UNIVERSITY OF SÃO PAULO
POLYTECHNIC SCHOOL

ADSON AGRICO DE PAULA

The airfoil thickness effects on wavy leading edge phenomena at low Reynolds number regime

São Paulo
2016

ADSON AGRICO DE PAULA

The airfoil thickness effects on wavy leading edge phenomena at low Reynolds number regime

Thesis submitted to the Polytechnic School of the University of São Paulo in partial fulfillment of the requirement for the Degree of Doctor of Science in Mechanical Engineering

São Paulo
2016

ADSON AGRICO DE PAULA

The airfoil thickness effects on wavy leading edge phenomena at low Reynolds number regime

Thesis submitted to the Polytechnic School of the University of São Paulo in partial fulfillment of the requirement for the Degree of Doctor of Science in Mechanical Engineering

Area of concentration:
Mechanical Engineering of Energy and Fluids

Advisor:
Prof. Dr. Julio Romano Meneghini

São Paulo
2016

Este exemplar foi revisado e alterado em relação à versão original, sob responsabilidade única do autor e com a anuência de seu orientador.

São Paulo, 02 de setembro de 2016.

Assinatura do autor _____

Assinatura do orientador _____

Catalogação-na-publicação

Agrico de Paula, Adson
The airfoil thickness effects on wavy leading edge phenomena at low Reynolds number regime / A. Agrico de Paula. -- ed.rev. -- São Paulo, 2016.
342 p.

Tese (Doutorado) - Escola Politécnica da Universidade de São Paulo. Departamento de Engenharia Mecânica.

1.Aerodinâmica 2.Aeronaves (Projeto e Construção) 3.Túneis de vento (Simulação numérica) 4.Escoamento (Controle) I.Universidade de São Paulo. Escola Politécnica. Departamento de Engenharia Mecânica II.t.

This thesis is dedicated to the memories of my mother, Mary Helena Agrico, and of the aerodynamicist and friend Rene Landman.

ACKNOWLEDGEMENT

Although the knowledge construction has a basis in the cognitive exercise of reason, affection brings to knowledge the possibility of something greater than simply a small step towards unveiling the unknown. It was thus with the French Revolution, thus with the cultural revolution of the Bossa Nova and shall always be.

Affection transforms knowledge and creation into something much greater than the measure of its metaphysics. In this sense, in these acknowledgements, I refer to the affection during this work to be able to show the magnitude of its importance in the construction of knowledge and reinvention of man.

First of all, I would like to thank my advisor that in 1999 opened the doors of the Polytechnic School of the University of São Paulo to me. Although, at the time, working in the aeronautical industry, in the field that I have affinity (aerodynamics), I endeavored to develop an academic accomplishment beyond the daily practice of engineering problems. In this condition Prof. Dr. Julio Meneghini received me at Polytechnic School and guided me in this career. Ever since then, this friendly atmosphere and desire of great accomplishments for science made me walk through academics, particularly in the environment of the Laboratory of Dynamic and Fluids (NDF). Besides this, I also thank all help (and support) during the phases of this research, whether in orientations of technical nature or even in support in materials and equipment, which made viable the finalization of this work. Also, I give special thanks to my advisor for his initial support on the theme of this work.

While I am at it, I would like to give thanks to all my laboratory colleagues, Reinaldo, Roque, Gustavo, João, Mariana, Fernanda, Cesar, Franzini, Provasi, Gioria, Stergios, Bonatto, Neomoto, Fabiano, Alfredo, Bruno, Ivan and Iago for the years of pleasant, harmonious conviviality, mutual co-operation and wonderful discussions. Also, I would like to thank our most lovable secretary Lucia, that always treated us in a sweet way, like a mother. I must remember to give thanks to the former laboratory secretary, Ivone that was always helpful and polite. Also I thank Prof. Gustavo Assi for supporting in the initial development of the Doctorate.

Technical problems lead me to conduct the experimental tests at the Technology Institute of Aeronautics and it was not different there from the Polytechnic School, in the sense that affection constructing knowledge. The difficulties of building the aerodynamic models to be tested were overcome by the support of the Aerodynamic Laboratory Technical Team through lots of professionalism and companionship. Likewise, I would like to immensely thank Devanildo, Rondinele, Wilson and Diego, also, the chief laboratory engineer Guedes. I also would like to thank the master student Bruno Massucato for his support during all the research on design and execution of the airfoil parts utilizing the rapid prototyping machine. Without the technical laboratory support, designer and executor of the models, the realization of this

work would not have been possible. I thank Prof. Aníbal and Cícero and technician Ana Pagotti of the Federal University of ABC for the support in prototyping during the first part of the wind tunnel tests. I also thank the technical team of the IAE (Space and Aeronautical Institute) for supporting in material regarding oil flow visualization. Thanks to Colleague Cavanha, who contributed to this thesis, of making the writing in the English language clear.

I would like to thank Prof. Gil Annes for providing a rapid prototyping machine, which made the realization of this thesis in adequate time. Also for your review in some texts. Special thanks to Prof. Roberto Girardi and Prof. Vitor Kleine for contributing immensely to making this work become clearer in the eyes of science. Between these pages hides long discussions in the hallways of the Aeronautical Engineering Division at ITA and thank you all for providing those moments. I thank my friend Pisani for providing moments of relaxing during this period. Thanks to my brother Alexandre, natural brother, and my other brothers "of being in the world" Ghandi, Ribeiro, Waldecy and Gaga for such great affection by supporting me in this most difficult journey. I thank my girlfriend Carolina for her patience and support during last year.

Last but not least in importance, I thank the great teachers that guided me through education, in the construction of the man I now am. I thank my mother and first teacher Mary Helena Agrico for teaching me the persistence, my teacher Manoelina Cabetti for teaching me sweetness and my teacher Silvio Marcondes for teaching me to be free to create a new world.

"*All human knowledge begins with intuitions, then goes to concepts, and is completed in ideas*"

Immanuel Kant (1724-1804)

RESUMO

Recentemente, aerofólios com bordo de ataque ondulados, inspirados na nadadeira da baleia jubarte, tem sido investigados como mecanismo de controle de escoamento para baixo número de Reynolds com a finalidade de se aumentar o desempenho aerodinâmico neste específico regime de escoamento.

O objetivo geral deste trabalho é investigar os efeitos geométricos do aerofólio nos fenômenos do bordo de ataque ondulado na condição de baixo número de Reynolds. Investigações experimentais foram realizadas correlacionando medições de forças com visualizações de lã e óleo a fim de compreender os efeitos da espessura do aerofólio sobre os fenômenos de bordo de ataque ondulado. Três conjuntos de espessura de aerofólios foram testados (NACA 0012, NACA 0020 e NACA 0030) na faixa de número de Reynolds entre 50,000 e 290,000, onde cada conjunto tem um aerofólio liso e três ondulados ($A = 0.11c$, $\lambda = 0.40c$; $A = 0.03c$, $\lambda = 0.40c$ e $A = 0.03c$, $0.11c$ $\lambda = 0.11c$).

O dados experimentais mostram importantes resultados que não foram possíveis em estudos anteriores devido às investigações serem restritas à geometria ou/e condição de escoamento específicas. O resultados de medida de força mostram que a diminuição da espessura do aerofólio conduz às características de separação de escoamento de bordo de ataque que causam menor deterioração aerodinâmica nos aerofólios ondulados finos quando comparados aos lisos no regime de pré-stall. Além disso, os resultados mostram um desempenho destacado do bordo de ataque ondulado para condição de menor número de Reynolds. Em quaisquer espessuras de aerofólio, os bordos ondulados apresentam valores de sustentação máxima maiores quando comparado aos aerofólios lisos mostrando assim resultado inédito na literatura para modelos ondulados bi-dimensionais.

As visualizações de óleo evidenciaram dois mecanismos de controle de escoamento desencadeadas pelo escoamento secundário: bolhas de separação laminar tridimensionais e estruturas vorticais. Os resultados confirmam alguns poucos estudos experimentais e numéricos anteriores relacionadas com bolhas tridimensionais, e apresenta pela primeira vez estas estruturas como um mecanismo muito eficiente de controle de escoamento em regime de pós-stall justificando o aumento de máxima sustentação para o menor número de Reynolds.

Adicionalmente, foram identificadas duas estruturas de bolhas tridimensionais nomeados aqui como "bolhas com pontas" e "bolhas alongadas" que causam distintos efeitos no regime de pré-stall.

Esta tese apresenta como resultado maior desempenho para aerofólios ondulados com menor espessura (NACA 0012) e/ou para condições de menor número de Reynolds (Re=50,000)mostrando claramente que estas características levam as ondulações a operarem em condições de stall de bordo de ataque assim tendo um desempenho superior. Portanto, um espaço de projeto para tubérculos conduz às características de stall de bordo de ataque confirmando a suposição de Stanway (2008) oitos anos antes.

Palavras-chave: *Aerodinâmica. Aeronaves (Projeto e Construção). Túneis de vento (Simulação numérica). Escoamento (Controle)*

ABSTRACT

Recently, the wavy leading edge airfoils, inspired by the humpback whale´s flipper, have been investigated, as flow control mechanisms, at low Reynolds numbers in order to improve aerodynamic performance in this particular flow regime.

The overall aim of this work is to investigate the airfoil geometric effects on wavy leading edge phenomena in the low Reynolds number regime. Experimental investigations were carried out correlating force measurements with mini-tuft and oil visualizations in order to understand the airfoil thickness effects on wavy leading edge phenomena. Three sets of airfoil thickness were tested (NACA 0012, NACA 0020 and NACA 0030), each set consisting of smooth plus three wavy configurations (A=0.11c, λ=0.40c; A=0.03c, λ=0.40c and A=0.03c, λ=0.11c); Reynolds number was varied between 50,000 and 290,000.

The results present many findings that were not possible in previous studies due the fact that these investigations were constrained to specific geometries and/or flow conditions. At higher Reynolds number, the decrease in airfoil thickness leads the airfoils to leading edge stall characteristics causing the lowest aerodynamic deterioration for the thinnest wavy airfoil as compared to smooth configuration in the pre-stall regime. In addition, the results show impressive tubercle performance in the lowest Reynolds number. For any tubercle geometry and airfoil thickness, the wavy leading edge airfoils present higher maximum lift values as compared to smooth configurations showing an unprecedented increase in performance for a full-span model tested in the literature.

The flow visualizations present two flow mechanisms triggered by secondary flow: three-dimensional laminar separation bubbles and vortical structures. Regarding three-dimensional laminar bubbles, the results confirm some of the few previous experimental and numerical studies, and presents for the first time these structures as a very efficient flow control mechanism in the post-stall regime justifying the impressive increase in maximum lift in the lowest Reynolds number. Besides that, two characteristics of laminar bubbles, "tipped-bubbles" and "elongated-bubbles", are identified with different effects in the pre-stall regime.

This thesis presents higher tubercle performance for thinner airfoils (NACA 0012) and/or lower Reynolds number conditions (Re=50,000) showing clearly that an optimum

performance lead the “tubercles” to operate under conditions of leading edge flow separation conditions. Therefore, a design space for tubercles conducted to leading edge stall characteristics confirming the hypothesis of Stanway (2008) eight years before.

Palavras-chave: *Aerodynamics. Aircraft (Design and build). Wind tunnels (Numerical simulation). Flow (Control)*

LIST OF FIGURES

LIST OF TABLES

LIST OF ABBREVIATIONS

AOA	Angle of Attack
APG	Adverse Pressure Gradient
AR	Aspect ratio
BLSB	Two-Dimensional Laminar Separation Bubble
CVP	Counter-rotating Vortex Pair
DLR	Deutsches Zentrum für Luft- und Raumfahrt
FFS	Full Flow Separation
FFSL	Full Flow Separation Line
ITA	Technological Institute of Aeronautics
LE	Leading Edge
LSB	Laminar Separation Bubble
M.A.C	Mean Aerodynamic Chord
MAV	Micro aerial vehicle
NACA	National Advisory Committee for Aeronautics
NASA	National Aeronautics and Space Administration
PLA	Polylactic acid
PIV	Particle Image Velocimetry
RMS	Root mean square
TEFS	Trailing Edge Flow Separation
TLSB	Three-dimensional Laminar Separation Bubble
UAV	Unmanned aerial vehicle
VG	Vortex generator

LIST OF SYMBOLS

A or L	Wavy leading edge amplitude
α	Angle of attack
α_{stall}	Stall angle
c	Chord of the airfoil
C_L	Lift coefficient
C_{LMAX}	Maximum lift coefficient
CD	Drag coefficient
C_{d0}	Drag coefficient at zero lift
C_M	Pitching moment coefficient
c_p	Pressure coefficient
ΔC_{LMAX}	Decrease or increase in C_{LMAX} caused by tubercles
ΔC_{d0}	Decrease or increase in C_{d0} caused by tubercles
$\Delta\alpha_{stall}$	Decrease or increase in α_{stall} caused by tubercles
L_B	Laminar bubble length
$\frac{L}{D}$	Aerodynamic efficiency
λ	Wavy leading edge wavelength
R_e	Reynolds number based on chord of the airfoil
X_S	Flow separation point
Γ_B	Bubble circulation distribution
Γ_S	Secondary flow circulation distribution
Γ_E	Trailing edge circulation distribution
U_∞	Freestream velocity
u_p	Peak velocity
u_t	Trough velocity
w_B	Bubble width

TABLE OF CONTENTS

1 INTRODUCTION

1.1 Flow control

Flow control devices caused significant changes in the aeronautical design and, as a consequence, in the aircraft performance of the last century. In this scenario, the flow control can be understood as any mechanism strategy or process through which the natural flow behaviour changes in order to reach design requirements. A good example of the flow control relevancy, from a technological point of view, is the application of the high lift devices in the early 1920s in order to reach design requirements. The aircraft design presumes a required increase of maximum take-off weight leading to an increased wing area, large enough to provide sufficient lift at takeoff and landing. On the other hand, cruise speed requirement is based on the idea of having less wing area, as long as the speed is high enough to provide the required lift. Therefore, a flow control mechanism using high lift devices relieved the problem of contradictory requirements by allowing wing area sized for cruise conditions, at the same time the system holds for takeoff and landing conditions (figure 1.1).

Figure 1.1: Modern high lift devices deployed during the landing of the aircraft Airbus 380. Reproduced from http://www.airliners.net/photo/Airbus/Airbus-A380-841/1062608/L/.

Gad-el-Hak (1996) generically describes how the flow changes due to flow control. The flow control mechanisms act by changing flow characteristics either by delay or by advancement of transition, prevention or provocation of flow separation and suppression or enhancement of the turbulence. These variations on flow promote, for example, drag reduction, lift effectiveness and noise suppression schematically represented in figure 1.2.

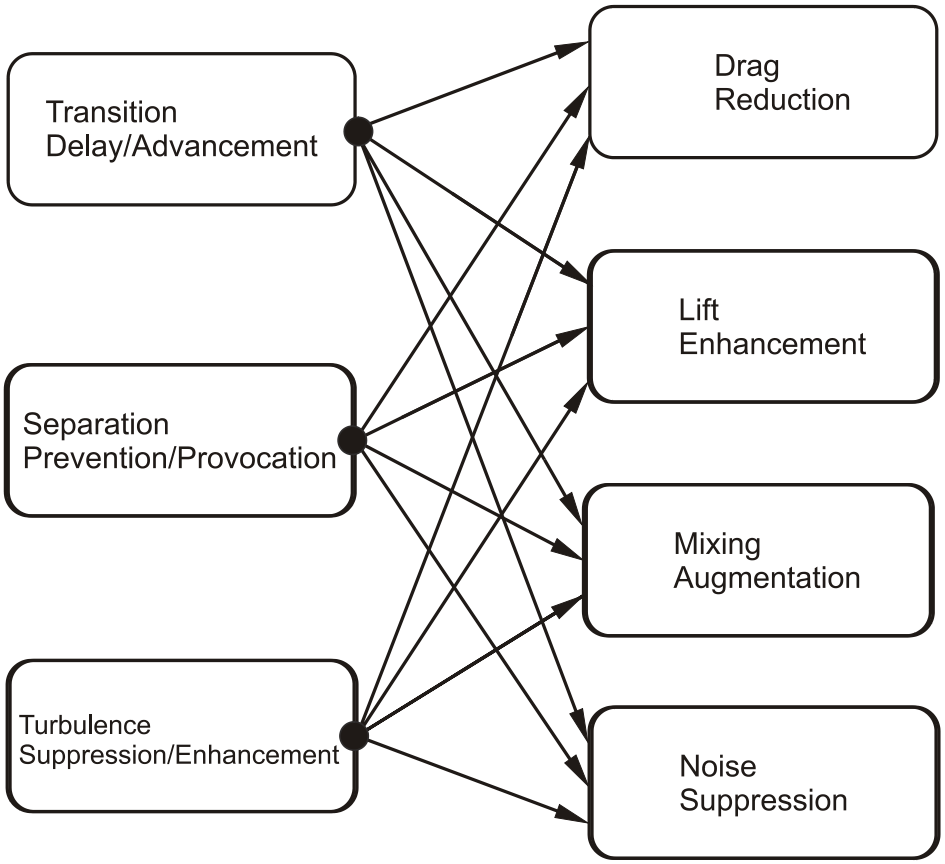

Figure 1.2: Changes on nature flow caused by flow control mechanisms and their benefits (GAD-EL-HAK, 1996).

Some changes on flow can cause simultaneous benefits. The flow control mechanism delaying the laminar-turbulent transition keeps the boundary layer laminar over an airfoil upper surface decreasing the skin friction drag and noise emission. On the other hand, some effects caused by flow control mechanisms can enhance some performance at same time decreasing others. The advancement in laminar-turbulent transition delays the flow separation condition increasing the maximum lift as consequence decreasing take-off and approach field

length. In contrast, increases in the skin friction drag compromises cruise performance. Figure 1.3 presents schematically different flow control goals and their interrelations.

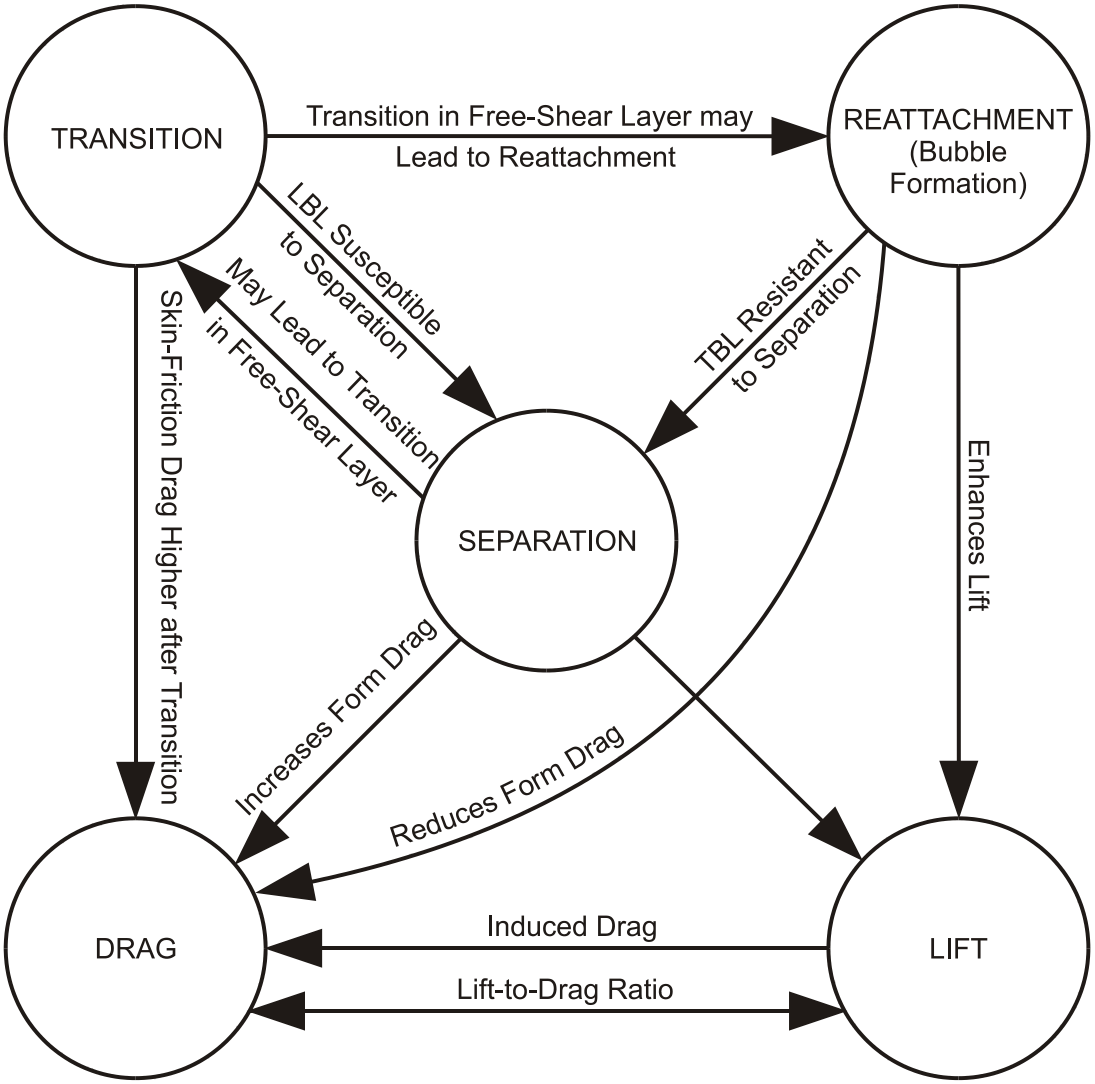

Figure 1.3: Interrelations among flow control goals (GAD-EL-HAK, 2000).

1.1.1 Historical Background

In order to understand the development of the research in flow control and its application, Gad-el-Hak (1996) splits into five distinct eras the knowledge in flow control: The empirical era (prior to 1900), the scientific era (1900-1940), the Word War II era (1940-1970), the energy crisis era (1970-1990), and the 1990s and beyond.

The empirical era can be understood as a quite productive period in which performance enhancements could be reached by changes in geometry even without a clear understanding of the lift, drag, and flow separation mechanisms. The earliest flow control mechanics could be spears, sickle-shape boomerangs, and fin-stabilized arrows developed empirically by archaic Homo sapiens as mentioned by Gad-el-Hak (1996).

Although during the 18^{th} century there occurred a clear improvement in the understanding of the flow physics provided by ideal flow theory connecting pressure, kinetic energy, and potential energy in moving streams of fluid, still the viscous effect from real fluids that leads to flow separation was not known, thus causing a lack of understanding in flow control phenomena. Continuing applying the empirical approach in this period in order to develop flow control mechanisms, the history of the golf ball appears as a good example. In the early 1800s, golfers realize that balls with roughened or scuffed surfaces flew farther than smooth balls. Robert Adams, in 1880, without understanding the flow control mechanisms that provided improvement in range for rough balls introduces roughness patterns in golf balls.

At the end of empirical era, the research in aeronautical engineering was growing, by applying an empirical approach in the investigations accompanied by theoretic calculations based on the ideal fluid theory. The calculations presented discrepancies with experimental results so that engineers and inventors at that time could not explain. However, the focus of flow control for early aeronautical engineers was the practical flight control solutions (JOSLIN; MILLER, 2009). In this context, the Wright brothers are first to understand the problem of adverse yaw created by asymmetric lift on wings in turn maneuver, and as consequence they added vertical stabilizer to compensate the adverse yaw (MACFARLAND, 2001).

Gad-el-Hak (1996) says that the science of flow control starts with Prandtl in 1904 introducing the boundary layer theory so explaining the physics of the separation phenomena and describing several experimental in which the boundary layer was controlled. Therefore, the flow control development entered an era where the physical understanding of the flow mechanisms leads to optimum engineering solution, in order to control the boundary layer.

As previously mentioned, in the beginning of the 1900s aeronautical engineering pursued aircraft´s controllability by flow control development. In 1908, ailerons were developed in order to perform turn maneuvers (ANDERSON, 1997). In 1914, as consequence

of the aileron development, it was realized that deflections downward caused in the aircraft´s pair of ailerons generate increase in lift (ANDERSON, 1997). Thus, the flow control mechanism as high lift device concept is applied establishing the first flap device. Later on, more sophisticated flaps were developed: Plain flap (1916), Split flap (1920), Slotted flap (1920) and Fowler flap (1924).

After the end of the First World War, the aircraft increase in size during 1920s. As a result, designers concern in increase the wing loading and keep appropriate take-off and approach field length requirements. The way to increase wing loading was to improve the aerodynamic efficiency under landing and take-off conditions. Therefore, in this period, active flow control mechanisms regarding high lift devices were tested, in order to increase the aerodynamic performance at take-off and landing conditions.

In the early 1920s, active flow mechanisms were tested, where air jets flow through slotted flaps reach the wing leading edge working as flow control mechanism designed to enhance lift (ANDERSON, 1997). In the late 1920s, suction control tests are performed in order to reattach the boundary layer under critical flight conditions (JOSLIN; MILLER, 2009). In the late 1930s, Jacob (1939) develops the early study in laminar-flow airfoil in order to decrease skin friction drag by keeping laminar flow over large areas of the airfoil upper surface.

The beginning of the Second World War motivated a large improvement in technology, mainly in aeronautical engineering. The key aeronautical technologies for air combat success promoted faster and highly maneuverable aircraft, besides operational requirements of an efficient aircraft in terms of cruise, take-off and landing. Thus, the design requirements established at the outbreak of World War II conducted the airfoil to have characteristics of higher wing loading, thinner profiles and smaller planform areas (HANSEN, 2012).

The development of laminar-flow airfoils comes from 1930s, and continued throughout the years of World War II and several thereafter. Over one hundred different airfoils were derived in the interest of reaching laminar conditions and so higher velocities (LOFTIN, 1985).

During the 1950s and 60s, the development of the fighter aircraft conducted the design towards smaller wings in pursuance of reducing drag at high speeds. Thus, the continue

interest in increasing wing loading keeps the development of high lift devices. In this context, in the late 1950s, a flap blowing system was developed called Boundary Layer Control System (BLCS). Internally-blown flaps bled air from jet engine compressor and blown over the back surface of the wing in order to keep the flow attached (figure 4.1). In addition, the continuing development in high lift devices leads to simplified systems with similar performance blowing gas from engine exhaust over the airfoil surface (externally-blown flaps).

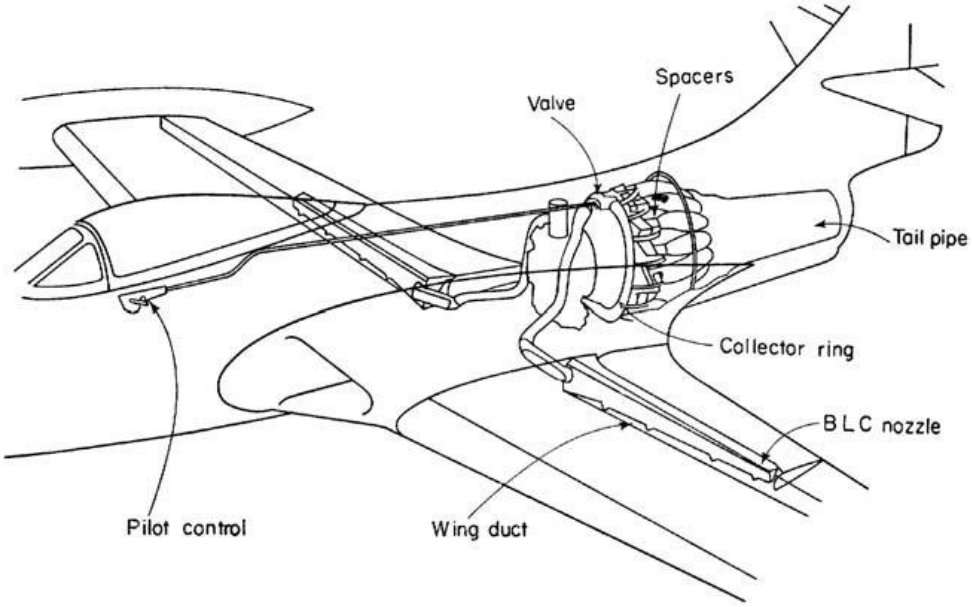

Figure 1.4: Schematic drawing of the plumbing system to control the blown flaps on the aircraft Grumman F9F-4 (ATTINELO, 1961).

The World War II era also presents some other important developments in flow control: suppression of instability modes by suction and heating/cooling, polymer drag-reduction, vortex generator, acoustic excitation, helical strakes and bluff-body splitter plates (HANSEN, 2012).

During the energy crisis era, the government institutions and industry led many researches in saving energy. Thus, the studies in drag reduction for commercial aircraft, land vehicles, pipelines and other devices were emphasized (GAD-EL-HAK, 1996). In addition, the advances in computational simulation helped to understand complex flow mechanisms proposing innovative flow control solutions.

Transition-delaying compliant coatings, Large-eddy breakup devices (LEBUs) and riblets are examples of flow control mechanisms that reduce skin-friction drag in turbulent layers in the era of saving energy and numerical approach (GAD-EL-HAK, 1996). The 1990s and beyond era starts few years before, in the mid1980s, changing the flow control strategies from controlling the time-averaged state to controlling flow instabilities by active control methods (JOSLIN; MILLER, 2009). A large number of active flow control methods were developed and applied in both open-loop and closed-loop configurations (HANSEN, 2012). Recently, sophisticated actuators are capable of controlling the flow at the stability timescale manipulating coherent structures present in transitional and turbulent shear flows (CANTWELL, 1981; ROBINSON, 1991).

1.1.2 Active and passive flow control devices

The wavy leading edge as a flow control device is based on the energy expenditure principle as a strategy to modify the overall fluid dynamic behaviour of the flow over a surface. In order to contextualize the research of the wavy leading edge as flow control mechanism, flow control devices will be classified based on the energy expenditure by the mechanism. A passive flow control mechanism does not need an auxiliary expenditure. On the other hand, active flow control devices require addition energy in order to change the flow characteristics.

Active flow control mechanisms present many advantages as compared to passive mechanisms. Generally speaking, flow control devices can act precisely in different flow conditions, and so reaching optimum performance for aircraft in entire flight envelope for example. In addition, as it was previously mentioned, they are capable of controlling the flow at the hydrodynamic stability level. Although active flow control mechanisms present high performance, the complexity of the devices still represent a technological challenge.

In contrast, the passive flow control mechanisms manipulates the flow characteristics to get benefits in terms of aerodynamic performance changing the geometry of the airfoil or adding fixed elements to airfoil surface, mainly related to energy expenditure principle. Thus, the technological simplicity in terms of physical mechanism brings reliability and low cost to implement passive devices as a success design. Because of these characteristics, even in

modern flow control research, many researchers dedicate investigations in passive flow control mechanisms.

1.1.3 Benefits of flow control on aeronautical design

Since the control of lift, drag and aerodynamic efficiency are the main aim in the aeronautical engineering, the understanding of the typical flow control mechanisms to "lift enhancement" or "drag reduction" is essential to realize the possible benefits of the wavy leading edge airfoils as flow control in aeronautical engineering. In the next paragraphs, it will be discussed the benefits of the passive flow control mechanism since this work regards passive devices.

1.1.3.1 Lift enhancement

Flow control devices present four important flow mechanisms in order to enhance lift: Pressure gradient design, Circulation augmentation, Momentum exchange and Restrictions of spanwise flow (HANSEN, 2012). Pressure gradient design is based on the improvement of the airfoil suction surface shape to avoid full flow separation. An optimum pressure profile near the leading edge increases maximum lift at higher angle of attack presenting benefits for take-off and landing performance. A straightforward approach is for example the design of a smooth leading edge shape keeping a high curvature radius in this region.

Another approach to increase lift can be an external free jet acting to energize the boundary layer over an airfoil upper surface, thus keeping attacked flow and establishing circulation augmentation. As discussed previously, the internally-blown flaps and externally-blown flaps are flow control devices based on this mechanism. Also the slat itself is a way to energize the boundary layer to delay separation. No external energy is added, only flow momentum changes through a slotted leading edge that provides a local flow velocity increase delaying boundary layer separation.

The momentum exchange mechanism at boundary layer of the airfoil suction surface is broadly used as flow control device in order to improve maximum lift values in aircraft

design. Basically, there are two flow mechanisms that exchange momentum inside boundary layer. The first one, already exemplified, is related to laminar-turbulence transition, it involves an increase of local flow momentum, which delays flow separation, as far as the local Reynolds number increases. Any geometry mounted over airfoil surface can cause an early laminar-turbulent transition. After transition, the flow becomes turbulent and so the turbulent mechanism exchange momentum between layers close and far from airfoil wall. It is used some small elements or sometimes physical tracks on spanwise direction at leading edge to cause flow transition.

Another approach is based on the placement of discontinued geometries over airfoil surface so as to induce vortex generation, by causing moment exchange between fluid layers. There are distinct geometries added to aerodynamic surfaces in order to generate vortices and improve maximum lift values. A classical device is the vortex generator, with a small rectangular or delta-shaped element. The figure 1.5 shows a schematic drawing of the vortex generators and their flow control mechanism.

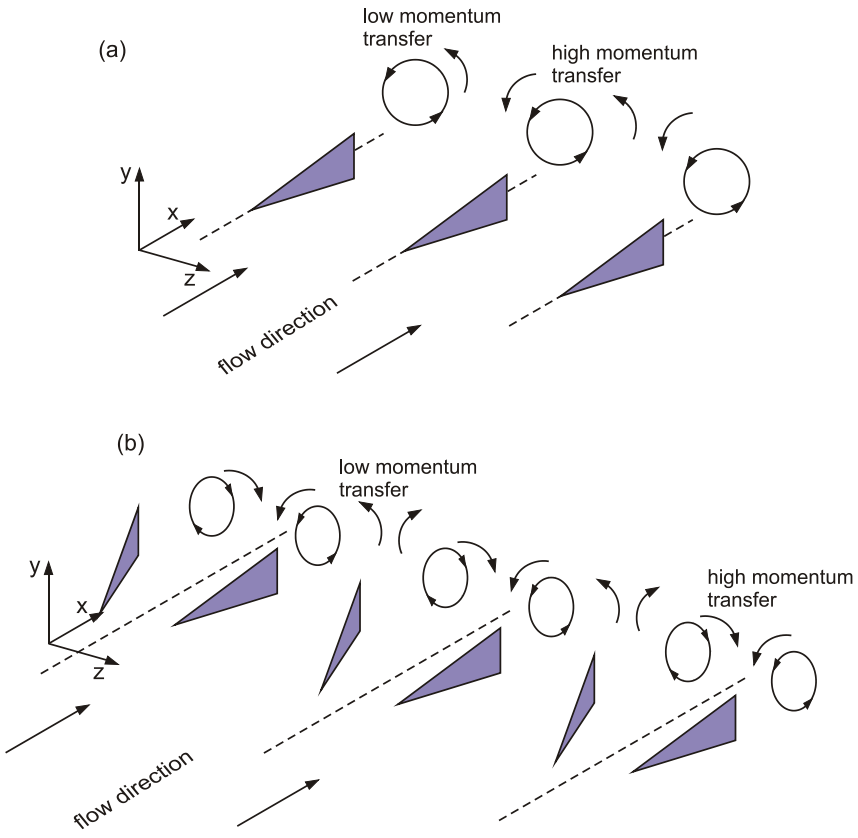

Figure 1.5: Vortex generators and their exchange moment flow mechanism. Adapted from Godard and Stanislas (2006).

The vortex generators are applied in aircraft usually after the first flight when the flight performance results do not fulfill the established requirements such as maximum lift for full flap deployment or control surface efficiency. Therefore, in order to fix unexpected problems in the end of an aircraft design process, the vortex generators are placed normally at forward position over upper surface or near control surface leading edge keeping the flow attached in critical flow conditions. Besides that, strakes over aircraft nacelle and small serration over the airfoil pressure surface are applied also in aircraft to get aerodynamic performance improvement with similar flow control mechanism.

The revolutionary new jet propulsion systems that had their beginnings in the 1940s require a new aerodynamic shape for wings to reach feasibility performance. Thus, the swept wing comes up as the new aerodynamic of wing for the jet era in order to minimize the wave drag. However, the new transonic-supersonic aircraft keep spanwise flow over the wing causing some penalties on flight quality.

The spanwise flow over the wing causes an increase in aerodynamic loads at span positions near wing tip, and, as consequence, early stall condition occur in this region. The stall onset at wing tip for sweep wings is the root of undesirable flight characteristics of the high speed configuration.

The early stall at wing tip causes asymmetric stall behaviour with roll tendency coupling with low aileron effectiveness caused by flow separation established in the wing tip area. These characteristics promote unsafely flight conditions. In addition, the onset stall at wing tip moves the wing pressure center forward, thus causing the undesirable pitch-up stall characteristics.

Therefore, flow control mechanisms that cause a barrier on wing span flow appeared as an aerodynamic need of the jet era. A classical mechanism is the wing fences that consist of a flat plate fixed perpendicular to airfoil upper surface skirting the leading edge and avoiding the span flow at wing tip region. Furthermore, vortex generator, sawtooth and notched leading edge appears as flow mechanisms that establish physical barrier to span flow and generate streamwise vortices avoiding flow separation. The figure 1.6 presents the distinct flow control mechanisms that establish a barrier for span flow over the wing avoiding flow separation at wing tip regions.

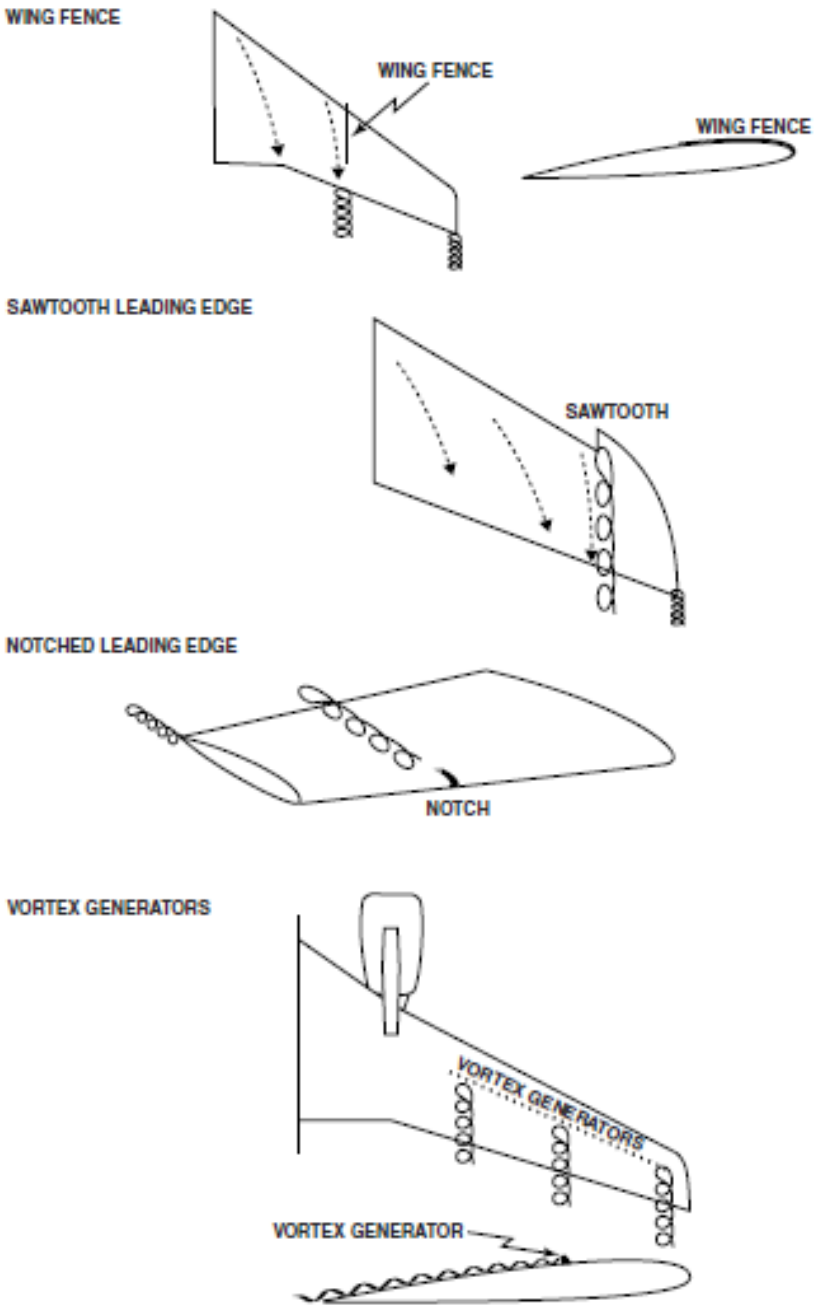

Figure 1.6: Spanwise flow attenuation devices (SWATTON, 2010).

1.1.3.2 Drag reduction

In terms of drag reduction, the flow control devices act in order to delay laminar-turbulent transition or attenuate turbulent fluctuations (HANSEN, 2012). The delay of the

laminar-turbulent transition over aerodynamic surfaces decreases areas with turbulent flow. This, in turn lowers skin friction drag causing large benefits for aircraft at cruise condition.

The embrionary studies in order to delay laminar-turbulent transition, as it was mentioned before, were motivated by researches that pursued higher speeds in aircraft in the late 1930s. Researchers developed many airfoils in order to minimize the adverse pressure gradient over suction surfaces so as to delay transition. Unfortunately, the researches only achieved partial success at that time, because some unstable atmospheric conditions can anticipate transition of the laminar airfoil designed. Currently, the computational capacity drives many projects to reach the design of laminar wings at transonic and supersonic conditions such as the projects LamAiR (Transonic) from DLR and F-16XL-2 (Supersonic) from NASA.

A sophisticated passive flow control mechanism in order to delay flow transition is the passive compliant coating. These coatings can suppress some instability mode such as Tollmien-Schlichting instabilities and traveling-wave flutter, so they delay transition and reduce skin friction drag (GAD-EL-HAK, 2000).

There are some flow control mechanisms that can attenuate the turbulent fluctuations physically avoiding fluctuating turbulent crossflow (riblets) or by shedding vortices canceling natural vorticity of the flow (Large-eddy break-up). In both cases the mechanisms conduct to drag reduction (HANSEN, 2012).

After describing briefly some characteristics of the flow control mechanisms, in the next subsection, the inspiration for this work and the general characteristics of the wavy leading edge as flow control mechanism will be discussed.

1.2 Wavy leading edge as flow control mechanism

This section discusses the current importance of the biomimetic research contextualizing with the aim of the present thesis. After that, the hydrodynamic characteristics of the humpback whales are described highlighting the flow control mechanism of the tubercles found in their pectoral flippers, so as to justify the wavy leading edges have potential benefits in engineered

systems as flow control device. Finally, some current and potential applications of the wavy leading edge are presented.

1.2.1 The flow control and the biomimetic of the marine mammals

The interest in biomimetic research is growing recently. In this kind of studies, engineers and researchers pay attention to nature's proven adaptation to specific environments so inspiring engineering solutions. The aim of the biomimetic research is to find inspiration in the biological environment, in order to emulate living organism performance in engineered system mainly in cases where organism's performance exceeds current mechanical technology (FISHER, 2009) (figure 1.7).

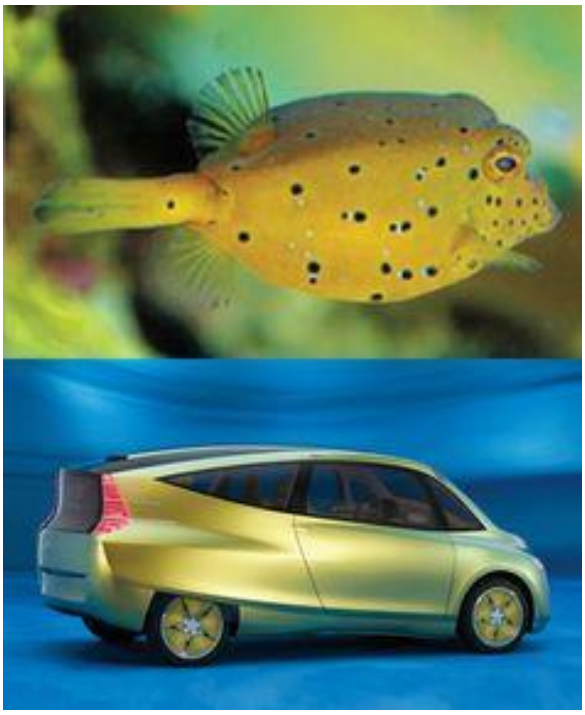

Figure 1.7: Biological methods applied in engineered systems. Reproduced from https://www.pinterest.com/hzonis/biomimetic/.

This work is related to biomimetic research where the investigation of the wavy leading edge phenomena comes from leading edge tubercles found on the humpback whales' pectoral flipper. Thus, in this context, it is important to understand some characteristics from aquatic environment as well as the humpback whale as a unique mammal.

The capability to control the fluid around the body establishes the marine mammal performance in the aquatic environment. The passive flow control mechanisms make the main role on morphological specializations of marine mammals that comes from natural selection. Besides the design of the marine mammal´s body shapes, some morphologic characteristics over bodies provide hydrodynamic advantages regarding drag, lift, thrust, and stall (FISH et al., 2008).

The dynamic characteristics of the marine mammals are established by laws of momentum, energy, and mass conservation establishing the energy demanding to live in the aquatic environment. The energy losses associated to movement through water determine the performance of the animal (speed, acceleration and manoeuvrability). Therefore, the flow control functionality in marine mammals determines the animal's survival and is potentially susceptible to strong evolutionary selection pressures (DANIEL; WEBB, 1987).

In this sense, the evolution of aquatic habits in marine mammals required, as a consequence, the evolution of adaptations that permitted these animals to optimize energy use with the decrease in resistive forces and the increase in propulsive force production and hydrodynamic efficiency (FISH, 1996; WILLIAMS, 1999).

Considering that the key to hydrodynamic improvements in marine mammals have been the flow control mechanisms, the morphological adaptations for flow control in these animals have technological application through the biomimetic approach (ANDERSON; BNADYOPADHYAY, 2004; KERREBROK, 2002; TAUBES, 2000; FISH, 2006; TRIANTAFYLLOU; TRIANTAFYLLOU, 1995).

1.2.2 Hydrodynamic characteristics of the unique marine mammal humpback whale

Although the blue whale, Balaenoptera musculus, is considered the greatest animal ever to have lived on the earth, the humpapback whale, Megaptera novaeangliae, has the largest pectoral flippers of any cetacean (TRUE, 1983). This is, probably, the reason why its latin name, Megaptera novaeangilae, means "giant wings of new England". In addition, humpback whale flipper´s shape is long, narrow, and thin (TRUE, 1983). However, the "giant" humpback whale flipper is also peculiar because of existence of great protuberances

or tubercles established at leading edge surface giving a scalloped appearance to this region (WINN; REICHLEY, 1985) (figure 1.8).

The spectacular length of the pectoral flippers of 28% of the whale total length has been speculated to provide many benefits to the humpback whale (FISH; BATTLE, 1995). One of these benefits is increase manoeuvrability (EDEL; WINN, 1978; JURASZ; JURASZ, 1979) that as consequence became the humpback whale the most “acrobatic” of baleen whales (EDLE; WINN, 1978; HOWELL, 1930; LEATHERWOOD et al., 1988; REICHLEY, 1985; TOMILIN, 1957; WINN).

Figure 1.8: A humpback whale breaches, with the Virginia Beach oceanfront in the background and the details of its pectoral flipper. The prominent tubercles sit on the flipper leading edge. Reproduced from http://pilotonline.com/news/photo-gallery-whale-sightings-spike-off-va-beach/article_1569b26a-871a-5c6f-ac83-885783e32f78.html.

The manoeuvrability characteristics of the humpback whale´s pectoral flipper indicate morphology for high hydrodynamic performance. Fisher and Battle (1995) were interested in this particular morphology in order to understand the hydrodynamic design of the humpback

whale flipper comparing with aerodynamics and hydrodynamic design of engineering systems.

The lift, drag and hydrodynamic efficiency (L/D) characteristics drive the humpback whale to remarkable manoeuvrability. The hydrodynamic characteristics are reached due to an appropriated morphology of the cross-section and planform of the pectoral flippers.

The symmetrical cross-section has characteristics of the streamlined airfoils decreasing drag. The mid-span sections are similar in design to the NACA 63_4-021 airfoil (ABBOT; VON DOENHOLFF, 1949). These cross-section characteristics decrease profile drag by reduction of the pressure gradient established by flow around the section (BLAKE, 1983; VOGEL, 1981; WEBB, 1975).

The favorable pressure distribution decreases the adverse pressure gradient delaying the stall condition and decreasing the pressure drag. Besides, a low adverse pressure gradient guarantees greater laminar flow areas over the flipper decreasing skin friction drag (FISH, 1995).

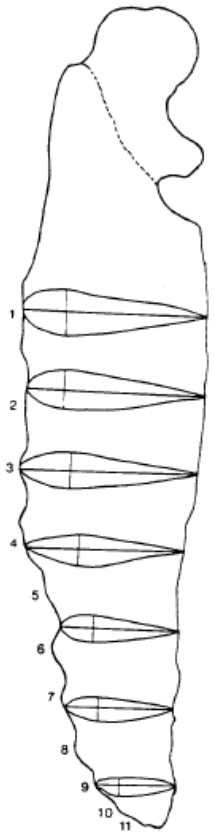

Figure 1.9: The planform of the humpback whale´s pectoral flipper and the tubercles positions (FISHER; BATTLE, 1995).

As in a desirable wing planform design for aeronautical engineering, the elliptical planform of the flipper establishes a uniform downwash and lift coefficient distribution along span minimizing the induced drag (HURT, 1965; VON MISES, 1945) (figure 1.9).

The maximum hydrodynamic efficiency is proportional to the square-root of the aspect ratio (LIGHTHILL, 1977). A flipper with higher aspect ratio causes a high-speed banking turn because of its hydrodynamic efficiency. A higher lift keeps a higher horizontal component of centripetal force keeping efficiently a turn.

Lift and bank angle are inversely related to turn radius (ALEXANDER, 1983; NORBERG, 1990). In addition, shorter wings can produce a quicker roll into a turn but produce less lift and thus a wider circle (Fisher; Battle, 1995). Therefore, the humpback whale flipper with aspect ratio of 6 and a span of 28% of the total length body justifies a greater manoeuvrability with high speed and low radius on turn.

Considering the swept shape of the pectoral flipper and the position and number of the tubercles (figure 1.9), the morphology at leading edge suggests a passive flow control mechanism originated from natural selection specialization.

The tubercles of the humpback whale flipper may function to generate vortices by unsteady excitation of flow to maintain lift and prevent stall at high angles of attack (WU et al., 1991). Fish and Battle (1995) said that the function of the tubercles may be analogous to strakes used in aircraft design where this device generates large vortices that exchange moment within the boundary layer having, as a consequence, the delaying of the stall. Thus, the flow control mechanism of the tubercles can be associated with the ability to perform fast turn maneuvers with small radius, since at higher angles of attack the humpback whales can maintain high lift values.

The high manoeuvrability of the humpback whales is particularly associated to perform some specific movements. Thus, the humpback whales are able to feed of plankton, euphausiidis, herring, and capelin (DOLPHIN, 1988; JURASZ; JURASZ, 1979; WINN; RICHLEY, 1985) performing varied feeding techniques. One of these feeding techniques is called “lunge feeding” where the whales swim at approximately 2.6 m/s toward their prey from below position to the water surface at angle of 30° to 90° (JURASZ; JURASZ, 1979).

The “inside loop” is another feeding technique where the whale swims away rapidly from the potential prey keeping its flippers abducted and protracted (EDEL; WINN, 1978)

then rolls 180° performing a sharp U-turn and lunges toward the prey (HAIN et al., 1982). The entire maneuver is performed approximately between 1.5 and 2.0 body lengths of the humpback whales.

Another feeding approach is known as the “bubbling” technique. This technique is the most popular feeding method of the humpback whales marveling millions of people in videos on internet. Air bubbles are exhaled by humpback whales while forming columns that concentrate the preys in a cylindrical region (WIN; REICHLEY, 1985). This bubble formation that involves the prey is called “bubble net”. The whales form the bubble nets swimming toward the surface and in a circular pattern (FISH; BATTLE, 1995). Therefore, the humpback whales performing smaller turning radius increases the density of preys due to a smaller volume of bubble net becoming more efficient the feeding technique.

Since lift and bank angle are inversely related to turn radius as it was previously said, small radius turns are reached with the increase in horizontal component of the lift vector by increase in bank angle or lift (figure 1.10).

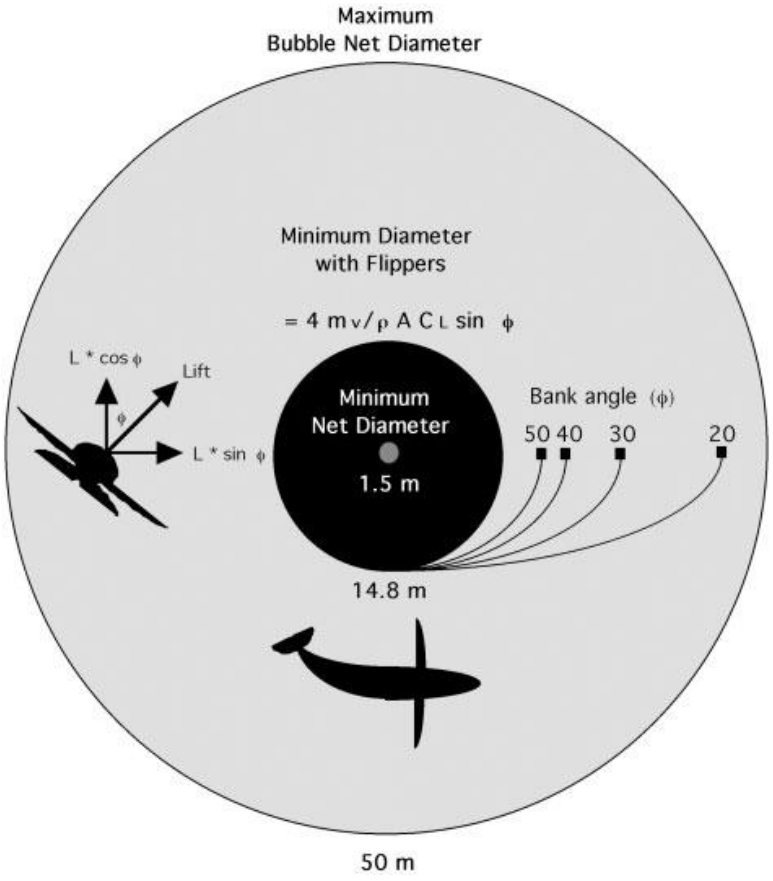

Figure 1.10: The centripetal force determines the turning radius that decrease by increase in bank angle and/or lift force (FISH et al., 2008).

The feeding requirement of the humpback whales establishes high values of lift in the bubbling technique maneuvers. In this sense, the tubercles have an essential role in increasing maximum lift supporting smaller turning radius so reaching high efficiency in feeding technique.

1.2.2.1 Current and potential applications for wavy leading edge as flow control mechanism

There are some current and potential applications in engineered systems related to flow control mechanism characteristics which are found in the tubercles of the humpback whale's flipper.

The benefits of the aerodynamic and hydrodynamic characteristics of the tubercle configuration in the post-stall regime are that it delays the stall condition and yields a soft stall behavior. In some cases, the tubercles increase the lift performance (HANSEN et al., 2009; JOHARI et al., 2007; MIKLOSOVIC et al., 2004; STANWAY, 2008). Therefore, it seems appropriated to mimic the humpback wale's pectoral flipper, in order to improve performance in control surface of the engineered systems, since control surfaces such as boat rudders, torpedo and missiles fins as well as rudder, ailerons, fins and tails of aircraft can take advantage in performance at their operational envelopes, by adding aerodynamic characteristics of the tubercles.

For instance, vertical tails, vertical fins and rudders are sized, in most cases, on the basis of a minimum speed at one engine inoperative that occur immediately after take-off. Thus, an increase in aerodynamic efficiency of control surfaces under this condition causes gains in take-off field length and/or decrease in weight with sizing of smaller surfaces.

Another example of application in control surface is related to aileron design in aircraft. The aileron surface control is susceptible to flow separation at swept wings due to the span flow along the wing that increases the aerodynamic loads at wing tip. Vortex generators near aileron leading edge are used currently in order to avoid this problem. Wavy leading edge at aileron potentially could cause benefits similar to vortex generators, while also decreasing weight and drag.

Weber et al. (2010) carried out investigations regarding tubercle effect on hydrodynamic performance at rudder with unswept leading edge and low aspect ratio. At high angle of attack, the protuberances increase lift performance. In addition, with increasing in Reynolds number condition, the effect is less effective, and it accelerates the cavitation onset.

Although the flow control mechanism related to tubercles applied on control surfaces seems appropriate, a potential application could be desirable for wings and their high lift elements in specific design requirements. Swept wings operate at high angle of attack, because of their low aerodynamic efficiency, which suggests desirable conditions for tubercle applications. In addition, as previously mentioned, swept wings present higher aerodynamic loads at wing tip that causes early stall in this region providing undesirable asymmetric stall characteristics. Thus, wavy leading edge at wing tip seems a potential application.

Airline aircraft design requires swept wings and high wing load, which makes it need to add high lift devices to the wing design in order to guarantee minimum aerodynamic performance regarding take-off and landing requirements. Thus, tubercles at leading edge of wing surfaces could improve lift performance for take-off and landing conditions in the best case replacing complex high lift devices (flaps and slats) decreasing weight and maintaining cost (figure 1.11). In addition, an improvement in flight quality could be reached with soft stall characteristics.

Particularly, at low Reynolds number regime, the tubercles seem to be a remarkable potential application. In this regime, Micro aerial vehicles (MAV) and small unmanned aerial vehicles (UAV) operate. These very small aircraft fly at low velocities with a small chord of wing at Reynolds number range 15,000-500.00 (MUELLER; DELAURIER, 2003).

In this regime, the laminar flow and laminar-turbulent transition dominate the flow characteristics. Even at low angle of attack, the flow over airfoil upper surface could undergo full flow separation causing a drastic deterioration in aerodynamic performance. Besides, in this flow regime, MAVs and UAVs could be affected by atmospheric turbulence causing premature flow separation (BOLZON et al., 2015).

Therefore, tubercles potentiality could improve aerodynamic performance in MAV and UAV design keeping desirable flight characteristics in a large range of angles of attack establishing stable flow conditions with tubercles reducing the sensitivity to atmospheric

turbulence excitation. Additionally, as in conventional aircraft designs, the tubercles could avoid addition of high lift devices. In this case, additions of high lift devices are not desirable because of the small aircraft size.

Figure 1.11: The tubercles replacing high lift devices needs decreasing weight and maintaining cost (FISH, 2011).

Even for unswept wing, the tubercle application could take advantage in general aviation. Because of the airfoil aerodynamic characteristics at low Reynolds number, some aircraft from general aviation could have abrupt stall behavior, which is undesirable for a training aircraft. Therefore, tubercles could add suitable flight characteristics to training aircraft.

The benefits of adding tubercles to lift surfaces are considered at subsonic regime. However, Bolzon et al. (2015) discusses a potential tubercle application in order to reduce the wavy drag associated to transonic and supersonic flight. The tubercles change the pressure distribution along spanwise when compared to a straight leading edge (SKILLEN et al., 2013; WATTS; FISH, 2001). Higher and lower pressures than for a smooth surface appear in different span stations for the wavy leading edge configuration. The critical Mach number is associated with lower pressure. Thus, the wavy airfoil will have local critical Mach number lower for some sections when compared to smooth configuration. On the other hand, other

sections will have higher Mach number. It is possible that the drag raise associated to critical Mach number is smaller for wavy configurations due to some sections keep higher values of critical Mach number.

An innovative tubercle application appears as an aerodynamic solution in the very competitive world of the Formula One cars. The flaps of the Formula One cars are high lift devices that increase downforce performance of the cars at specific conditions during the race. The flaps work as aircraft wing generating lift and drag where during turns the car needs great increase in downforce to maintain high speed and take advantage in this critical condition. On the other hand, during straights the flaps need to perform minimum drag in order to reach maximum speed. Therefore, the aerodynamic flaps need to be optimized during the race to present high efficiency. However, at the Reynolds number regime of the Formula One car races, it is not possible to have a broad range of angles of attack with high aerodynamic efficiency.

In this sense, tubercles were added to the leading edge of the top flap of Formula One cars, in order to keep higher efficiency as compared to a straight leading edge configuration at greater range of angle of attack (BOLZON, 2015) (Figure 1.12).

Figure 1.12: Wavy leading edge adds to top flap in order to improve aerodynamic performance. Reproduced from http://www.somersf1.co.uk/2014/07/bite-size-tech-mclaren-mp4-29-new.html.

The application of tubercles has been a success on rotary wings. It seems clear that energy efficiency is enhanced by addition of tubercles on leading edge of fan and turbine blades. The industrial ceiling fans for great buildings with addition of tubercles at leading edge blade have been produced. The WhalePower Corporation demonstrates increase in electrical generation at moderate wind speeds adding tubercles at leading edge turbine blades (WIND ENERGY INSTITUTE OF CANADA, 2008). Additionally, the WhalePower Corporation reported benefits in reducing fatigue. Murray et al. (2010) investigated the addition of tubercles to blades of marine tidal turbine, where the blades with wavy leading edge presented significantly improvement in performance at lower flow speed.

Another benefit when tubercles are added to the blade leading edge of fans and turbines is the reduction in noise emission. Hansen et al. (2010) carried out experimental tests showing the suppression of tonal noise by adding tubercles to an airfoil at low Reynolds number condition. Furthermore, still on rotary wings, the tubercles seem to present benefits regarding problems with dynamic stall on loads of the rotor blades by reducing the cyclical loading (BOLZON, 2015).

1.3 Aims of this thesis

The overall aim of this work is to investigate the airfoil geometry effect on wavy leading edge phenomena at low Reynolds number regime. However, the broad variation of the flow conditions and geometric parameters proposed to reach the overall aim brings some specific investigations to establish a rational path, and to clarify the comprehension of the wavy leading edge phenomena in many aspects that were not accomplished in previous studies due to their restrictions to specific geometries or flow conditions. Therefore, the aim of this thesis will be split into some specific investigations that will contribute to expand the knowledge of the wavy leading edge phenomena. In the next paragraphs, the specific aims in this current research and its relevance will be described.

Stanway (2004) said that the tubercle performance depends on stall type of the smooth airfoil. Therefore, it is supposed that airfoil geometry causes influence on wavy leading edge phenomena since thin airfoils, as a result of the small leading edge radius, present leading edge stall characteristics, whereas thick airfoils with great radius establish trailing edge stall

characteristics (JACOB et al., 1935; JACOB et al., 1937). Thus, an aim of this work is to characterize clearly the pre-stall and post-stall characteristics of the smooth airfoils in order to support preliminarily the investigation of the airfoil geometry effect on tubercle phenomena.

There is a lack of knowledge in airfoil geometry effects on tubercle phenomena owing to the fact that most previous researches focus investigations on airfoils similar to the whale humpback flipper´s morphology. Thus, in order to expand the knowledge out of the humpback whale morphology, this work will investigate the airfoil geometry effect by exploring the extremes of airfoil thickness.

The wavy leading edge phenomena will be evaluated at low Reynolds number regime. In this regime, a complex laminar flow is sensitive to Reynolds number varation. The flow separation determines the aerodynamic characteristics over airfoil upper surface at any angle of attack. A laminar separation bubble or full flow laminar separation can occur at leading edge of the airfoil. In addition, trailing edge flow separation also appears in this flow regime. Thus, as in the airfoil geometric variation, it is expected that the Reynolds number changes can cause modifications of wavy leading edge effect on aerodynamic characteristics of an airfoil. Therefore, another aim of this work is to investigate the Reynolds number effect on wavy leading edge phenomena.

The understanding of the flow control mechanism of the tubercle phenomena is restrict to some specific flow conditions and airfoil geometries performed by previous researchers. In addition, the previous studies generalize the flow control mechanism understanding it as behaviour similar to vortex generator at any flow conditions (angle of attack and Reynolds number) and airfoil geometry. Since there is a poor understanding of the flow control mechanism regarding tubercles, and in order to contribute to expand this understanding in the literature, it will carry out investigation related to flow control mechanism of wavy leading edge at broad parameter variation, in order to understand the mechanism in detail as well as to find potential distinct flow control mechanism.

Although previous researchers have investigated the effect of changing the tubercle amplitude and wavelength on wavy leading edge performance (HANSEN et al., 2009; JOHARI et al., 2007; LEVSHIN et al., 2006), there is a poor understanding why specific configurations show optimum performance. Thus, another aim of this thesis is to confirm the tubercle geometry effect on aerodynamic performance of the airfoils, and to understand the

aerodynamic characteristics that lead to the best performance. In addition, Reynolds number and airfoil geometry effects on tubercle geometry performance will be evaluated.

After we have described the aims of this thesis and their potential contributions, we can summarize them as follows:

- To understand the aerodynamic characteristics of thin and thick smooth airfoils.
- To determine and understand the airfoil geometry effect on wavy leading edge phenomena caused by airfoil thickness variation.
- To determine and understand the changes caused on wavy leading edge phenomena due to Reynolds number variation.
- To understand the flow control mechanism that involves the wavy leading edge airfoils at broad geometric and flow condition variations.
- To confirm the tubercle geometry effect on aerodynamics performance of the airfoils, and to understand its causes. In addition, to evaluate the Reynolds number and airfoil geometry effect on tubercle geometry performance.

In order to achieve the aims of this thesis, the follows activities were performed during the investigation:

- Measurements of lift, drag and moment for set of NACA 0012, NACA 0020 and NACA 0030 at distinct wavy leading edge configurations for low Reynolds number regime, ranging from Re = 50,000 up to 290,000.
- Mini-tuft and oil flow visualizations were carried out at higher and lower Reynolds numbers conditions for all configurations, where the Reynolds numbers were chosen (higher and lower) based on the force measurement results.

1.4 Structure of the thesis

This work is presented in eight chapters, each one with a specific aim, in order to clarify the overall work regarding wavy leading edge phenomena. The first chapter presents introductory aspects from this research. The section 1.1 shows the motivation of the research.

The characteristics of the flow control as well as the importance of this topic for technology in engineering mainly in aeronautics are described briefly.

After that, in the next section, the imitation of nature is presented as inspiration for the currently study in wavy leading edge airfoil as passive flow control mechanism. The humpback whale (Megaptera novaeangliae) is presented as a mammal with unique hydrodynamic performance caused by its tubercles. They are located at the flipper leading edge, and cause an improvement in performance due to passive flow control mechanisms. In addition, it is described some currently and potential applications regarding wavy leading edge airfoils. The section 1.3 describes the aims of this currently research. Finally, the last section presents the structure of the work.

The second chapter discusses the phenomenology involved in this research. The characteristics of the low Reynolds number regime are discussed by detailing phenomena such as laminar separation bubble and full flow laminar separation. Besides, Reynolds number and airfoil geometry effect on flow characteristics also are discussed.

The second part of this chapter makes a bibliography review that gives details of different aspects of wavy leading edge researches, such as first researches, wavy leading edge and airfoil geometry effects, topology flow and flow control mechanism.

The third chapter describes the experimental equipment and methodology. The general characteristics of the equipment used during the research, such as wind tunnel and hot wire anemometers, are presented. Moreover, experimental procedure and methodology are described such as uncertainty calculation, sensor calibration, flow visualization and test executions.

The fourth chapter presents the force and moment measurements for wavy and smooth airfoils, with distinct tubercle geometries, at Reynolds number regime between 50,000 and 290,000. Besides, it is discussed the aerodynamics performance presented by experimental results. Effects on smooth and wavy airfoils regarding airfoil thickness, wavy geometry and Reynolds number were analysed.

The fifth chapter presents the description of the flow topology for smooth and wavy airfoils at lower and higher Reynolds numbers. Section 5.1 and 5.2 describe the flow topology over the airfoils based on mini-tuft and oil flow visualizations correlating with force results.

The sixth chapter shows the most important discussions of this current research. It discusses at length all phenomena that were visualized and associated with the force measurements. The distinct flow control mechanisms that appear in different configurations and flow conditions are discussed in depth. Besides, the effects of the parameter variations on tubercle aerodynamic performance (airfoil thickness, wavy geometry, Reynolds number) are clearly explained.

The seventh chapter presents the conclusions summarizing main discoveries and the understanding of the wavy leading edge phenomena regarding flow control mechanisms and airfoil thickness, wavy geometry and Reynolds number effect.

Finally, chapter eight presents suggestions of the new works that could continue some aspects of the wavy leading edge phenomena that this thesis opened.

2 PHENOMENOLOGY AND LITERATURE REVIEW

2.1 Phenomenology

The main focus of this work is to evaluate changes in the boundary layer of aerodynamic airfoils at low Reynolds number, which are caused by a wavy leading edge. In this Reynolds number regime, the flow has complex characteristics. The laminar boundary layer is susceptible to separation even at low angles of attack. Furthermore, in a laminar boundary layer, the separation can take place with reattaching in a laminar or turbulent flow condition, or without reattaching. Finally, when the boundary layer separation occurs in the turbulent regime it is denominated as turbulent detaching.

The aforementioned different characteristics of boundary layer detachment over an airfoil upper surface at low Reynolds number regime depend on the incoming flow Reynolds number (based on the airfoil chord), airfoil geometry, free flow turbulence intensity and external perturbations. Therefore, the following discussions regarding flow characteristics over an airfoil and their dependency on essential parameters (Reynolds number and airfoil geometry) can help the understanding of the wavy leading edge phenomena at low Reynolds number studied in this work.

Within the boundary layer, the Reynolds number, which establishes the balance between viscous and inertial forces, characterizes the velocity profile near the wall along the airfoil surface. In addition, the presence of pressure gradient over the airfoil surface affects the boundary layer development changing also the velocity profile. In this context, the flow characteristics are sensitive to the airfoil geometry (defined by geometrical parameters). In the following subsection, the influence of the Reynolds number and airfoil geometry parameter over flow characteristics of the aerodynamic airfoil is discussed.

2.1.1 Reynolds number dependence on flow characteristics

The Reynolds number is the most important non-dimensional parameter in the study of aerodynamics. The variation of Reynolds number can strongly modify the flow characteristics implying in changes in the aerodynamic coefficients. The Reynolds number definition associated with non-dimensional form of the Navier-Stokes equations can help the understanding of the Reynolds number effects on flow.

The Reynolds number is defined as:

$$Re = \frac{\rho UL}{\mu} \tag{2.1}$$

where

U is a characteristic velocity scale

L is a characteristic length scale

ρ is the density of the fluid

μ is the dynamic viscosity of the fluid

The nature is governed by different density, viscosity and scales of characteristic velocity and length resulting in many flow phenomena. In order to find the meaning of Reynolds number, and to quantify it, it is helpful to determine the characteristics of particular flow observed on nature.

The Reynolds number is determined by inertial forces *F (mass, velocity, size)* and viscous forces *F (viscosity)*. In this sense, the Reynolds number can be understood as the ratio of inertial forces to viscous forces in the flow or even the measure of the relative importance of inertial forces and viscous forces. This balance of forces on flow involves forces with distinct characteristics.

Inertia is the physical concept that describes the fact that any particle tends to remain at the same speed and direction when there are no external forces on it. Therefore, a body with large inertia will strongly resist to a change in its direction (velocity), whereas a body with small inertia changes almost instantaneously its motion by acting of external forces.

The inertia of fluid flow is related to flow instability. Inertia in fluid flow is associated to the non-linear interactions that occur within the flow field. These non-linearities may cause instabilities in the flow with a growth potential.–Therefore, the flow can become turbulent when inertial forces are dominant what happens for large Reynolds numbers.

Viscosity is a property of the fluid related to the resistance of a fluid to flow under the application of an external force. At sufficiently low Reynolds number, the viscosity is dominant, the flow is laminar and smooth where the viscosity has the major role of distributes and transports momentum throughout the flow.

The main characteristic of the fluid flow regarding laminar or turbulent state depends on the ratio of inertial forces to viscous forces in the flow. At laminar flow conditions (low Reynolds number), viscous forces affect the flow dynamic where the viscosity damps out disturbances within the flow. As a consequence, disturbances tend to decay or to not sustain themselves through the flow.

In contrast, under turbulent flow conditions (large Reynolds number), inertial forces drive the flow dynamic, and viscous forces cannot prevent the disturbance from growing the flow. Therefore, the Reynolds number is a parameter used to characterize the flow behaviour regarding laminar or turbulent conditions.

We can evaluate the role of the Reynolds number on flow by analyzing the Navier-Stokes in non-dimensional formulation for an incompressible and Newtonian fluid presented in the following form:

$$\nabla . u = 0 \tag{2.2}$$

$$\frac{\partial u}{\partial t} + (u.\nabla)u = \nabla p + \frac{1}{Re}\nabla^2 \mathrm{u} \tag{2.3}$$

where

$\bigtriangledown$ is the spatial gradient operator normalized by some length scale (L)

u is the velocity vector normalized by some velocity scale (U)

t is the time normalized by the convective time scale (L/U)

p is the pressure normalized by the dynamic pressure (ρU^2)

The inertial terms (acceleration) are on the left-hand side of equation 2.3. The first term (on the left hand side) represents the unsteady inertial component (local acceleration), that is, time-dependent. The second term is the non-linear inertial term (convective acceleration). On the right-hand side of equation 2.3, the first term is the pressure gradient, and the second term represents the viscous force.

As discussed before, at low Reynolds number, the fluid viscosity dominates the flow forces damping out the flow instabilities. This phenomenon can be understood on equation 2.3 where a sufficiently low Reynolds number makes the Laplacian term, on the right-hand side, to dominate the equation and govern the fluid dynamics. The non-linear term on the left-hand side has not significant effect on the flow. In this case, the flow is laminar and keeps stability characteristics.

On the other hand, it can also be justified in equation 2.3 that at high Reynolds number the flow becomes turbulent because local momentum exchange causes instability. The non-linear terms on the left-hand side will start to affect the flow dynamics. Thus, at sufficiently high Reynolds number, the non-linear terms dominate, and the fluid is considered fully turbulent.

Although the Reynolds number dominates the Navier-Stokes equation and consequently the fluid dynamics determining laminar or turbulent behaviour, the pressure gradient on the left side of the Navier-Stokes equation also has a considerable influence on flow characteristics. Geometric characteristics of a body immerses in flow determine the pressure gradient over its surface. Therefore, besides Reynolds number effect, geometric characteristics are important to determine the flow behaviour.

As a consequence of the body´s geometric effect on flow characteristics, the fluid flow on Blunt and streamlined bodies present flow behaviour totally distinct at same Reynolds number. Thus, the shape of the geometry can affect the flow characteristics distinguishing Blunt and streamlined bodies aerodynamic characteristics. In this context, the Reynolds

number effects have been studied for distinct geometric bodies. The figure 2.1 shows different Reynolds number effects on wetted area drag coefficients for cylinder, sphere, profile and plate indicating geometric effects on flow at same Reynolds number.

The flow around a circular cylinder has been extensively studied due to its geometric simplicity and widespread application in engineering. Although the study of flow around circular cylinders is interesting, and has many applications such as risers on petroleum exploration, the main goal of this thesis is to study boundary layer control mechanisms on aerodynamic airfoils. Thus, the focus in this chapter is to understand the flow phenomena over aerodynamic airfoils at different Reynolds number regimes.

Even though this work studies flow phenomena at Reynolds number between 50,000 and 290,000, it is helpful to understand the flow characteristics at specific Reynolds number regime studied in this thesis as a particular band in the larger range of Reynolds number conditions. This helps to show how the peculiarities of the studied regime are established and connected to the broad band of the Reynolds number effects. In addition, this view gives support to clarify phenomena, limitations and speculations in this work.

Generally speaking, aerodynamic airfoils present, above Reynolds number one million, most of boundary layer in turbulent state where the Reynolds number is referenced by the chord of the airfoil. In the intermediate Reynolds number regime ($10^3 < Re < 10^6$), the boundary layer presents laminar, transitional and turbulent state depending on geometric characteristics of the airfoil. Below Reynolds number 100,000, the viscosity effect grows so that hardly the flow presents transition to turbulent state.

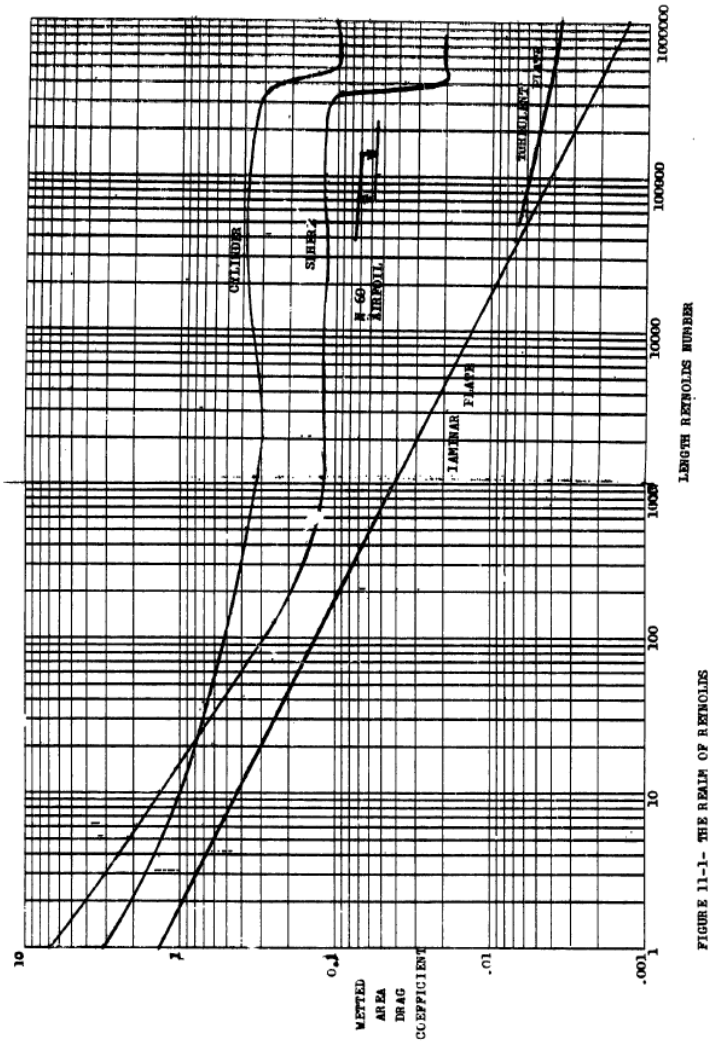

FIGURE 11-1- THE REALM OF REYNOLDS

Figure 2.1: Reynolds number effects on wetted area drag coefficients for different geometries (CARMICHAEL, 1981).

In order to understand the flow characteristic around airfoils over the large Reynolds number range explored by man, the discussions regarding flow regime by Carmichael (1981) are very useful. The following discussions related to different Reynolds number regime is a modified version of the Carmichael´s original work.

- *Very low Reynolds number*, at fractional Reynolds numbers, the flow is completely viscous.

- *Reynolds numbers below 150,* this regime becomes of interest in the design of turbulence reducing screens and smoke streak producing wires for low turbulence wind tunnels.

- *Reynolds numbers between 1,000 and 10,000,* in this regime the boundary layer is strongly laminar and it is very difficult to cause artificially transition to turbulent flow.

- *Reynolds numbers between 10,000 and 30,000,* the boundary layer is full laminar and artificial tripping on boundary layer has not been successful. At higher lift coefficients, the flow produces flow separation at laminar boundary layer without reattachment.

- *Reynolds numbers between 30,000 and 70,000,* in this regime above Reynolds number 50,000, the separation transitions to turbulent condition reattaching the flow forming a laminar separation bubble. In addition, the critical Reynolds number can be decreased by artificial boundary layer tripping.

- *Reynolds numbers between 70,000 and 200,000,* extensive laminar flow is typical.

- *Reynolds numbers between 200,000 and 700,000,* in this regime, an extensive laminar flow still is present, and the airfoil performance keeps improving with raise of Reynolds number condition. The fail in reattachment can occur after mid-chord causing laminar separation. However, the laminar separation bubble still has significant relative length and causes some loss of performance.

- *Reynolds numbers between 700,000 and 3,000,000,* the laminar bubble can still cause deterioration in performance at Reynolds number of one million.

- *Reynolds numbers between 3,000,000 and 9,000,000,* it is possible to reach very low drag coefficients through extensive natural laminar flow at specific conditions. The laminar separation bubble at fifty percent of chord is no longer a problem for this regime. The turbulent boundary layer on the rear wing can stay attached through very severe adverse pressure gradients by using modern airfoil design methods.

- *Reynolds numbers between 9,000,000 and 40,000,000,* even in this high Reynolds number regime is possible to maintain extensive natural laminar flow using strong favorable pressure gradient.

- *Reynolds numbers between 40,000,000 and* 10^9, boundary layer flow is mostly turbulent.

- *Reynolds numbers greater than* 10^9, the drag is mainly turbulent.

In the next subsection, the flow characteristics at low Reynolds number will be discussed in order to help the understanding of the aerodynamic phenomena involved in this research.

2.1.2 Low Reynolds number phenomena

The understanding of the flow phenomena over aerodynamic airfoils at low Reynolds number has shown interesting results since early studies. During the 1930s, Schmitz (1942) carried out experimental investigations on wind tunnel for some airfoil shapes at low Reynolds number ($20{,}000 < Re < 200{,}000$). In this low Reynolds number range, for a thick cambered airfoil, the experimental results presented an abrupt change in aerodynamic performance at specific flow conditions, so showing the existence of a *Critical Reynolds number*. The results plotted by Schmitz (1942) showed remarkable improvement in all aerodynamic coefficients after a critical Reynolds number (figure 2.2).

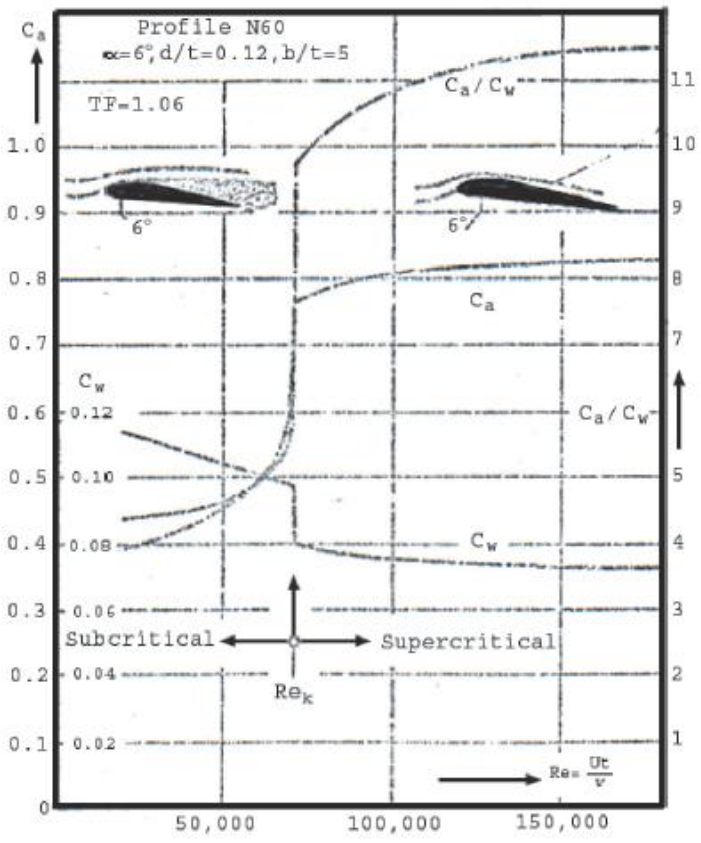

Figure 2.2: Remarkable aerodynamic changes above critical Reynolds number (SCHIMITZ, 1942).

The figure 2.2 shows values of maximum lift (Ca), minimum drag (Cw) and aerodynamic efficiency (Ca / Cw) for a thick cambered airfoil at Reynolds number variation. Above the critical Reynolds number, the maximum lift coefficient (Ca) goes up and the minimum drag coefficient (Cw) goes down abruptly. Besides, the maximum aerodynamic efficient (Ca / Cw) is much higher for Reynolds number above the critical number.

The critical Reynolds number can be understood in a similar way to Reynolds number that forces to appear the “drag crisis” at a circular cylinder. Below critical Reynolds number, the viscous forces affect strongly the flow phenomenon, thus becoming minor the inertial force effect. Therefore, the flow over the entire airfoil upper surface remains laminar. In contrast, at higher values than the critical Reynolds number, the flow becomes turbulent in somewhere on the airfoil upper surface.

The results from Schimitz (1942) bring a great interest in studying the laminar-turbulent transition effects on airfoil performance in the future decades. Thus, with new experimental results (ABBOTT, 1945; ALTHAUS, 1972; REIGELS, 1961) became clearer

the turbulent-laminar transition phenomenon, by generalizing of the understanding of tests with different airfoil geometries in a large range of Reynolds numbers. As consequence of these results, it can be assumed that most aerodynamic airfoils have the critical Reynolds number between 10^4 and 10^5.

McMasters and Henderson (1979), using the previous works cited, generalized the critical Reynolds number for a wide Reynolds number band. The results (figure 2.3) show distinct aerodynamic performances for smooth and rough airfoil surfaces. At Reynolds number lower than 100,000, the smooth airfoils have a large deterioration in aerodynamic efficiency when compared to rough airfoils. In contrast, above this Reynolds number, the smooth airfoils have superior aerodynamic efficiency.

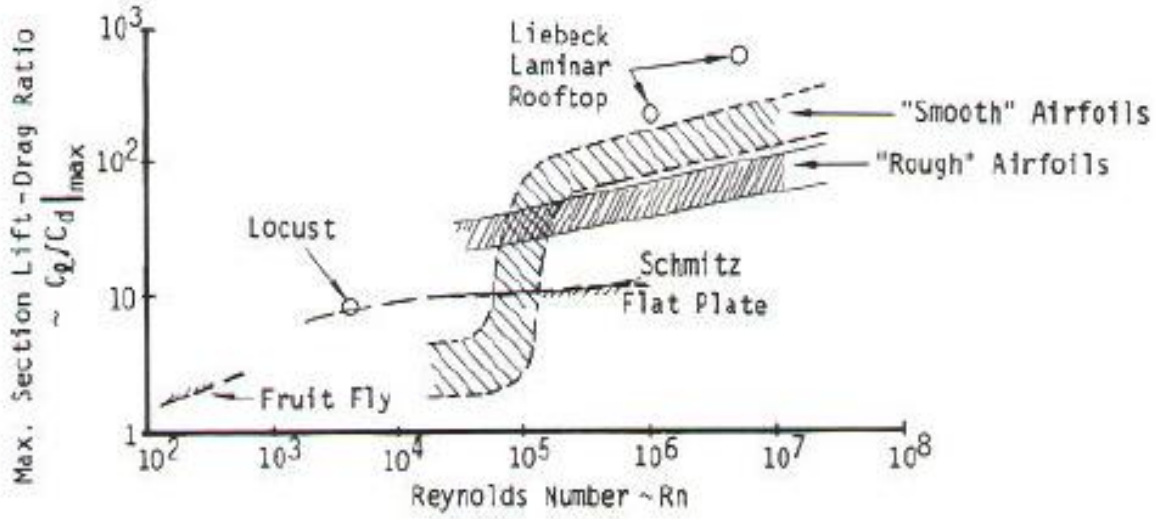

Figure 2.3: Reynolds number effect for smooth and roughness airfoil surfaces. (MCMASTERS; HENDERSON, 1979).

Additionally, there are no drastic changes for rough airfoils at wide Reynolds number range tested. Considering the relationship between flow transition and roughness, the results indicate the correlation between critical Reynolds number and the laminar-turbulent flow state. For smooth airfoils (laminar flow state), the critical Reynolds number appears at lower Reynolds number lower than 100.000 whereas for rough airfoils (turbulent flow state) occurs the absence of critical Reynolds number.

In order to understand the cause of drastic aerodynamic changes at critical Reynolds number shown by McMasters and Henderson (1979), Mueller and Batill (1982) carried out experimental tests correlating force measurements and flow visualizations. The NACA 66_3-018 airfoil was tested at Reynolds number between 40,000 and 400,000.

Mueller and Batill (1982) show that, at Reynolds number 40,000, the lift curve has a large non-linearity ($\alpha = 8^{o}$). On the other hand, at Reynolds number greater than 100,000, the lift curve linearly increases with angles of attack (figure 2.4).

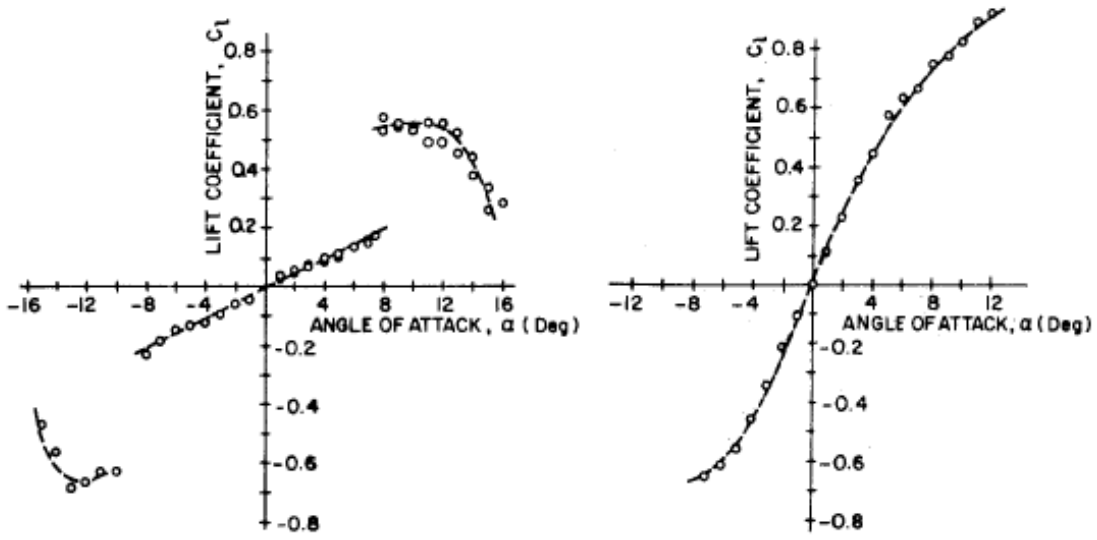

(a) $Re = 4 \times 10^4$ (b) $Re = 4 \times 10^5$

Figure 2.4: Lift curves for Re = 40,000 and 400,000 (MUELLER; BATILL, 1982).

Mueller and Batill (1982) show, using smoke visualization, that the non-linearity on lift curve at Re= 40,000 and $\alpha = 8\ ^{o}$ is due to the formation of a laminar separation bubble under that specific flow condition. It seems that the decrease in performance verified firstly by Schimitz (1942) has a likely explanation on laminar separation bubble phenomenon suggested by Mueller and Batill (1982).

Although the laminar bubble formation is related to abrupt increase in lift, this result does not seem contradictory since the maximum lift coefficient reaches values at Reynolds number 40,000 much smaller than at Reynolds number 400,000. Thus, the Mueller and Batill

(1982) results indicate that when the laminar separation bubble appears over the airfoil surface, the maximum lift coefficient has a large decrease.

Actually, the laminar separation bubble phenomenon is related to laminar separation at low Reynolds number, and a consequent low aerodynamic performance. When the laminar separation occurs, the evolution of the separated shear layer has a strong influence on the entire flow. The boundary layer separation can occur reattaching over the airfoil with a transitional separation bubble and a narrow wake formed behind the airfoil (figure 2.5) or the separation shear layer may fail to reattach to the airfoil surface and a wide wake is formed behind the airfoil (fig 2.6). In both flow conditions, the airfoil undergoes aerodynamic deterioration.

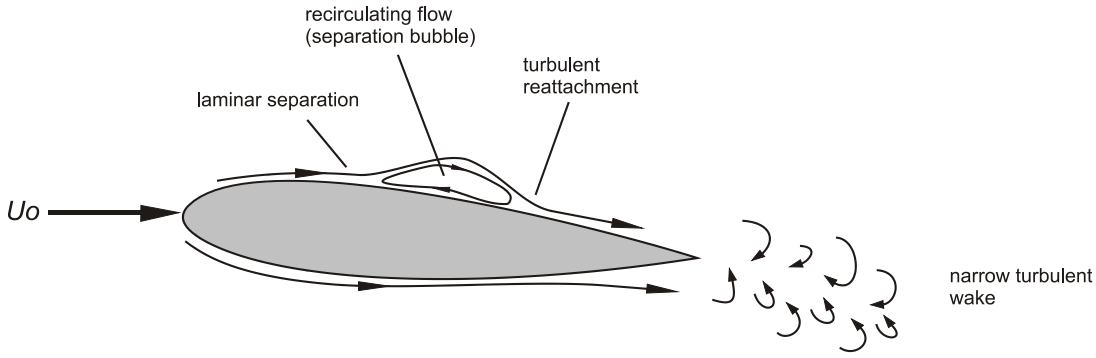

Figure 2.5: Flow separation with subsequent reattachment. Adapted from Gerakopulos (2011).

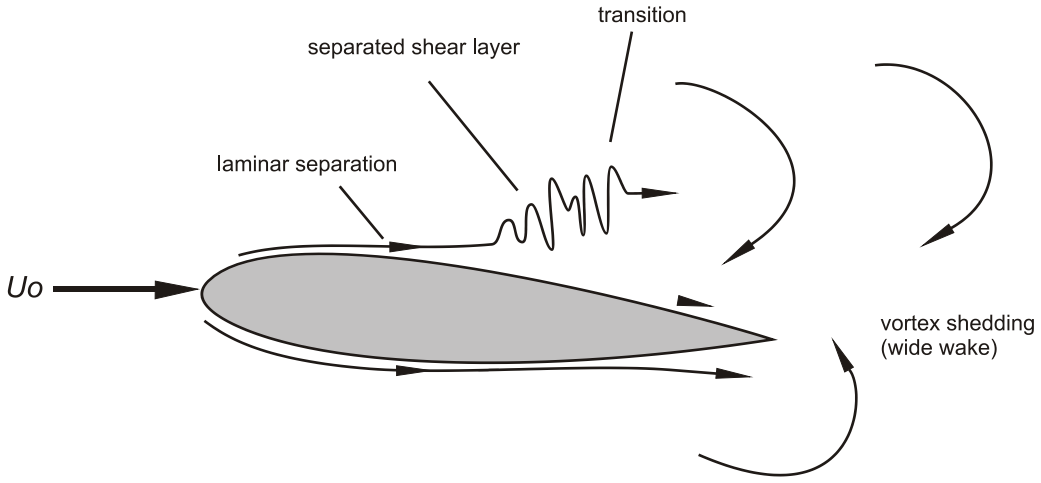

Figure 2.6: Flow separation without subsequent reattachment. Adapted from Gerakopulos (2011).

The Mueller and Batill (1982) results indicate that the critical Reynolds number drives the transition from laminar flow separation, with or without separation bubble phenomenon, to turbulent flow condition as consequent increase in aerodynamic performance.

2.1.3 Laminar bubble separation

As shown in previous subsection, the laminar separation bubbles appear at Reynolds number below 100,000 causing large changes on aerodynamic performance of airfoils. Thus, investigations regarding laminar separation bubble phenomenon could improve the understanding of flow characteristics at low Reynolds number regime.

The stall behaviour of airfoils motivated the earliest remarkable investigations conducted by Crabtree (1959) and Tani (1964) in the 1960s regarding laminar separation bubbles. In the same decade, Gaster (1967) and Horton (1968) contributed with works in order to explain the laminar separation bubble mechanism.

Horton (1968) proposed a physical model for explaining the separation bubble mechanism shown in the figure 2.7. A short separation bubble starts at separation point (S) and covers a complex flow region up to reattachment point (R). The short separation bubble phenomenon comes from interaction between two main areas: the free shear layer (S´T´R´) and the re-circulation bubble (ST´R).

The transition frontier (T´T) split the flow into two phenomena. Upstream from the transition frontier line, the free shear layer is laminar. As a consequence, the viscous shear stresses remain low in this region, not resisting to pressure gradient. In this region, between separation and transition point, the pressure distribution is virtually constant. This “plateau” pressure distribution is a general characteristic of the laminar flow separation. After the flow undergoes transition to turbulent state, the viscous shear stresses increase keeping enough pressure values to take place reattachment at pressure values of non-viscous conditions.

A re-circulation flow occurs over entire bubble because of a pressure rise in this region, however, as the higher pressure values appears on turbulent region, the re-circulation occurs mainly in the called reverse-flow vortex region (TT´R). The region upstream of the

reverse-flow vortex area is called dead-air region, and is characterized by very small velocity magnitude (BRENDEL; MUELLER, 1988; LEBLAC et al., 1987).

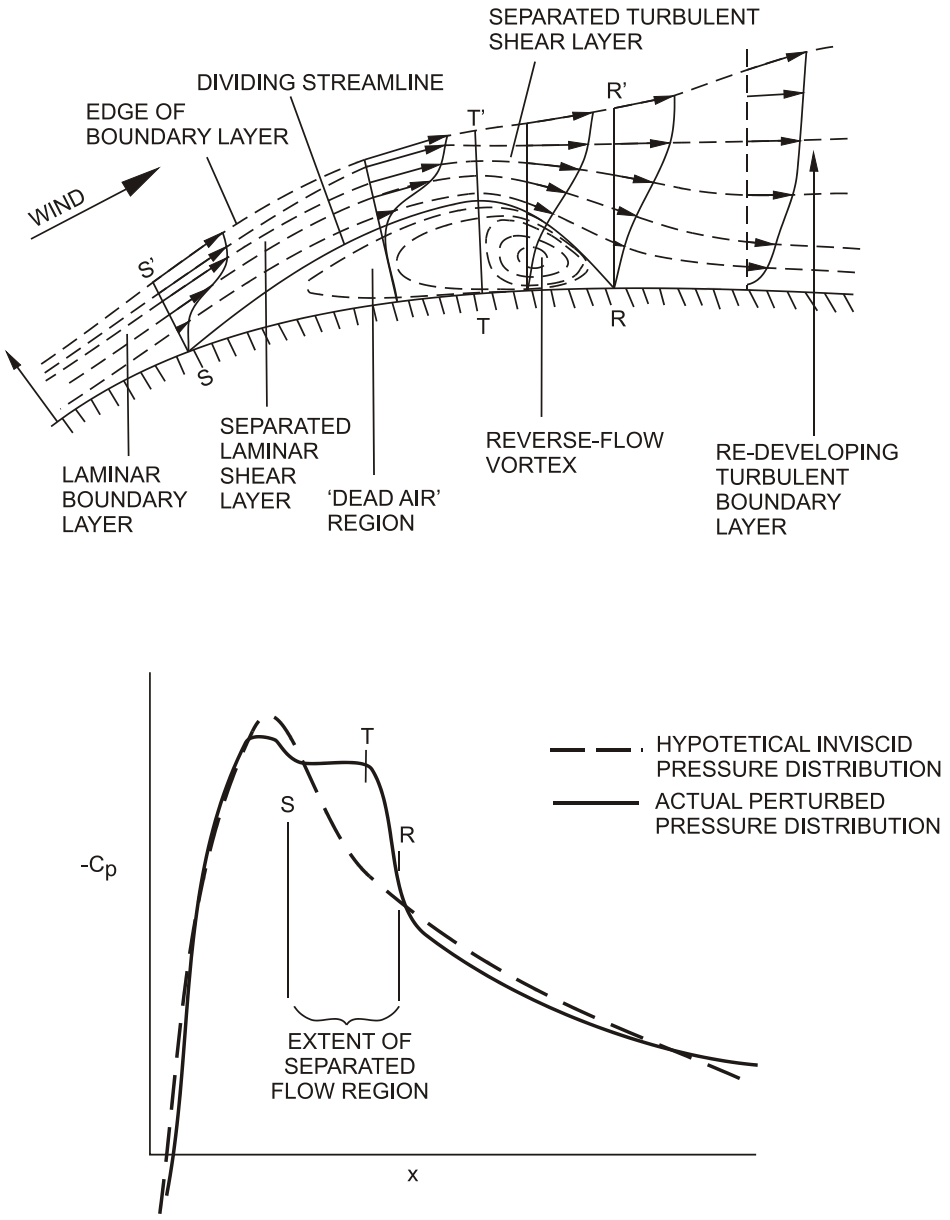

Figure 2.7: Two-dimensional short laminar separation bubble proposed by Horton. Adapted from Horton (1968).

Carmichel (1981) says that at Reynolds number below 50,000 the laminar separation bubble does not appear because its length would be of the same magnitude of the profile chord. Generally speaking, for airfoils at Reynolds number higher than 70,000, there are conditions for flow reattachment so that a laminar bubble can form (LISSAMAN, 1983).

At a fixed airfoil shape, the flow separation characteristics depend on the energy of the lower levels of the boundary layer. In other words, the flow separation type is established by the Reynolds number condition. Therefore, at low Reynolds number, two distinct types of separation bubbles can be formed: a short separation bubble and a long separation bubble.

At Reynolds number higher than 100,000, a short separation bubble appears occupying up to 15% of airfoil chord at forward position (BRENDEL & MUELLER, 1989; TANI, 1964, 1989). The bubble effect on pressure distribution over the airfoil surface is little. Although the suction peak has lower values as compared to non-viscous flow condition, it maintained high suction values varying angles of attack. Downstream of the suction peak, the bubble establishes a constant pressure level in a small region. After that, the airfoil undergoes a drastic increase in pressure returning to levels of non-viscous flow condition (figure 2.8).

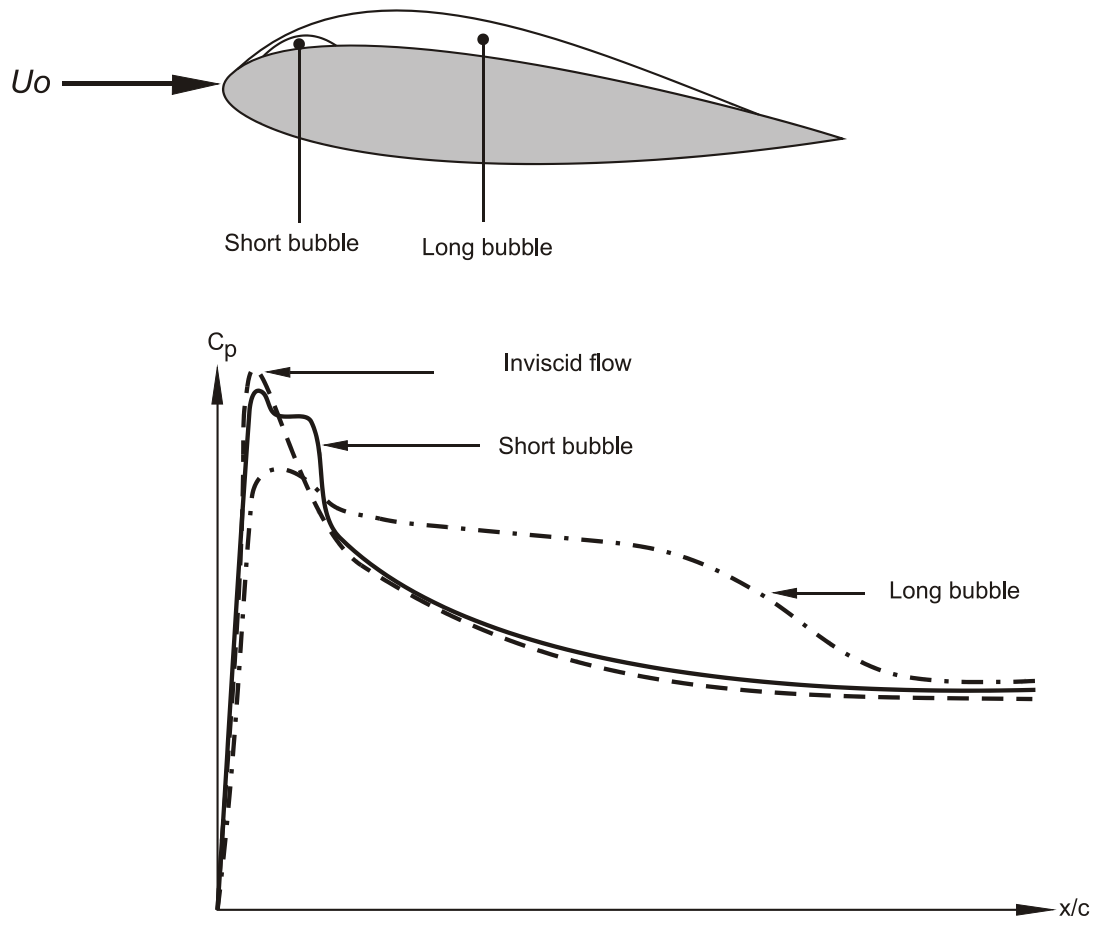

Figure 2.8: Short (a) and long (b) bubble effect on pressure distribution. Adapted from Gerakopulos (2011).

Tani (1964) discusses the formation of short bubbles at moderate angles of attack on thick airfoils, and its role on stall characteristics. Such airfoils undergo trailing edge stall where increasing the angle of attack the bubble contracts, but never bursts before it reaches the maximum lift, which is established by the forward movement of the separation point of the turbulent boundary layer. The role of the bubble is to force the boundary layer to be turbulent, and change the stall characteristics through the thickness onset of the turbulent boundary layer (VON DOENHOFF; TETERVIN, 1942).

In contrast with short separation bubble characteristics, at Reynolds numbers below 100,000, a long separation bubble may occupy from 30% of chord up to entire airfoil surface (BRENDEL; MUELLER, 1989; TANI, 1964, 1989). The pressure distribution is much different from inviscid flow distribution. The suction peak near the leading edge undergoes a large decrease when compared to inviscid flow path, and the constant pressure region extends over a great area. After that, as in the case of the short bubble, the pressure levels goes to inviscid flow path, but by a smooth way (figure 2.8).

Crabtree (1959), O´Meara & Mueller (1987), Brendel & Mueller (1988), Sharma & Poddar (2010), Karasu (2012) and Genç (2012) studied the dependency in size and separation point position of the bubble regarding Reynolds number and angle of attack conditions. They noticed that increasing the incidence angle the bubble moves to forward position. The bubble size, generally, contracts with increase in angles of attack in streamwise extent increasing thickness. However, O´Meara and Mueller (1987) show results with opposite behaviour, and Crabtree (1959) mentions that the long bubble grows rapidly with the increase in angle of attack. In terms of Reynolds number, the bubble position is less sensitive than angle of attack variation whereas the bubble length and thickness decrease with Reynolds number increasing.

After describing briefly the laminar separation bubble phenomenon, it is desirable related to stall characteristics of the aerodynamic airfoils at low Reynolds number. Three stall types are described by Jones (1933, 1934) at low Reynolds number where the first one is related to flow separation near the trailing edge, and the last two ones to flow separation near leading edge. However, the understanding in detail of the stall behaviour correlating with boundary layer changes was possible due to McCullough and Gault (1951). Thus, they classified stall types in trailing edge stall, leading-edge stall and thin-airfoil stall (figure 2.9).

A *trailing-edge stall* is characterized by a forward movement of the turbulent separation point that comes from airfoil trailing edge caused by an increase in angle of attack.

When the separation bubble is established at airfoil surface due to high angle of attack and/or low Reynolds number may cause another two stall types: *leading-edge stall and thin-airfoil stall*. These stall characteristics are related to bubble types established before full separation reaches the stall condition.

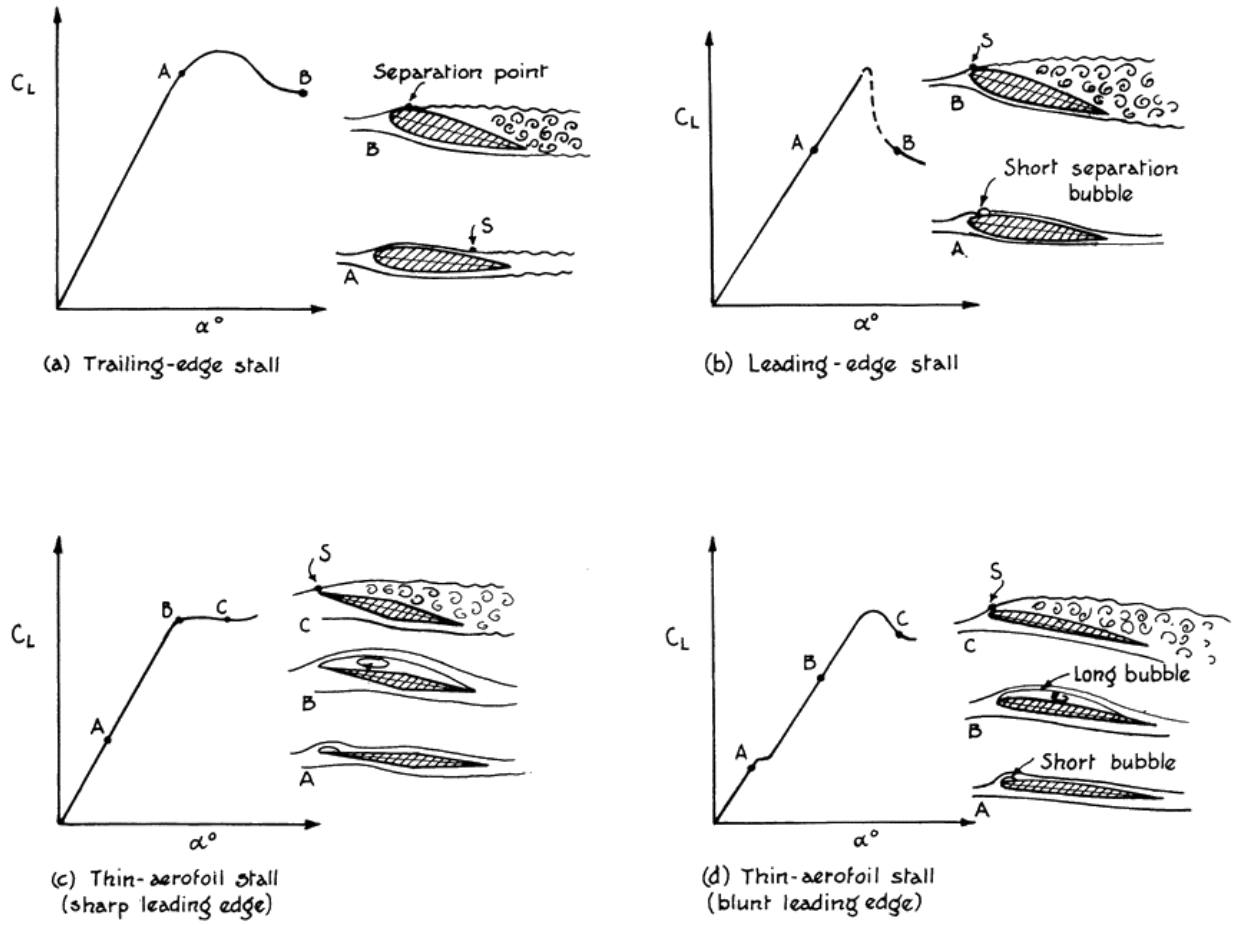

Figure 2.9: Three stall types depending on airfoil geometry (WHITFORD, 1987).

Leading-edge stall is related to short laminar separation bubbles near to the leading edge where the laminar boundary layer undergoes an abrupt separation without reattaching, forming a wide wake causing a large deterioration in aerodynamic performance, decreasing lift and increasing drag. Thus, the leading-edge stall is related to a short bubble bursting.

The *thin-airfoil stall* is characterized when a long separation bubble occurs on the airfoil surface before full flow separation. The long separation bubble occupies upwards almost the entire chord length keeping a constant pressure distribution. After stall, the constant pressure distribution reaches the trailing edge characterizing soft stall behaviour.

2.1.4 Geometric shape and Reynolds number effects on flow over an airfoil

The wavy leading edge effect on flow characteristics over an airfoil depends on the stall type of the smooth airfoil (STAWAY, 2008). Thus, it is important to characterize the airfoil stall behaviour for straight leading edge airfoils in order to help the understanding of this influence on tubercle performance. As previously mentioned, the stall characteristics are determined by the development of the boundary layer behaviour over the airfoil surface. Geometric shape and Reynolds number determine the aerodynamic characteristics of an airfoil by driving the development of the boundary layer. In this context, the effect of these parameters on stall characteristics of the airfoil will be discussed in this subsection.

2.1.4.1 Airfoil geometric shape

The airfoil geometric shape, at a fixed Reynolds number, determines the aerodynamic performance of the airfoil. Thus, the airfoil circulation and its consequent lift as well as drag (friction and pressure) will be established by the airfoil geometry. Besides, the nonlinear phenomena that involve separation flow show greater dependence of the airfoil geometry. The minimum pressure or maximum velocity point and the adverse pressure gradient over the airfoil upper surface will drive nonlinear flow conditions for subsonic and supersonic regime.

At low speed regime, the adverse pressure gradient, depending on airfoil geometric characteristics, causes reversal in the velocity profile of the boundary layer leading to flow detachment with consequent large decrease in lift (large lift loss) and increase in drag at stall condition (figure 2.10).

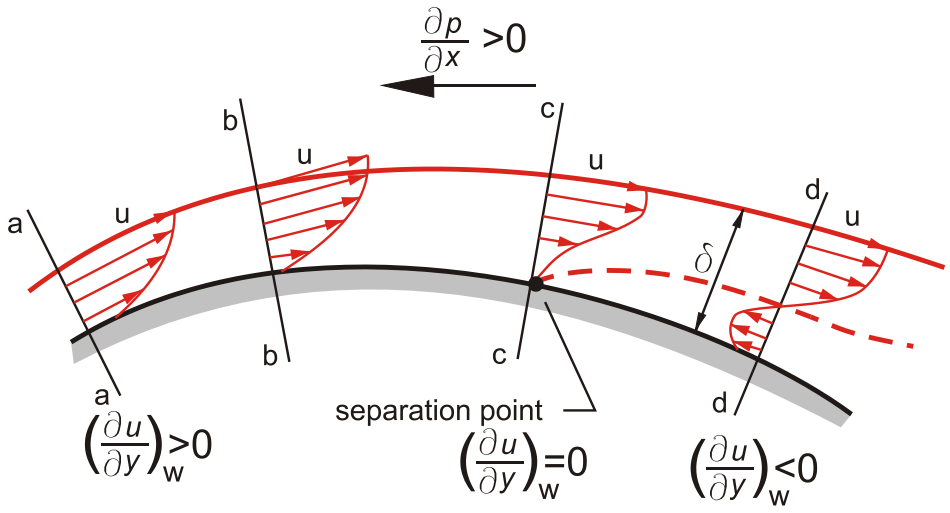

Figure 2.10: Development of the Boundary layer over an airfoil surface.

On the other hand, at high speed regime, the minimum pressure established by the airfoil geometric shape can overcome the critical pressure coefficient value causing shock wave formation which also leads to a decrease in lift (changes on lift curve slope) and increase in drag (Figure 2.11).

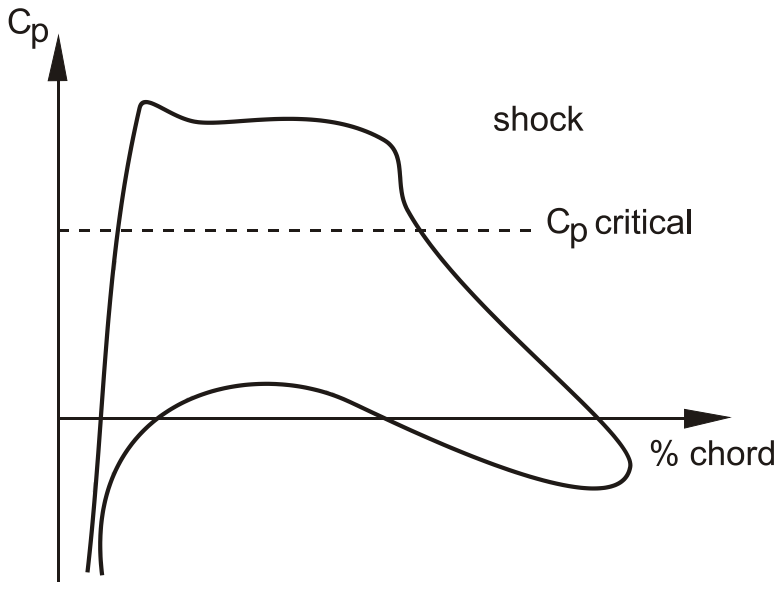

Figure 2.11: Pressure distribution at shock wave condition.

The geometric parameters that determine the airfoil shape and its aerodynamic characteristics are thickness, camber and nose radius (figure 2.12). The maximum thickness

and its position determine the thickness characteristics, and the maximum camber and its position determine the camber characteristics. The nose is defined by the radius of a circle tangent to the airfoil at the leading edge. In this subsection, it will be discussed only the effect of maximum thickness since this thesis evaluates the influence of this parameter on wavy leading edge performance.

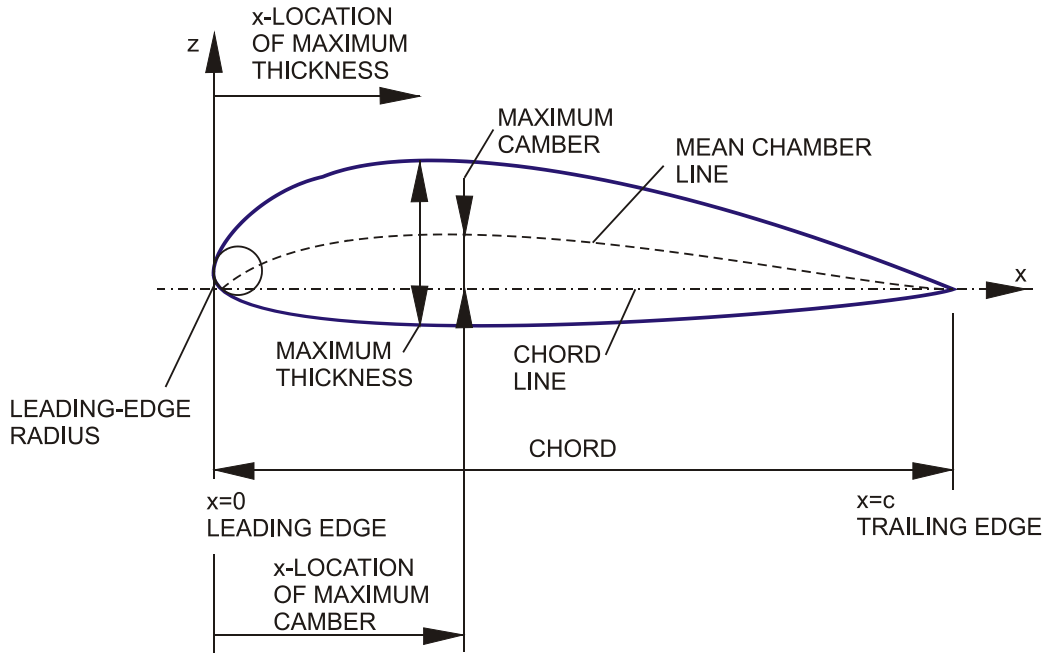

Figure 2.12: Main geometric parameters of an aerodynamic airfoil.

The variation in the airfoil thickness causes considerable changes in the pressure distribution over the upper surface of the airfoil, particularly in the location near the leading edge due to the geometric change caused in the leading edge radius (figure 2.13).

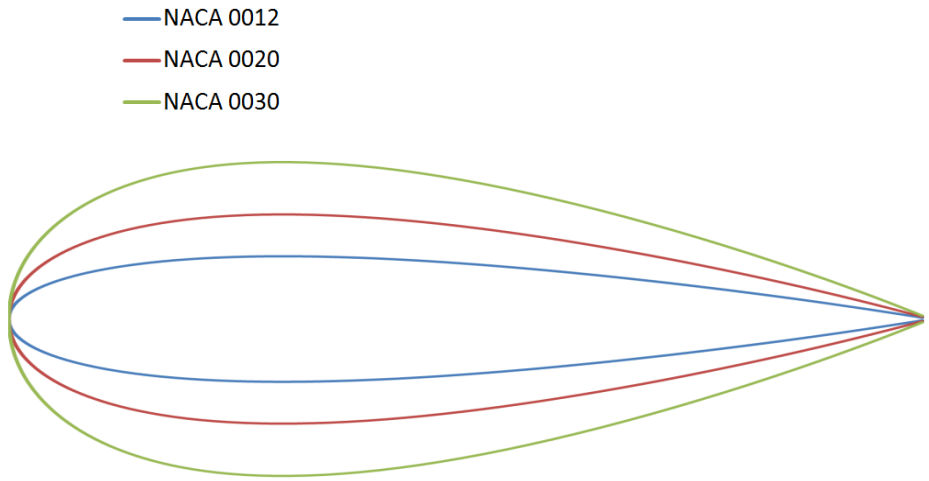

Figure 2.13: Geometric changes caused by airfoil thickness variation.

Regarding airfoil thickness effects, changes in drag and lift on the linear regime (pre-stall conditions) and in the stall characteristics (post-stall regime) are consequences of the pressure distribution modification over airfoil surface due to increase in thickness. The dependence between pressure distribution and thickness can be seen through the non-viscous results of the XFOIL PROGRAM (figures 2.14).

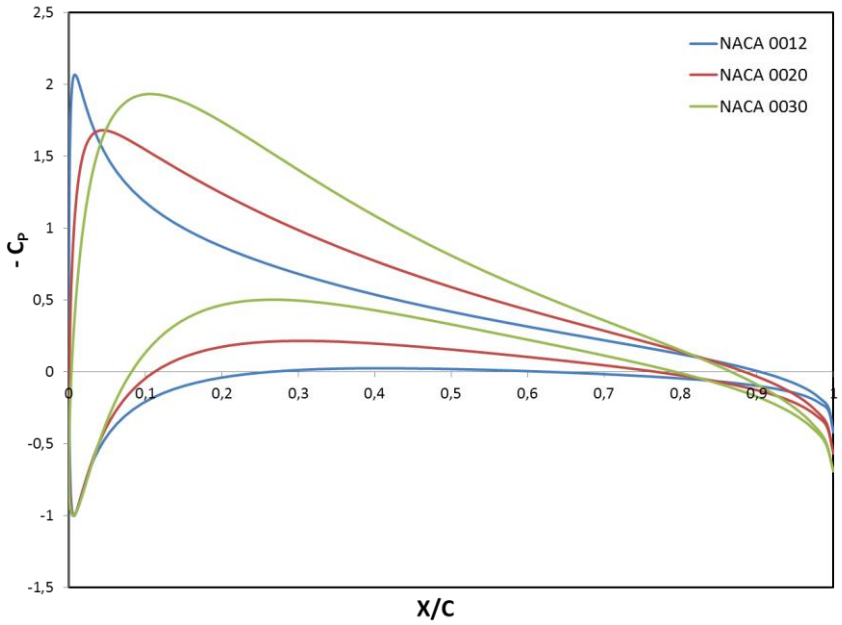

Figure 2.14: Changes in the pressure distribution due to airfoil thickness variation (alpha =5º).

It can be seen in figure 2.14 with increase in airfoil thickness that the expansion and recovery region around the leading edge (minimum pressure or maximum velocity) has decreased its suction peak and pressure adverse gradient over upper surface of the airfoil keeping higher velocities along the chordwise direction. A decrease in adverse gradient at thicker airfoils makes them more resistant to velocity profile inversion and consequently boundary layer detachment so as to delay delaying the stall condition. Additionally, the pressure distribution areas have a little raise with increasing thickness so as consequent an improve in lift occurs.

Jacob et al. (1935) carried out an investigation of a large group of airfoils under high Reynolds number conditions in order to study changes in aerodynamic characteristics of the airfoils by variation in thickness and mean-line form. Regarding the airfoil thickness effects, Jacob et al. (1935) evaluated several airfoils with various thicknesses (NACA0006, NACA 0009, NACA 0012, NACA 0015, NACA 0018, NACA 0021, NACA 0025) at Reynolds number 3 million. The figure 2.15 shows the lift curve for various airfoils varying the thickness.

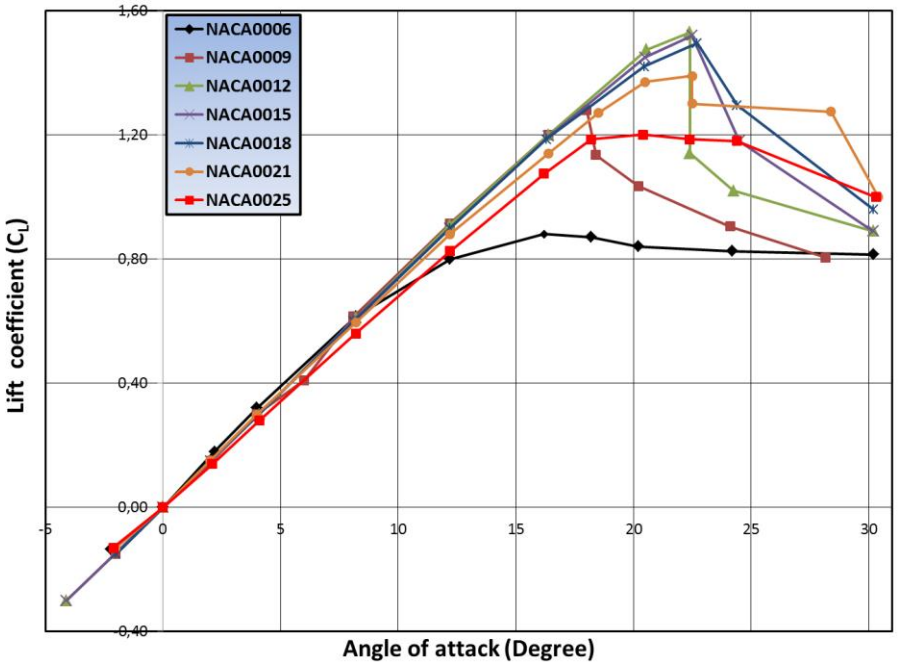

Figure 2.15: Airfoil thickness effects on lift curve of symmetrical airfoils at Re = 3 million (Source: Jacob et al. (1935)).

It is observed that the maximum lift values increase with airfoil thickness up to 15% of chord in thickness. In contrast, for higher airfoil thicknesses the values of maximum lift decrease. A generalization of this trend can be seen in the Raymer (1989) and Torembeek (1982). This characteristic is considered as a reference for choice of airfoil in terms of maximum lift in aircraft design.

Besides the results bring a correlation between maximum lift and airfoil thickness that is used in aircraft design, the correlation between airfoil thickness and stall type in figure 2.15 presents a clear understanding of how the airfoil shape affects the boundary layer development along chordwise direction. It is observed in the figure 2.15 three stall type characteristics.

At the lowest airfoil thickness value (NACA 0006), thin-airfoil stall characteristics are observed where the lift values in the post-stall regime keep close to maximum lift value (Fig 2.9-c). At intermediate values of thickness (NACA 0009, NACA 0012, NACA 0015, NACA 0018, NACA 0021), the lift curves present characteristics of leading-edge stall as an abrupt stall behaviour in the post-stall regime (Fig 2.9-b). The thickest NACA 0025 airfoil presents trailing-edge stall characteristics associated with soft stall behaviour (Fig 2.9-a).

A raise in airfoil thickness, as previously mentioned, minimizes the adverse gradient increasing the resistance to flow separation preserving the flow attached at leading edge region. Therefore, the transition of stall type from thin-airfoil stall passing by leading edge stall, going to trailing edge stall with increasing airfoil thickness is justified in figure 2.15 under high Reynolds number conditions.

2.1.4.2 Reynolds number effects

As it was discussed before, the variation in Reynolds number condition can cause large changes on aerodynamic characteristics of a body. Although the Reynolds number effects on flow characteristics of an airfoil have been discussed earlier, this subsection will describe the scale effects based on practical results from airfoils typically applied in aircraft design.

The evaluation of the Reynolds number effects on aerodynamic characteristics of classical airfoils shows that these effects are also related to stall characteristics as changes

caused by geometric modification on airfoil shape. Jacobs and Sherman (1937) carried out experimental investigation for a set of airfoils over a wide range of Reynolds number conditions extending into the flight range.

Figures 2.16 and 2.17 show the Reynolds number effects on aerodynamic characteristics of a thin airfoil (NACA 0009) and a thick airfoil (NACA 0018) at Reynolds number range between 40,000 and 3 million. For both airfoil thicknesses, values substantially greater of maximum lift are observed at higher Reynolds number. These results are justified since at higher Reynolds number the viscous effects are minimized on boundary layer levels near airfoil surface leading the fluid to resist to greater adverse pressure gradient keeping the flow attached. Besides, the increase in maximum lift at high Reynolds number regime is related to turbulent state of the boundary layer under these conditions.

As for the airfoil thickness effects, the stall type is also driven by Reynolds number variation. The NACA 0009 airfoil presents a thin-airfoil stall type at lower Reynolds number (up to 1.29×10^6) whereas leading edge stall occurs at higher Reynolds number. On the other hand, in the case of the thick NACA 0018 airfoil, at Reynolds number up to 328,000, it presents leading-edge stall type. After that, the airfoil shows trailing edge stall characteristics.

Generally speaking, as the increase in airfoil thickness, an increase in Reynolds number changes the stall characteristics transitioning from leading edge to trailing edge stall type. This behaviour is justified due to an increase in Reynolds number avoids flow separation at leading edge and shifts it to trailing edge areas.

Therefore, a lower Reynolds number condition and thin airfoils leads flow separation to leading edge stall characteristics. This stall type will be discussed in the chapters five and six since under these conditions the wavy leading edge airfoils present better aerodynamic performance.

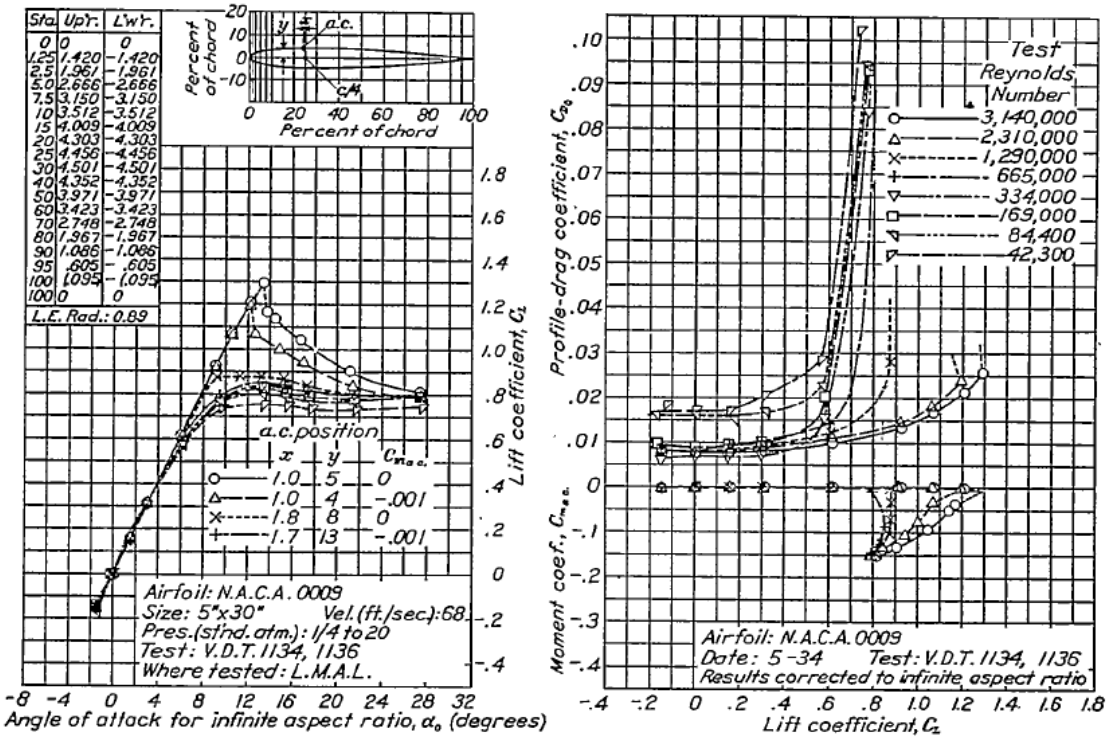

Figure 2.16: Reynolds number effects on NACA 0009 airfoil (JACOBS; SHERMAN, 1937).

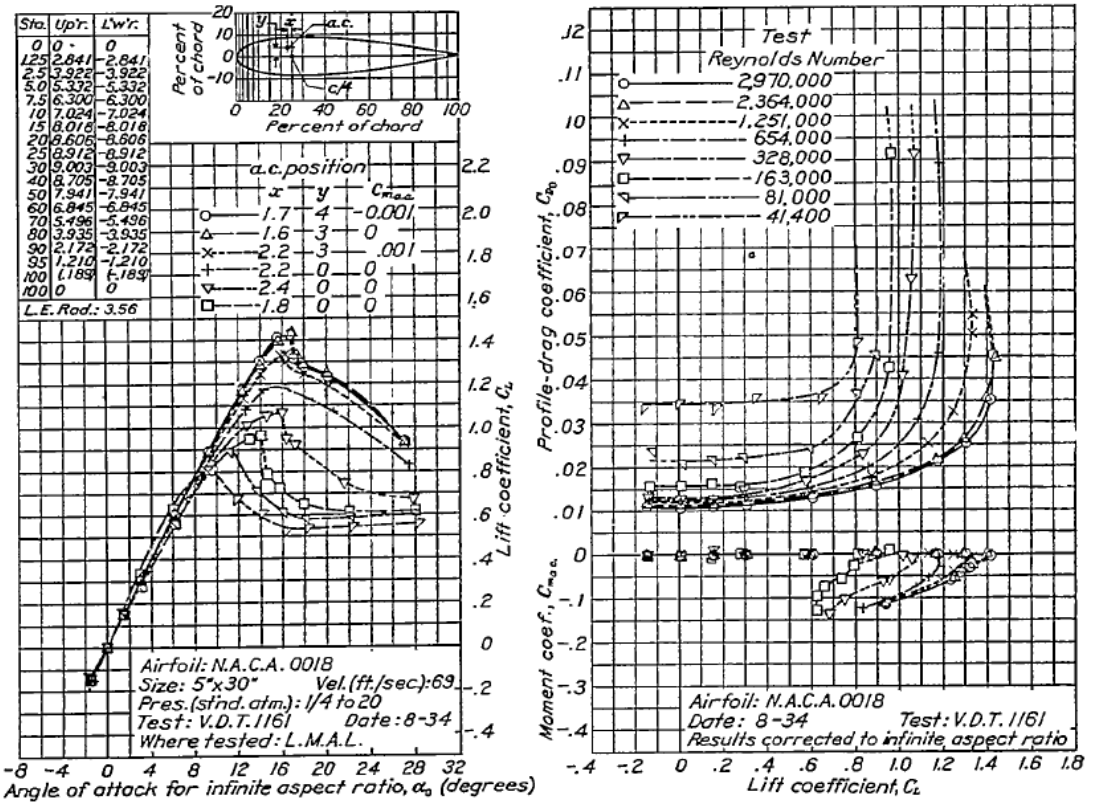

Figure 2.17: Reynolds number effects on NACA 0018 airfoil (JACOBS; SHERMAN, 1937).

2.2 Literature Review

The interest in wavy leading edge airfoils as a field of research in flow control has its inspiration in scientific works from the 80s that investigated morphological characteristics in humpback whales, mammals who display spectacular manoeuvrability in the aquatic environment (EDEL; WINN, 1978; JURASZ; JURASZ, 1979; HAIN et al., 1982; TRUE, 1983; TYACK, 1981; WINN; REICHLEY, 1985).

These researches gave support to an important work that characterized the morphology of the humpback whale in terms of its geometric parameters that drives its high performance in the water (FISH; BATTLE, 1995). This impressive work inspired mankind to mimic nature based on the representation of the humpback whales' flippers' tubercles in the form of wavy leading edges to aerodynamic and hydrodynamic surfaces.

Although the first work to mimic tubercle morphology applied to an aerodynamic surface showed some aerodynamic improvements using wavy leading edges (WATTS; FISH, 2001), it was with Miklosovic et al. (2004) that the potential aerodynamic gains in maximum lift, stall angle and aerodynamic efficiency effectively brought scientific interest into the understanding of wavy leading edge phenomena and its application.

The research of wavy leading edges as applications of flow control is therefore recent. Over the past twelve years, since Miklosovic et al. (2004), researchers have tried to mimic the morphological characteristics of humpback whales flipper's geometries (planform, airfoil, tubercle geometry), and, in this process, they have fully answered some of the questions regarding flow phenomena such as the soft stall behaviour in the post-stall regime provided by tubercles. On the other hand, many questions remain (some at least partially) such as the clear understanding of the flow control mechanisms and the effect of the Reynolds number and the airfoil shape on tubercle performance.

In order to clarify the state of the art in the understanding of the phenomena associated with wavy leading edges as well as to contextualize the contribution of the present work, the following subsections discuss the major discoveries in the past twelve years regard leading edge wavy research as flow control mechanism.

2.2.1 First researches: pre-stall and post stall performance

Although the investigation of Fish and Battle (1995) regarding the morphology of the humpback whale flipper is considered in this subsection in order to contextualize the first works in the field, the first researches in wavy leading edge phenomena as a flow control mechanism (WATTS; FISH, 2001; MIKLOSOVIC et al., 2004; STEIN; MURRAY, 2005; LEVSHIN et al., 2006; JOHARI et al., 2007; STANWAY, 2008; NIEROP et al., 2008) evaluated the main characteristics of the tubercle aerodynamic performance at pre-stall ($dC_L/ d\alpha$, C_{D0}) and post-stall ($C_{Lmaximum}$, α_{stall}, post stall behaviour) regimes.

Fish and Battle (1995) characterize the morphology of the humpback whale flipper highlighting the geometric parameters that determine its hydrodynamic performance. The design suggests high manoeuvrability relative to the humpback whale´s singular feeding habits. In this context, Fish and Battle (1995) analyse the tubercle characteristics and conduct a literature review of the tubercle function, suggesting that the morphology and placement of leading edge tubercles work as lift-enhancing devices to control the flow over the flipper surface and maintain to high lift values at high angles of attack. This embryonic work motivated interest in mimicking the whale's tubercles in order to improve hydrodynamic and aerodynamic performance.

Inspired by the whale's flippers' tubercles, Watts and Fish (2001) carried out studies of sinusoidal leading edges that showed some potential gain in aerodynamic and hydrodynamic efficiencies. Inviscid (a panel method) and viscous flow simulations using a NACA 63021 airfoil with finite span – an aspect ratio (AR) of 2.04 – at large Reynolds numbers were conducted. At an angle of attack of 10 degrees, the wavy shape incorporated at the leading edge increased lift by 4.8%, decreased induced drag by 10.9%, increasing the lift-to-drag ratio by 17.6%. The wavy leading edge enhanced wing performance at modest angles of attack while offering no detrimental effects at zero angle of attack. However, for a viscous calculation form drag increased 11% at $\alpha = 10^{o}$.

The first experimental study of wavy leading edge is carried out by Miklosovic et al. (2004). The NACA 0020 airfoil was used to build a scale model of the pectoral flipper of humpback whale, which was tested in a wind tunnel at the Reynolds number range of 505,000-520,000. The tests showed promising results (figure 2.18) with an increase of 40% on the stall angle and 6% in maximum lift, while decreasing drag in 32% in the post-stall

regime for the configuration with tubercles compared to the smooth flipper model. At low angles of attack, both lift and drag showed similar results compared to smooth model. Moreover, the scalloped flipper showed better lift-to-drag ratio (L/D), achieving higher performance at all angles of attack range except at $10º < \alpha < 12º$. Miklosovic et al. (2004) concluded that the scalloped leading edge of the whale flipper has the function of delaying the stall by providing higher lift at higher angles of attack. These results have been essential for the rapid increase in the interest in the study of wavy leading edge phenomena that followed.

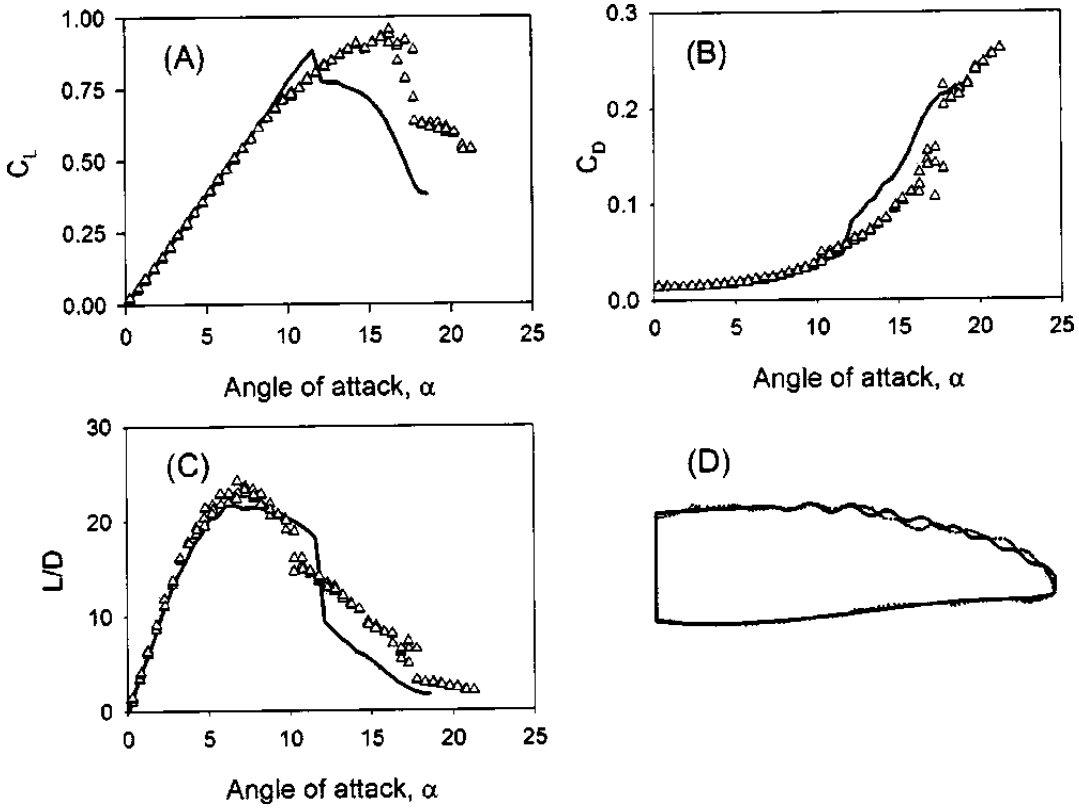

Figure 2.18: Flipper with tubercles (triangles) vs flipper without tubercles. Tubercles increasing stall angle, maximum lift and aerodynamic efficiency (MIKLOSOVIC et al., 2004).

Stein and Murray (2005) are first to carry out experimental tests with full-span models to demonstrate performance of the tubercles. The results showed a reduction in lift and increase in drag compared to the smooth airfoil. Experiments were carried out for a specific angle of attack range ($0º < \alpha < 12º$) at Reynolds number 250,000 using a full-span model with

an incorporated sinusoidal leading edge with amplitude and wavelength equal to the average values found in the humpback whale´s flippers.

Levshin et al. (2006) and Johari et al. (2007) carry out experimental tests with a full-span model to study in detail the nature of the flow imposed by wavy leading edge as well as the tubercle performance. The tests were performed in a water tunnel using a NACA 63_4021 airfoil, an airfoil similar to the humpback whale morphology, for different wavy leading edge geometries at a Reynolds number of 183,000. The results (figure 2.19) show deterioration in performance at the pre-stall with lift reduction and increased drag observed for the modified airfoil. On other hand, softer stall progression is observed and the post-stall performance advantage is reverted towards the wavy airfoil with 50% increase in lift in with little or no drag penalty.

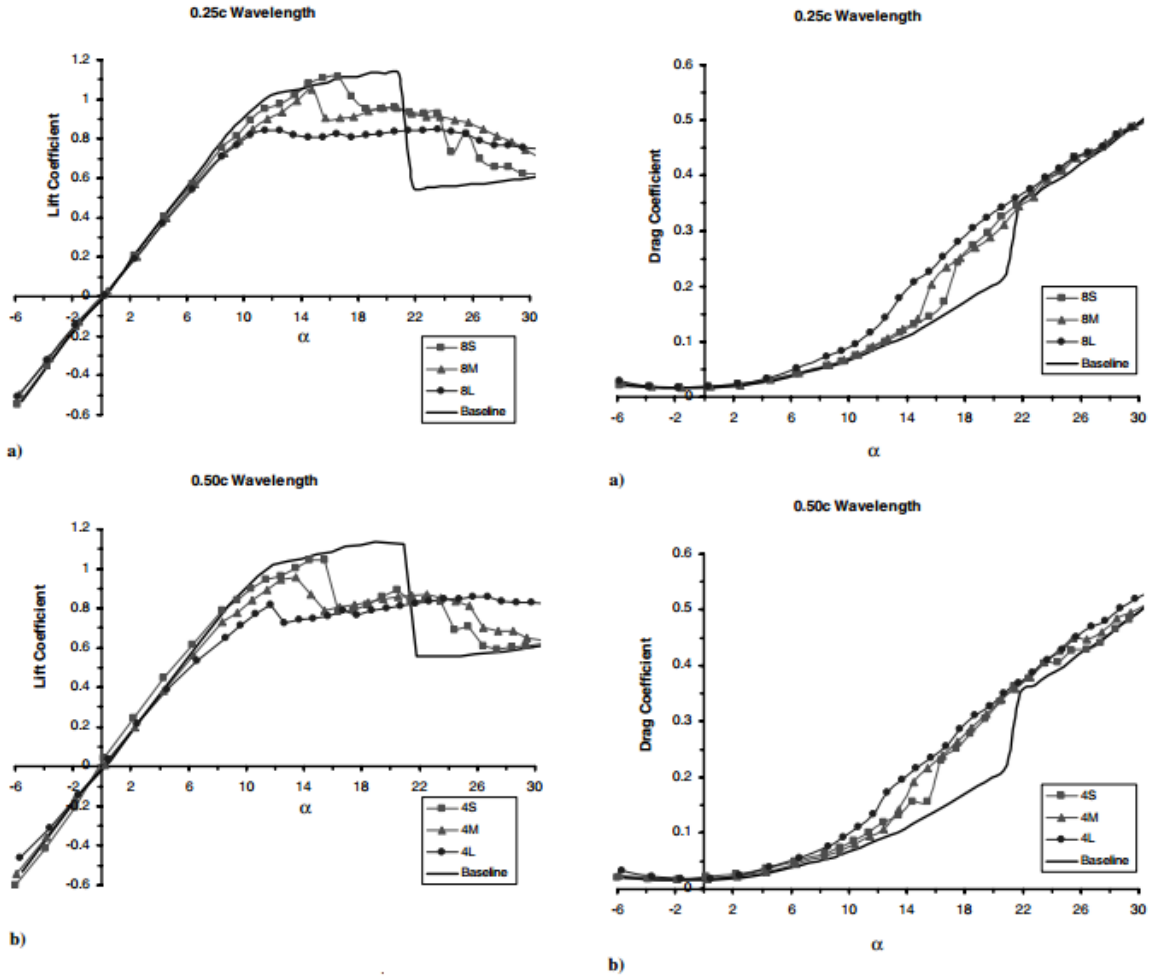

Figure 2.19: The tubercle effect on pre-stall and post stall regime for distinct wavelengths (4 for 0.5c and 8 for 0.25c) and amplitudes (S, M and L for 0.025c, 0.05c and 0.12c) (JOHARI et al., 2007).

Miklosovic et al. (2007) study the wavy leading edge effect in full-span and partial-span models. Wind tunnel tests were performed with geometries based on the NACA 0020 airfoil at Reynolds numbers between 274,000 and 277,000 for two-dimensional and from 534,000 to 631,000 for the three-dimensional geometries. The two-dimensional results show delay in the stall angle, accompanied by increased drag and decreased lift. The three-dimensional results also showed a delay in the stall angle of 5 degrees with the maximum lift increasing by 4%, however with increased drag values.

Stanway (2008) performed tests in a water tunnel with a model similar to Miklosovic et al. (2004) configuration based on the NACA 0020 airfoil, in the Reynolds number range between 44,000 and 120,000. The tubercle configuration presented softer stall characteristics and delayed stall onset at all Reynolds numbers. The maximum lift decreased in all cases except for the highest Reynolds number, while the drag polar plots show that the tubercle decreased the range of low drag coefficient (figure 2.20).

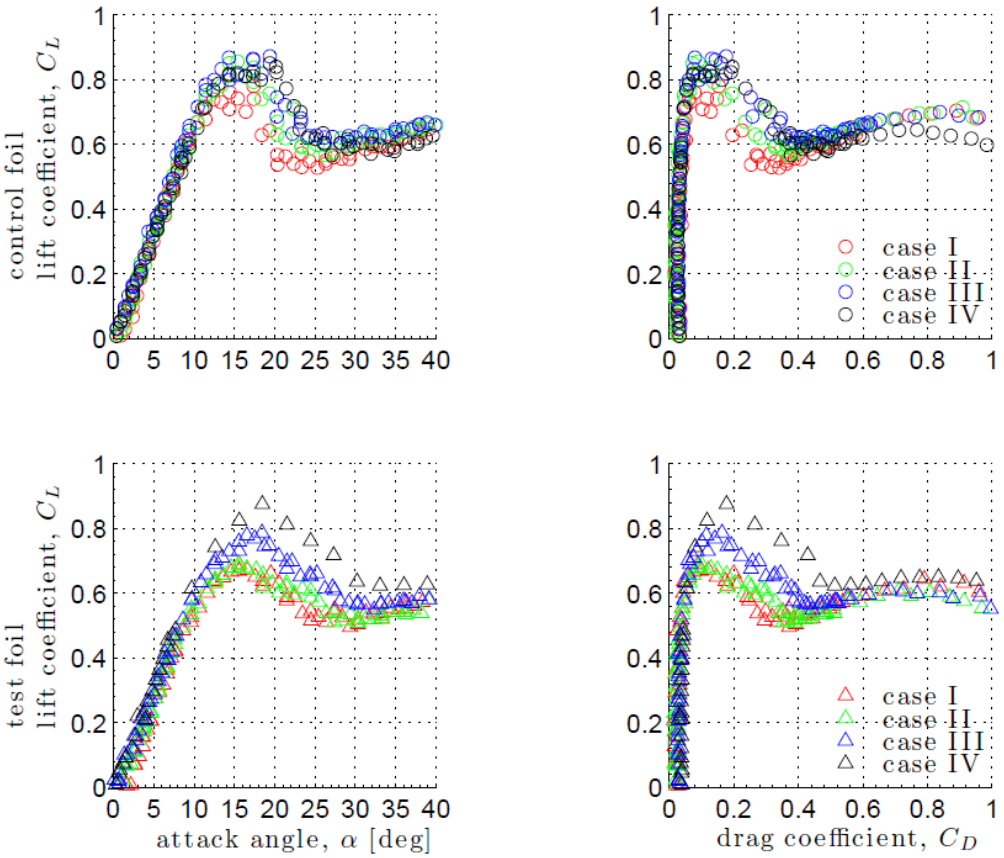

Figure 2.20: Force measurement results for smooth airfoil (circle) and wavy airfoil (triangle), presented as lift curve and drag polar. Reynolds numbers for each case were: case I: 44648, case II: 59530, case III: 89295, case IV: 119060 (STANWAY, 2008).

Although Miklosovic et al. (2004) conducted experimental investigations at a different Reynolds number regime (Re = 500,000), results showed delay in stall. However, Miklosovic et al. (2004) results present an increase in maximum lift. Stanway (2008) explains the increase in maximum lift at higher Reynolds number justifying that the tubercle effect has a dependency on the stall type. He suggests that the tubercle performance will be superior for wings with short bubble stall characteristics rather than for wings with trailing edge stall. This remarkable suggestion from Stanway (2008) is the initial motivation of this thesis.

The studies from Nierop et al. (2008) are considered significant since their theoretical model presented similar results to experimental data. They model the wavy leading edge phenomena considering that tubercle causes a cyclic variation in chord and thickness along the wing span, causing a variation in circulation which consequently generates a sheet of streamwise vortices behind the wing. Nierop et al. (2008), by using lifting-line theory and applying a smooth elliptic wing model, predicated aerodynamic characteristics at pre-stall and post-stall conditions for tubercle configurations.

2.2.2 Tubercle geometry effects

Since the first studies published on the subject, the investigation of tubercle geometry details on aerodynamic performance has instigated researchers in the quest for finding any remarkable improvements in aerodynamic efficiency due to tubercle shape. The studies have parameterized tubercle geometry in terms of wavelength (λ) and amplitude (A) parameters.

Levshin et al. (2006) and Johari et al. (2007) were the first to investigate the tubercle geometry effect on aerodynamic performance. Geometric variation investigations of wavy leading edges were performed for amplitudes ranging from 2.5% to 12% and wavelengths from 25% to 50%, all relative to the mean chord length. These ranges of tubercle geometry variations represent typical values found in the humpback whales' flippers' morphology.

Results (figure 2.19) show that amplitude variation had a great effect on the wavy leading edge performance. For the configuration with wavelength of 25%, for the smallest amplitude at pre-stall conditions, the lift curve shows a tendency to follow the baseline airfoil characteristics up to its stall angle (α_{stall} = 17°). Moreover, the smallest amplitude

configuration has much softer stall characteristics than the smooth airfoil, with only a small drop in lift coefficient after stall angle.

On the other hand, for the largest tubercle amplitude the pre-stall and post-stall characteristics are quite different than the smallest amplitude configuration. The largest amplitude decreases the stall angle (α = 10º) compared to smallest amplitude, and the lift coefficient remains constant up to α = 26º. The lift curve slope on the linear range decreases with an increase in amplitude.

In terms of drag coefficient, all wavy leading edge configurations have values close to the smooth configuration at low angles of attack. After that, the drag curves follow the stall onset characteristics for each configuration, increasing drag values as compared to the baseline airfoil. For α > 22°, the drag coefficients are similar to the smooth configuration. The largest amplitude show the highest drag values for entire angle of attack range. The amplitude effect in lift and drag for the wavelength 50%c is similar to the wavelength 25%c.

If on the one hand the wavy leading edge amplitude has a remarkable influence on the airfoil's aerodynamic characteristics, on the other hand the wavelength variation seems to have a smaller influence. However, airfoils with shorter wavelengths delay the stall onset and have slightly more lift and less drag in the post-stall regime. In addition, the longer wavelength configurations present a noticeable, albeit small increase in lift at pre-stall conditions.

Hansen et al. (2009) carried out experimental tests of full-span models to investigate the variation effect of amplitude (6%c to 11%c) and wavelength (21%c to 86%c) for NACA 0021 airfoils at Reynolds number 120,000 (figure 2.21). In the pre-stall range, the smallest amplitude (6%c) at 43%c wavelength reaches larger C_{Lmax} and a higher maximum stall angle among wavy airfoils. In Addition, decreasing amplitude, for the symmetrical airfoil, increases the lift in the second linear range on lift curve. In the post stall regime, the larger amplitude reaches smoother stall characteristics.

With regard to drag characteristics, at lower angles of attack (α < 8º), the drag values are roughly similar for different amplitudes. At intermediate angles of attack (8º < α < 15º), the smallest amplitude reaches lower drag coefficients, and for α > 15º the largest amplitude configuration shows a lower drag coefficient.

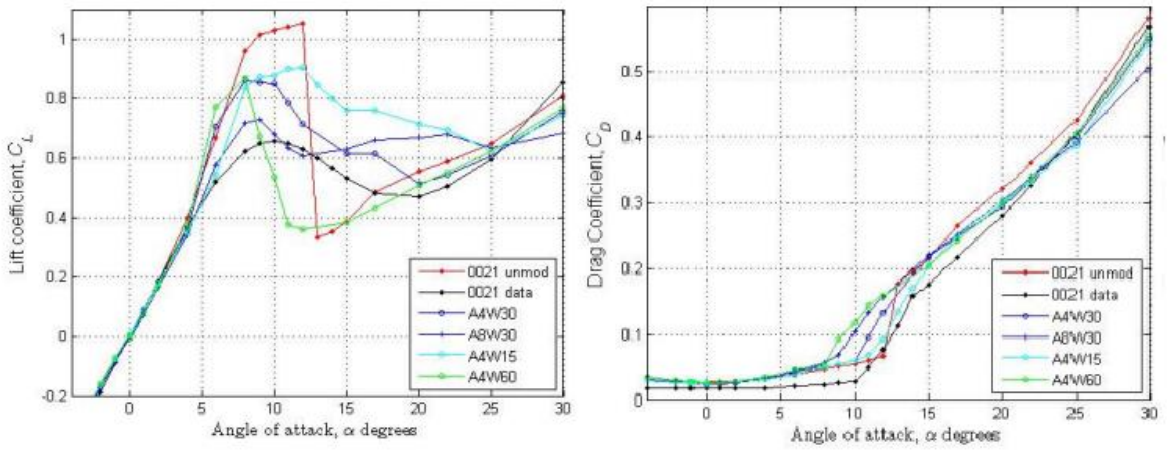

Figure 2.21: Tubercle geometry effect at pre-stall and post-stall conditions for distinct wavelengths (15 for 0.21c, 30 for 0.43c and 60 for 0.86c) and amplitudes (4 for 0.06c and 8 for 0.11c) (HANSEN et al., 2009).

At pre-stall conditions, increasing the wavelength causes an increase in the lift slope; on the other hand, at post-stall conditions for longer wavelengths the stall angle decreases, and loss of lift is substantially amplified.

Although Hansen et al. (2009) says that the wavelength reduction appears to have more advantage than reduction in amplitude when one considers the achieving of both higher C_{Lmax} and desirable post-stall characteristics, the amplitude effect is more effective to reach higher maximum lift.

At lower angles of attack, the effect of wavelength variation on drag is negligible. In addition, for decreasing wavelength, the drag decreases at intermediate angles of attack (between 8º and 15º), and at $\alpha > 15º$, the longer wavelength reaches only slightly lower drag coefficient.

Most researches in wavy leading edge performance focus on thick airfoils (around 20%c). Chen et al. (2012) show interesting experimental results for a thinner airfoil (NACA 0012). Tests were carried out to evaluate the effect of wavy leading edge shape and aspect ratio on aerodynamic performance of wings. Regarding tubercle shape, three wavy leading edge configurations are tested with amplitudes 0.05c, 0.1c and 0.15c for the same wavelength (λ=0.25c) at Reynolds number 123,000.

Results from figure 2.22, for the largest aspect ratio (AR=3), show that the lift curve for the smallest amplitude configuration has a similar behaviour to the smooth airfoil up to α =13 º, and delays the stall angle by 6 degrees. At the pre-stall condition, increasing tubercle amplitude results in increased aerodynamic deterioration. In the post stall regime, increasing the amplitude a characteristic stall angle tend to disappear. All wavy leading edge configurations reach similar maximum lift, all lower than the smooth configuration (ΔC_{Lmax} = -14%). In terms of aerodynamic efficiency, all wavy configurations have better L/D for angles of attack above the stall angle for smooth configuration. In addition, the larger amplitude reaches the highest value of maximum aerodynamic efficiency (L/D).

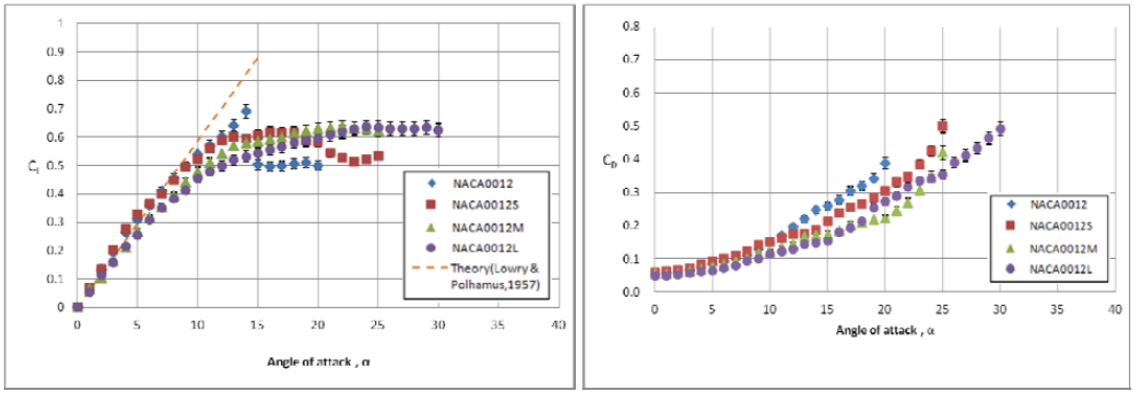

Lift and drag coefficients at various attack angles (AR=3)

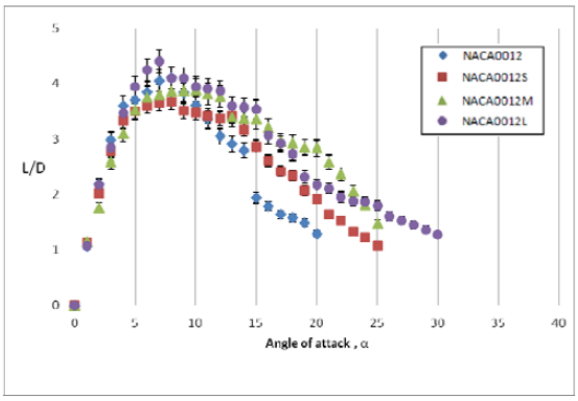

Lift-to-drag ratio at various attack angles (AR=3)

Figure 2.22: Tubercle geometry effect on aerodynamic performance for λ=0.25c and amplitudes S=0.05c, M=0.1c and L=0.15c (CHEN et al., 2012).

At lower angles of attack, the drag coefficients are similar to the smooth configuration with the largest amplitude achieving the lowest drag values. For α > 10º, the smooth

configuration has higher drag coefficient than wavy leading edge configurations, and the drag decreases with increasing amplitude.

In general, Levshin et al. (2006), Johari et al. (2007), Hansen et al. (2009) and Chen et al. (2012) present similar results altogether where the larger amplitude configurations cause greater aerodynamic deterioration and achieving lower maximum lift values. On the other hand, the tubercle wavelength effect has a smaller overall effect, however it influences the characteristics in the post-stall region.

2.2.3 Tubercles on wings

A distinct wavy leading edge performance for finite wings can be expected in comparison to the infinite wing, due to the differences in geometry and flow conditions. An infinite span wing, unlike a partial span model, has a unique local Reynolds number, sweep angle, thickness and camber. In addition, there is not wing tip phenomenon which changes the pressure coefficient along span, and as consequence the adverse pressure gradients. These differences on the flow over finite and infinite span geometries cause differences in tubercle performance, which has motivated several works, in order to investigate the influence of flow three-dimensionality on wavy leading edge performance.

Miklosovic et al. (2007) claim that the effect of wavy leading edges on aerodynamic characteristics for finite and infinite span wings is remarkably different, even though the flow mechanism produced by the tubercles is similar.

At pre-stall conditions, results for both full-span (infinite wing) and partial span (finite wing) models show similar behaviour, following the trend of the smooth configuration at lower angles of attack. For higher angles of attack up to the stall, the full-span model shows significant aerodynamic deterioration, with substantial decrease in maximum lift. In the case of the partial-model, only a small penalty occurs up to the stall angle, with the configuration overcoming the maximum lift of the smooth airfoil. In the post-stall regime, the full-span model presents softer stall characteristics when compared to the partial span model (figure 2.23).

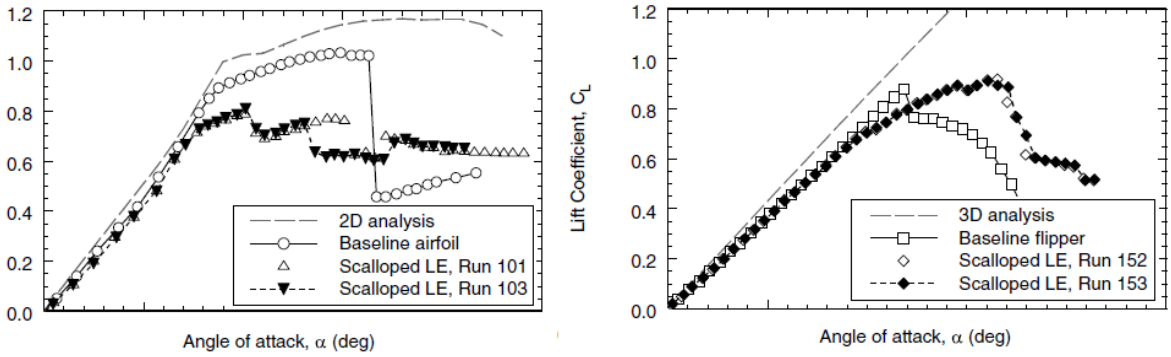

Figure 2.23: Three-dimensional effect on wavy leading edge performance (MIKLOSOVIC et al., 2007).

Miklosovic et al. (2007) explain that the vortices induced by the wavy Leading edge reduced the performance of the full-span model by triggering early flow separation. On other hand, the higher Reynolds number condition and the planform shape of the partial span model established favorable conditions that contained the spanwise stall progression. Despite tubercle performance differences between full-span and partial span results being justified by a combination of effects, Stanway (2008), as previously mentioned, affirms that the Reynolds number has a strong impact on wavy leading edge performance as a consequence of change in stall type. Thus, it is important to carry out experiments that isolate the effect of Reynolds number in order to correctly identify the effects of flow three-dimensionality.

Guerreiro (2010) carried out experimental investigations in order to evaluate the effect of the wing planform in wavy leading edge performance. Models using the NASA LS(1)-0417 airfoil with different aspect ratios (AR = 1 and 1.5) and sweep angles (0º,15º and 30º) at Reynolds numbers between 70,000 and 140,000. Amplitude of L=0.12c and S=0.06c and wavelengths of L=0.5c and S=0.25c were tested.

At moderate Reynolds numbers, the wing with lower aspect ratio (AR=1 (B1)) does not improve its post-stall as aerodynamic performance with the introduction of a wavy leading edge as in previous works (figure 2.24). This is due to the absence of sharp stall behaviour on wing with smooth leading edge. This characteristic can be typically found in low aspect ratio wings (TORRES; MUELLER, 2001, 2004), thus not being an efficient geometry for a wavy leading edge performance. The wavy configurations have slightly lower lift values than smooth configuration up to $\alpha = 20º$ (“fake stall”). The configuration LL (A=0.12c, λ =0.25c) shows optimum performance.

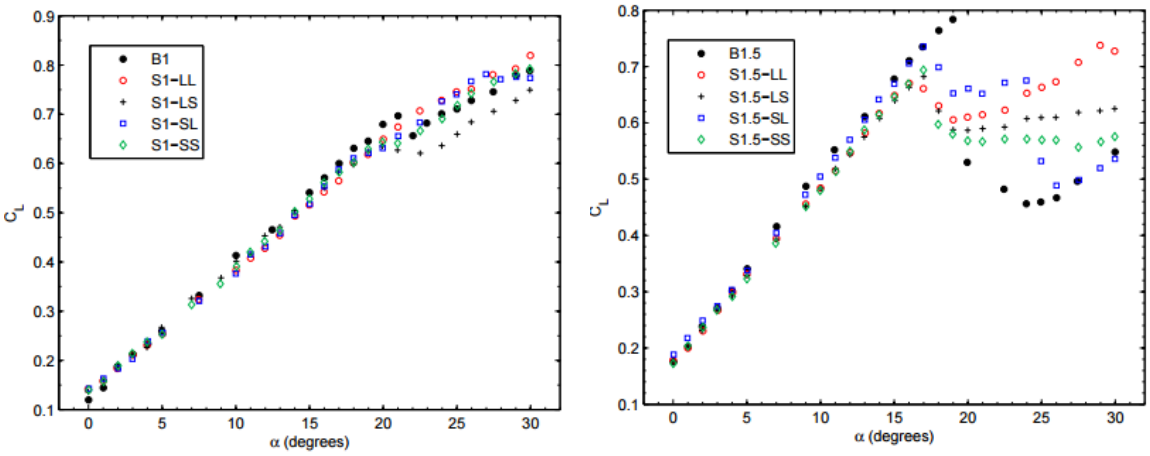

Figure 2.24: Wavy leading edge effect for distinct aspect ratio (B1 and S1 = 1.0; B1.5 and S1.5 = 1.5) at Re = 140,000 (GUERREIRO, 2010).

In contrast with the stall characteristics for lower aspect ratio observed at AR = 1 (B1), the smooth wing with AR =1.5 (B1.5) shows an abrupt stall behaviour with a lift drop of 32% after stall.

In this case, the wavy leading edge wings presented benefits in the post-stall regime with soft stall characteristics, and maintaining higher lift coefficients than smooth configuration. The wavy configurations undergo significant deterioration on maximum lift compared to the smooth leading edge. The configuration SL reaches the highest maximum lift. However, the highest lift values among wavy configurations are obtained for the largest amplitude and longer wavelength past the stall angle. There is a loss in lift in the pre-stall regime similar to the geometry with aspect ratio 1.0 for all wavy configurations.

At the lower Reynolds number (figure 2.25), the wings with aspect ratio of 1.0 present higher performance for all wavy leading edge configurations in the entire angle of attack range, being worth of notice that a classical stall is absent in all configurations. In the case of AR =1.5, there is an improvement in performance up to $\alpha = 9\ °$. Beyond that, the smooth airfoil retains higher lift values up to the stall. However, in the case of the low Reynolds number the wavy configurations reach similar maximum lift compared to the baseline configuration.

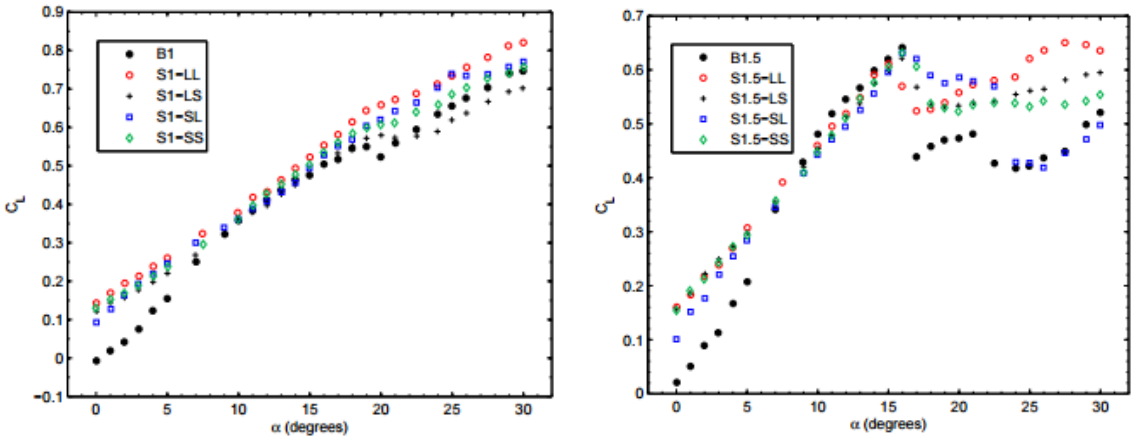

Figure 2.25: Wavy leading edge effect for distinct aspect ratio (B1 and S1 = 1.0; B1.5 and S1.5 = 1.5) at Re = 70,000 (GUERREIRO, 2010).

Hansen (2010), in order to distinguish possible benefits from Reynolds number effects from those arising from flow three-dimensionality, evaluated various wavy leading edges geometries for full and half-span models with NACA 0021 airfoils without sweep nor taper. The tests are performed at a Reynolds number of 120,000 for a range of amplitudes and wavelengths of 3%c to 11%c and 11%c to 86%c respectively. It was observed that wavy leading edge performance for full-span and half-models is similar, in contrast with results from Miklosovic et al. (2007). In addition, in both models the optimum configuration was reached by the configuration wavy leading edge with the smallest amplitude and shortest wavelength. Hansen (2010) suggests that the wavy leading edge could increase the performance in wings with sweep and/or taper due to the fact that these geometries carry significantly more spanwise flow.

Custodio et al. (2012) conducted the most comprehensive study of finite-span airfoil effect on wavy leading edge performance to date. Experimental tests with partial span and full-span models with NACA 63_4021 airfoils were conducted. Four different planform geometries were used: full-span rectangular, partial span rectangular (AR=2.15) with sweep (AR=2.0, Λ=26º), and a model representative of a humpback whale's flipper (AR=4.43). The geometrical effect on tubercle performance was evaluated specifically at the Reynolds number of 450,000 due to previous analyses showing that this effect was not sensitive to Reynolds number.

In terms of lift values, considering the full-span rectangular airfoil results from Custodio et al. (2012) and Johari et al. (2007), the maximum lift and stall angle for wavy

leading edge configurations are lower than smooth airfoil for all tubercle geometries. At pre-stall conditions, wavy airfoils have similar behaviour than the baseline airfoil in the linear region. However, the wavy leading edge configurations have a soft post-stall behaviour whereas the smooth configuration shows abrupt stall characteristics.

Experimental tests for partial span rectangular wings show an increase of 18% in maximum lift for the optimum wavy configuration (λ=25%, A=2.5%) when compared to the smooth airfoil. The wavy leading edge affects the lift curve slope similarly to the full span model. However, the effect of tubercles in the post-stall regime is opposite from two-dimensional tests: the sinusoidal leading edge configuration established an abrupt stall for the partial span model, in contrast with a soft stall for the full span model.

The partial span swept airfoil, at lower angles of attack ($\alpha < 6º$) for smooth and λ=50%, A=12% wavy configurations have a similar linear behaviour on lift curve. For higher angles of attack, the smooth configuration keeps the linear behaviour until an abrupt stall occurs at $\alpha = 26º$. The wavy configuration keeps linear characteristics but with a decrease in the lift curve slope. In addition, the wavy configuration has a slightly higher maximum lift coefficient than smooth configuration, also not showing a remarkable stall.

The results from the flipper model show, at lower angles of attack ($\alpha < 8º$), no differences for wavy configuration relative to the baseline. After that, the tubercle causes a decrease in the lift slope up to stall. The wave leading edge configuration has a slightly increase in the stall angle as well as in the maximum lift coefficient. At post-stall, both configurations have an abrupt stall with the wavy configuration keeping higher lift values.

Regarding drag coefficient values, all tested models had similar characteristics where, at lower angles of attack, the wavy leading edge configurations did not cause substantial changes in drag. On other hand, at higher angles of attack, the wavy airfoils showed higher drag values than the smooth configuration. The aerodynamic efficiency was thus reduced for entire angle of attack range for all wavy models tested.

Chen et al. (2012) show that the effect of aspect ratio on wavy leading edge performance is minimum. The same tendencies are noticed for AR = 1, 2 and 3. The only effect is the increase in stall angle with decreasing aspect ratios.

2.2.4 Reynolds number effects

Although the tubercle effect seems favorable in improving the humpback whales performance, it is necessary to evaluate the flow conditions in which tubercles may work effectively. Thus, the Reynolds number condition appears as a fundamental flow parameter that potentially drives the tubercle performance. The Reynolds number determines the momentum level on the boundary layer over the surface of an airfoil. It seems reasonable that the changes caused by a wavy leading edge on aerodynamic characteristics of an airfoil will depend on momentum level imposed on the boundary layer by the tubercles. Some works have investigated the Reynolds number effects on wavy leading edge performance.

Stanway (2008) was the first to carry out tests to evaluate the Reynolds number effects on wavy leading edge performance. His study was conducted at a critical Reynolds number range (Re = 44,000 to 120,000) where the onset of formation of laminar separation bubble occurs (CARMICHAEL, 1981). The scale effect seems more important for the Higher Reynolds number end (figure 2.20).

The wavy leading edge configurations follow the linear curve of the smooth configuration up to $\alpha = 6$ °. After that, a second linear segment goes up to stall onset having a decrease in slope. The reduction in slope increases with decreasing in Reynolds number. For higher Reynolds number (89,295 and 119,060), the tubercles are more effective in delaying the stall onset, even though the maximum lift decreases in all cases except for the highest Reynolds number as mentioned previously.

Custodio et al. (2012), aside from studying three-dimensional effects on wavy leading edge performance, also evaluated the Reynolds number effects for a full span model within the same investigation. The wavy leading edge configuration with amplitude and wavelength respectively of 12%c and 50%c was tested in a range of Reynolds numbers between 90,000 and 450,000.

The results (figure 2.26) show that at all Reynolds number conditions the maximum lift and stall angle for wavy leading edge configuration are lower than for the smooth airfoil. At pre-stall conditions, wavy airfoils follow the linear trend of the lift curve from smooth configuration with a slight decrease in slope up to $\alpha = 7$º. After that, all wavy configurations

undergo a second decrease in slope where at the lowest Reynolds number condition the slope eventually flattens until the stall finally takes place.

In the post-stall regime, for all Reynolds number conditions, the wavy leading edge configurations do not present an abrupt stall as the smooth airfoil. The wavy configuration at the lowest Reynolds number increases linearly lift with angle of attack whereas, at higher Reynolds number conditions, lift is nearly constantly increases with Reynolds number.

In terms of drag, the wavy leading edge performance shows not to be sensitive to Reynolds number variation except at Reynolds number 90,000 where drag values significantly increase in the range $7º < \alpha < 15º$.

Dropkin (2012) carries out numerical simulations to evaluate Reynolds number effects on wavy leading edge performance for an infinite span geometry for a NACA 63_4021 airfoil with A = 12%c and λ = 50%c. The large spectrum of Reynolds numbers between 180,000 and 3,000,000 shows similar behaviour where the tubercles decrease substantially the maximum lift presenting no well-defined stall conditions, and increasing lift with angle of attack. The lift coefficient increases with Reynolds number for the wavy leading edge configuration, even though the dependency is less sensitive than for smooth airfoil, and the maximum lift is similar for all conditions of Reynolds number.

Custodio et al. (2015), continuing their previous experimental work (CUSTODIO et al., 2012), evaluate the Reynolds number effects for wavy leading edge performance for a rectangular planform model testing six tubercle geometries (A= 2.5%c [S], 5%c [M], 12%c [L]; λ = 25%c [8], 50%c [4]) at a range of Reynolds numbers between 90,000 and 450,000.

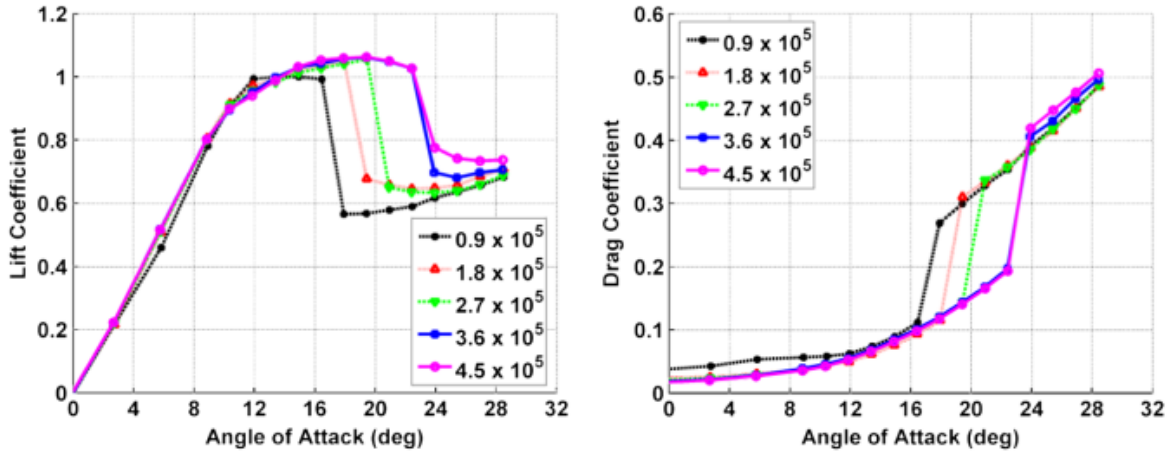

Smooth configuration

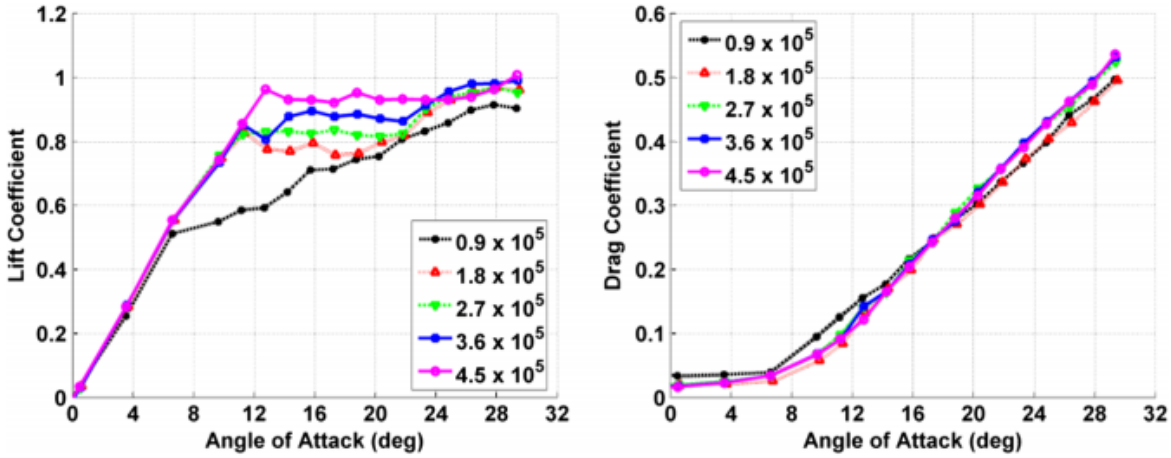

Wavy configuration

Figure 2.26: The Reynolds number effects on smooth and wavy full span models for tubercle geometry with A= 12%c and λ = 50%c (CUSTODIO et al., 2012).

The results in figure 2.27 show that in the linear regime, the effect of Reynolds number seems not to be major for all tubercle configurations, except for the lowest Reynolds number condition (Re = 90,000). However, for angles of attack outside the linear regime, the wavy leading edge performance presents a clear dependency on Reynolds number up to 360,000. The results show that the aerodynamic deterioration caused by decreasing the Reynolds number intensifies with increasing amplitudes and decreasing wavelengths.

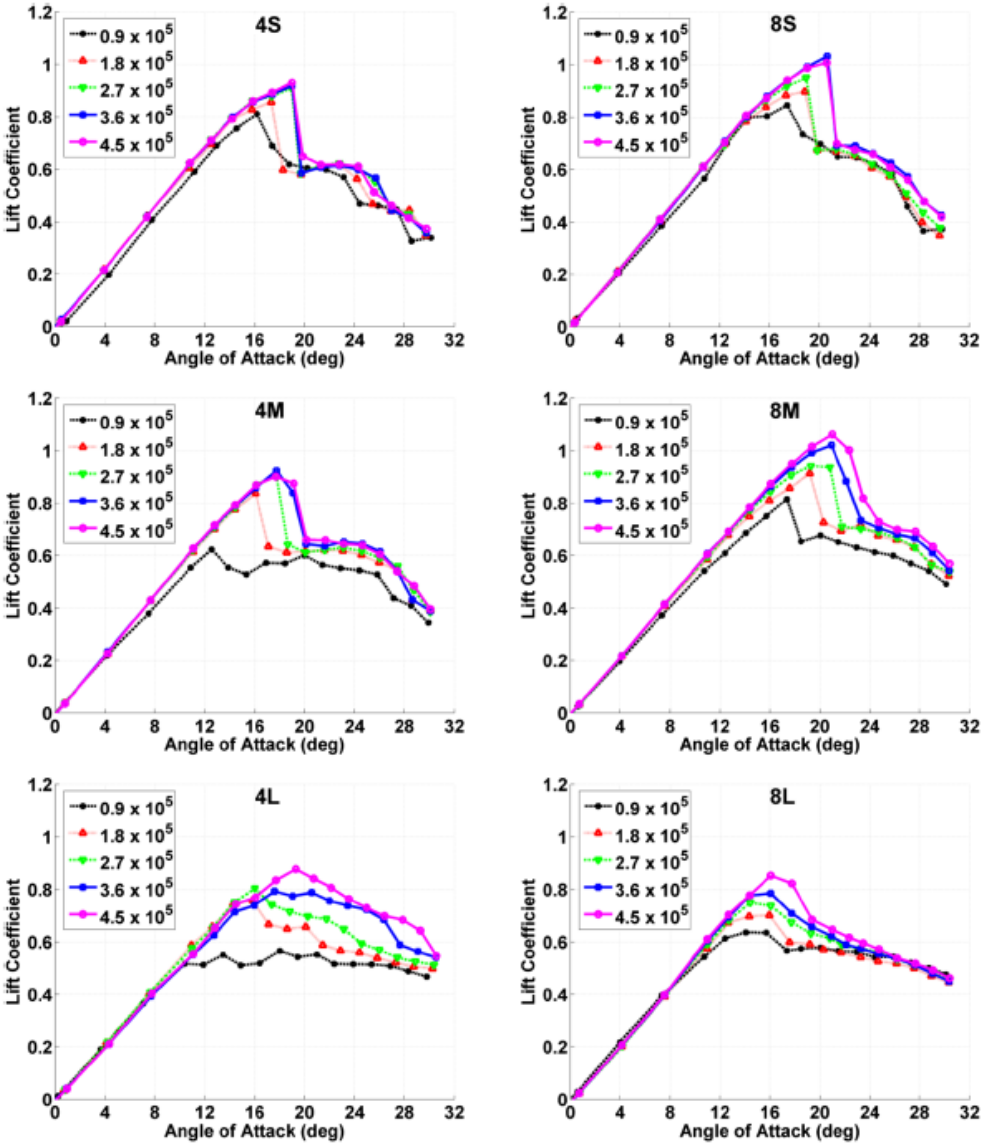

Figure 2.27: The Reynolds number effects on smooth and wavy rectangular partial span models with AR = 4.3 (CUSTODIO et al., 2015).

2.2.5 Airfoil geometry variation

The airfoil geometry is supposed to have influence on wavy leading edge performance since, not unlike the influence of Reynolds number, the leading edge geometry determines the boundary layer conditions over the airfoil's upper surface by the means of an adverse pressure gradient. In addition, the combination of amplitude and wavelength tubercles with airfoil

geometry determines the overall geometric variation on the critical area of the leading edge. However, there are few studies that consider airfoils outside the morphologic limits of the humpback of whales' flippers. In addition, there is only a single study regarding the effect of airfoil geometry on wavy leading edge phenomena.

Hansen et al. (2009) carried out, for the first time, systematic experimental investigations in order to assess the dependency of airfoil geometry on wavy leading edge performance. Tests on the airfoils NACA 0021 and NACA 65021 were conducted at a Reynolds number of 120,000.

The results (figure 2.28) show that the wavy leading edge geometries reach maximum lift values similar to the smooth configuration for the cambered airfoil (NACA 65021) whereas the symmetrical airfoil suffers a deterioration in maximum lift. Both airfoils maintain higher lift values past the stall angle with softer stall characteristics. At pre-stall, the cambered and symmetrical wavy airfoils presented similar characteristics to smooth configuration.

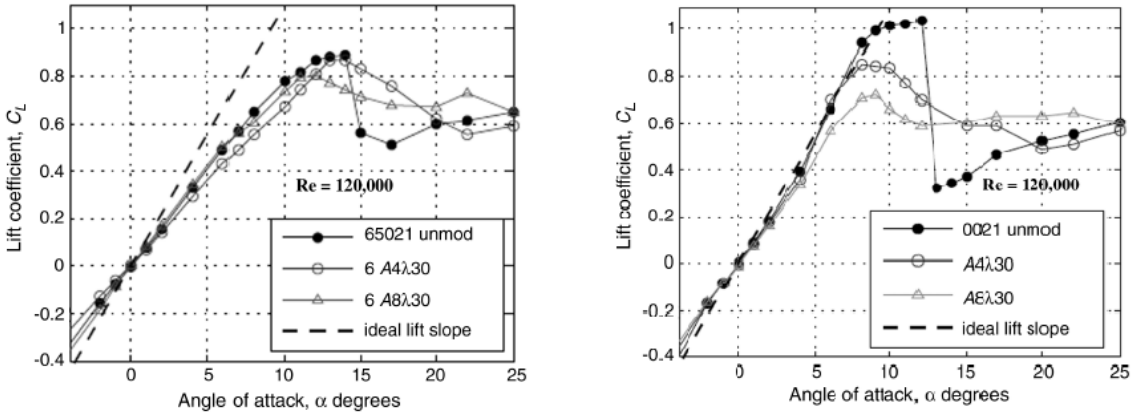

Figure 2.28: Tubercles effect on lift curve for NACA 0021 and NACA 65021 (HANSEN et al., 2011).

2.2.6 Flow topology

Although the first researchers focused their studies in evaluating the aerodynamic performance of tubercles, studies of flow topology have been of increasing interest in order to understand the changes in flow caused by tubercles and its consequence on performance as well as in the understanding of the flow control mechanisms involved.

Fish and Watts (2001), having performed non-viscous numerical simulation, identified lower pressure regions between tubercles rather than behind their peaks. In addition, the leading edge region shows substantial variations in pressure intensity when compared to a plain leading edge. The streamlines become closer between tubercles, indicating higher velocities in these regions. This study supports hypothesis from Fish and Battle (1995) that tubercles channel the flow, creating regions of higher velocities (figure 2.29).

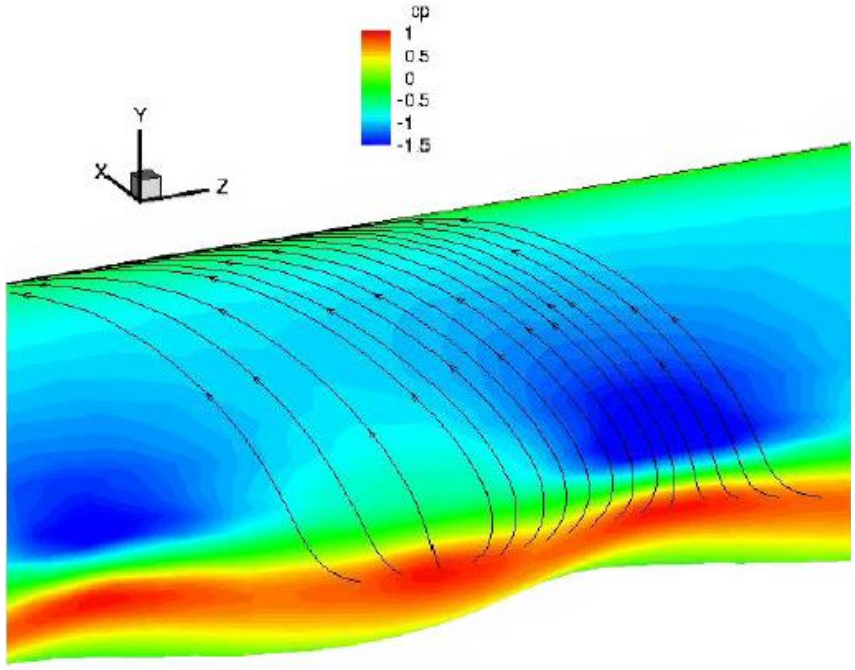

Figure 2.29: Streamlines outside of the boundary layer yet near the surface (FISH; WATTS, 2001).

Paterson et al. (2003) conducted unsteady Reynolds-averaged Navier-Stokes (RANS) simulations in order to evaluate changes caused on flow over an NACA 63021 airfoil due to tubercles present at the leading edge. The results show that the tubercles cause flow separation, generating vorticity on troughs in chord-wise direction, increasing velocity downstream of the tubercles´ peaks which in turn locally reduces the adverse pressure gradient. Thus, flow separation in peak regions is delayed while in trough regions the separation flow seems to be anticipated.

Paterson et al. (2003) bring the first work that supported the idea of momentum exchange between peaks and troughs of the tubercles by the means of vortices generated which effectively act as a flow control mechanism (figure 2.30). The introduction of viscous

flow considerations in this study lead to different results from Fish and Battle (1995) and Fish and Watts (2001), where vortices generated at troughs that increased velocity downstream of the tubercle peaks were found.

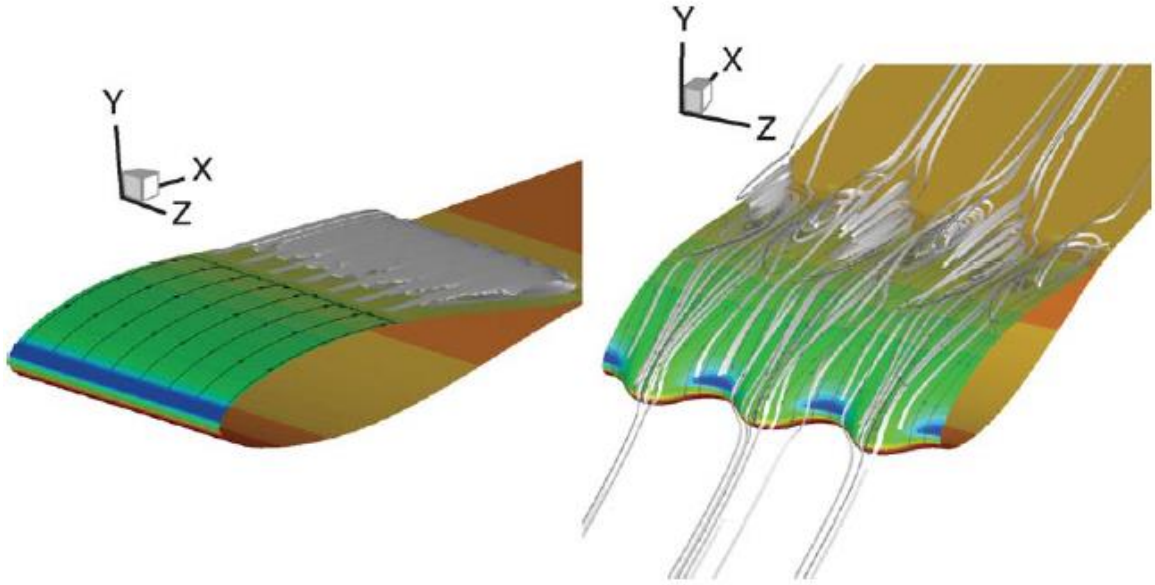

Figure 2.30: Pressure contours and streamlines at α =10◦ for NACA 63–021 with straight leading edge (left) and with tubercles (right) (PATERSON et al., 2003).

Levshin et al. (2006) and Johari et al. (2007) were the first to carry out flow visualizations. In order to understand the wavy leading edge phenomena, they used the mini-tuffs technique for flow visualization.

In the pre-stall regime ($\alpha = 12°$), figure 2.31 indicates that the smooth configuration has the flow attached over the first three-quarters of the airfoil, showing an onset of trailing edge flow separation which justifies a substantial decrease in the lift curve slope on figure 2.19. On the other hand, the wavy leading edge configurations show that at least half of the airfoil has detached flow. In addition, the flow separation is irregular and cyclic. The results of this work show that flow separation initially occurs at troughs between tubercles, confirming the tendency from Paterson et al. (2003). The largest amplitude configuration highlights this flow characteristic.

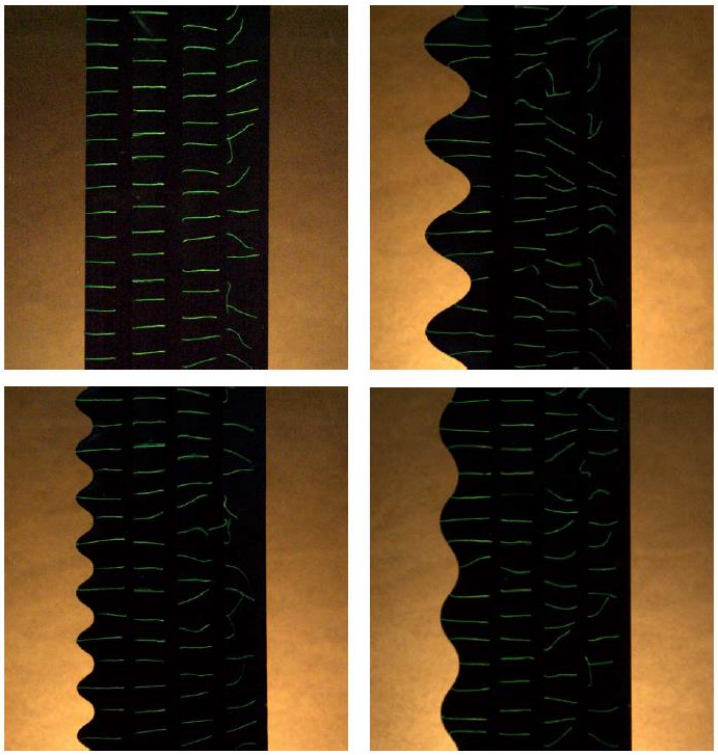

Figure 2.31: Photographs of airfoils at 12° angle of attack. Clockwise from top left: baseline, 4L, 4M, 8M (JOHARI et al., 2007).

In the post-stall regime (α = 24°), figure 2.32 shows the flow over the entire smooth airfoil detached. In contrast, the wavy configurations keep the flow attached locally in the leading edge region.

The numerical simulations carried out by Pedro and Kobayshi (2008) at a Reynolds number of 500,000 using a similar model from Miklosovic et al. (2004) contributed to the understanding of the flow changes due to tubercles in a whale´s pectoral flipper.

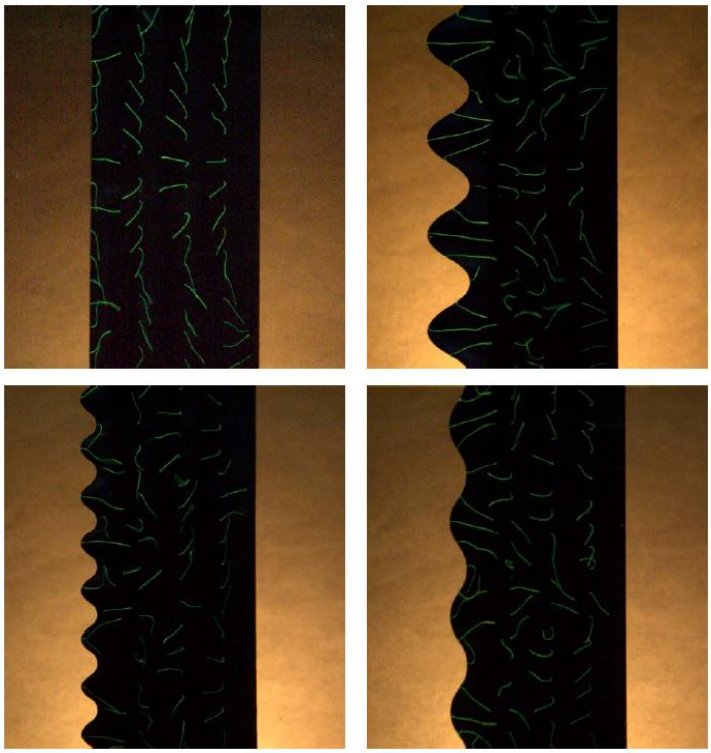

Figure 2.32: Photographs of airfoils at 24° angle of attack. Clockwise from top left: baseline, 4L, 4M, 8M (JOHARI et al., 2007).

The results show distinct stall behaviour for outboard and inboard spanwise positions of the flipper for smooth and tubercles configurations (figure 2.33-34). These characteristics are justified due to different Reynolds number regime at the outboard (Re < 200,000) and inboard (Re > 500,000) regions of the flipper.

The visualization of the averaged shear stress streaklines show that near the wing tip's leading edge flow detachment occurs whereas in the region near the wing root the detachment occurs at the trailing edge. Increasing angle of attack, the detachment is propagated towards the flipper´s root. The tubercles on the flipper´s outboard sections prevent that the propagation of the leading edge stall towards the root. On other hand, in the inboard region, the tubercles generate vortices which add momentum into the boundary layer, delaying the trailing-edge separation.

It can be therefore seen that tubercle effects are different for inboard and outboard regions and the global effect is dependent on Reynolds number, aspect and taper ratios as pointed out by Miklosovic et al. (2007).

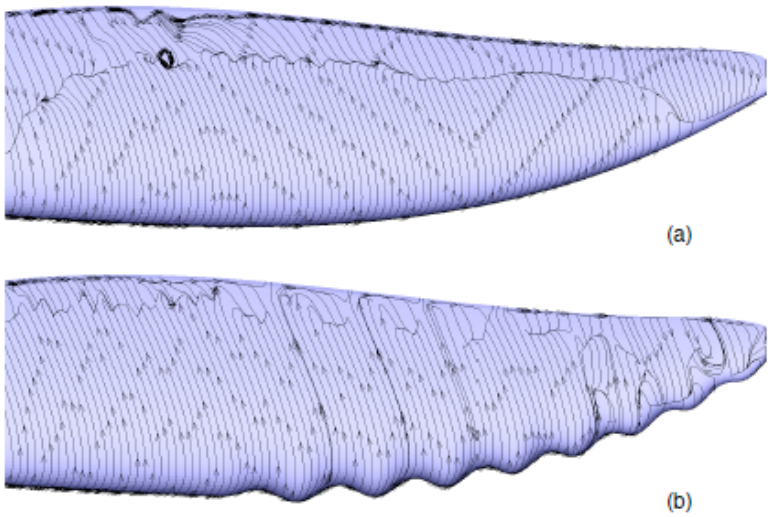

Figure 2.33: Averaged shear stress streaklines for alpha= 12.5°.(a) Scalloped flipper, (b) smooth flipper (PEDRO; KOBAYSHI, 2008).

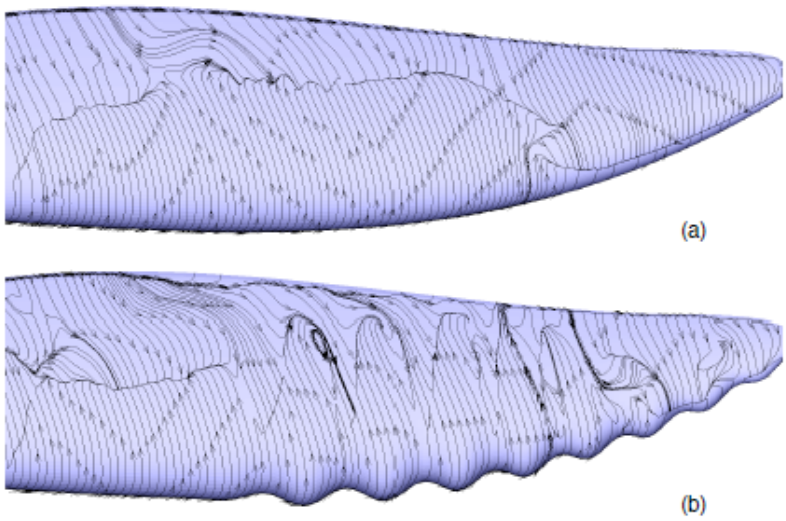

Figure 2.34: Averaged shear stress streak-lines for alpha= 15°.(a) Scalloped flipper, (b) smooth flipper (PEDRO; KOBAYASHI 2008).

Stanway (2008), for first time, carried out flow visualizations using PIV (Particle Image Velocimetry) in order to understand the wavy leading edge phenomena. The velocity field results show changes caused by wavy leading edge, at Reynolds number 89,000, for distinct angles of attack (figure 2.35). Remarkable changes were observed at higher angles of attack (14º and 18º).

At α = 14º, the smooth configuration has a large region along span of low velocity that comes from the flipper´s tip, indicating flow separation. In contrast, the wavy leading edge configuration has a smaller region of fully separated flow confined near the tip. Moreover, the inboard area presents some low velocity cells downstream of the troughs.

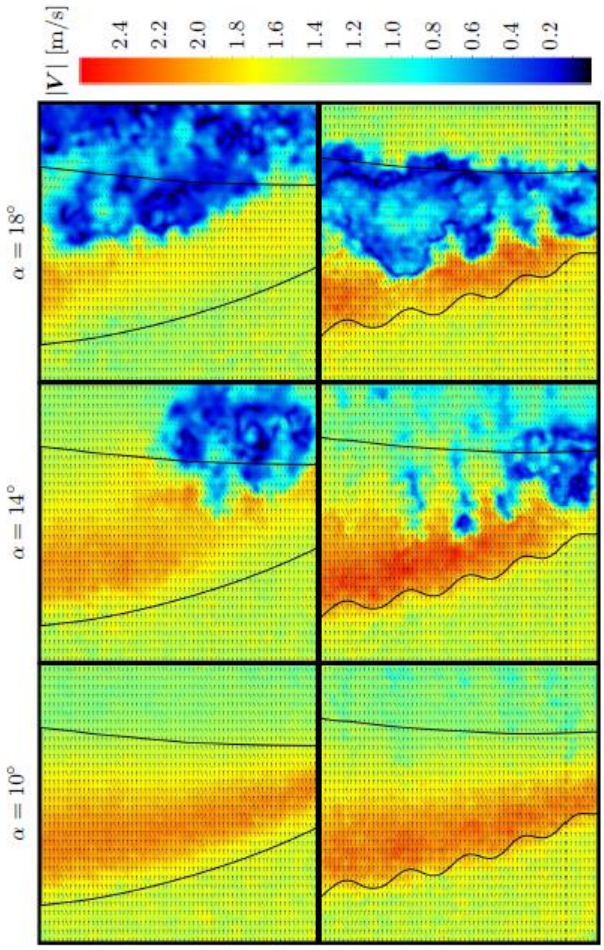

Figure 2.35: Comparison of representative instantaneous velocity fields at α = 10◦, 14◦, 18◦. Control airfoil is in the top row, and test airfoil in the bottom row. Areas in blue represent lower velocities, indicating flow separation and stall (STANWAY, 2008).

Near the stall angle (α = 18º), the rear half of the smooth model presents flow separation characterizing the progression of a typical trailing edge stall. On the other hand, the wavy configuration maintains the low velocity cells along the span, covering downstream of half-chord in the model. The flow downstream of the peaks remains attached longer, contributing to guarantee lift. The results agree with investigation from Pedro and Kobayashi (2008).

Zeverkov et al. (2008) is the first to carry out oil flow visualizations in order to investigate the tubercle effect on aerodynamic characteristics of a wing. Figure 2.36 shows that, for Re < 200,000, that flow topology is quite different for a wing equipped with a wavy leading edge when compared to a smooth configuration. The baseline configuration presents a long laminar separation bubble near the stall angle (α =15°). After that, a stall condition characterized by full separation at the leading edge is observed. On the hand, the wavy configuration at α =20° presents three-dimensional laminar bubbles downstream of the troughs while the flow is kept attached downstream of the peaks, justifying a delay in the leading edge stall. In addition, measurements were performed in order to obtain the velocity profiles of the boundary layer. Based on these results, an early laminar-turbulent transition at troughs was observed.

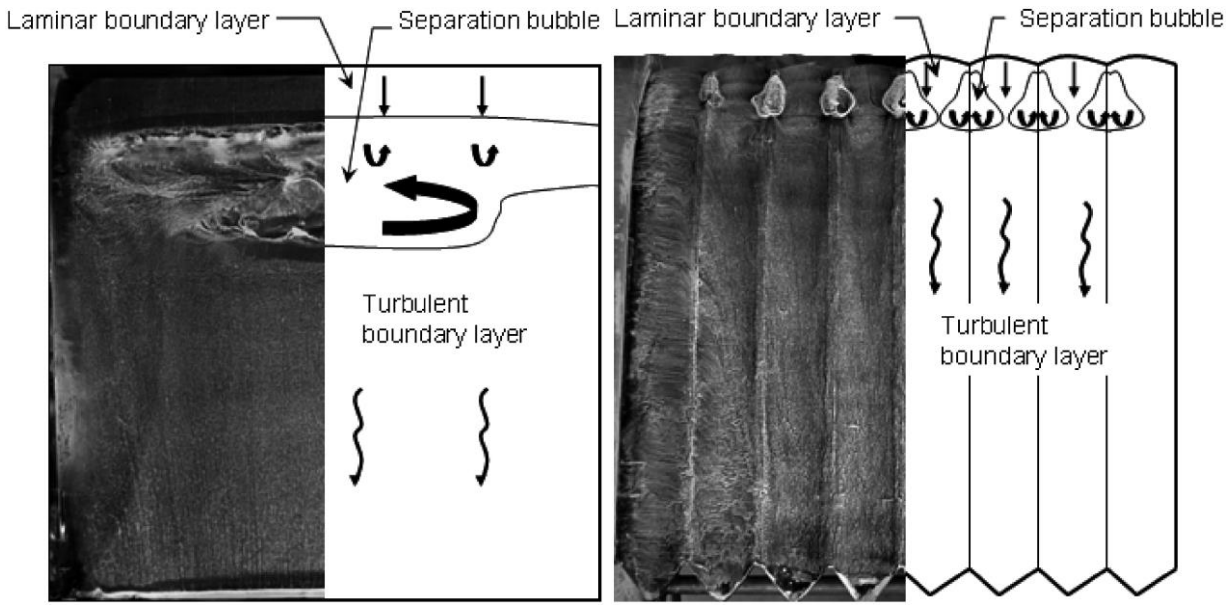

Figure 2.36: Oil flow visualization and its interpretation for the smooth (α =15°) and wavy (α =20°) configurations (ZEVERKOV et al., 2008).

Chen et al. (2012) used oil flow visualization over a partial span model of the thin NACA 0012 airfoil in order to understand the effect caused by tubercles on the airfoil performance. Figure 2.37, the smooth configuration with AR = 3 presents full flow separation at the leading edge for high angles of attack. In contrast, the wavy model (A = 0.10c and λ =0.25c) shows locally separated flow along the span where the flow attached remains in certain small areas downstream of the peaks so that a periodic separation line is established along the span close to the leading edge. These remaining areas of attached flow justify high lift observed at the post-stall.

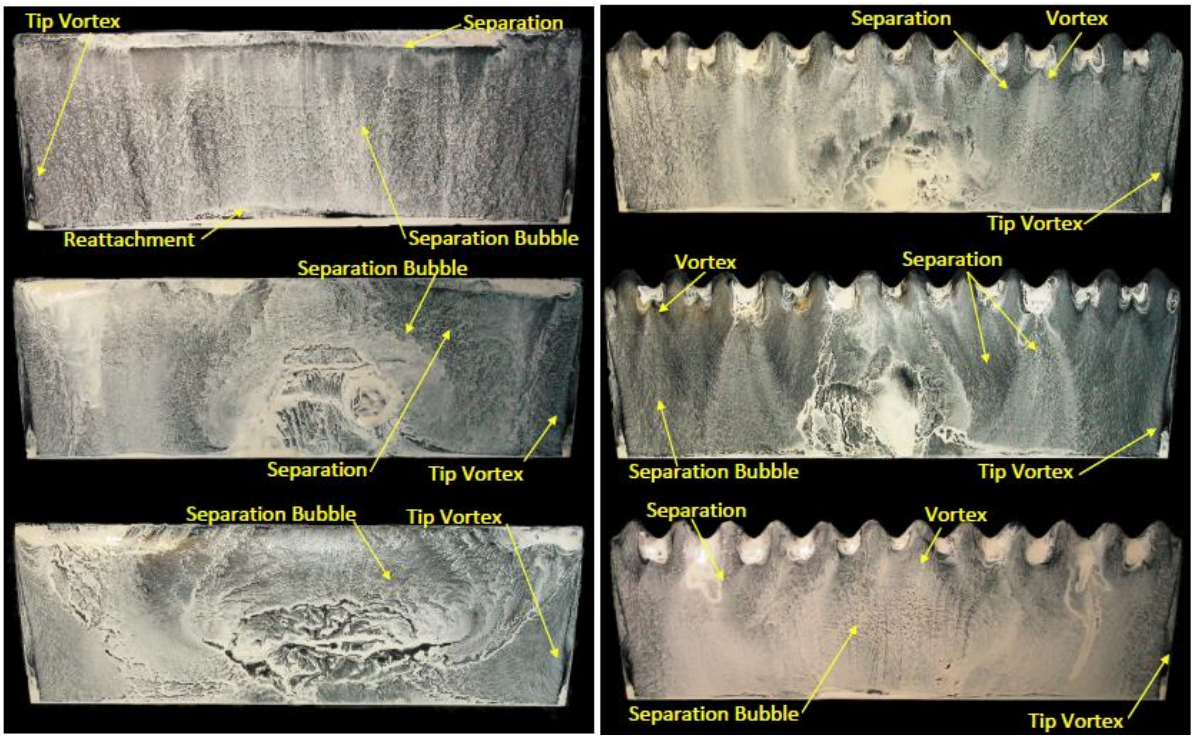

Figure 2.37: Oil flow visualization for smooth (left) and wavy (right) configuration model α = 13º, 15º and 17º (top to bottom) (CHEN et al. (2012)).

Karthikean et al. (2014) carried out oil flow visualizations, PIV and pressure measurements to investigate the flow topology on a NACA 4415 airfoil modified with a wavy leading edge (A=25%, λ = 25%) at the low Reynolds number 120,000.

Pressure distribution measurements and flow oil visualizations of the smooth airfoil indicate in the pre-stall regime ($\alpha = 6^{o}$) a clear onset of flow separation, along with regions of dead air and reverse flow as well as point of flow reattachment on suction surface (figure 2.38). The flow visualization show a bubble separation located at 0.35c with extension of 0.30c.

In contrast, figure 2.39 shows that the wavy configuration establishes a complex flow topology on the airfoil's upper surface. The two-dimensional separation bubble is split into three smaller three-dimensional bubble pockets. These bubble pockets have the flow separation point moving towards the trailing edge behind peaks, forming a "heart-shaped" shaped bubble. As a consequence, the separation and reattachment lines are wavy indicating that the adverse gradient is favorable to flow separation downstream of the troughs, agreeing with other aforementioned works.

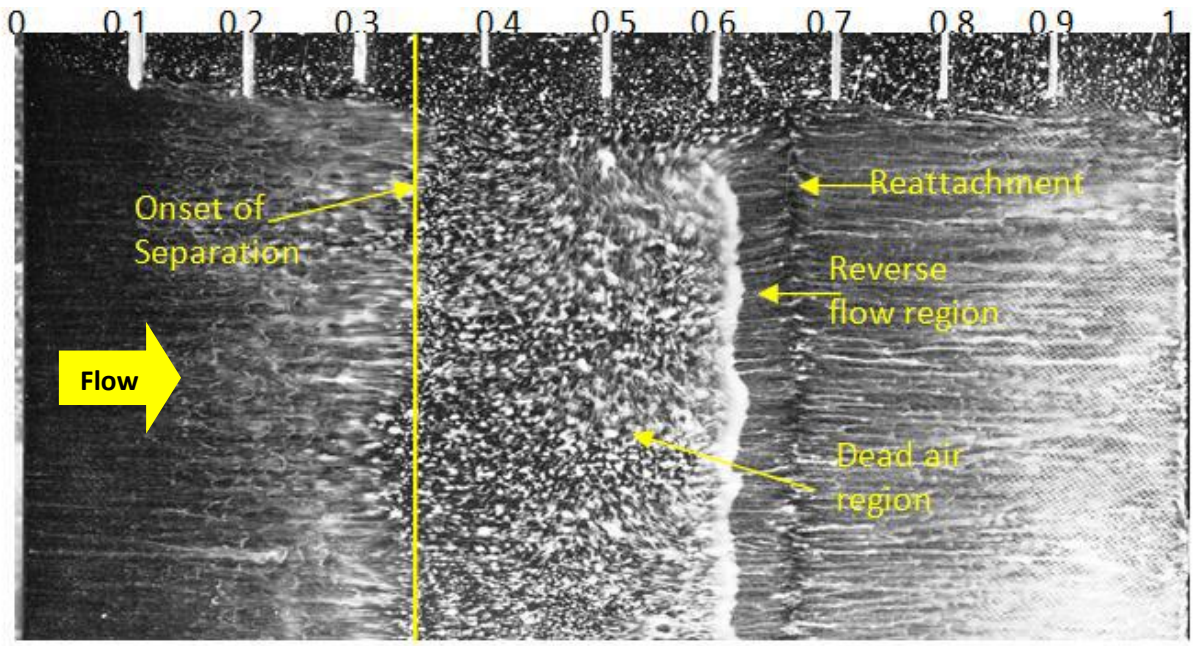

Figure 2.38: Surface oil visualization at smooth NACA 4415 airfoil ($\alpha = 6°$) (KARTHIKEAN et al., 2014).

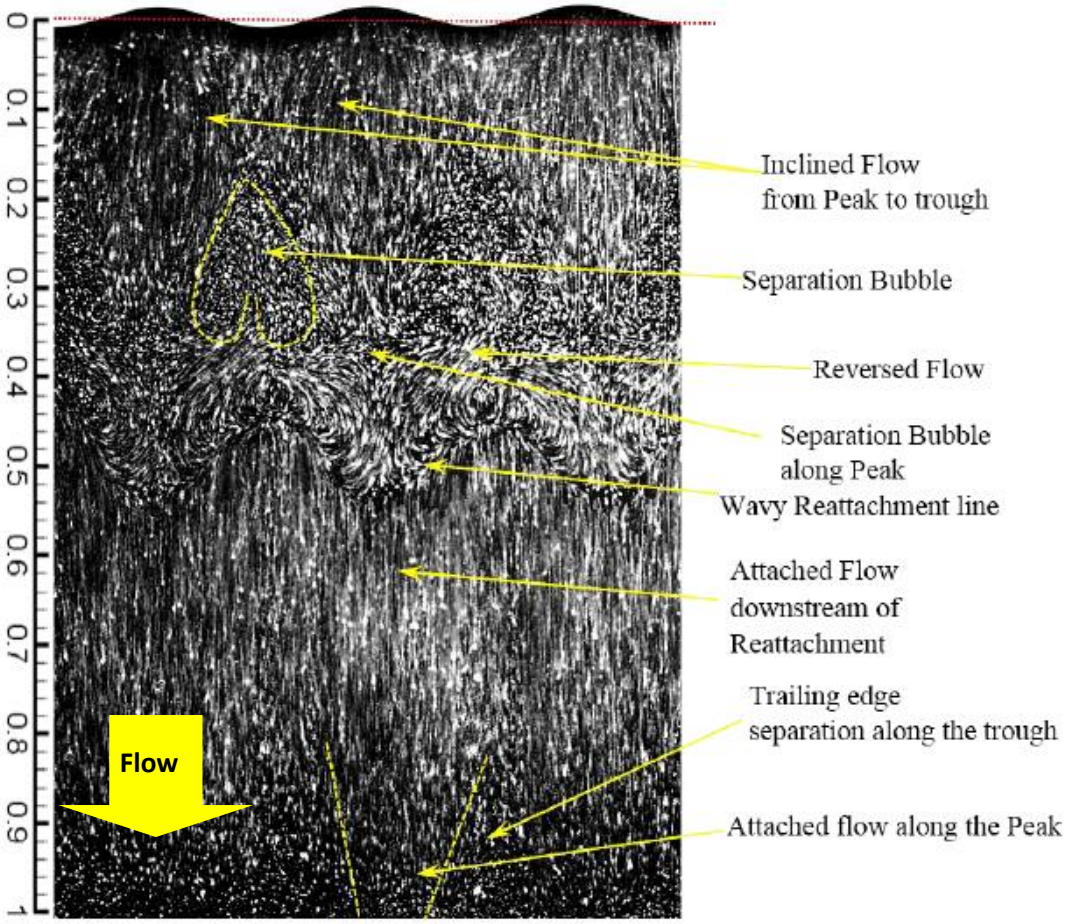

Figure 2.39: Surface oil visualization of wavy configuration on a NACA 4415 airfoil (α = 6°) (KARTHIKEAN et al., 2014).

At the post-stall condition (α=18º), pressure distribution and flow visualization show full flow separation at the leading edge for the smooth airfoil (figure 2.40). On the other hand, for the wavy leading edge configuration, figure 2.41 indicates that the flow downstream of the tubercle peaks remains attached close to leading edge, and the pressure distribution on the upper surface does not indicate a bubble in this region. Downstream of this region, a laminar bubble appears. In contrast with lower angles of attack, the flow forms an inverted "heart-shaped" behind tubercle peaks. Downstream of the trough region, a small bubble region occurs and further downstream a small area of reversed flow is noted. In addition, as with the lower angle of attack case, the analysis of oil streaks near the leading edge suggests that the direction of flow is from peak region towards troughs.

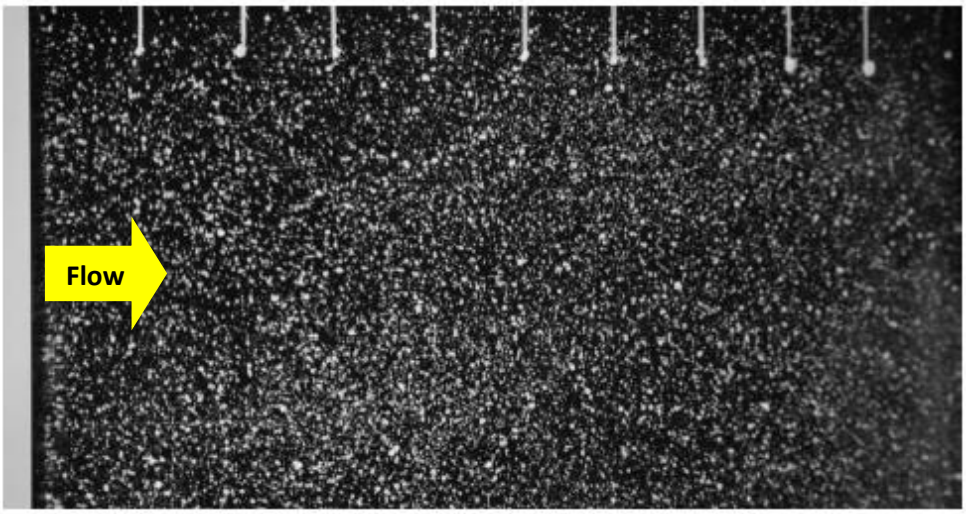

Figure 2.40: Surface oil visualization at smooth NACA 4415 airfoil (α = 18°) (KARTHIKEAN et al., 2014).

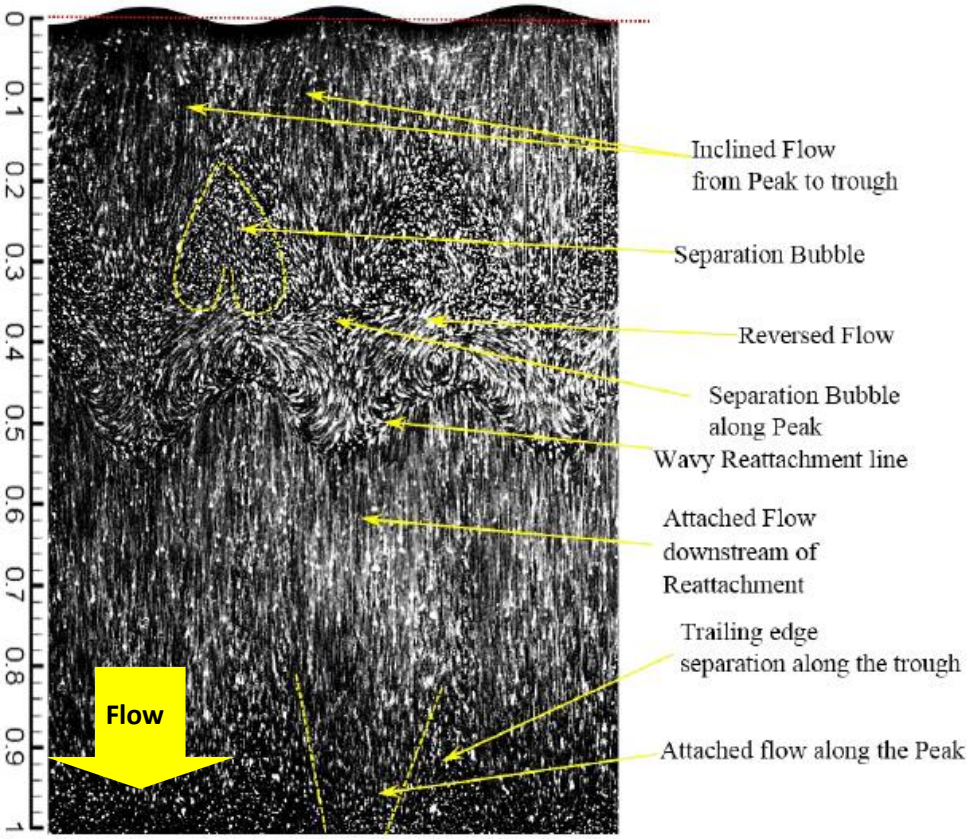

Figure 2.41: Surface oil visualization at wavy NACA 4415 airfoil (α = 18°) (Karthikean et al., 2014).

The mean streamwise velocity field over the upper surface measured by PIV apparatus confirms flow characteristics shown by pressure distributions and oil flow visualizations. In the pre-stall regime (α = 6º), for the smooth airfoil, figure 2.42 presents an enclosed region of reversed flow characterizing a laminar separation bubble. On the other hand, for the wavy leading edge configuration, the region downstream of the tubercle peaks does not present a laminar separation bubble. In addition, the trough and middle regions show a laminar separation bubble presenting smaller thickness when compared to smooth configuration.

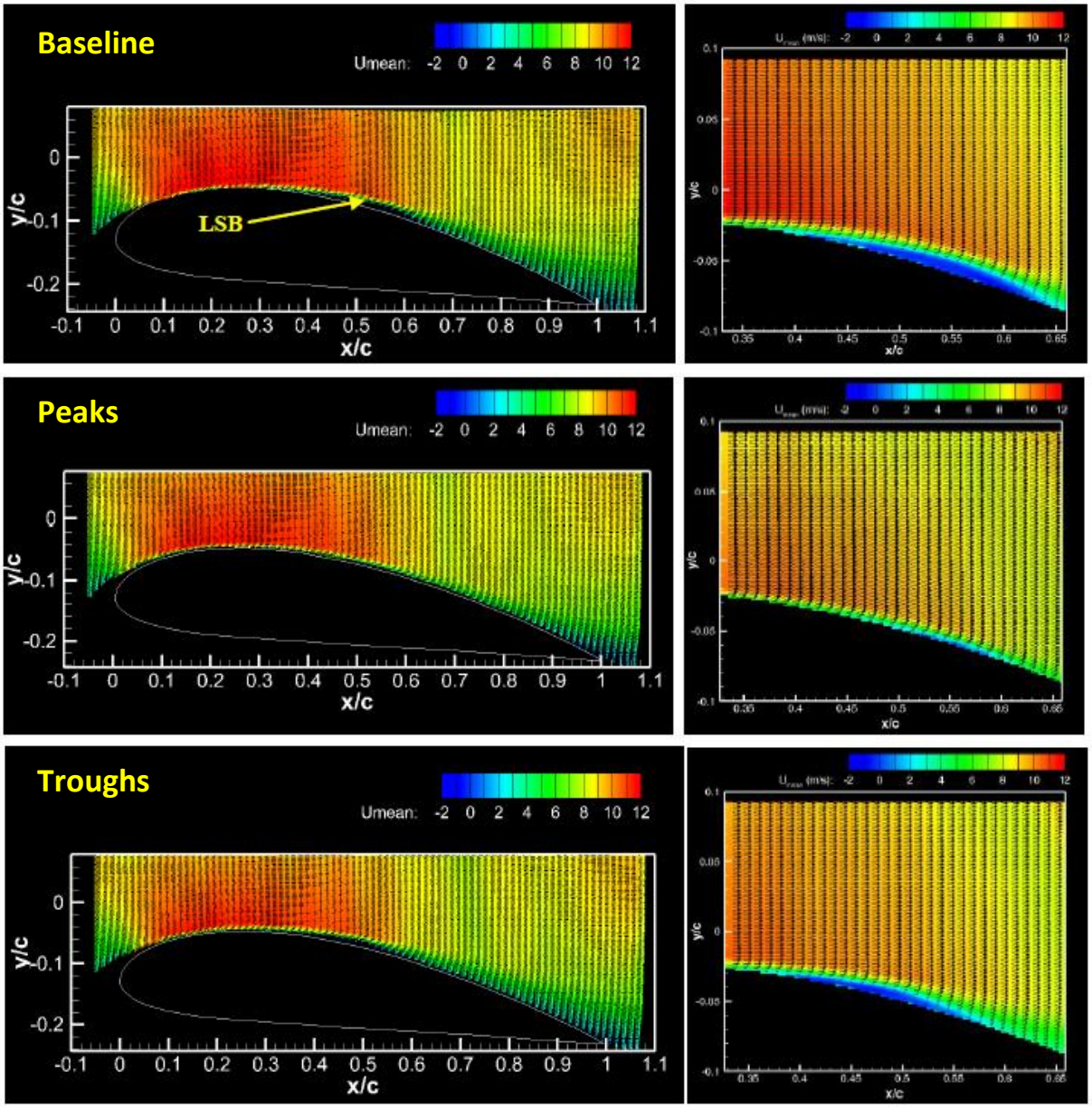

Figure 2.42: Mean velocity filed and zoomed in view near the surface at NACA 4415 airfoil (α = 6°) (KARTHIKEAN et al., 2014).

In the post-stall regime ($\alpha = 18^{o}$), PIV measurements show that the wavy leading edge is efficient in keeping the flow attached at higher angles of attack (figure 2.43). For the baseline configuration, flow separation appears immediately at the leading edge. A massive recirculating area occurs over almost the entire airfoil. In contrast, for the wavy leading edge airfoil a reduced recirculation region occurs downstream of the tubercle peaks and troughs. The height and the chordwise extent of the recirculation region increase from peak to trough. In addition, the separation point moves upstream towards the leading edge from tubercle peak to trough.

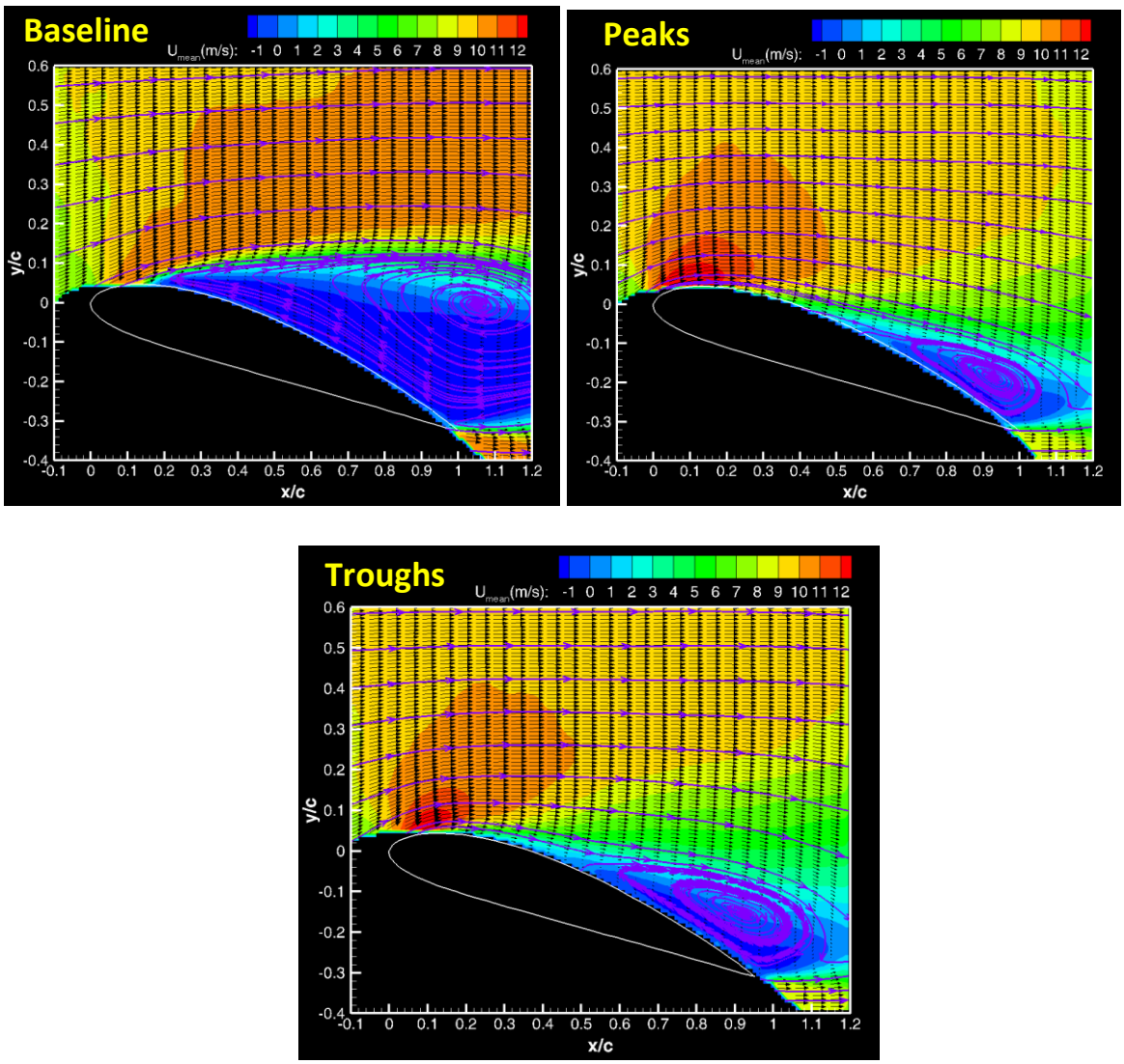

Figure 2.43: Mean velocity filed and zoomed in view near the surface at NACA 4415 airfoil ($\alpha = 18°$) (KARTHIKEAN et al., 2014).

Although Zeverkov et al. (2008) and Karthikean et al. (2014) identify three-dimensional laminar separation bubbles at peaks and troughs of the wavy airfoils giving remarkable contribution for the understanding of tubercle phenomena, Rostamzadeh et al. (2014) clarify, for first time, by numerical simulation, the complex structure that involves the flow topology of wavy airfoils. They identify, for the NACA 0021 airfoil at Re=120,000, the three-dimensional laminar separation bubble distribution that occurs at the leading edge in the pre-stall regime (figure 2.44). In addition, the early flow separation downstream of the troughs identified by Paterson et al. (2003), Levshin et al. (2006) and Johari et al. (2007) is presented in detail as delta-shaped regions near the trailing edge. Besides, in the post-stall regime, it is shown that, for wavy configurations, attached flow regions downstream of the peaks justify higher lift values (figure 2.45).

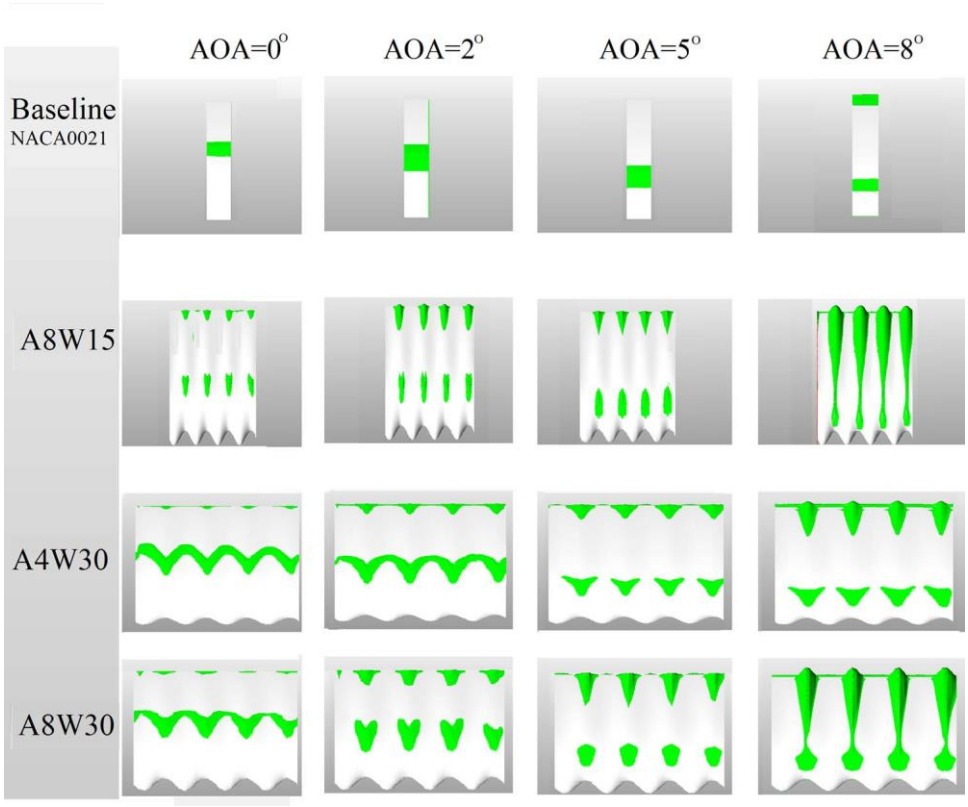

Figure 2.44: Separated flow regions (green areas) over the suction surface of the smooth and wavy airfoils in the pre-stall regime (ROSTAMZADEH et al., 2014).

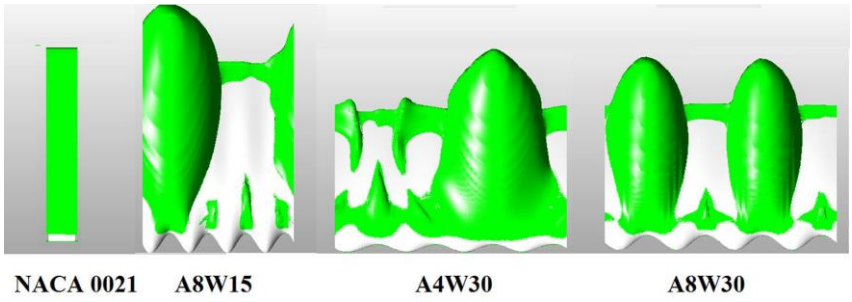

Figure 2.45: Separated flow regions (green areas) over the suction surface of smooth and wavy airfoils in the pos-stall regime (α = 15°) (ROSTAMZADEH et al., 2014).

2.2.7 Flow control Mechanism

Researchers have proposed many explanations for changes in flow caused by tubercles and the consequent effect on aerodynamic performance. All these efforts have contributed to build the knowledge around the understanding of tubercles as a flow control mechanism. The understanding of the flow mechanisms help to clarify the improvements and downsides of using tubercles.

Although most researchers propose explanations in order to respond the performance gains at the post-stall, a more general understanding of the mechanisms should consider the different regimes (pre-stall and post-stall).

Hansen (2012) summarized the following explanations for flow control mechanism of the wavy leading edge airfoils found in literature:

- Increased boundary layer momentum exchange by vortex generation (CUSTODIO, 2008; FISH; BATTLE, 1995; JOHARI et al., 2007; MIKLOSOVIC et al., 2004; PEDRO; KOBAYASHI, 2008)
- Compartmentalization of the flow along the span minimizing tip stall (FISH; BATTLE, 1995; MIKLOSOVIC et al., 2007; PEDRO; KOBAYASHI, 2008; STEIN; MURRAY, 2005)

- Non-uniform separation characteristics (FISHER; LAUDER, 2006; JOHARI et al., 2007; KOBAYASHI, 2008; VAN NIEROP et al., 2008; PEDRO; ZEVERKOV et al., 2008)
- Alteration of the pressure distribution over the airfoil (VAN NIEROP et al., 2008)
- Vortex lift (CUSTODIO, 2008; MIKLOSOVIC et al., 2007)

Fish and Battle (1995) are first to suggest an explanation to the flow control mechanism of the humpback whale´s tubercles. They make an analogy with leading edge strakes that are basically large vortex generators fixed to airplanes' wings, increasing the maximum lift and stall angle. It was supposed that, working as strakes, the vortices generated by tubercles exchanged momentum within the boundary layer to maintain the flow attached over the flipper´s surface, thus increasing aerodynamic performance for higher angles of attack.

Miklosovic et al. (2004) justify the enhancement in stall performance due to tubercles in their experimental results by also interpreting that the tubercles work as vortex-inducing devices exchanging momentum within the boundary layer.

Pedro and Kobayashi (2008) show that a wavy leading edge configuration presents high values of vorticity over the midsection of the flipper because of vortices generated by tubercles. These vortices re-energize the boundary layer adding high momentum to the upper surface of the flipper.

Miklosovic et al. (2007) and Custodio (2008) argue that the geometric modification caused by tubercles creates a variation in the leading edge sweep angle along the span, introducing spanwise flow along the leading edge and inducing streamwise vortices.

The first explanation regarding tubercle flow control mechanism seems more reasonable for flow over a full span model in the wind tunnel tests. However, the humpback whale´s pectoral flipper has a complex three-dimensional flow that involves an additional spanwise flow component over the flipper.

Thus, the low Reynolds number at the outboard flipper sections cause early flow separation as compared to the inboard region, causing a progressive flow separation along the

span with increasing angles of attack. Stein & Murray (2005), Miklosovic et al. (2007), Pedro and Kobayashi (2008) explain that streamwise vortices generated by tubercles establish a physical barrier, preventing progression of flow separation towards inboard areas.

Van Nierop et al. (2008) refused the hypotheses of momentum exchange by vortex generation since the dimensions of the tubercle amplitude and wavelength are much bigger than the boundary layer thickness. They explain that the flow control mechanism from tubercles is triggered by geometry differences between profiles at peaks and troughs. Despite the sections having similar thicknesses, the smaller chords at troughs cause higher adverse pressure gradients and as a consequence early flow separation. In order to clarify the bi-periodic characteristics along the span, Van Nierop et al. (2008) explain that a non-uniform downwash component distribution along the span imply lower local angles of attack at peaks, locally delaying the stall. This characteristic would explain the delay in stall for tubercle configurations. Previous studies than Van Nierop et al. (2008) support this explanation since they present early flow separation downstream of the troughs (FISHER; LAUDER, 2006; JOHARI et al., 2007; ZEVERKOV et al., 2008).

The delta wing phenomenon at higher angles of attack is proposed by Miklosovic et al., (2007) and Custodio (2008) in order to explain the flow control mechanism at post-stall conditions due to tubercles.

Custodio (2008) describes that a pair of counter-rotating streamwise vortices starts between tubercle peaks, growing toward troughs and coalescing in this region causing suction areas, helping in high lift generation. However, in the pre-stall regime, flow separation at troughs cause loss of suction which is not compensated by the suction generated by weak vortices.

As mentioned previously, recently Rostamzadeh et al. (2014) brought very important results to explain the flow topology of three-dimensional laminar separation bubble distribution caused by tubercles. However, the most important contribution of their work is a clear understanding of the flow control mechanism involved.

Rostamzadeh et al. (2014) as well as Nierop et al. (2008) establish the understanding of tubercle effect as an element that generates vorticity. They mention in their previous work that the effect of a wavy leading edge on spanwise circulation distribution is to generate a cyclic pattern and, as a consequence, a similar pattern appears for vorticity distribution

(ROSTAMZADEH et al., 2013). It is identified that the cyclic variation of spanwise circulation establishes the development of pairs of counter-rotating streamwise vortices as in a finite wing.

As streamwise vorticity is introduced by tubercles, it is considered the two main mechanisms for generating it, which are called as “skew-induced” and “stress-induced”. The skew-induced occurs with presence of flow vorticity on streamwise or transverse direction. On the other hand, stress-induced appears as consequence turbulence anisotropy conditions.

The flow skewness is identified by the change in the curved streamlines at the leading-edge. However, three-dimensional bubbles forming at tubercle troughs drive the formation of streamwise vortices (primary vortices) adding streamwise vorticity to the flow downstream of the bubbles. In addition, streamwise vortices are formed (secondary vortices) at the region near the trailing edge establishing a delta-shaped flow separation (figure 2.46).

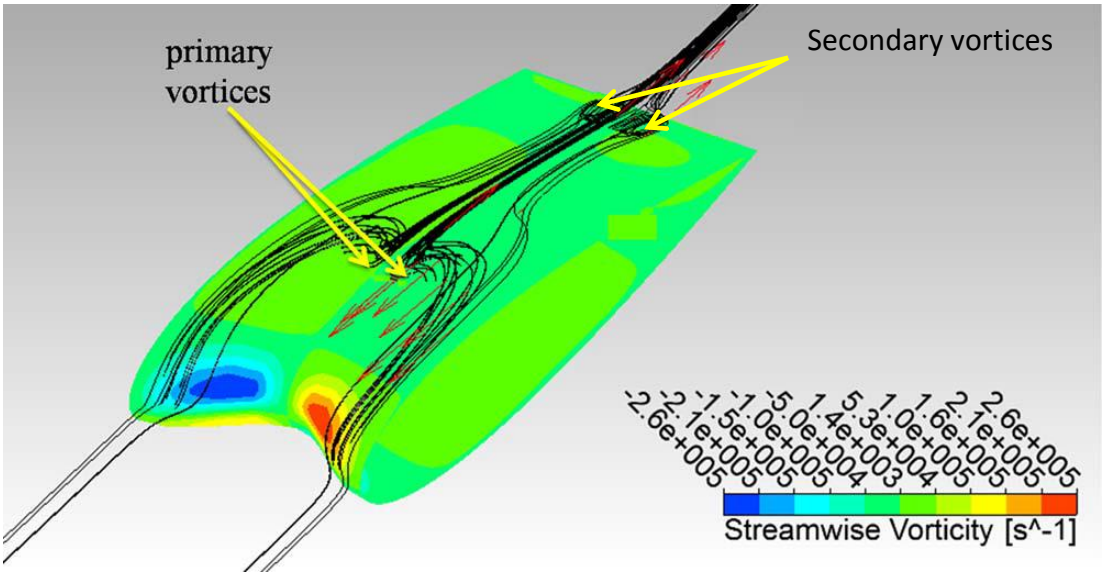

Figure 2.46: Normalized streamwise vorticity vectors plotted for one-half of the 3D-streamlines. Surface coloured by streamwise vorticity (Re = 120. 000, α = 2◦) (ROSTAMZADEH et al., 2014).

Figure 2.47 presents vortex lines in agreement with the presence of a long separation bubble in the trough regions. Vortex lines are convected downstream of the bubbles fed by

primary and secondary vortices turning into the streamwise direction due to spanwise velocity gradients. These frontiers established by vortex lines are called “chordwise separation lines”.

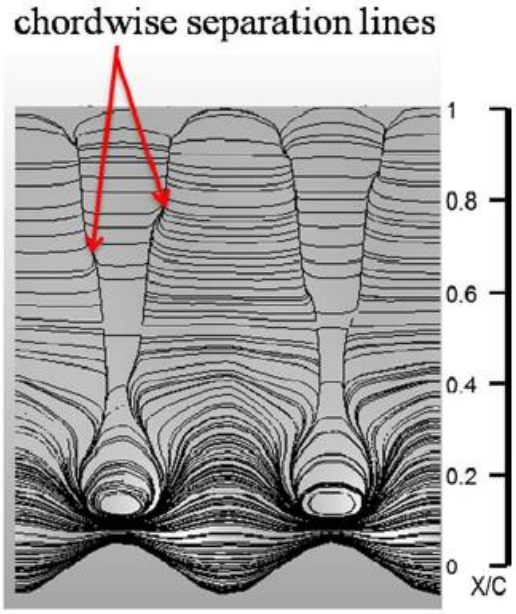

Figure 2.47: vortex lines on the suction side of the tubercled foil section A8W30 (Re = 120. 000, α = 8◦) (ROSTAMZADEH et al., 2014).

Skillen et al. (2014) present important results regarding stress-induced mechanisms produced by turbulence anisotropy conditions caused by tubercles. The flow at trough areas undergoes higher adverse pressure gradients causing flow separation with consequent reattachment and forming a laminar separation bubble. The laminar bubble drives a newly re-energised boundary layer downstream of the reattachment point causing flow transition at different spanwise positions. Figure 2.48 presents flow instabilities at the leading edge in the trough location whereas laminar flow remains further downstream behind peaks.

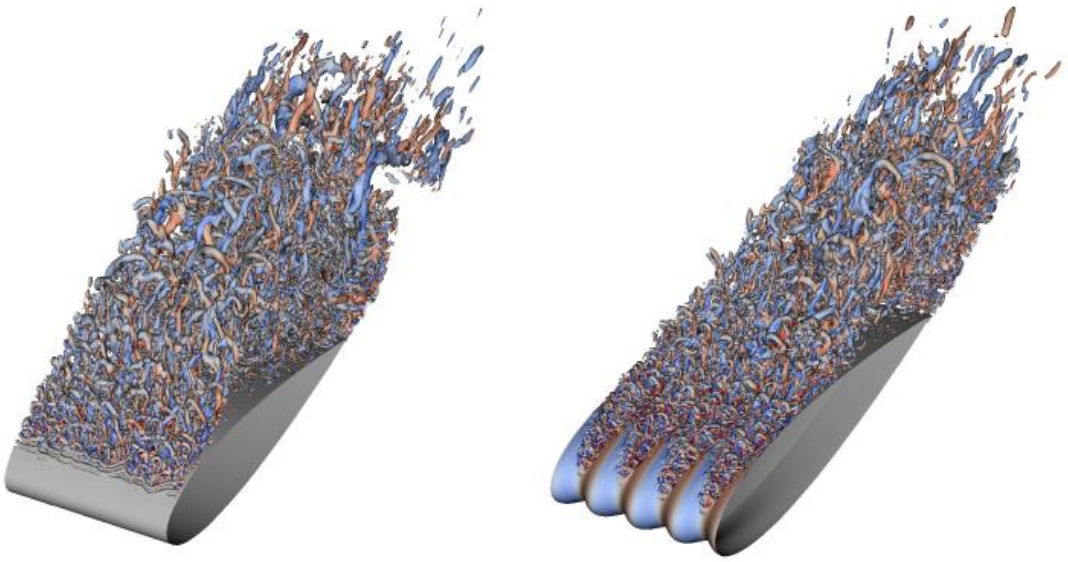

Figure 2.48: Iso-surfaces of the second invariant of the velocity gradient tensor, Q = 200. Left: Unmodified; Right: Modified. Coloured by streamwise vorticity (blue to red) (SKILLEN et al., 2014).

2.2.8 Summary and discussions

The present bibliographical review has shown that since the pioneering work of Fisher and Battle (1995), which proposed tubercles as responsible for hydrodynamic improvements, many aspects of the wavy leading edge phenomena were clarified at least partially.

The first researchers brought up important insights that motivated the rapidly growing interest in wavy leading edge phenomena. Miklosovic et al. (2004) present remarkable tubercle performance at higher angles of attack, increasing lift and decreasing drag for a geometry representing the humpback whale´s morphology. However, results from full span models have shown that the aerodynamic performance benefit in that case was restricted to the post-stall regime with softer stall behaviour (JOHARI et al., 2007; LEVSHIN et al., 2006; STEIN; MURRAY, 2005), indicating distinct tubercle effects between wings and airfoils.

Miklosovic et al. (2007), presumably stimulated by differences that had been found between results from full and partial span wind tunnel models, conducted tests in order to

evaluate the three-dimensional effects on tubercle performance. Their results were similar to previous studies. The justification provided was that tubercles avoid the spanwise progression of the stall thus improving the maximum lift; however, the tests were performed at Reynolds number distinct from previous works, casting doubt about the effects of Reynolds numbers.

Stanway (2008), investigating the Reynolds number effects carried out tests using similar models from Miklosovic et al. (2004), however, at lower Reynolds numbers. The deterioration in lift, when compared to Miklosovic et al. (2004) results, brought up the hypothesis that the Reynolds number affects the tubercles' performance.

In fact, Stanway (2008) hypothesized that the stall characteristics of the smooth configuration itself as imposed by Reynolds number variation caused changes on tubercle performance. The differences between infinite and finite span configurations would not be only attributable to the tri-dimensionality of the flow, since the Reynolds number conditions were different in previous studies.

With regards to tubercle geometry, Levshin et al. (2006), Johari et al. (2007), Hansen et al. (2009) and Chen et al. (2012) evaluate the morphologic variation of the humpback whale´s tubercles; similar results are presented among the researches. The tubercle amplitude variation seems to have a larger effect on performance, in comparison to the influence of the wavelength; larger amplitude configurations at pre-stall condition suffer greater aerodynamic deterioration with a substantial decrease in lift (lower maximum lift) and increase in drag. However, this particular configuration has a soft behaviour in the post-stall regime, and its stall angle is reduced. On the other hand, the tubercle wavelength presents a small effect on performance. An increase in wavelength at pre-stall shows a little raise in lift. In contrast, this increase causes an early stall angle and decrease in soft stall behaviour.

As mentioned above, the first results showing decrease in aerodynamic performance for wavy configuration of full span wind tunnel models when compared to partial models intrigued researchers. Although Miklosovic et al. (2004) suggested that tubercles acted as flow mechanism that prevents the stall progression along the span, the question that remained was the role of Reynolds number effects on the results. Hansen (2010) tries to answer this question at least partially. For the case of an unswept or tapered wing, the tubercle performance shows similar results for finite and infinite wings.

The results from Hansen (2010) and the morphology of the humpback whale´s pectoral flippers motivated Custodio et al. (2012) investigate the role of the flipper's sweep angle on tubercle performance. Therefore Custodio et al. (2012) carried out the most extensive study of three dimensional effects on tubercle performance. The results show disagreement from Hansen (2010). All partial span models presented an increase in maximum lift compared to two-dimensional models including the rectangular wing. The wings had similar lift performance at lowers angle of attack. At higher angles of attack, an aerodynamic deterioration on lift curve slope was observed. However, higher maximum lift is reached. In the post-stall regime, there is remarkably an absence of soft stall behaviour in contrast with the characteristics of the full span model. A surprising result, when compared to previous study from Hansen (2010), was that the highest increase in maximum lift was reached for the unswept wing configuration.

Guerreiro (2010) investigates the effect of aspect ratio on wavy leading edge performance. The results show that at the lower aspect ratio tested (AR=1.0), due to the absence of a proper stall for the smooth configuration, the tubercles do not become effective. On the other hand, for AR = 1.5, the tubercle provided a soft stall behaviour in contrast with baseline configuration that had an abrupt stall. Chen et al. (2012), contrary to Guerreiro (2010) results, show that by varying the aspect ratio the tubercle performance is minimally affected.

The studies regarding Reynolds number effects have positively identified that the Reynolds has an important role on tubercle performance. Stanway (2008), Custodio et al. (2012), Dropkin (2012) and Custodio et al. (2015) present similar results where the aerodynamic deterioration caused by tubercles decreases with increasing of Reynolds number, although Guerreiro (2010) presents some improvement in performance with decreasing Reynolds numbers. However, all Reynolds number effect cases presented a decrement in maximum lift for wavy configurations when compared to baseline geometries. In addition, Custodio et al. (2012) and Custodio et al. (2015) show significant deterioration at Reynolds number in the order of 100,000. The larger amplitude and the shorter wavelength configuration were shown to be more prone to degradation at low Reynolds numbers (CUSTODIO et al., 2015). Although the collection of results show interdependency between Reynolds number condition and tubercle performance, the results cannot be generalized since all airfoil used had thicknesses in the order of 20% of chord.

The investigation of the airfoil geometry with regards to the phenomena associated to wavy leading edges is certainly an aspect of research that needs to be extended since the investigations so far have been focused mostly thick airfoils, similar to morphology of a flipper. The only specific investigation carried out by Hansen et al. (2009) showed similar results for symmetrical and cambered airfoils. However, the cambered airfoil had a maximum lift close to smooth configuration, differently from the decrement observed in the symmetrical airfoil.

The first researches that investigated the effect of tubercles on flow topology brought an important contribution to the understanding of the wavy leading edge performance both at pre-stall and post-stall. Paterson et al. (2003), Levshin et al. (2006) and Johari et al. (2007) show that the tubercles anticipate trailing edge flow separation, inducing early flow detachment downstream of the tubercle troughs, justifying the aerodynamic deterioration at pre-stall conditions observed in force measurements. The mini-tuft flow visualizations carried out by Levshin et al. (2006) and Johari et al. (2007) present, in the post-stall regime, flow attached downstream of the tubercle peaks, agreeing with high lift values at higher angles of attack for wavy configuration.

Contributing to the understanding of differences in tubercle performance for finite and infinite span geometries, Stanway (2008) and Pedro and Kobayashi (2008) present experimental and numerical topological analyses suggesting that tubercles work as a flow control mechanism, avoiding the stall progression along the span of a flipper.

Although Paterson et al. (2003), Levshin et al. (2006) and Johari et al. (2007) contributed to describe the mechanisms of tubercles, only recently flow topology analysis have been carried out to explain the complex flow structure caused by wavy leading edges. The oil flow visualizations conducted by Zeverkov et al. (2008) and Karthikean et al. (2014) show three-dimensional laminar separation bubbles forming at the leading edge of wavy airfoils for specific geometric configurations and flow conditions. The results present three-dimensional laminar bubbles downstream of the troughs and peaks respectively at forward and aft chordwise positions. In addition, Karthikean et al. (2014) show PIV measurements that confirm these flow structures. Rostamzadeh et al. (2014) bring, by numerical investigations, a clearer understanding of the flow structures at leading edges presented by Zeverkov et al. (2008), Chen et al. (2012) and Karthikean et al. (2014). In addition, the effect

of the flow structures near to trailing edge could be understood as part of the overall phenomena.

The flow control mechanisms that involve the wavy leading edge phenomena could be considered the aspect that causes the most controversy. Most researchers (FISH; BATTLE, 1995; JOHARI et al., 2007; MIKLOSOVIC et al., 2004; MIKLOSOVIC et al., 2007; CUSTODIO, 2008; PEDRO; KOBAYASHI, 2008) believe that vortex structures at the leading edges, exchanging momentum within the boundary layer, are responsible for any flow control mechanism generated by wavy leading edge airfoils. However, the supposition that such vortices at the leading edge are the only flow structure that governs the overall flow pattern seems questionable, since little understanding about flow structures caused by tubercles as well as the broad flow conditions imposed by Reynolds number and geometric properties were not explored by current researches.

In this direction, recently Rostamzadeh et al. (2014) present new and detailed views on the flow control mechanisms caused by tubercles, although Zeverkov et al. (2008) are in fact the first to mention the ideas from Rostamzadeh et al. (2014). They clearly present three-dimensional laminar bubble distributions that work as flow control mechanism even at higher angles of attack. At the leading edge, a secondary flow increases velocities, driving three-dimensional bubbles at troughs, whereas at peaks low velocities maintain the flow attached. In addition, downstream of the bubbles, vortex lines are formed in the chordwise direction, which meet the secondary vortices at the airfoil's trailing edge. This finding motivates an in-depth investigation of which conditions determine these counter-rotating vortices or three-dimensional bubble distributions which act as flow control mechanisms. In addition, Skillen et al. (2014) contributed to the perspective from Rostamzadeh et al. (2014) adding considerations regarding turbulence.

The main limitation of the current researches is in restricting the studies to a space of geometries within the realm of the humpback whale´s morphology and flow conditions of the aquatic environment. Therefore most airfoils tested in wavy leading edge studies had thickness around 20% of chord. The wing planform of the partial span models tested presented low aspect and taper ratios. Besides geometric constraints restricted to the pectoral flipper's morphology, the Reynolds number condition was limited in most cases between 100,000 and 500,000. Future investigations should not be constrained by these geometric and flow limitations in order to contribute to further understand the wavy leading edge phenomena

in a more general context. Besides, exploring new frontiers could open the possibility to apply tubercles to a design space suitable for use in engineering applications. In this sense, investigations of airfoil thickness and camber variations, higher aspect ratios, sweep angle and taper ratio explorations could help to rapidly expand the knowledge towards new discoveries. Moreover, at extremes of low and high Reynolds numbers, tubercles may present different behaviours from current studies, since these extremes establish fully laminar and turbulent flow conditions not achieved in previous works.

Particularly regarding flow control mechanisms, the findings from Rostamzadeh et al. (2014) need experimental confirmation using flow visualization techniques. In addition, as previously mentioned, it seems to be the logical next step in the research to identify the limits of both flow mechanisms cited.

Finally, the exploration of higher Mach numbers in transonic and supersonic regimes in order to investigate any potential benefits in wave drag with theoretically lower velocities at tubercle peaks as Bolzon et al. (2015) commented could be a possibility.

Considering the scenarios of possibilities for new investigations envisioned above, this work was directed towards the evaluation of the influence of the airfoil geometry on wavy leading edge phenomena by exploring the extremes of airfoil thickness. In addition, the Reynolds number effects are also evaluated since, as discussed previously, the current studies on Reynolds number effects do not consider the parametric influence of geometries. Besides, it is an opportune chance to explore the preliminary findings from Rostamzadeh et al. (2014) and experimentally confirm and understand the flow structures in order to bring up a broader view of the aerodynamic phenomena with the wide space of conditions to be investigated.

3 EXPERIMENTAL EQUIPMENT AND METHODOLOGY

3.1 Introduction

This chapter describes the procedures of the experimental methodology applied during the wind tunnel tests in order to guarantee reliability of the results. The following paragraphs discuss the experimental equipment techniques, apparatuses, model design and configurations. As a starting point, the design of the tested airfoil models and their configurations are described. Subsequently, relevant wind tunnel characteristics are commented as well as experimental techniques that enable the control of flow parameters such as turbulence intensity in order to attain adequate flow quality.

Also, the instrumentation and related methodology to obtain the forces and moment measurements are described. The tunnel balance, calibration procedures and applicable corrections are described in detail. Finally, the flow visualization techniques are an important experimental component of this work, and the procedures in order to obtain appropriate flow visualizations are delineated.

3.2 Design and configuration of the airfoils

In order to investigate the dependency between the wavy leading edge phenomena and the airfoil geometry, wavy leading edge configurations were built for three symmetrical airfoils with distinct airfoil thickness. The airfoils chosen are symmetrical NACA profiles with maximum thicknesses of 12%, 20% and 30% of the chord, respectively NACA 0012, NACA 0020 and NACA 0030.

The choice of NACA airfoils arises from the fact that this family of airfoils is thoroughly documented in literature, therefore permitting the comparison to the experimental results of smooth airfoils from the present work. The airfoil thickness of 20% of chord has been considered because it is a reference from previous studies in terms of wavy leading edge performance. This airfoil has a representative thickness of the Humpback whale flipper´s

cross-section profile. There are many previous experimental studies regarding wavy leading edge aerodynamic performance for the NACA 0020 airfoil, as the promising results from Miklosovic et al. (2004) that motivated several studies based in this geometry.

The other two airfoil thicknesses were selected in order to evaluate extremes of the airfoil geometric effects on wavy leading edge phenomena. On one hand, the NACA 0012 airfoil represents the characteristics of a thin airfoil with a small leading edge radius; on the other hand, the NACA 0030 airfoil represents an extremely thick airfoil with a very large leading edge radius.

Smooth and wavy airfoils were built in order to evaluate the wavy leading edge effect. All of them were designed using the software Autodesk/Inventor, computer-aided design (CAD) tool. The airfoils with wavy leading edges were built based on two-dimensional profiles with variable chord lengths. The three dimensional models were created using leading edges based on a sinusoidal repetitive path as defined for each wavy geometry, along with straight trailing edges perpendicular to the chords(figure 3.1).

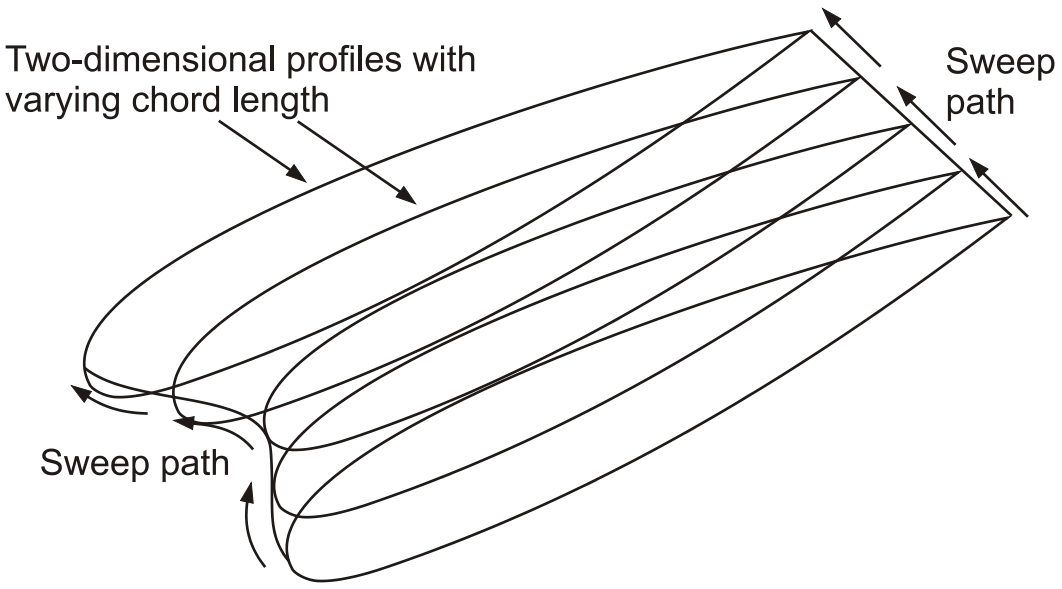

Figure 3.1: Wavy leading edge airfoil model design. Adapted from Hansen (12012).

The airfoils were fabricated of PLA using a prototype machine type 3D Cloner ST. After that, the models were sanded in order to reach appropriate superficial roughness and

homogeneity. All airfoils were painted in black color in order to provide appropriate color contrast with mini-tufts and oil visualization tests.

The airfoil model dimensions were chosen based on a compromise between installation effects on the wind tunnel minimizing blockage and three dimensional effects by the choice of proper aspect ratio and an adequate chord length allowing the appropriate Reynolds number range for this work.

Essentially, larger chords allow more flexibility in the choice of the Reynolds numbers. On the other hand, shorter chords minimize the blockage which in turn improves the accuracy of results. In addition, lower values of chord length imply in higher aspect ratios, therefore increasing two-dimensionality characteristics of the flow around the airfoils tested. In the decision of the chord length, the endplates used in order to minimize three-dimensional effects on the flow over the airfoil upper surface caused by wind tunnel sidewalls has also been taken into account.

Furthermore, aspect ratios of airfoil models used in previous two-dimensional studies of wavy leading edge performance were considered as reference. For instance, Johari et al. (2007) and Miklosovic et al. (2007) used aspect ratios of 2.0 and 3.3, respectively. The chord length chosen for the airfoil models of this work have was 150 mm, and given the span of 410 mm the plan form areas are 650 mm^2 and the aspect ratio 2.73.

The wavy leading edge geometries were varied by combining tubercle amplitudes and wavelengths within the range of the Humpback whale flipper´s morphology, in order to evaluate the effect of these parameters on flow characteristics and the implied consequence on their performance (lift, drag and pitching moment).

Since this work carries out a broad variation of parameters (wavy leading edge and airfoil geometries as well as Reynolds number), the wavy leading edge geometries were limited to three configurations in order to maintain a manageable number of tests to be conducted in the wind tunnel campaigns.

Considering that previous studies investigating tubercle geometry variation (JOHARI et al., 2007; HANSEN et al. 2009; LEVSHIN et al., 2006) clearly demonstrated some of the aspects pertaining to amplitude and wavelength effects, and keeping sight of the main goal of this work which is to evaluate the airfoil geometry effect on wavy leading edge phenomena, three wavy configurations were chosen for the experimental investigations. The values of

amplitude and wavelength were chosen in order to be comparable with previous studies at different airfoil shape and Reynolds number conditions.

Three sets of four airfoils were built, each set having a unique profile geometry (specifically the profile thickness); in each set, one airfoil consists of a straight (smooth) leading edge while the other three have wavy leading edges. Table 3.1 summarizes the twelve airfoil configurations tested and shows the nomenclature used in the result chapters 4, 5 and 6. Additionally, figure 3.2 shows the set of smooth and wavy NACA 0020 airfoils tested at the wind tunnel facilities.

Airfoil	Amplitude	Wavelength	Configuration
NACA 0012	0% chord	0% chord	NACA0012 BASELINE
NACA 0012	3% chord	40% chord	NACA 0012 A3λ40
NACA 0012	3% chord	11% chord	NACA 0012 A3λ11
NACA 0012	11% chord	40% chord	NACA 0012 A11λ40
NACA 0020	0% chord	0% chord	NACA 0020 BASELINE
NACA 0020	3% chord	40% chord	NACA 0020 A3λ40
NACA 0020	3% chord	11% chord	NACA 0020 A3λ11
NACA 0020	11% chord	40% chord	NACA 0020 A11λ40
NACA 0030	0% chord	0% chord	NACA 0030 BASELINE
NACA 0030	3% chord	40% chord	NACA 0030 A3λ40
NACA 0030	3% chord	11% chord	NACA 0030 A3λ11
NACA 0030	11% chord	40% chord	NACA 0030 A11λ11

Table 3.1: Profile and wavy geometry for twelve airfoils tested.

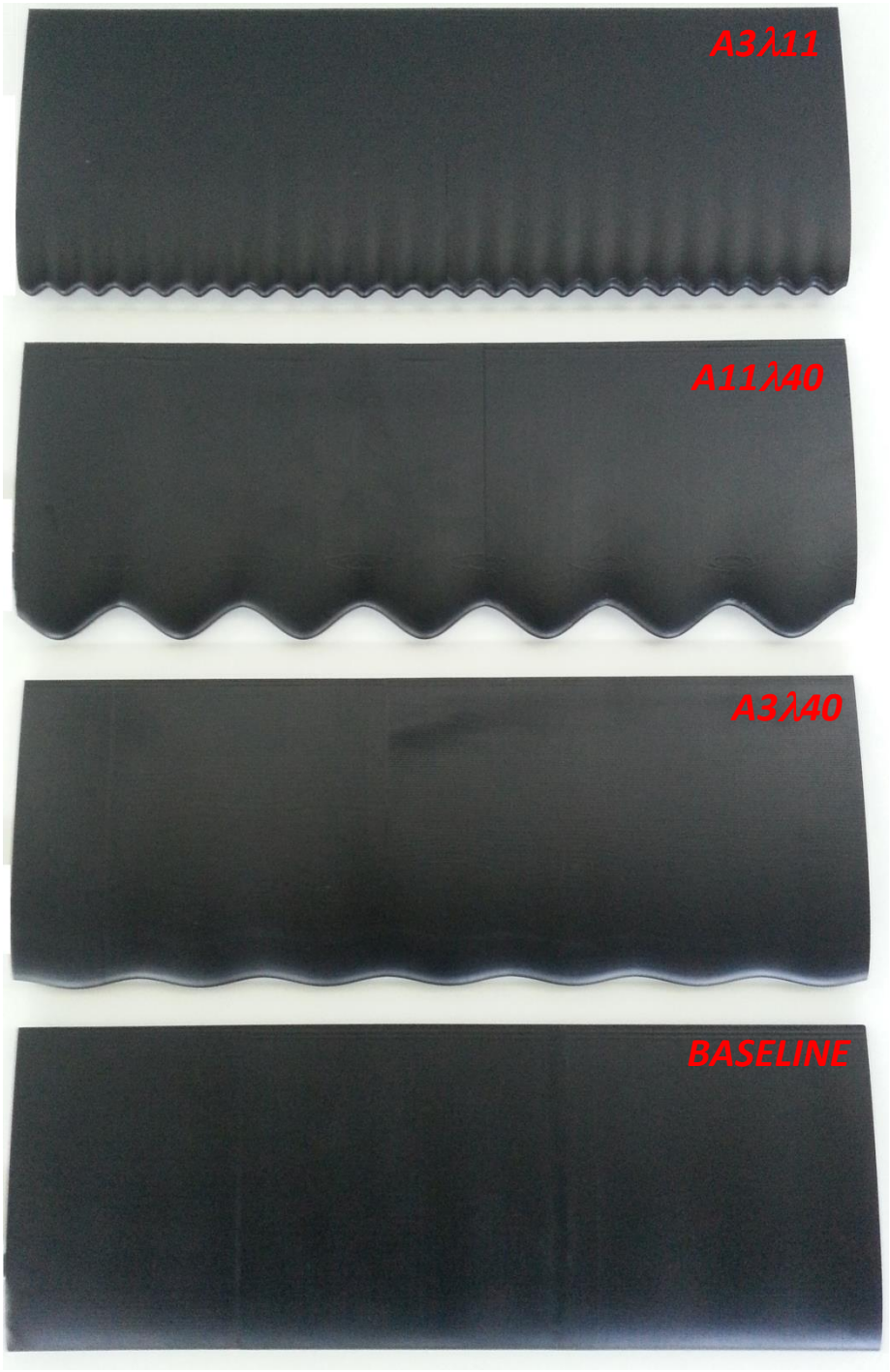

Figure 3.2: Set of NACA 0020 airfoils (Smooth, A3λ40, A11λ40 and A3λ11) tested at wind tunnel facilities.

3.3 Wind tunnel facility characteristics

The experimental investigations were carried out in a subsonic blower-type wind tunnel with open loop circuit and a closed test section at Professor Feng Laboratory of the Aeronautical Engineering Division of the Technological Institute of Aeronautics (ITA). The wind tunnel designer was Professor G. Jackson of the Department of Aeronautics at Imperial College and it was implemented by the company Plint & Partners.

The internal dimensions of the test section are 457 mm x 457 mm x 1200 mm, and excluding the areas of the side corners, the transverse area at beginning of the test section is 0.2027 m^2.

The energy introduced into the wind tunnel (blowing air) is provided by a centrifugal blower which rotates at 1000 rpm connected directly to an A.C engine that produces 25 HP in power. The blower speed, and therefore the tunnel flow velocity, is regulated by the belt system.

General view of the wind tunnel facility at ITA and its components as well as the cross section view of the test section can be seen in the figures 3.3 and 3.4 respectively.

The wind tunnel open loop circuit begins by admitting atmospheric air that is sucked in by the fan and undergoes compression due to the energy injected into the flow, therefore increasing the total or stagnation pressure.

Downstream from the blower, the air enters a short diffuser fitted with three screens with different meshes. In this wind tunnel element, the velocity flow decreases and the static pressure increases to a level close to the local stagnation pressure at the diffuser outlet.

The screens have the function of breaking up the large vortices that exit from the blower fan. So, a uniform flow is produced with low turbulence level at the diffuser outlet. However, the increase in total pressure provided by the fan is partly consumed by power losses from the flow path through the screens as well as due to flow friction with the diffuser's walls. The flow coming from the diffuser outlet goes to a settling chamber of constant section in which the flow has low velocity and low level of fluctuation when passing through the last screen with the smallest mesh at the diffuser.

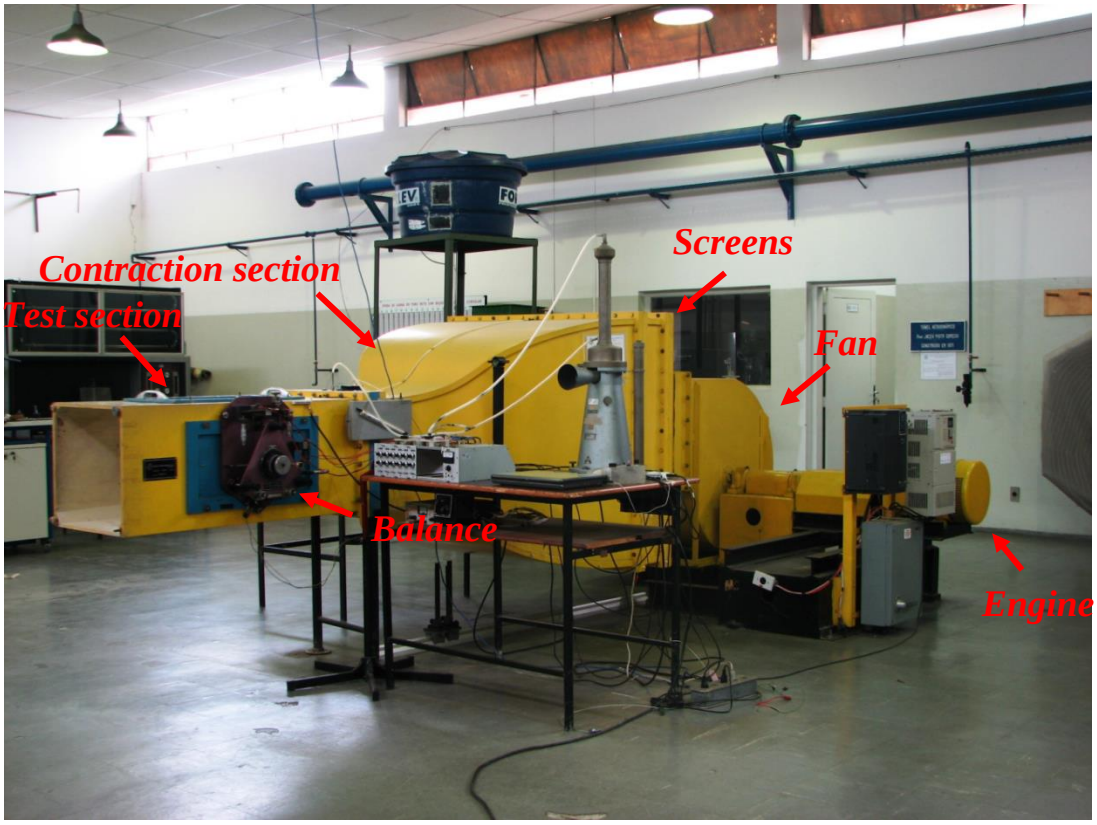

Figure 3.3: An overall view from wind tunnel facility at ITA and its component.

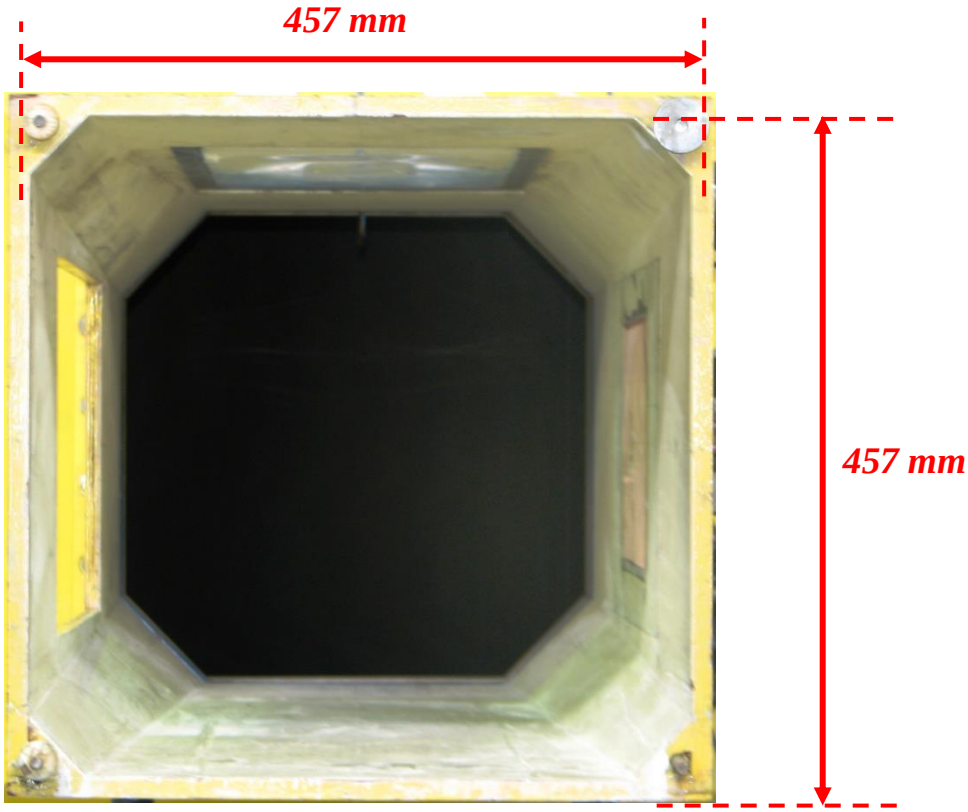

Figure 3.4: A cross section view of the test section from wind tunnel at ITA.

After the settling chamber, the flow passes through a contraction section with ratio of 7.2:1 to arrive to the test section. In the contraction process, the flow undergoes steep acceleration and, consequently, a decrease in static pressure, i.e, the remainder of total pressure increment is converted into flow velocity (kinetic energy increment). During the acceleration process, the flow velocity fluctuations do not increase, resulting in low turbulence levels in the test section.

Static and total pressure measurements are taken from free flow in a section upstream of the test section at the end of the contraction region. At the test section entrance, the flow velocity profile is not uniform because the cross-sectional area changes at the contraction element. Due to this non uniform flow, the total and static pressure ports, which are located upstream of the test section, provide erroneous measurements to represent the free flow pressures at the test model position, therefore the measurements need to be corrected. After the inlet test section, the velocity profile becomes uniform so that the flow quality is very high at center of the test section where the models sit. In the outlet section, the flow has static pressure equal to the atmospheric pressure.

The maximum flow velocity reached at the wind tunnel test section is 30.6 m / s. An investigation at the central plane of the test section using hot a wire anemometer showed that the RMS values of the axial velocity fluctuation are approximately 0.5 % of the average velocity, indicating a low turbulence level. The turbulence level investigation is shown in details on subsection 3.4.1. A three axes balance is fixed at lateral window of the wind tunnel and its characteristics will discussed in detail in the section 3.6.

3.4 Flow characteristics at test section

The flow characteristics in the test section need to meet specific criteria in order to reach good results in the experimental investigations. In this work, the boundary layer profile and turbulence intensity at test section are controlled in order to attain the desired conditions for the wind tunnel test campaign. Thus, hot wire anemometry was used in preliminary tests to control the flow parameters in order to check the flow characteristic requirements for tests.

The anemometry system used for characterizing the flow was of the constant temperature type which operates by means of a feedback system that keeps unchanged the sensor's temperature.

The sensor response to variation in flow velocity is not linear. However, a linear response is desired since the signal processing is facilitated and accuracy in turbulence measurements is increased. Therefore, a linearizer was coupled to the anemometer amplifier output.

There are different sensor types offered by manufacturers for a variety of applications (DANTEC). According to the conditions under which the tests were carried out, the probe DISA 55P01 (Gold-Plated wire sensor type) was chosen. Figures 3.5 show a schematic drawing of the anemometry system. In addition, the probe used in the experimental tests is presented in figure 3.6.

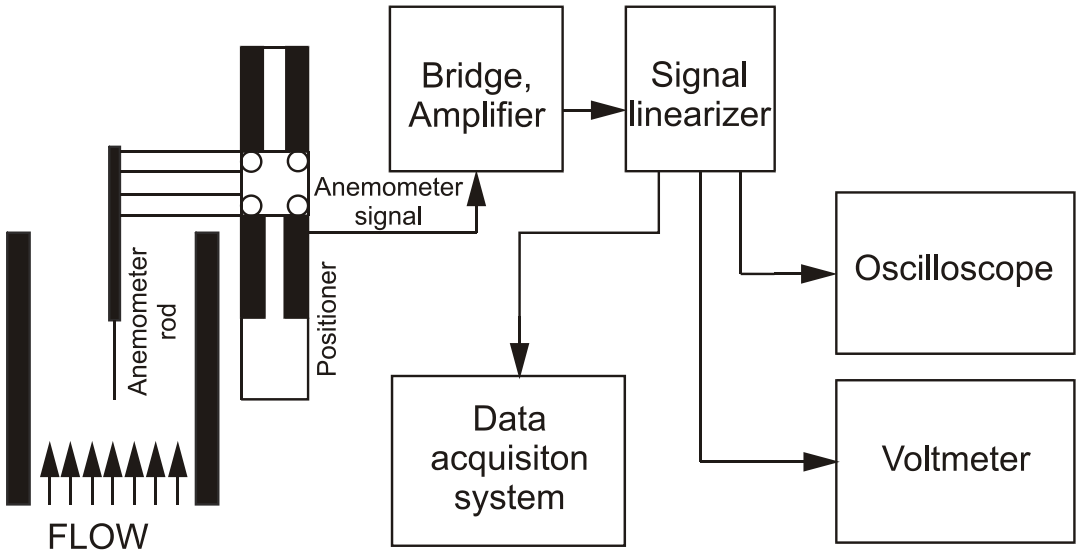

Figure 3.5: Anemometry system used in the experimental tests.

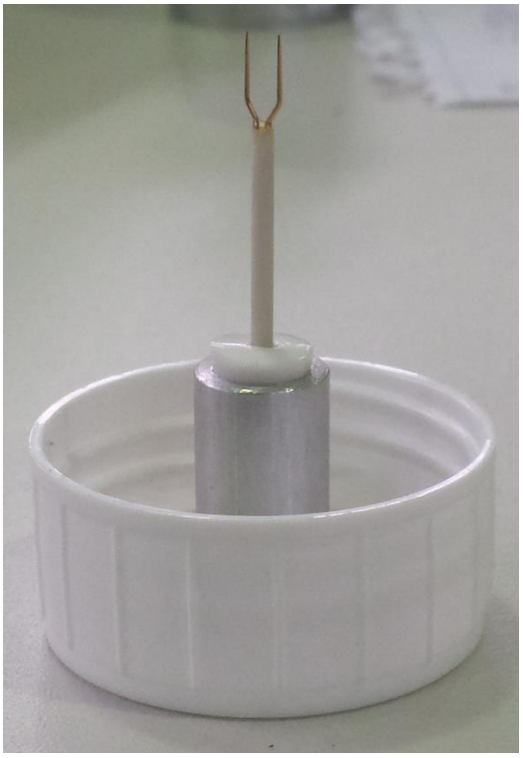

Figure 3.6: Probe used in the experimental tests (DISA 55P01).

The placement of the sensor inside the wind tunnel test section was performed using a three-axis positioner (DANTEC 57H00), which allowed the positioning of the anemometer in any point of the test section with a resolution of 0.1 mm. The anemometer sensor mounting rod is fixed to the positioner by means of a wooden sting support such that the assembly interference inside the wind tunnel is minimal. The figure 3.7 shows a schematic drawing of the positioner.

The anemometer calibration was performed using a TSI 1125 caliper. This equipment has been specially built for calibration of hot wire/film anemometers in air or liquids. During the calibration, the sensor was fixed to a vertical arm that positions the wire in the output of a small hole where a free jet is produced.

The sensor was calibrated by calculating the free jet's velocity and correlating it with anemometer output signal. The free jet comes from a pressurized chamber so its velocity is calculated as a function of the pressure measurement in the chamber, with relation to atmospheric pressure, measured with a Betz anemometer.

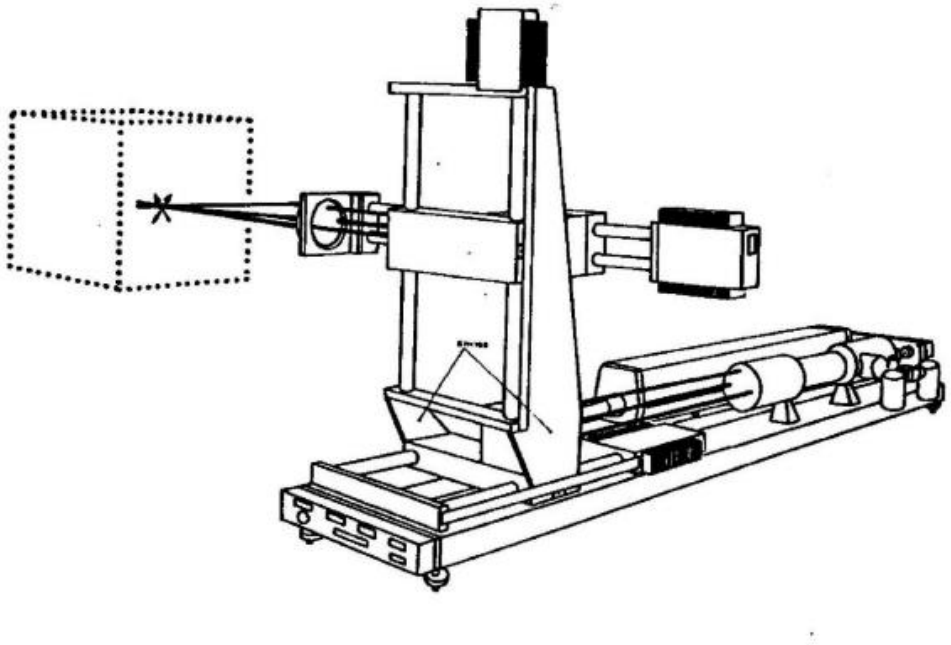

Figure 3.7: Three-axis positioner DANTEC supporting the anemometer sensor.

3.4.1 Turbulence intensity mesurement

The turbulence level characteristics of a wind tunnel may affect the experimental results. The role of the turbulence levels can be more significant at low Reynolds numbers due to instable aerodynamic phenomena at this flow condition such as laminar-turbulent transitions and laminar separation bubble formation.

McArthur (2007) justifies that change in turbulence levels result in variations in airfoil aerodynamic performance for different wind tunnel facilities in the range of Reynolds numbers between 60,000 and 300,000. Thus, it is important to control the turbulence fluctuation level parameter, mainly at low Reynolds number conditions, during wind tunnel tests in order to correlate aerodynamic phenomena with the turbulence conditions as well as to keep the turbulence intensity in levels acceptable for the objectives of wind tunnel tests.

The turbulence intensity is defined as:

$$I = \frac{u}{U} = \frac{\sqrt{\frac{1}{3}\left(\overline{u'^2} + \overline{v'^2} + \overline{w'^2}\right)}}{U_\infty} \quad (3.1)$$

Where,

u = the Root-Mean-Square (RMS), or Standard Deviation, of the turbulent velocity fluctuations.

U = the average of the free-stream velocity.

An isotropic turbulence condition can be assumed at a distance behind the wind tunnel mesh screen (SCHLICHTING; GERSETEN, 2000). Thus, the equation 3.1 can be simplified as follows:

$$I = \frac{u}{U} = \frac{\sqrt{\overline{u'^2}}}{U_\infty} \quad (3.2)$$

Prior to the wind tunnel campaign, the turbulence level was measured at center of the test section for different velocities and consequently different Reynolds number conditions. Figure 3.8 shows the turbulence intensity along the operational velocity range of the wind tunnel.

Barlow et al. (1999) present turbulence intensity around 0.5% in streamwise direction as acceptable to conduct wind tunnel tests. In this context, the results present low level of the turbulence intensity so that the most velocity range has values lower or equal 0.50%.

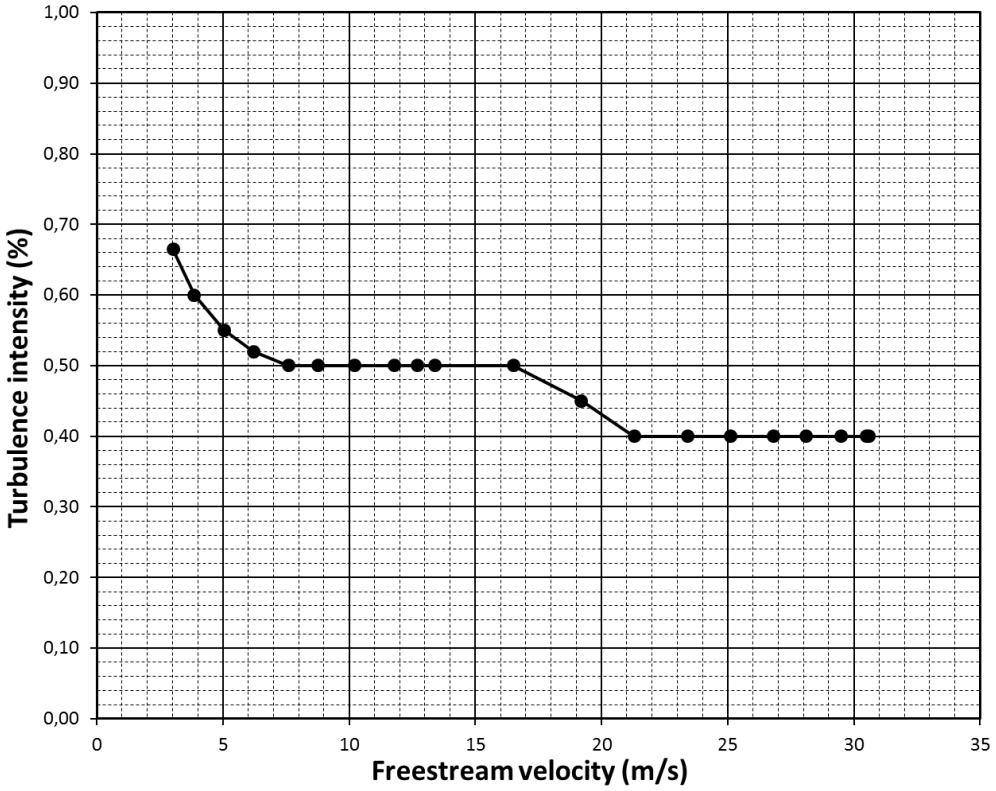

Figure 3.8: Turbulence intensity variation along the operation velocity range of the wind tunnel at ITA.

3.4.2 Wind tunnel sidewall boundary layer profile

The boundary layer of the wind tunnel sidewalls significantly affects the flow parameters over the airfoil's upper surface. This occurs because the low pressure regions in the model interacts with the low velocities on boundary layers of the wind tunnel sidewalls which cause a massive efflux from the wall to the model's surface, thus changing the pressure distribution over entire airfoil span.

In order to minimize the boundary layer effects of the wind tunnel sidewalls, shields called "endplates" are placed at the ends of the airfoils at a certain distance from the wind tunnel sidewalls so that they isolate the wall´s boundary layer from the flow over the model.

Kubo et al. (1989) shows that, for a circular endplate, the relationship between the endplate diameter and the characteristic length of the body tested being greater than 8.5 provides a two-dimensional flow along the wing span of various body shapes (flat plate,

circular cylinder, rectangle and square). Kubo et al. (1989) also suggested that the endplate part upstream of the test section body does not interfere in the interaction between the wall's boundary layers and the body´s wake. Thus, the endplates could be extended only downstream of the model.

However, Standby (1977) found that the endplate length upstream of the model also influences the flow parameters. Actually, he noticed that using rectangular endplates for testing a circular cylinder, the distance in flow direction from the cylinder center to the endplate leading edge should be equal to at least 2.5 times the cylinder diameter. He also notes that this distance cannot be very large, which would nullify benefits of the endplate.

Based on these considerations and on the internal dimensions of the wind tunnel test section, rectangular endplates were sized considering minimum blockage and desired model dimensions.

In order to determine the distance between the tunnel walls and the endplates, the boundary layer thickness of the wind tunnel sidewalls was verified using hot wire anemometer. It was observed that, for all the operational speed range of the wind tunnel, the boundary layer does not exceed the thickness of 20.0 mm at the central plane of the test section.

Since the boundary layer thickness of the wind tunnel sidewalls is known, endplates with thickness of 5 mm were positioned 17 mm away from the wind tunnel walls. So, the model has a clearance of 23 mm from each sidewall, which leads to an effective model span of 410 mm (figure 3.9).

As the endplates start 350 mm ahead of the test section central plane (Standby, 1977), it can be assured that the spacing of 23 mm is sufficient to isolate the models from wind tunnel boundary layer because at the endplate leading edge the boundary layer thickness is smaller than 20 mm.

The endplates are fixed to the wind tunnel walls forming a sort of false wall. This choice is justified by considering the interference that the endplates could cause on the model's drag if they were fixed directly to it. Besides, inherent complications could occur with models of the different sizes and geometries. The edges of the endplates are in contact with the floor and ceiling of the test section.

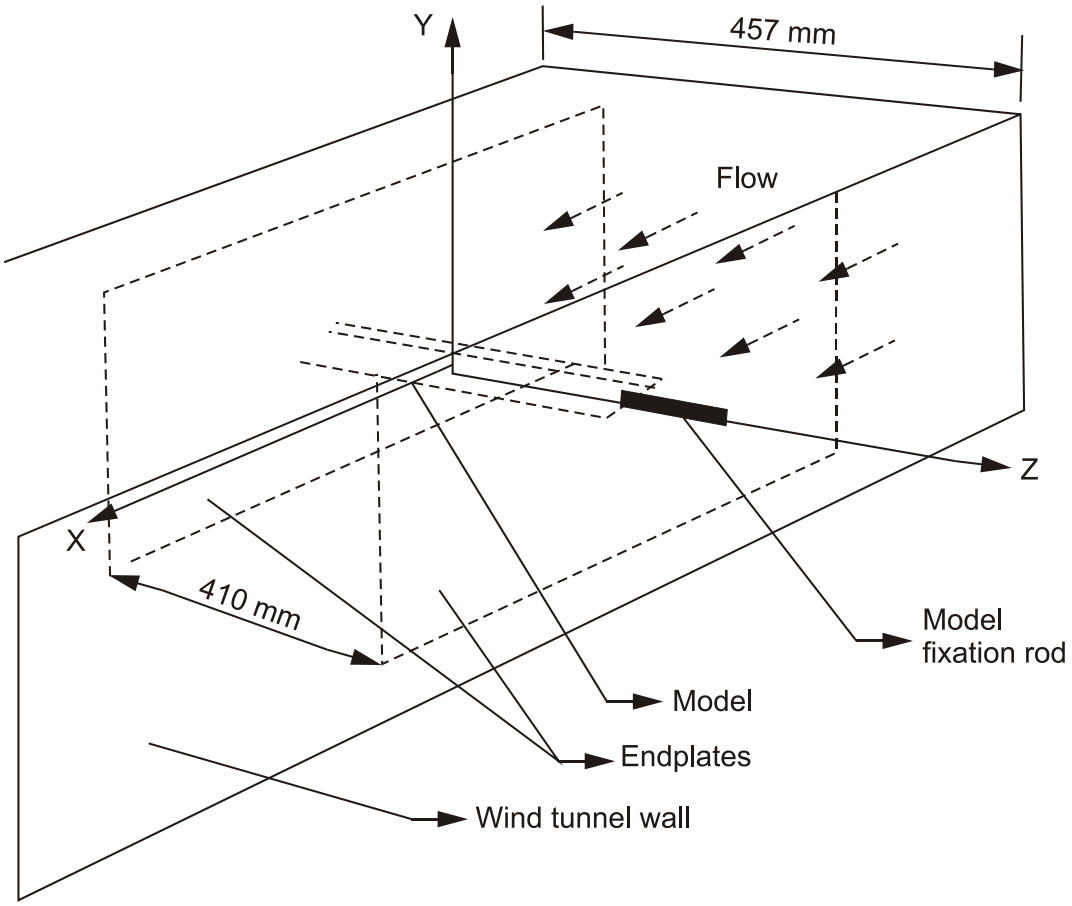

Figure 3.9: Endplate system assembly at wind tunnel test section.

The mounting of the endplates to the wind tunnel walls are accomplished by four screws of 4.5 mm in diameter for each false wall, using spacers. Thus, there is a system which allows the correct adjustment of the distance between the wind tunnel walls and the false walls while also providing good rigidity to the assembly. The assembly was positioned so that the origin of the endplate longitudinal axis either coincides or is very close to the position of the axis of the model's mounting rod (figure 3.9).

3.5 Wind tunnel wall corrections

The flow over an aerodynamic airfoil at a given Reynolds in a wind tunnel test section number is distinct from the free flow condition. The bounds established by wind tunnel walls and model supporting system cause changes to the flow over the tested body. It is therefore necessary to correct the aerodynamic data measured in the wind tunnel in order to represent the conditions out the influence of wind tunnel's apparatus. In this context, wind tunnel corrections regarding the solid blockage, wake blockage and streamline curvature effect were carried for the wind tunnel campaign of this work.

3.5.1 Solid blockage

The physical boundaries that are imposed by wind tunnel walls to the flow over a model in the test section reduce the cross-sectional area through which the air can flow when compared to free stream flow conditions. Therefore, as consequence of the continuity law, the flow near to model surface increases velocities due to solid blockage effect. This effect is represented by changes in velocity or dynamic pressure and must be taken into account. The wind tunnel correction due to solid blockage, considering a two-dimensional body is calculated from a doublet summation and an effective increment in velocity is established by Glaubert (1933) as:

$$\varepsilon_{sb} = \left(\frac{\Delta V}{V_u}\right) = \frac{\pi^2}{3} . \frac{\lambda_2}{4} . \frac{t^2}{h^2} = 0.822 \lambda_2 . \frac{t^2}{h^2} \tag{3.3}$$

Where,

ΔV = axial velocity

V_u = uncorrected velocity

λ_2 = shape factor = 1.5

t = airfoil thickness

h = height of the wind tunnel test section

3.5.2 Wake blockage

Wake blockage is a result of the constraint that is imposed by the test section wall on the wake of the tested model. The body´s wake in a wind tunnel section produces pressure and velocity fields lower than the freestream. The velocity outside of the wake under physical constraint (closed wind tunnel test section) will be higher than under freestream conditions as consequence of the law of continuity. The higher velocity outside of the wake induces lower pressures according to Bernoulli´s principle which grow over the model establishing a pressure gradient and resulting in an increment in velocity at the model surface.

In order to establish a mathematical correction for wake blockage effect, a theoretical model needs to properly represent the model´s wake and the wind tunnel walls. The model´s wake is modeled by a line source at the model's trailing edge. A sink of equal strength is established far downstream to satisfy the continuity law. The wind tunnel ceiling and floor are presented using the image system concept that maintains an infinite vertical row of source-sink pairs. The image sources avoid axial velocity at the model surface whereas the image sinks will induce a horizontal velocity. Maskell (1965), based on the mathematical modeling discussed, suggests the following velocity correction for a two-dimensional model:

$$\varepsilon_{wb} = \frac{\Delta V}{V_u} = \frac{c/h}{2} C_{D_u} \tag{3.4}$$

Where,

ΔV= axial velocity

V_u= uncorrected velocity

c= airfoil chord

h= height of the wind tunnel test section

C_{D_u}= uncorrected drag coefficient

3.5.3 Streamline curvature

The streamlines around any lifting body limited by ceiling and floor of a wind tunnel undergo deformation when compared to free flight. These streamline changes cause an apparent increase in the model's camber. As a consequence, an airfoil close to wind tunnel walls has increased lift and moment about the quarter chord as compared to the free air condition.

A mathematical model based on the image-system concept predicates the geometric effect of the streamline deformations. It is assumed that the airfoil is small, and that it can be considered as a single vortex located at the quarter-chord. Following the image-system approach, vortices of alternating signs are placed from and to infinity above and below the airfoil.

The horizontal velocities induced by image pairs cancel mutually. In contrast, the vertical components are added. Thus, a boundary-induced upwash angle appears and it is represented by an angle of attack correction. The following corrections add the effect on lift and pitching moment coefficients due to streamline curvature:

$$\Delta C_{L_{SC}} = \sigma C_L \tag{3.5}$$

$$\Delta C_{M1/4_{SC}} = -\frac{\sigma}{4}\Delta C_{L_{SC}} \tag{3.6}$$

Where,

$$\sigma = \frac{\pi^2}{48}\left(\frac{c}{h}\right)^2$$

In this work, the correction due to streamline curvature effect applied a more complex mathematical modeling that considers a vorticity distribution along the airfoil chord instead of a concentrated point at the quarter-chord (ALLEN; VINCENTI, 1944). However, the simple previous lift and moment correction formulation is still valid. The following equation corrects the angle of attack change that is caused by streamline curvature:

$$\Delta\alpha_{sc} = \frac{57.3\sigma}{2\pi}\left(C_{L_u} + 4C_{M_{1/4_u}}\right) \tag{3.7}$$

Where,

C_{L_u} = uncorrected lift coefficient

$C_{M_{1/4_u}}$ = uncorrected pitching moment coefficient about the quarter chord

The wall effect on lift distribution was neglected since the chord of the airfoils tested is lower in length than 70% of the wind tunnel height (BARLOW et al., 1999).

3.5.4 The overall wind tunnel wall corrections

The complete low speed wall effects for two-dimensional tests of this work are computed by following formulae:

$$\alpha = \alpha_u + \frac{57.3\sigma}{2\pi}\left(C_{L_u} + 4C_{M_{\frac{1}{4}u}}\right) \tag{3.8}$$

$$C_L = C_{L_u}(1 - \sigma - 2\varepsilon) \tag{3.9}$$

$$C_D = C_{D_u}(1 - 3\varepsilon_{sb} - 2\varepsilon_{wb}) \quad (3.10)$$

Where,

α = angle of attack

$\varepsilon = \varepsilon_{sb} + \varepsilon_{wb}$

C_L = lift coefficient

C_D = drag coefficient

$C_{M_{1/4}}$ = pitching moment coefficient about the quarter-chord position

3.6 Force and moment measurements

3.6.1 Balance Apparatus

Measurements of lift, drag and pitching moment of the experimental investigations were obtained using a three-axis balance (PLINT & PARTNERS LTD) suitable for measurements of two-dimensional bodies. The apparatus was fixed at one of the side windows of the wind tunnel's test section. Figures 3.10 and 3.11 show the balance schematics.

The balance is composed of two parts, respectively the base and force plates. The base plate is attached to the sidewall whereas the force plate is fixed to the model's mounting rod. These two plates are interconnected by three springs working as a cantilever beam, respectively the after spring (spring A), forward spring (spring F) and drag spring (spring D).

The lift and drag forces and the pitching moment effected by the wind over the model are transmitted to the force plate by the model's mounting rod. In turn, the force plate transmits such efforts to the base plate through the springs which act as sensing elements.

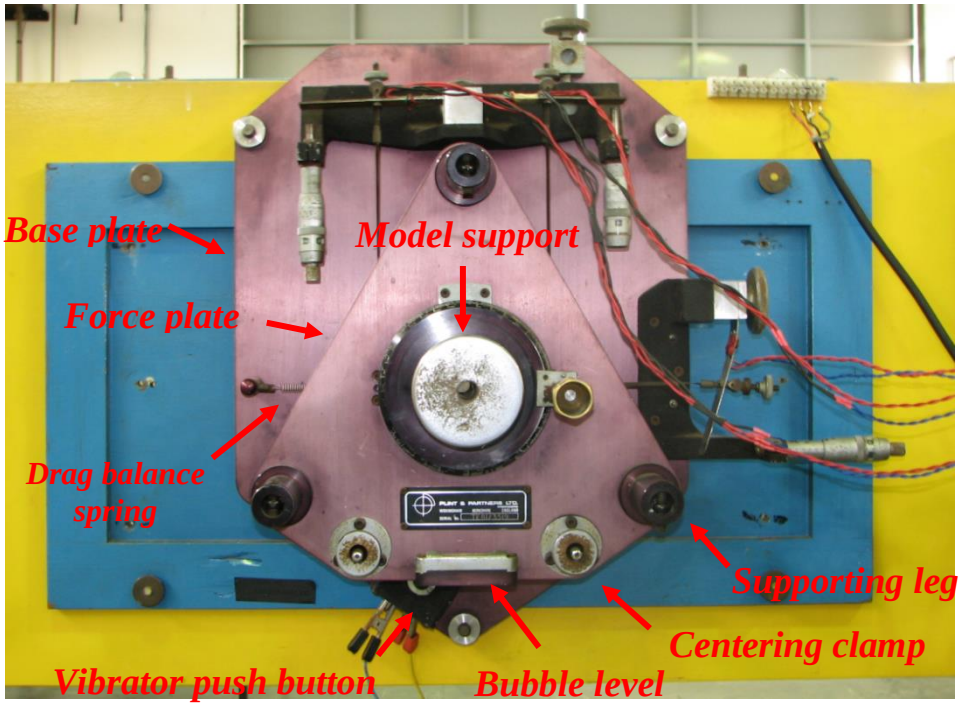

Figure 3.10: Front view of the three-axis balance Plint & Partners.

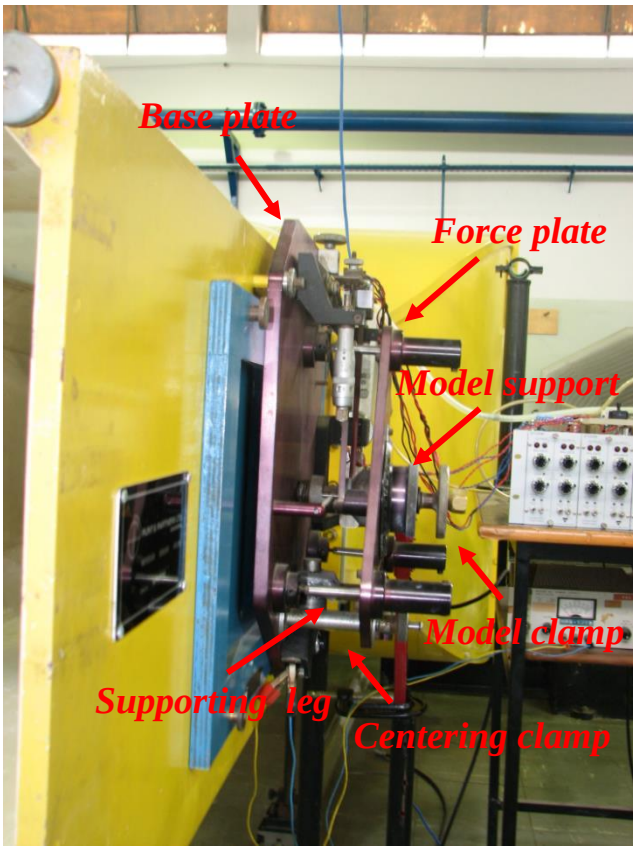

Figure 3.11: Lateral view of the three-axis balance Plint & Partners.

In each of these springs were installed four strain gauges, two on each spring´s side forming a complete Wheatstone bridge which increases the sensor element sensitivity and further promotes temperature compensation, avoiding that environment temperature variations affect the balance's measurements (figure 3.12).

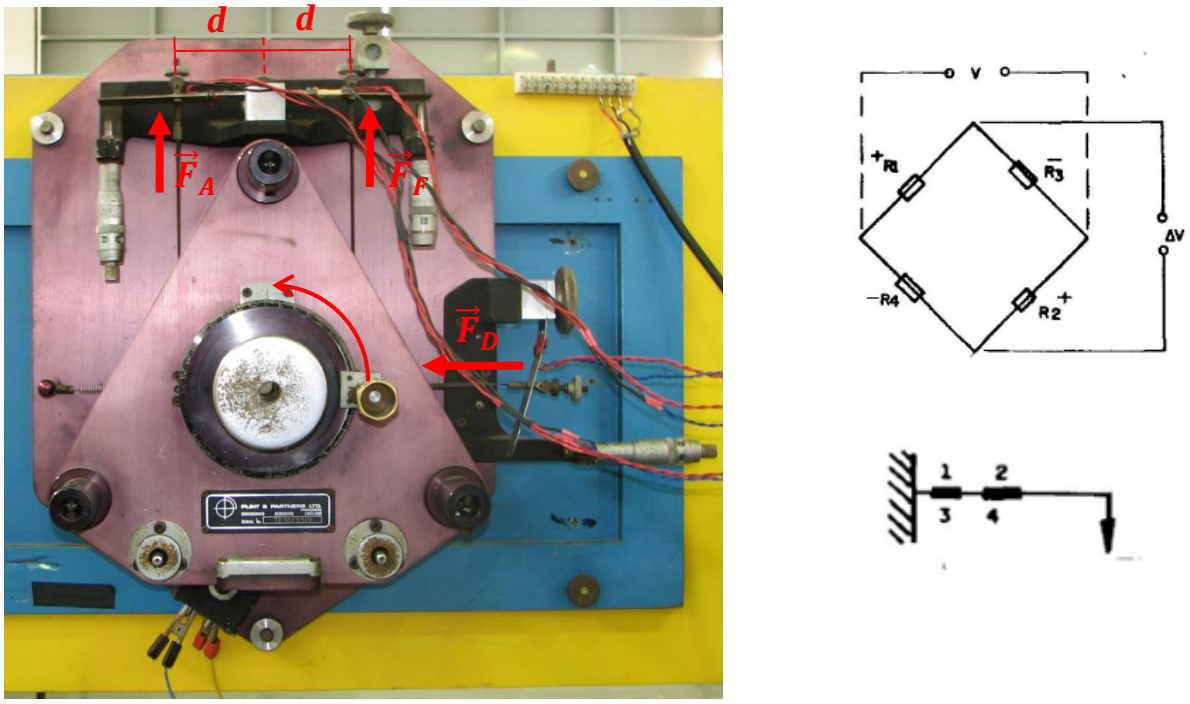

Figure 3.12: Strain gauge installed in the spring for drag and lift forces and strain gauge electrical scheme.

Each Wheatstone bridge must be supplied with a DC voltage (approximately 6 volts). Since the signal produced by each of the springs has a low amplitude (in the order of millivolts), signal amplification is necessary. Thus, the electric wires containing the bridge´s output signal were connected to a signal conditioner, which executes the signal amplification. The conditioner gains were checked for limit voltages at full loading conditions (figure 3.13).

Figure 3.13: Signal conditioner used to amplify the bridge´s output signal.

Coupled to the model's mounting rod (figure 3.10), the mechanism for measuring angle of attack can be observed, graduated from 0 to 360 degrees with one degree markings. Therefore any modification on angle of incidence can be directly read visually, which can be locked to allow measurements of the aerodynamic loads at a fixed angles of attack.

At the bottom of the force plate (figures 3.10) is located a bubble level responsible for the alignment of the plate with respect to the gravity vector, ensuring that lift and weight forces are supported in the same way by the springs "A" and "F".

Attached to the bottom of the base plate (figure 3.10) is installed a vibrating device connected to the balance in order to promote the stabilization of the spring output signals after each loading introduced during calibration, thus decreasing the waiting time for each reading. The balance also has two latches that fix the force plate to the base plate.

3.6.2 Applied load determination at balance device

The figure 3.14 shows a schematic drawing of the balance, showing the sensor elements (springs) "A", "F" and "D", which are cantilevered blades embedded in the fixed part of the balance called base plate.

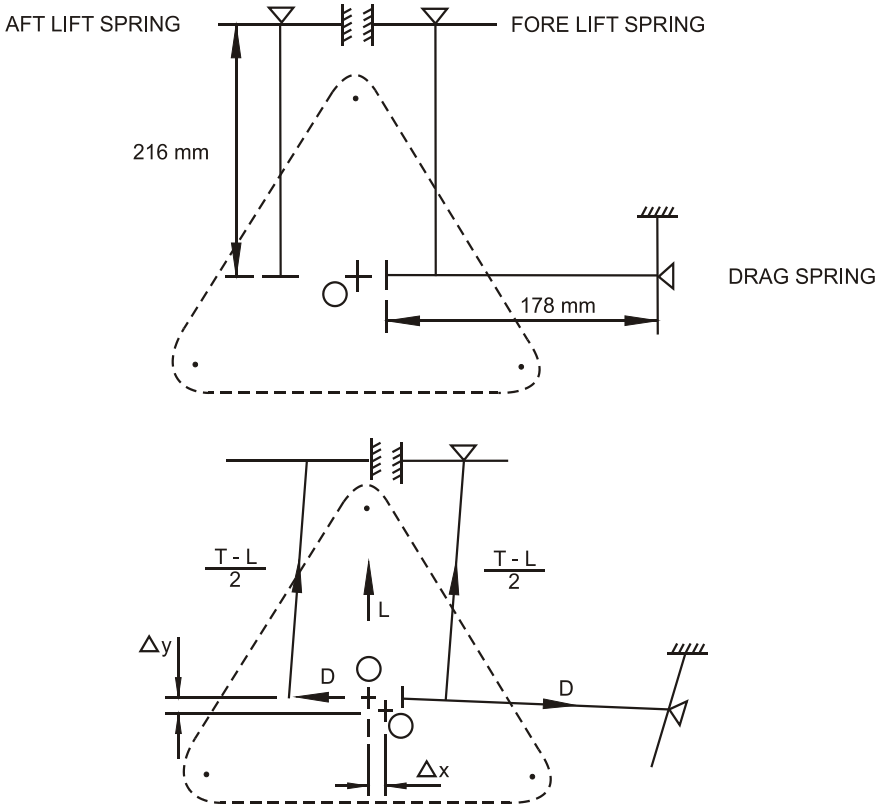

Figure 3.14: a) Schematic view of the sensing elements A, D and F. b) interaction of the sensor elements A, D and F due to the movement of the deflection point O.

The aerodynamic loads are transmitted to the balance's springs. The drag force (D) is transmitted to the "D spring", which is deflected with increasing drag. The lift force (L) has opposes the weight force (model and force plate), compressing the springs "A" and "F". As the mounting rod is located at the middle point between the application point of the lift forces (springs "A" and "F"), it can be considered that the lift loads are equal.

The pitching moment (referenced at point "O") applied to the model has anti-clockwise movement (positive sign convention), it can be seen that the effect of this moment (M) is a misbalance between sensors A and F, where the sensor "F" will undergo a force with

same intensity and opposite direction than the force imposed on the sensor "A". Thus, the resulting of forces in the springs can be written as follows:

$$F_A = \frac{P}{2} - \frac{L}{2} + \frac{M}{2d} \tag{3.11}$$

$$F_F = \frac{P}{2} - \frac{L}{2} - \frac{M}{2d} \tag{3.12}$$

$$F_D = D \tag{3.13}$$

Adding up equations 3.11 and 3.12, we have the final formulations to obtain the lift force from sensors A and F:

$$L = -(F_A + F_F) \tag{3.14}$$

Subtracting the equations 3.11 and 3.12, we have the final formula to obtain moment force from sensors:

$$M = (F_A - F_F)d \tag{3.15}$$

In short the lift force is obtained directly from the sum of forces from sensors A and F, the moment from the difference between the same sensor forces and the drag force comes directly from D sensor.

Figure 3.14b shows that the spring deflections produce a coupling effect between lift and drag forces, that is, the balance presents lift values for a model that has only drag force and vice-versa. However, as it can be seen in the balance manual, this coupling is very small and, to a first approximation, can be neglected.

3.6.3 Calibration procedure

In order to measure lift, drag and pitch moment of the model in the test section, a calibration procedure was performed on the balance´s three load cells to establish the correlation between the voltage read by the acquisition system and the forces applied to the model.

The calibration procedure for the load cells was carried out by a standard mass weight set connected with a pulley and wire system, which was assembled in order to allow the application of forces in a specific axis (lift and drag) of the balance. Figure 3.15 shows the assembly for the calibration procedure.

The limit loads of the calibration were established based on a load envelope of the tests. The calibration was done by incrementing loads from zero to the estimated maximum value and the inverse process was done in order to evaluate balance system hysteresis. Approximately 20 different loads were used in each calibration process, and during a sampling time of one second 1000 measurements were performed.

The average value of voltage measurements was correlated with each applied force. The sensors A and F were calibrated simultaneously considering that the vertical force applied to the balance was distributed equality to both sensors. On the other hand, the sensor D was calibrated without lift loading.

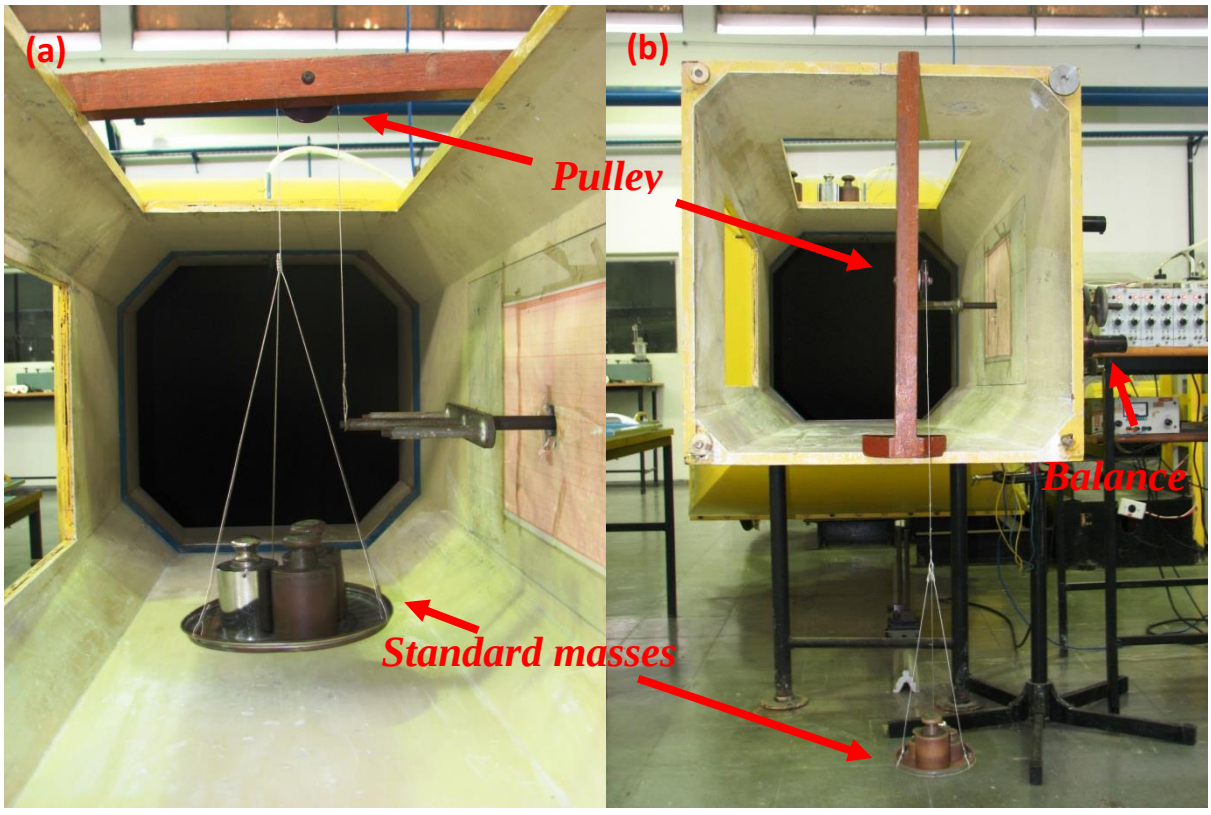

Figure 3.15: Calibration assembly for a) sensors A and F b) sensor D.

For pitching moment measurements, calibration was not performed because moment measurements are obtained in an indirect way as mentioned previously. However, a correlation between model angle of attack of and center of gravity position changes was performed. The calibration procedure was done after the model had been assembled into the test section and attached to the balance plate by its metal axis. Pitching moment was measured (indirect CG measurement) for angles of attack of 0, 15, 30 and 45 degrees in order to establish a correlation between angle of attack and CG changes.

During the calibration procedure of the load cells for lift (A, F) and drag (D), a small vibration was applied to the model in order to accelerate the accommodation of structural parts. The vibration was applied before starting the measurement of each calibration point. This procedure was also applied during the test execution.

The anemometric calibration procedure is similar to perform for force calibration. The pressure measurements were performed by a pressure transducer with limits between 0 to 100 mm H_2O that was calibrated using a Betz manometer as reference.

Initially, the pressure was increased and decreased at least three times in order to wet the internal walls of the Betz manometer and so guaranteeing the zero pressure datum. The pressure was then increased from zero in increments up to the maximum pressure verified in the experimental tests. After reaching the maximum pressure value, the pressure was then decreased back to zero with the same stepping.

As in the force calibration procedure previously described, a minimum of 20 pressure values were used. One thousand measurements were obtained during one second. For each measuring point the average of these data was used to calculate the calibration values.

The calibration procedures were performed at each wind tunnel test session that lasted four hours in order to minimize changes on load sensors characteristics due to environment temperature variation along the day. The figures 3.16-19 present one calibration set performed for lift (A, F) and drag (D) load cells as well as the pressure transducer. The calibration curve used is a linear regression obtained by least squares method.

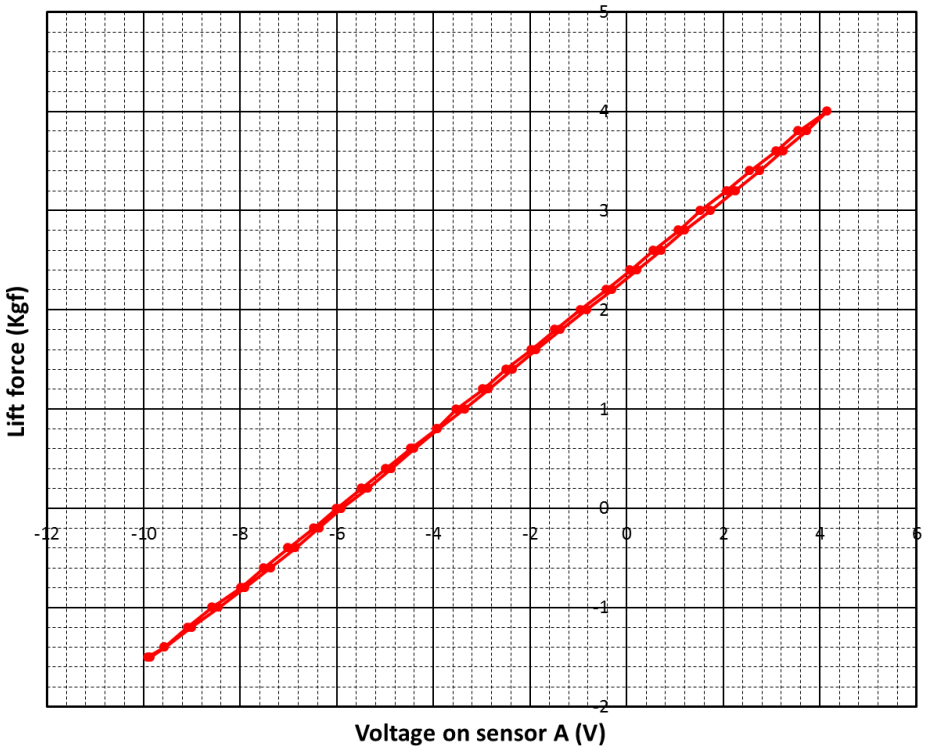

Figure 3.16: Calibration curve of the sensor A (Lift force).

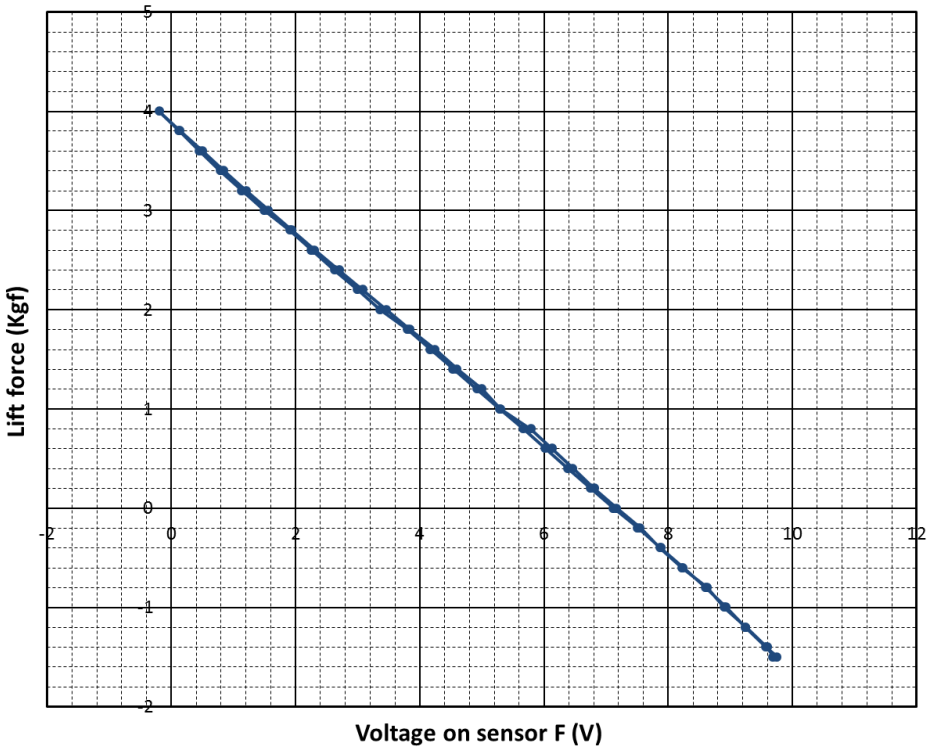

Figure 3.17: Calibration curve of the sensor F (Lift force).

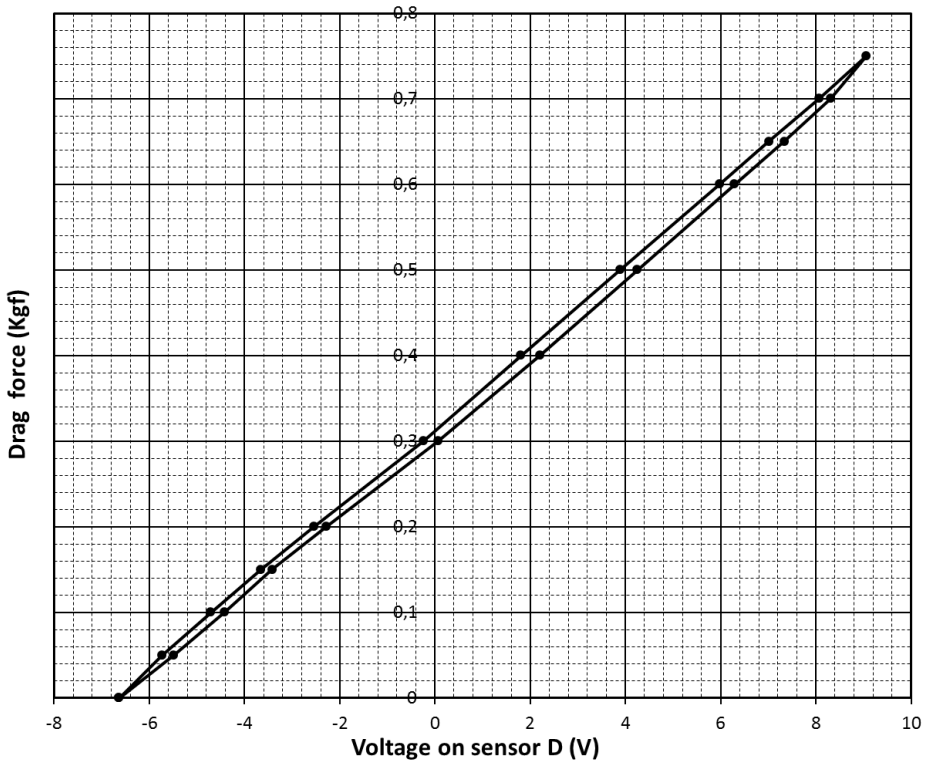

Figure 3.18: Calibration curve of the sensor D (Drag force).

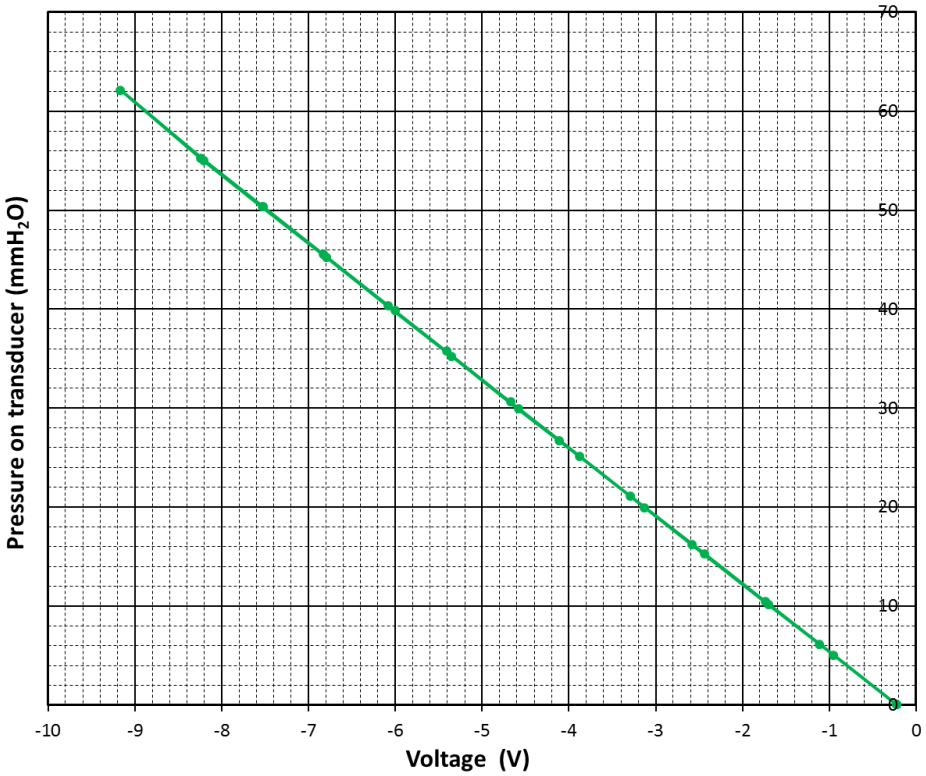

Figure 3.19: Calibration curve of the pressure transducer (Dynamic pressure).

3.6.4 Test performance procedures

During the course of the experimental investigation, the same test performance procedure was repeated in order to maintain correlation between the great number of wind tunnel results of the straight and wavy leading edge configurations.

Once each calibration procedure for three load cells was completed, the test procedure started with coupling the model to the test section by its metal axis connected to the balance. After that, the alignment of the airfoils (at zero angle of attack) was performed with the help of a template attached to the test section wall with a fixed a horizontal marking. The trailing edge of the tested airfoil was then aligned to this mark.

Following the airfoil alignment, the initial signals of the three sensors were read by the acquisition system. In order to guarantee that all initial load cells were well accommodated, the same vibration device used at the calibration process was applied. Signals of the experiment initialization (flow velocity at zero value) need to be especially accurate since the aerodynamic coefficients, in all tests, were obtained from difference of measured values for wind tunnel on and off.

After measuring the initial voltages for the wind tunnel off condition, the wind tunnel was turned on and a desired Reynolds number condition was adjusted by stabilizing a specific dynamic pressure. The Reynolds number condition was kept constant throughout all the measurements for a particular model configuration (wavy geometry and airfoil thickness).

During the performance of the experimental tests, each angle of attack was fixed manually by a rotating device attached to the model's metal axis (figure 3.10). The rotating device is free to rotate 360 degrees with an uncertainty of ±0.5 degrees.

In general, the measurements for each model configuration were performed for a range of angles of attack between -4º and 25º. In the pre-stall regime, the angle of attack was increased every one degree and fixed to perform measurements. In the case of the post-stall regime, it was performed measurements each increase in two degree.

During the wind tunnel tests, a data acquisition code written in LabView performed the acquisition of the sensors three load cells signals as well as of the pressure transducer. Each measuring point was performed for four channels (sensors A,F,D, transducer) where

each one was sampled 3000 times during a sampling time of 3 seconds so performing a sampling rate of 1000 Hz.

The average values from each channel were used in combination with calibration data, environmental conditions and airfoil geometric parameters by the data acquisition code in order to calculate aerodynamic coefficients and the Reynolds number condition.

3.6.5 Uncertainy analysis

The characteristics of this experimental investigation involve many complex aerodynamic phenomena due to the low Reynolds number regime and the wavy leading edge airfoils.

At the low Reynolds number regime, the flow over aerodynamic airfoils is susceptible to hysteresis, formation of laminar bubbles, unsteadiness at higher angles of attack as well as it can be sensitive to turbulence intensity. In addition, the wavy leading edge phenomena can cause small changes in terms of aerodynamic coefficients. Thus, the experimental uncertainties and so the measurement reliability becomes very important in order to evaluate precisely changes caused by complex phenomena on aerodynamic coefficients evaluated in this thesis.

The main goal of this subsection is to describe the calculation of the uncertainties on lift, drag and pitching moment coefficients for the wind tunnel tests.

The uncertainties measured relate to aerodynamic coefficients and the dynamic pressure depends on following formulations:

$$C_L = \frac{L}{q_\infty . c} \tag{3.16}$$

$$C_D = \frac{D}{q_\infty . c} \tag{3.17}$$

$$C_M = \frac{M}{q_\infty . c} \tag{3.18}$$

$$q_\infty = \frac{\rho . V_\infty^2}{2} \tag{3.19}$$

The uncertainties found in the experimental tests can be split into uncertainties regarding procedures and conditions of the tests and measurement equipment.

Procedures and conditions of the tests cause uncertainties related to model geometry, environmental conditions (air density, temperature and humidity), freestream velocity and force determination, data acquisition time and wind tunnel characteristics.

On the other hand, measurement equipment uncertainties are associated to the methods used to indirectly measure physical quantities. Typical examples are load cell and hot wire anemometer measurements.

In this work, statistical uncertainties relative to procedures and conditions of the tests will be considered for freestream velocity and force measurements since they represent the larger components on uncertainty calculation process.

At each test measurement point, a set of velocity and forces measurements (lift, drag and dynamic pressure) are obtained during each sample time. In order to estimate uncertainties from measurements, the standard deviation formula (σ) was applied for the temporal measurements of lift, drag and dynamic pressure according to the following equation:

$$\sigma = \sqrt{\frac{\sum_{i=0}^{n}(x_i - \bar{x})}{n-1}} \tag{3.20}$$

Where,

x_i = single measurement

$\bar{x}$ = mean of data set

n = total number of measurements

In order to minimize the uncertainties in the test procedures, measurement samples were collected between 1000 and 10000 times. A number of 3000 samples presented adequate results considering minimum uncertainties and time of the tests. Thus, measurements are done 3000 times during a time span of 3 seconds so performing a sampling rate of 1000 Hz.

After calculating the standard deviation for dynamic pressure and forces (lift and drag), the overall uncertainties of the procedures and conditions of the tests need to be computed. The overall uncertainties can be calculated appropriately by the Root Sum Square (RSS) formula (SCARBOROUGH, 1955):

$$\delta = \left[\left(\frac{\partial f}{\partial \delta_1}.\delta_1\right)^2 + \left(\frac{\partial f}{\partial \delta_2}.\delta_2\right)^2 + \cdots + \left(\frac{\partial f}{\partial \delta_n}.\delta_n\right)^2\right]^{\frac{1}{2}} \quad (3.21)$$

Applying the formulation 3.16-19 to the overall uncertainty equation in order to obtain uncertainties of lift, drag and pitching moment coefficient, it follows that:

$$\delta_{C_D} = \sqrt{\frac{{C_D}^2.{\delta_D}^2}{D} + \frac{{C_D}^2.{u_{q_\infty}}^2}{q_\infty}} \quad (3.22)$$

$$\delta_{C_L} = \sqrt{\frac{{C_L}^2.{\delta_L}^2}{L} + \frac{{C_L}^2.{\delta_{q_\infty}}^2}{q_\infty}} \quad (3.23)$$

$$\delta_{C_M} = \sqrt{\frac{{C_M}^2.{\delta_D}^2}{M} + \frac{{C_M}^2.{\delta_{q_\infty}}^2}{q_\infty}} \quad (3.24)$$

The uncertainties regarding forces and pressure sensors are obtained by the sensor calibration procedure presented in the subsection 3.6.4. The Gaussian distribution of uncertainties with 95% of confidence (2σ) was considered for all uncertainty calculations.

The data acquisition code computes automatically the uncertainties of the sensors as well as forces and dynamic pressure. Subsequently, the overall uncertainties of the aerodynamic coefficients are calculated.

Table 3.2 shows the overall uncertainties of the aerodynamic coefficients ($C_{L,}$ C_D and C_M) for smooth NACA 0030 airfoil at highest Reynolds number condition tested. The lift coefficients present the lowest uncertainties with an average value of 0.4%. In addition, the drag and pitching moment coefficients have average values of the 1.9% and 1.6% respectively.

The uncertainties show to be quite sensitive to Reynolds number variation, with increasing uncertainties for decreasing Reynolds numbers. In addition, when the uncertainties between different configurations are compared, they show to be less relevant than Reynolds number effects.

α°	C_L	2σ	% 2σ	C_M	2σ	% 2σ	C_D	2σ	% 2σ
-3,3	-0,282	0,004	-1,41	-0,0112	0,00169	-15,0458	0,0319	0,0014	4,28
-1,3	-0,114	0,003	-3,05	-0,0054	0,00147	-27,4353	0,0296	0,0014	4,68
0,7	0,058	0,003	5,18	0,0030	0,00127	42,8379	0,0286	0,0014	4,92
1,7	0,129	0,003	2,17	0,0077	0,00119	15,4463	0,0288	0,0014	4,90
2,7	0,216	0,003	1,20	0,0109	0,00110	10,0907	0,0299	0,0014	4,67
3,7	0,289	0,002	0,85	0,0139	0,00103	7,4133	0,0331	0,0014	4,15
4,7	0,377	0,002	0,61	0,0158	0,00095	6,0294	0,0366	0,0013	3,67
5,7	0,444	0,002	0,50	0,0174	0,00090	5,1813	0,0416	0,0013	3,14
6,7	0,525	0,002	0,41	0,0189	0,00085	4,4920	0,0460	0,0013	2,75
7,7	0,603	0,002	0,35	0,0203	0,00082	4,0118	0,0494	0,0012	2,51
8,7	0,673	0,002	0,32	0,0197	0,00081	4,0994	0,0571	0,0012	2,07
9,7	0,748	0,002	0,29	0,0198	0,00081	4,0673	0,0655	0,0011	1,72
10,7	0,797	0,002	0,27	0,0211	0,00079	3,7566	0,0697	0,0011	1,59
11,7	0,862	0,002	0,26	0,0175	0,00082	4,6637	0,0819	0,0011	1,28
12,7	0,941	0,002	0,26	0,0037	0,00086	23,0479	0,0971	0,0010	1,05
13,7	1,014	0,003	0,25	-0,0059	0,00087	-14,7367	0,1061	0,0010	0,96
14,7	1,057	0,003	0,25	-0,0231	0,00092	-4,0000	0,1286	0,0011	0,83
15,7	1,086	0,003	0,25	-0,0343	0,00095	-2,7521	0,1471	0,0012	0,80
16,7	1,104	0,003	0,25	-0,0443	0,00096	-2,1754	0,1647	0,0013	0,79
17,7	1,124	0,003	0,25	-0,0493	0,00097	-1,9714	0,1769	0,0014	0,80
18,7	1,143	0,003	0,25	-0,0624	0,00100	-1,5949	0,1992	0,0016	0,82
19,7	1,166	0,003	0,25	-0,0787	0,00104	-1,3188	0,2189	0,0018	0,84
20,7	1,190	0,003	0,26	-0,0911	0,00108	-1,1850	0,2432	0,0021	0,87
21,7	1,202	0,003	0,25	-0,0988	0,00108	-1,0963	0,2470	0,0022	0,88
22,7	1,210	0,003	0,25	-0,1015	0,00109	-1,0727	0,2485	0,0022	0,88
23,7	1,217	0,003	0,25	-0,1056	0,00110	-1,0426	0,2484	0,0022	0,88
24,7	1,227	0,003	0,25	-0,1117	0,00111	-0,9974	0,2480	0,0022	0,88
25,7	1,232	0,003	0,26	-0,1185	0,00113	-0,9504	0,2491	0,0022	0,88
26,7	0,600	0,002	0,41	-0,1218	0,00101	-0,8285	0,2552	0,0022	0,87
27,7	0,631	0,003	0,40	-0,1305	0,00102	-0,7815	0,2554	0,0022	0,87
28,7	0,714	0,003	0,36	-0,1552	0,00105	-0,6734	0,2569	0,0022	0,87
30,7	0,845	0,003	0,34	-0,1992	0,00113	-0,5686	0,2606	0,0023	0,87
32,7	0,913	0,003	0,34	-0,2305	0,00124	-0,5361	0,2619	0,0023	0,87
35,7	1,018	0,004	0,35	-0,2861	0,00143	-0,4988	0,2668	0,0023	0,87

Table 3.2: Overall uncertainties of the aerodynamic coefficients for the smooth NACA 0030 airfoil at Re=290,000.

3.6.6 Repeatability analysis

The previous subsection detailed the uncertainty calculation procedures. However, even for an experimental process controlled by parameters and uncertainties, the tests can have non-deterministic results with apparently random behavior caused by aerodynamic phenomena.

This is the main reason why when both in industry and academia carry out experimental wind tunnel investigations, besides controlling uncertainties, repeatability tests are performed in order to understand deterministic and non-deterministic aerodynamic characteristics of the phenomena under scrutiny.

Initially, repeatability tests are performed in the beginning of a wind tunnel campaign in order to conduct appropriate evaluation of the deterministic aerodynamic characteristics. For instance, a flapped airfoil could present aerodynamic hysteresis at low Reynolds numbers. Repeatability tests must provide the understanding of whether the understanding of deterministic conditions is sufficient for the proper airfoil design.

After brief discussions regarding repeatability tests in experimental investigations, the repeatability tests of this work will be presented in order to demonstrating proper accuracy in the evaluation of the wavy leading edge phenomena based on the experimental tests performed.

In the beginning of the experimental investigation, three independent tests for each airfoil thickness of the smooth configuration were carried, at Re=290,000, in order to evaluate the repeatability of the tests.

Figures 3.20-22 plot present the lift repeatability for airfoils NACA 0012, NACA 0020 and NACA 0030. Good repeatability is seen for almost every range of angles of attack, since repeated points fall inside of the uncertainty boundaries. For airfoils NACA 0012 and NACA 0020, the repeatability points slightly fall outside of uncertainty limits at $3°<\alpha< 6°$ and $8°<\alpha< 10°$ respectively. In addition, the thinnest airfoil reaches the same maximum lift values, however with decreased stall angle equal to one degree.

The thickest airfoil presents the best result in terms of repeatability with whole range of angles of attack totally covered by uncertainty limits.

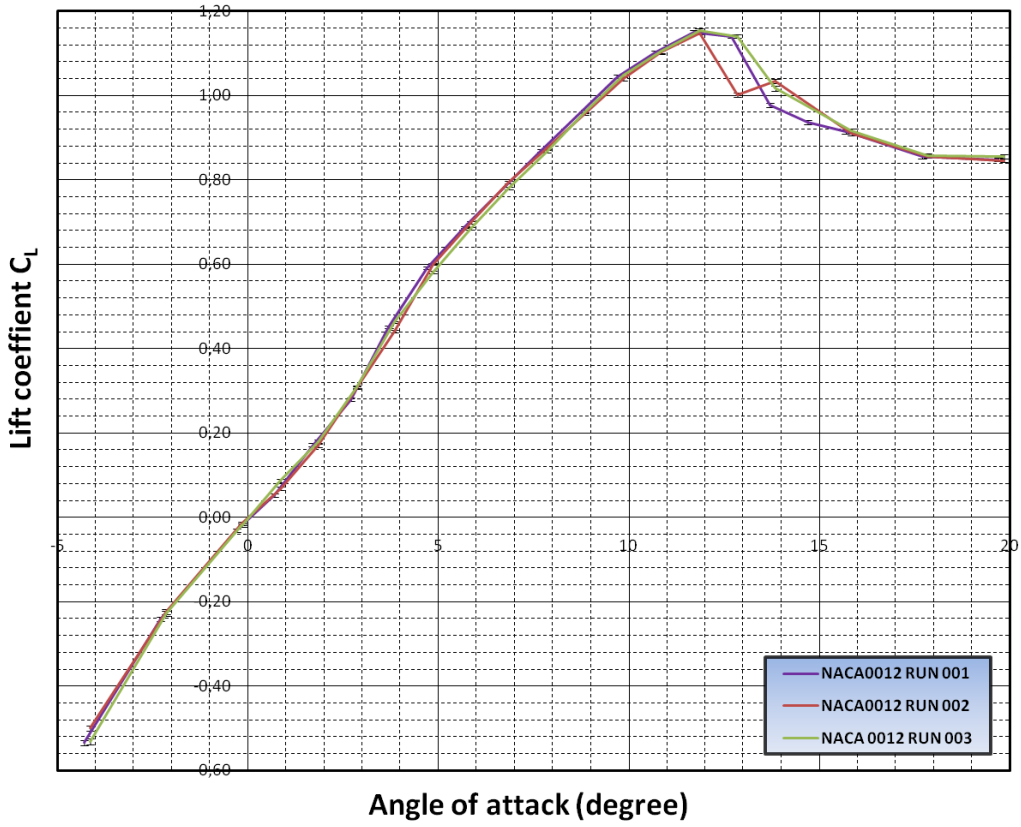

Figure 3.20: Repeatability curves (lift) for smooth NACA 0012 airfoil (Re=290,000).

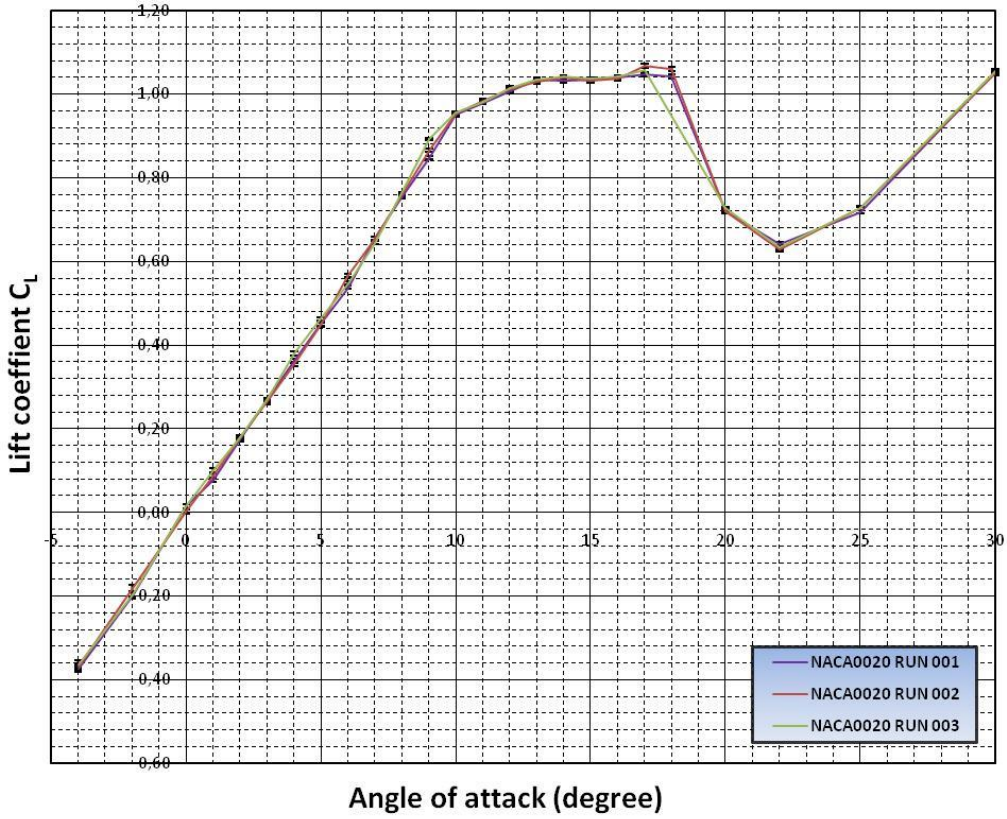

Figure 3.21: Repeatability curves (lift) for smooth NACA 0020 airfoil (Re=290,000).

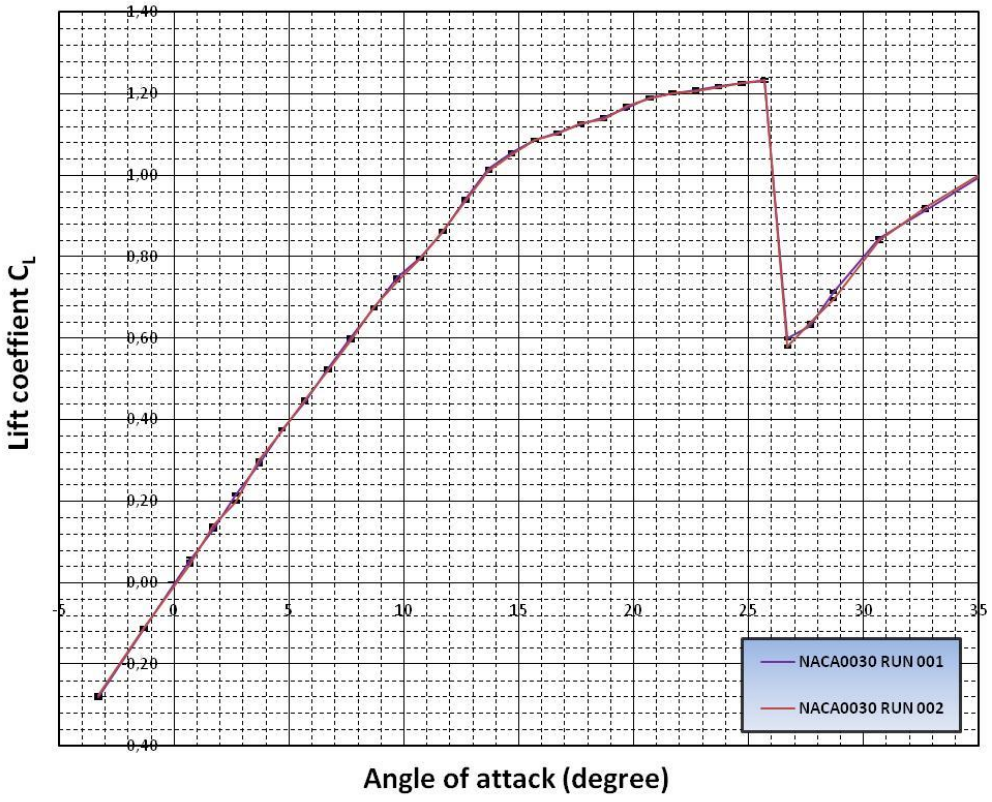

Figure 3.22: Repeatability curves (lift) for smooth NACA 0030 airfoil (Re=290,000).

The figures 3.23-25 show drag repeatability characteristics similar to the lift curves. The thinner airfoils present repeatability points outside of the uncertainty limits for ranges of angles of attack similar to lift curve. However, the drag curves present higher dispersion showing to be less repeatable. The airfoils NACA 0012 and NACA 0020 present drag values outside the uncertainty limits at $3°<\alpha< 10°$ and $7°\alpha< 13°$ respectively. In addition, as in the lift curve, the thickest NACA 0030 airfoil presents drag repeatability values within the uncertainty limits of the tests over the entire range of angles of attack.

It seems likely that a systematic aerodynamic phenomenon is present on repeatability tests in specific ranges of angles of attack for the thinner airfoil. On the other hand, the thickest airfoil does not present this characteristic.

Actually, the airfoils NACA 0012 and NACA 0020 after angle of attack 2° and 6° respectively undergo an increase in lift curve caused by mainly by flow separation at the trailing edge of the airfoil lower surface. These characteristics will be discussed in detail in chapter six. This aerodynamic characteristic is related to the poor repeatability in the specific

angle of attack range, since the flow separation at lower surface seems susceptible to physical parameter variations such as turbulence intensity, uncertainty of the angle of attack device (0.5°) and velocity variation cause by the wind tunnel engine.

Static tests were performed to evaluate the drag variation at similar flow conditions. At a fixed angle of attack and wind tunnel freestream velocity, many were collected presenting similar results under uncertainty limits. The results contribute to the hypothesis that little physical parameter variation, during the execution of the repeatability tests, is responsible for changes on aerodynamic phenomena.

In addition, at low angles of attack, the repeatability tests for thinner airfoils do not present symmetrical results at $-4° < \alpha < 4°$, where only for negatives angle of attack the drag values are under uncertainty limits. These results indicate asymmetry characteristics in the wind tunnel facilities.

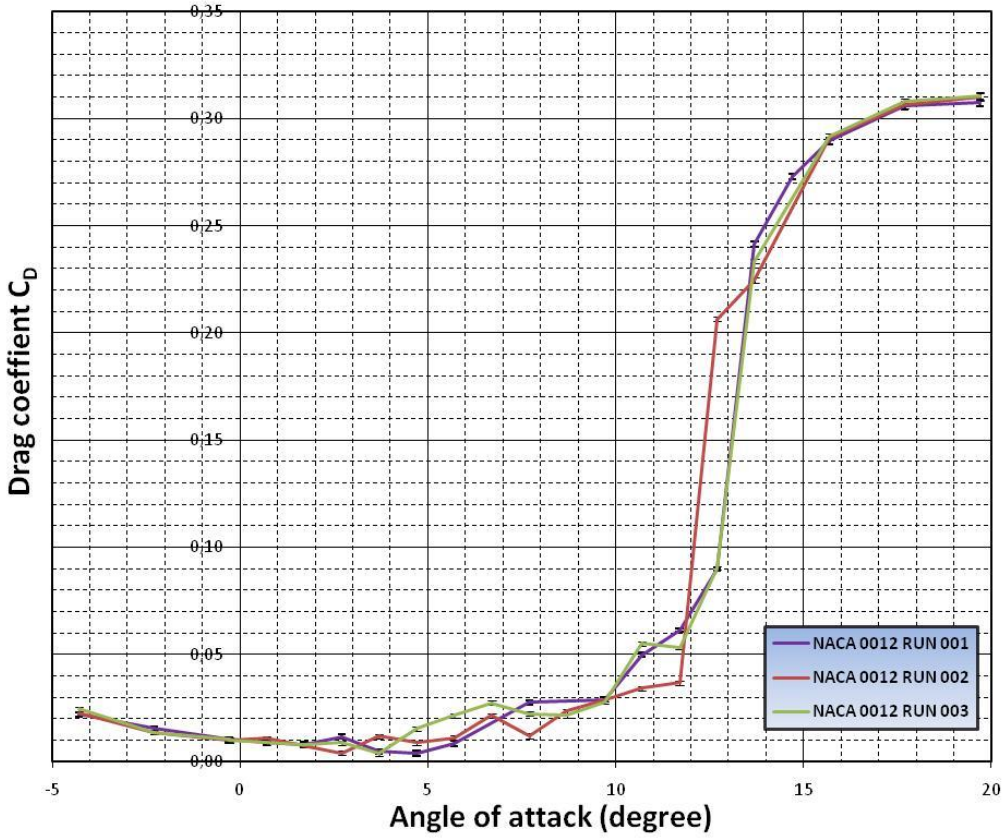

Figure 3.23: Repeatability curves (drag) for smooth NACA 0012 airfoil (Re=290,000).

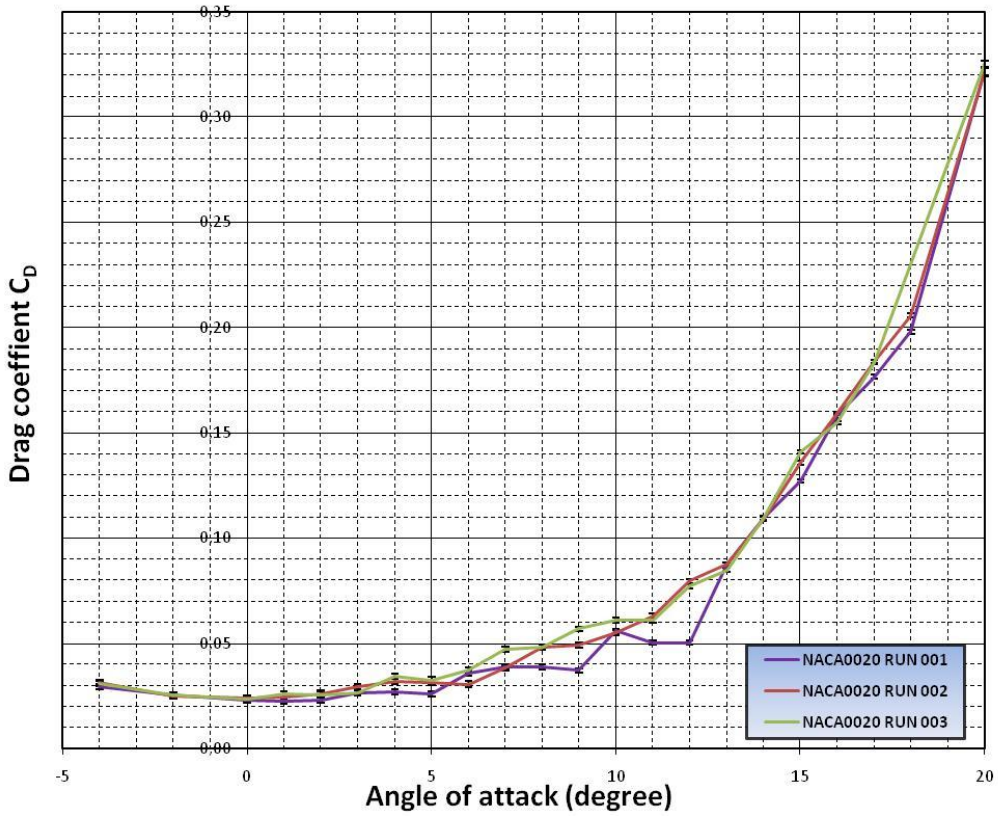

Figure 3.24: Repeatability curves (drag) for smooth NACA 0020 airfoil (Re=290,000).

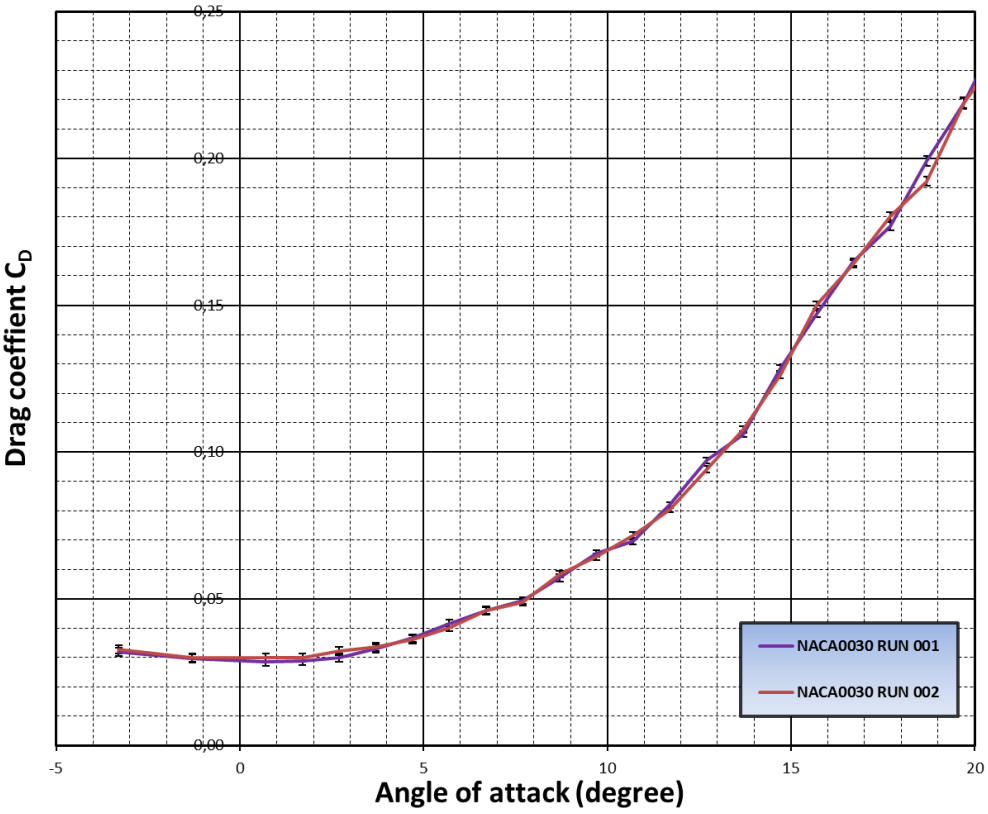

Figure 3.25: Repeatability curves (drag) for smooth NACA 0030 airfoil (Re=290,000).

Figures 4.26-28 show the repeatability characteristics for pitching moment curves. The thinner airfoils present moment values outside of uncertainty limits similar to the lift and drag curves. In addition, the NACA 0030 airfoil has the pitching moment coefficient under uncertainty limits for the entire range of angles of attack.

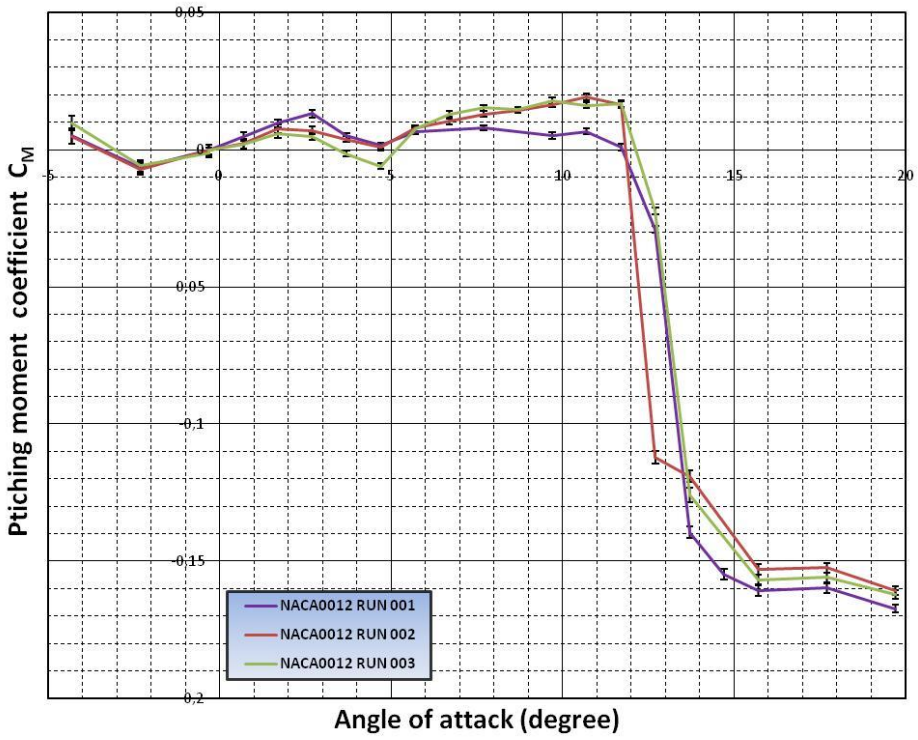

Figure 3.26: Repeatability curves (pitching moment) for smooth NACA 0012 airfoil (Re=290,000).

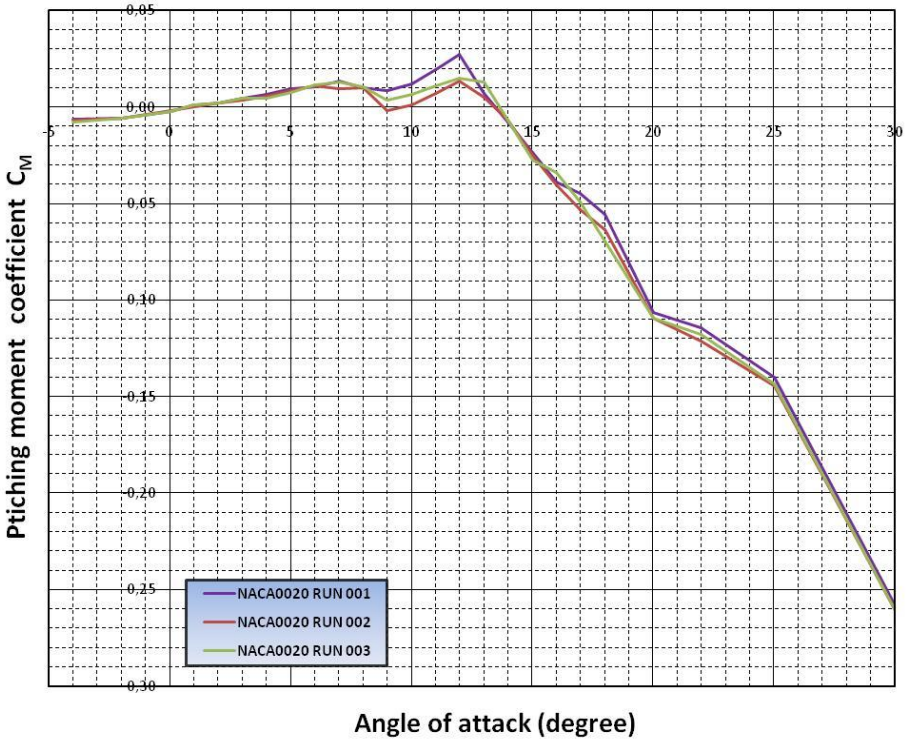

Figure 3.27: Repeatability curves (pitching moment) for smooth NACA 0020 airfoil (Re=290,000).

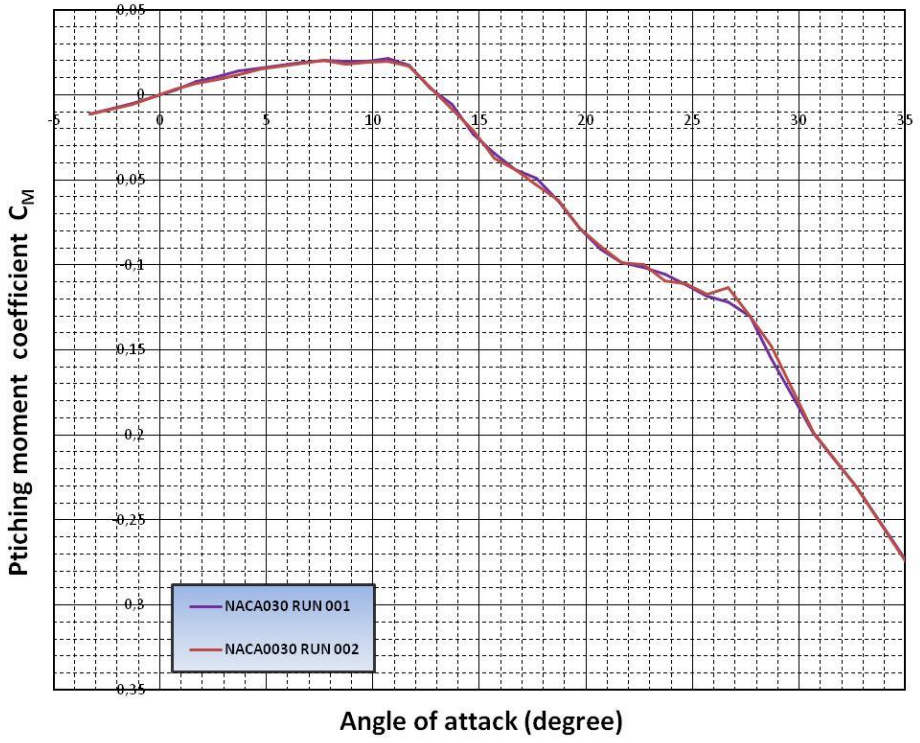

Figure 3.28: Repeatability curves (pitching moment) for smooth NACA 0030 airfoil (Re=290,000).

The repeatability results for wavy configurations present similar dependency on airfoil thickness. In terms of Reynolds number effects, with decreasing of Reynolds number condition the repeatability becomes worse, in part because of increased uncertainty limits.

In general, the repeatability analysis presented discrepancies in lift values that remain themselves under uncertainty limits of the tests for all airfoil thickness. On the other hand, the pitching moment and mainly the drag coefficient show values outside of the uncertainty limits for thinner airfoils. Therefore drag and pitching moment coefficients obtained in this work are based on an average of three runs. This procedure provides smoother curves, especially with regards to the drag curve which assumes an expected parabolic shape at intermediate angles of attack. Additionally, at low angles of attack, the average curve recovers the physical symmetry at $-4° < \alpha < 4°$.

The qualitative analysis of the wavy leading edge effect on aerodynamic coefficients is not affected by experimental accuracy. Both averaged and a simple runs indicate the same tendencies in terms of increase or decrease in lift, drag and pitching moment. Besides, values near zero angle of attack have higher repeatability and the effect on stall behavior caused by wavy leading edge is not sensitive to repeatability.

3.7 Flow visualization

3.7.1 Mini-tuft flow visualization

The flow topology of the smooth and wavy airfoils at distinct angle of attack and Reynolds number was investigated using mini-tuft flow visualization with attached mini-tufts at the upper surface of the airfoils. The mini-tuft flow visualizations were performed for all configurations where force measurements were taken. The tests were carried out for specific angles of attack at high (Re=290,000) and low (Re=50,000) Reynolds number conditions.

Different types of fabric with distinct outside lengths and diameters were tested in order to choose the most appropriate light and flexible fabric for the specific flow condition so that the mini-tufts properly align with flow as a consequence of the local flowfield.

Stockinet yarns were used as mini-tufts, and chosen dimensions were 25 mm in length and 2 mm in diameter. The mini-tufts were attached to the entire airfoil upper surface in order to identify flow patterns in important areas such as leading edges, trailing edges and interference areas between airfoil and test section wall. The tufts were attached using adhesive tape with spanwise spacing of 25 mm in. In addition, in the streamwise directions the mini-tufts are aligned very close each other.

Special attention was taken to attaching mini-tufts along the wavy leading edges in order to have at least one mini-tuft at tubercle peaks and another one at troughs. Figure 3.29 shows the mini-tufts attached to a wavy leading edge airfoil.

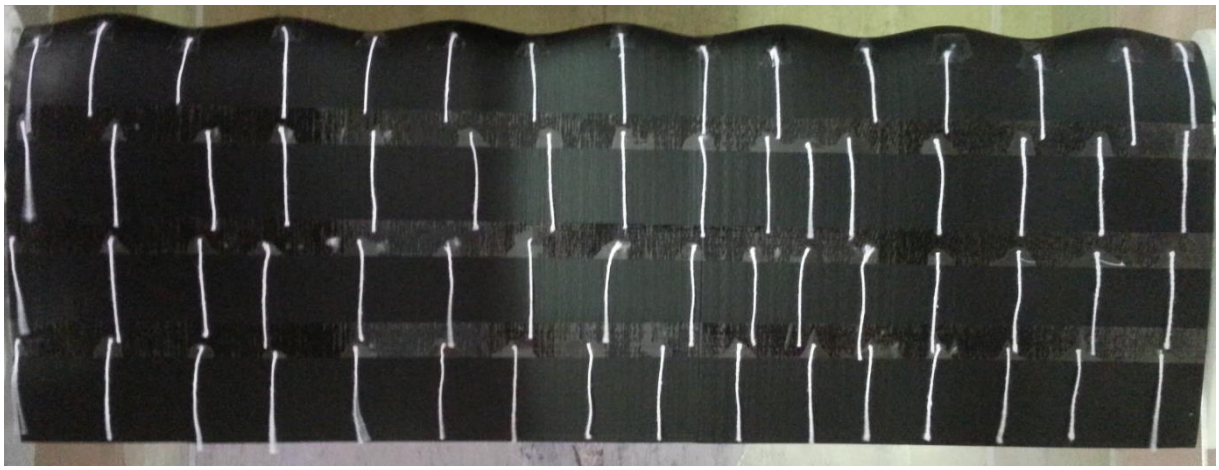

Figure 3.29: The mini-tufts attached at wavy leading edge airfoil upper surface.

The flow topology was captured using image photography. At each angle of attack and Reynolds number condition, a series of pictures were taken. In addition, film recordings were performed in order to evaluate the continued changes caused by the variation of angles of attack and unstable flow conditions. The images and movies were taken using Canon PowerShot S3 IS camera with resolution of 24M pixels.

As previously mentioned, the airfoil was painted in black color and the stockinet yarns chosen had white color in order to provide good contrast, consequently better supporting the flow topology analyses. In addition, the pictures were edited reaching better brightness and contrast. Artificial lights were used at all times during the entire wind tunnel test campaign.

3.7.2 Oil flow visualization

The oil flow visualizations were performed in order to clarify some characteristics of the flow topology that the mini-tufts are not capable such as laminar separation bubbles over airfoil upper surface. The mini-tuft and oil flow visualization are complementary flow visualization techniques.

The oil flow over the airfoil upper surface is influenced by the shear stress of the airflow and gravity. Therefore, on one hand the oil mixture needs to have proper viscosity so that it does not flow rapidly over the airfoil upper under influence of gravity. On the other hand, the oil needs to be sufficiently viscous so that the airflow momentum is able to guide the oil in order to impress the shear stresses and reveal the flow pattern over the airfoil surface.

The oil flow visualization was performed by applying a classical oil flow technique with the use of a mixture of titanium dioxide powder, kerosene and oleic acid in the ratio of 6:20:1. However, before reaching an appropriate oil mixture for high (Re=290,000) and low (50,000) Reynolds number conditions, many oil flow visualizations were performed in order to reach an adequate mixture that was used for all oil flow visualizations. As in the mini-tuft flow visualization, all configurations from force measurement campaign were tested.

The mixture was sprayed to the upper airfoil surface by the use of a paint brush so to uniformly cover the entire surface and guarantee that the oil would not move under gravity influence. After that, initial pictures were taken with wind tunnel off. As in the mini-tuft visualizations, many pictures are taken during the test at specific angles of attack. Additionally, video recordings are done during the tests showing the evolution of the oil mixture over the airfoil surface. With the wind tunnel off and after the tests, photographs were taken of details of the oil impression over upper airfoil surface. The figure 3.30 shows the three phases of the oil flow visualizations. The photographic equipment was the same used in mini-tuft flow visualizations.

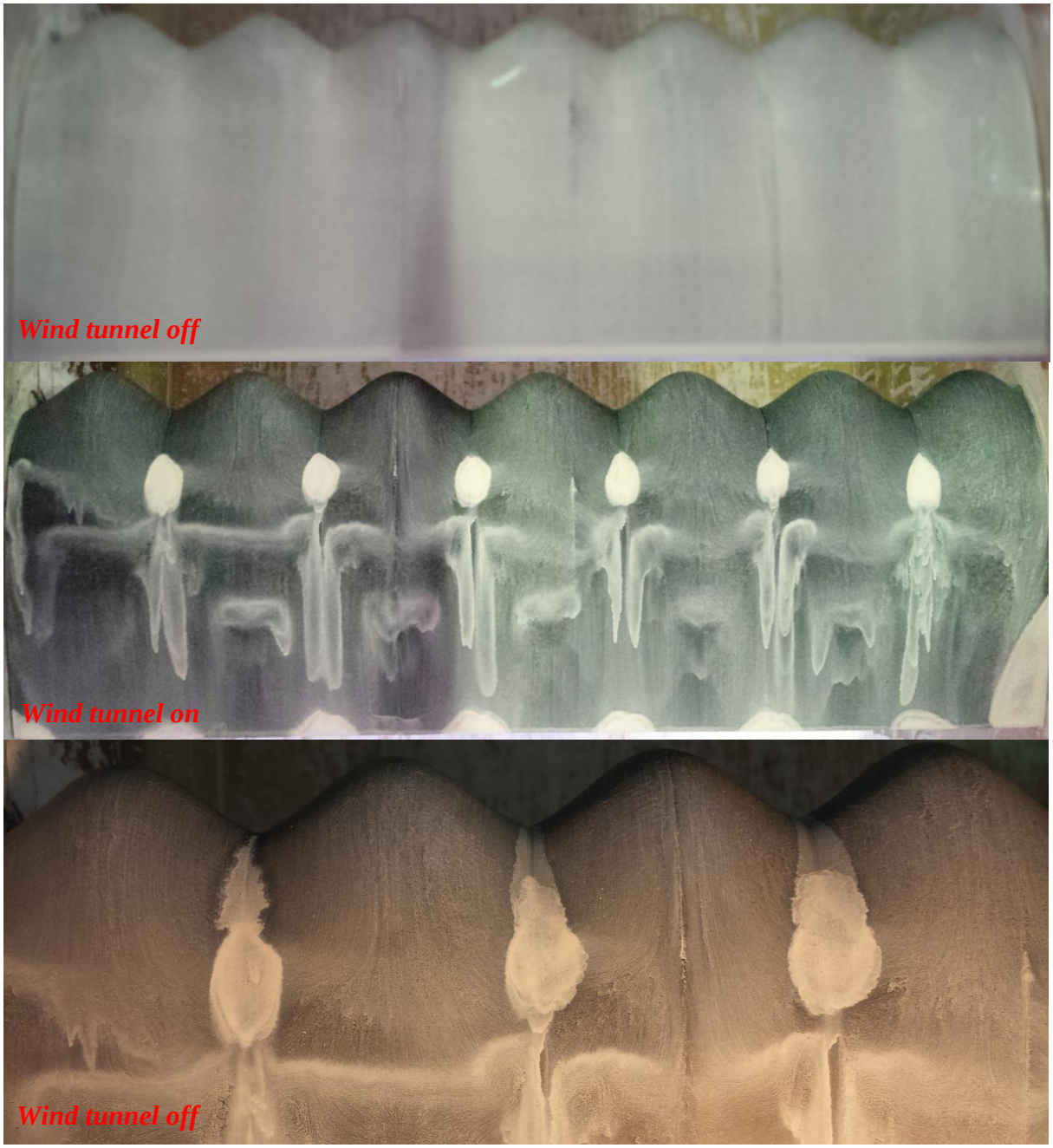

Figure 3.30: Oil flow visualization procedure during the wind tunnel tests.

4 WAVY LEADING EDGE EFFECT ON AERODYNAMIC PERFORMANCE

4.1 Introduction

As previously described, the wavy leading edge performance depends on stall type of the smooth airfoil. Also as mentioned, the stall behaviour is affected by airfoil geometric parameters (thickness and camber) and the Reynolds number condition. Thus, this chapter presents the force and moment measurement results in order to quantify quantitatively the airfoil geometric parameters by evaluating the airfoil thickness effects on wavy leading edge aerodynamic performance. Moreover, the Reynolds number effect on tubercle performance is also investigated. The investigations, in both cases, were performed by evaluating lift, drag and moment curves in the pre-stall and post-stall regime.

Wind tunnel results were shown and discussed for different airfoil geometries by changing the airfoil thickness (NACA 0012, NACA 0020, NACA 0030) at a low Reynolds number range (50,000-290.00). First of all, it will be evaluated the smooth airfoil configuration to establish the aerodynamic characteristics of the baseline airfoils, helping to understand the flow changes caused by wavy leading edge. The wavy leading edge performance will be evaluated in detail at Reynolds 290,000 because, at these flow conditions, the experimental apparatus reaches the minimum uncertainty. In Addition, the Reynolds number effects will be evaluated by changes on the plots of the experimental tests at Re = 50,000, 80,000, 120,000, 200,000 and 290,000. Although the uncertainty increases with decreasing Reynolds numbers, the qualitative evaluation of the Reynolds number effect is not affected. Exceptions occurred for drag and pitching moment measurements below Re=100,000 and the results were omitted.

4.2 Wavy leading edge performance for NACA 0012 airfoil

4.2.1 Baseline Airfoil in the range of the Reynolds number between 50,000 and 290,000

Figures 4.1-3 show the aerodynamic characteristics of the thin NACA 0012 airfoil at low Reynolds number regime. Figure 4.1 presents the lift curves for different Reynolds number conditions. Considering the pre-stall regime, the theoretical curve that comes from thin profile theory is indicated in plot. At lower Reynolds number (Re = 50,000, 80,000 and 120,000), there is a first straight line segment ($\alpha < 2^o$) with higher curve slope when compared to the theoretical curve. This characteristic is attributed to flow behaviour at low Reynolds number which imposes the presence of a separation bubble on the airfoil upper surface and full flow separation at the low surface of the trailing edge. It will be discussed this characteristic in the chapter 6 in detail. After that, a second linear segment starts with the same slope as the theoretical curve, and decreases the curve slope approaching stall condition. However, at the lowest Reynolds number (Re = 50,000) there is a drop in lift coefficient at $\alpha = 5^o$.

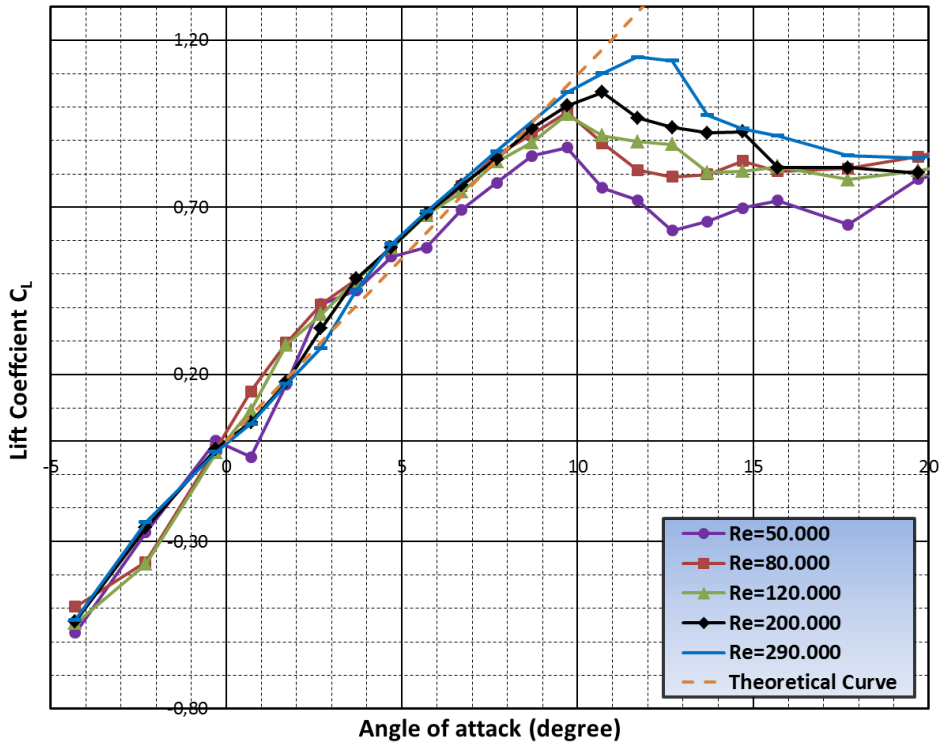

Figure 4.1: Lift curve for the NACA 0012 airfoil at low Reynolds number regime (Re = 50,000 - 290,000).

For higher Reynolds number conditions, the increase in curve slope when compared to the theoretical curve, i.e. potential flow theory, occurs later than a lower Reynolds numbers condition at $\alpha = 2^{\circ}$ and 3°, respectively for Re = 200,000 and 290,000. After that, the slope curve follows the same tendency observed for a higher Reynolds number. The delay in curve slope change occurs because of the dependency of laminar separation bubble and full flow separation characteristics over airfoil surface with Reynolds number (O´MEARA; MUELLER, 1987). Thus, for higher Reynolds number when compared to low Reynolds number, a similar effect in increase in lift curve slope occurs at higher angle of attack.

At post-stall regime, the NACA 0012 airfoil, at all Reynolds number conditions, has characteristics of a typical leading edge stall (JONES, 1933, 1934; MCCULLOUGH, 1951). There is a stall behavior lightly abrupt with an intermediate drop in lift coefficient values as consequence of a short laminar bubble burst. The stall angle and maximum lift coefficient increase with the raise of the Reynolds number.

Figure 4.2 shows the drag curves for the NACA 0012. The drag coefficients, at low angle of attack ($\alpha < 5^{\circ}$), decrease with the Reynolds number increase as consequence of the decrease in skin friction coefficient. The drag coefficient at Re = 50,000 has a significant raise in the entire range of angles of attack. Besides, for all Reynolds number conditions a great increase in drag occurs at stall angle as a result of the laminar bubble burst. The greatest increase in drag occurs earlier with decrease in Reynolds number as consequence of the stall onset anticipation caused by decreasing of the Reynolds number. Moreover, for higher angle of attack the scale effect is less sensitive ($\alpha > 15^{\circ}$).

It can be seen on figure 4.3 the Reynolds number effects on pitching moment characteristics. The pitching moment coefficient at 25% of M.A.C (reference point). for higher Reynolds number conditions (Re = 200,000 and 290,000) keeps constantly null up to stall angle as consequence of a symmetrical thin airfoil establishing the aerodynamic center at reference point and keeps null over attached flow conditions. After that, it can be noticed a large decrease in moment as results of the full flow separation moving the pressure center towards the backward position.

At Re = 120,000, the moment coefficient presents a negative curve slope at a lower angle of attack. After that, it follows the tendency of the post-stall regime at higher Reynolds number condition. At Re=80,000, the pitching moment characteristics change drastically. The moment curve keeps a quite linear behaviour decreasing values from the lower angle of

attack. At the lowest Reynolds number, up to α = 5º, the moment coefficient reaches negative values. After that, its values increase up to stall condition where it occurs a significant decrease in moment values following the same tendency of the higher Reynolds numbers.

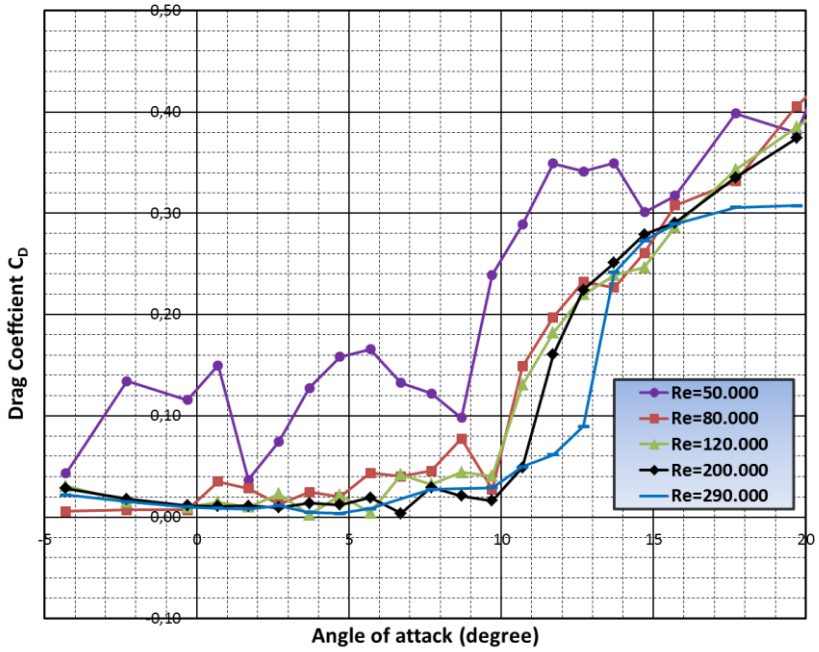

Figure 4.2: Drag curve for the NACA 0012 airfoil at low Reynolds number regime (Re = 50,000 - 290,000).

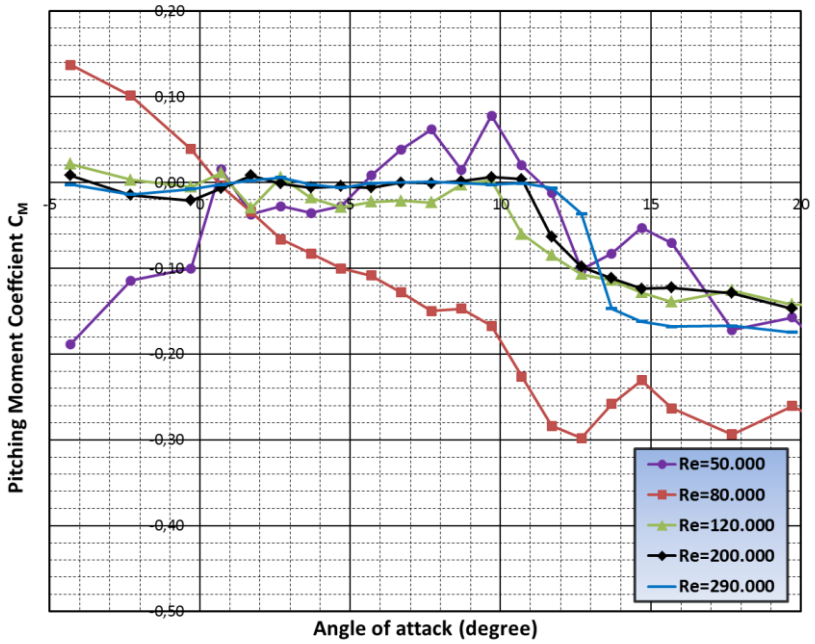

Figure 4.3: Pitching moment curve for the NACA 0012 airfoil at low Reynolds number regime (Re = 50,000 - 290,000).

4.2.2 Wavy leading edge performance at Reynolds number 290,000

Considering the wavy leading edge effect for lift performance on thin NACA 0012 airfoil, the lift coefficient values were plotted in figure 4.4 as function of angle of attack for wavy and smooth configurations. At pre-stall regime, all wavy leading edge configurations follow the smooth airfoil curve up to $\alpha = 2°$. The wavy configurations delay the increase in lift curve slope by one degree when compared to the baseline airfoil. In addition, for higher angles of attack up to stall, the configurations A3λ40 and A3λ11 keep close and with similar tendency as the smooth configuration one (remaining the theoretical curve slope), having lift values slightly lower.

In the case of the configuration A11λ40, it can be observed a large aerodynamic performance deterioration for higher values of angle of attack ($\alpha > 5°$) where the lift curve linearity decreases significantly when compared to the smooth configuration. In terms of maximum lift coefficient and stall angle, the configurations A3λ40 and A3λ11 reach similar values close to the baseline configuration. For configuration A11λ40, the C_{Lmax} is lower than other configurations with the highest stall angle. At post-stall regime, all wavy leading edge configurations have a soft stall keeping the lift coefficients near C_{Lmax} at higher angles of attack, differently from the abrupt stall that occurs for the baseline airfoil indicating a leading edge stall.

The wavy leading edge geometries defined by amplitude (A) and wavelength (λ) affect the pre-stall and post-stall characteristics. By increasing the tubercle amplitude at the same wavelength (λ40) a large decrease in linearity is observed on lift curve at pre-stall regime where the configuration A11λ40 presents significantly lower lift values than those for the baseline configuration, whereas the smaller amplitude configuration (A3λ40) has similar performance to the smooth airfoil up to stall. However, as consequence of a higher stall angle at greater amplitude, the configurations A11λ40 and A3λ40 reach similar maximum lift coefficients with values of 1.05 (ΔC_{Lmax} = -8.7%) and 1.06 (ΔC_{Lmax} = -7.8%), respectively. In contrast with pre-stall conditions, an increase in amplitude does not change the post-stall characteristics keeping a soft stall behaviour.

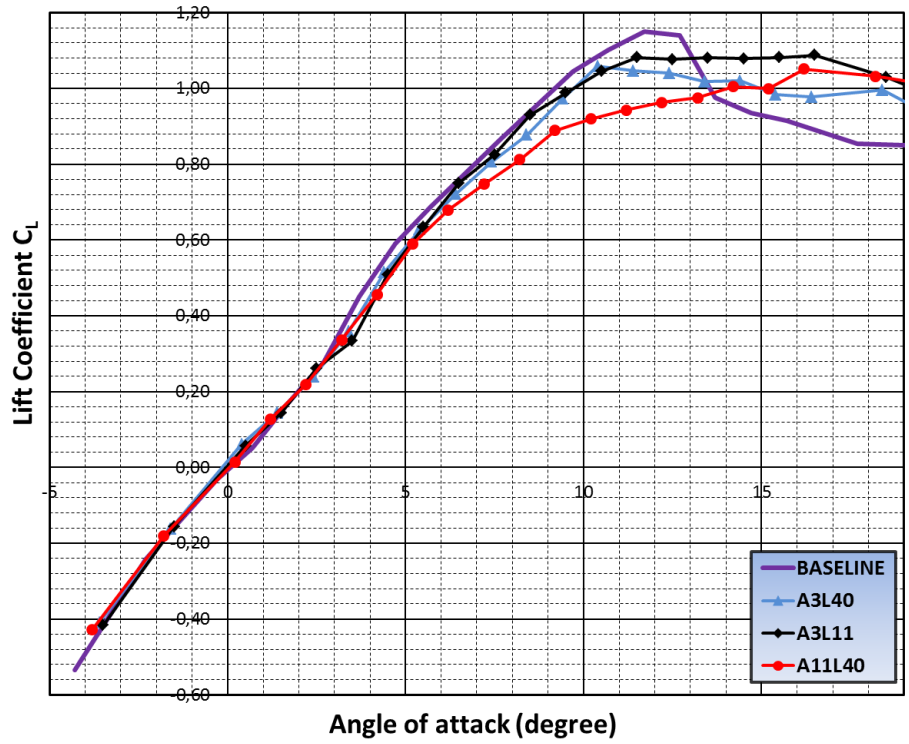

Figure 4.4: Lift curves for the smooth and wavy configurations at Re = 290,000 (NACA 0012 airfoil).

By increasing the wavy leading edge wavelength for the same amplitude (A3), significant changes on the lift curve at pre-stall and post-stall regime do not occur where the shorter wavelength has a little softer post-stall behaviour. The maximum lift coefficient for configurations A3λ40 and A3λ11 reach values of 1.06 (ΔC_{Lmax} = -7.8%) and 1.08 (ΔC_{Lmax} = -6.1%), respectively.

In terms of maximum lift, the amplitude and wavelength effect does not cause effective changes, but at pre-stall regime, the effect is considerable where the wavy leading edge configurations with smaller amplitude (A3λ11 and A3λ40) reach better aerodynamic performance.

This indicates that smaller tubercle amplitude establishes for NACA 0012 airfoil a better aerodynamic performance at pre-stall and post-stall characteristics having similar pre-stall behaviour and C_{Lmax} to those of the smooth airfoil keeping a soft stall.

Figure 4.5 shows the wavy leading edge performance in terms of drag. At low angle of attack ($\alpha < 2°$). The longer wavelength configurations (A3λ40 and A11λ40) have similar higher drag coefficient values than the smooth configuration. For the shorter wavelength

configuration (A3λ11) the drag coefficient at zero lift reaches the highest value when compared to smooth airfoil (ΔC_{d0} = +79%).

For intermediate angles of attack ($2° < \alpha < \alpha_{stall}$), the tubercle geometry effect on drag coefficient curves depends on how the configurations resist to beginning of the stall. The configuration A11λ40 anticipates the stall onset at $\alpha = 5°$ and thus reduce the extent of the drag bucket increasing drag at early angles of attack. On the other hand, the configurations A3λ40 and A3λ11 keep a parabolic rise in the drag curve up to $\alpha = 10°$ with the A3λ11 presenting higher drag values, and both configurations overcoming the drag values of the smooth airfoil.

At post-stall regime, a great increase in drag coefficient occurs for configurations A3λ40 and A3λ11 at stall angle keeping drag values quite higher than baseline configuration up to $\alpha = 20°$ where the drag coefficient for the shorter wavelength airfoil overcomes the values of the configuration A3λ40 at $\alpha = 12°$. In the case of the configuration A11λ40, the stall anticipation condition keeps the highest drag coefficient values from $\alpha = 5°$ up $\alpha = 20°$.

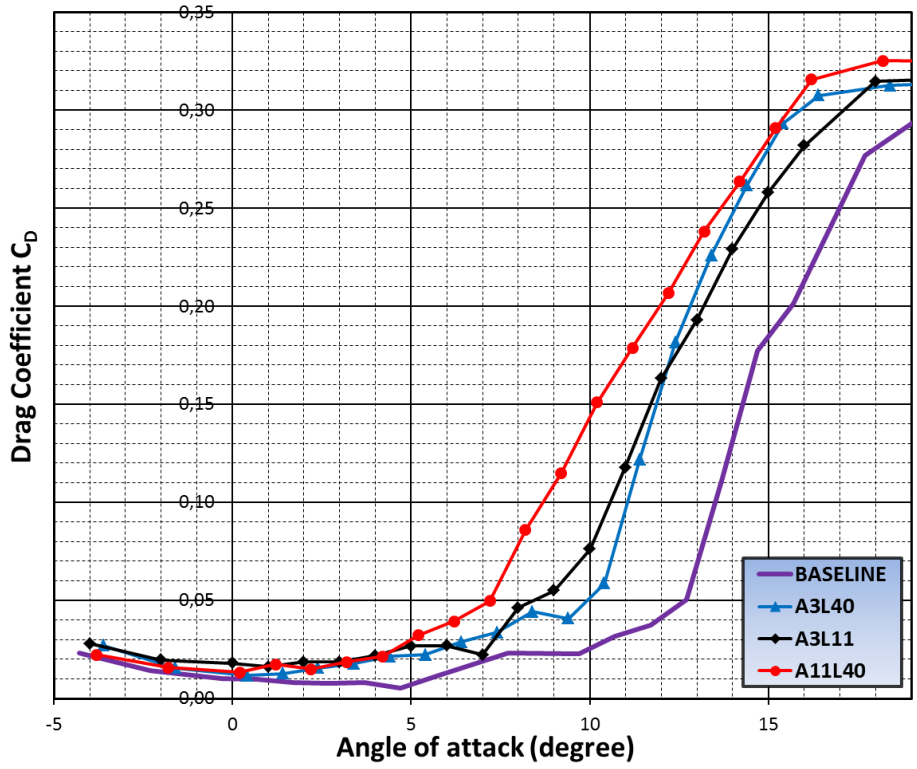

Figure 4.5: Drag curves for the smooth and wavy configurations at Re = 290,000 (NACA 0012 airfoil).

In terms of amplitude effect, an increase in amplitude at a fixed wavelength (λ40) reduces the drag coefficient at lift zero and anticipates the stall onset resulting in a large increase in drag. Considering the wavelength effect, except at zero lift, the configurations A3λ40 and A3λ11 present similar drag values showing a negligible wavelength variation effect at low angle of attack. For higher angles of attack at post-stall regime, the longer wavelength configuration shows higher drag values.

Figure 4.6 shows pitching moment results for smooth and wavy leading edge configurations. Except for the configuration A11λ40, All wavy airfoils remain with similar pitching moment characteristics presenting moment coefficient close to null values up to stall as consequence of the airfoil symmetry characteristics and the reference point to be on aerodynamic center (25% c.m.a).

The configuration A11λ40 presents lower values of pitching moment since $\alpha = 1°$. Additionally, this configuration, as discussed previously, anticipates the stall onset changing the pitching moment characteristics by a large decrease in the curve slope at an early angle of attack ($\alpha = 5º$). The configurations A3λ40 and A3λ11 follow the baseline curve trend with values near null moment up to $\alpha = 11°$. After that, it occurs an abrupt decrease in pitching moment near the drastic decrease for smooth airfoil. The amplitude effect is effective on pitching moment characteristics decreasing moment values with increasing amplitude in most of the angle of attack range.

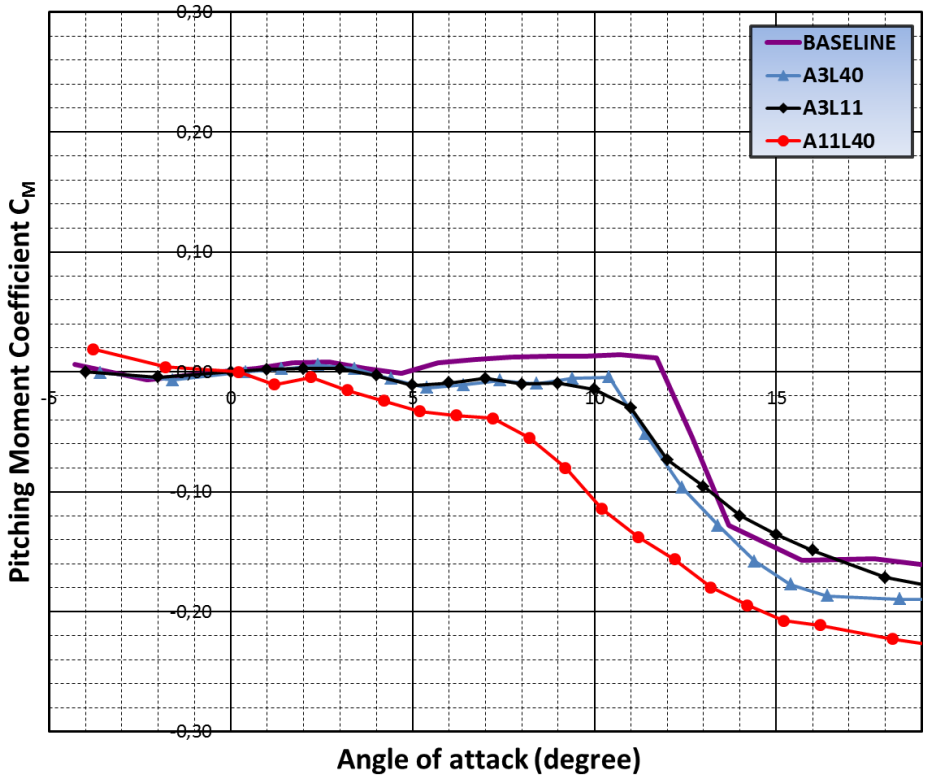

Figure 4.6: Figure 4.6 Pitching moment curves for the smooth and wavy configurations at Re = 290,000 (NACA 0012 airfoil).

Table 4.1 summarizes the changes caused by wavy leading edge geometries on aerodynamic performance of the thin NACA 0012 airfoil.

Configuration	C_{d0} *(counts)*	ΔC_{d0}	C_{Lmax}	ΔC_{Lmax}	α_{stall}	$\Delta \alpha_{stall}$	*Lift drop*	*Stall type*
Baseline	100	reference	1,15	reference	11,7	reference	26.30%	lightly abrupt
A3λ40	125	+ 25%	1.06	-7.8%	10.40	-1.7%	-15.80%	soft
A11λ40	135	+ 35%	1.05	-8.7%	16.20	38.5%	-9.64%	soft
A3λ11	179	+ 79%	1.08	-6.1%	11.50	-11.1%	-12.00%	soft

Table 4.1: The wavy leading edge effect on aerodynamic performance for thin NACA 0012 airfoil.

4.2.3 Reynolds number effect on wavy leading edge performance

Figures 4.7-11 show the Reynolds number effect on wavy leading edge performance at lift curve for the NACA 0012 airfoil. The maximum lift coefficient for the smooth configuration keeps higher than wavy airfoils at all Reynolds number regimes, except for the lowest Reynolds number condition (Re = 50,000). Besides, at Reynolds number 290,000 and 200,000, the wavy leading edge configurations A3λ40 and A3λ11 keep stall angle lower than baseline airfoil. In contrast, at Re = 120,000, 80,000 and 50,000, the stall angle overcomes the smooth configuration. In addition, the greater amplitude configuration keeps greater stall angles at any Reynolds number condition.

Considering the pre-stall regime, for the configurations A3λ40 and A3λ11, there is not a sensitive Reynolds number effect on the performance where the lift curves are very close to the smooth airfoil curve, at any Reynolds condition. In the case of the greater amplitude configuration (A11λ40), there is a decrease in aerodynamic deterioration with increase in Reynolds number when compared to the smooth airfoil.

The greater stall angles for wavy airfoils at Reynolds number lower than 120,000 indicates that at a certain *Critical Reynolds number* the wavy leading edge resist more to full flow separation than the smooth configuration. The aerodynamic deterioration in terms of maximum lift coefficient caused by wavy configurations decreases with Reynolds number reduction, overcoming the smooth performance at Re = 50,000 (figure 4.12).

At post-stall regime, for higher Reynolds number (Re = 290,000, 200,000 and 120,000) the all wavy leading edge configurations have a soft stall behaviour in contrast with the slightly abrupt stall of the smooth airfoil. At Reynolds number 80,000 and 50,000 the configuration A3λ40 follows abrupt stall as the smooth airfoil.

The tubercle geometric effect is not sensitive to Reynolds number. In other words, for entire Reynolds number regime, the configuration A3λ11 reaches the best performance. On the other hand, the configuration A11λ40 undergoes the highest aerodynamic deterioration.

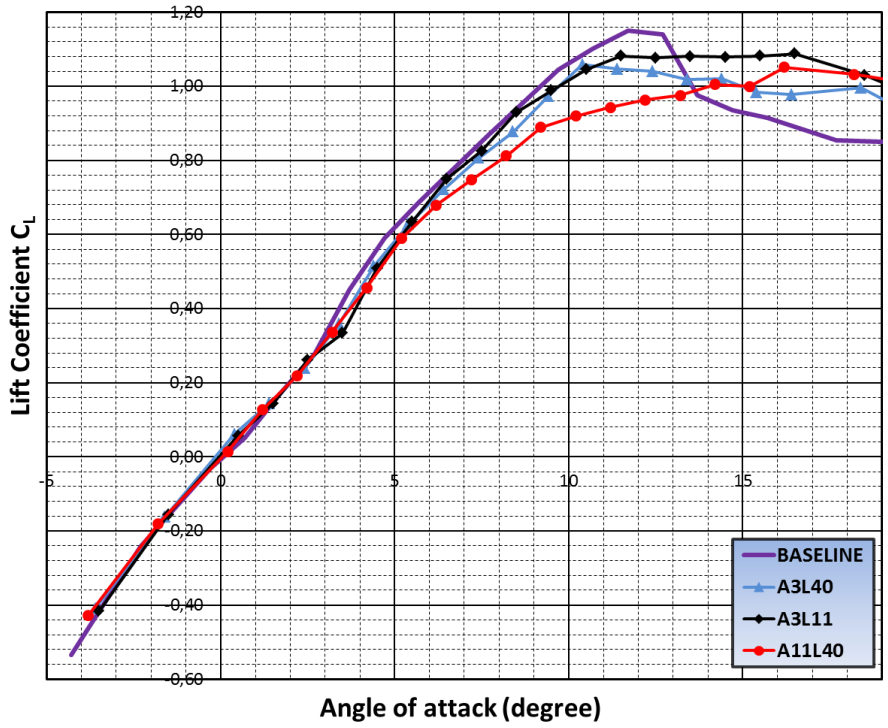

Figure 4.7: Lift curves for the smooth and wavy configurations at Re = 290,000 (NACA 0012 airfoil).

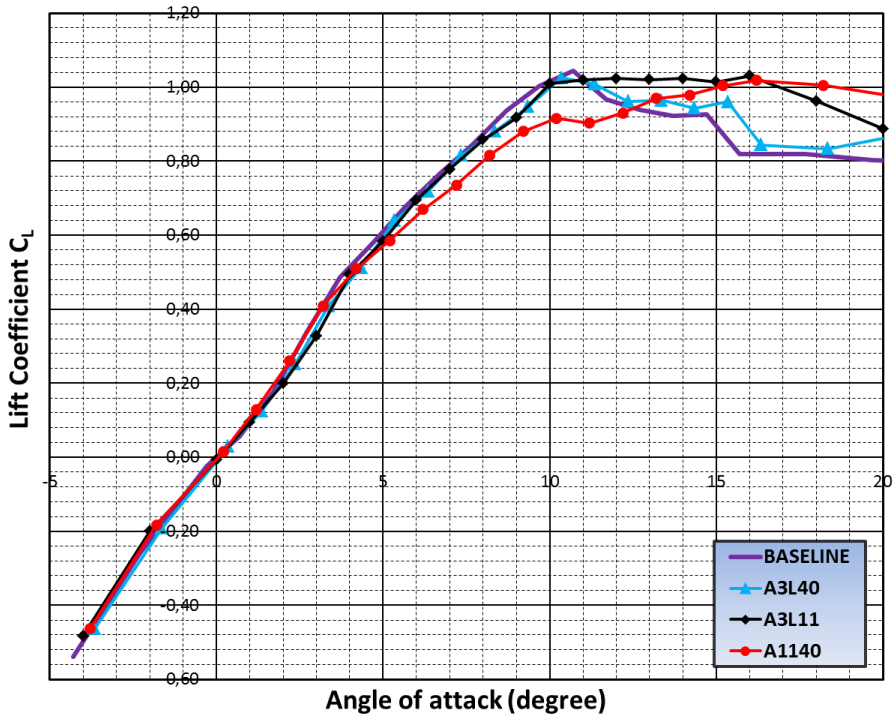

Figure 4.8: Lift curves for the smooth and wavy configurations at Re = 200,000 (NACA 0012 airfoil).

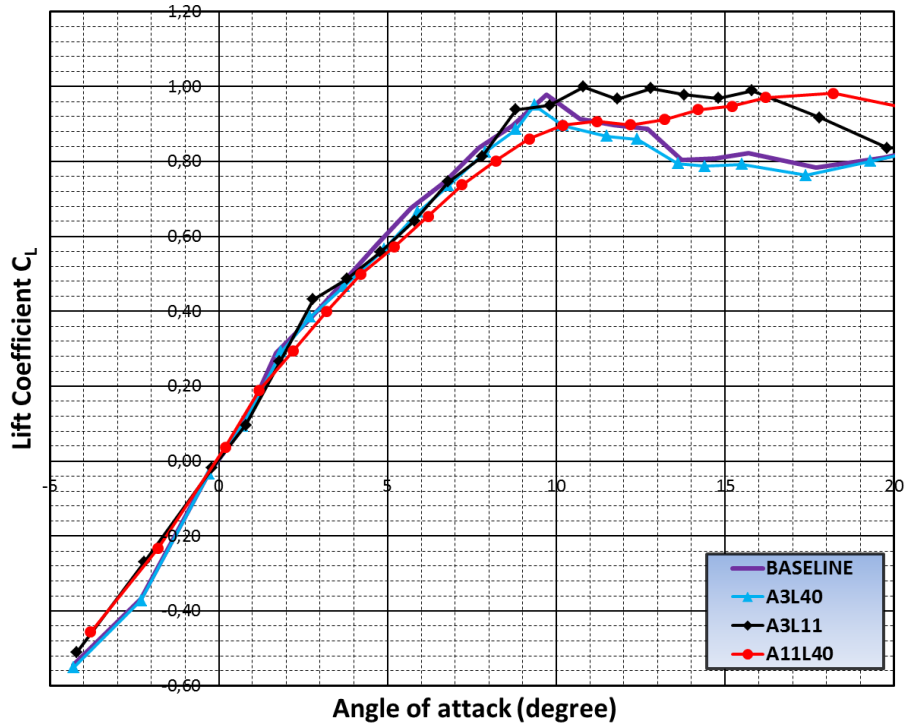

Figure 4.9: Lift curves for the smooth and wavy configurations at Re = 120,000 (NACA 0012 airfoil).

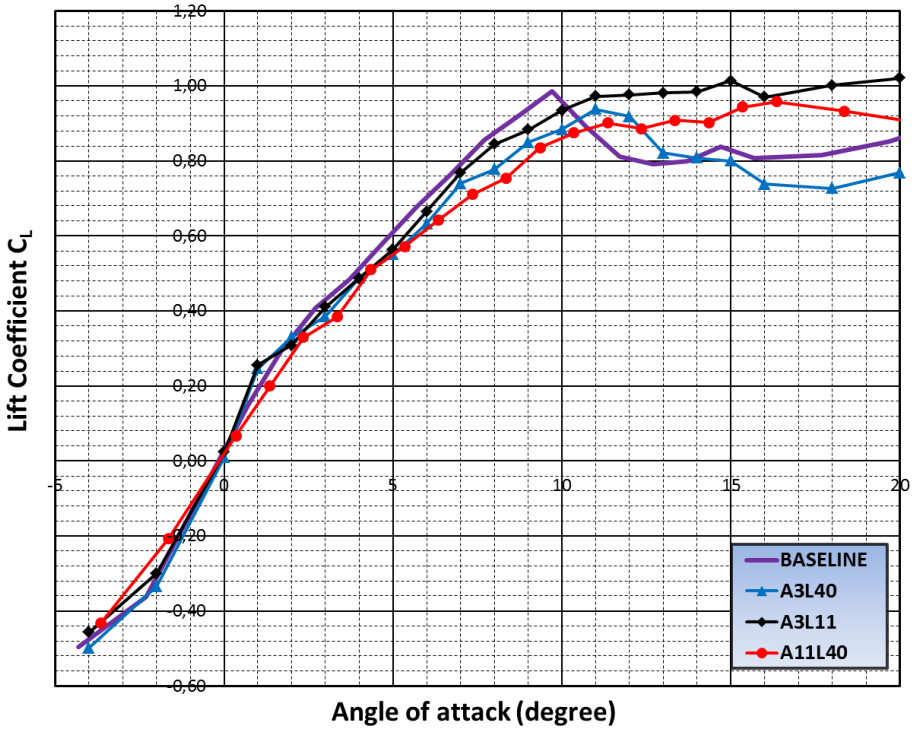

Figure 4.10: Lift curves for the smooth and wavy configurations at Re = 80,000 (NACA 0012 airfoil).

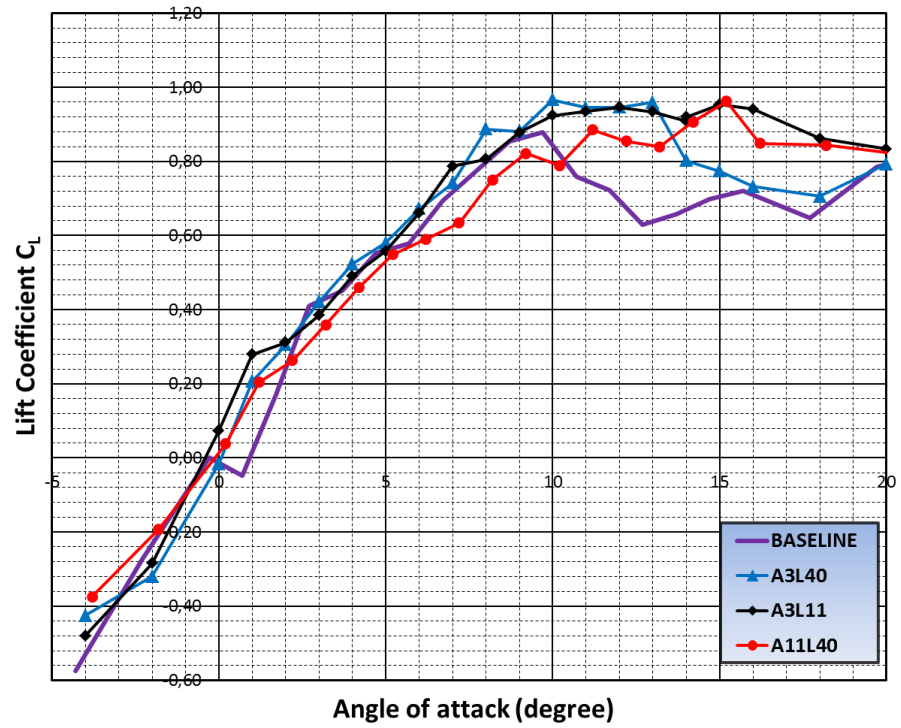

Figure 4.11: Lift curves for the smooth and wavy configurations at Re = 50,000 (NACA 0012 airfoil).

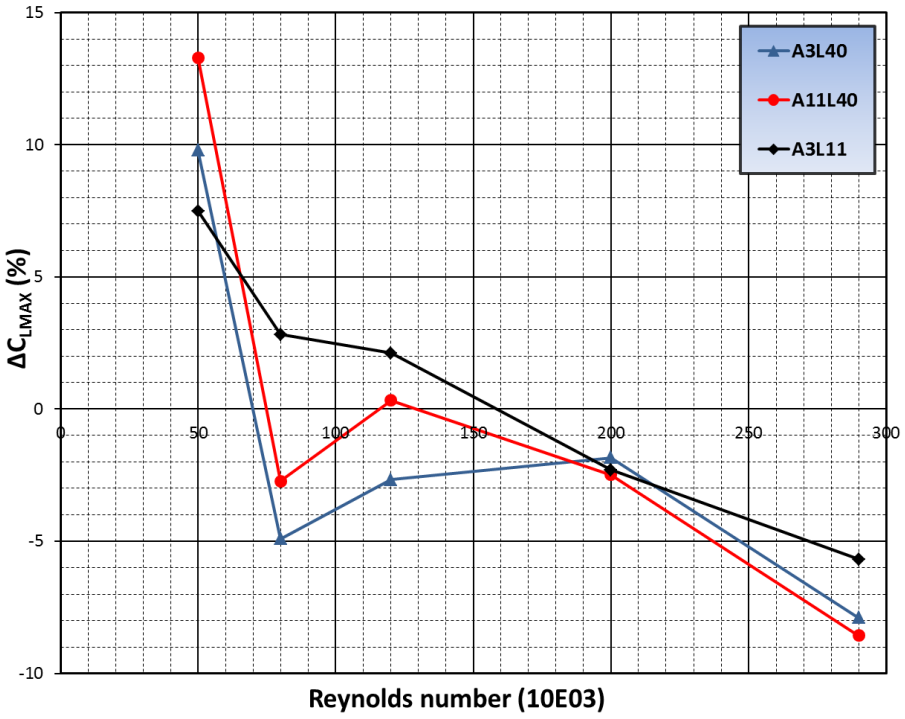

Figure 4.12: Reynolds Number effect on C_{LMAX} for the wavy configurations (NACA 0012 airfoil).

Regarding drag coefficient (figures 4.13-15), at Reynolds numbers 290,000 and 200,000, the wavy leading edge performance is similar, increasing drag at low angles of attack for all wavy airfoils with similar values for configurations A11λ40 and A3λ40. In addition, the configuration A3λ11 reaches the highest values. The significant increase in drag is anticipated for the configuration A11λ40 as consequence of the early stall onset in both Reynolds number conditions.

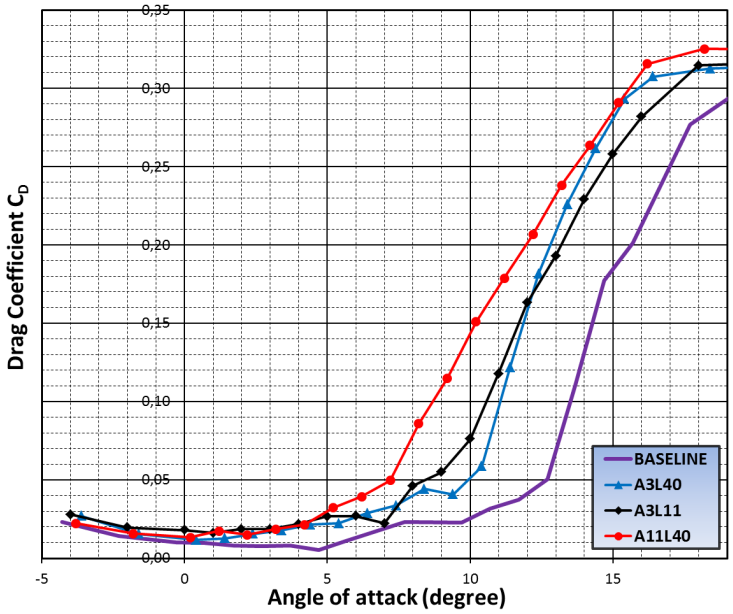

Figure 4.13: Drag curves for smooth and wavy NACA 0012 airfoils at Re=290,000.

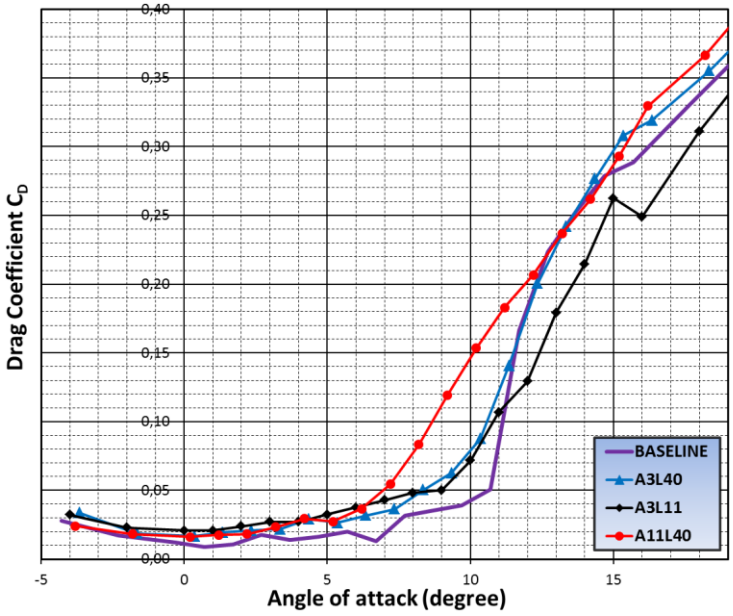

Figure 4.14: Drag curves for smooth and wavy NACA 0012 airfoils at Re=200,000.

At Reynolds number 120,000, the Reynolds number effects cause great changes on tubercle performance. The greater amplitude configuration keeps significantly greater drag coefficient values in the entire range of angles of attack. In contrast, the configurations A3λ40 and A3λ11 present values closer to smooth airfoil up to $\alpha = 9°$.

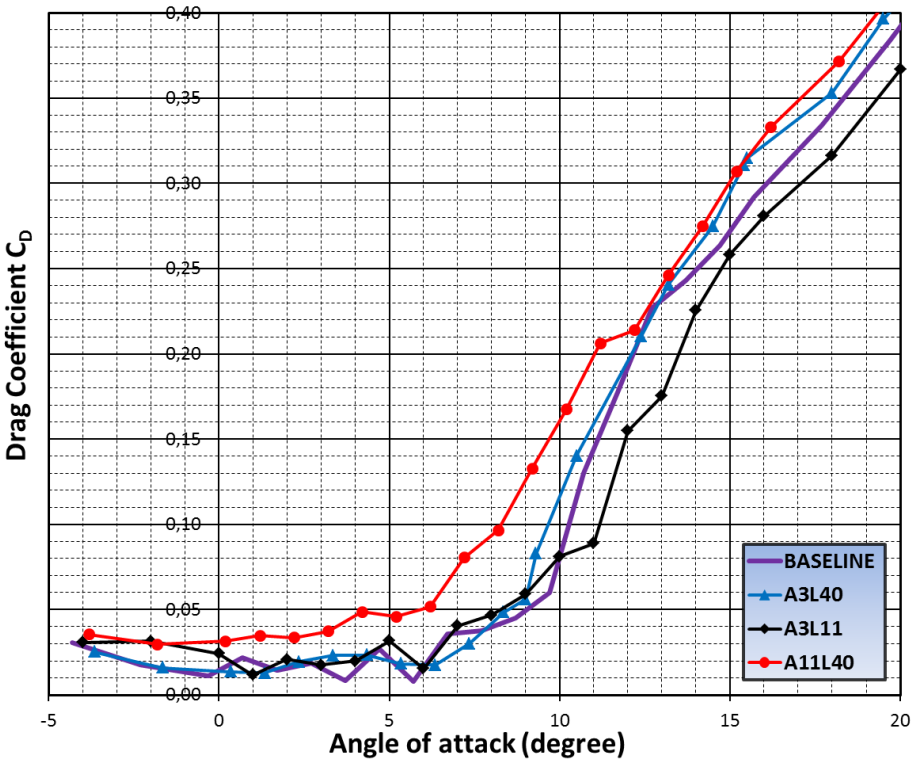

Figure 4.15: Drag curves for smooth and wavy NACA 0012 airfoils at Re=120,000.

Figures 4.16-17 show that there are no significant changes on pitching moment curves increasing Reynolds number from 200,000 to 290,000. Except for the configuration A11λ40, all wavy airfoils keep moment coefficient near null values with the wavy configurations presenting slightly lower values than the ones in the smooth airfoil. This behaviour follows up to stall onset of each configuration where it occurs an abrupt decrease in pitching moment. The greater amplitude configuration presents the earliest abrupt decrease in moment values.

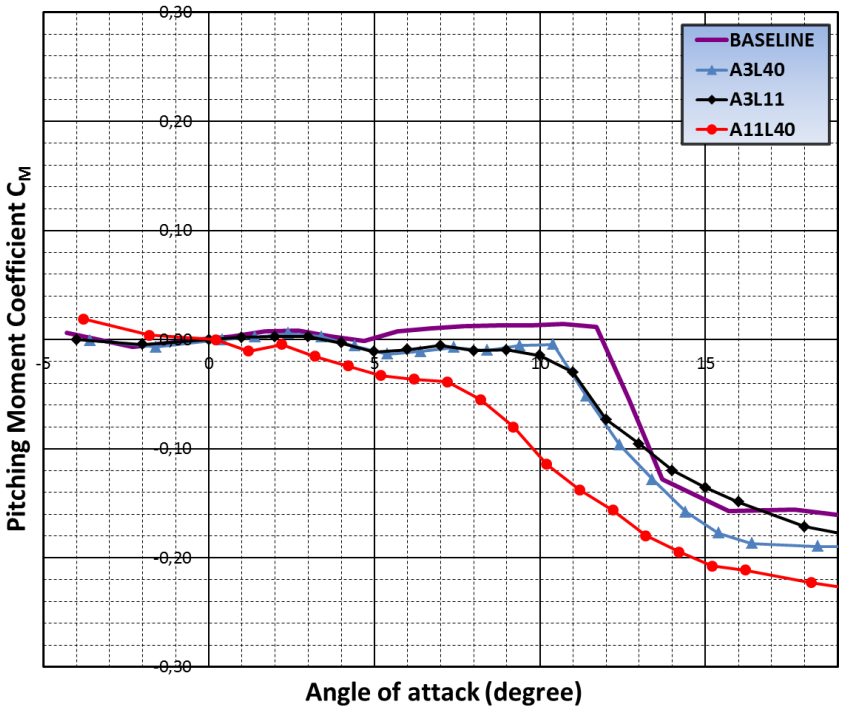

Figure 4.16: Pitching moment curves for smooth and wavy NACA 0012 airfoils at Re=290,000.

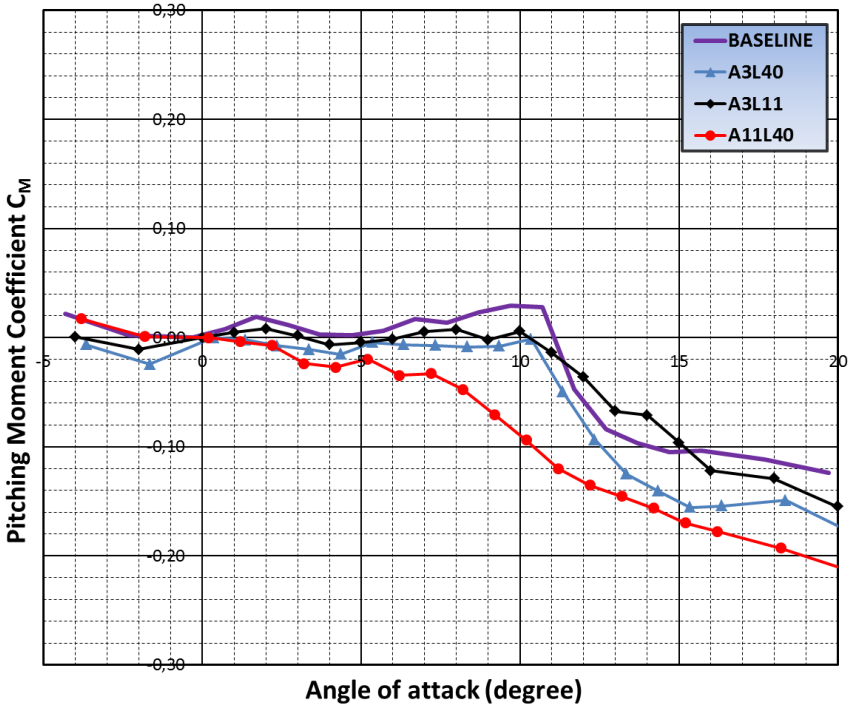

Figure 4.17: Pitching moment curves for smooth and wavy NACA 0012 airfoils at Re=200,000.

The pitching moment characteristics at Re =120,000 (figure 4.18) present the smooth and higher wavelength (λ40) configurations establishing a negative curve slope since zero lift values. On the other hand, the configuration A3λ11 presents positive moment values up to stall angle where it undergoes an abrupt decrease in pitching moment.

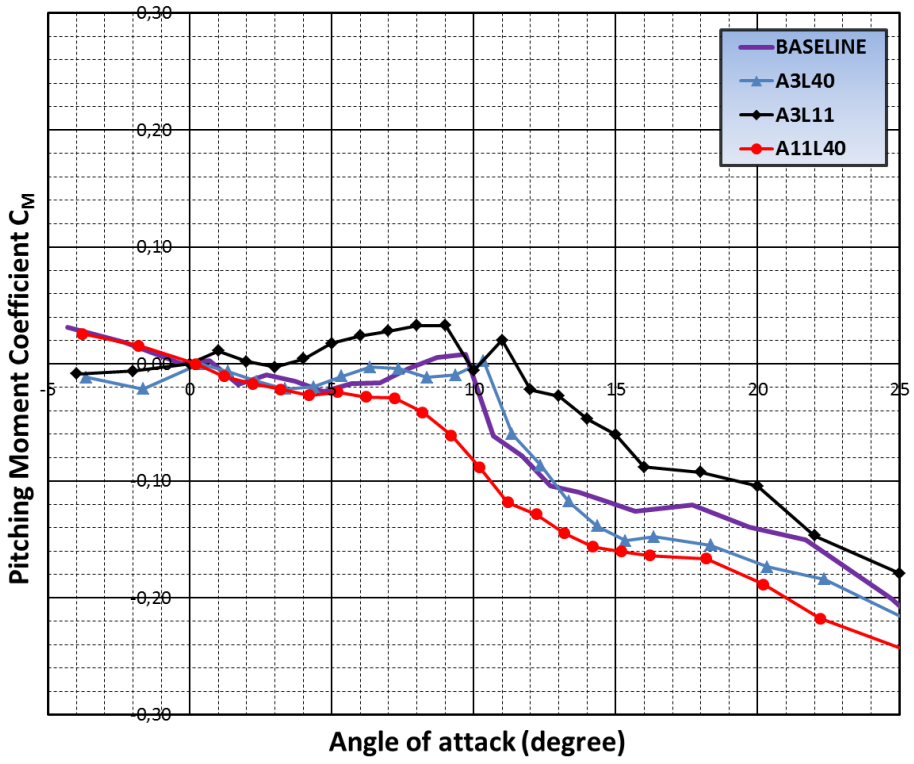

Figure 4.18: Pitching moment curves for smooth and wavy NACA 0012 airfoils at Re=120,000.

4.3 Wavy leading edge performance for NACA 0020 airfoil

4.3.1 Baseline Airfoil in the range of the Reynolds number between 50,000 and 290,000

Figures 4.18-20 show aerodynamic characteristics of the thick NACA 0020 airfoil, quite different from the thin NACA 0012 at low Reynolds numbers. The lift curves of the thicker airfoil present an increase in the abrupt stall characteristics and lower maximum lift coefficient values than the ones observed for the thin airfoil.

The lift curves (figure 4.19) present two straight line segments with distinct curve slopes. Except for Re = 50,000, the first one has lower slope curve than the theoretical curve, probably as consequence of the boundary layer thickening. The second one presents an increase in the slope curve at different α´s, depending on the Reynolds number, when compared to the theoretical curve. The improvement in curve slope decreases with increasing Reynolds numbers. The Reynolds number dependency in changing the curve slope, as discussed previously, is a consequence of the flow separation over the airfoil trailing edge that depends on Reynolds number condition.

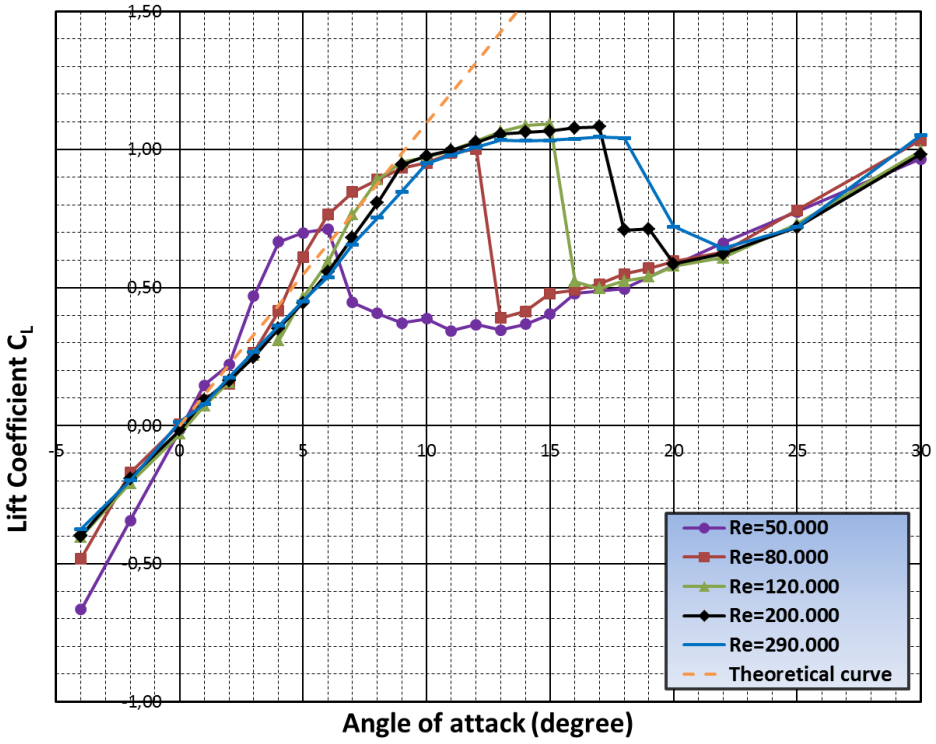

Figure 4.19: Lift curves for NACA 0020 airfoil at low Reynolds number (Re= 50,000-290,000).

A third curve segment appears with an asymptotic shape and as consequence of the trailing edge stall onset indicated by the flow visualizations. These curves go into abrupt stall condition. With increase in Reynolds number the asymptotic curves start later and reach higher stall angle. Furthermore, the maximum lift coefficient has similar values for Reynolds

number from 80,000 up to 290,000. The abrupt stall characteristic is a result of the short separation bubble burst on the airfoil upper surface.

In terms of drag (figure 4.20), the thicker NACA 0020 airfoil has a minimum drag coefficient higher than the thinner NACA 0012. The Reynolds number effects on drag characteristics is similar to thinner airfoil ones, with decreasing drag values at low angles of attack and extending the drag bucket with increasing Reynolds numbers. Higher Reynolds numbers delay the large drag increase due to stall condition. In addition, at higher angles of attack, as with the thin airfoil, the scale effect is not much sensitive to changes in Reynolds number conditions. The negatives values of drag, at low angles of attack, do not represent physical results. These results are consequence of low measurement precision at Re = 50.000.

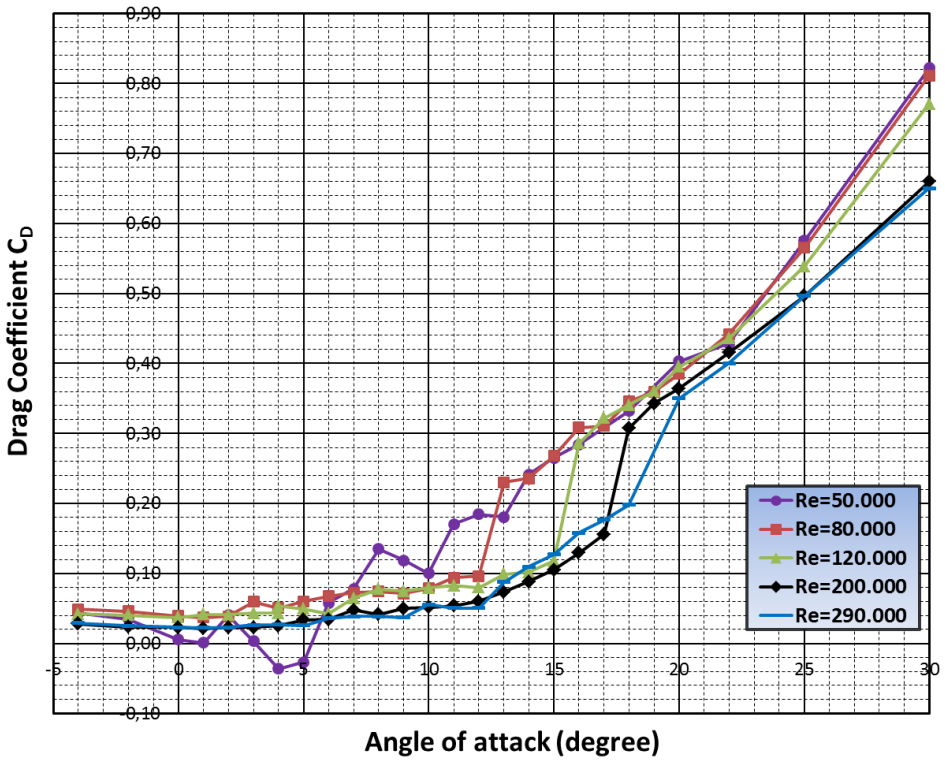

Figure 4.20: Drag curves for NACA 0020 airfoil at low Reynolds number (Re=50,000-290,000).

Figure 4.21 shows a similar pitching moment behaviour on the NACA 0020 for higher Reynolds numbers (Re= 200,000 and 290,000), keeping values constantly close to null up to stall angle as consequence of the symmetrical airfoil. After that, it can be observed a large

decrease in pitching moment as a result of a back movement on the pressure center caused by trailing edge flow stall as in the thin NACA 0012 airfoil.

At lower Reynolds number conditions, a large decrease in pitching moment values is anticipated because of the great increase in lift curve slope at lower angles of attack. In addition, at higher angle of attack, for flow conditions Re=80,000 and 50,000 the pitch moment assumes positive values.

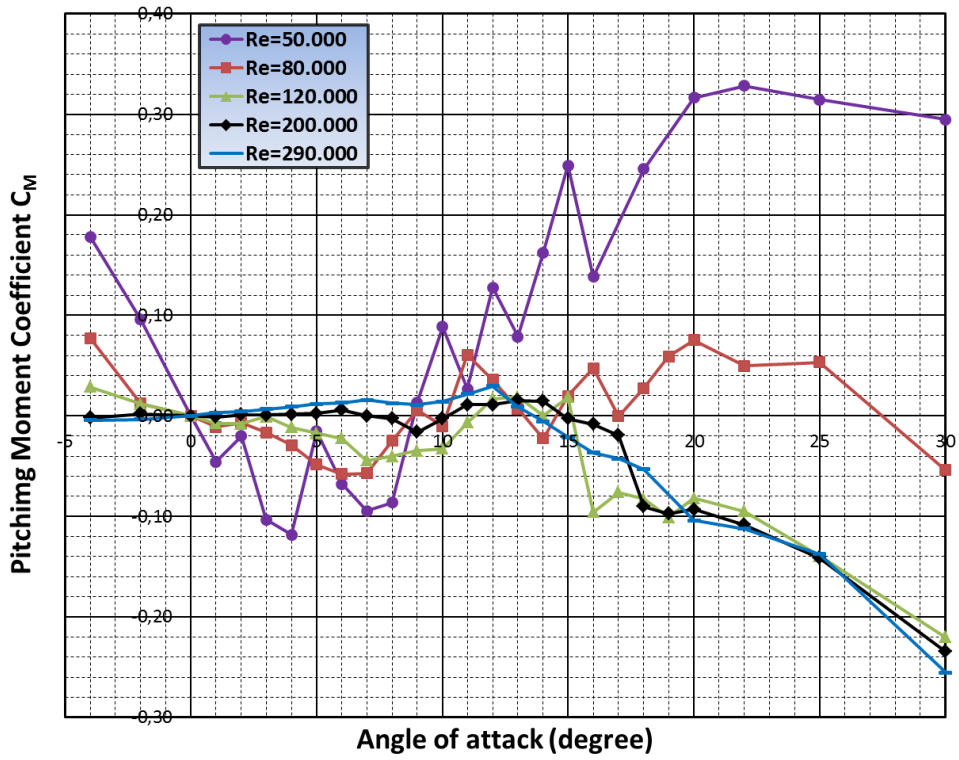

Figure 4.21: Pitch moment curve for NACA 0020 airfoil at low Reynolds number (Re=50,000-290,000)

4.3.2 Wavy leading edge performance at Reynolds number 290,000

Figure 4.22 shows the wavy leading edge performance at lift curve for thick NACA 0020 airfoil. At pre-stall regime, differently from thinner NACA 0012 airfoil, all configurations reach the angle of attack 5º keeping the linear lift curves very close.

The configuration A3λ40 follows the linearity of the baseline airfoil curve up to α = 4º. For configurations A11λ40 and A3λ11, it is kept the same linearity up to α = 4º and 6º, respectively. After the first straight line segment, the configuration A3λ40 undergoes an increase in slope curve earlier than the smooth configuration achieving higher lift coefficient values up to stall angle.

On the other hand, in the case of the configurations A11λ40 and A3λ11, it occurs a decrease in curve slope on the second straight line segment keeping lower lift values when compared to baseline airfoil.

As in the baseline airfoil, the configurations A3λ40 and A3λ11 present a third curve segment on the lift plot. The configuration A3λ40 follows an asymptotic curve as the smooth configuration does, whereas A3λ11 shows straight line segments with decrease in curve slope. Despite the fact the airfoil A3λ11 undergoes higher aerodynamic deterioration than smooth airfoil does, at pre-stall regime, both configurations reach the same maximum lift coefficients. In contrast with smaller amplitude configurations, the configuration A11λ40 keeps the second straight line segment up to stall.

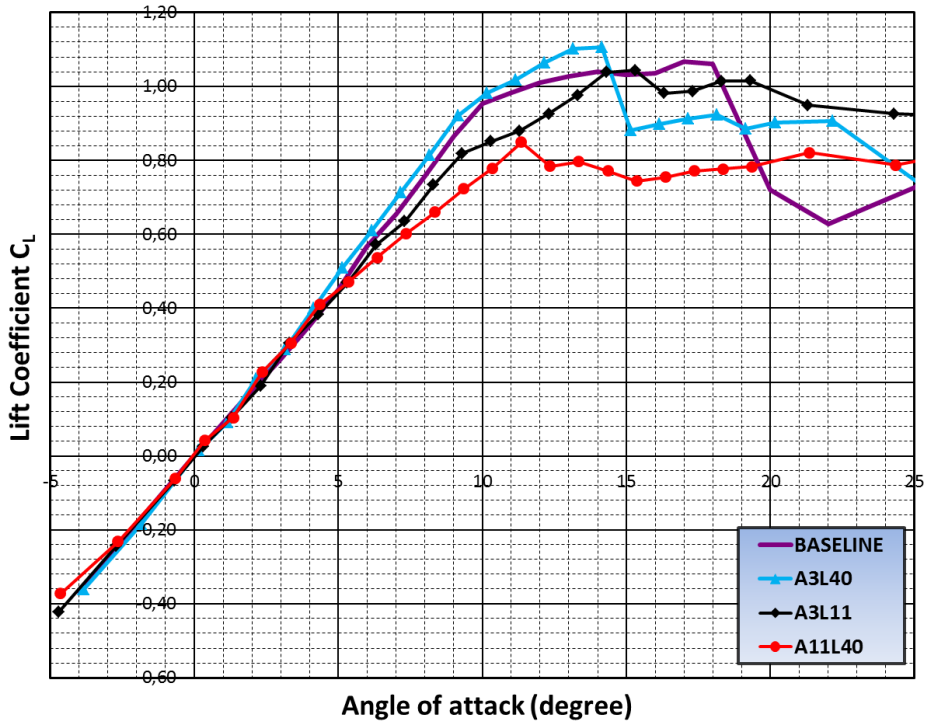

Figure 4.22: Lift curves for smooth and wavy configurations at Re = 290,000 (NACA 0020 airfoil).

In on hand, the wavy leading edge for the NACA 0020 airfoils does not cause aerodynamic deterioration up to $\alpha = 5º$, in opposition to thin airfoils, keeping very close values to smooth configuration. On the other hand, the configurations A11λ40 and A3λ11 present a significant decrease in performance for higher angles of attack up to stall when compared to NACA 0012 airfoil.

At post-stall regime, the wavy leading edge configurations, except for A3λ40, have a soft stall behaviour, differently from the abrupt stall for the smooth airfoil, keeping the lift coefficients near C_{Lmax} at higher angles. In contrast, in the case of the NACA 0012, the configuration A3λ40 also keeps a soft stall behaviour.

The amplitude effect on tubercle performance for the NACA 0020 shows that a decrease in amplitude from A11 to A3 at higher wavelength (λ40) approaches the lift curve to the smooth configuration. Besides, an increase in tubercle amplitude causes a decrease in stall angle in 12.5%.

On the other hand, an increase in amplitude guarantees a smooth stall in opposition to abrupt stall at configuration A3λ40. For amplitude variation at a fixed wavelength, as a result of the combination of the pre-stall and post-stall characteristics, it is reached for configurations A11λ40 and A3λ40 C_{Lmax} = 0.89 (ΔC_{Lmax} = -16.80%) and 1.12 (ΔC_{Lmax} = +4.78%), respectively.

The wavelength effect causes an expressive increase in lift values at the $\alpha = 5º$ for configuration A3λ40 when compared to shorter wavelength (A3λ11). However, the stall angle decreases from 14 °to 15° and the maximum lift coefficients reached for both configurations are close. Considering the post-stall regime, a wavelength increase keeps the airfoil at an abrupt stall condition. As global consequence of the increasing in wavelength, the airfoils reach C_{Lmax} = 1.12 (ΔC_{Lmax} = +4.78%) and 1.08 (ΔC_{Lmax} = -0,1%), respectively, for the configurations A3λ40 and A3λ11.

Although the wavelength increase rises the maximum lift, the effect of decreasing amplitude appears to be more effective increasing C_{Lmax} by 23% whereas there is an increase of 5% for wavelength variation.

Even though the configuration A3λ40 reaches the highest maximum lift coefficient (1.10) and overcomes the value of the smooth configuration, the wavy leading edge

configuration for smaller amplitude and shorter wavelength (A3λ11) reaches better overall result, having maximum lift coefficient close to smooth configuration (ΔC_{Lmax} = -2,28%), and, in addition, keeping desirable soft stall characteristics.

This wavy leading edge geometric combination indicates that smaller amplitude and shorter wavelength (A3λ11) establish a better arrange between pre-stall and post-stall characteristics achieving a highest C_{Lmax} and soft stall characteristics for both airfoils NACA 0012 and NACA 0020.

The changes caused on drag characteristics by wavy leading edge are showed in figure 4.23. At low angles of attack regime ($\alpha < 5°$), the configurations with smaller amplitude (A3λ11 and A3λ40) have similar smaller drag coefficient values than the ones of the smooth airfoil. The minimum drag coefficient for smaller amplitude configurations decrease in -14.52% (A3λ11) and -23.93 % (A3λ40). The configuration A11λ40 has a similar drag coefficients values than the baseline airfoil at low angle of attack.

For intermediate angle of attack ($5° < \alpha < \alpha_{stall}$), the drag coefficient depends on stall characteristics for each wavy leading edge configuration. The configuration A11λ40 anticipates the stall onset at $\alpha = 5°$ and thus reduces the extent of the drag bucket increasing drag as in the thinner NACA 0012 airfoil. In contrast, the configuration A3λ40 keeps a parabolic raise in drag coefficient up to $\alpha = 11°$ with values lower than the smooth configuration. The configuration A3λ11 has similar characteristics to A3λ40 except that the parabolic raise in drag goes up to $\alpha = 8°$. After that, this configuration overcomes the drag values from the configuration A3λ40.

At post-stall regime, a significant increase in drag for wavy leading edge configurations occurs at stall angle so that for angles of attack higher than 14° the configurations A3λ40 and A11λ40 have greatest drag coefficient values. Additionally, the configuration A3λ11 also keep values quite higher than those of the smooth airfoil.

In terms of amplitude effect, a decrease in amplitude reduces the C_{d0} and delays the large increase in drag due to the stall condition (A3λ40 and A11λ40). Considering the wavelength effect, the configurations A3λ40 and A3λ11 have similar drag values, at low angle of attack, showing a negligible effect of wavelength variation in this condition.

However, the stall onset is anticipated for shorter wavelength increasing drag values. At post-stall regime (from $\alpha = 15°$), the longer wavelength reaches higher values of drag coefficient.

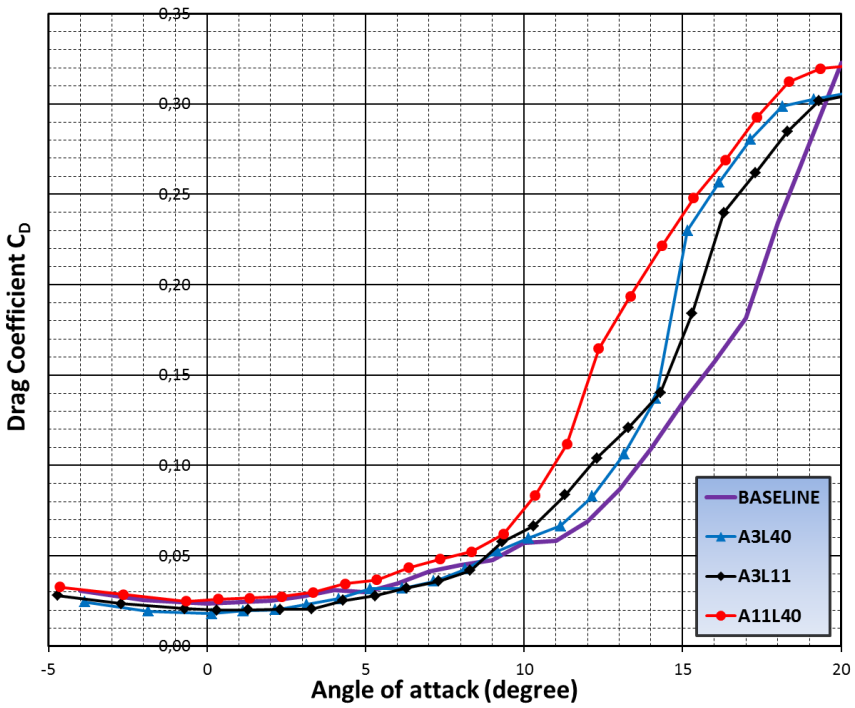

Figure 4.23: Drag curves for smooth and wavy configurations at Re = 290,000 (NACA 0012 airfoil).

Figure 4.24 shows pitching moment results for different wavy leading edge configurations. At low angle of attack (up to 10º), the smooth and A3λ11 configurations has similar pitching moment characteristics increasing moment coefficient slightly from null values. In addition, the configurations A11λ40 and A3λ40 keep lower pitching moment coefficients than the smooth configuration does, where the greater amplitude configuration reaches the lowest values.

For higher angle of attack, the wavy leading edge configurations follow the smooth configuration trend having a significant decrease in pitching moment curve slope after stall angle, however, anticipating this moment characteristic. The configuration A11λ40 keeps the earliest abrupt decrease in moment values as in the thin NACA 0012 airfoil.

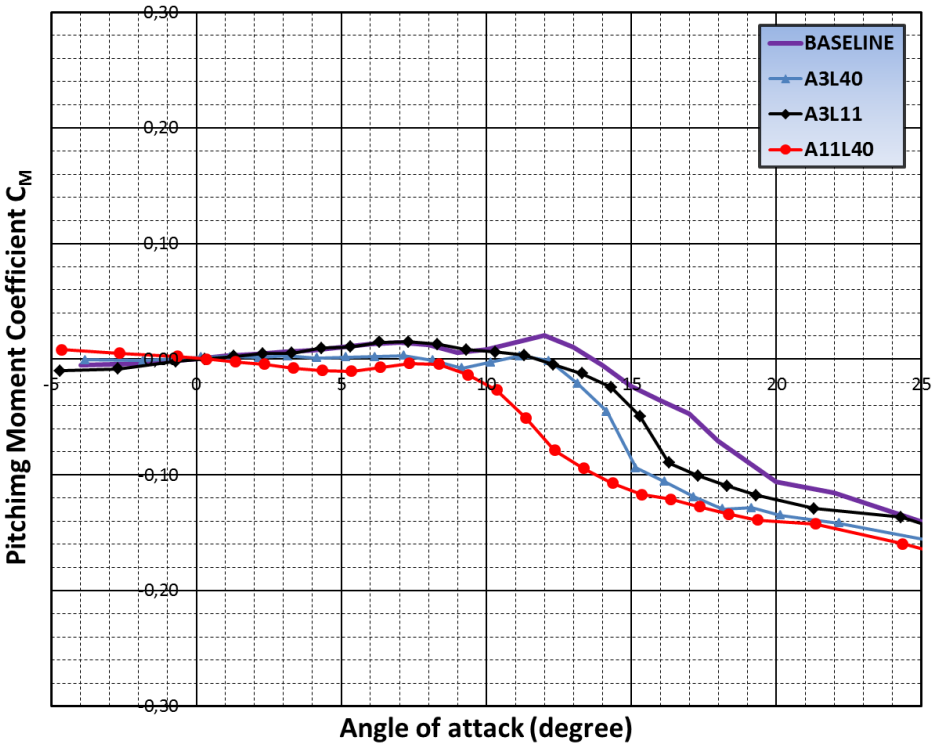

Figure 4.24: Pitching moment curves for smooth and wavy configurations at Re = 290,000 (NACA 0020 airfoil).

Table 4.2 summarizes the changes caused by wavy leading edge geometries on aerodynamic performance of the thin NACA 0020 airfoil.

Configuration	C_{d0} *(counts)*	ΔC_{d0}	C_{Lmax}	ΔC_{Lmax}	α_{stall}	$\Delta \alpha_{stall}$	*Lift drop*	*Stall type*
Baseline	234	reference	1,07	reference	18.0	reference	-40.8%	abrupt
A3λ40	181	-22.64 %	1.12	+4.78%	14.15	-19,4%	-20.3%	abrupt
A11λ40	258	+10.25%	0.89	-16.8%	11.35	-36,9%	-6.25%	soft
A3λ11	203	-13.24%	1.08	-0.10%	15.30	-15,0%	-11.2%	soft

Table 4.2: The wavy leading edge effect on aerodynamic performance for thin NACA 0020 airfoil.

4.3.3 Reynolds number effects

The increase in Reynolds number does not affect, except for at Re = 50,000, the main aerodynamic characteristics of the wavy leading edge for the thick NACA 0020 airfoil (figure 4.24-28).

It is kept the same geometric dependency of amplitude and wavelength in aerodynamic performance as mentioned in the previous subsection for Re = 290,000 where the configuration A3λ11 shows the best performance in contrast with the worst result for configuration A11λ40.

The Reynolds number effect causes small changes at pre-stall conditions. The wavy configurations follow the smooth airfoil at linear curve up to lower values with decrease in Reynolds number where it reaches $\alpha = 5^{o}$ at Re = 290,000 and $\alpha = 2^{o}$ at Re = 80,000. Except for Reynolds numbers 290,000 and 50,000, the smooth configuration has higher maximum lift coefficient. Furthermore, only at Re =50,000, the stall angle of the baseline airfoil reaches values lower than the wavy configuration ones.

The maximum lift coefficient deterioration caused by tubercle decreases with increasing Reynolds number, reaching an improvement for all wavy configurations at Reynolds number 50,000 (figure 4.29). At post-stall regime, the configuration A3λ40 remains with abrupt stall characteristics, like the smooth airfoil. Moreover, the configurations A11λ40 and A11λ40 keep soft stall at any Reynolds number condition.

As for wavy NACA 0012 airfoils, at the lowest Reynolds number (Re = 50,000), there are large changes when compared to higher Reynolds number regimes. At pre-stall regime, the configurations A11λ40 and A3λ11 decrease values in lift coefficient since lower angles of attack whereas the configuration A3λ40 follows the baseline airfoil, reaching higher maximum lift and stall angle, but keeping an abrupt stall. The configurations A11λ40 and A3λ11 overcome the baseline maximum lift coefficient presenting soft a stall at post-stall regime.

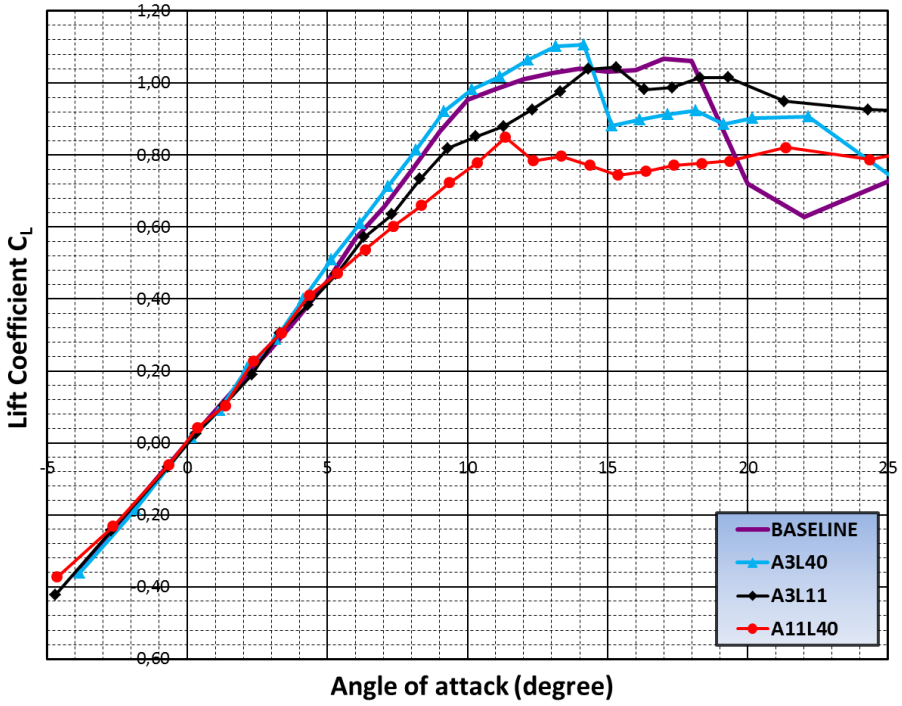

Figure 4.25: Lift curves for the smooth and wavy configurations at Re = 290,000 (NACA 0020 airfoil).

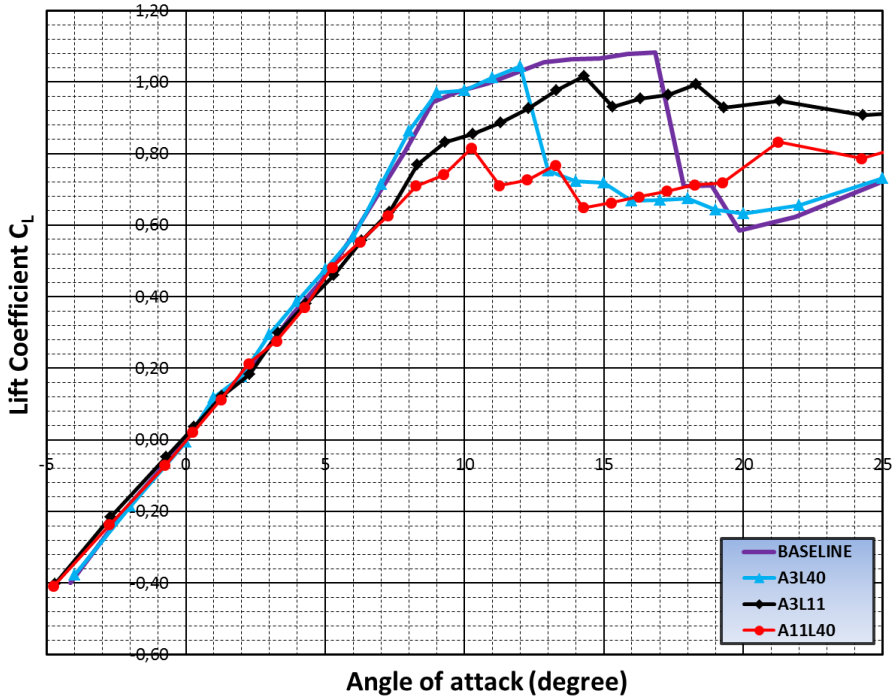

Figure 4.26: Lift curves for the smooth and wavy configurations at Re = 200,000 (NACA 0020 airfoil).

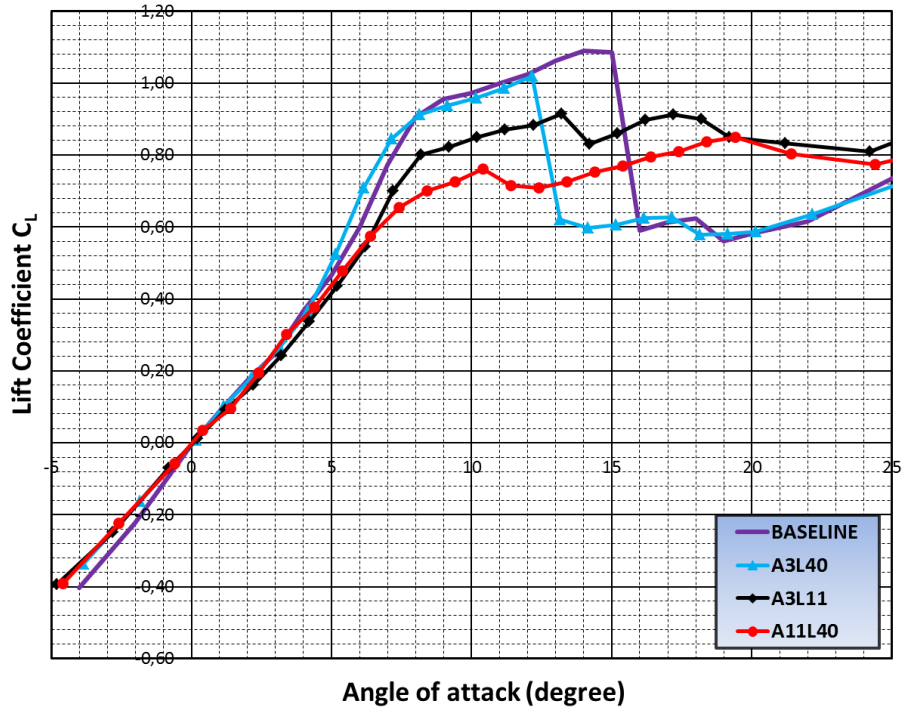

Figure 4.27: Lift curves for the smooth and wavy configurations at Re = 120,000 (NACA 0020 airfoil).

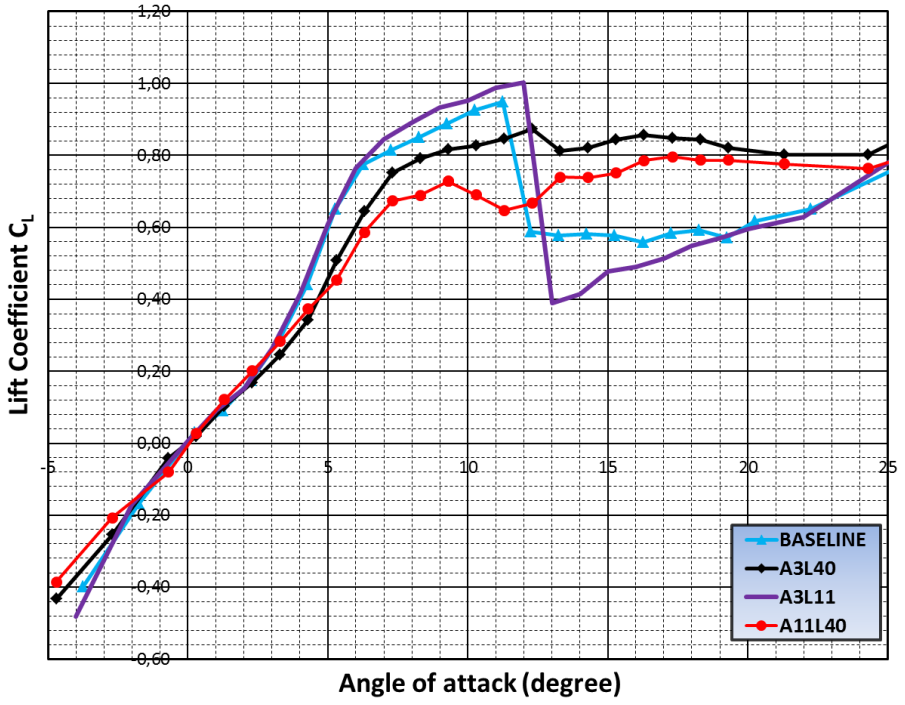

Figure 4.28: Lift curves for the smooth and wavy configurations at Re = 80,000 (NACA 0020 airfoil).

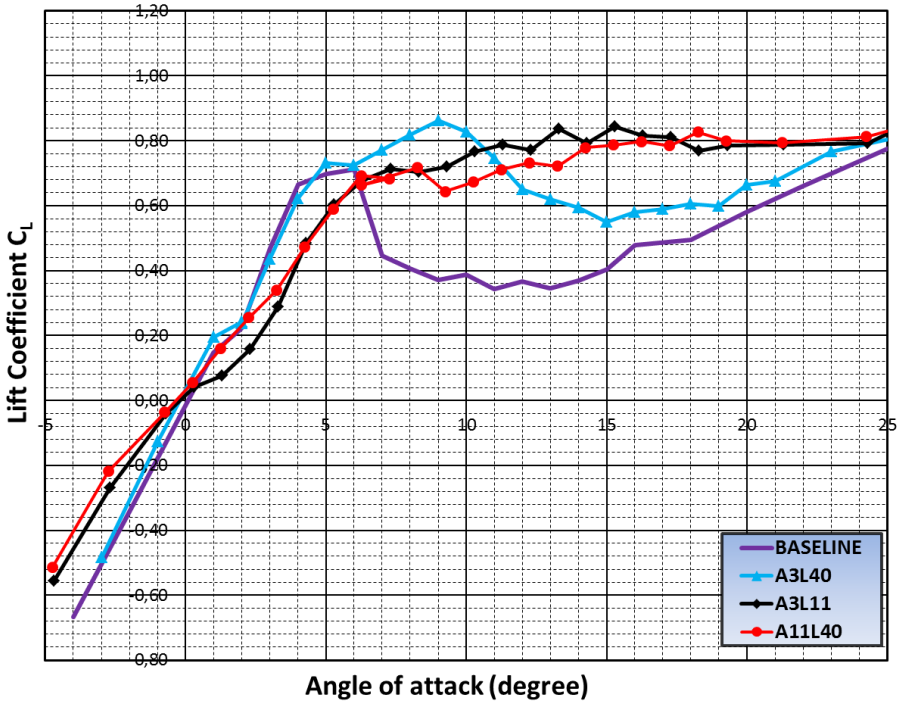

Figure 4.29: Lift curves for the smooth and wavy configurations at Re = 50,000 (NACA 0020 airfoil).

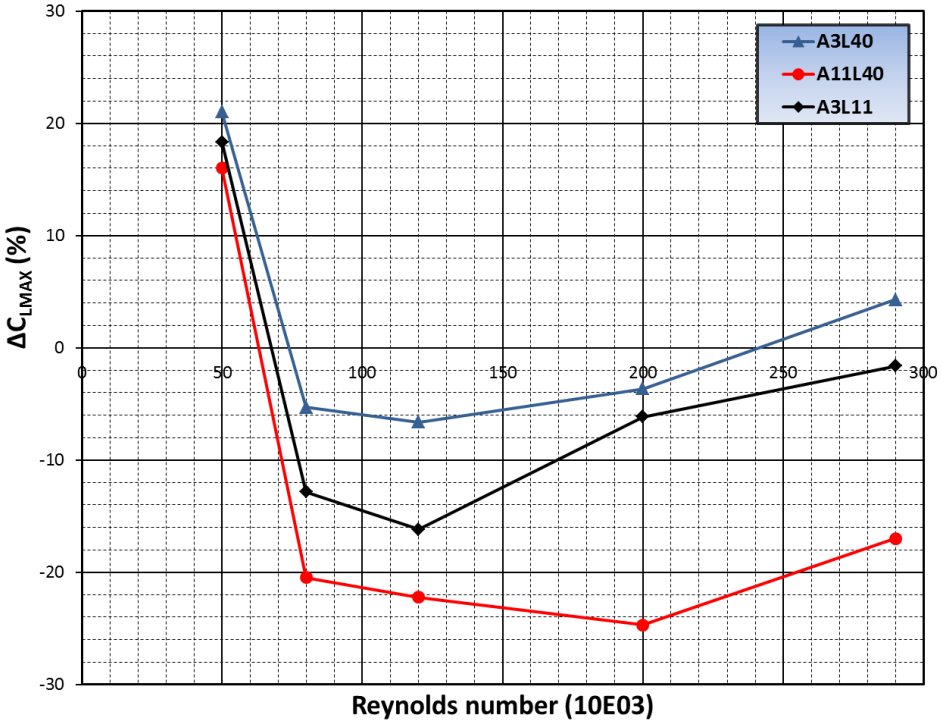

Figure 4.30: Reynolds Number effect on C_{LMAX} for the wavy configurations (NACA 0020 airfoil).

As it was shown previously, at Reynolds number 290,000, the configurations A3λ40 and A3λ11 present lower drag values than the smooth configuration at lower angles of attack whereas the airfoil A11λ40 shows similar values (figure 4.31). However, the drag performance of the tubercles changes with decreasing of the Reynolds number condition.

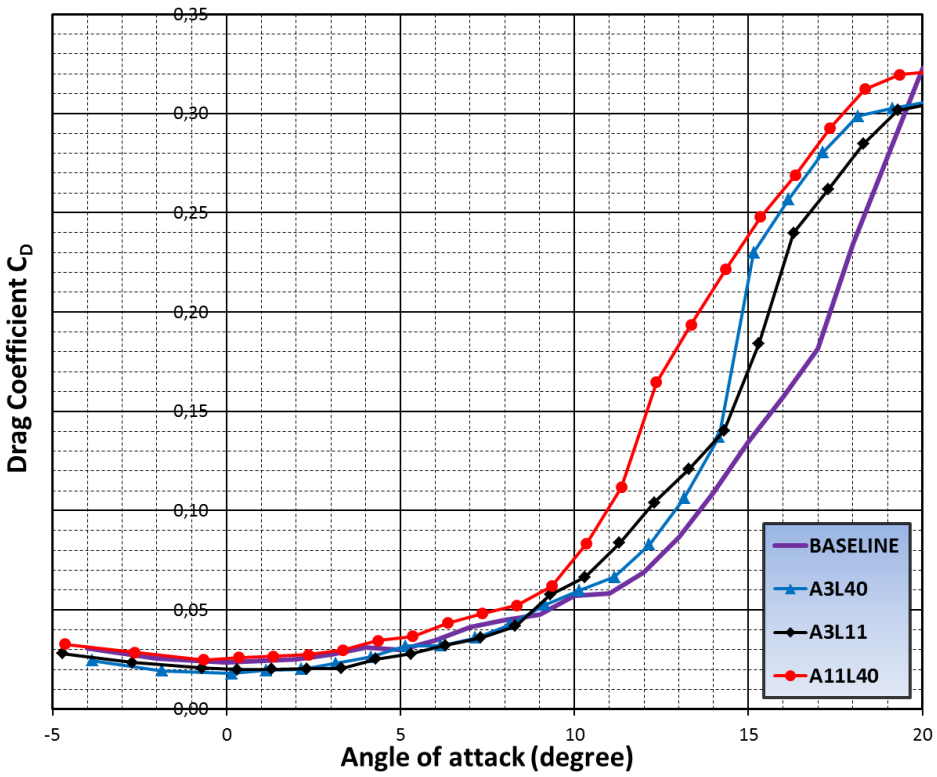

Figure 4.31: Drag curves for the smooth and wavy configurations at Re = 290,000 (NACA 0020 airfoil).

At Re = 200,000, all wavy configurations reach values higher than baseline configuration for lower angles of attack (figure 4.32). In contrast, at Reynolds number 120,000, the wavy airfoil reaches lower values than the smooth configuration at lower angle of attack conditions (figure 4.33).

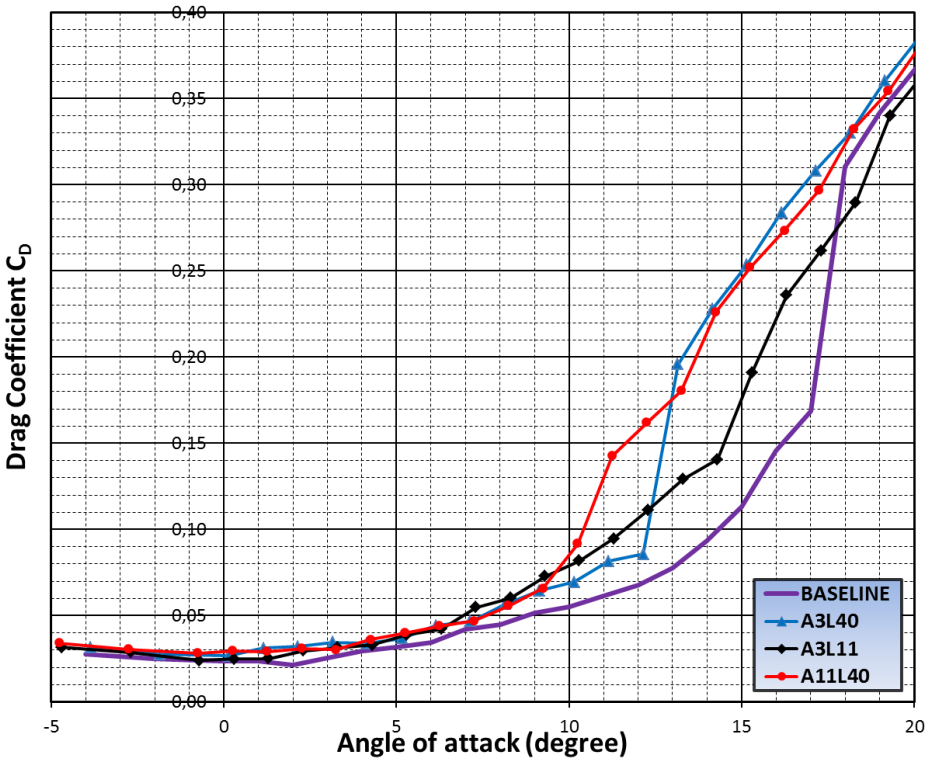

Figure 4.32: Drag curves for the smooth and wavy configurations at Re = 200,000 (NACA 0020 airfoil).

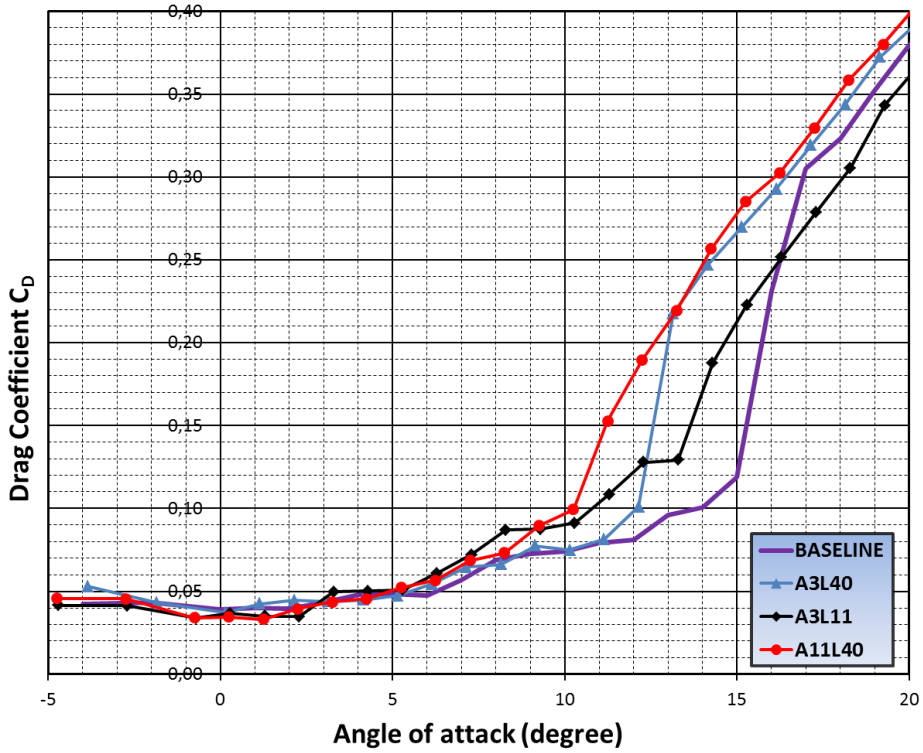

Figure 4.33 Drag curves for the smooth and wavy configurations at Re = 120,000 (NACA 0020 airfoil).

The Reynolds number effect regarding pitching moment characteristics seems not be sensitive at higher Reynolds numbers flow conditions (Re = 290,000 and 200,000) (figures 4.34 and 4.35) where the wavy configurations decrease moment curve slope slightly, at a lower angle of attack, when compared to the smooth airfoil. Additionally, it also anticipates the large decrease in moment curve slope. The configuration A11λ40 keeps the lowest pitching moment values in the entire range of angle of attack.

However, at Reynolds number 120,000 (figure 4.36), the wavy and smooth configurations remain within similar values at low angles of attack. In contrast, the configuration A3λ11 presents the highest pitching moment values over the entire angle of attack range. The Reynolds number effects on pitching moment characteristics seem similar to those of the thin NACA 0012 airfoil.

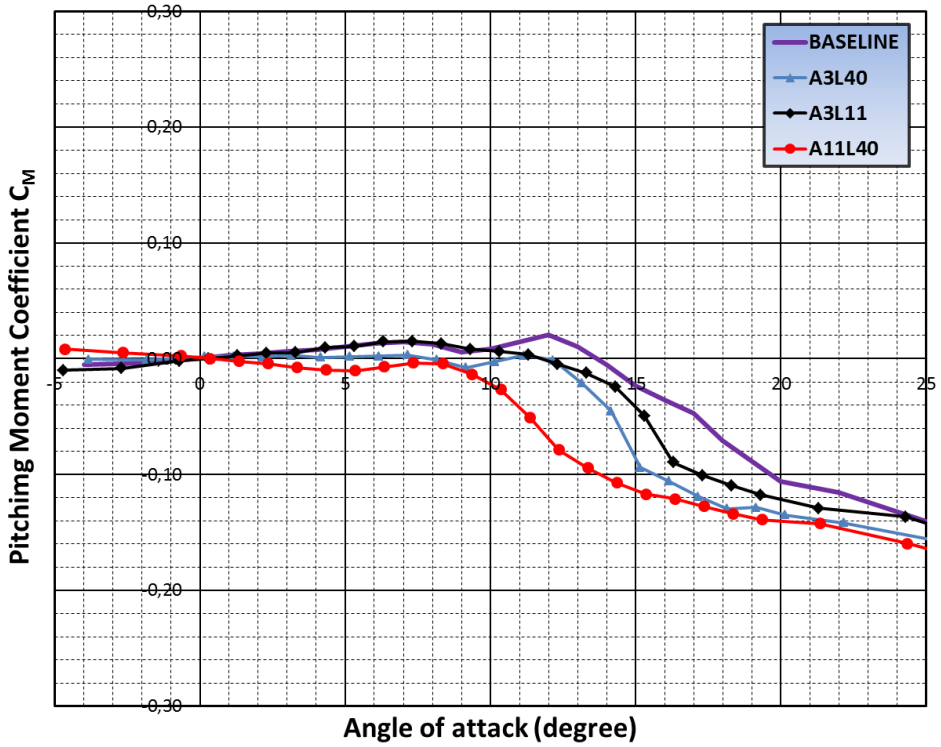

Figure 4.34: Pitching moment curves for the smooth and wavy configurations at Re = 290,000 (NACA 0020 airfoil).

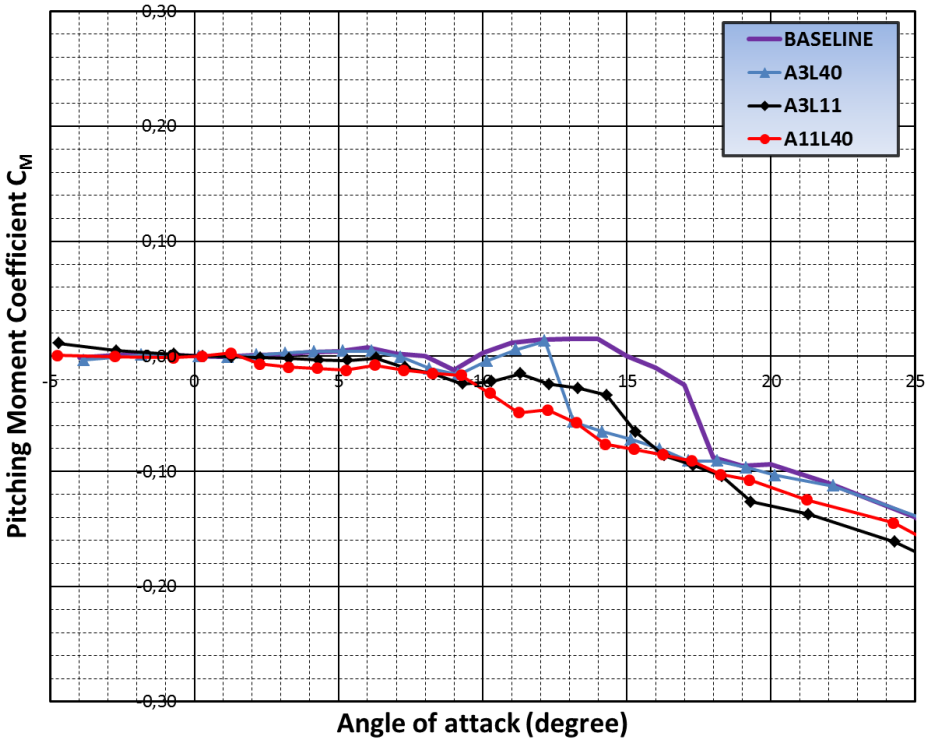

Figure 4.35: Pitching moment curves for the smooth and wavy configurations at Re = 200,000 (NACA 0020 airfoil).

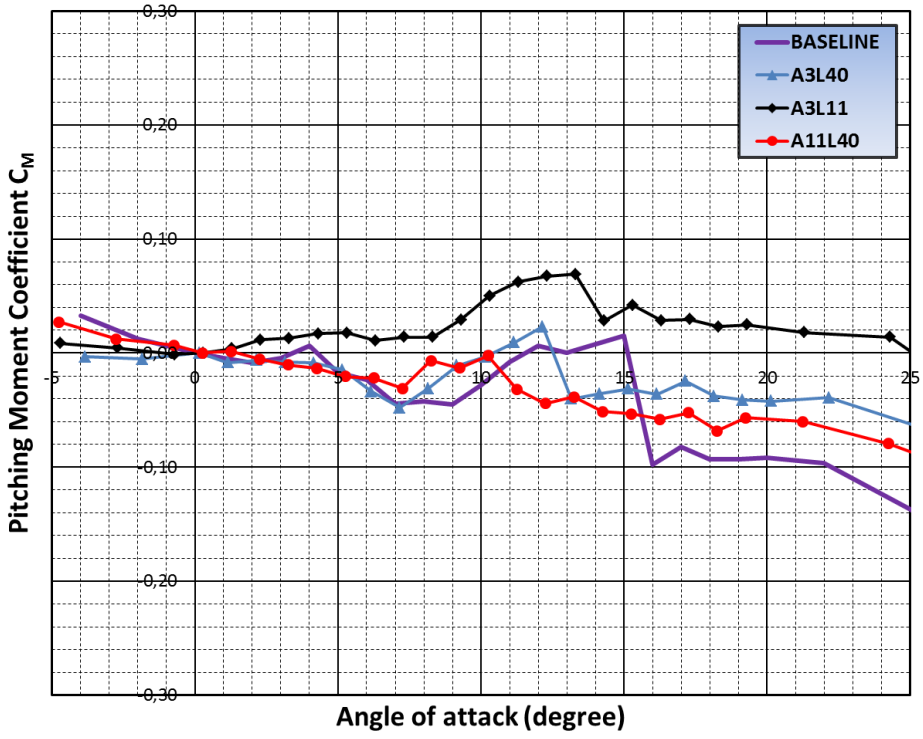

Figure 4.36: Pitching moment curves for the smooth and wavy configurations at Re = 120,000 (NACA 0020 airfoil).

4.4 Wavy leading edge performance for NACA 0030 airfoil

4.4.1 Baseline Airfoil in the range of the Reynolds number between 50,000 and 290,000

Figures 4.37-39 show the aerodynamic characteristics of the thickest NACA 0030 airfoil at low Reynolds number regimes. When compared to thinner airfoils, NACA 0012 and NACA 0020, the thickest airfoil shows a greater abrupt stall behaviour (lift loss) and decrease in performance caused by Reynolds number variation.

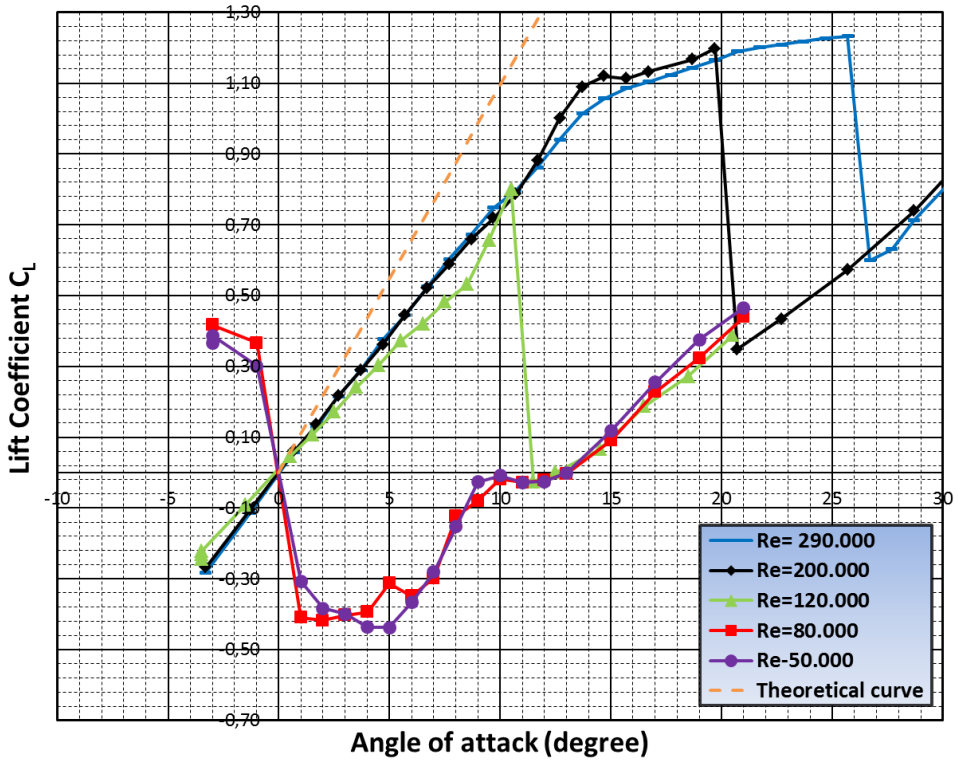

Figure 4.37: Lift curves for NACA 0030 airfoil at low Reynolds number (Re=50,000-290,000).

At a higher Reynolds number (Re = 200,000 and 290,000), it can be seen at lift curve a similar behaviour than the one of NACA 0020 airfoil where the first straight line segment keeps a lower curve slope than the theoretical curve. After that, it follows an increase in curve slope, greater at Re = 200,000, that finishes with the beginning of asymptotic curves. In addition, there is a large Reynolds number effect on stall angle (decrease in five degrees) and

a small effect on maximum lift coefficient (decrease in 3%) with decreasing in Reynolds number condition.

At an intermediate Reynolds number condition (Re=120,000), the lift characteristics shows a higher decrease in curve slope in the first straight line segment. After that, occurs an increase in slope curve earlier than in higher Reynolds number conditions. However, the airfoil undergoes stall condition before achieving an asymptotic behaviour in the lift curve. Thus, the airfoil at Re =120,000 has a large decrease in stall angle and maximum lift coefficient.

For lower Reynolds number (Re = 80,000 and 50,000), there is a large deterioration in aerodynamic performance. At angles of attack up to 10º, the airfoil reaches negative lift values. After that, the lift curves kept a linear behaviour achieving very low lift coefficient at higher angles of attack.

Figure 4.38 shows similar characteristics in terms of drag for the Reynolds number range between 120,000 and 290,000. As for previous thinner airfoils, with decrease in Reynolds number, there is a positive shift in drag values at low angle of attack, and the anticipation of the significant increase in drag because of the stall onset where at Re = 120,000 appears the earliest abrupt increase in drag at the lowest angle of attack ($\alpha = 10º$).

At lower Reynolds numbers 80,000 and 50,000, in the entire range of angles of attack, there is a large aerodynamic deterioration with enormous increase in drag indicating a full flow separation from lower angles of attack showed by flow visualizations in the chapter five.

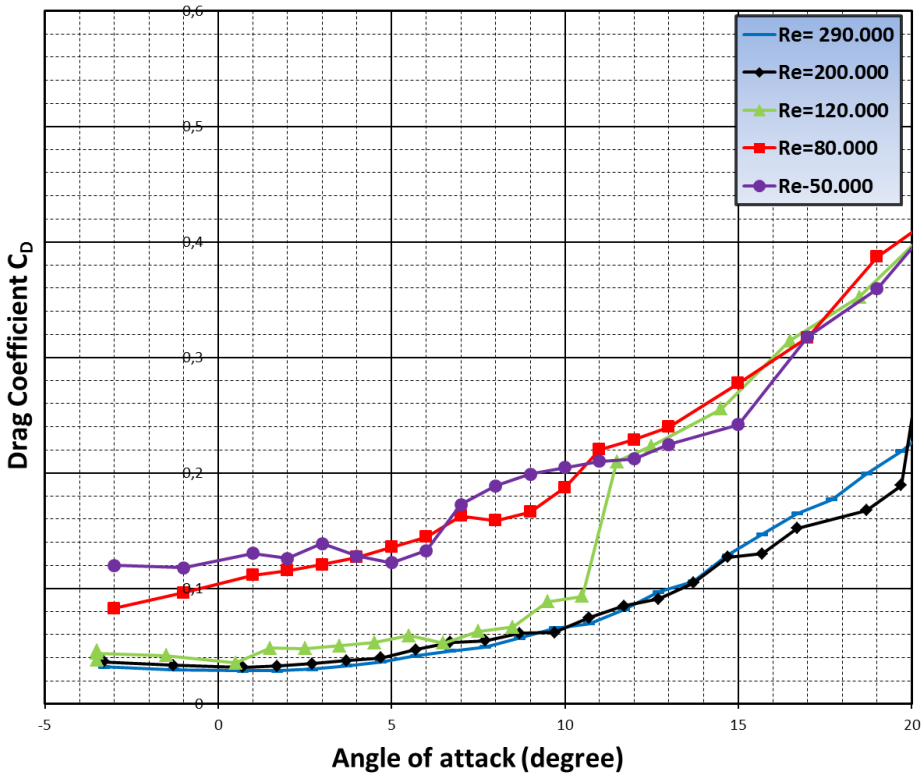

Figure 4.38: Drag curves for NACA 0030 airfoil at low Reynolds number (Re=50,000-290,000).

In figure 4.39, it can be seen the pitching moment characteristics for NACA 0030 airfoil. At low angles of attack, it occurs a linear behaviour, increasing pitching moment values with increase in angle of attack up to the stall angle. This behaviour indicates that for the thickest NACA 0030 airfoil the aerodynamic center is not valid at 25% of M.A.C anymore. Thus, the pitching moment increases as consequence of the forward movement of the pressure center position. The positive curve slope increases with decreasing in Reynolds number. After that, the pitching moment curve slope changes in signal and amplitude decreasing values with increasing angle of attack, indicating the stall condition behaviour. As for thinner airfoils the pitching moment undergoes a large decrease due to the backward movement of the pressure center position caused by wake of the trailing edge flow separation. The change in moment curve slope occurs earlier with decrease in Reynolds number as consequence of the onset stall anticipation for lower Reynolds number conditions. In addition, below Re=120,000 the pitching moment curves present a large increase in curve slope at lower angles of attack.

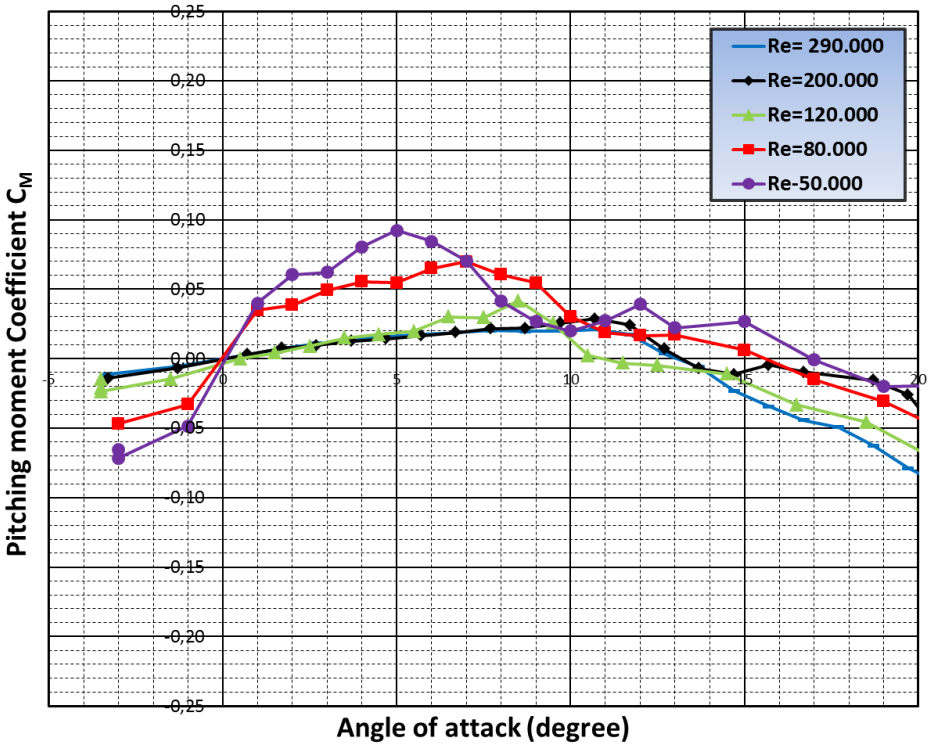

Figure 4.39: Pitching moment curve for NACA 0030 airfoil at low Reynolds number (Re=50,000-290,000).

4.4.2 Wavy leading edge performance at Reynolds number 290,000

It can be seen in figure 4.40 that the thickest wavy airfoils clearly present higher aerodynamic deterioration when compared to thinner airfoils (NACA 0012 and NACA 0020). At pre-stall regime, the configurations A3λ40 and A3λ11 follow the linearity of the smooth airfoil curve up to α = 7.5º keeping the lift coefficient very close to the smooth configuration values. After that, the configurations A3λ40 and A3λ11 decrease linearity up to α = 11 º and 13 º, respectively, with lift values remaining lower than those of the smooth airfoil. At these angles of attack, the curves increase the curve slope, and after continuing an asymptotic curve with the same trend of the baseline configuration. They reach maximum lift values lower than those of the smooth airfoil.

In the case of the configuration A11λ40, the first straight line segment has a significant decrease in curve slope when compared to the smooth airfoil. At α = 6º there is a great

increase in slope curve keeping the linearity up to stall angle, reaching the lowest maximum lift coefficient.

At post-stall regime, differently from the abrupt stall that is observed for the smooth configuration, the airfoil A3λ11 undergoes a soft stall, keeping the lift coefficients near C_{Lmax} at higher angles of attack. The configurations A3λ40 and A11λ40 still keep an abrupt stall like in the baseline airfoil where the lower amplitude configuration reaches a higher lift drop.

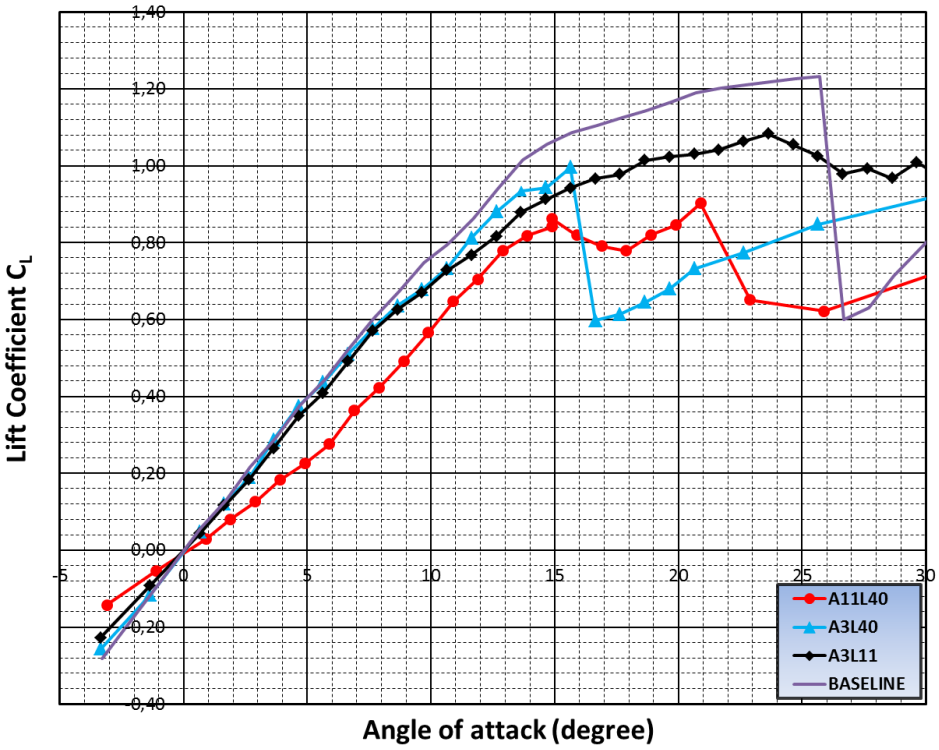

Figure 4.40: Lift curves for the smooth and wavy configurations at Re = 290,000 (NACA 0030 airfoil).

The wavelength effect can be seen when the configuration A3λ11 is compared to the configuration A3λ40. A decrease in wavelength delays the curve slope change and the stall angle. Moreover, the wavelength reduction changes the stall behaviour from an abrupt to soft characteristic. In terms of wavelength effect on maximum lift coefficient, the configurations A3λ40 and A3λ11 reach C_{Lmax} = 0.99 (ΔC_{Lmax} = -19.5%) and 1.08 (ΔC_{Lmax} = -12.2%), respectively.

The amplitude effect causes, as in the other thinner airfoils, a significant aerodynamic deterioration. However, in this case, the decrease in lift performance appears in the entire

angle of attack range. The configuration A11λ40 has the first straight line segment slope decreased since lower angles of attack when compared to configuration A3λ40 keeping the lowest lift values up to stall. As consequence, the configurations A11λ40 and A3λ40 present values of C_{Lmax}´s 0.90 (ΔC_{Lmax} = -26.8%) and 0.99 (ΔC_{Lmax} = -19.5%), respectively. However, the stall angle and drop in lift decrease with increasing amplitude.

Also as in the thinner airfoils, an arrange of shorter wavelength and greater amplitude (A3λ11) establishes a better combination between pre-stall and post-stall characteristics reaching the C_{Lmax} closest to baseline configuration keeping soft stall characteristics.

Figure 4.41 shows the drag performance for wavy leading edge airfoils. At low angle of attack regime ($\alpha < 3°$), the configurations A3λ11 and A11λ40 have similar drag coefficient values little higher than those on the smooth configuration. The greater amplitude configuration anticipates the trailing edge stall onset reaching highest drag from $\alpha = 4º$ whereas the configuration A3λ11 keeps similar drag values to the smooth configuration ones up to $\alpha = 7º$. After that, as consequence of the stall onset, it increases the drag coefficient maintaining higher values.

The configuration A3λ40 presents lower drag values compared to the baseline airfoil up to $\alpha = 8º$. For $\alpha > 8º$, the drag coefficient reaches higher values than the smooth configurations, and this configuration shows stall onset characteristics earlier than for the airfoil A3λ11.

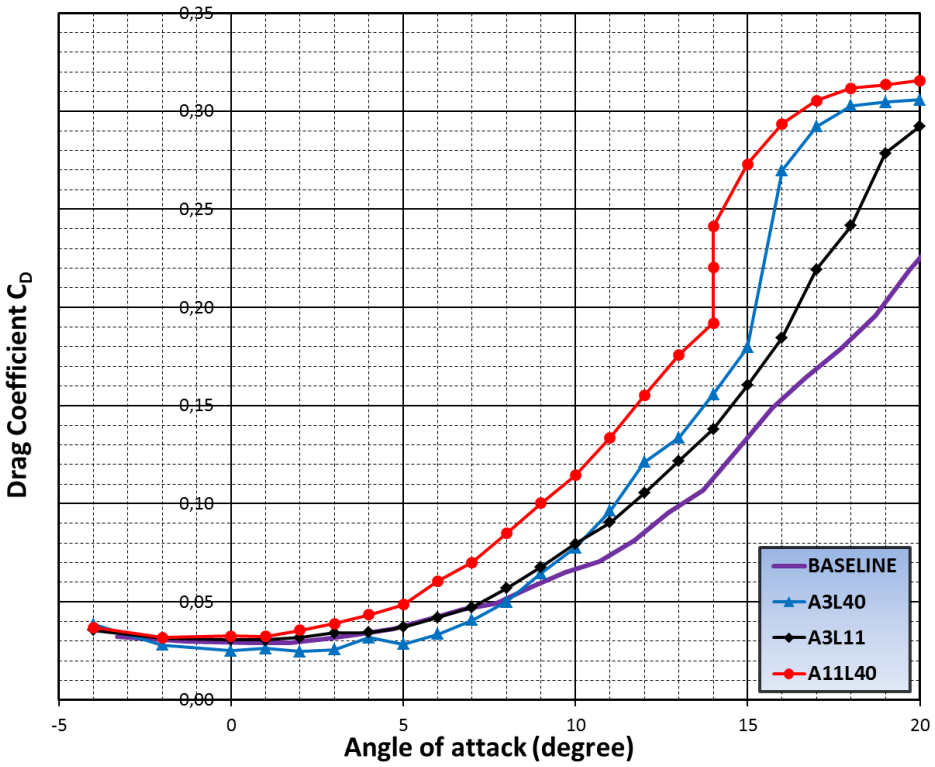

Figure 4.41: Drag curves for the smooth and wavy configurations at Re = 290,000 (NACA 0012 airfoil).

Figure 4.42 shows the results of the pitching moment characteristics for different configurations. All configurations, smooth and wavy, have similar pitching moment behaviour following a linear characteristic with positive slope up to $\alpha = 5°$ as consequence of the pressure center position moving ahead and the aerodynamics center is no longer valid at 25% M.A.C for a thick airfoil. All wavy configurations cause an anticipated change in curve slope because of the early flow separation that moves the pressure center position backwards. The greater amplitude configuration reaches the earliest slope curve change at $\alpha = 5º$ as a result of a large increase in lift slope curve at this angle of attack. On the other hand, the configuration A3λ40 and A3λ11 undergoes a large decrease in curve slope later ($\alpha = 10º$).

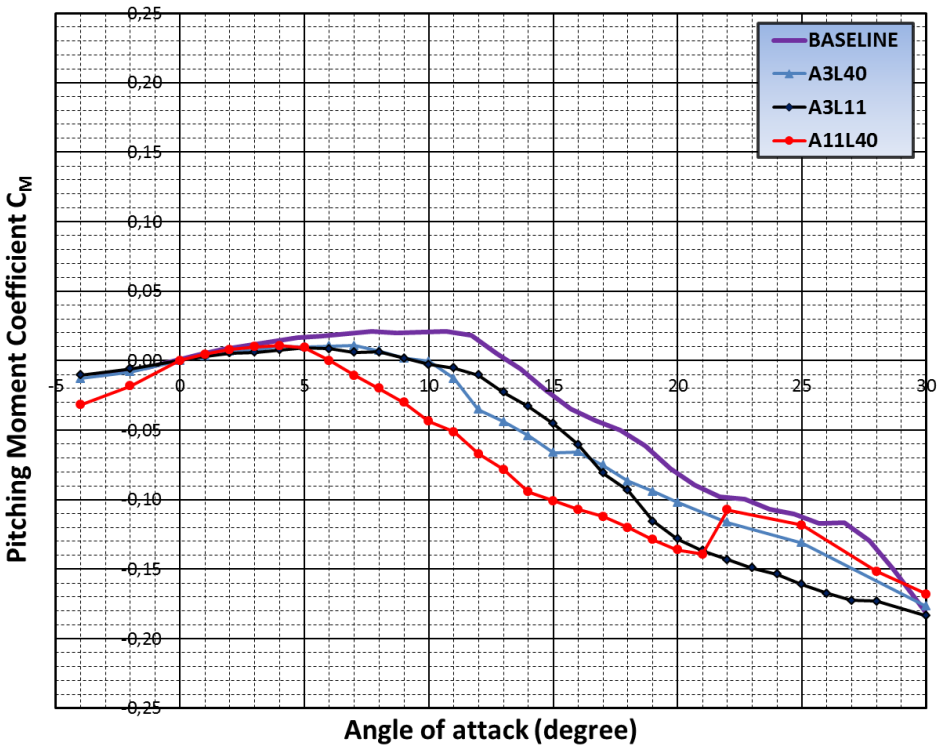

Figure 4.42: Pitching moment curves for the smooth and wavy configurations at Re = 290,000 (NACA 0012 airfoil).

Table 4.3 summarizes the changes caused by wavy leading edge geometries on aerodynamic performance of the thin NACA 0030 airfoil.

Configuration	C_{d0} *(counts)*	ΔC_{d0}	C_{Lmax}	ΔC_{Lmax}	α_{stall}	$\Delta \alpha_{stall}$	*Lift drop*	*Stall type*
Baseline	293	reference	1,23	reference	25.70	reference	-51,21%	abrupt
A3λ40	251	-14.33%	0.99	-19.5%	15.65	-39.10%	-40.00%	abrupt
A11λ40	325	+10.92%	0.90	-26.8%	20.90	-18.70%	-31.13%	abrupt
A3λ11	307	+4.77%	1.08	-12.20%	23.65	-8.00%	-8.35%	soft

Table 4.3: The wavy leading edge effect on aerodynamic performance for thin NACA 0030 airfoil.

4.4.3 Reynolds number effects

Figures 4.42-46 show a greater Reynolds number effect on wavy leading edge lift performance for the thickest NACA 0030 airfoil when compared to thinner airfoils (NACA 0012 and NACA 0020). At higher Reynolds numbers 290,000 and 200,000, the wavy configurations have a similar performance for both flow conditions (figures 4.43 and 4.44).

At lower angles of attack, the lift behaviour for smaller amplitude is very close to baseline lift curve up to $\alpha = 7.5^{o}$ and 5^{o} for Re = 290,000 and 200,000, respectively. After that, the curves decrease their linearity earlier than in the smooth airfoil, however, following its tendency up to stall condition achieving lower lift values. In contrast, the greater amplitude configuration shows a decrease in lift curve slope since the lower angles of attack keeping a significant aerodynamic deterioration on lift curve up to stall.

At stall condition, the smooth configuration has the highest maximum lift coefficient for an abrupt stall. The configuration A3λ11 reaches the highest maximum lift coefficient for wavy configurations keeping soft stall behaviour whereas the bigger amplitude configuration presents the lowest maximum lift coefficient. Both configurations A3λ40 and A11λ40 present an abrupt stall. However, the drop in lift is lower than in the smooth configuration. The drop in lift increases for all configurations with decreasing Reynolds number conditions. The decrease in Reynolds number also causes a large increase in aerodynamic deterioration on maximum lift coefficient caused by wavy leading edge configurations.

At an intermediate Reynolds number 120,000 (figure 4.45), the smaller amplitude and shorter wavelength configuration shows a great performance keeping the same linearity of the smooth airfoil at a lower angle of attack, and overcomes the baseline maximum lift coefficient in 19.4% and the stall angle in 44% showing an unprecedented result when compared to previous studies regarding wavy leading edge performance. The configuration A3λ40 has similar characteristics to baseline airfoil ones, reaching abrupt stall on the second straight line segment (higher curve slope) at an early angle of attack ($\alpha = 12^{o}$). The bigger amplitude configuration follows the characteristics from higher Reynolds number.

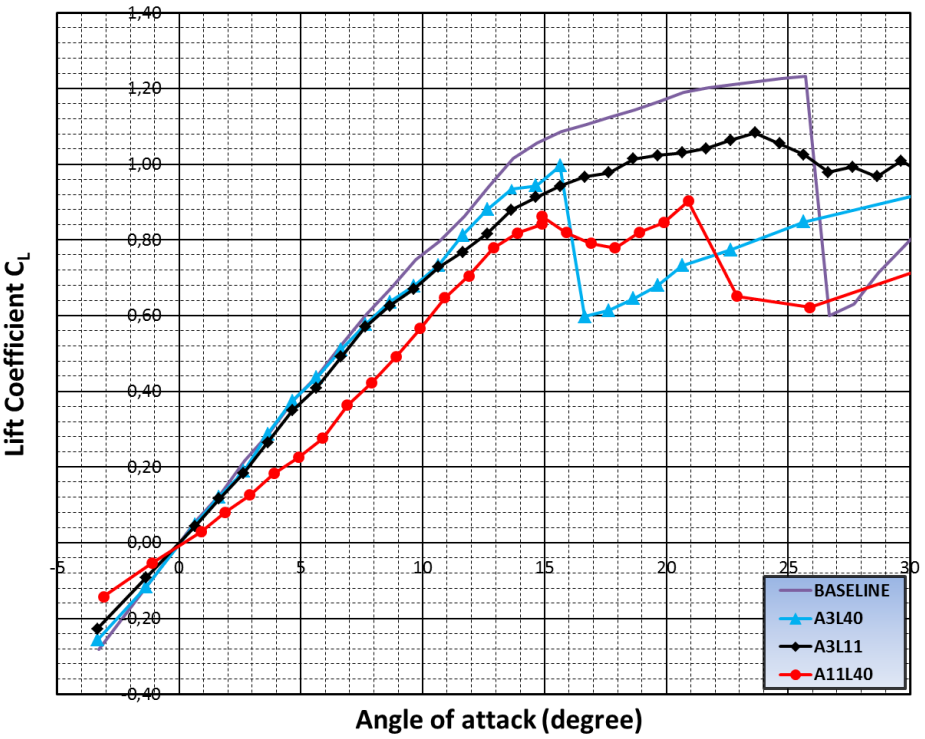

Figure 4.43: Lift curves for the smooth and wavy configurations at Re = 290,000 (NACA 0030 airfoil).

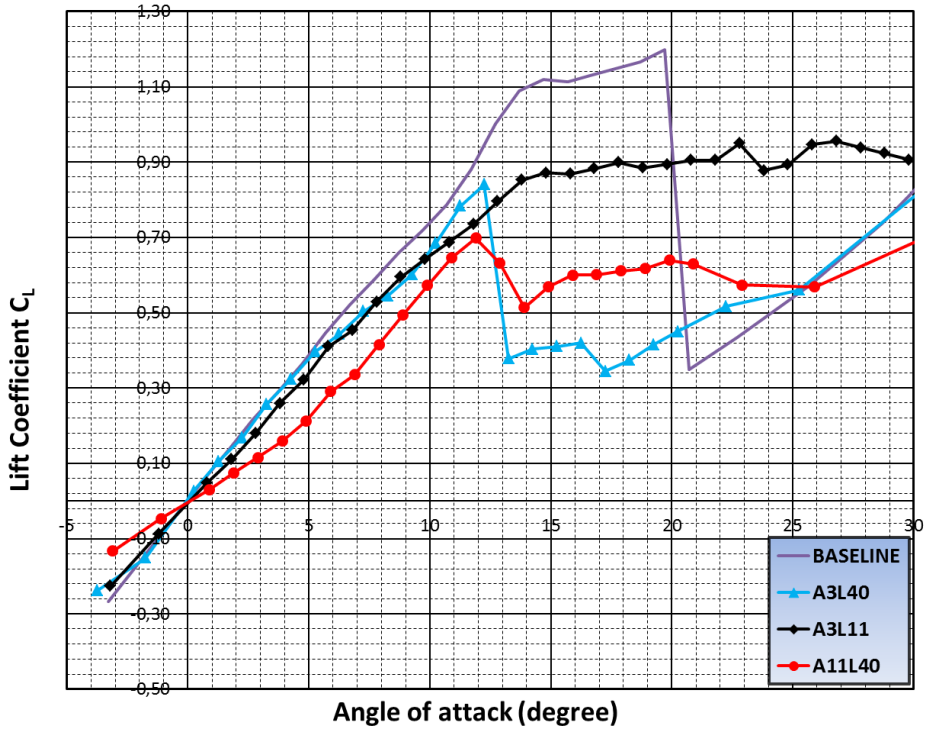

Figure 4.44: Lift curves for the smooth and wavy configurations at Re = 200,000 (NACA 0030 airfoil).

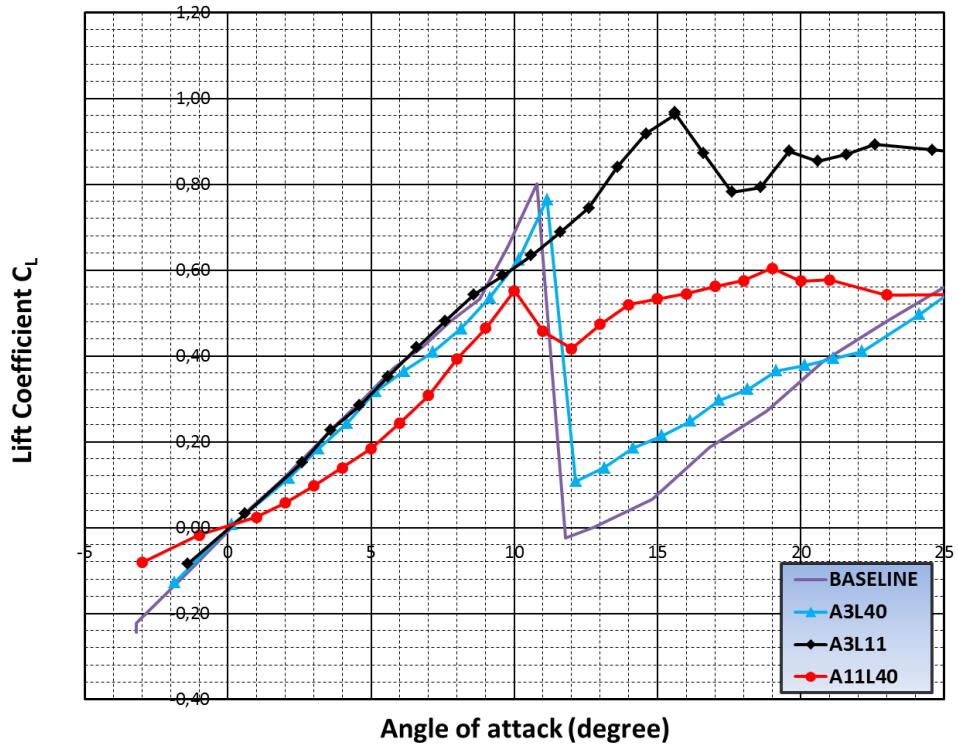

Figure 4.45: Lift curves for the smooth and wavy configurations at Re = 120,000 (NACA 0030 airfoil).

At Reynolds numbers 80,000 the smooth airfoil undergoes greater changes on lift curve (figures 4.46). There is no linearity on lift curve for lower angles of attack where the configuration reaches negative lift values up to α = 10º. After that, the lift coefficient increases with angle of attack, but reaching low values. On the other hand, the configuration A3λ11 remains the typical aerodynamic characteristics of an airfoil for lift performance. The configuration keeps the linearity on lift curve up to stall as on the smooth configuration for higher Reynolds numbers so reaching the highest lift. The configuration A3λ40 follows a behaviour similar to the configuration A3λ11, however, it presents early drop in lift (α = 4°) indicating flow separation condition. The airfoil A11λ40 keeps linearity on lift curve up to higher angles of attack with lower curve slope. Figure 4.47 presents at Re=50,000 an increase in aerodynamic deterioration for configuration A3λ40. In addition, the performance of the configurations A11λ40 and A3λ11 become close.

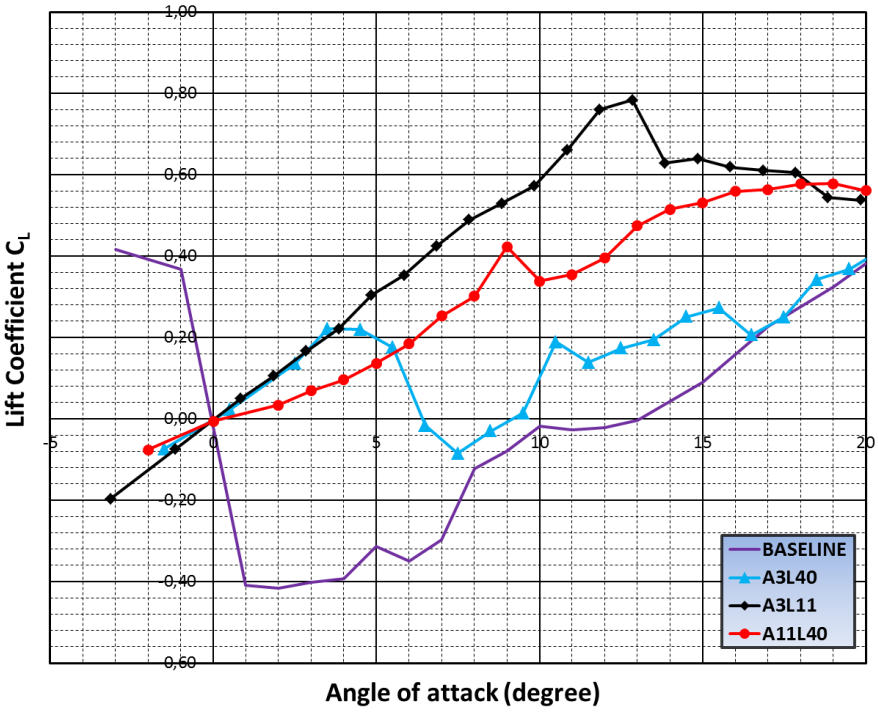

Figure 4.46: Lift curves for the smooth and wavy configurations at Re = 80,000 (NACA 0030 airfoil).

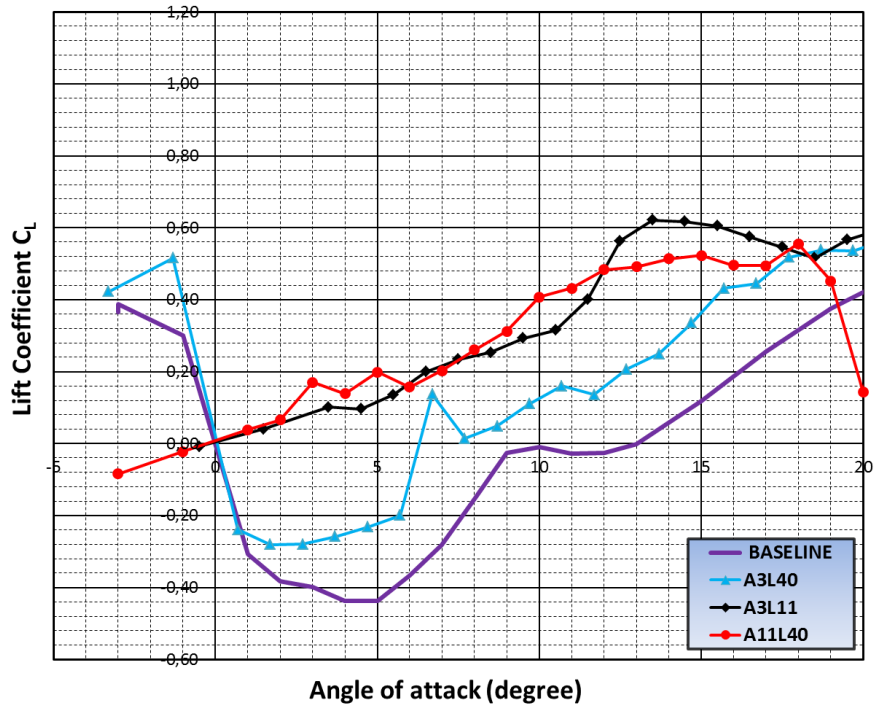

Figure 4.47: Lift curves for the smooth and wavy configurations at Re = 50,000 (NACA 0030 airfoil).

Figure 4.48 shows the tubercle effect in performance in term of maximum lift ($\Delta C_{L_{MAX}} = \frac{C_{L_{MAX\ wavy}} - C_{L_{MAX\ smooth}}}{C_{L_{MAX\ smooth}}}$) where there is a decrease in Reynolds number condition for Re > 200,000. On the other hand, an increase in performance occurs by decreasing Reynolds number for Re < 200,000.

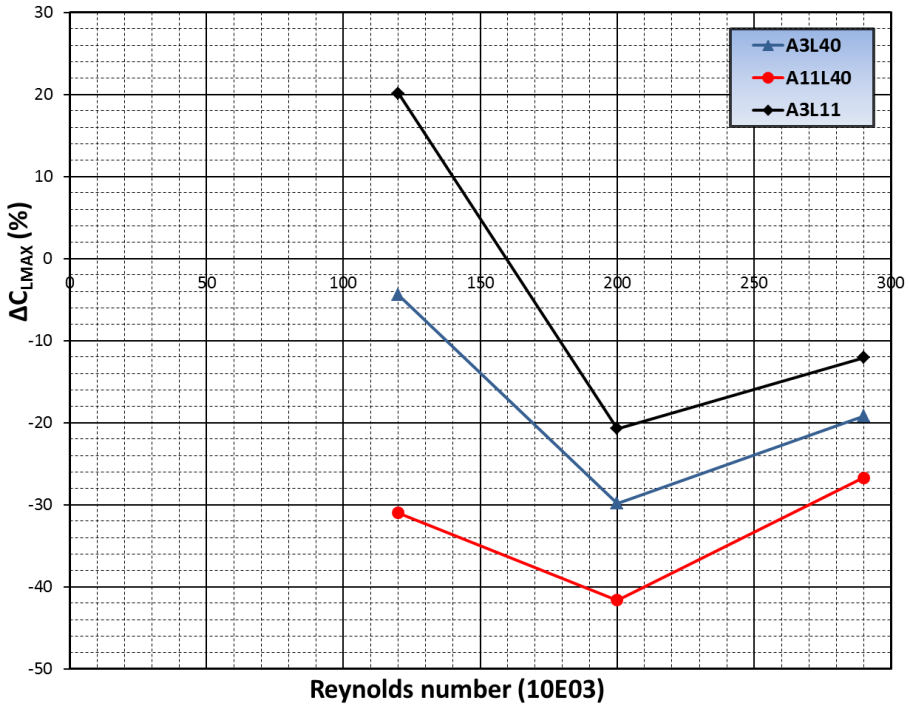

Figure 4.48: Reynolds number effect on maximum lift coefficient for the NACA 0030 airfoil.

For the thickest NACA 0030 airfoil, as on lift curve, the Reynolds number variation causes large changes in terms of drag at the entire Reynolds number range (figures 4.49-52). At Re = 290,000, the configuration A3λ40, as discussed previously, presents lower values than the smooth configuration does at lower angles of attack and the configuration A11λ40 shows an early and expressive increase in drag because of the anticipation on the flow separation onset.

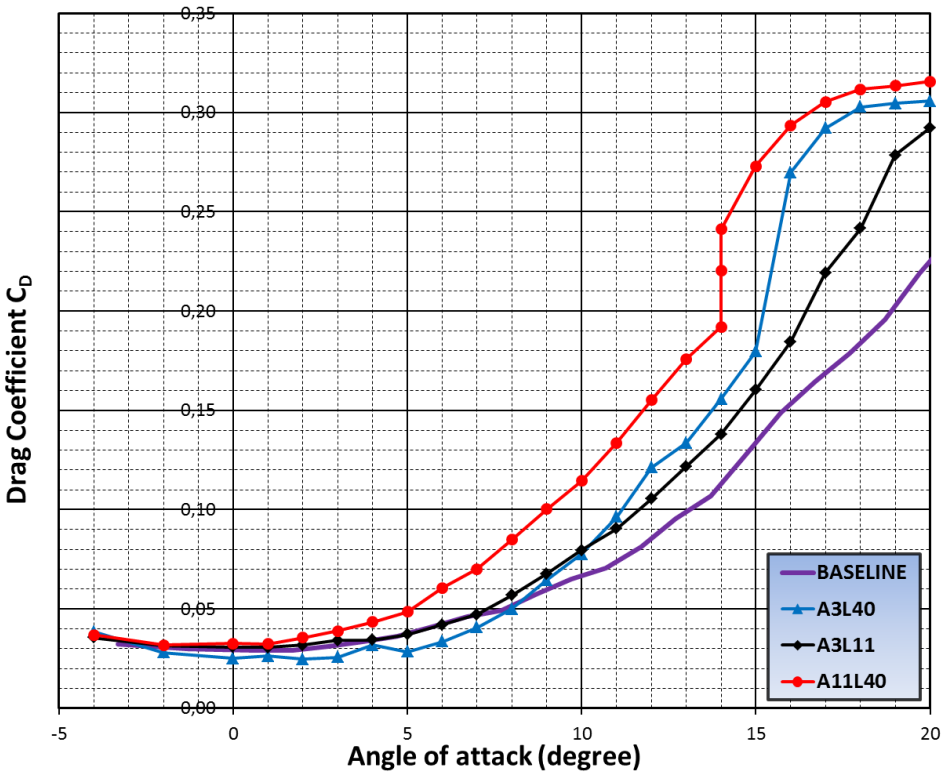

Figure 4.49: Drag curves for the smooth and wavy configurations at Re = 290,000 (NACA 0030 airfoil).

In the case of Reynolds number conditions 200,000 and 120,000, the configuration A3λ11 presents lower drag values when compared to the smooth airfoil at a lower angle of attack whereas the longer wavelength configurations establish higher values. In addition, the configuration A3λ40 undergoes a large increase in drag overcoming the values of the configuration A11λ40 at α = 13º and 10º for Re = 200,000 and 120,000, respectively.

At Reynolds number 80,000, the wavy configurations, following the lift behaviour, undergo great changes in drag performance when compared to smooth configuration. At lower angle of attack, the wavy configuration reaches extraordinary lower drag values. The configuration A3λ11 decreases drag in 800 drag counts when compared to baseline airfoil, and it keeps this difference up to α = 13º. In addition, the wavy configurations A3λ11 and A11λ40 remain with lower drag when compared to the smooth airfoil in the entire range of angle of attack whereas the configuration A3λ40 keeps lower values up to α = 6°.

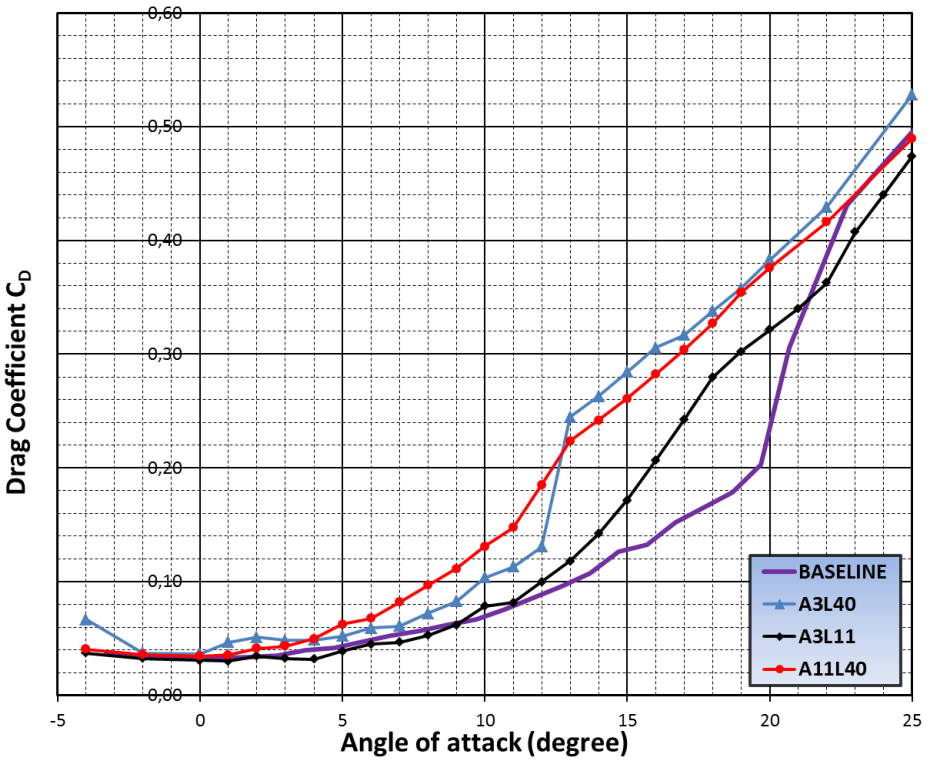

Figure 4.50: Drag curves for the smooth and wavy configurations at Re = 200,000 (NACA 0030 airfoil).

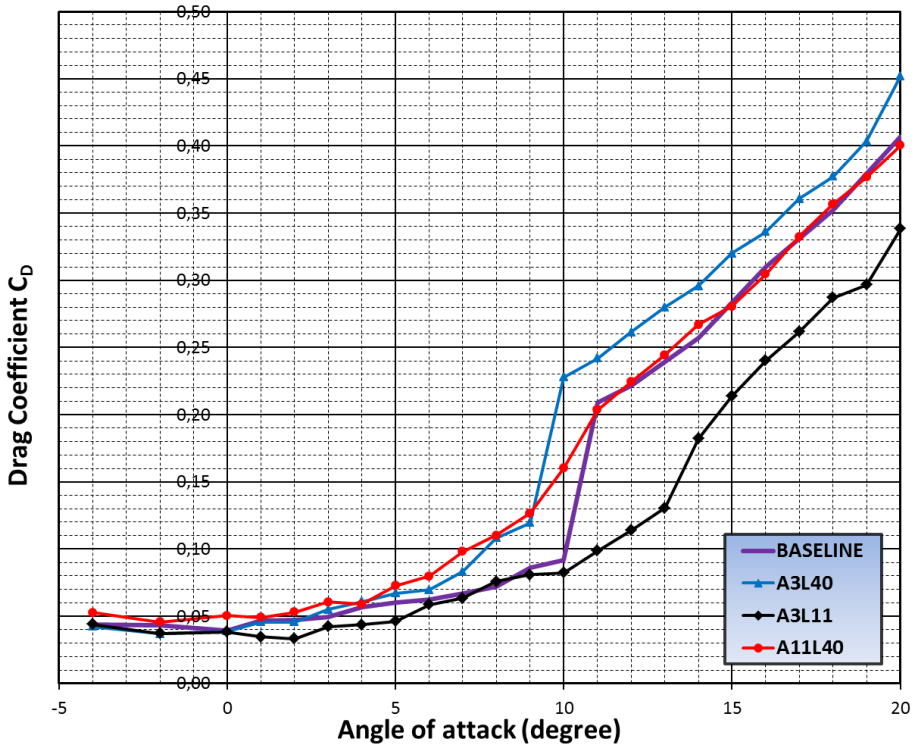

Figure 4.51: Drag curves for the smooth and wavy configurations at Re = 120,000 (NACA 0030 airfoil).

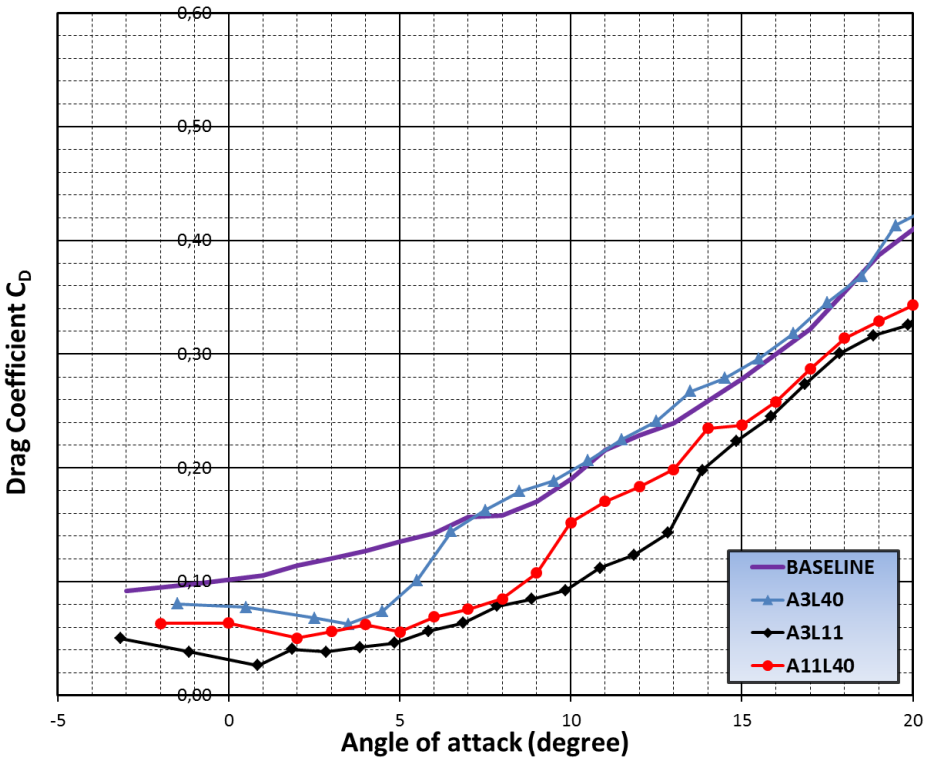

Figure 4.52: Drag curves for the smooth and wavy configurations at Re = 80,000 (NACA 0030 airfoil).

Figures 4.53-55 show the Reynolds number effects on pitching moment curves. For the highest Reynolds number condition (Re=290,000), at lower angles of attack, the wavy configuration keeps similar pitching moment values with a positive curve slope lower of the smooth configuration ($\alpha < 5^o$). After that, the configurations A3λ11 and A3λ40 keep lower values as in those of the smooth airfoil, and the configuration A11λ40 anticipates the change to negative curve slope at the moment plot ($\alpha = 5^o$). The configurations A3λ11 and A3λ40 changes the moment curve slope at a similar angle of attack ($\sim \alpha = 10^o$) later than in greater amplitude configurations, but still earlier than the smooth airfoil.

At lower Reynolds number (Re= 200,000 and 120,000), the wavy leading edge performance is similar to Re = 290,000. However, the configurations A3λ40 and A3λ11 show pitching moment values lower than the smooth airfoil does since lower angles of attack. In addition, a decrease in Reynolds number anticipates the appearance of a negative curve slope for the configuration A11λ40.

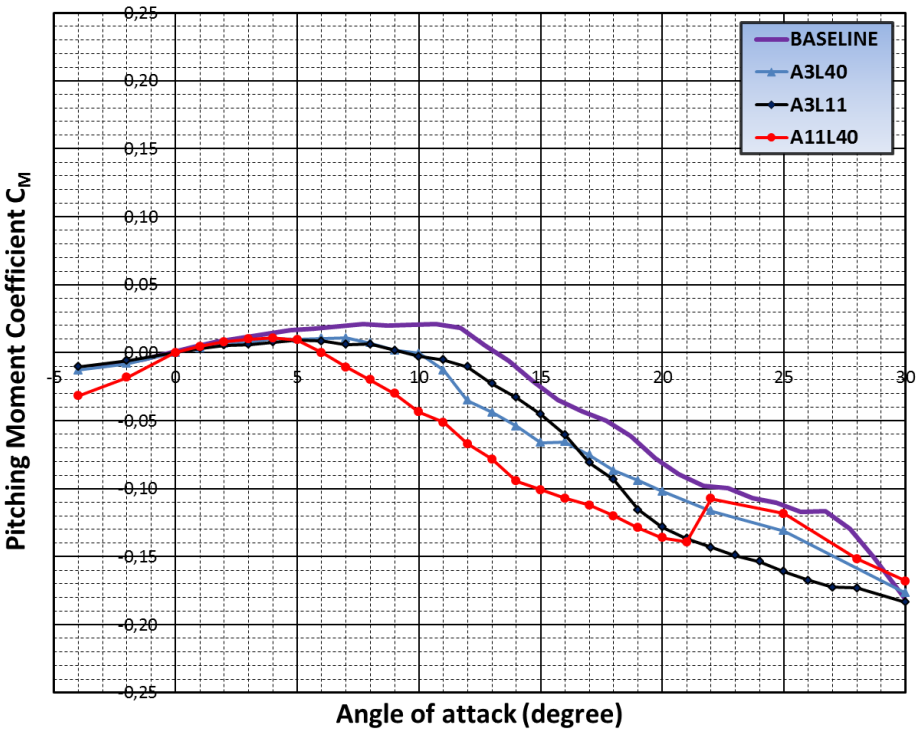

Figure 4.53: Pitching moment curves for the smooth and wavy configurations at Re = 290,000 (NACA 0030 airfoil).

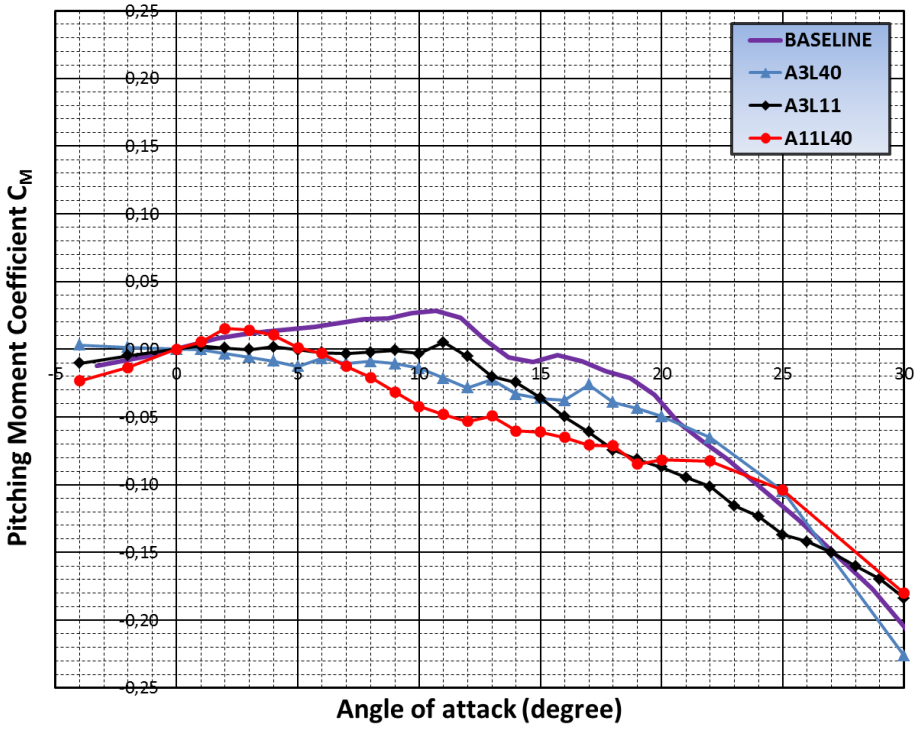

Figure 4.54 : Pitching moment curves for the smooth and wavy configurations at Re = 200,000 (NACA 0030 airfoil).

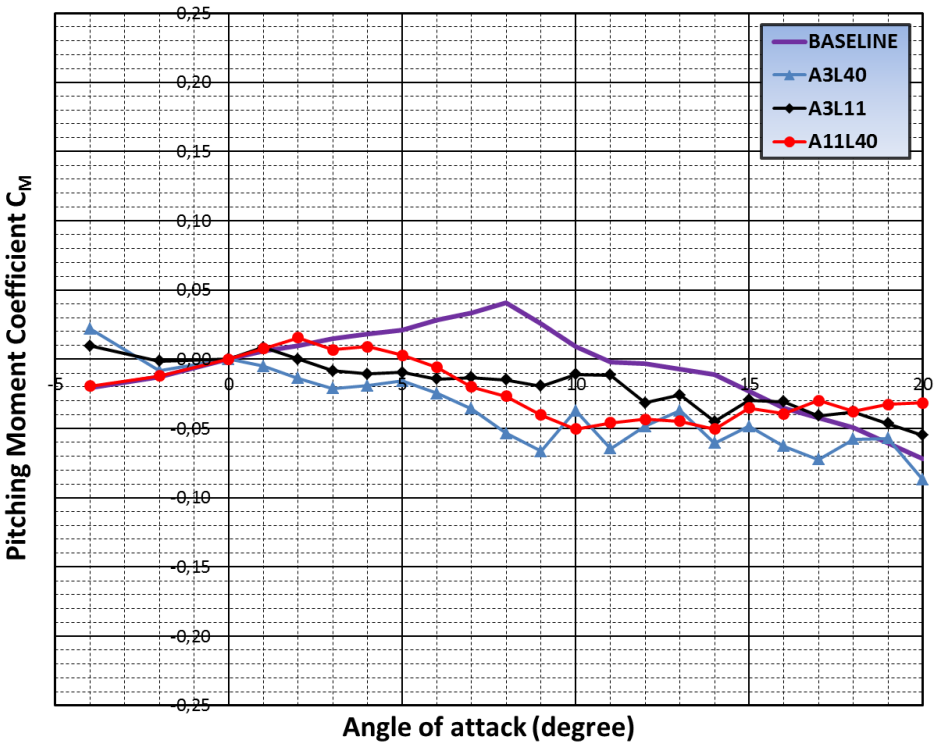

Figure 4.55: Pitching moment curves for the smooth and wavy configurations at Re = 120,000 (NACA 0030 airfoil).

4.5 Summary and discussions

The increase in thickness for the smooth airfoils, as shown in this work, causes distinct changes on flow characteristics over the airfoil surface for different flow conditions. Figure 4.56 shows the airfoil thickness effects on lift curve at Reynolds number 290,000. The thinnest NACA 0012 airfoil follows the theoretical curve up to α = 3º. The lift curve slope increases when compared to the theoretical curve up to α = 5º. After that, a linear segment starts with the same slope as the first segment. At angle of attack = 10°, a short asymptotic curve follows up to stall. For the thicker NACA 0020 airfoil it is also observed four distinct lift curve segment. However, the first one has lower slope than the theoretical curve, differently from NACA 0012. Furthermore, the second one has a little increase in curve slope

when compared to the theoretical curve. The third straight line segment maintains the theoretical curve slope. At angle of attack = 10°, a long asymptotic curve follows up to stall. The thickest NACA 0030 airfoil has similar lift performance than that of NACA 0020. However, after the highest slope curve, a very long asymptotic curve that goes to stall condition appears.

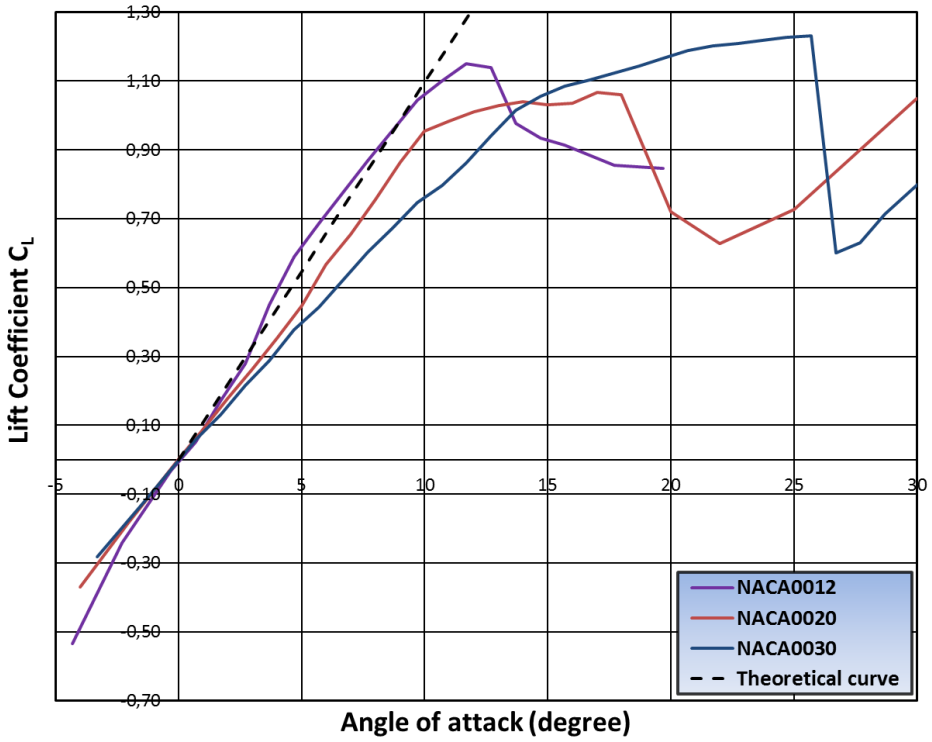

Figure 4.56: Thickness effects on lift curve performance at Re= 290,000.

As consequence of the thickness effects on lift curve at Reynolds number 290,000, it is clear that some distinct aerodynamic characteristics appear at pre-stall regime driving the maximum lift coefficient values. For thinner airfoils, the increase in lift curve slope at pre-stall regime establishes a high maximum lift value tendency. On the other hand, the airfoil does not resist to higher stall angle of attack indicating leading edge full flow separation. In the case of the thick airfoils, the airfoil does not undergo a substantial increase in lift curve slope, however, it resists without full flow separation up to higher angles of attack having a significant decrease in lift curve slope near to stall indicating trailing edge flow separation.

Although the thickness effects causes similar modifications on airfoil lift performance at higher Reynolds number (Re > 100,000), the large change on lift performance occurs at lower Reynolds number (Re < 100,000) as shown in figure 4.57. The NACA 0020 airfoil keeps the lift curve slope higher than NACA 0012 airfoil. However, the thicker airfoil reaches a lower stall angle and maximum lift coefficient than NACA 0012 airfoil. The thickest NACA 0030 airfoil undergoes a massive aerodynamic deterioration achieving negative lift values in almost the entire range of angle of attack.

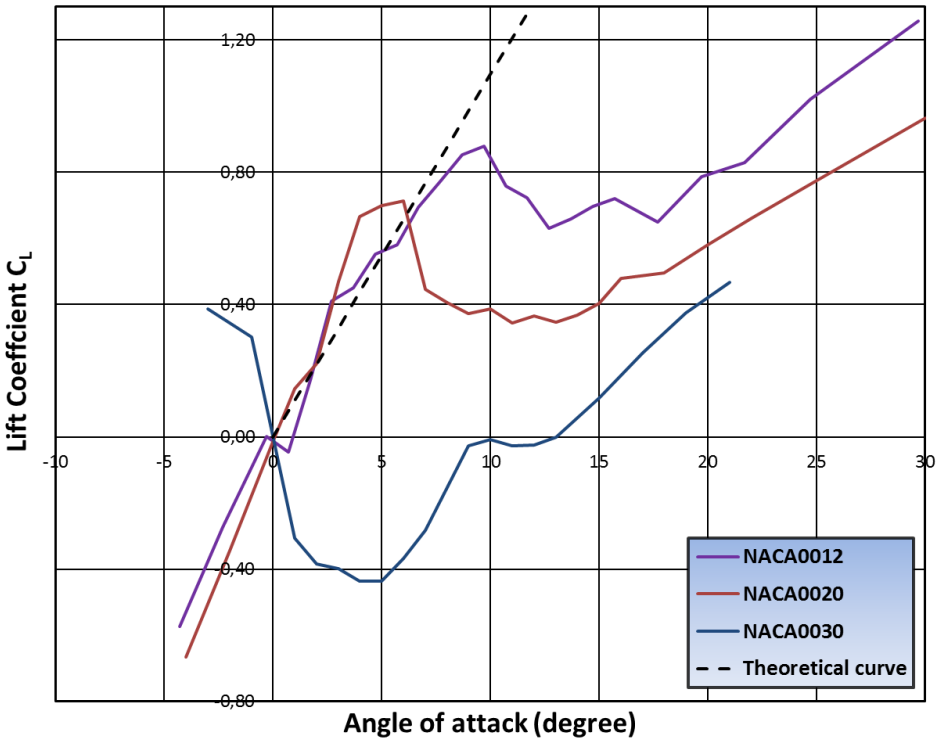

Figure 4.57: Thickness effects on lift curve performance at Re= 50,000.

Figure 4.58 shows the thickness effect on maximum lift coefficient at low Reynolds number regime between Reynolds number 50,000 and 290,000. The maximum lift coefficient increases for all airfoil thicknesses with increasing Reynolds number. The thickness effect establishes different characteristics depending on Reynolds number condition. At lower Reynolds numbers, thinner airfoils reaches higher maximum lift values. In contrast, at higher Reynolds number, the thickest airfoil reaches the greater maximum lift coefficient. The characteristics presented in figure 4.58 indicate that the airfoil design of MAV and UAV depends on the Reynolds number of the design point.

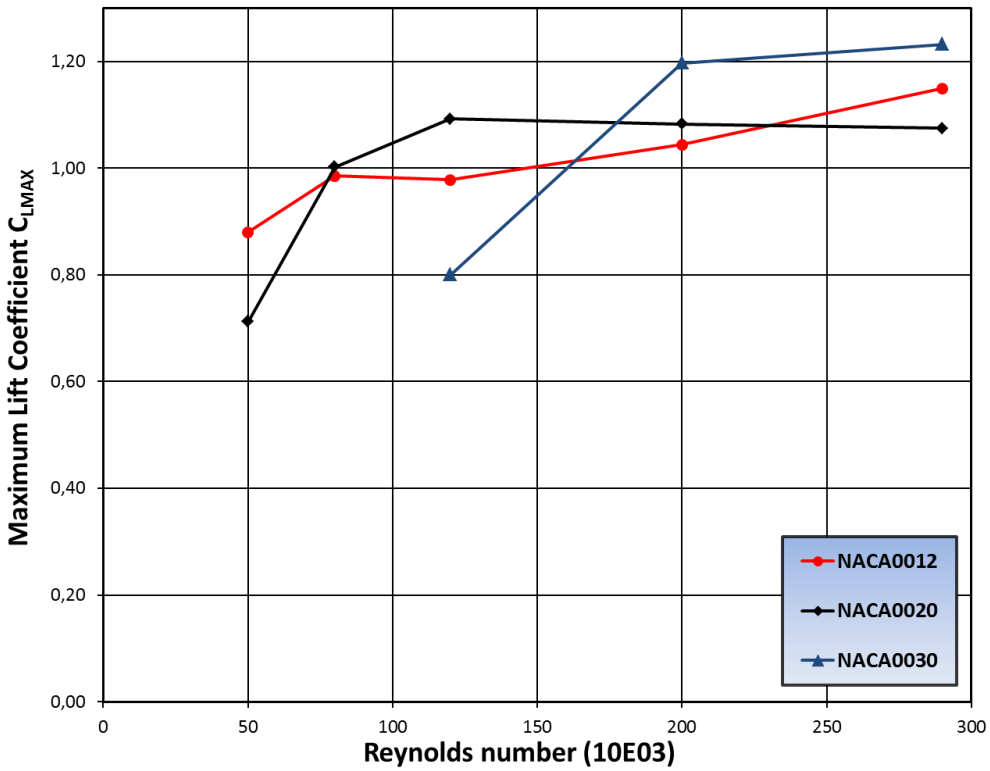

Figure 4.58: Thickness effect on maximum lift coefficient at low Reynolds number.

The drag characteristics (figures 4.2, 4.20 and 4.38) are affected by the thickness effect in increasing the drag coefficient at zero lift with increasing thickness. In addition, the thicker airfoils increase the extent of the drag bucket and delay the stall behaviour avoiding an early large increase in drag values.

In terms of pitching moment coefficient, the thin NACA 0012 airfoil follows with close to null values up to the stall angle as consequence of its symmetrical condition and aerodynamic center at 25% of M.A.C. With increasing thickness, the supposition of the aerodynamic center at 25% of M.A.C is no longer valid. Thus, the pitching moment increases with angle of attack as a result of the movement towards the leading edge of the pressure center. At stall angle, for all airfoil thicknesses, the full flow separation condition moves the pressure center towards the trailing edge causing an abrupt decrease in pitching moment. The Reynolds number effects cause changes on pre-stall characteristics of the pitching moment. The increase in lift curve slope, at pre-stall regime, decreases the moment curve slope. The decrease in Reynolds number anticipates changes in lift curve slope affecting the pitch

moment characteristics at pre-stall. In addition, a decrease in Reynolds number anticipates the large decrease in moment coefficient caused by stall condition.

As for the aerodynamic performance of the smooth airfoils, the wavy leading edge performance shows distinct results, at pre-stall regime, for the thin NACA 0012 airfoil and thick airfoils (NACA 0020 and NACA 0030).

At higher Reynolds number (Re > 100,000), the wavy thin NACA 0012, at pre-stall, presents lift curves very close to the smooth airfoil, except for configuration A11λ40. In contrast, the thicker airfoils NACA 0020 and NACA 0030 undergo a greater aerodynamic deterioration on lift curve up to stall where the thickest airfoil presents the highest decrease in performance for wavy configurations.

Figure 4.59 presents, in terms of maximum lift coefficient, at Reynolds number higher than 100,000, aerodynamic deterioration caused by the wavy leading edge. The wavy configurations reach lower values than the smooth airfoil except at Re = 120,000 for specific configuration A3λ11. As consequence of the thickness effects on wavy leading edge performance at pre-stall conditions, the aerodynamic deterioration in maximum lift coefficient, caused by wavy leading edge airfoils, increases with increasing in airfoil thickness. In addition, the wavy thinnest airfoil establishes the stall angle close to baseline configuration. On the other hand, thicker airfoils have significant decrease in stall angle for wavy configurations.

Figure 4.60 also clearly shows for the NACA 0020 airfoil an increase in maximum lift reduction caused by wavy leading edge with decreasing of the Reynolds number condition. In addition, it can be seen, at Re > 100,000, that the effect of the wavy leading edge geometry is not sensitive to changes in thickness where the configuration A3λ11 establishes the best performance, whereas the A11λ40 remains the worst among all airfoil thicknesses.

At post-stall regime, the thin airfoil presents soft stall behaviour for all wavy leading edge configurations in contrast with abrupt stall for baseline airfoil. The thicker airfoils show similar wavy leading edge effect at post-stall regime but for configuration A3λ40 it keeps abrupt stall behaviour. In addition, the wavy leading edge thick airfoils have more benefits in terms of keeping high lift values at post-stall regime because the lift drop for thick smooth configuration is higher than for thin airfoils (tables 4.1, 4.2 and 4.3).

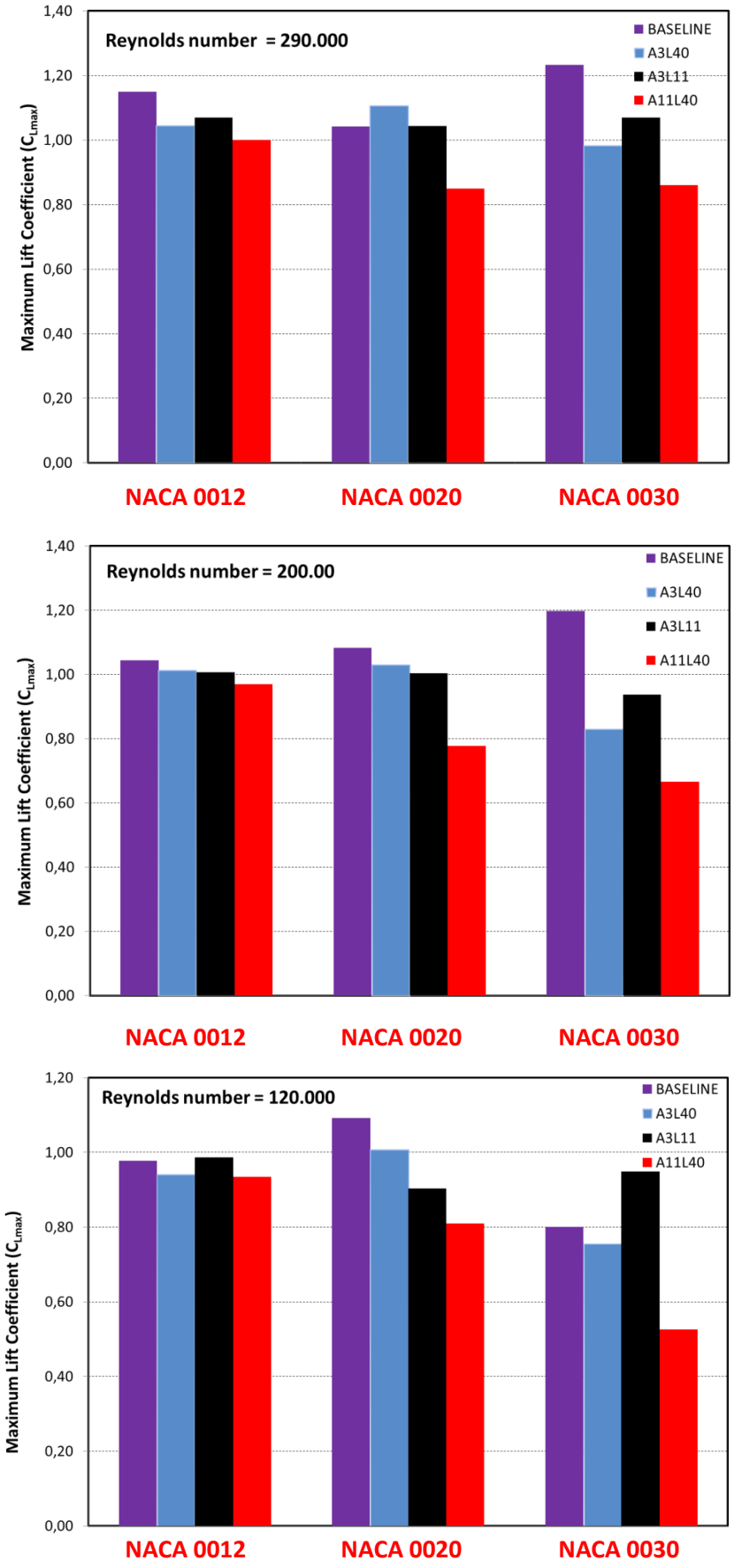

Figure 4.59: Thickness effect on maximum lift coefficient (Re > 100,000).

At lower Reynolds numbers (Re < 100,000), for different airfoil thicknesses, in contrast with higher Reynolds number conditions, there is no significant changes on wavy leading edge performance at pre-stall conditions. In addition, there is a minimum aerodynamic deterioration in terms of maximum lift coefficient with an increase in some cases.

Figure 4.60 shows the maximum lift values for wavy and smooth configurations in the case of airfoils NACA 0012 and NACA 0020. At Reynolds number 80,000 the wavy airfoils show decrease in maximum lift values with lower reduction for the thinner NACA 0012 airfoil. In contrast, at Re = 50,000, the wavy airfoils increase the maximum lift values reaching better performance with higher increase for the thicker NACA 0020 airfoil.

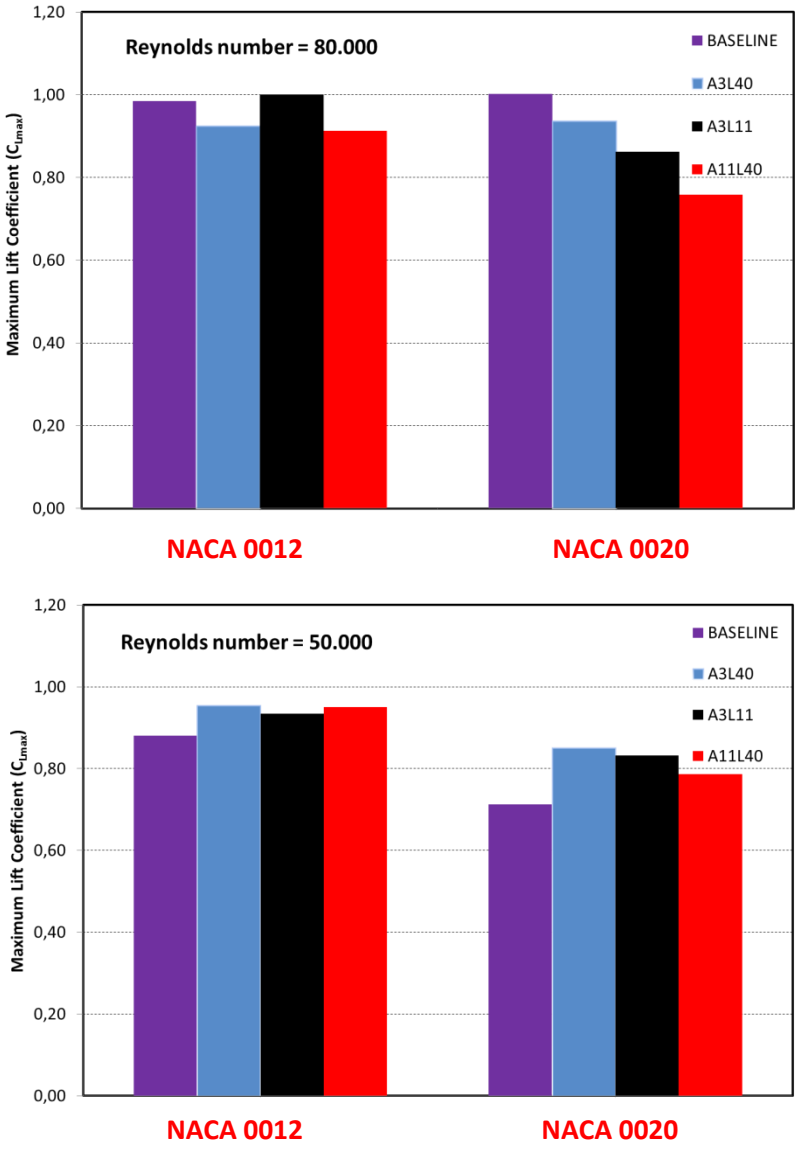

Figure 4.60: Thickness effect on maximum lift coefficient (Re < 100,000).

At Reynolds numbers below 100,000, the wavy thickest NACA 0030 airfoil (figures 4.45-47) presents the greatest and most impressive improvement in aerodynamic performance. Even at Reynolds numbers higher than 100,000 (Re = 120,000) an improvement occurs in maximum lift coefficient for the specific wavy leading configuration A3λ11. At this Reynolds number regime, the smooth configuration undergoes an expressive aerodynamic deterioration. The baseline airfoil presents non-linearity since lower angle of attack range, starting with negative lift coefficient and reaching low values at high angles of attack. There are no maximum lift values for all configurations of the NACA 0030 except for configuration A3λ11 it keeps a classical lift curve shape with the greatest performance. Thus, the thickest NACA 0030 shows, at the lowest Reynolds number condition, the highest wavy leading edge performance for airfoils and flow conditions tested in this work.

In terms of drag values, in general, the wavy leading edge configurations increase drag coefficient values at lower angles of attack when compared to baseline airfoil. In addition, the wavy airfoils anticipate the stall condition and consequently the large increase in drag at a high angle of attack where the configuration A11λ40 presents the earliest raise in drag values. Furthermore, the wavy airfoils in some specific cases show a decrease in drag compared to baseline configuration, as for configuration A3λ40 and A3λ11 with NACA 0020 airfoil and Re = 290,000. Moreover, a large decrease in drag in the entire angle of attack range occurs for NACA 0030 airfoil at Reynolds numbers below 100,000.

Regarding pitching moment coefficient values, at low angles of attack, the wavy leading edge configurations cause a decrease in the curve slope reaching lower moment values than the smooth configuration. Furthermore, the wavy configurations anticipate the stall onset, thus undergoing earlier significant decrease in pitching moment values. The configuration A11λ40 establishes the earliest large decrease in moment coefficient and, in most cases, keeps the lowest moment values in the entire angle of attack range.

The discussions regarding aerodynamic performance presented here continue in the next chapters 5 and 6 in order to explain the results found based on topology analyses.

5 FLOW TOPOLOGY

Flow topology analysis is a very important part of this work. This chapter presents, based on mini-tufts and oil visualization and correlating with force measurements, general flow characteristics of the wavy leading edge airfoils of distinct airfoil thicknesses at different flow conditions.

The experimental tests were carried out for full span models in the wind tunnel section. Although the endplates eliminate the boundary layer effects caused by wind tunnel sidewalls, still the endplates cause three-dimensional effects on flow topology over the airfoil's upper surface due to the interaction between the boundary layers of the endplates and the models. However, this effect is not discussed in the analysis of results due to the main aim of this work being in the understanding of the wavy leading edge effects on airfoil aerodynamic performance. The evaluation of the configurations is therefore focused on relative analyses. Since all visualizations were performed with the test section ceiling window removed, the results are qualitatively comparable.

In steady conditions of angles of attack, photographs of flow visualizations were taken in order to document the main changes in the flow over the airfoils caused by wavy leading edges across a large range of angles of attack spanning pre-stall and post-stall regimes. The sets of angles of attack were chosen based on changes caused in lift curves due to tubercles.

The tests were carried out at Reynolds number 290,000 and 50,000 since the force measurement showed significant changes on tubercle performance below Re= 100,000 when compared to the highest Reynolds number tested (Re=290,000).

In order to reach a clear understanding of the wavy leading edge phenomena based on mini-tuft flow visualizations, video recordings were performed in order to evaluate the dynamics of flow phenomena over the airfoils' upper surfaces. These recordings were carried out in angle of attack sweeps from $\alpha = 0°$ to 30°.

The figures in this chapter show static characteristics of the flow over airfoil surfaces at fixed angles of attack; the set of photographs (i.e. static conditions) and filming (dynamic conditions) that provide the basis for the following flow topology descriptions.

5.1 Mini-tuft visualization

5.1.1 Wavy leading edge effect on NACA 0012 airfoil at Re = 290,000

For the thinnest airfoil – the NACA 0012 – in mini-tuft flow visualizations at an angle of attack of 0° (figure 5.1), show identical flow topology for all configurations presenting mini-tufts fully aligned and attached to the airfoil's upper surface, indicating an absence of any flow separation.

Increasing the angle of attack to 5°, figure 5.2 shows that all configurations still present similar flow characteristics, with the flow fully attached over the whole upper surface. The flow topology similarity for all configurations justifies similar lift performance up to $\alpha = 5^{o}$ for smooth and wavy airfoils (figure 4.4).

At an angle of attack of 10°, the flow over almost the entire airfoil upper surface remains attached for configurations smooth (fig. 5.3a) and A3λ40 (fig. 5.3b). The flow visualizations show a very small trailing edge flow separation for smooth and wavy configurations.

Configuration A11λ40 (fig. 5.3c) shows detached flow characteristics at the leading edge as indicated by misaligned mini-tufts at troughs. On the other hand, the mini-tufts behind peaks remain aligned characterizing attached flow in this region.

Configuration A3λ11 (fig.5.3d) presents similar flow characteristics to configuration A11λ40 at the leading edge. The configuration shows a misalignment in the mini-tufts between peaks, bending towards troughs and indicating flow separation in this location.

The flow characteristics presented by mini-tufts at the leading edge, including a small perturbation downstream from the leading edge, indicate possible vortex structure present at leading edge for configurations A3λ11 and A11λ40.

Figure 5.4 shows clearly, at angle of attack 12°, that the wavy leading edge anticipates the full flow separation at the airfoil leading edge (stall condition). The smooth configuration keeps the flow attached over almost the entire airfoil surface, presenting trailing edge flow separation at 22% of the chord whereas the wavy configurations undergo flow separation in almost entire airfoil upper surface reaching stall condition onset.

The wavy configurations present a separation cell centered at middle-span achieving the leading edge. In addition, configuration A3λ40 (fig.5.4b) preserves attached flow over almost the whole leading edge span. Both configurations A3λ11 (fig.5.4d) and A11λ40 (fig.5.4c) remain flow attached at the leading edge downstream of the peaks as indicated by the always aligned mini-tufts. However, the smaller amplitude configuration keeps a larger area with attached flow downstream of the leading edge, similar to configuration A3λ40.

At an angle of attack of 15° (figure 5.5), configurations baseline (fig.5.5a) and A3λ40 (fig.5.5b) present flow separation over entire airfoil surface whereas configurations A3λ11 (fig.5.4d) and A11λ40 (fig.5.4c) maintain the flow attached downstream of the tubercle peaks so presenting softer stall behaviour as compared to configuration A3λ40 (figure 4.4).

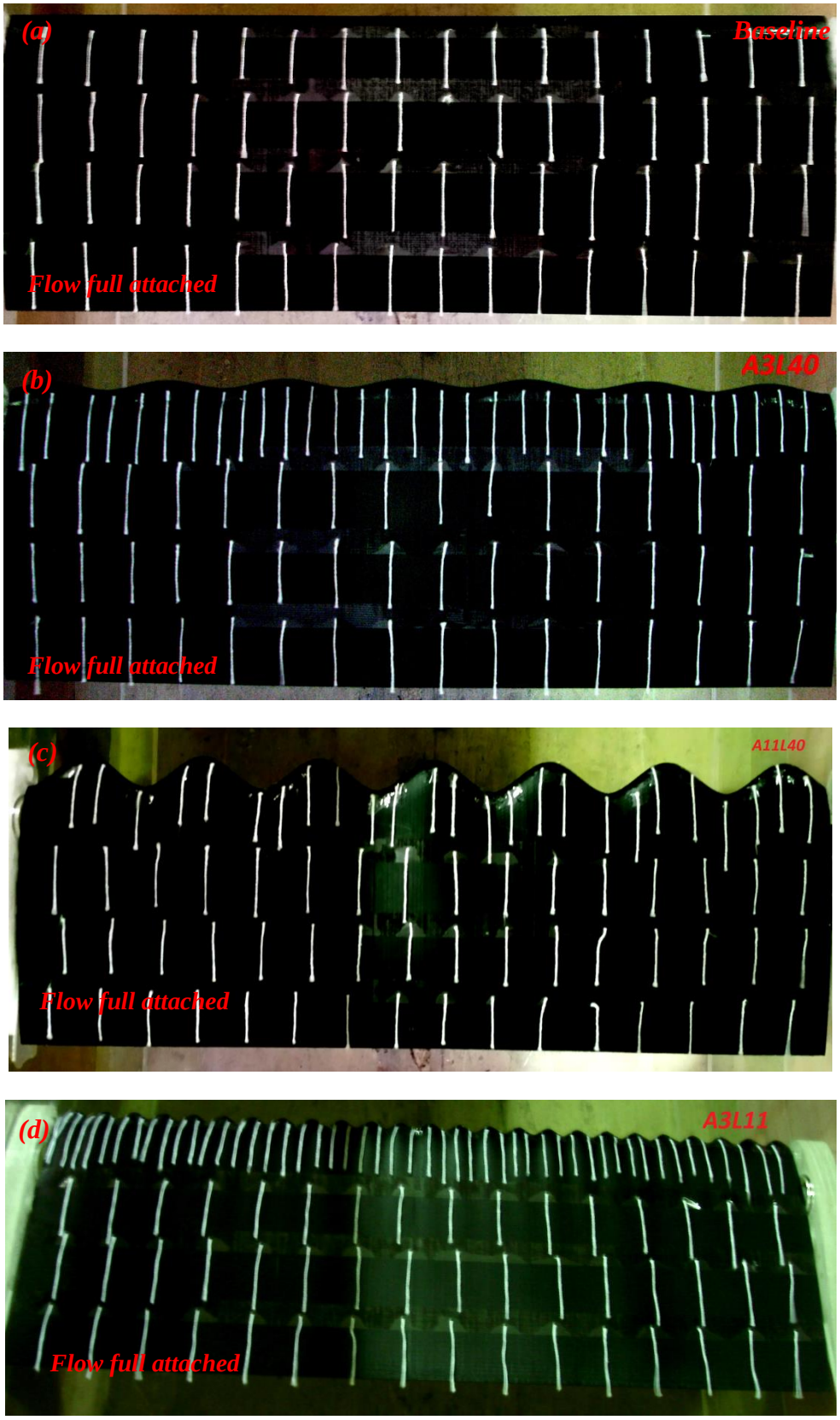

Figure 5.1: All configurations at α =0°and Re = 290,000 (NACA 0012).

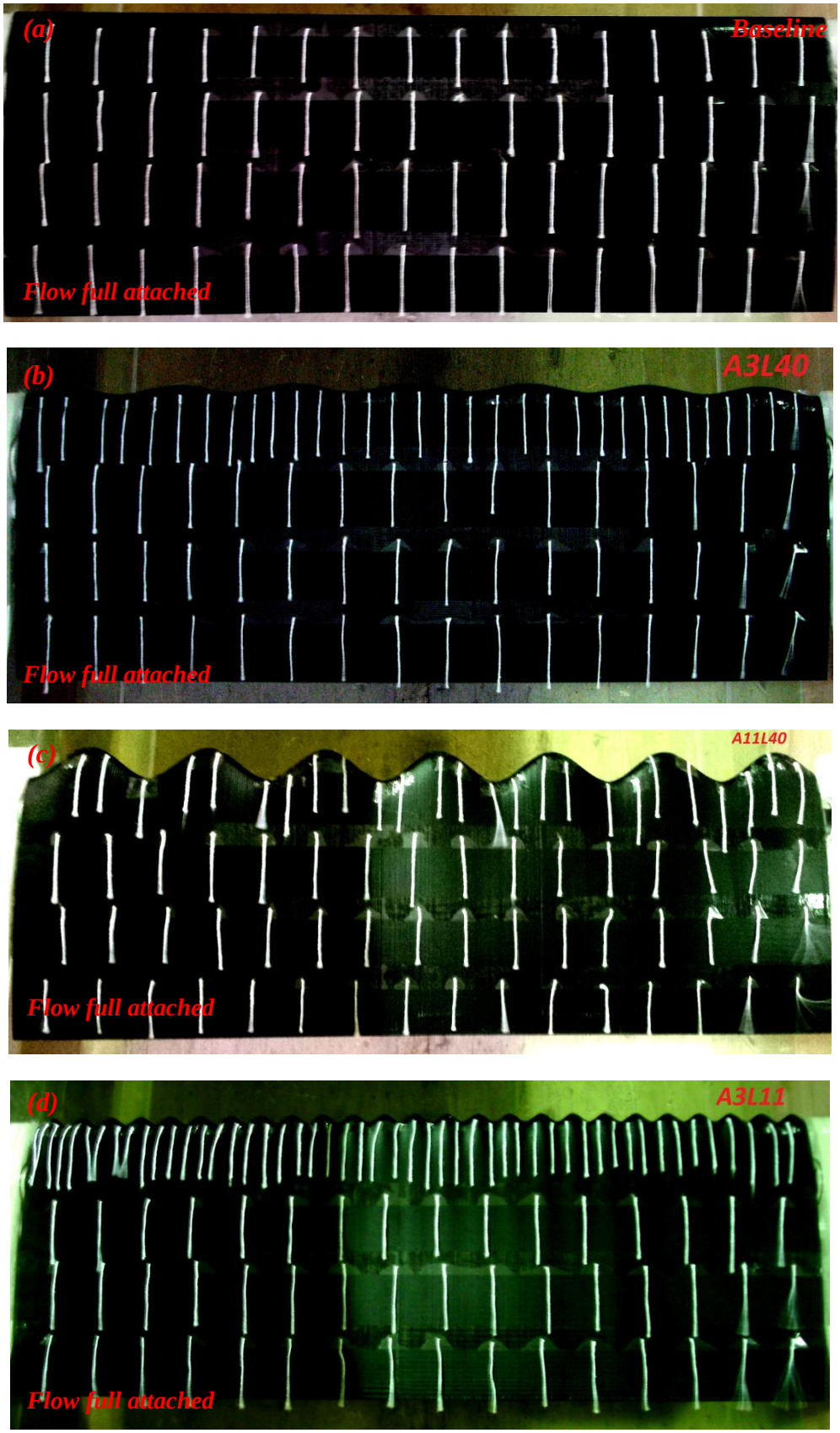

Figure 5.2: All configurations at α = 5°and Re = 290,000 (NACA 0012).

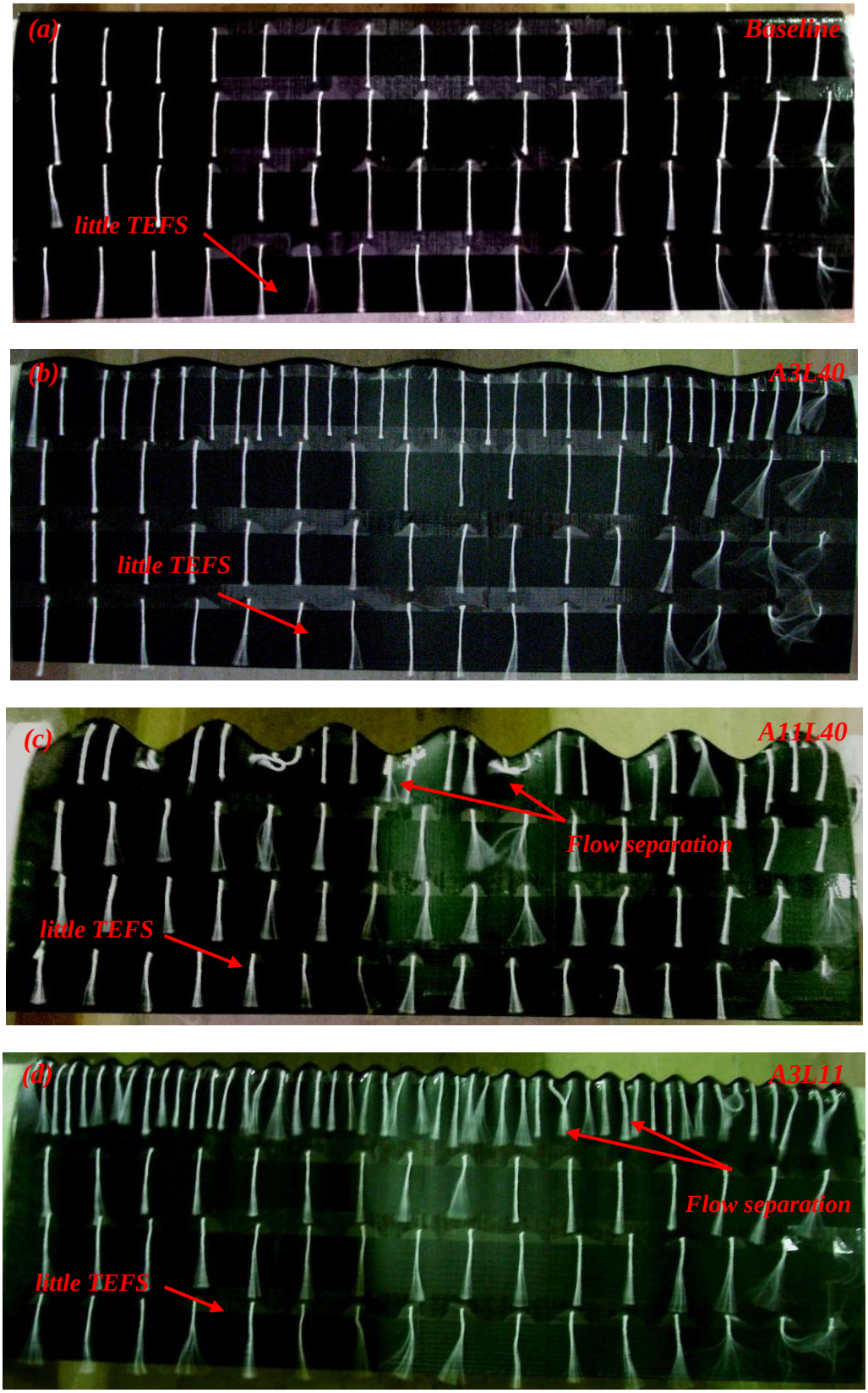

Figure 5.3: All configurations at α = 10°and Re = 290,000 (NACA 0012).

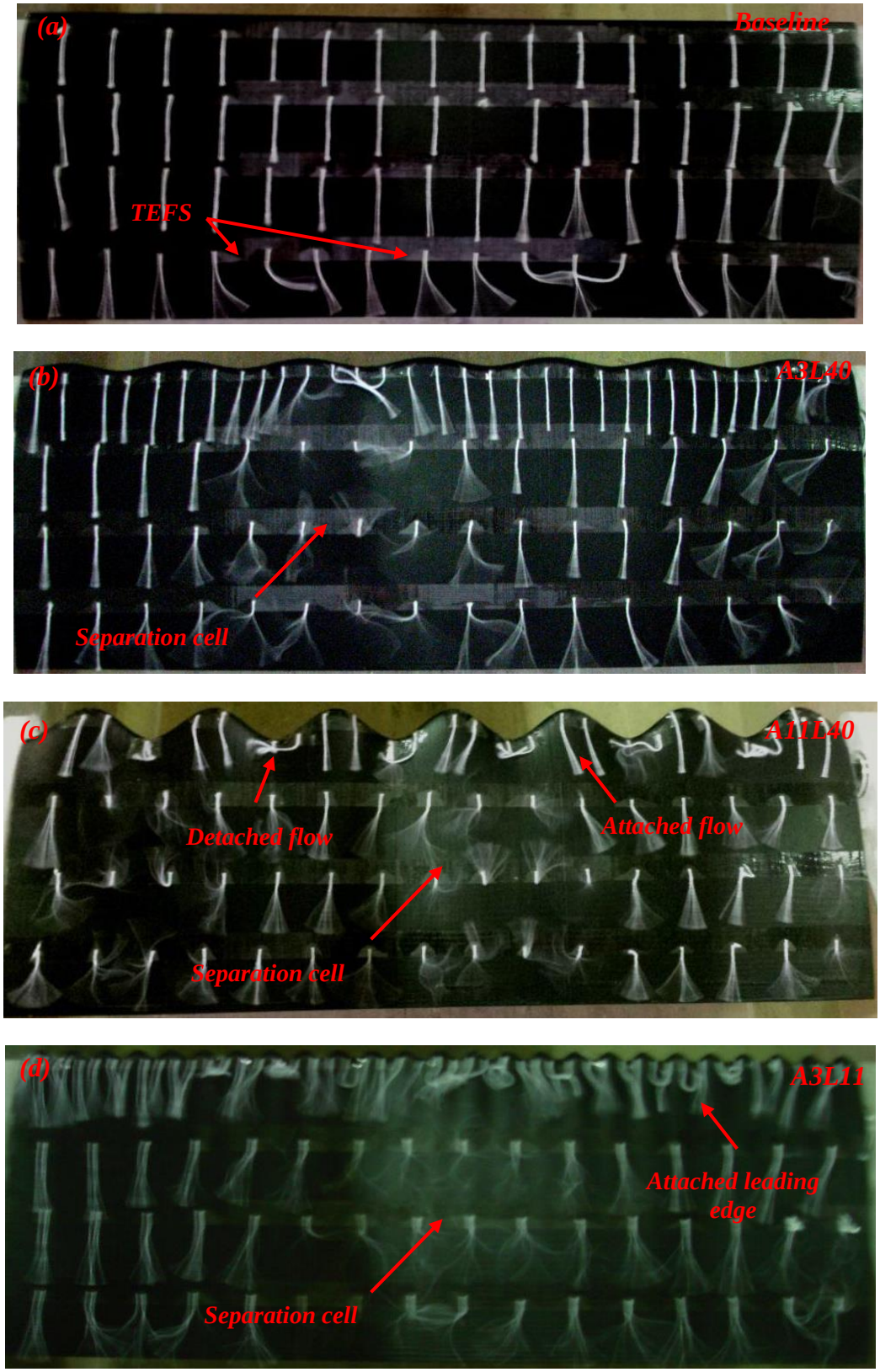

Figure 5.4: All configurations at α = 12°and Re = 290,000 (NACA 0012).

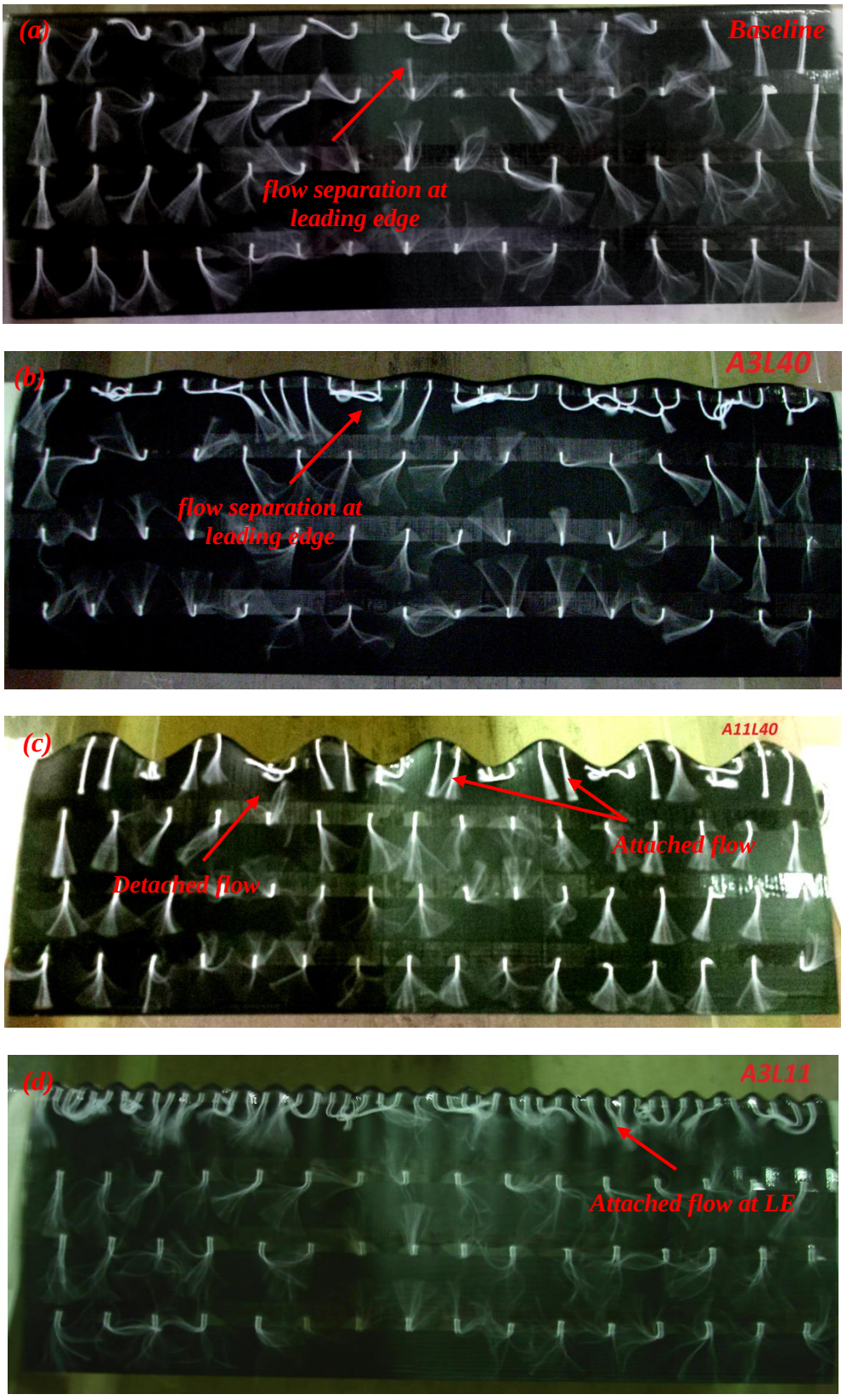

Figure 5.5: All configurations at α = 15°and Re = 290,000 (NACA 0012).

5.1.2 Wavy leading edge effect on NACA 0020 airfoil at Re = 290,000

Figure 5.6 shows that at an angle of attack of 0°, the NACA 0020 airfoil presents similar flow characteristics to the thinner NACA 0012 airfoil where for smooth and wavy configurations, the flow is fully attached over the entire airfoil upper surface, and this flow behaviour is maintained at increased angles of attack, guaranteeing similar characteristics on the lift curves for all configurations up to $\alpha = 6°$ (figure 4.22).

At an angle of attack of 7°, the smooth configuration (fig.5.7a) maintains the flow attached over the entire airfoil upper surface. In contrast, for wavy airfoils, the mini-tufts located at the trailing edges indicate the onset of flow separation at this location. In addition, the mini-tufts at the trailing edge are not aligned downstream from tubercle troughs for configurations A11λ40 (fig.5.7c) and A3λ40 (fig.5.7b), indicating that flow separation starts downstream of the tubercle troughs. In contrast, configuration A3λ11 presents trailing edge flow separation downstream of the tubercle peaks.

Thus, the wavy configurations anticipate the trailing edge flow separation for the NACA 0020 airfoil at higher angles of attack in different ways where earlier flow separation occurs downstream of the tubercle troughs and peaks respectively for longer and shorter tubercle wavelengths. The earlier trailing edge flow separation at troughs caused by the wavy leading edge at the pre-stall regime was shown by Custodio (2007) for a thick NACA 63_4-021 airfoil. The flow characteristics of wavy leading edge justify the values of the lift curve for configurations A11λ40 and A3λ11 being lower than for the smooth airfoil (figure 4.22).

The anticipation of the trailing edge flow separation caused by the wavy leading edge at $\alpha = 7°$ increases for $\alpha = 10º$. The flow separation at the trailing edge for the baseline airfoil reaches 10% of the chord (fig.5.8a). Moreover, the larger amplitude configuration causes trailing edge flow separation over 30% of the chord (figure 5.8c). On the other hand, configuration A3λ40 (fig.5.8b) has the least effect of the wavy leading edge on trailing edge flow separation. The large aerodynamic deterioration of the lift curve (figure 4.22) for configurations A11λ40 (fig.5.8c) and A3λ11 (fig.5.8d) agrees with the flow separation area observed on mini-tuft visualizations.

At an angle of attack of 15º (figure 5.9), the smooth configuration (fig.5.9a) reaches trailing edge flow separation at 45% of chord over the entire span, accompanied by a

separation cell centered in the middle-span achieving 65% of chord. Besides, the wavy leading configuration undergoes a greater aerodynamic deterioration with a separation cell covering a vast area. Configuration A11λ40 (fig.5.8c) presents the worst aerodynamic deterioration with the largest area of separated flow.

At an angle of attack of 20º for the baseline airfoil (fig.5.10a), the flow separation reaches almost the entire leading edge, characterizing the onset of the post-stall regime. In contrast, configuration A3λ40 (fig.5.10b) does not undergo a complete flow separation but rather the separation cell is raised up to the leading edge. This characteristic agrees with a smaller drop in lift at the stall angle for configuration A3λ40 when compared to the smooth airfoil (figure 4.22).

Despite the fact that configuration A11λ40 (fig.5.10c) at $\alpha = 20^\circ$ presents great flow separation areas, the mini-tufts aligned at leading edge areas indicate attached flow behind wavy leading edge peaks, keeping similar lift values when compared to flow condition at $\alpha = 15^\circ$ (figure 4.22). As consequence of this behaviour, the configuration establishes soft stall characteristics in the post-stall regime.

The leading edge flow characteristics indicate possible vortex structures in this region as observed for the NACA 0012 airfoil at a lower angle of attack (α =10º). Configuration A3λ11 (fig.5.10d) keeps attached flow over the entire leading edge, which is consistent with the highest lift values reached in the post-stall regime and its soft stall characteristics (figure 4.22).

Figure 5.6: All configurations at α = 0°and Re = 290,000 (NACA 0020).

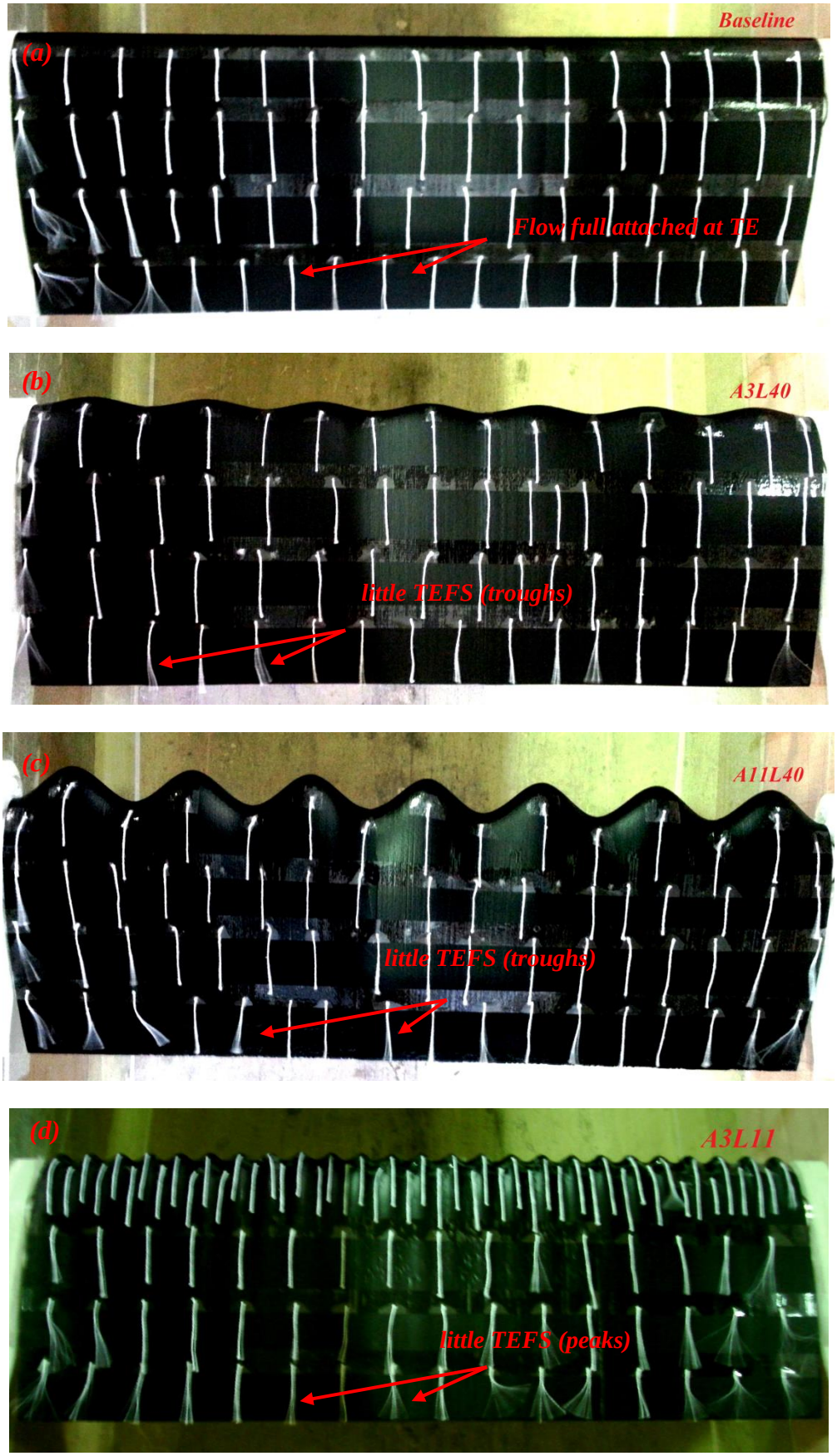

Figure 5.7: All configurations at α = 7°and Re = 290,000 (NACA 0020).

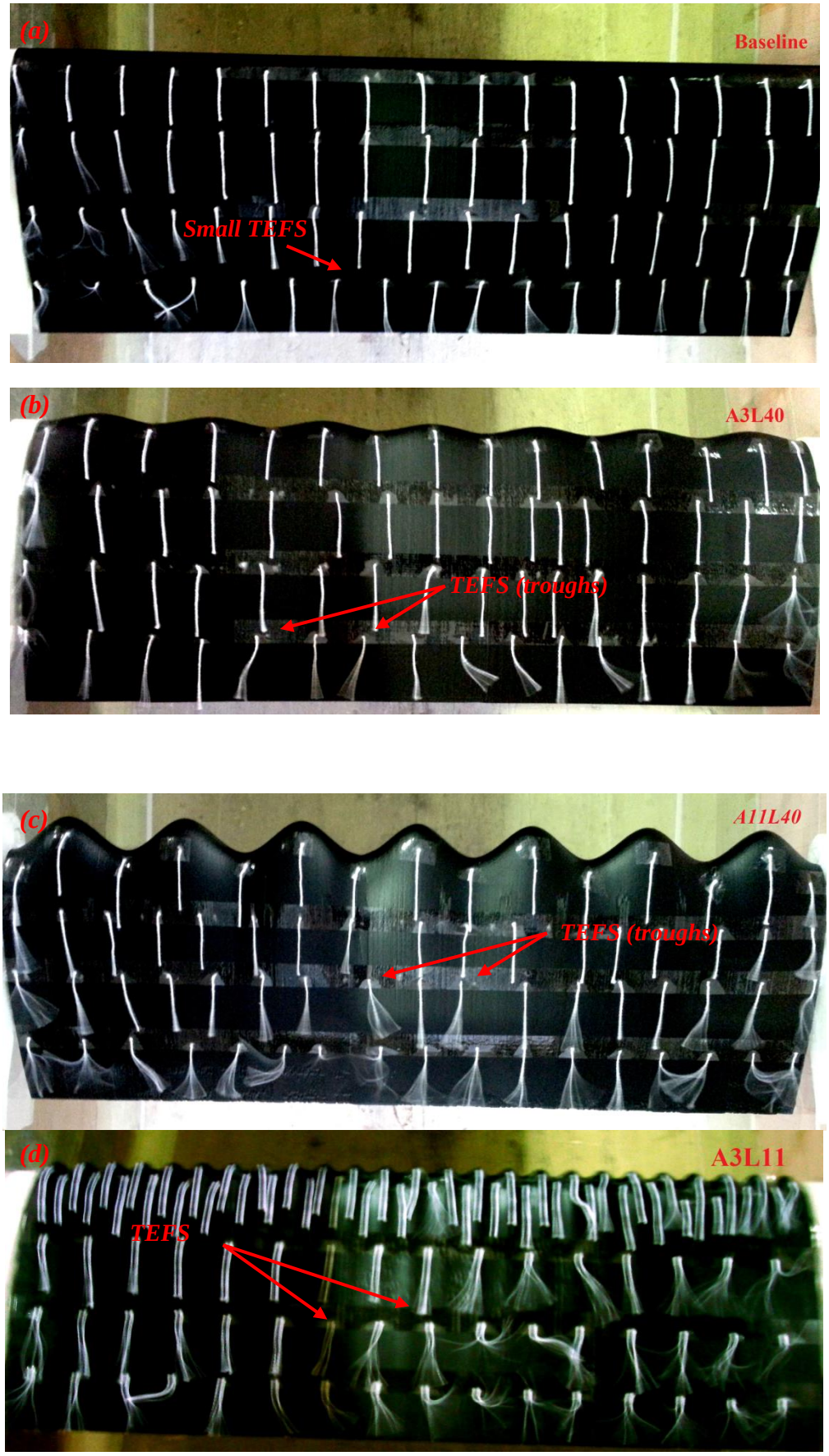

Figure 5.8: All configurations at α = 10°and Re = 290,000 (NACA 0020).

Figure 5.9: All configurations at α = 15°and Re = 290,000 (NACA 0020).

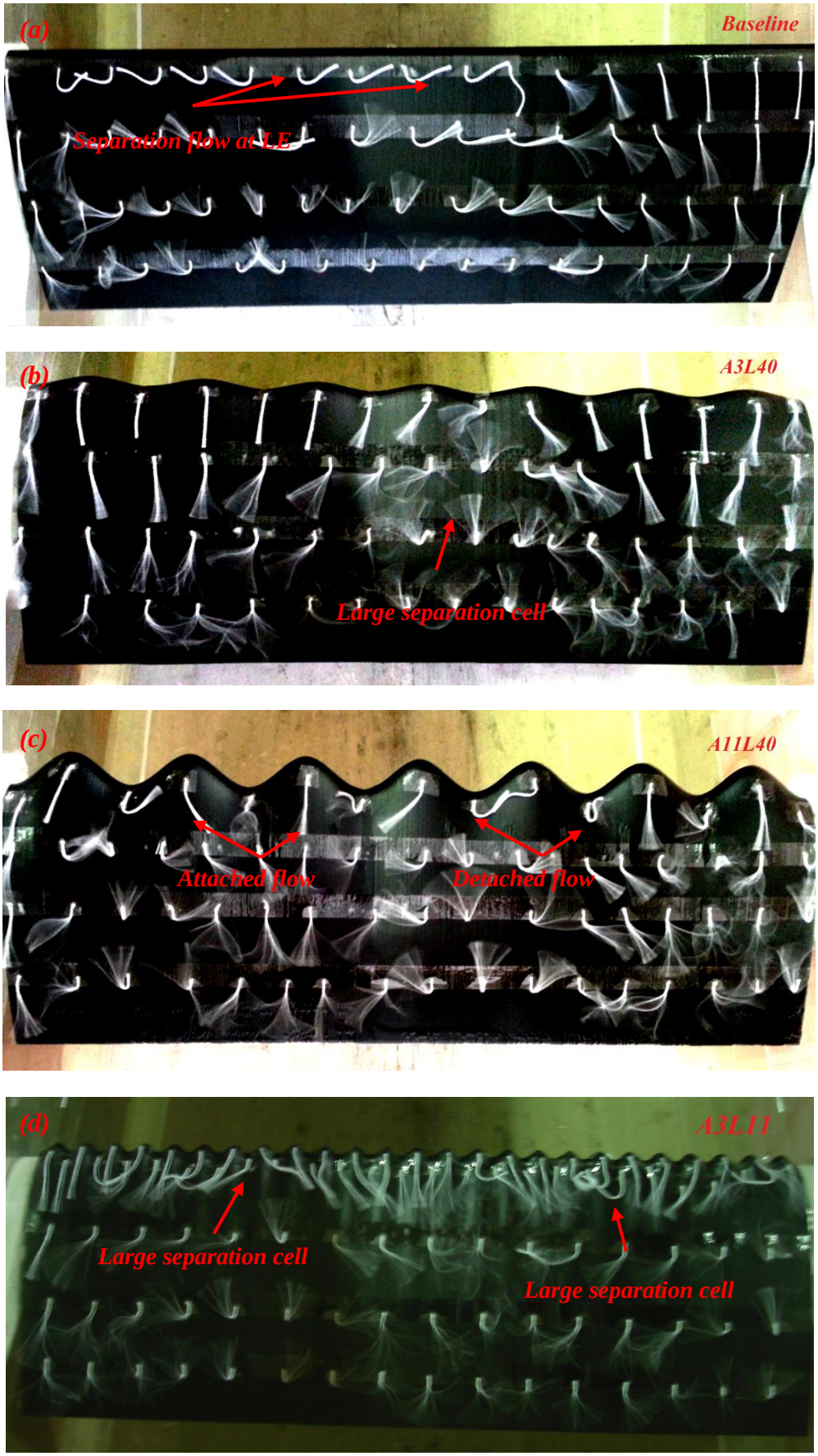

Figure 5.10: All configurations at α = 20°and Re = 290,000 (NACA 0020).

5.1.3 Wavy leading edge effect on NACA 0030 airfoil at Re = 290,000

Differently from thinner airfoils, the wavy leading edge causes changes in flow topology for the thickest NACA 0030 airfoil even at an angle of attack of 0°. The smooth configuration (fig.5.11a) shows mini-tufts aligned and attached in the entire airfoil upper surface. In contrast, the wavy leading edge configurations show trailing edge flow separation. Configurations A11λ40 (fig.5.11c) and A3λ11 (fig.5.11d) present flow separation areas spanning respectively 20% and 10% of chord. In addition, configuration A3λ40 (fig.5.11b) shows a small flow separation at the trailing edge.

At an angle of attack of 5°, all configurations undergo a growth in trailing edge flow detachment. The smooth airfoil (fig.5.12a) presents trailing edge flow separation at 20% of chord. In the case of wavy configurations, the separated flow area depends on tubercle geometry. The larger amplitude configuration (fig.5.11c) shows trailing edge flow separation reaching 65% of chord, and thus establishing the greatest flow separation area explaining the large deterioration in the lift curve (figure 4.40). For this configuration, it can be clearly seen that the flow separation areas are concentrated downstream of the tubercle troughs. The aerodynamic deterioration seen in the larger amplitude configuration is similar for all airfoil thicknesses. However, for the thickest airfoil the deterioration occurs earlier, at a lower angle of attack. Configuration A3λ11 (fig.5.12d) presents trailing edge flow separation reaching 35% of the chord. Besides, the wavy airfoil A3λ40 (fig.5.12b) presents flow separation similar to the smooth configuration, justifying similar values on lift curve (figure 4.40).

At an angle of attack of 10°, the flow separation increases towards the leading edge for smooth and wavy configurations. The larger amplitude configuration (fig.5.13c) maintains the largest separation flow area increasing up to 75% of chord and anticipating flow separation downstream of the troughs. Configurations baseline (fig.5.13a) and A3λ40 (fig.5.13b) have similar flow separation areas. Additionally, the airfoil A3λ11 (fig.5.13d) presents two separation cells with a slightly larger separation area.

At an angle of attack of 15°, the smooth configuration (fig.5.14a) remains the largest attached area among the configurations, with a separation cell at 24% of chord from the leading edge. Configurations A3λ40 (fig.5.11b) and A3λ11 (fig.5.11d) have similar flow separations, preserving almost the entire leading edge attached.

Although the larger amplitude configuration (fig.5.11c) preserves the leading edge attached, this configuration still presents greater flow separation area downstream from the leading edge than the smaller amplitude configurations, justifying lower lift values (4.40).

At an angle of attack of 20º, in contrast with thinner airfoils, the smooth configuration (fig.5.15a) still guarantees high lift values keeping the attached flow over the entire leading edge. On the other hand, configuration A3λ40 (fig.5.15b) presents two separation cells achieving the leading edge characterizing the post-stall regime.

Configuration A3λ11 (fig.5.15d) preserves the flow attached over almost the entire leading edge similar to $\alpha = 15º$, although the areas of the twin separation cells are increased. The flow topology for configuration A11λ40 (fig.5.15c) is also similar to $\alpha = 15º$. The flow characteristics from configurations A3λ11 and A11λ40 agree with soft stall behaviour at figure 4.40.

At an angle of attack of 25º, the baseline configuration (fig.5.16a) undergoes full flow separation at 60% of airfoil span characterizing post-stall regime. The flow is preserved attached close to the left wind tunnel wall.

Configurations A3λ40 (fig.5.16b) and A3λ11 (fig.5.16d) show similar flow separation areas, justifying similar lift values (figure 4.40). Moreover, configuration A11λ40 (fig.5.16c) increases the flow separation areas, reaching the leading edge.

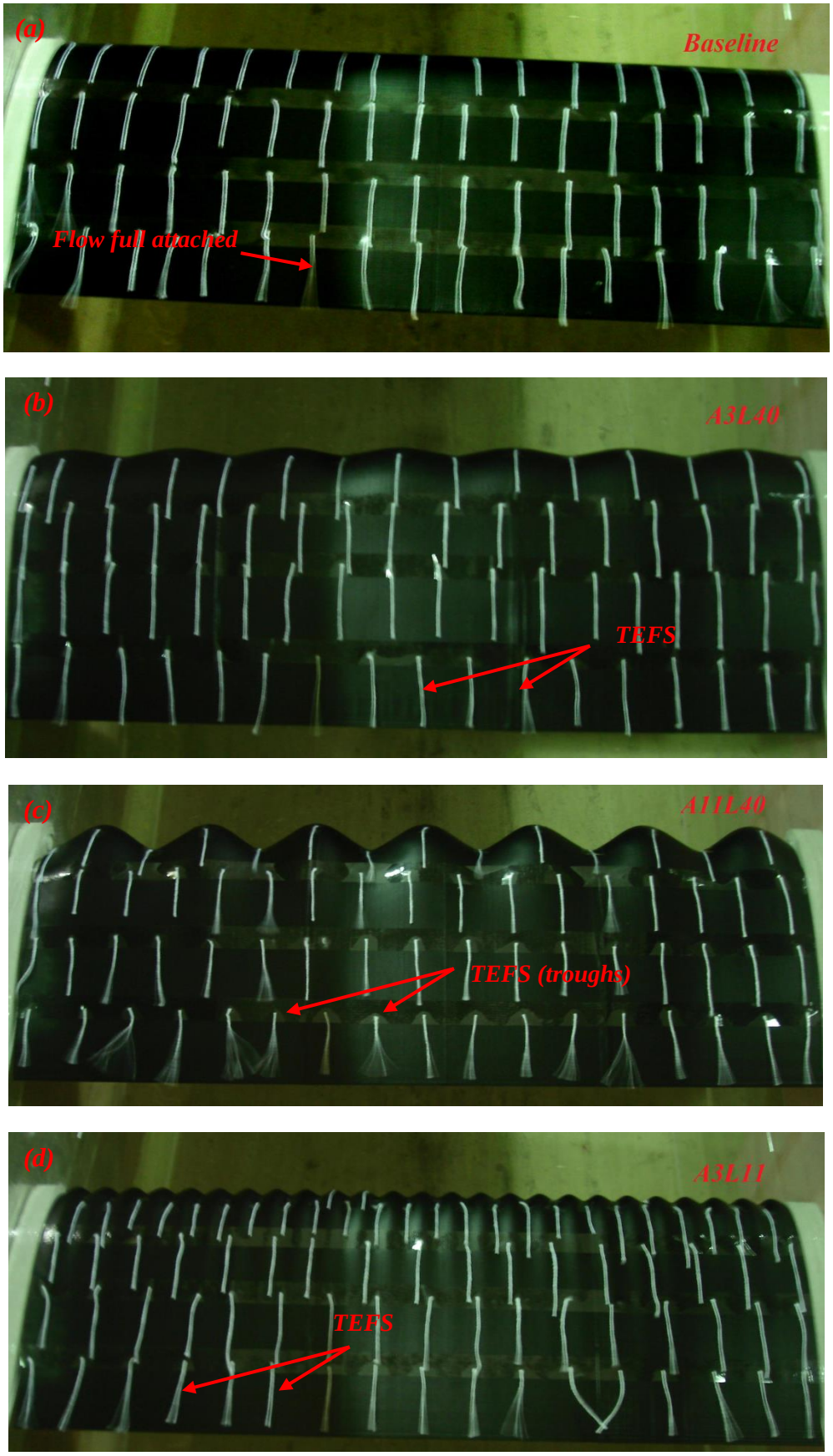

Figure 5.11: All configurations at α = 0°and Re = 290,000 (NACA 0030).

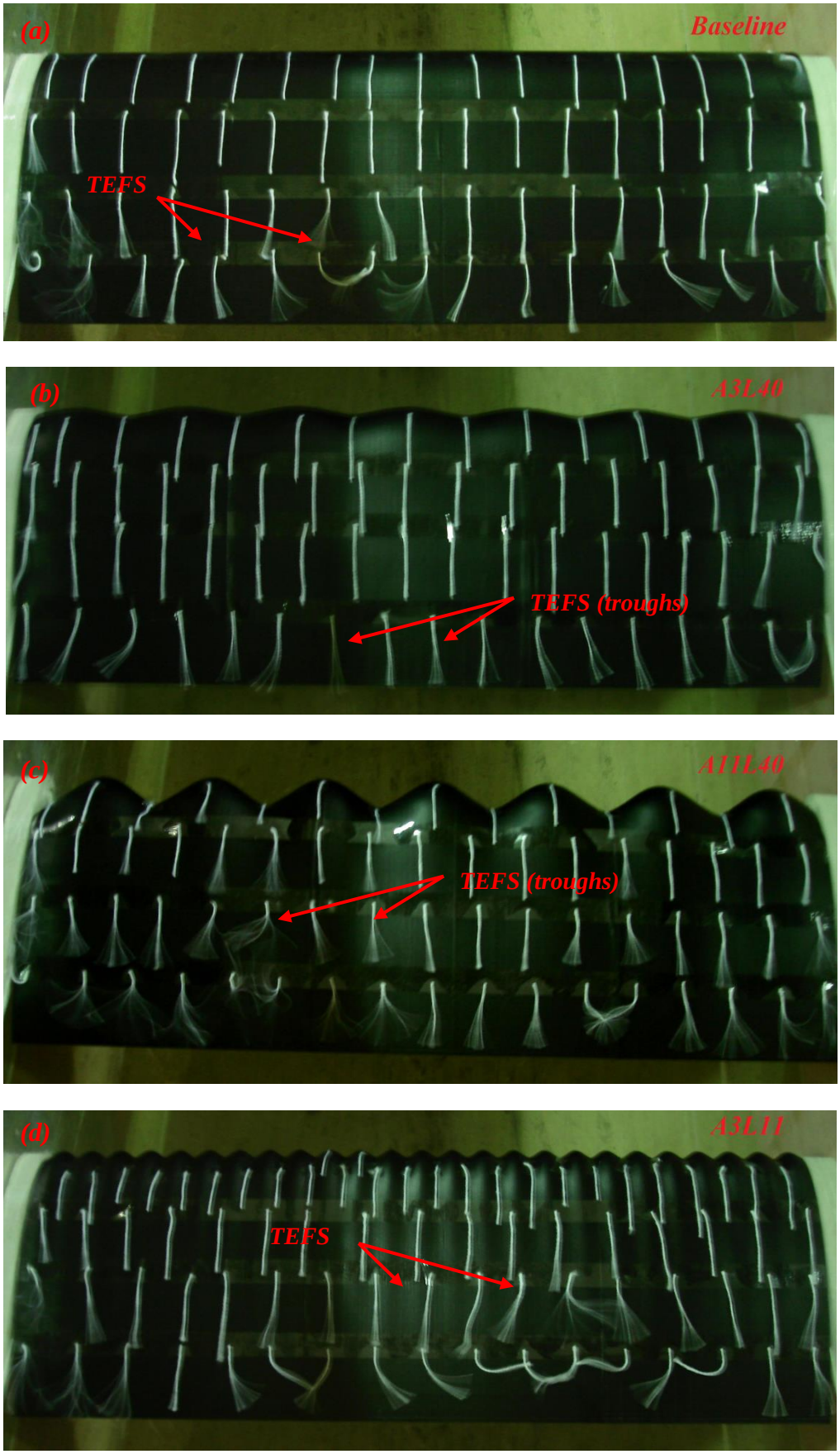

Figure 5.12: All configurations at α = 5°and Re = 290,000 (NACA 0030).

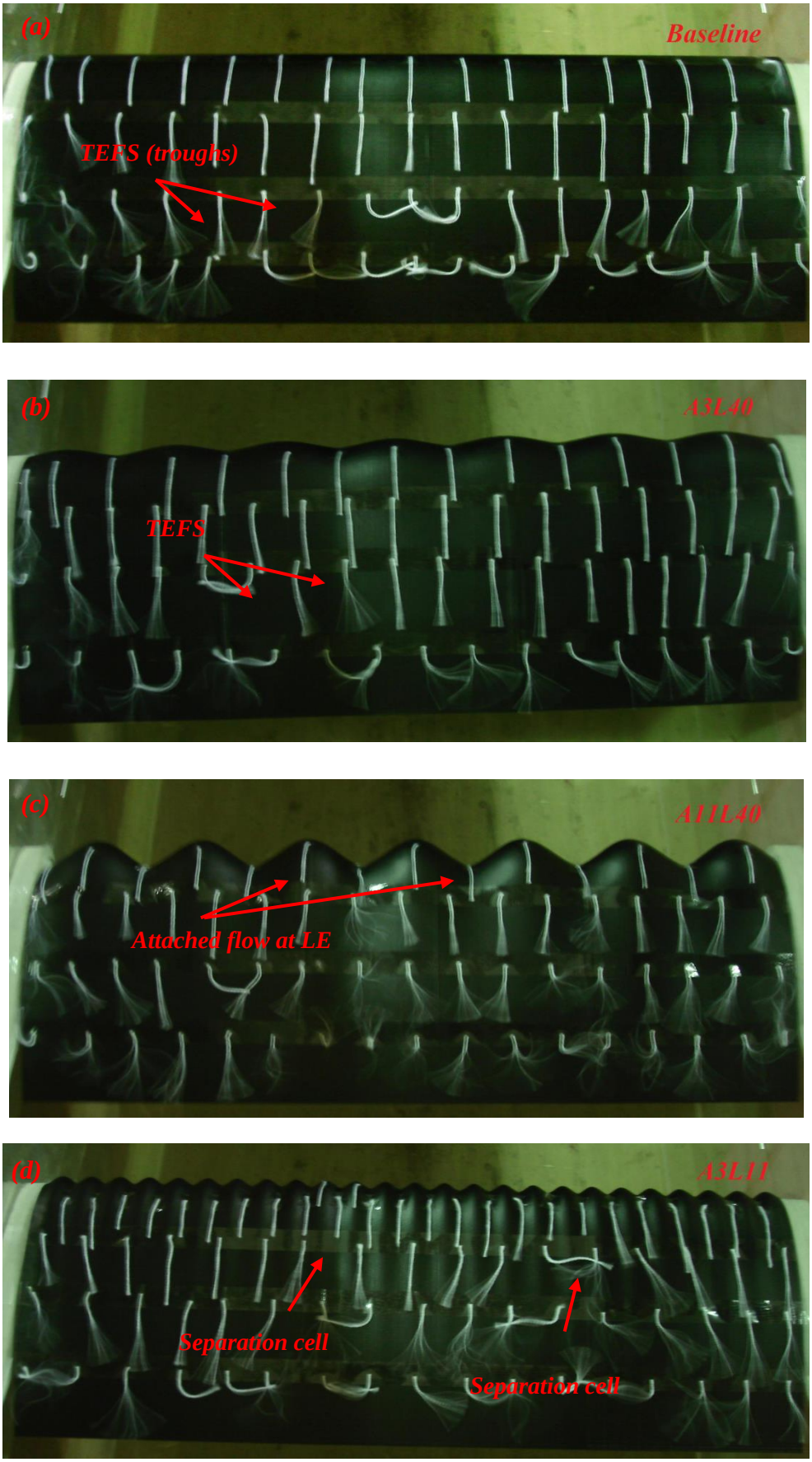

Figure 5.13: All configurations at α = 10°and Re = 290,000 (NACA 0030).

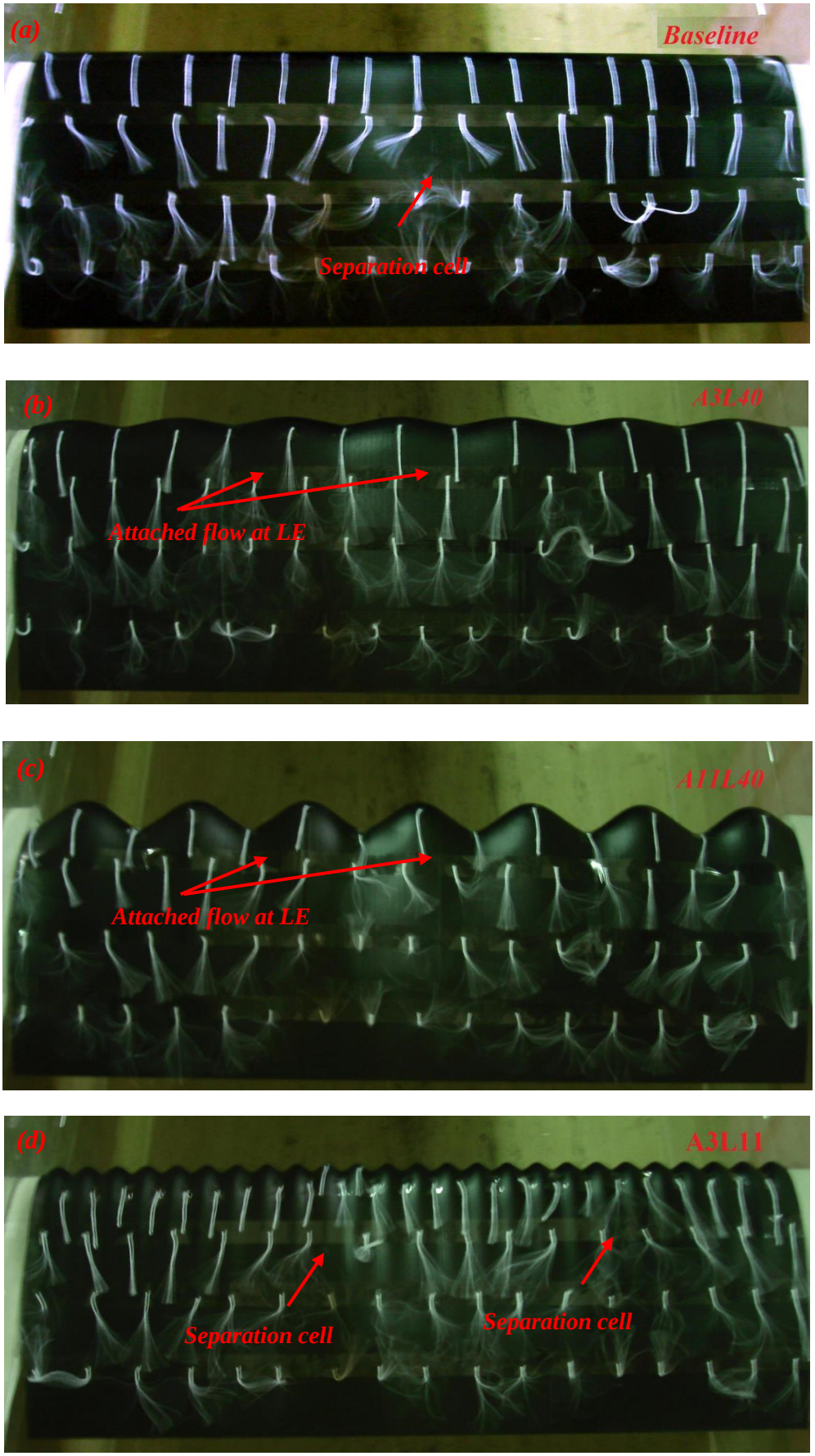

Figure 5.14: All configurations at α = 15°and Re = 290,000 (NACA 0030).

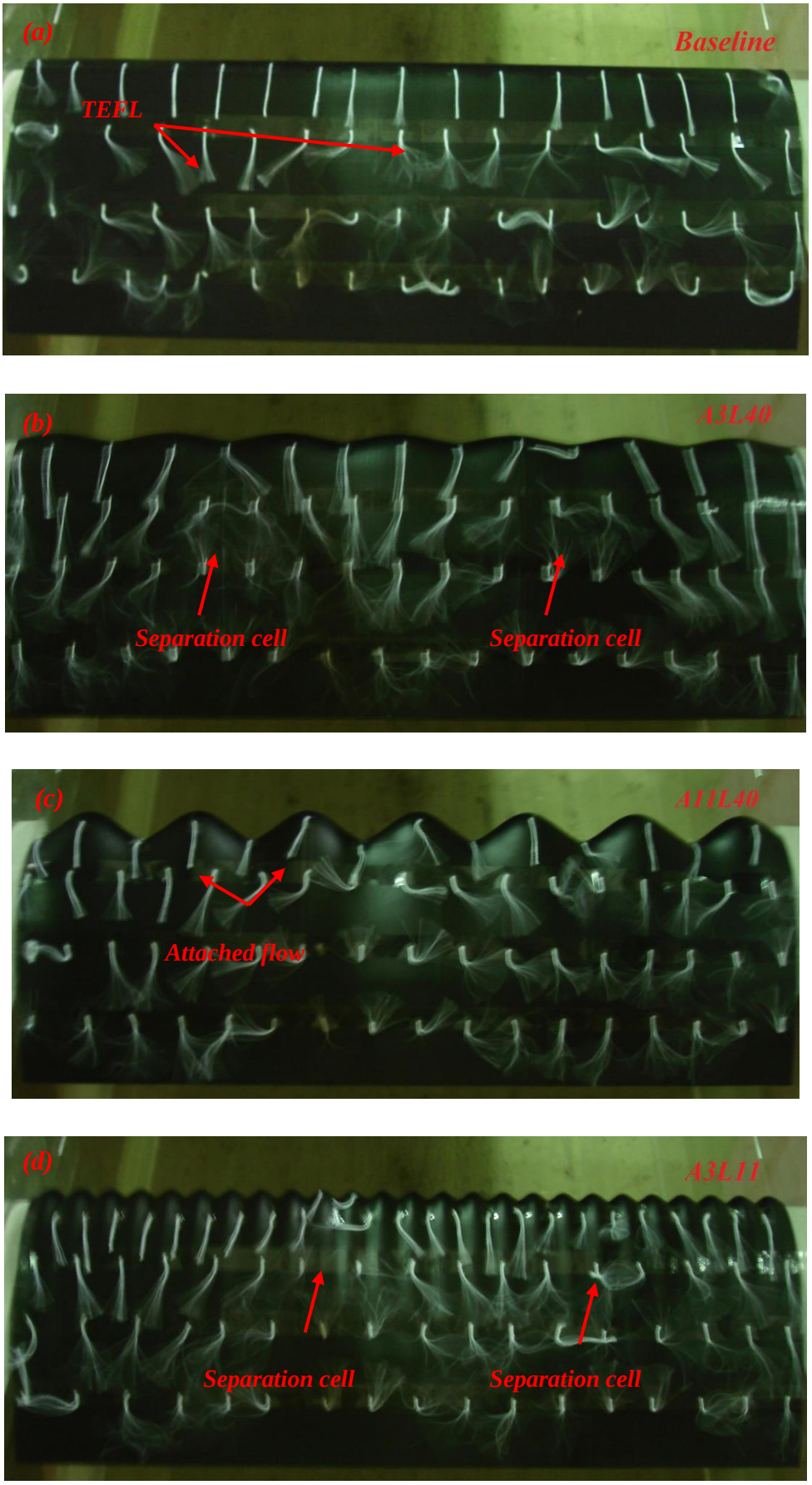

Figure 5.15: All configurations at α = 20°and Re = 290,000 (NACA 0030).

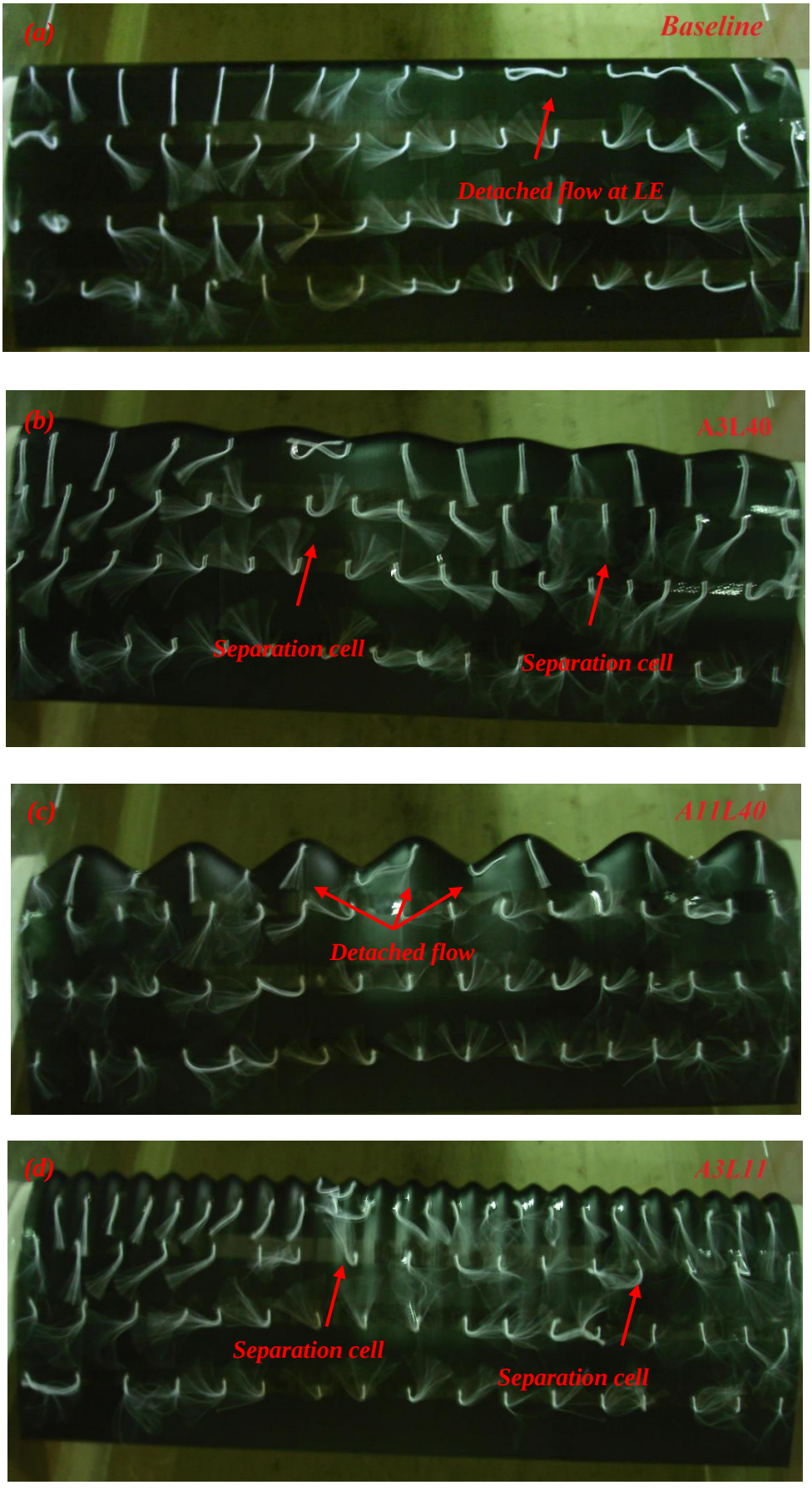

Figure 5.16: All configurations at α =25°and Re = 290,000 (NACA 0030).

5.1.4 Wavy leading edge effect at the lowest Reynolds number (Re = 50,000)

The NACA 0012 airfoil keeps mini-tufts attached and aligned at an angle of attack of 0º (figure 5.17), indicating the flow fully attached over the entire airfoil upper surface for all configurations. Although not presented, the flow visualizations up to $\alpha = 10º$ show similar flow topology than angle of attack 0º.

At an angle of attack of 11º (figure 5.18), the smooth airfoil undergoes flow separation at the leading edge, justifying the abrupt stall condition presented on lift curve (figure 4.11). On the other hand, the wavy configurations preserve attached flow over the entire leading edge. Besides, the configurations keep a large area of attached flow, indicating that at low Reynolds numbers, differently from higher Reynolds number conditions, the tubercle preserves the flow attached over larger areas downstream from leading edge. This flow characteristic agrees with higher values on lift curve at $\alpha = 11°$ (figure 4.11). At an angle of attack of 15º (figure 5.19), the baseline configuration keeps a flow pattern similar to $\alpha = 11º$. The wavy configurations still have attached flow at the leading edge.

The tubercle effect on the flow topology of the airfoils NACA 0020 (figures 5.22 and 5.22) and NACA 0030 (figures 5.23 and 5.24) is similar to NACA 0012 airfoil.

The aerodynamic characteristics at low Reynolds number present on the smooth configuration imply an abrupt leading edge stall at earlier angle of attack whereas the wavy configurations do not cause trailing flow separation at the pre-stall condition. The tubercles delay the stall keeping flow attached over large areas of the airfoil upper surface, thus establishing higher lift values and soft stall behaviour (figure 4.11 and 4.29).

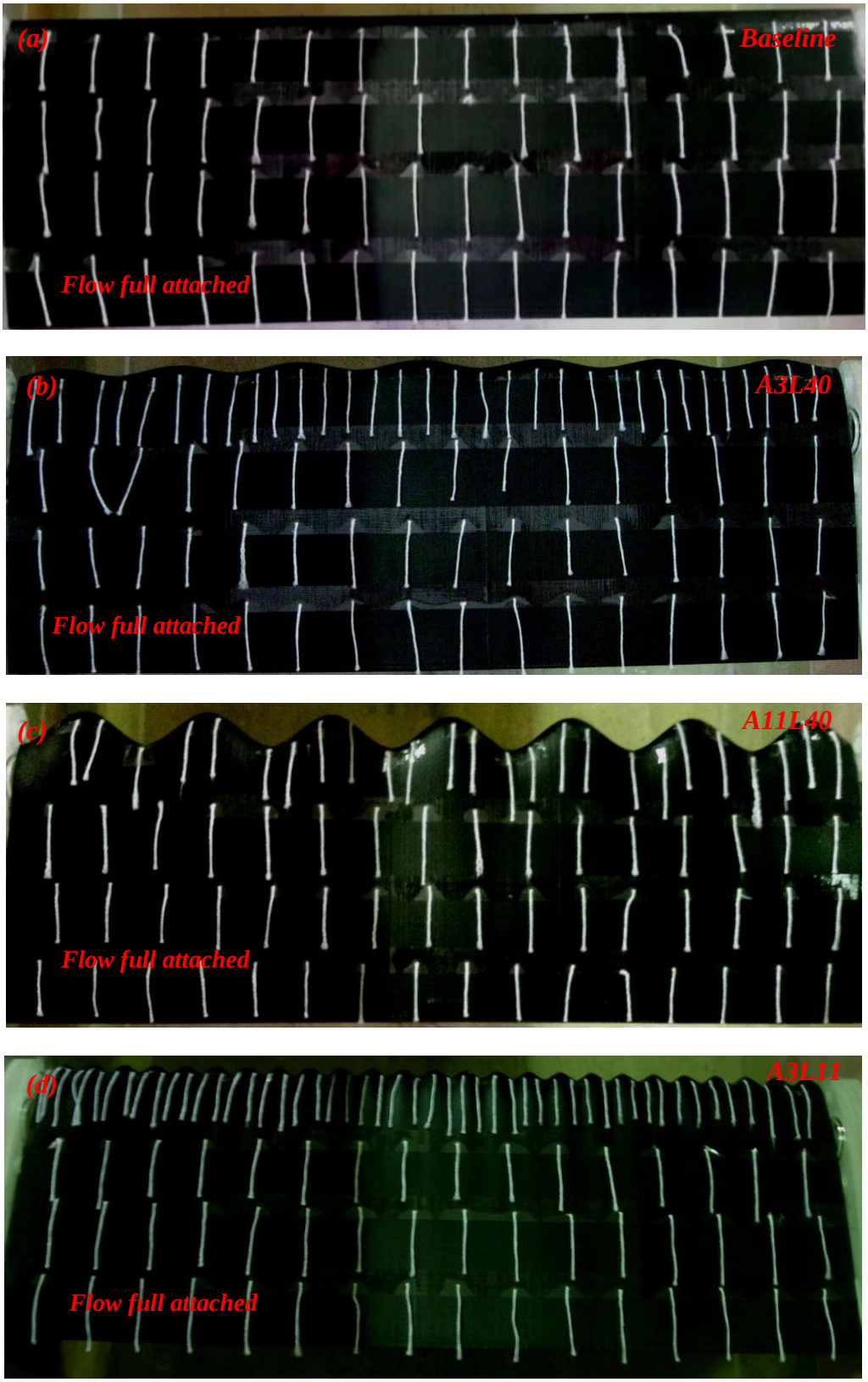

Figure 5.17: All configurations at α =0°and Re = 50,000 (NACA 0012).

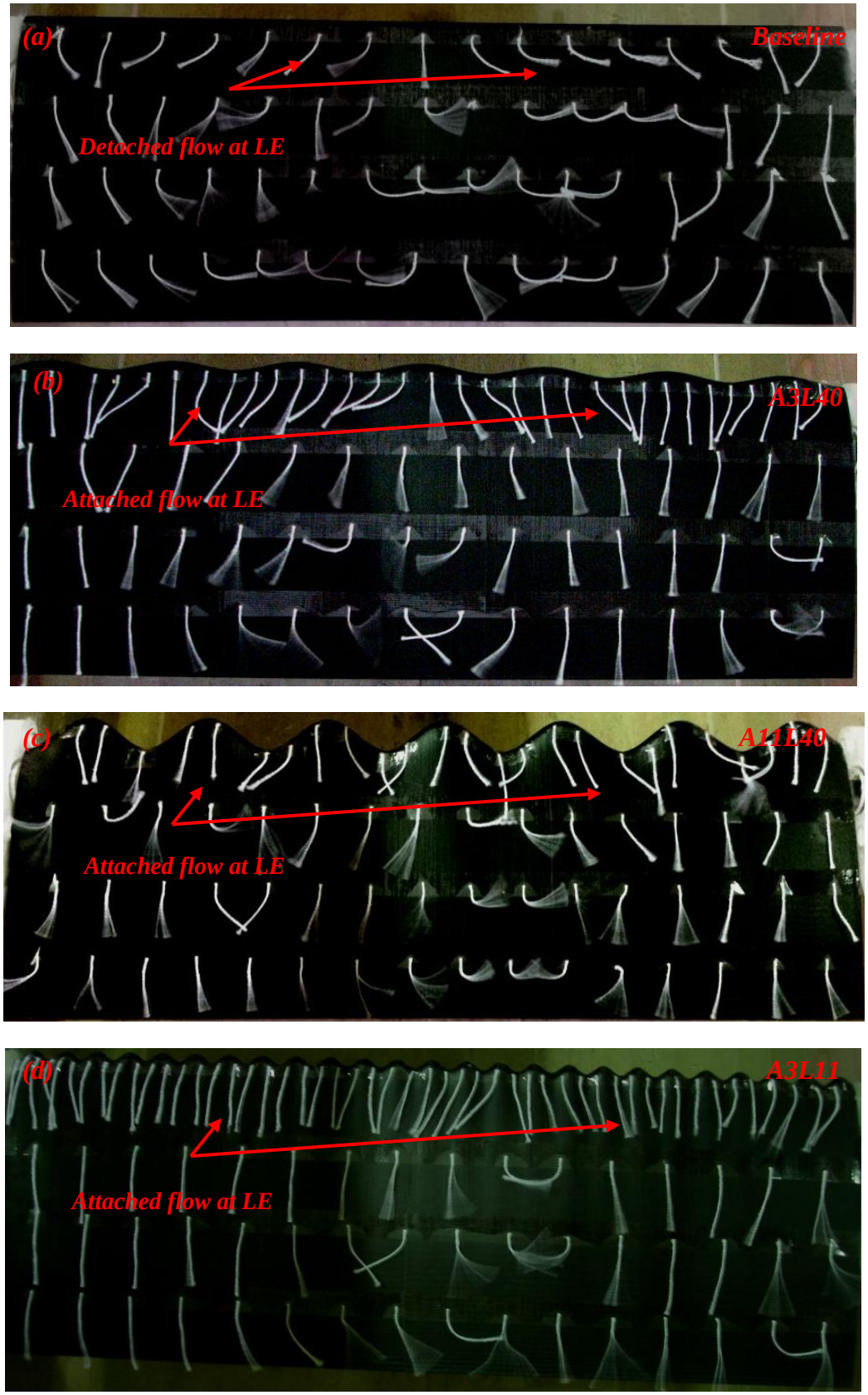

Figure 5.18: All configurations at α =11°and Re = 50,000 (NACA 0012).

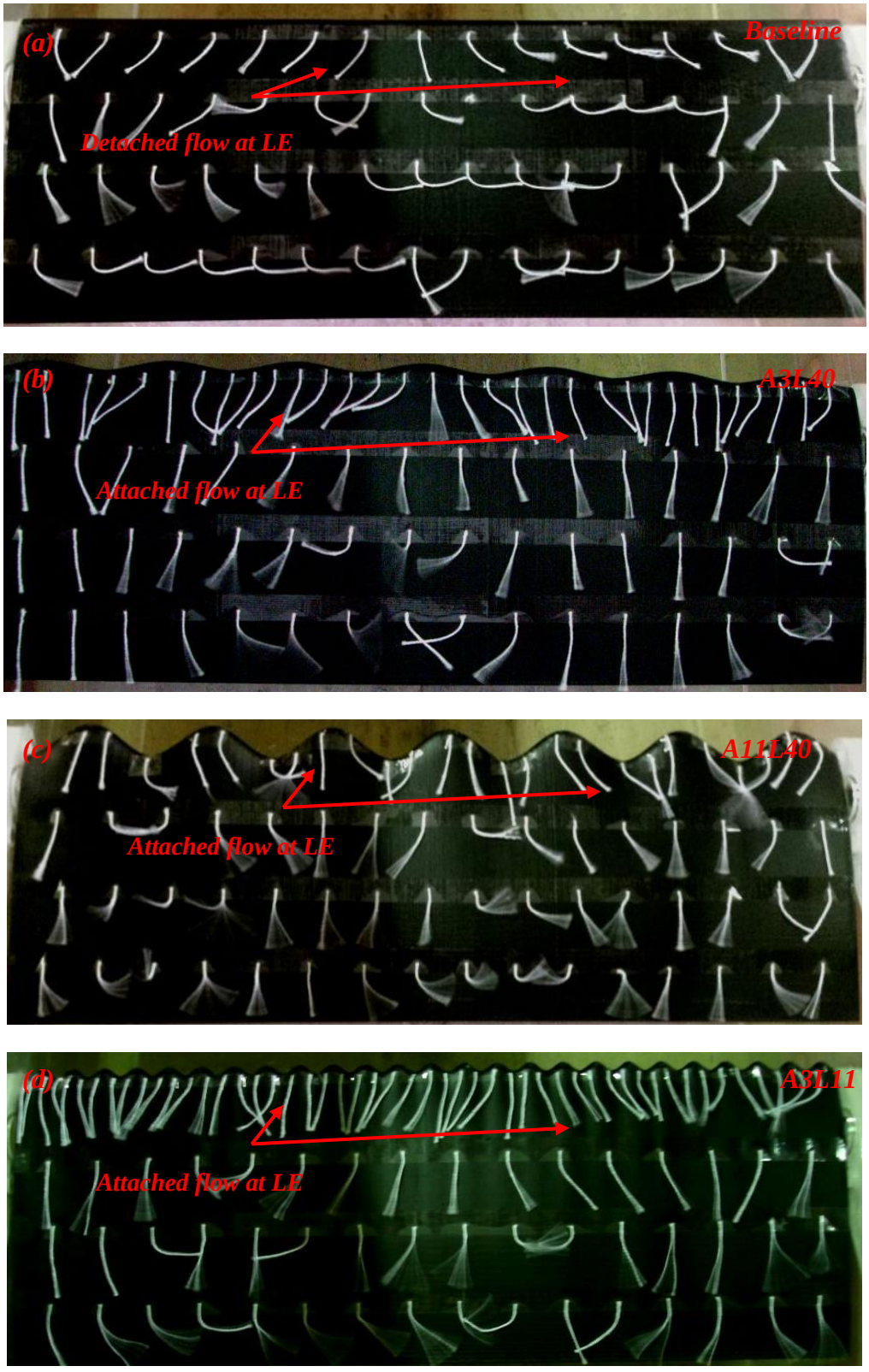

Figure 5.19: All configurations at α =15°and Re = 50,000 (NACA 0012).

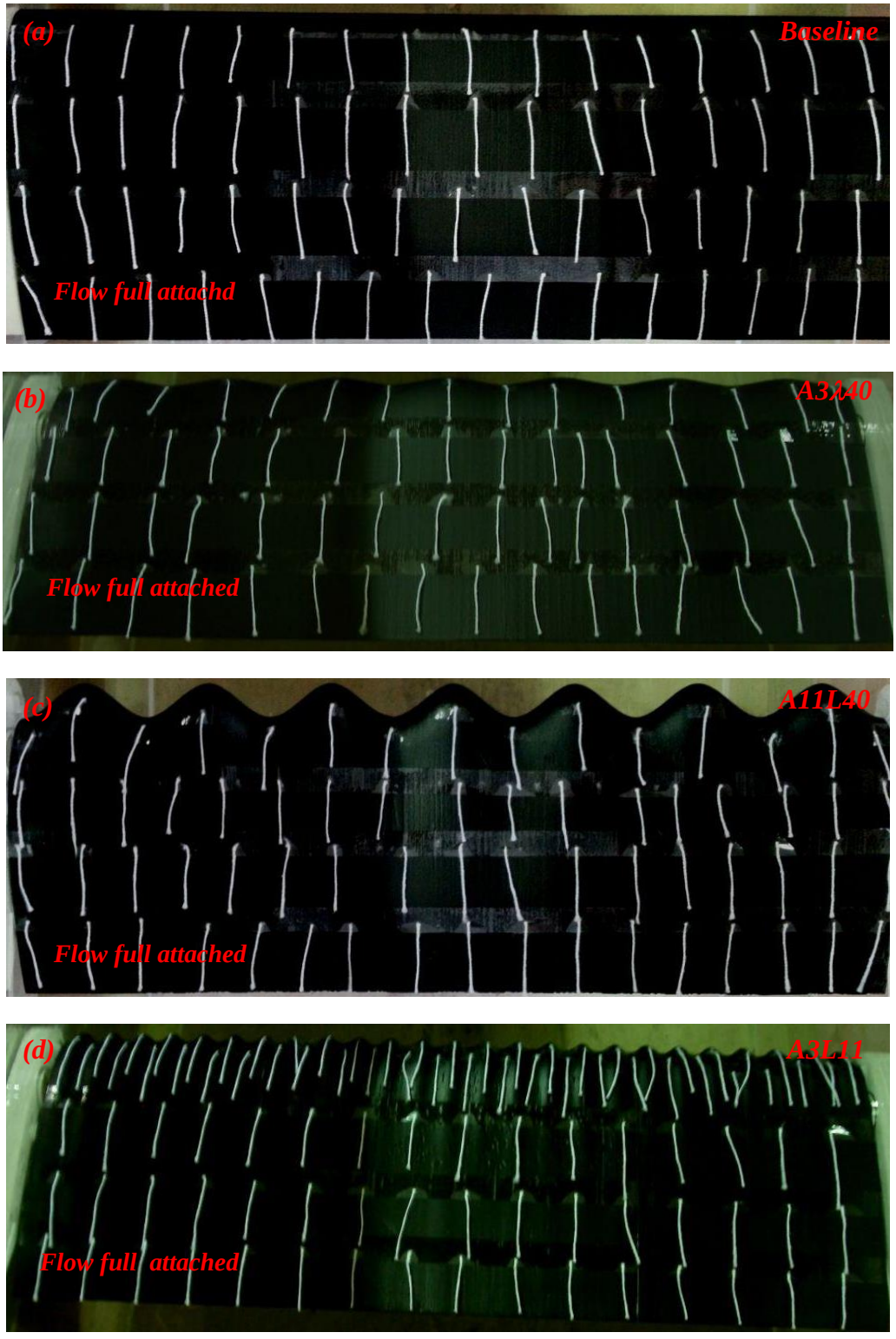

Figure 5.20: All configurations at α =0°and Re = 50,000 (NACA 0020).

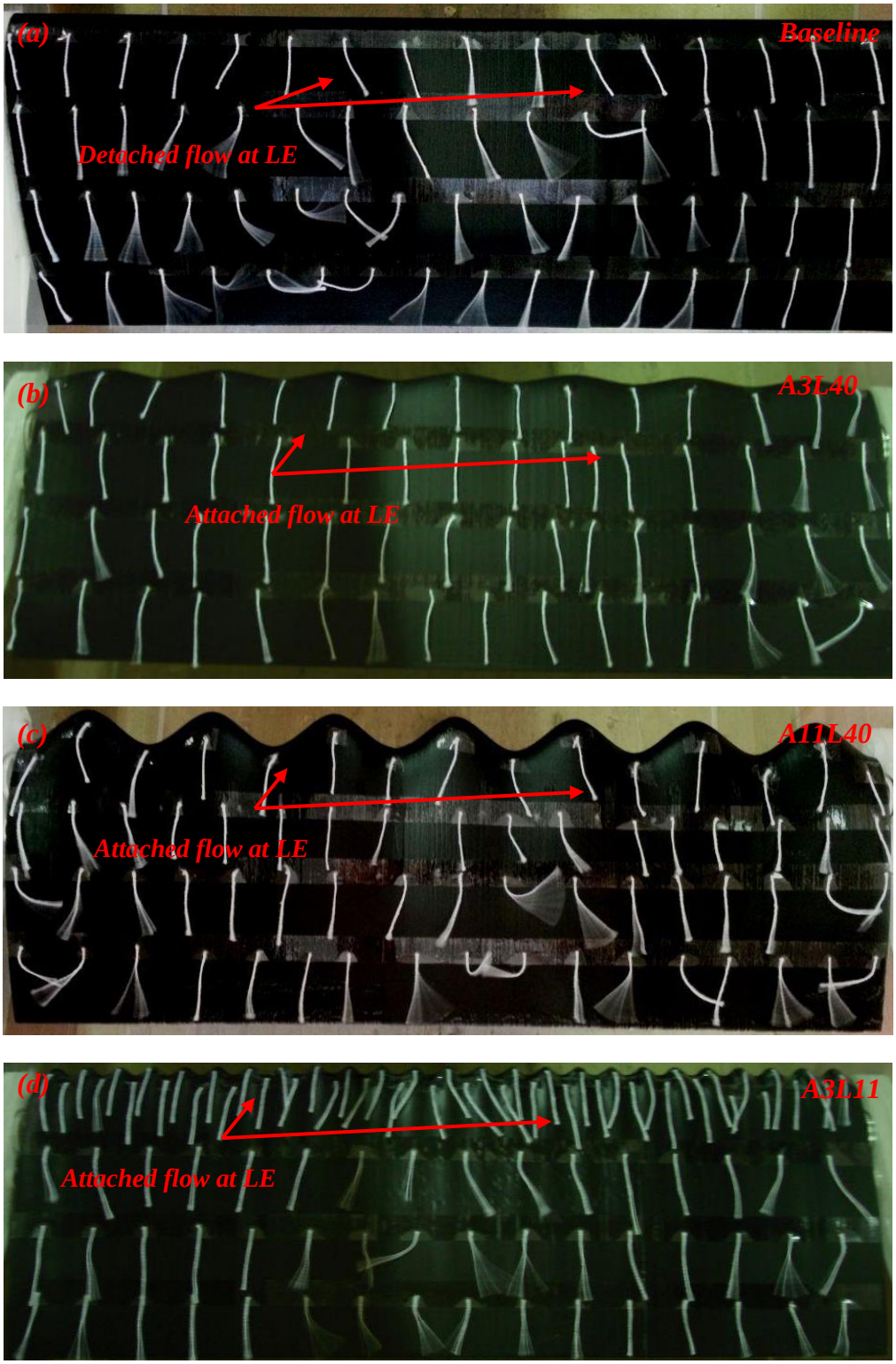

Figure 5.21: All configurations at α =11°and Re = 50,000 (NACA 0020).

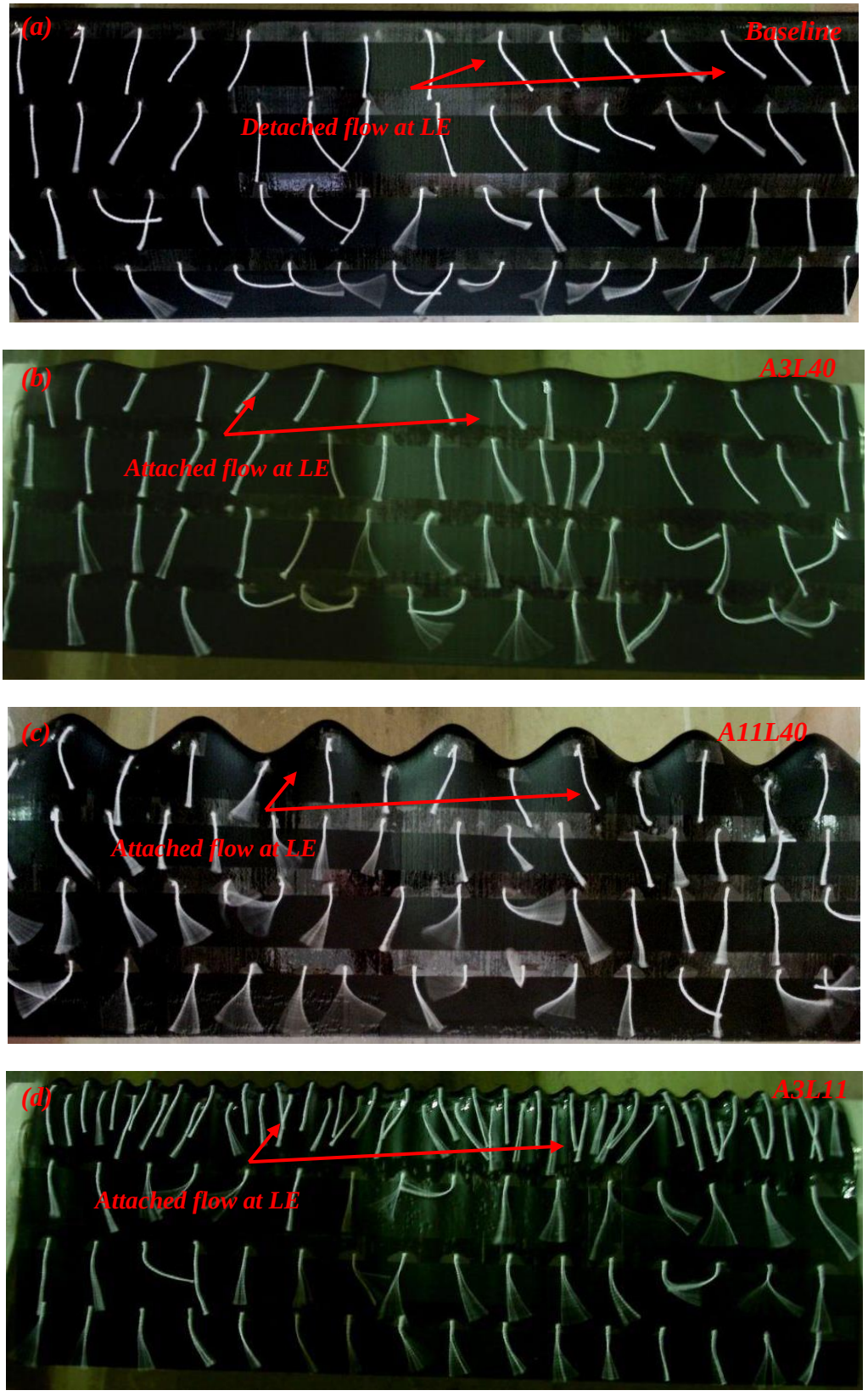

Figure 5.22: All configurations at α =15°and Re = 50,000 (NACA 0020).

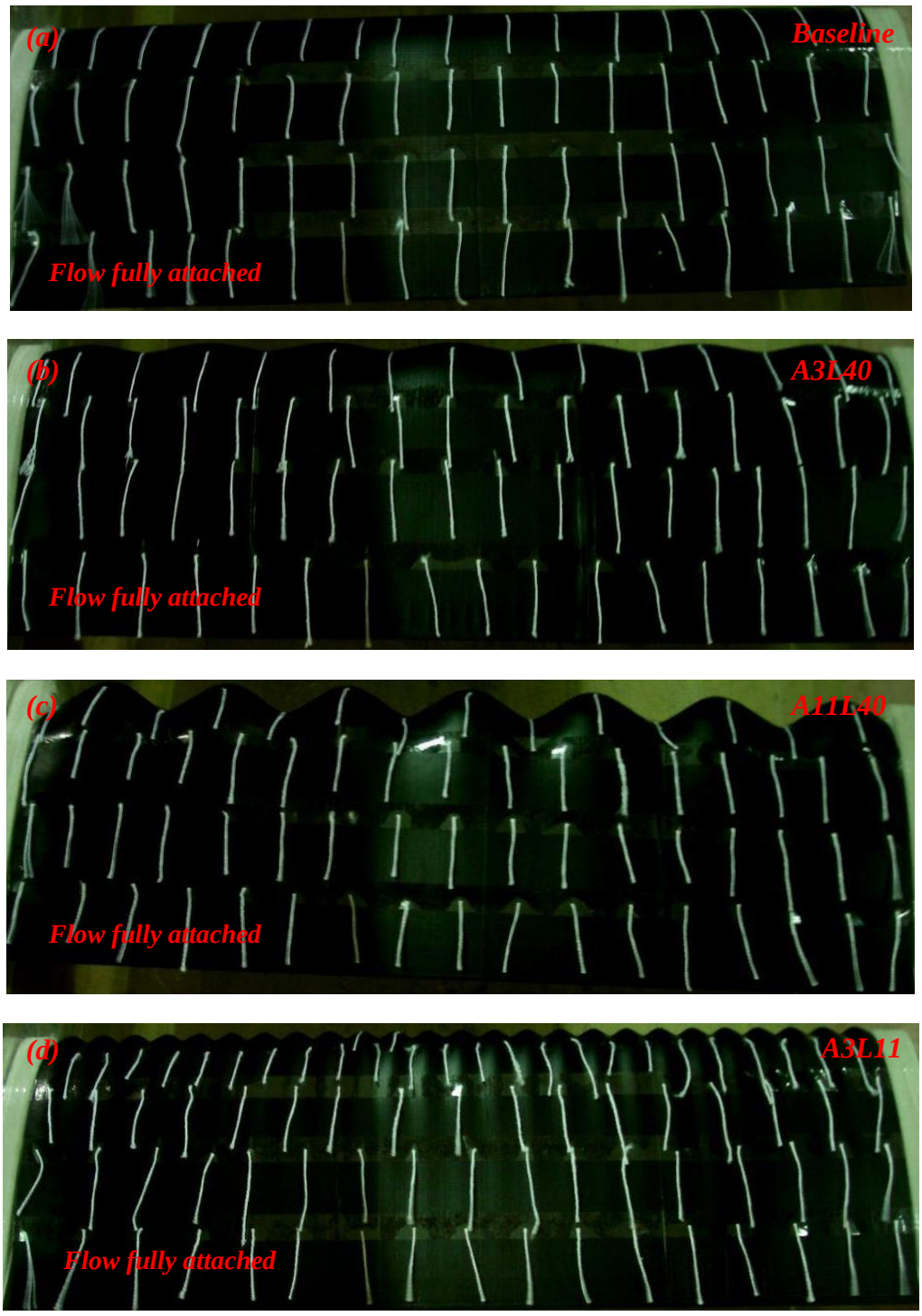

Figure 5.23: All configurations at α =0°and Re = 50,000 (NACA 0030).

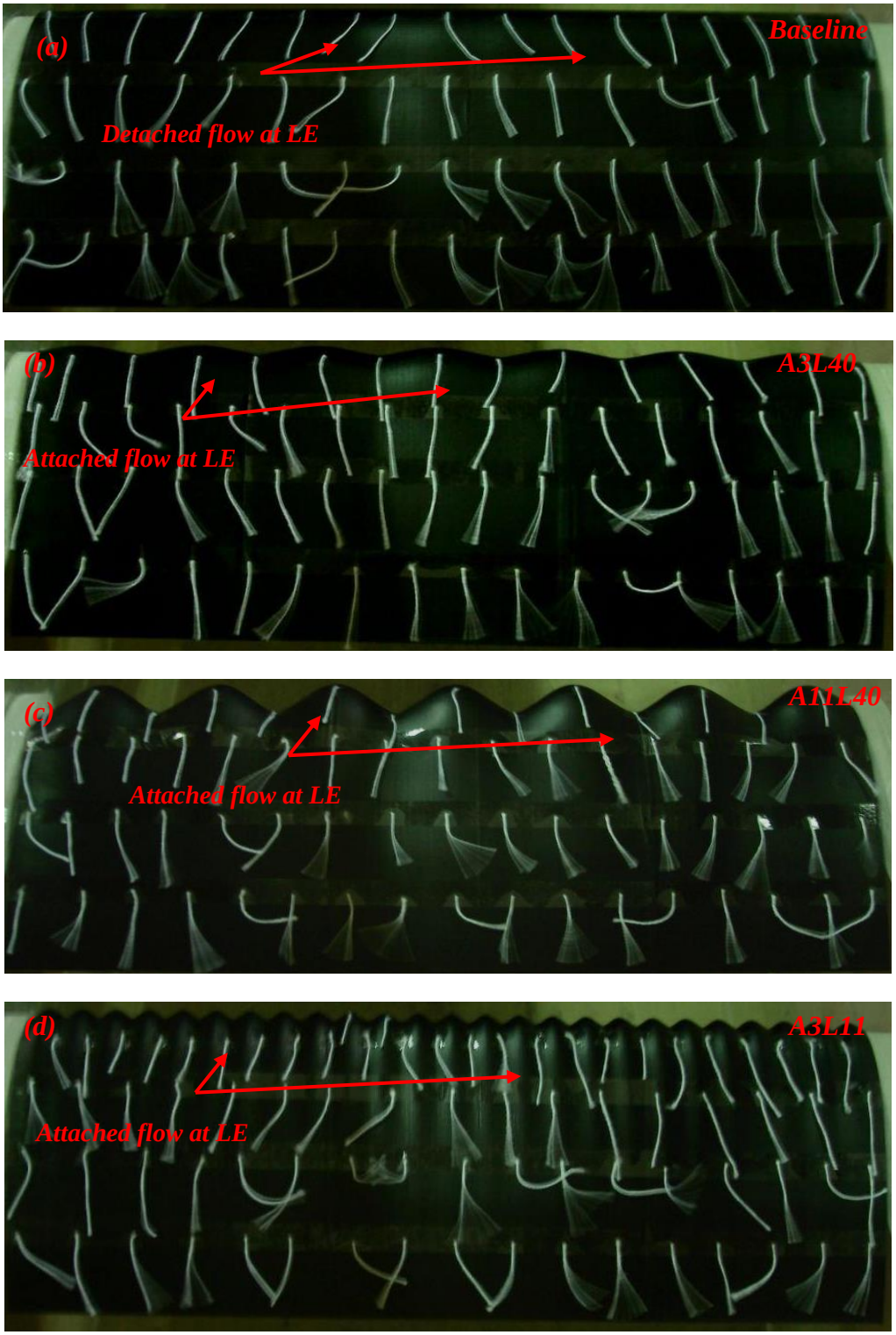

Figure 5.24: All configurations at α =15°and Re = 50,000 (NACA 0030).

5.2 Oil visualization

5.2.1 Wavy leading edge effect on NACA 0012 airfoil at Re = 290,000

Evidenced in Figure 5.25a, for the smooth configuration at an angle of attack of 0°, is a two-dimensional laminar separation bubble at a relatively rearward position on upper surface of the NACA 0012 airfoil. The flow undergoes separation at 0.52c from the leading edge, reattaching near the trailing edge and forming a long bubble 0.46c in length. Configuration A3λ40 (fig.5.25b) presents a quasi-two-dimensional LSB (laminar separation bubble) showing a wavy line along the span at flow separation points.

For the larger amplitude configuration (fig.5.25c), a bi-periodic flow pattern occurs where a three-dimensional long laminar bubble forms downstream of the troughs in a forward position whereas a staggered, smaller bubble occurs near the trailing edge. In contrast, configuration A3λ11 (fig.5.25d) presents only an elongated laminar bubble downstream of the troughs.

Increasing the angle of attack to $\alpha = 5°$ generally makes the laminar bubble to decrease in length and move towards the leading edge. At this angle of attack, the separation point (X_S =0.21c) and length (L_B =0.24c) of the two-dimensional bubble distribution on the smooth configuration is significantly altered (fig.5.26a).

On the other hand, the laminar bubbles reach the leading edge for configurations A11λ40 (fig.5.26c) and A3λ11 (fig.5.26d), presenting the three-dimensional structures only downstream of the troughs. Configuration A3λ40 (fig.5.26b) establishes a laminar bubble reaching 16% of chord from the leading edge (L_B = 0.16c), and possibly bubbles form downstream of the peaks. The flow for all configurations is attached, only with a separation visible at the intersection between the profile and the wind tunnel sidewalls.

At an angle of attack of $\alpha = 10°$, the smooth configuration (fig.5.27a) has a very short laminar bubble (L_B =0.04c) starting virtually at the leading edge (X_S =0.01c). For the wavy configurations A11λ40 (fig.5.30c) and A3λ11 (fig.5.27d), the flow mechanism at the leading edge changes from a three-dimensional laminar bubble formation at tubercle troughs to a counter-rotating vortex pair (CVP) forming between peaks. The flow mechanism that forms

the CVP´s is evidenced clearly by the flow topology for the larger amplitude configuration (fig.5.27c).

It is evidenced by the video recordings that configurations A11λ40 and A3λ11establish, between peaks, two pockets of “tooth-shaped” oil accumulation abutting swirl lines between peaks and troughs, indicating a counter-rotating vortex pair. The area downstream of the peaks does not accumulate oil, with the dark surface evidencing the presence of attached flow in this location. The “tooth-shaped” structure decreases in size with reduction of the wave amplitude. Configuration A3λ11 reaches smaller counter-rotating vortex pair.

Configuration A3λ40, as documented in figure 5.27b, has a three-dimensional laminar bubble distribution at the leading edge where a short bubble occurs at tubercle troughs and another, distinct laminar bubble forming a narrow line at peaks.

Three-dimensional flow separations are evident for wavy and smooth airfoils at an angle of attack 15°. The baseline configuration (fig.5.28a) shows fully separated laminar flow, without reattachment without further reattachment, forming a complex three-dimensional flow downstream from separation line. Configuration A3λ40 (fig.5.28b) also presents full flow separation without further with similar flow topology.

In contrast, configuration A11λ40 (fig.5.28c) preserves a bi-periodic pattern where the flow keeps attached in over a significant area downstream of the peaks.

Configuration A3λ11 (fig.5.28d), besides maintaining the flow attached downstream of the peaks due to CVP´s, preserves an area attached far downstream from the leading edge, thus guaranteeing the highest lift values at post-stall regime among wavy configurations. However, the “tooth-shaped” structure could not be more clearly identified due to unstable flow as observed from video recordings.

At α = 20°, the smooth configuration (fig.5.29a) and A3λ40 (fig.5.29b) have similar flow as compared to the α = 15º condition, where the entire airfoil upper surface is fully separated. Configurations A3λ11 (fig.5.29d) and A11λ40 (fig.5.29c) keep the counter-rotating vortex pair topology between peaks at the leading edges, clearly establishing attached flow areas (in dark color) downstream of the peaks. The results from configurations A3λ11 and A11λ40 agree with mini-tufts visualizations at higher angles of attack, showing a vortical flow control mechanism that maintain higher lift values in the post-stall regime (figure 4.4).

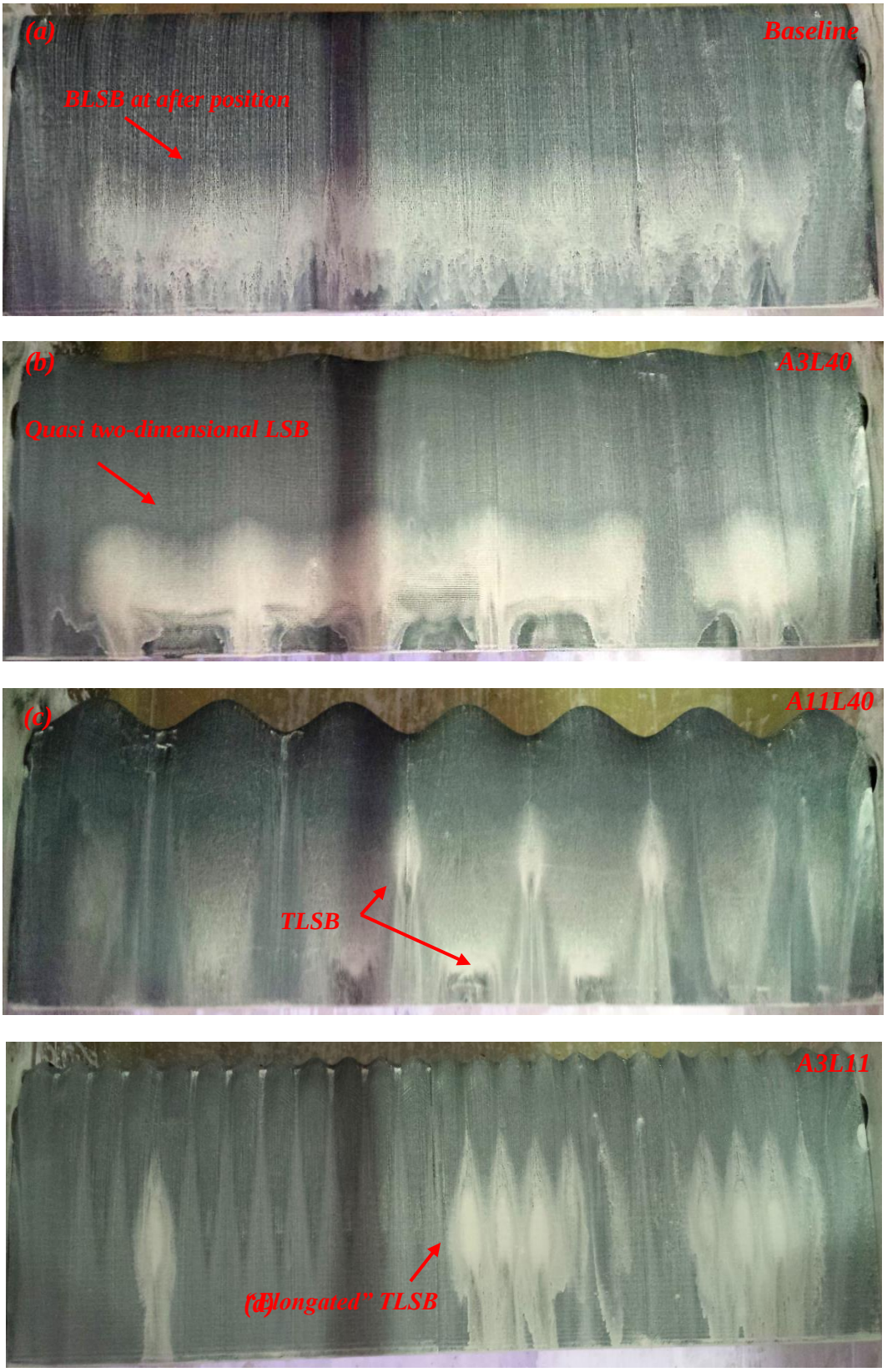

Figure 5.25: All configurations at α = 0°and Re = 290,000 (NACA 0012).

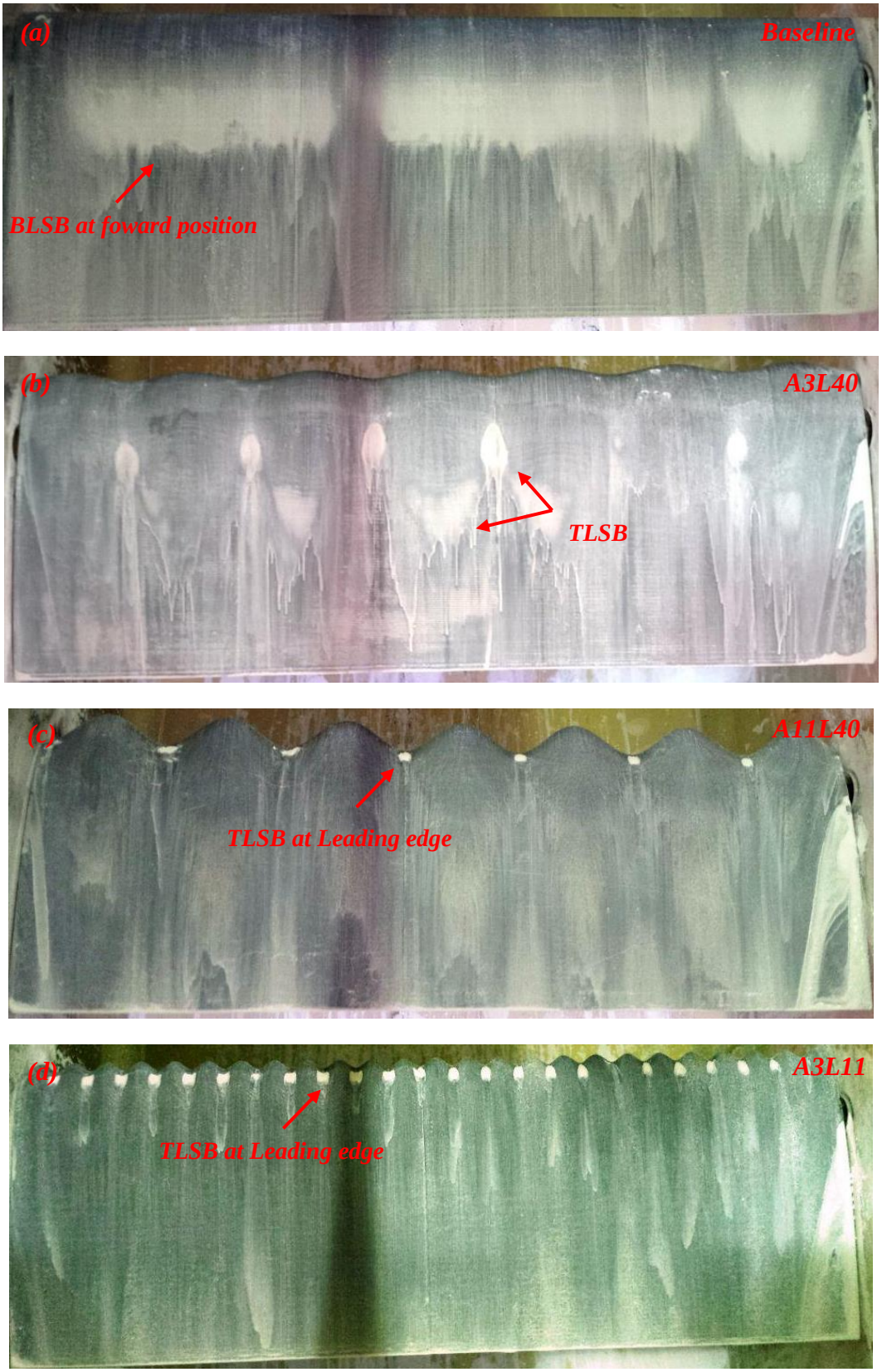

Figure 5.26: All configurations at α = 5°and Re = 290,000 (NACA 0012).

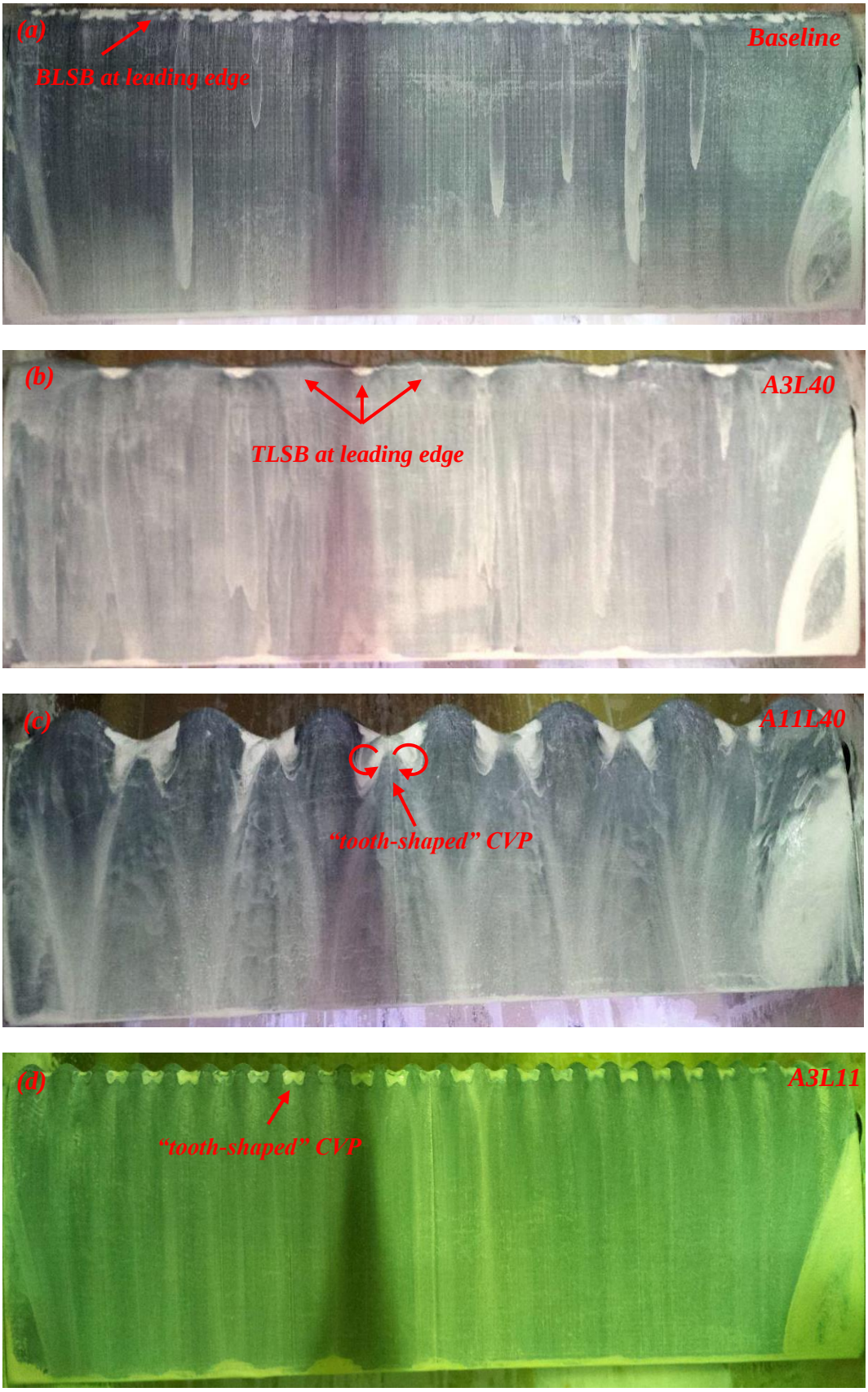

Figure 5.27: All configurations at α = 10°and Re = 290,000 (NACA 0012).

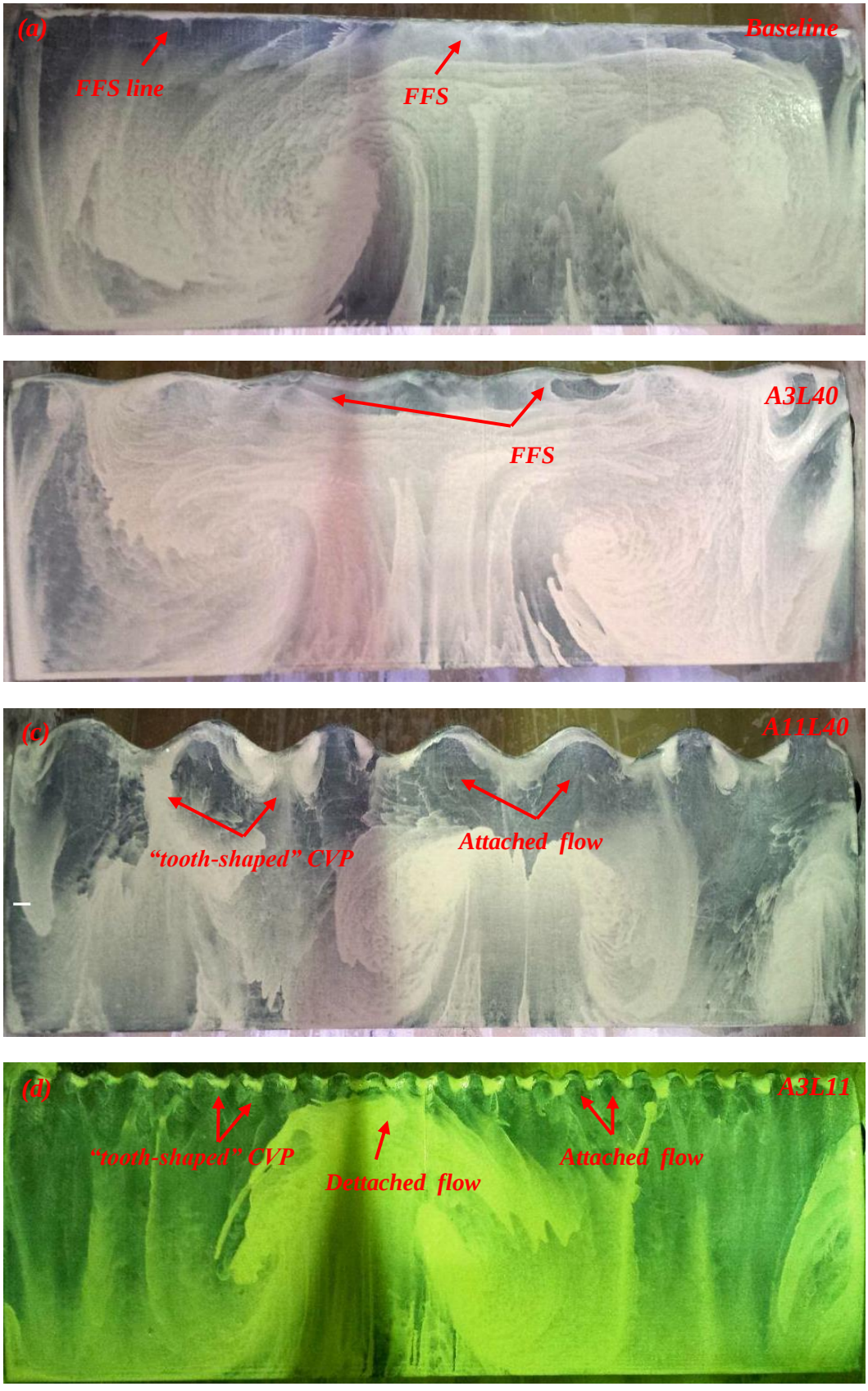

Figure 5.28: All configurations at α = 15°and Re = 290,000 (NACA 0012).

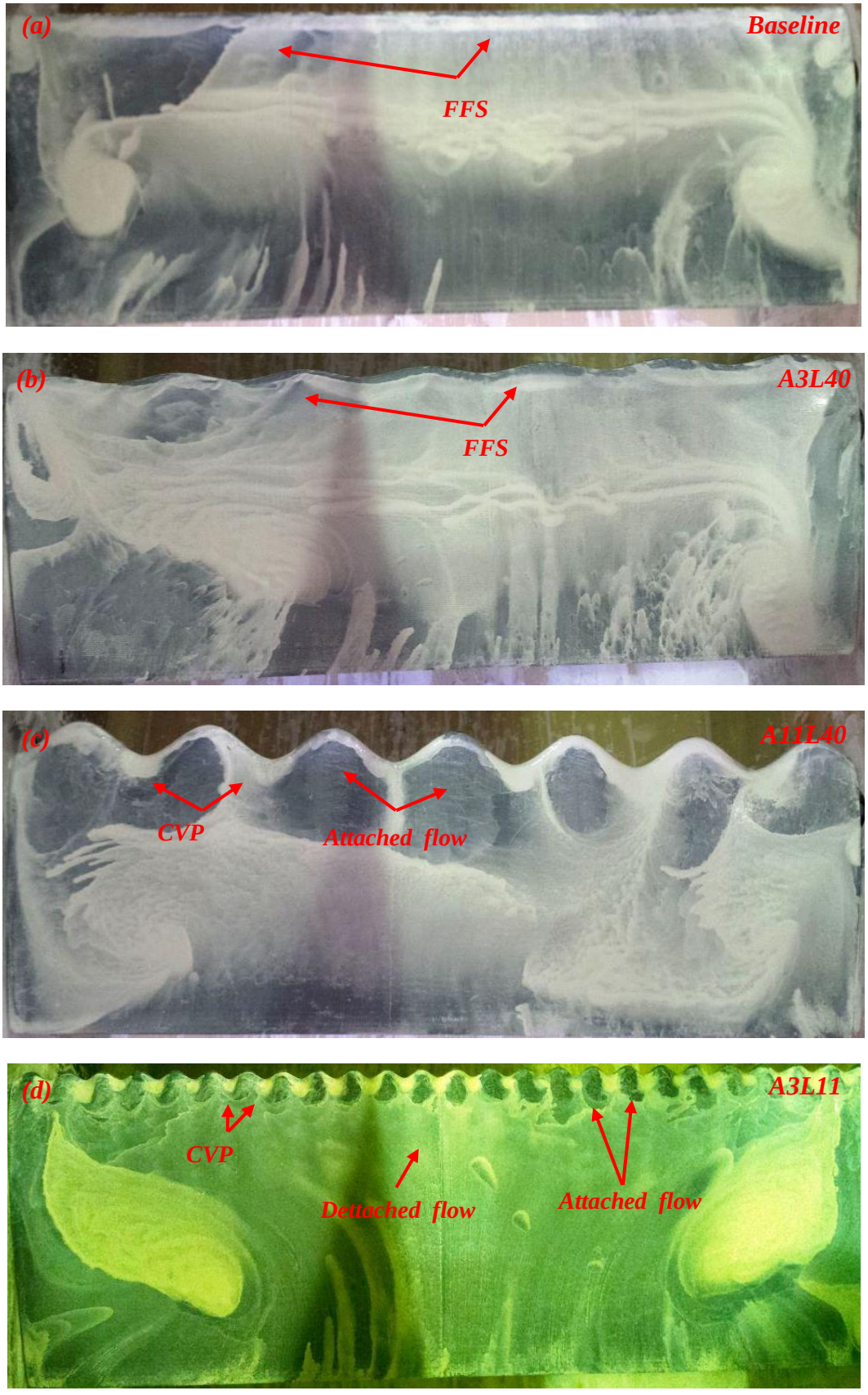

Figure 5.29: All configurations at α = 20°and Re = 290,000 (NACA 0012).

5.2.2 Wavy leading edge effect on NACA 0020 airfoil at Re = 290,000

The wavy leading edge configurations of the medium-thick NACA 0020 airfoil are similar to the thinner NACA 0012 airfoil , with the flow topology changing from a two-dimensional laminar bubble distribution for the smooth airfoil to a bi-periodic three-dimensional laminar separation bubble distribution along the span, depending on leading edge geometry and angle of attack.

At an angle of attack of 0°, the smooth configuration (fig.5.30a) holds a two-dimensional laminar bubble distribution. A short laminar separation bubble (L_B = 0.24c) separates at 0.37c from the leading edge. As for the NACA 0012 airfoil at the same angle of attack, configuration A3λ40 (fig.5.30b) presents wavy edges at the separation points along the span (quasi-two-dimensional LSB).

Configuration A11λ40 (fig.5.30c) shows a complex bi-periodic three-dimensional flow structure where laminar bubbles appear downstream of the troughs in a forward position, whereas bubbles downstream of the peaks occur at a more rearwards chordwise position, at near mid-chord location. Configuration A3λ11 (fig.5.30d) presents bubbles only downstream from tubercle troughs with length and position of respectively L_B =26%c and X_S =24%c. Additionally, the laminar bubbles present elongated characteristics.

At an angle of attack of 5°, the bubbles tend to move forward and to decrease in length. Whilst the baseline configuration (fig.5.31a) has a short separation bubble with length 0.19c and chordwise position 0.20c along the entire airfoil span, configuration A3λ40 (fig.5.31b) establishes a short bubble (L_B =0.15c) downstream of the troughs located at a more forward position (X_S =0.12c) and, downstream of the peaks, a very short bubble (L_B = 0.02c) occurs at position X_S =0.18c. In this configuration, the bubbles at troughs and peaks are aligned.

On the other hand, configurations A11λ40 (fig.5.31c) and A3λ11 (fig.5.31d) present laminar bubbles only downstream of the troughs, where the larger amplitude configuration establishes a short laminar bubble (L_B = 0.12c) very close to local leading edge (X_S =0.12c). Moreover, configuration A3λ11 maintains the trend seen at $\alpha = 0^{\circ}$, presenting an elongated laminar bubble (L_B = 0.15c) located at X_S = 0.08c.

Configurations A11λ40 and A3λ11 also undergo trailing edge separation onset just below α = 5º. For the larger amplitude configuration, a delta-shaped separation appears at the trailing edge, anticipating the flow separation downstream of the troughs, confirming the tendency observed in mini-tuft visualizations. This "delta-shaped" trailing edge flow separation was identified by Rostamzadeh et al. (2014). In the larger amplitude configuration, an extended flow separation area reaching 16% of chord is observed. In contrast, configuration A3λ11 presents a wavy line of separated flow very close to the trailing edge, evidencing the earlier onset of flow separation downstream of the peaks.

At an angle of attack of 10º, the laminar separation bubbles continue decreasing in length for all configurations, moving forwards and reaching the leading edge in all cases but the smooth configuration. The later (fig.5.32a) establishes a very short laminar bubble with a length of 4%c, with separation point at X_S = 9%c. Flow separation at the trailing edge is visible at α = 10º, confirming the mini-tuft visualizations and justifying a decrease in the lift curve slope at this angle of attack (figure 4.22).

Configuration A3λ40 (fig.5.32b) also show three-dimensional laminar separation bubbles downstream of the peaks. However, the bubbles form a curved line behind peaks, differently from the straight separation line observed at α = 5º. In addition, this flow pattern triggers the delta-shaped trailing edge separation structure achieving 28% of chord.

The trailing edge separation moves towards leading edge for configurations A11λ40 (fig.5.32c), establishing a massive flow separation at troughs and preserving flow attached at peaks, thus intensifying the delta-shaped trailing edge separation structure. The larger amplitude configuration has the largest trailing edge separation area for all wavy configurations. In contrast, configuration A3λ11 (fig.5.32d) maintains a wavy separation line at the trailing edge, where flow separation is amplified at peaks. The figures show clearly that tubercles cause increase in trailing edge flow separation, and increasing the tubercle amplitude implies an increase of the separated area.

At an angle of attack of 15º, the trailing edge flow separation characterizes the flow topology for all configurations in different ways. The laminar separation bubble, however, remains close to the leading edge in all cases.

The smooth configuration (fig.5.33a) has a very short laminar bubble (L_B = 0.03c) very close to the leading edge (X_S = 0.04c). In addition, the trailing edge flow separation area increases, covering 40% of trailing edge in chord.

Configuration A3λ40 (fig.5.33b) extends the delta-shaped flow separation pattern; the separations observed at α = 10º grow into two massive separation cells which appear asymmetrically over the profile: one at mid-span the other one close to the right wind tunnel wall. The separation cells grow directly from the leading edge troughs.

The larger amplitude configuration (fig.5.33c) undergoes the largest flow separation, with a massive separation cell at middle-span covering a large area and approaching the leading edge. Configuration A3λ11 (fig.5.33d) presents the smallest flow separation area achieving the trailing edge at 36% of the chord.

At an angle of attack of 20º, although the smooth configuration (fig.5.34a) still presents a very short laminar bubble (L_B = 0.01c) at the leading edge (X_S = 0.01c), flow separation occurs just aft of the bubble reattachment point, keeping small areas of attached flow along the leading edge. This observation agrees with mini-tuft visualizations and justifies a significant lift drop after the stall angle (figure 4.22).

Configuration A3λ40 (fig.5.34b) presents a similar behaviour compared to the smooth configuration, also keeping small attached areas of flow between the reattachment point and the flow separation line. However, larger areas of attached flow close to wind tunnel wall (right border) explain the smaller lift drop as compared to the baseline configuration at the stall condition.

In contrast, vortical structures appear at the leading edge between peaks for the larger amplitude configuration (fig.5.34c), which are responsible for preserving the flow attached downstream of the peaks down to 25% of chord therefore guaranteeing soft post-stall characteristics (figure 4.22).

Configuration A3λ11 (fig.5.34d) holds the smallest flow separation area at α = 20º, with short laminar bubbles at tubercle troughs, and shows two separation cells, one at middle span and the other close the right tunnel wall. These flow characteristics establish a soft stall and high maximum lift value (figure 4.22). The figure 5.34d presenting three-dimensional bubbles at the leading edge and significant attached flow areas states a new flow control

mechanism at post-stall regime distinct from vortical structures indicates by previous researchers.

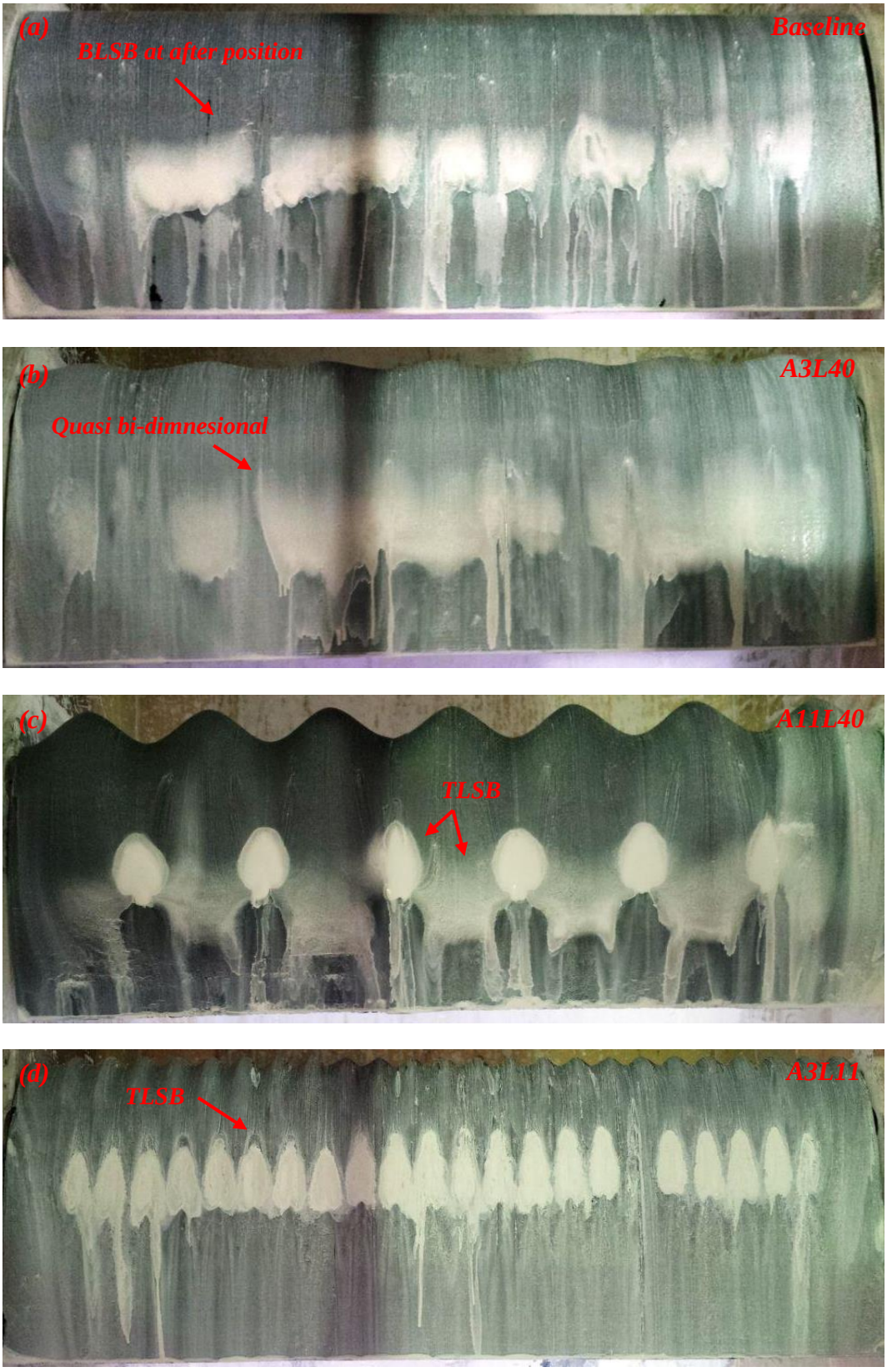

Figure 5.30: All configurations at α = 0°and Re = 290,000 (NACA 0020).

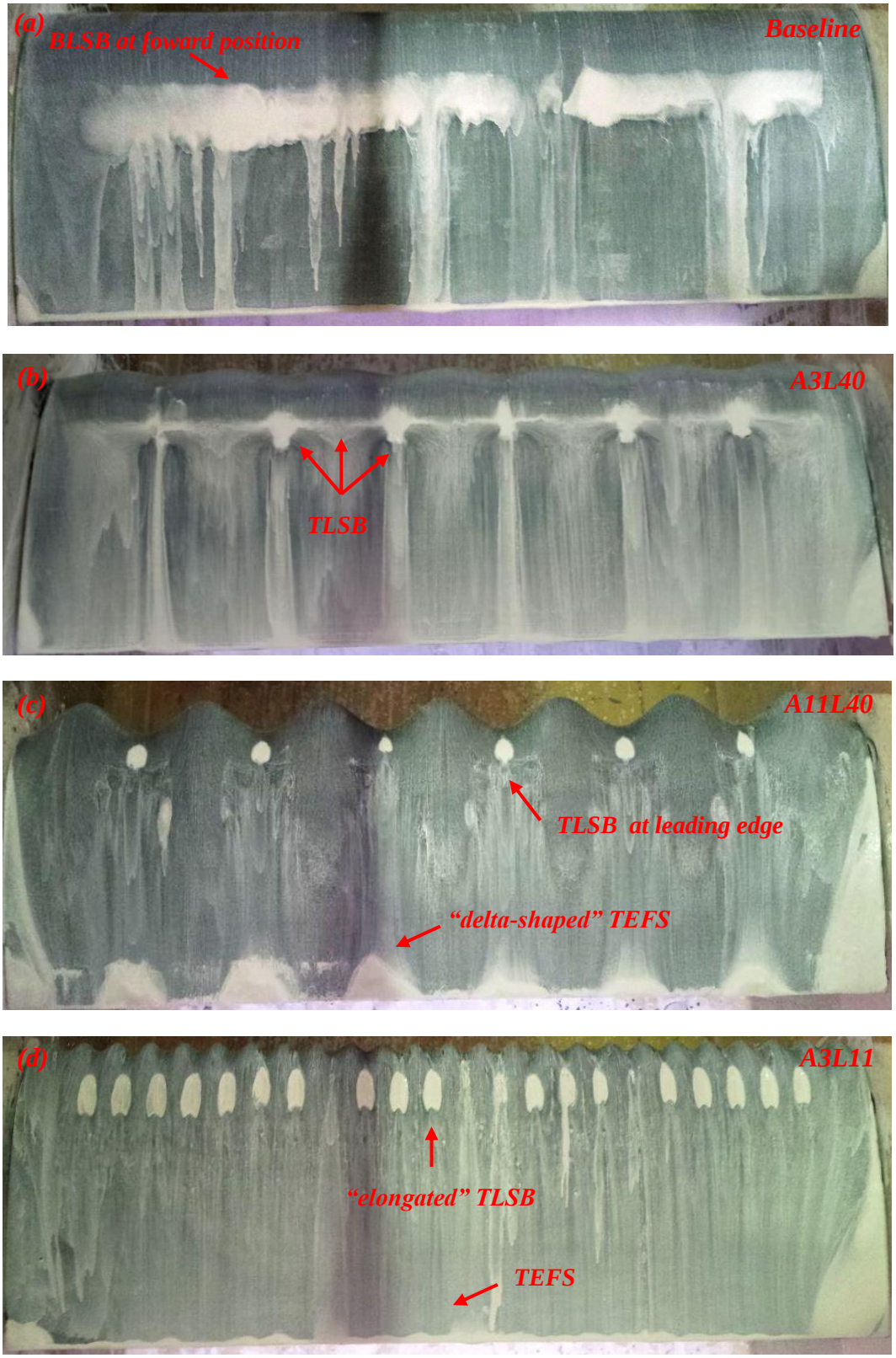

Figure 5.31: All configurations at α = 5°and Re = 290,000 (NACA 0020).

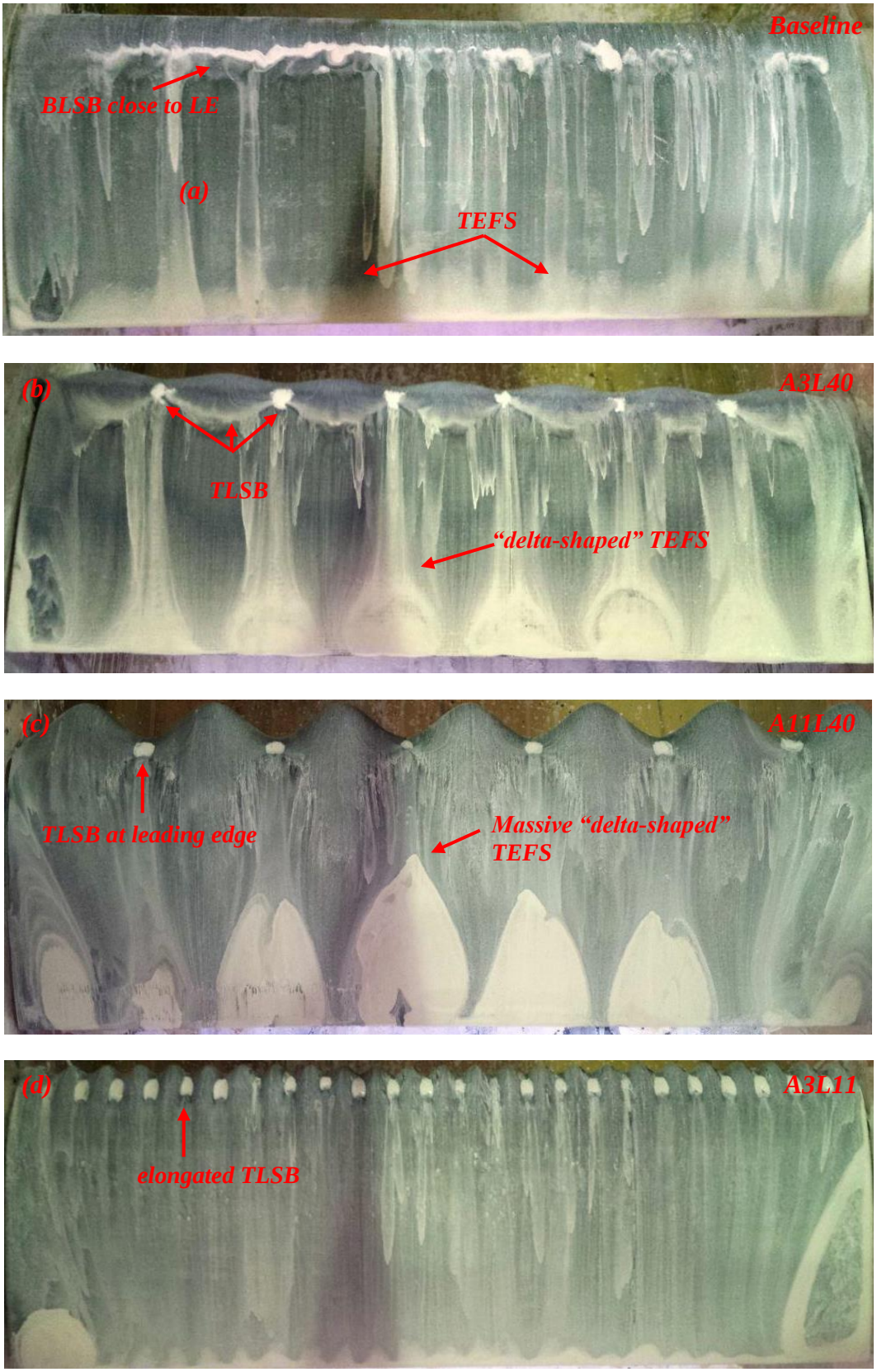

Figure 5.32: All configurations at α = 10°and Re = 290,000 (NACA 0020).

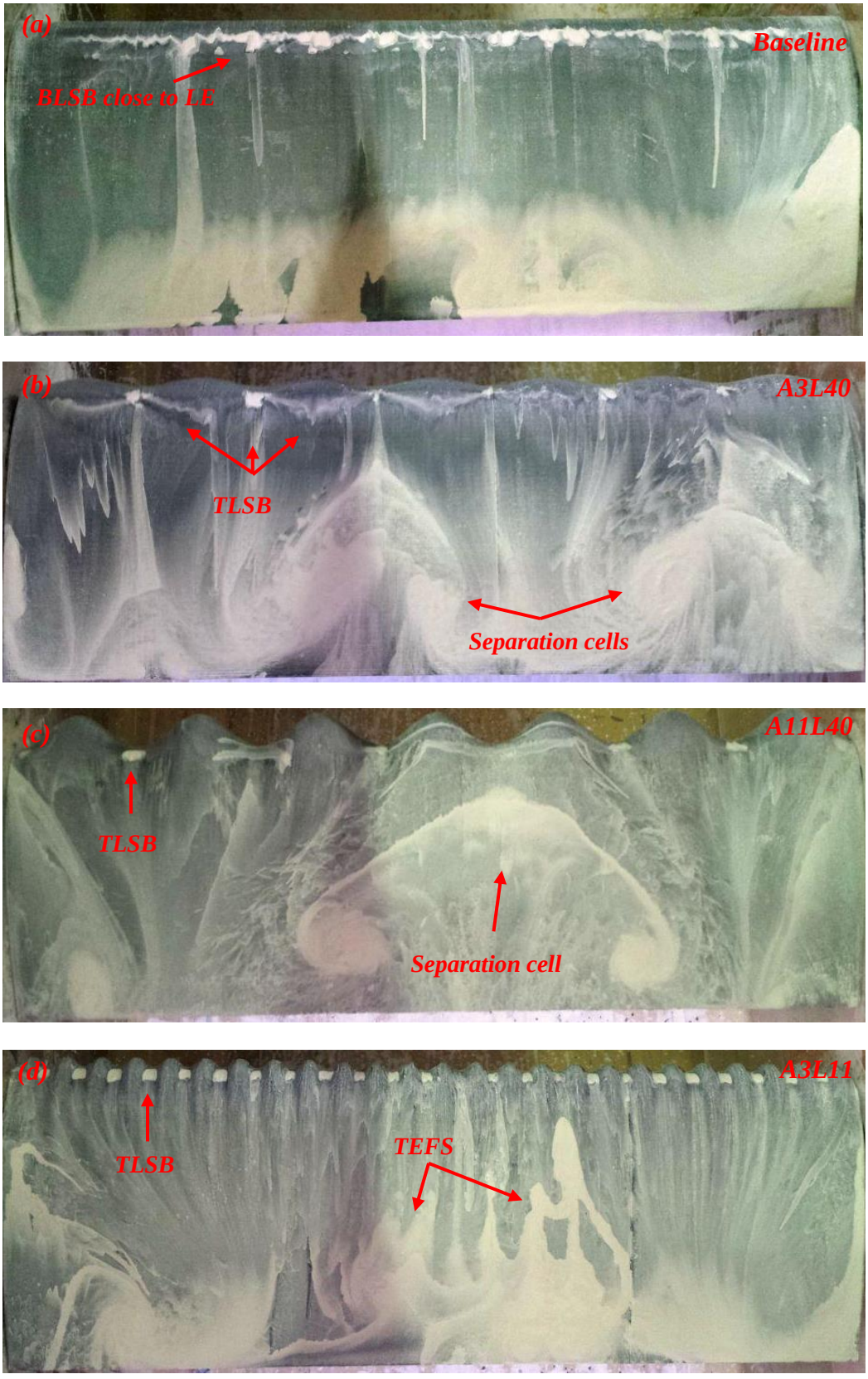

Figure 5.33: All configurations at α = 15°and Re = 290,000 (NACA 0020).

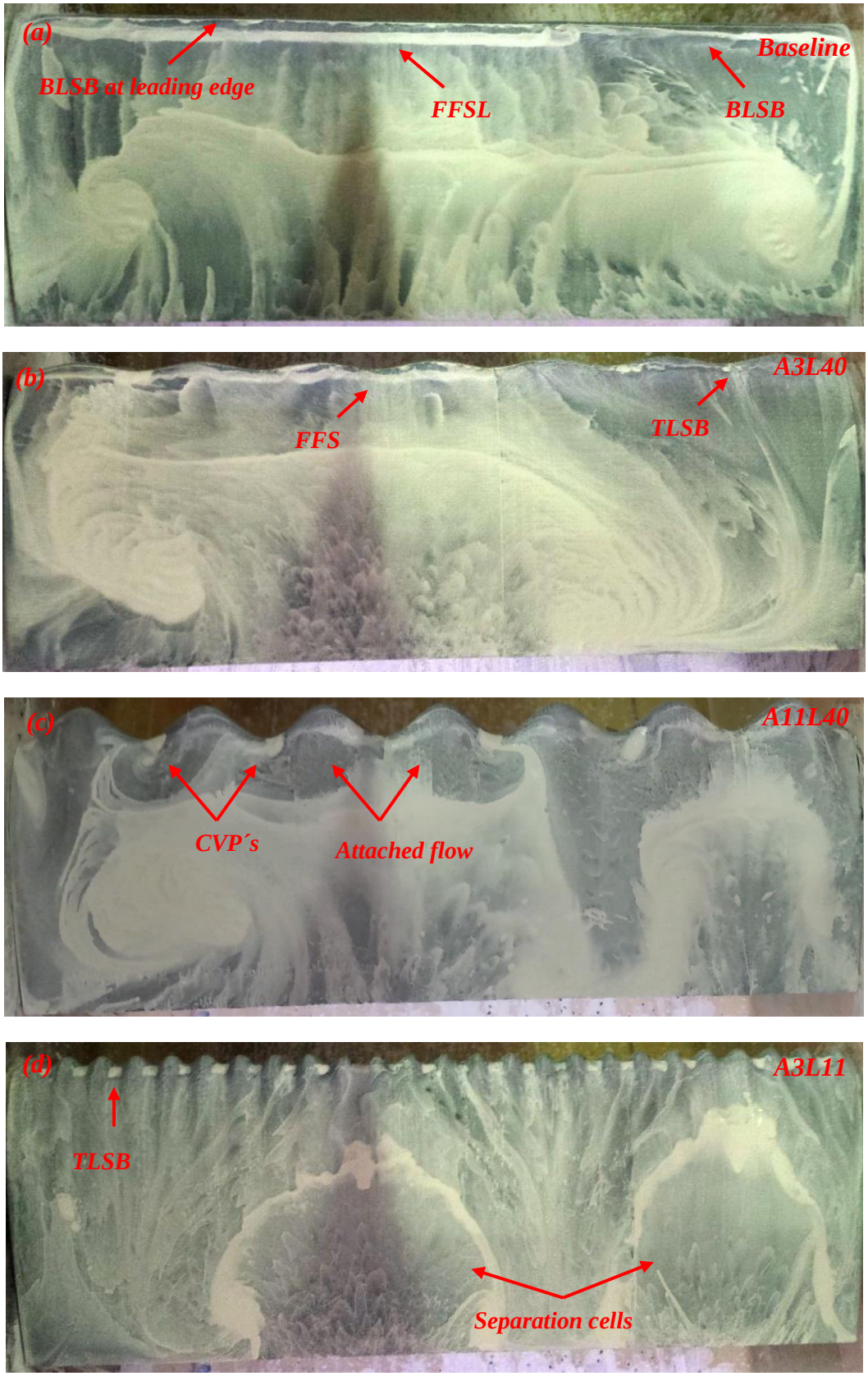

Figure 5.34: All configurations at α = 20°and Re = 290,000 (NACA 0020).

5.2.3 Wavy leading edge effect on NACA 0030 airfoil at Re = 290,000

At an angle of attack of 0°, the smooth configuration (fig.5.35a) presents a short laminar separation bubble at 0.29c from the leading edge with a length of 0.21c along the entire span, keeping flow at the trailing edge fully attached.

In contrast, configuration A3λ40 (fig.5.35b) shows a bi-periodic three-dimensional laminar bubble distribution along the span. The laminar bubbles formed downstream of the troughs move forward to 0.22c with length of 0.32c whereas the shorter bubbles formed downstream of the peaks reach more aft positions at 0.36c and a length of 0.09c. Although the flow topology undergoes a drastic change when compared to smooth configuration, the flow at trailing edge still remains attached.

Configuration A11λ40 (fig.5.35c) presents some differences in terms of the laminar bubble distribution along the span when compared to configuration A3λ40. The bubbles are not anymore aligned along the span and an additional bubble occurs downstream from bubbles formed behind peaks. The laminar bubbles downstream of the peaks reaches X_s = 0.42c and with a L_B = 0.1c whereas bubbles downstream of the troughs reaches X_s = 0.21c with a L_B = 0.16c. The additional bubbles appear at 0.59c from leading edge with length of 0.09. These flow characteristics point out to a possible boundary layer relaminarized.

Differently from configuration A3λ40, the greater amplitude configuration (fig.5.35c) presents trailing edge flow separation even at the angle of attack 0° following a delta-shaped pattern, with the flow starting to separate downstream of the troughs similar to wavy NACA 0020 airfoils.

Configuration A3λ11 (fig.5.35d) presents elongated short bubbles downstream of the troughs and an absence of bubbles downstream of the peaks. The laminar bubble starts 0.12c from leading edge with length of 0.22c. In addition, the configuration shows the trailing edge flow separation onset, with larger flow separation areas downstream of the peaks (differently from longer wavelength configurations, which tend to have extended separated areas downstream of the troughs) confirming the tendency already seen on the NACA 0020 airfoil.

At an angle of attack of 10°, the trailing edge flow separation with distinct three-dimensional characteristics for each of tubercle geometries, as noticed for the NACA 0020 airfoil, is observed. The smooth configuration (fig.5.36a) still presents a laminar bubble

(X_s=0.20c, L_B =0.18c) along full span. Additionally, the trailing edge presents flow separation at 22%c continuously along the span.

Configuration A3λ40 (fig.5.36b) presents a bubble distribution along span similar to α = 0º. However, the bubbles downstream of the peaks (X_s = 0.2c, L_B =0.02c) and troughs (X_s =0.10, L_B =0.16) move towards the leading edge. In contrast with the lower angle of attack case, trailing edge flow separation occurs forming a bi-periodic delta structure.

For the case of configuration A11λ40 (fig.5.36c), a very short laminar bubble is established at the trough close to the local leading edge (X_s =0.13, L_B =0.09), and a curved laminar bubble distribution occurs downstream of the peaks. Strong flow separation areas in delta-shaped structures appear at the trailing edge, forming the widest separation area of all configurations.

The elongated bubbles presented by configuration A3λ11 (fig.5.36d) reach the leading edge (X_s =0.15, L_B =0.06) at troughs. Besides, the trailing edge flow separation keeps growing with increased angle of attack.

At an angle of attack of 20º, the baseline configuration (fig.5.37a) still possesses a laminar bubble preserving the flow attached (X_s=0.02c, L_B =0.01c) in a narrow strip along the entire leading edge guaranteeing high lift values even at α = 20° . Downstream of the leading edge, a full separation line (X_S =0.08c) triggers a three-dimensional flow separation over the remaining surface of the airfoil.

The flow topology for configuration A3λ40 (fig.5.37b) is similar to the smooth configuration, with a laminar bubble distribution over the entire leading edge but at troughs where the bubble vanishes. The flow separation downstream of the laminar bubbles forms a curved line along the span, preserving areas of attached flow downstream of the peaks.

Configuration A11λ40 (fig.5.37c) retains flow similarity to the α = 10° case at the leading edge. However, in this case flow separation occurs over entire airfoil downstream from laminar bubble distribution.

For the configuration A3λ11 (fig.5.37d), elongated bubbles at the leading edge with decreased length occurs. A massive separation cell centered at mid-span extends all the way to the leading edge and over a significant portion of the trailing edge. However, this

configuration comparatively has the largest attached flow area in comparison to the other wavy configurations, thus justifying the highest lift values (figure 4.40).

At an angle of attack of 25º, the smooth configuration (fig.5.38a) has a very short laminar bubble over entire leading edge (X_s=0.00c, L_B =0.01c). However, the flow undergoes an immediate turbulent reattachment, followed by a separation over almost the total leading edge span aside from the very left side near the wind tunnel wall, characterizing the onset of an abrupt stall as evidenced by the lift curve (figure 4.40). Configuration A3λ40 (fig.5.38b) presents similar flow topology to α = 20º with greater attached flow areas at the leading edge as compared to the smooth configuration; as consequence, this geometry presents higher lift values (figure 4.40).

The larger amplitude configuration (fig.5.38c) shows a combination of three-dimensional laminar bubbles and vortical structures at the leading edge which prevent flow separation downstream of the peaks. The configuration with smaller amplitude and wavelength (fig.5.38d) presents two large massive cells. Interestingly, even at α = 25º, it has the smallest flow separation area of the configurations, which is reflected in the soft stall behaviour and the highest maximum lift value recorded, warranting the best wavy lift performance (figure 4.40). At the leading edge, elongated bubbles still are present on troughs working as an efficient flow control mechanism similar to the shorter wavelength configuration on the NACA 0020 airfoil.

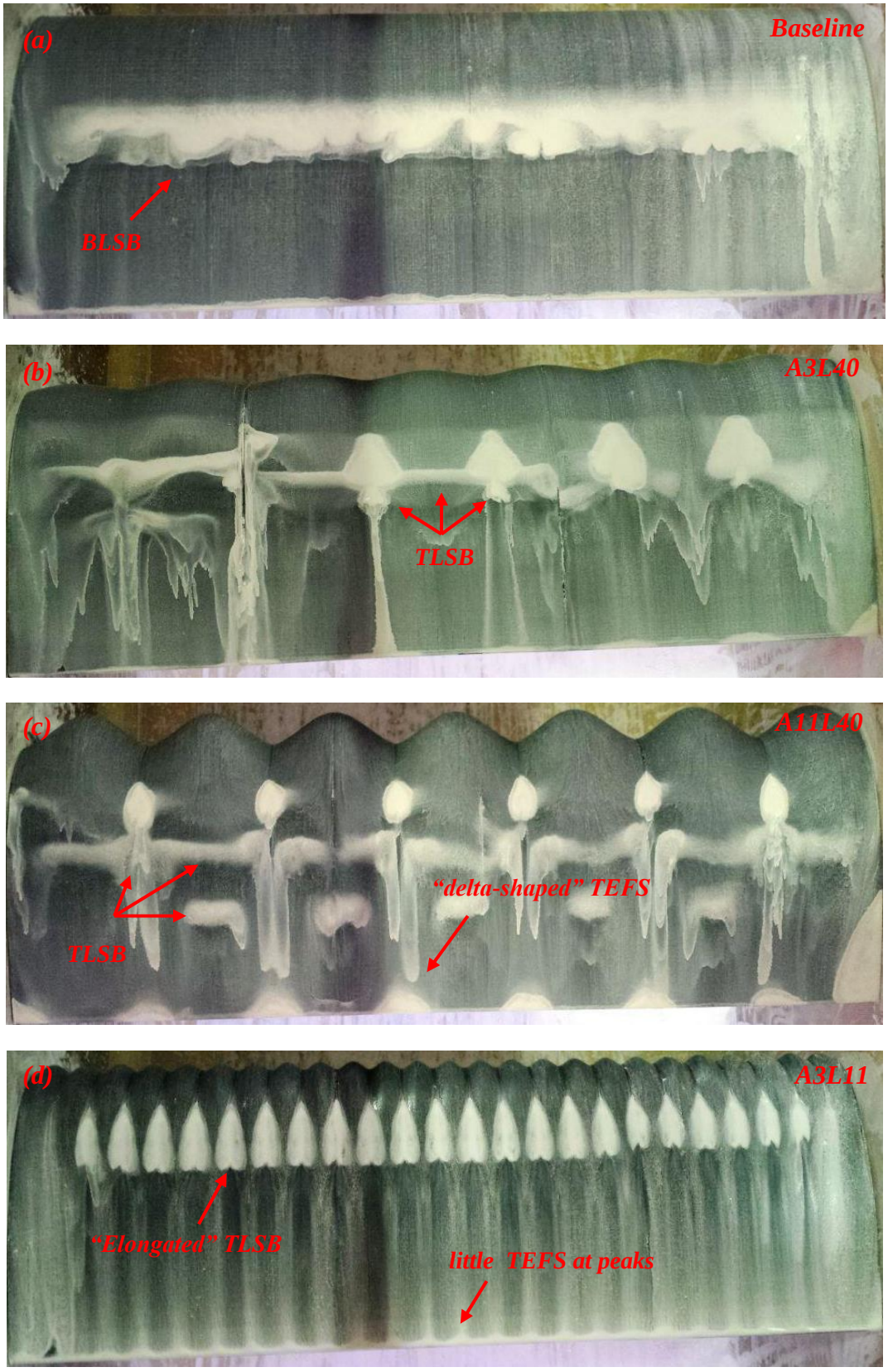

Figure 5.35: All configurations at $\alpha = 0°$and Re = 290,000 (NACA 0030).

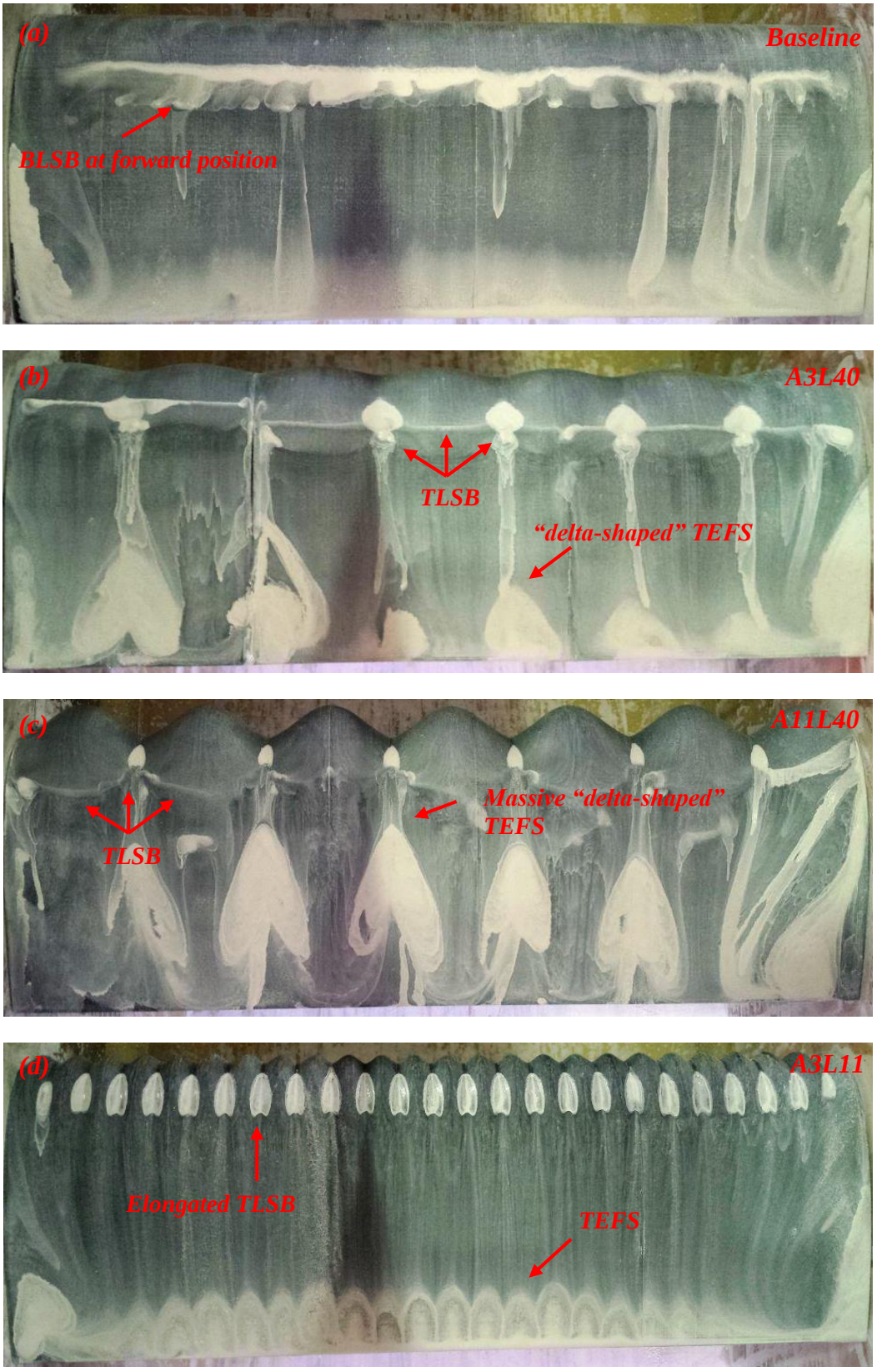

Figure 5.36: All configurations at α = 10°and Re = 290,000 (NACA 0030).

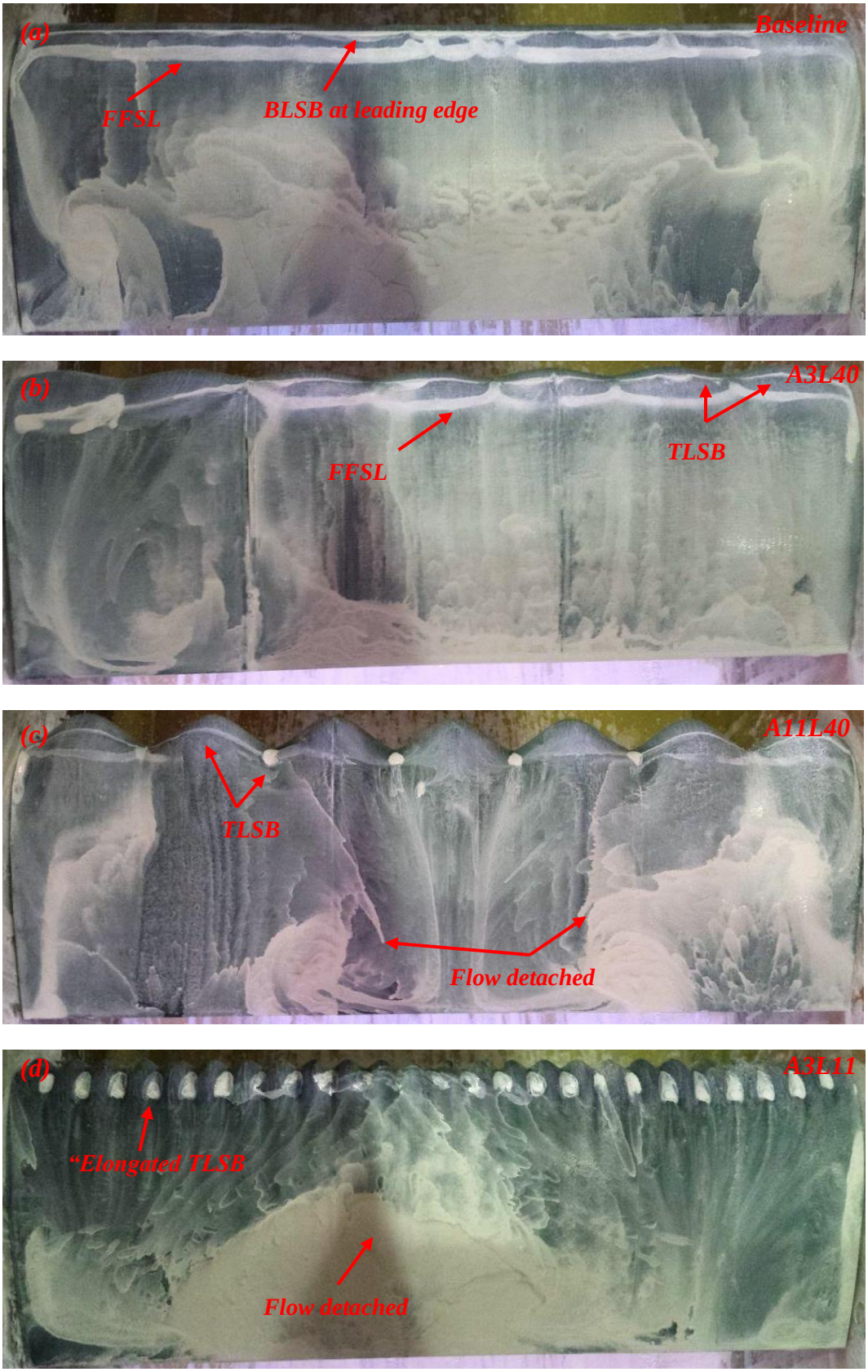

Figure 5.37: All configurations at α = 20°and Re = 290,000 (NACA 0030).

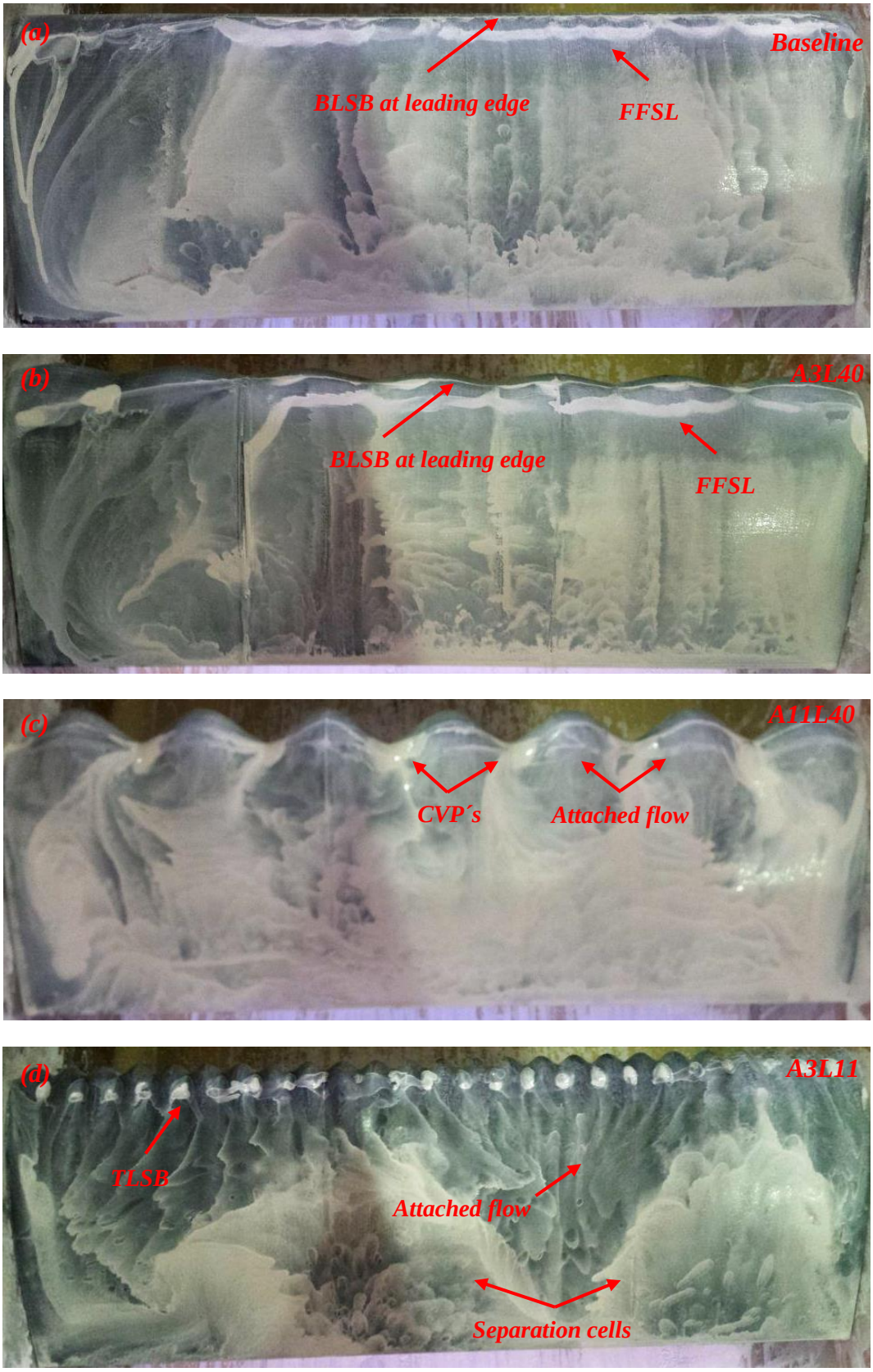

Figure 5.38: All configurations at α = 25°and Re = 290,000 (NACA 0030).

5.2.4 Wavy leading edge effect on NACA 0030 airfoil at Re = 120,000

At Reynolds number 120,000, as previously discussed in the chapter four, the wavy leading configuration A3λ11 reaches an impressive aerodynamic performance, keeping the linearity of aerodynamic lift curve up to higher angle of attack ($\alpha = 16°$), reaching a sizeable increase in maximum lift coefficient when compared to smooth configuration (figure 4.45). Figures 5.39 and 5.40 present the flow mechanisms responsible for the higher efficiency for this specific wavy configuration.

At $\alpha = 5º$, the smooth configuration (fig.5.39a) presents a two-dimensional laminar separation bubble distribution along the span whereas configuration A3λ11 (fig.5.39b) shows a typical distribution for the shorter wavelength configuration, thus establishing a three-dimensional bi-periodic structure with the presence of elongated bubbles downstream of the troughs; the bubbles stand in close proximity to each other. The three-dimensional bubble distribution is located closer to the leading edge as compared to the smooth configuration; the bubble lengths of both configurations are comparable. Besides, both configurations have the flow attached over entire upper airfoil surface. Thus, at the angle of attack 5º, both smooth and wavy configurations present similar lift coefficients (figure 4.45).

On the other hand, at an angle of attack of 15º, the flow topologies of both configurations are quite distinct from each other. The baseline configuration (fig.5.40a) presents flow separation near leading edge along the entire span without reattachment, characterizing fully separated flow over virtually the entire airfoil upper surface. In contrast, configuration A3λ11 (fig.5.40b) maintains a flow similar topology to $\alpha = 5°$, with an attached leading edge which remains working as a high suction region. The configuration indeed has trailing edge flow separation, however 50 % of the chord is able to preserve the flow attached. Therefore, the shorter wavelength configuration works as an efficient flow control mechanism at a Reynolds number of 120,000, similarly to the higher Reynolds condition, but with increased efficiency since the tubercle configuration does not cause early trailing edge flow separation as compared to smooth airfoil in this case, differently from higher Reynolds number conditions.

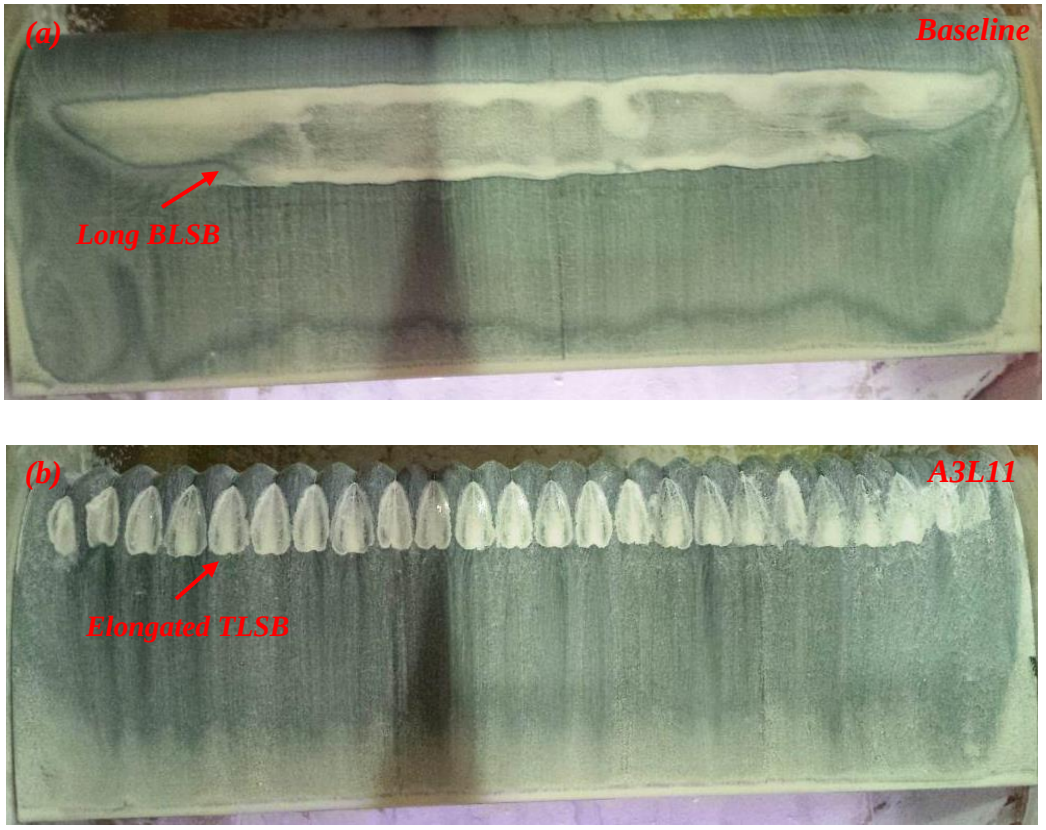

Figure 5.39: Smooth and wavy configurations at α = 5°and Re = 120,000 (NACA 0030).

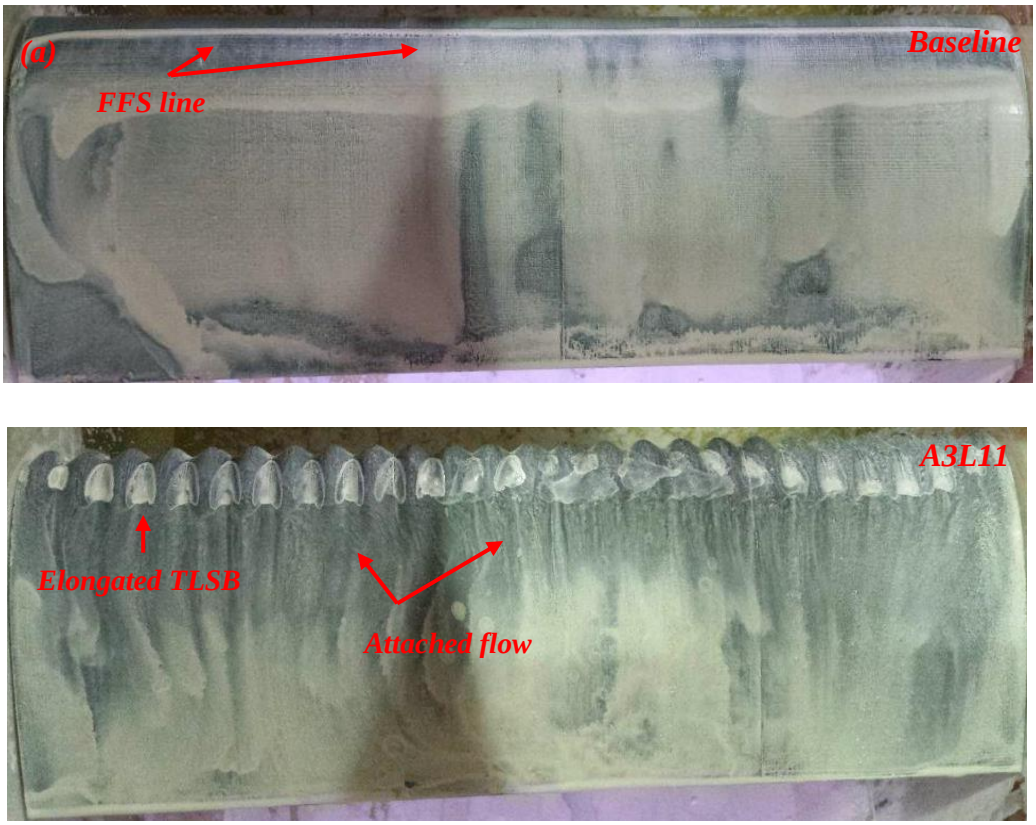

Figure 5.40: Smooth and wavy configurations at α = 15°and Re = 120,000 (NACA 0030).

5.2.5 Wavy leading edge effect at the lowest Reynolds number (Re = 50,000)

In the lowest Reynolds number condition, the smooth NACA 0012 airfoil presents a very long laminar separation bubble at α = 0° (fig.5.41a). Besides, the wavy configurations (fig.5.41b-c-d) present a three-dimensional laminar bubble distribution, similar to higher Reynolds number conditions. In all cases, the flow condition maintains the flow attached over the entire airfoil. The three-dimensional bubble structures present are longer and wider in comparison to higher Reynolds number conditions.

At an angle of attack of 5° (figure 5.42), the laminar bubble distribution shifts towards the leading edge while decreasing in length, reaching the leading edge location at troughs for all wavy configurations; flow is attached downstream of the laminar bubble distribution for all configurations.

At an angle of attack of 10º, the smooth configuration (fig.5.43a) presents flow separation near the leading edge. A very short laminar separation bubble appears at the leading edge, and very close to behind of the bubble formation a full flow separation occurs. The wavy configurations (fig.5.43b-c-d) still present laminar bubble distributions at the leading edge, with the flow attached over entire airfoil.

At an angle of attack of 15°, the smooth (fig.5.44a) and A3λ40 (fig.5.44b) configurations suffer full flow separation at leading edge. On the other hand, configurations A3λ11 (fig.5.44d) and A11λ40 (fig.5.44c) still have laminar bubbles at the troughs with the flow attached in the leading edge region, thus justifying higher lift values and soft behaviour at post-stall conditions (figure 4.11).

The NACA 0020 airfoil undergoes changes in flow characteristics caused by wavy leading edge similar to the thinnest airfoil. At an angle of attack of 0º, the smooth airfoil (fig.5.45a) keeps a very long laminar bubble over entire span. Moreover, for the wavy configurations (fig.5.45b-c-d), the laminar bubble distributions assume very long length and width. With increasing in angles of attack, they decrease size and move towards the leading edge (figure 4.49).

However, at the post-stall condition at α = 8º, the baseline airfoil presents full flow separation at leading edge (fig.5.47a). The wavy configurations (fig.5.47b-c-d) still retain a three-dimensional laminar bubble distribution with the flow attached at the leading edges.

Therefore the wavy airfoils reach higher lift value than smooth configuration for the angle of attack 8º (figure 4.29).

At an angle of attack of 15º (figure 5.48), similarly the NACA 0012 airfoil, configurations A3λ11 and A11λ40 for the NACA 0020 retain laminar bubble structures with attached flow at the leading edges; consequently, they reach higher lift values and soft stall behaviour (figure 4.29).

The thickest NACA 0030 airfoil exhibits fully separated flow even at low angles of attack. This characteristic causes a distinct wavy leading edge effect as compared to thinner configurations.

At an angle of attack of 0°, the smooth (fig.5.49a) and A3λ40 (fig.5.49b) configurations already show fully separated flow at leading edge. On the other hand, the wavy configurations A3λ11 (fig.5.49d) and A11λ40 (fig.5.49c) are characterized by three-dimensional laminar bubble distributions with attached flow over entire airfoil upper surface.

At an angle of attack of 5º, the smooth (fig.5.50a) and A3λ40 (fig.5.50b) configurations show fully separated flow progressing towards the leading edge over the airfoil upper surface whereas at the lower surface a long bubble is found. These characteristics cause significant aerodynamic deterioration on the lift curve with negative values of lift up to α = 10º (figure 5.51).

Configurations A3λ11 (fig.5.50d) and A11λ40 (fig.5.50c) display a flow topology similar to the α = 0° case. However, the three-dimensional laminar distribution progresses towards the leading edge with attached flow areas up to an angle of attack of 10° (figure 5.51). Therefore these configurations of the NACA 0030 profile are significantly more aerodynamically efficient than the smooth and A3λ40 (figure 4.47).

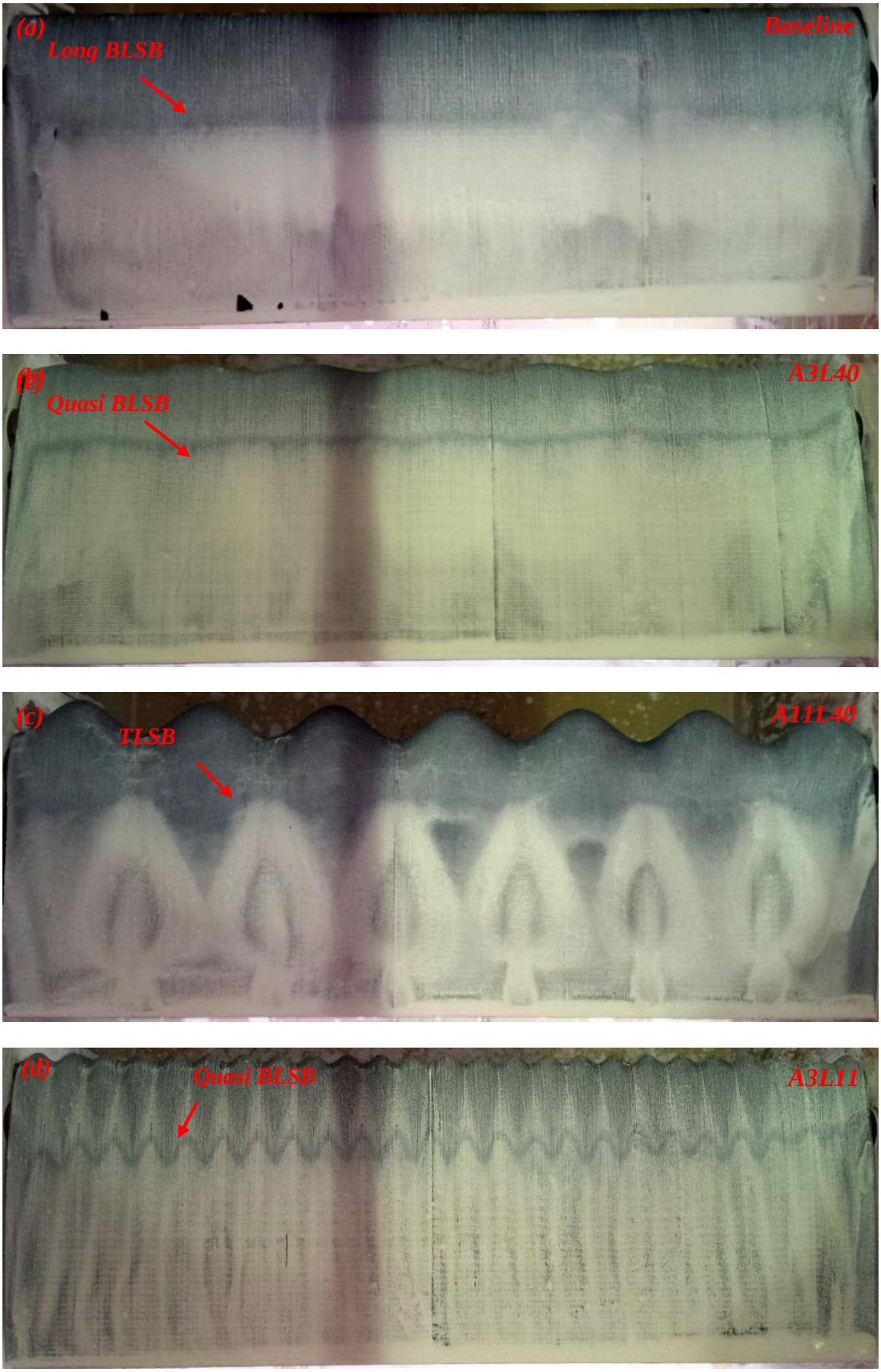

Figure 5.41: All configurations at α = 0°and Re = 50,000 (NACA 0012).

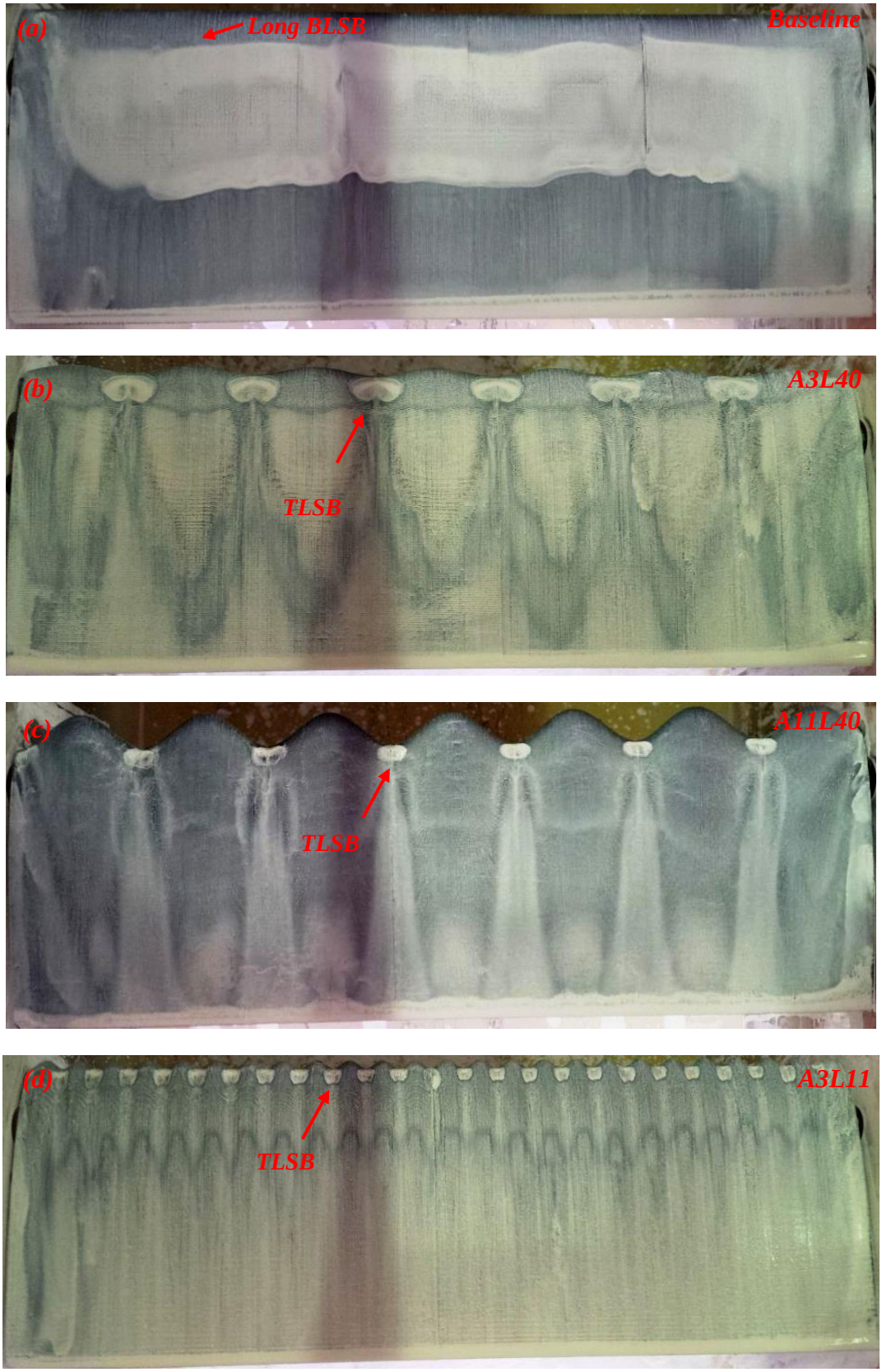

Figure 5.42: All configurations at α = 5°and Re = 50,000 (NACA 0012).

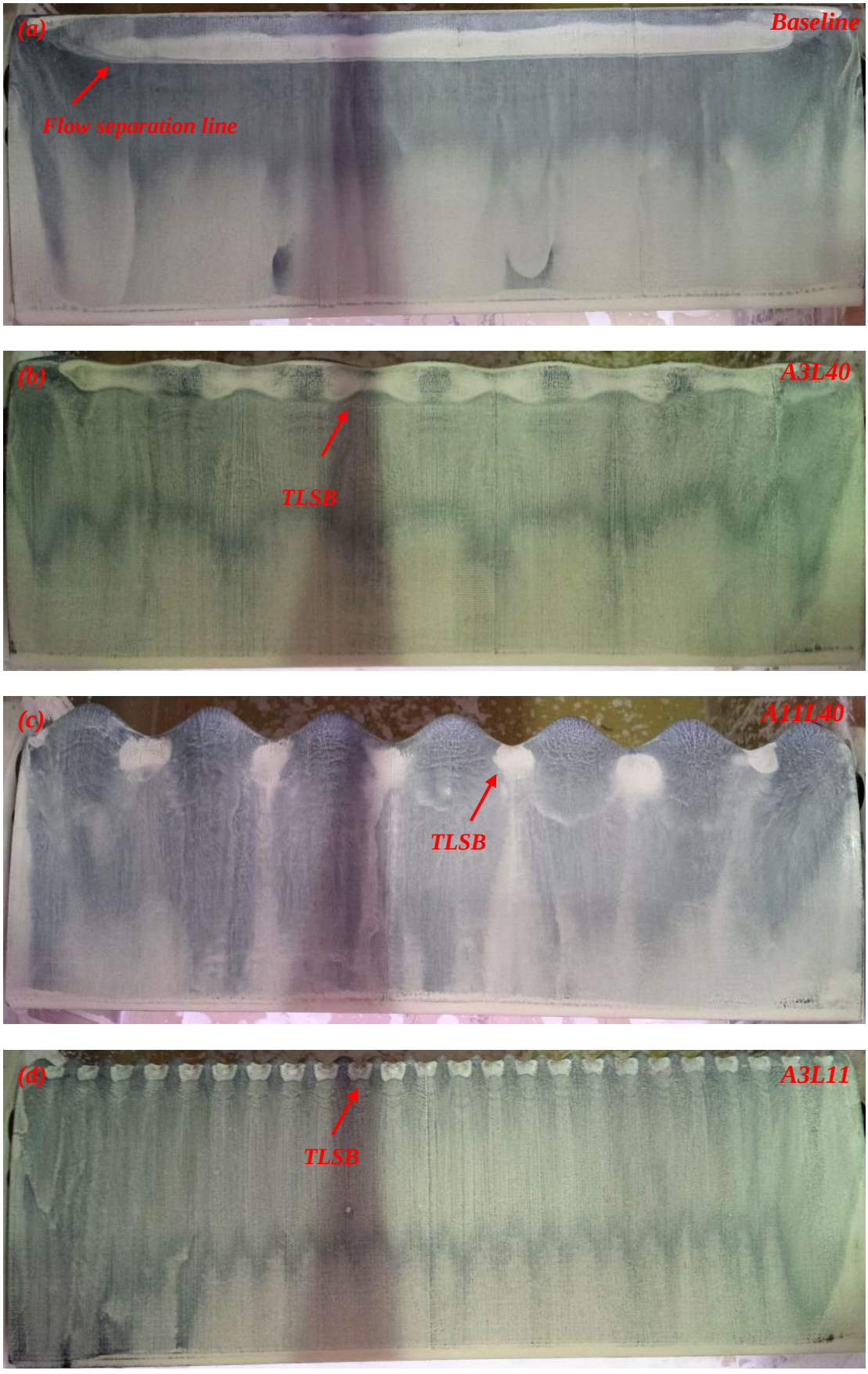

Figure 5.43: All configurations at α = 10°and Re = 50,000 (NACA 0012).

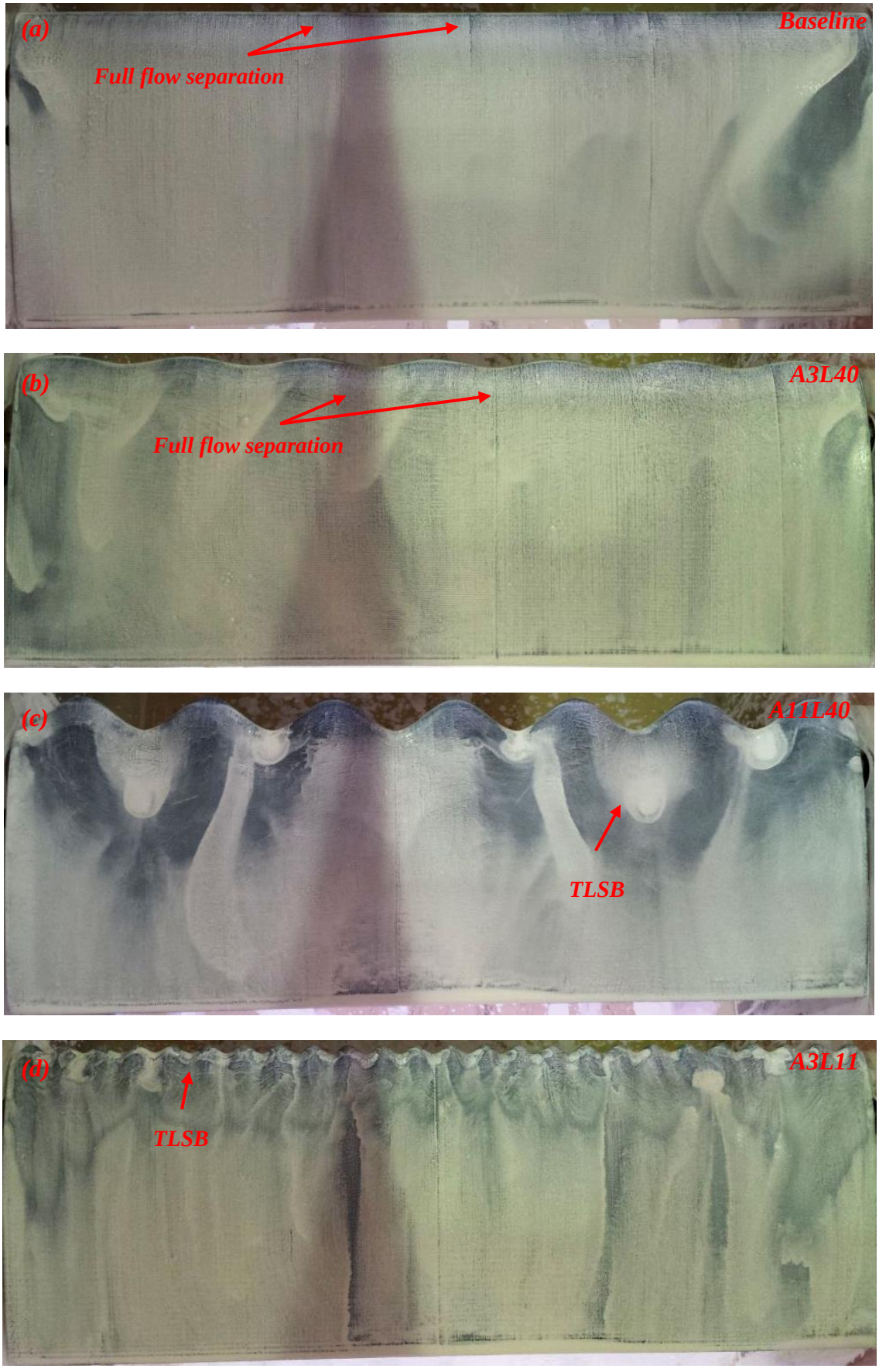

Figure 5.44: All configurations at α = 15°and Re = 50,000 (NACA 0012).

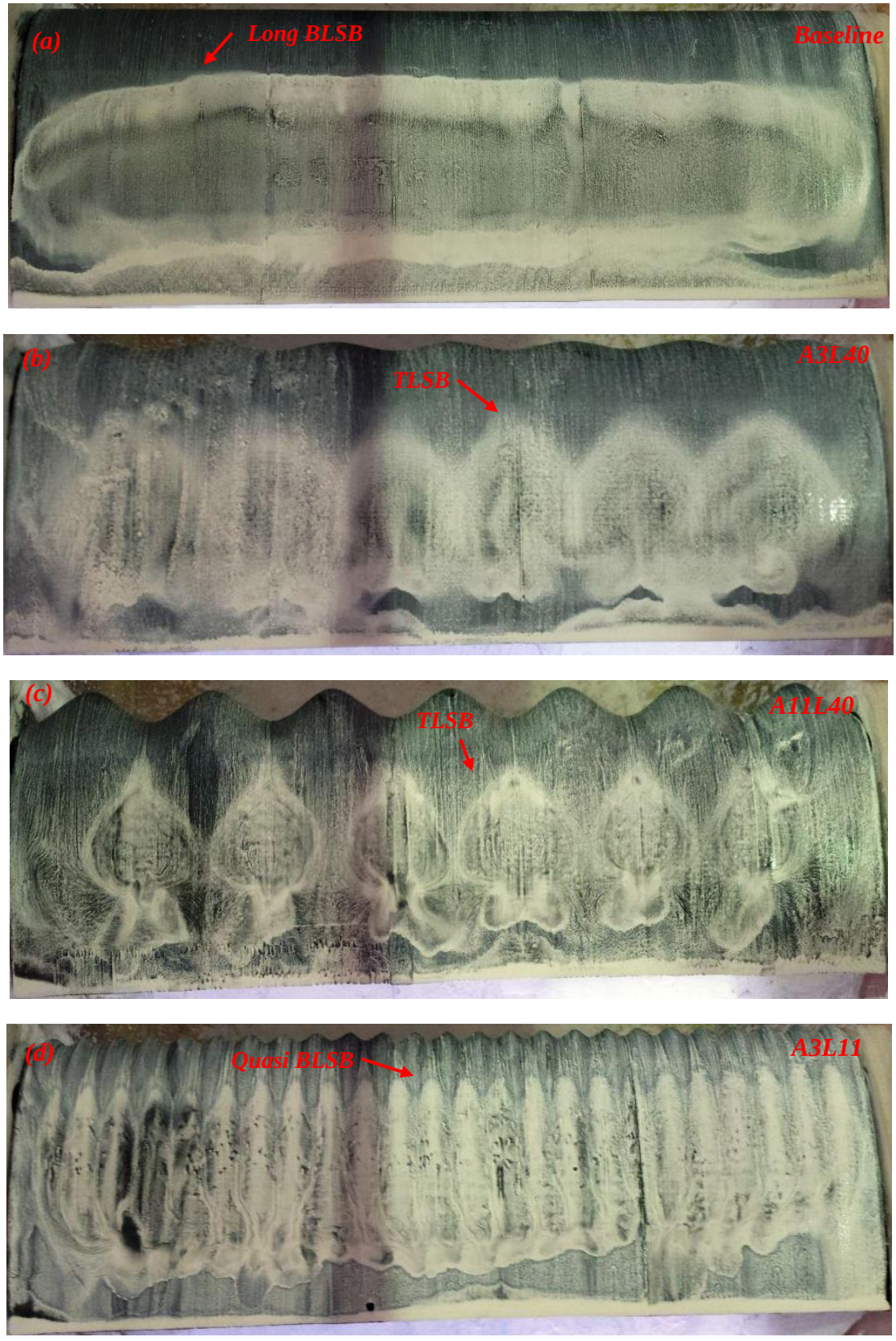

Figure 5.45: All configurations at α = 0°and Re = 50,000 (NACA 0020).

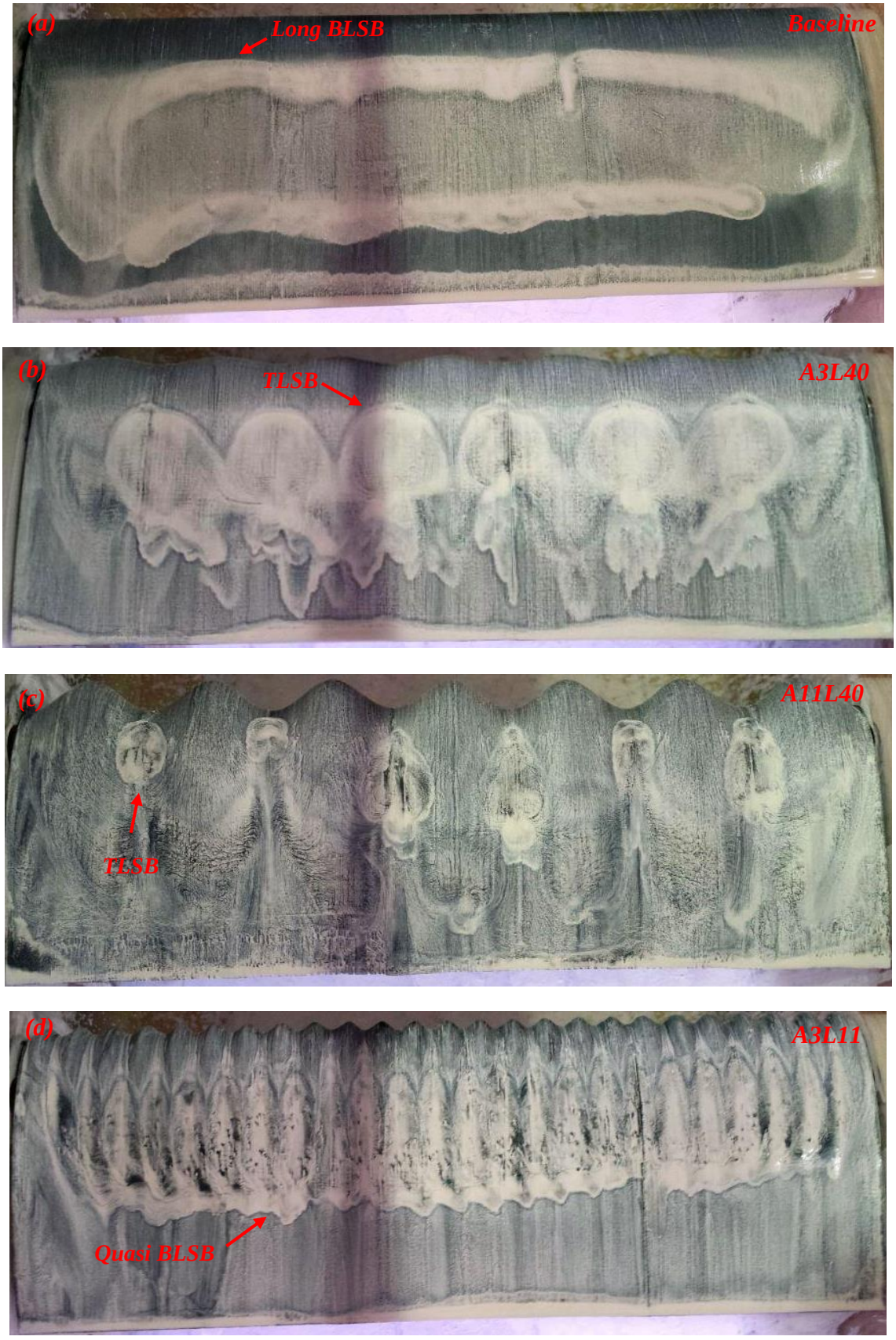

Figure 5.46: All configurations at α = 3°and Re = 50,000 (NACA 0020).

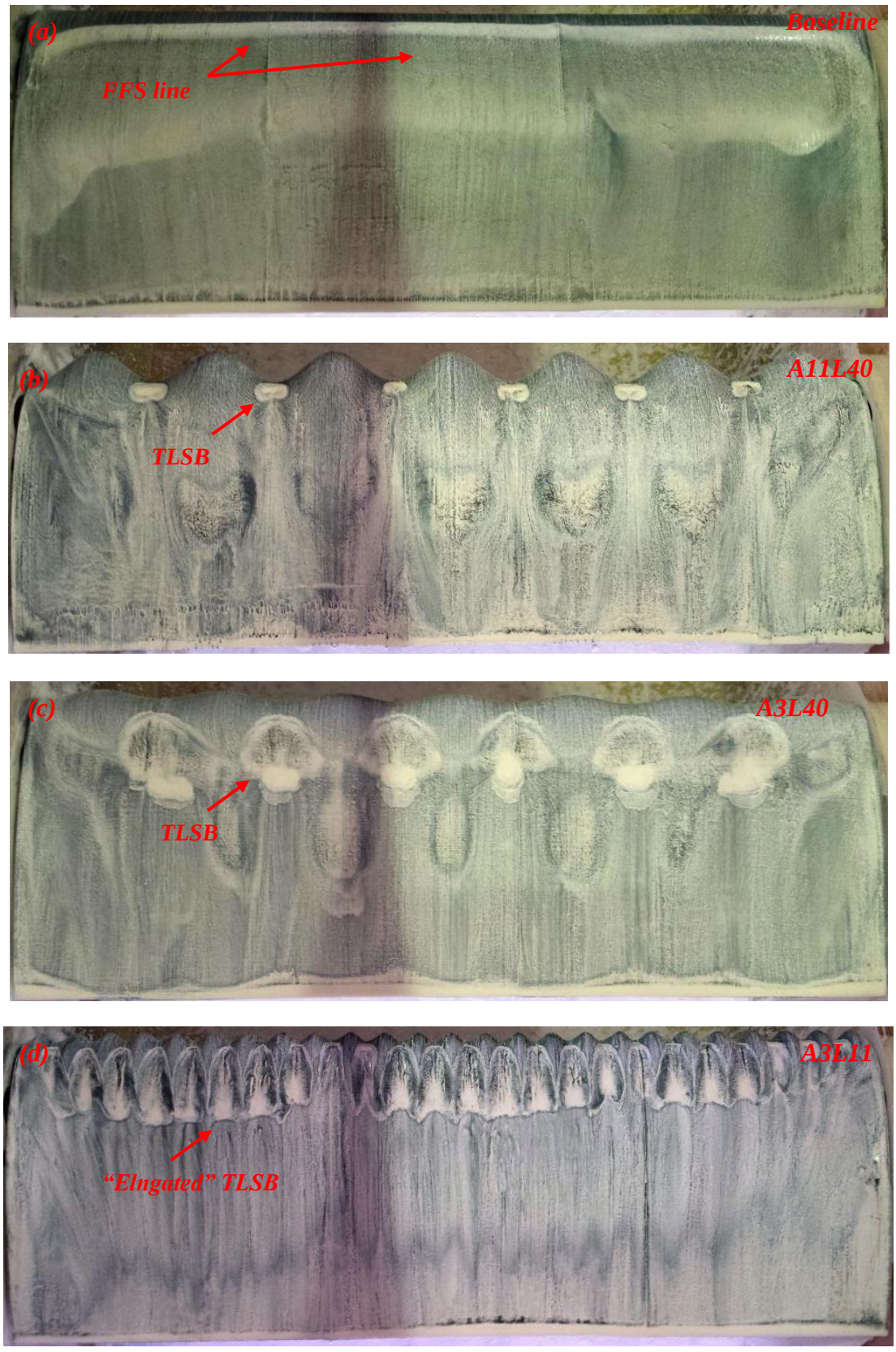

Figure 5.47: All configurations at α = 8°and Re = 50,000(NACA 0020).

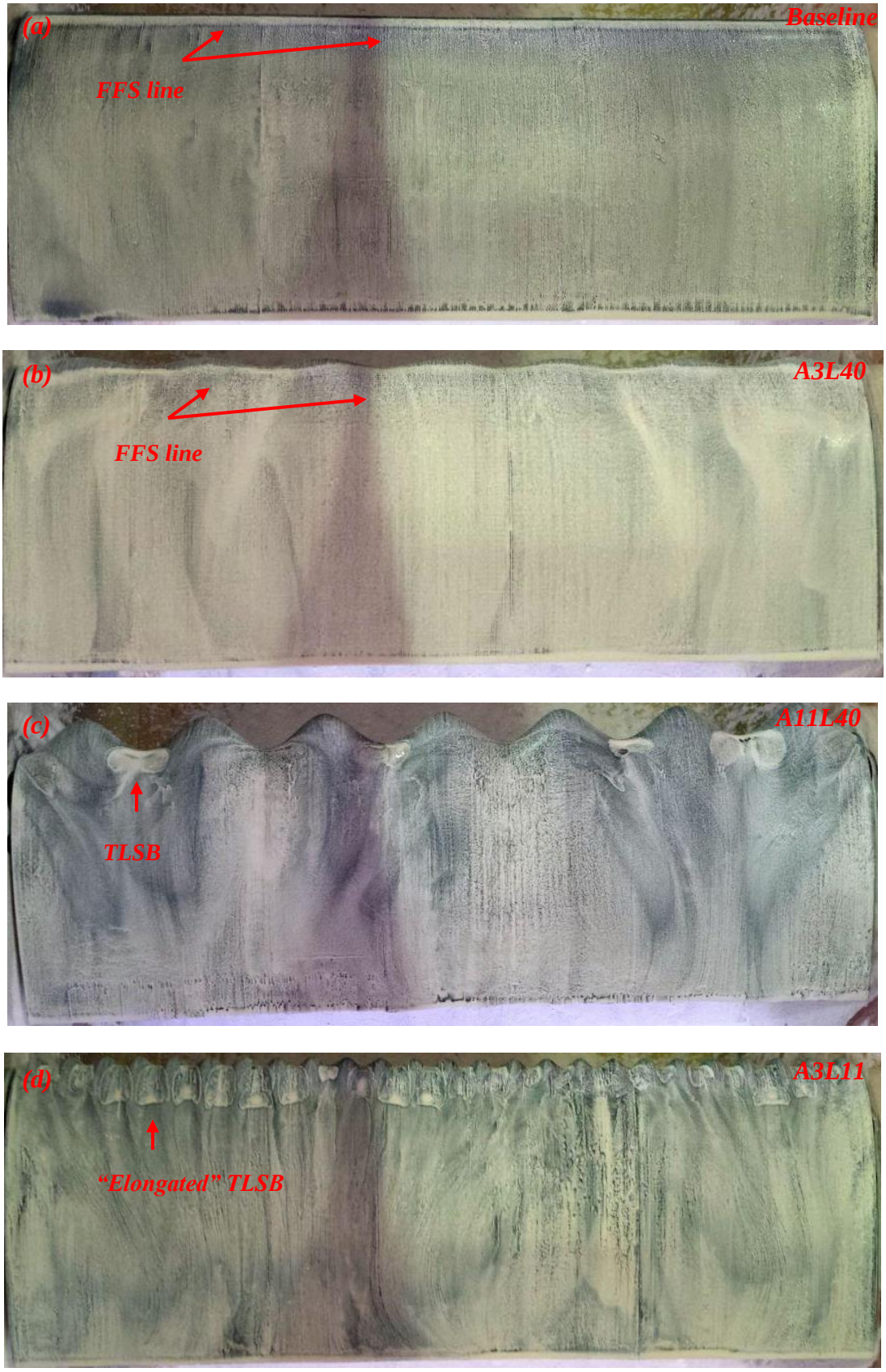

Figure 5.48: All configurations at α = 15°and Re = 50,000 (NACA 0020).

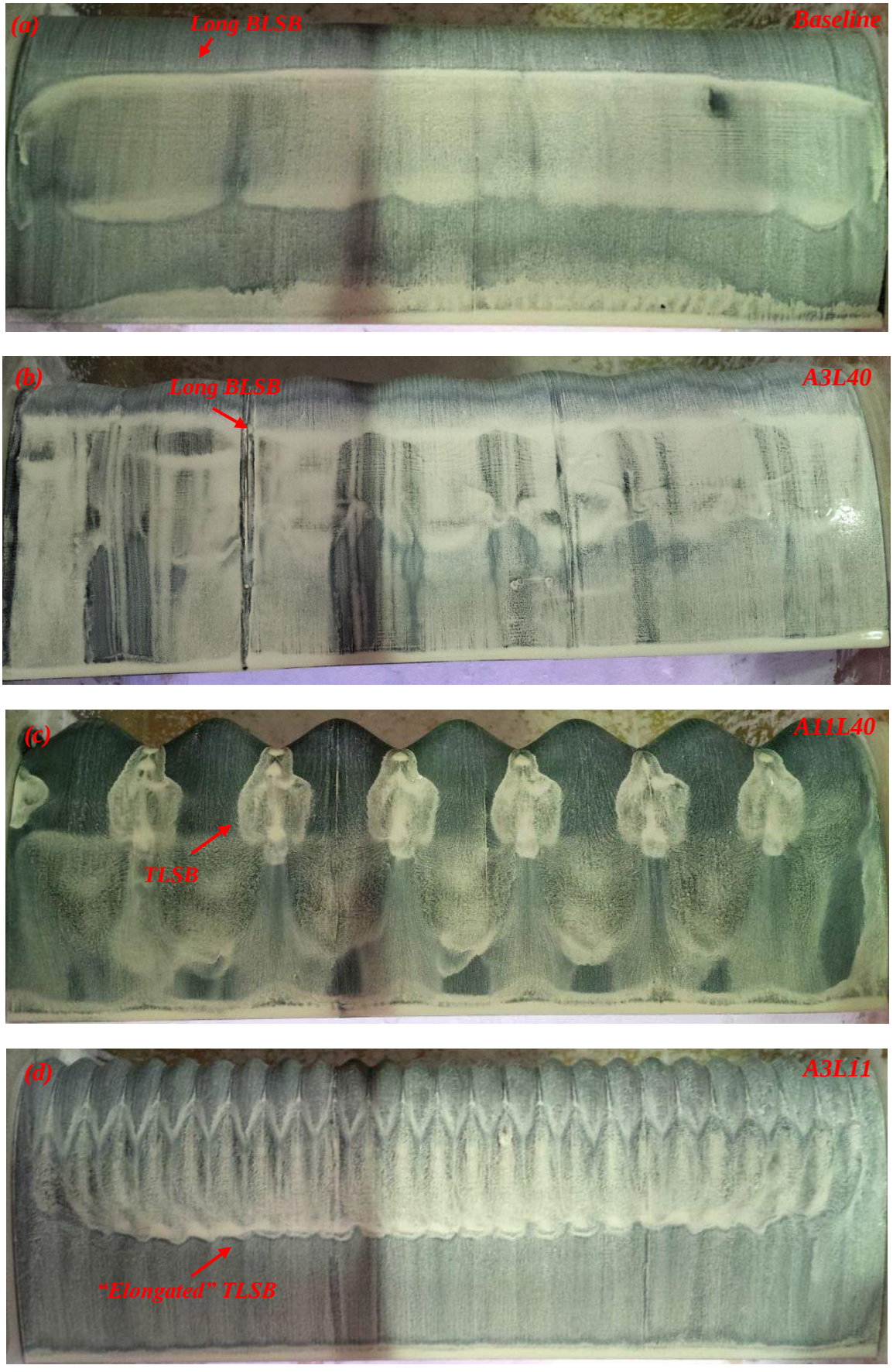

Figure 5.49: All configurations at α = 0°and Re = 50,000 (NACA 0030).

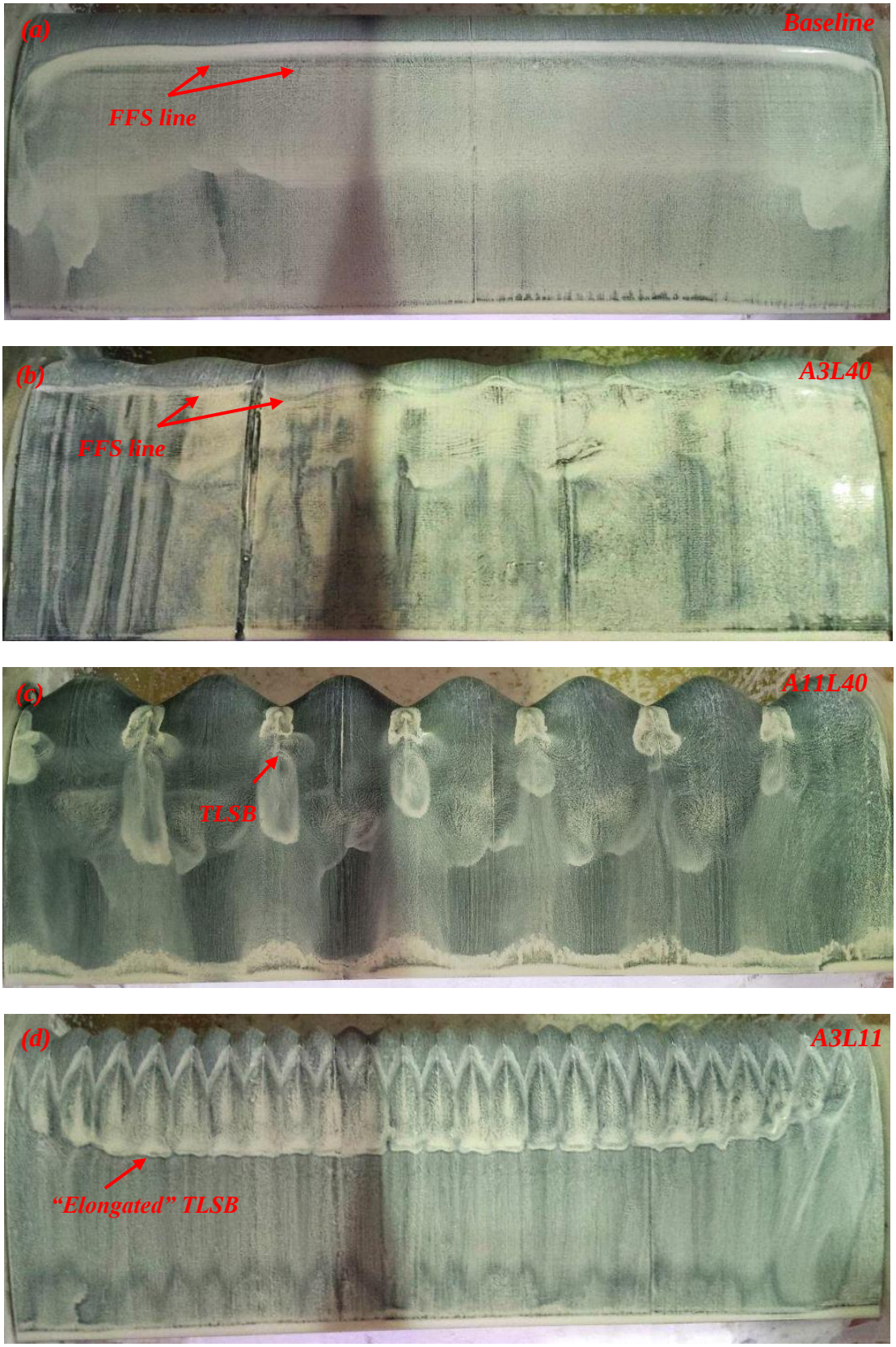

Figure 5.50: All configurations at α = 5°and Re = 50,000 (NACA 0030).

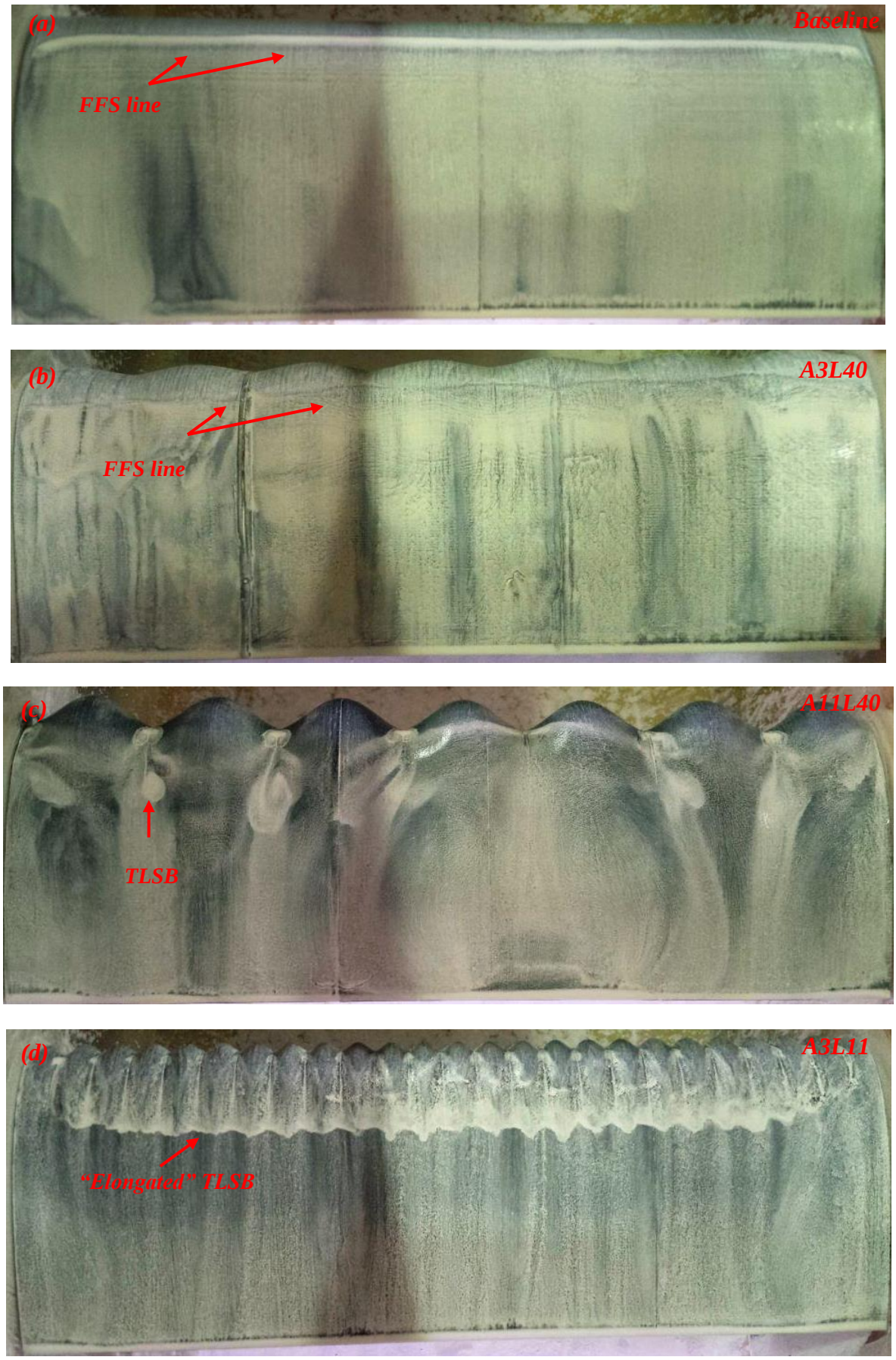

Figure 5.51: All configurations at α = 10°and Re = 50,000 (NACA 0030).

6 WAVY LEADING EDGE PHENOMENOLOGY

In this chapter, the results from oil and mini-tuft flow visualizations in agreement with force measurements are discussed in detail to clarify all physical phenomena, flow characteristics and overall effects on airfoil performance found in this work. In the first three sections, the evaluation is done for the highest Reynolds number (Re=290,000). The fourth section presents the Reynolds number effects. Firstly, the airfoil thickness effects for smooth airfoil are analysed in the following sections, aiming towards the understanding of the wavy leading edge phenomena.

In section 6.2, the tubercle phenomenology at the pre-stall regime is evaluated. Some previously discussed topics (HANSEN et al., 2009; JOHARI et al., 2007; LEVSHIN et al., 2006) are taken up in detail such as secondary flows and evaluation of tubercle geometry effects on aerodynamic performance. New results published in recent researches (ROSTAMZADEH et al., 2014; SKILLEN et al., 2015) are presented with regards to flow control mechanism in the pre-stall regime. Flow mechanisms are evaluated in detail, and mathematical models to describe the physical flow topology over wavy airfoils are proposed. Some flow mechanisms determined numerically are confirmed experimentally first-hand. In addition, a new flow mechanism is discovered, supporting the understanding of optimum values of tubercle geometry in order to reach the best attainable performance. It has also been found that the airfoil thickness effect present distinct flow separation characteristics which determine the pre-stall regime for wavy airfoils.

In the sequence, the post-stall phenomenology is investigated in section 6.3. Flow control mechanism in the post-stall regime is discussed. Although previous researchers (CUSTODIO, 2008; FISH; BATTLE, 1995; KOBAYASHI, 2008; MIKLOSOVIC et al., 2004; MIKLOSOVIC et al., 2007) describe vortices generated at the leading edge as main flow control mechanism to maintain the flow attached at higher angles of attack in wavy configurations, a new flow mechanism is described in this section. In addition, the tubercle geometry is related to flow mechanisms at the post-stall regime.

In the final section of this chapter (6.4), the Reynolds number effects are evaluated and impressive results are presented, showing a desirable design space for optimal tubercle

performance similar to a thin airfoil in the higher Reynolds number regime. The new flow control mechanism found at the post-stall regime is discussed in detail since it dominates the flow properties in the low Reynolds number regime.

6.1 Smooth airfoil flow characteristics

The lift curves and flow visualizations show a significant effect of airfoil thickness on a smooth configuration impacting on tubercle performance; a thin airfoil presents distinct characteristics compared to thicker airfoils with regard to wavy leading edge phenomena. It becomes clear that it is imperative to understand the thickness effect on a smooth airfoil since a clear understanding of the flow characteristics over the straight leading edge configuration helps to clarify the changes caused by the wavy leading edge airfoil on flow topology. With this approach, the current investigation avoids some of the difficulties faced by previous researchers due to the lack of knowledge regarding smooth airfoil flow topology.

Although the thickness airfoil effect on the lift curve has been discussed previously (figures 4.56-57), the flow visualizations are capable to fully clarify this effect evidencing the flow characteristics over the airfoil.

The distinct characteristics on the lift curves caused by an increase in airfoil thickness comes mainly from the flow over the airfoil leading edge affected by the leading edge radius (JACOBS; SHERMAN, 1936),which imposes flow separation conditions in this region dominated by laminar separation bubbles. In addition, the airfoil thickness parameter also has an influence in the boundary layer downstream of the laminar bubble establishing the flow separation conditions at the trailing edge.

The oil flow visualization results showed that over a smooth airfoil upper surface a laminar separation bubble is formed with different characteristics in terms of length (L_B) and flow separation point (X_S), depending on the airfoil geometry and flow conditions (Reynolds number and angle of attack).

In figures 6.1 and 6.2, results obtained from oil flow visualizations are shown and distinct characteristics in terms of length (L_B) and flow separation point (X_S) of the laminar separation bubbles can be observed for varying airfoil thickness. It can be seen from plots that with increased airfoil thickness, the laminar bubble length decreases more slowly with

increasing angle of attack (figure 6.1). Figure 6.2 shows a quick movement of the laminar bubble towards the leading edge in the thinnest airfoil. Thus, the thickness effect will dictate the location and length of the bubble around the leading edge of the airfoil.

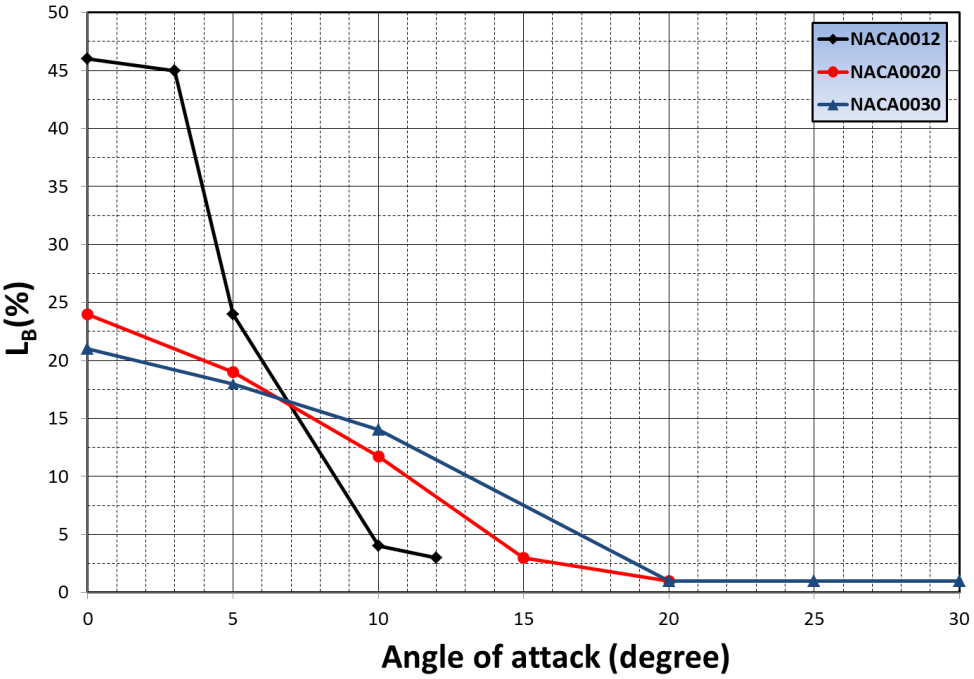

Figure 6.1: Laminar bubble length vs angle of attack for distinct airfoil thickness (Re=290,000).

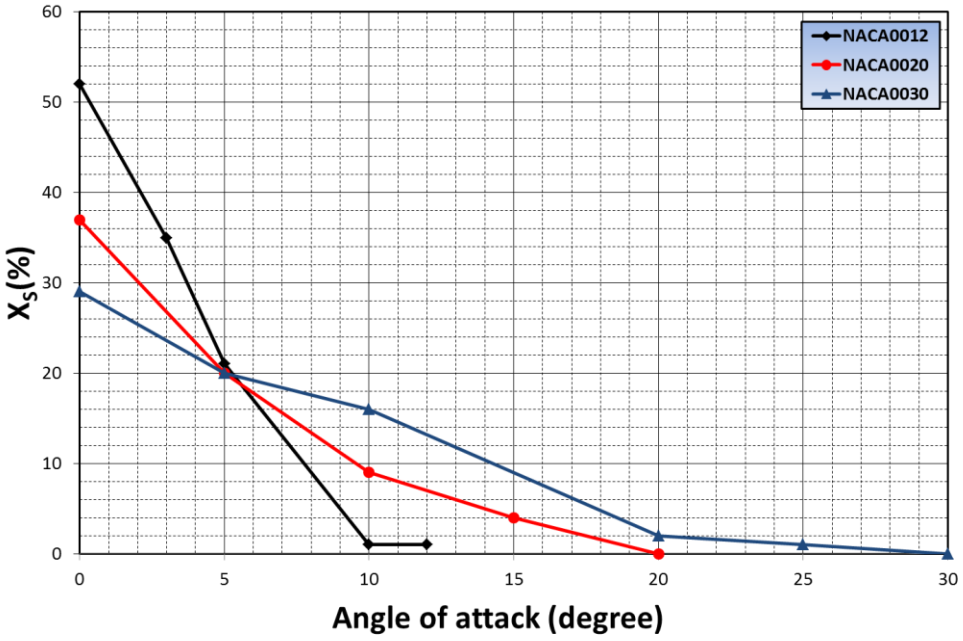

Figure 6.2: Laminar bubble separation point vs angle of attack for distinct airfoil thickness (Re=290,000).

As previous discussion, the thinnest NACA 0012 airfoil, at Re = 290,000 shows the best lift performance in the pre-stall regime compared to thicker airfoils (figure 4.56). The behaviour can be attributed to laminar separation bubble characteristics and the boundary layer development downstream of the laminar bubble.

At an angle of attack of zero degrees, it can be seen in figure 6.3 that the thinnest airfoil shows a long laminar separation bubble, caused by the small leading edge radius, at same rearward position on upper and lower surfaces (symmetrical airfoil). Increasing the angle of attack, the laminar bubble on the upper surface moves towards the leading edge whereas the bubble on the lower surface moves towards trailing edge keeping similar flow characteristics up to $\alpha = 3°$, thus justifying a lift curve slope equal to the theoretical curve.

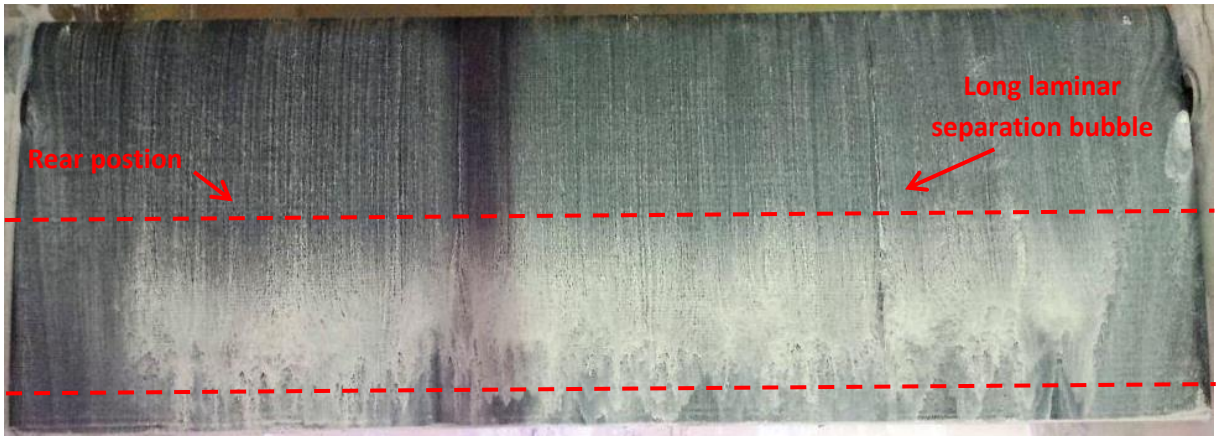

Figure 6.3: Flow topology for upper and lower surface (NACA 0012; $\alpha = 0º$ and Re=290,000).

In the range $3° < \alpha < 5°$, the figure 6.4 shows the laminar bubble still present and assuming a more forward position over the airfoil's upper surface. In contrast, on the lower surface, a full flow separation occurs at the trailing edge. This flow separation causes an increment in flow deflection at the trailing edge (an increase in momentum variation), causing a raise in the lift curve slope as seen on figure 4.56. This physical reasoning justifies the increase in effective camber mentioned by Simons (2002) for airfoils at a low Reynolds number condition. The increase in the lift curve slope disappears for $\alpha > 5º$ due to the disappearance of the separation on the lower surface at higher angles of attack. Similar characteristics have been observed in different angle of attack ranges for other airfoil thickness and Reynolds number combinations.

The mini-tuft and oil visualizations show that the thin NACA 0012 airfoil reaches angles of attack very close to stall angle (α = 12º) with a little flow separation on the trailing edge (figure 5.4) that causes a small decrease in lift curve slope close to the stall condition (figure 4.1).

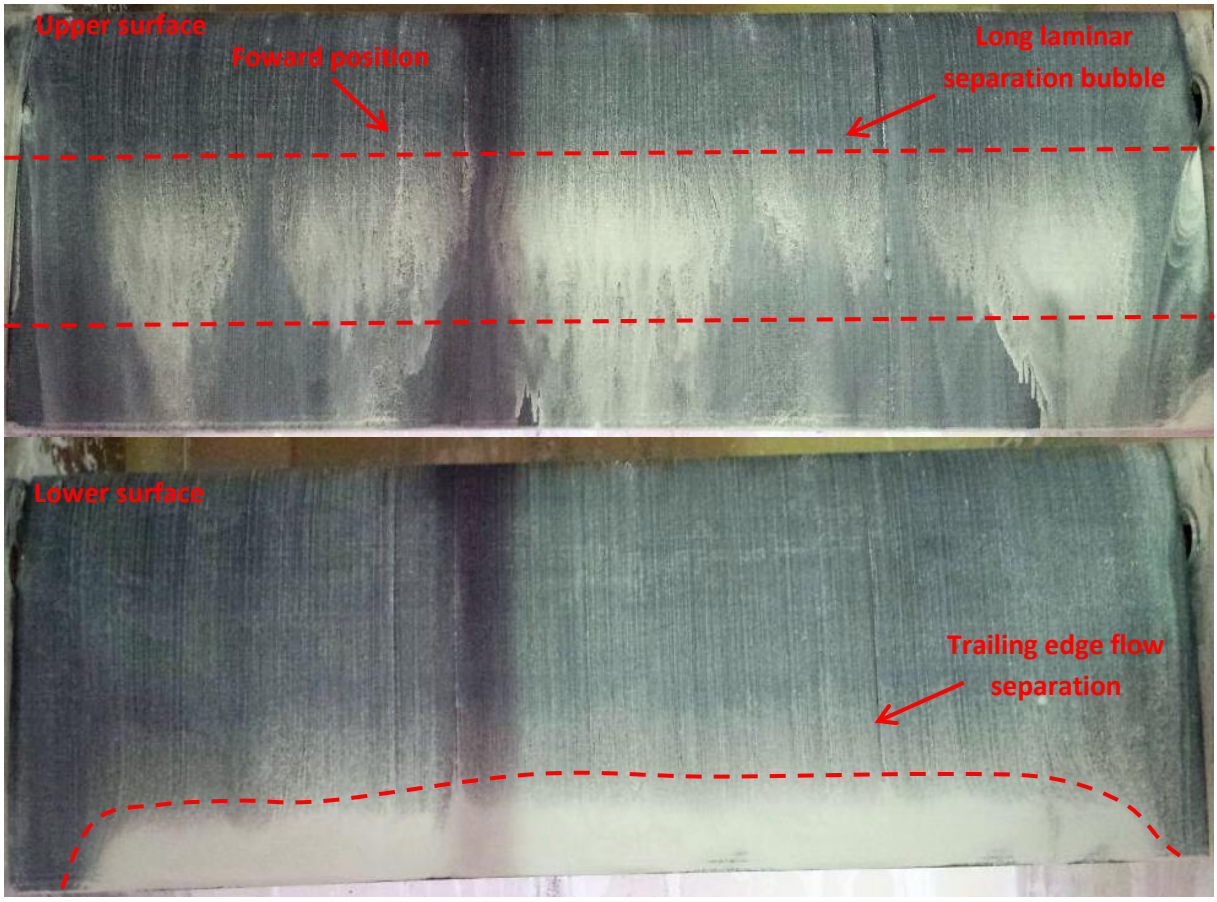

Figure 6.4: Flow topology for upper and lower surface (NACA 0012; α = 3º and Re=290,000).

At an angle of attack of 13º, a partial abrupt stall occurs with a short laminar bubble burst characterizing a full flow separation over entire airfoil upper surface (figure 5.5 and 5.28). Therefore the NACA 0012 airfoil reaches the stall angle without continuous trailing edge separation progression at the pre-stall condition. In addition, it is noteworthy that the laminar separation bubble resists to full flow separation up to the stall angle (α = 13°). Thus, the thin airfoil thickness demonstrates *leading edge stall characteristics*. The figure 6.5 describes the *leading edge stall characteristics* for the thin NACA 0012 airfoil, and its consequence on lift performance.

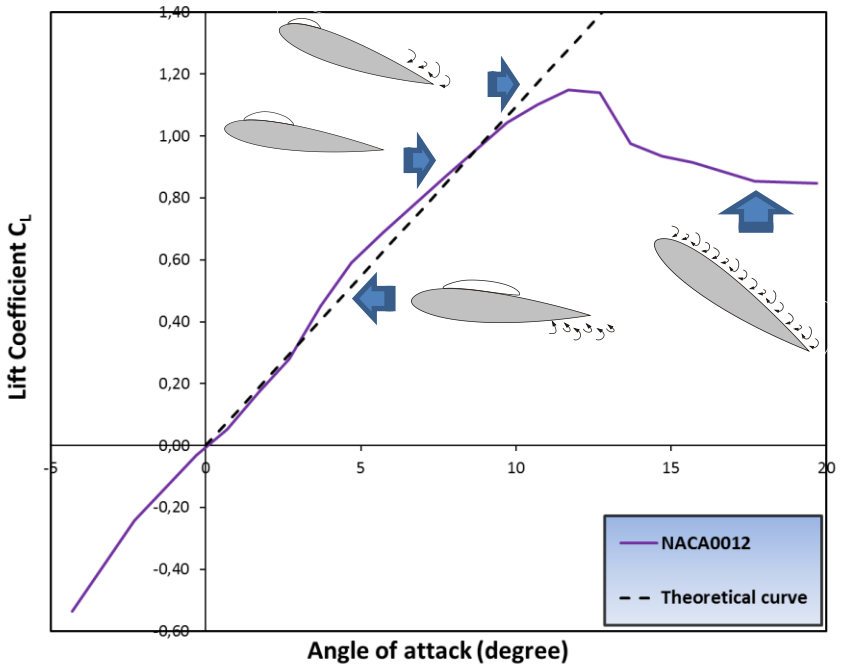

Figure 6.5: Leading edge stall characteristics for the NACA 012 airfoil with consequent lift performance (Re = 290,000).

The absence of trailing edge flow separation can be attributed to the early leading edge stall condition being triggered by a smaller leading edge radius that establishes a laminar bubble rapidly moving towards the leading edge and decreasing in length, with a consequently violent burst (figure 6.1 and 6.2).

The trailing edge flow characteristics for the NACA 0012 airfoil are distinct from thicker airfoils (NACA 0020 and NACA 0030) and it will provide better aerodynamic performance for wavy leading edge at the pre-stall regime as discussed later.

The figure 4.56 shows that the NACA 0020 airfoil undergoes a decrease in lift curve slope up to $\alpha = 10^{o}$ when compared to the theoretical curve. This aerodynamic deterioration is attributed to boundary layer thickening since the flow is almost fully attached over the airfoil upper surface up to $\alpha = 10^{o}$ (figures 5.30-32). In addition, there is a little increase in curve slope in the range $5^{o} < \alpha < 6^{o}$, similar to the increment observed in the thinner NACA 0012 airfoil.

At an angle of attack 10^{o}, the trailing edge flow separation onset occurs (figures 5.8 and 5.32), causing a major decrease in the lift curve slope. Differently from the NACA 0012 airfoil, here the laminar bubble at the leading edge resists to full flow separation up to a

higher angle of attack (α = 18º) due to a greater leading edge radius. Therefore from α = 10º up to the stall angle (α = 18º) there is a continuous decrease in lift curve slope, forming an asymptotic curve up to the stall condition caused by a progressive trailing edge flow separation.

The flow visualizations (figures 5.10 and 5.34) at α = 20º indicate that an abrupt stall occurs due to flow separation present at the leading edge at least over half-chord. However, a very small laminar separation bubble remains close to the stagnation point.

The NACA 0020 airfoil, in contrast with its thinner counterpart NACA 0012, does not resist to trailing edge flow separation up to the stall condition. However, it reaches higher angles of attack while keeping the flow attached at the leading edge. It can be seen in figures 5.9 and 5.33, at higher angles of attack (α = 15º), a short laminar separation bubble at the leading edge sustains the flow attached in this region along with the presence of trailing edge flow separation. Figure 6.6 describes the *trailing edge stall characteristics* with consequent lift performance for NACA 0020 airfoil. However, a very small LSB remains attached close to the stagnation point.

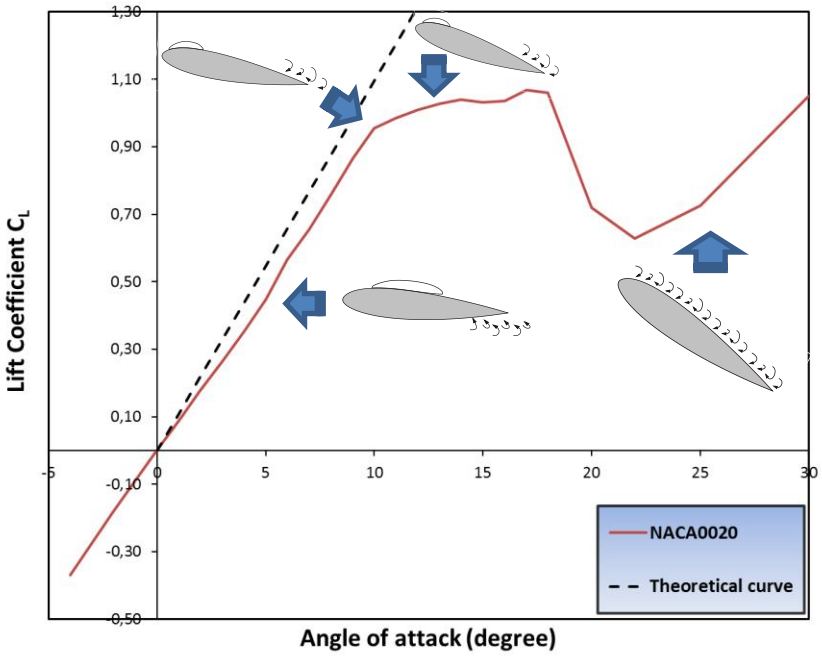

Figure 6.6: Leading edge stall characteristics for the NACA 020 airfoil with consequent lift performance (Re = 290,000).

The thickest NACA 0030 airfoil has similar flow characteristics to the NACA 0020 airfoil (figure 6.7). However, for the NACA 0030, even at lower angles of attack, trailing

edge flow separation is present with a slow growth up to α = 15º (figures 5.11-14 and 5.35-36), establishing a lift curve with lower values than the NACA 0020 up to α = 14º. The boundary layer thickening and an early trailing edge flow separation justify a lower lift curve slope. At 15º < α < 25°, as for NACA 0020 airfoil, a massive trailing edge flow separation occurs, establishing an asymptotic lift curve. On the NACA 0030 airfoil, the laminar separation bubble causes a slow movement of the flow separation point towards leading edge (figure 6.2) at higher angles of attack. Thus, the thickest airfoil resists to full flow separation at the leading edge up to the extraordinarily high angle of attack of 25º. The stall behaviour is abrupt, similar to the NACA 0020 having flow separation over half-span at α = 25º (figures 5.16 and 5.39). In addition, the thickest airfoil also keeps very small laminar bubbles at the leading edge of the airfoil.

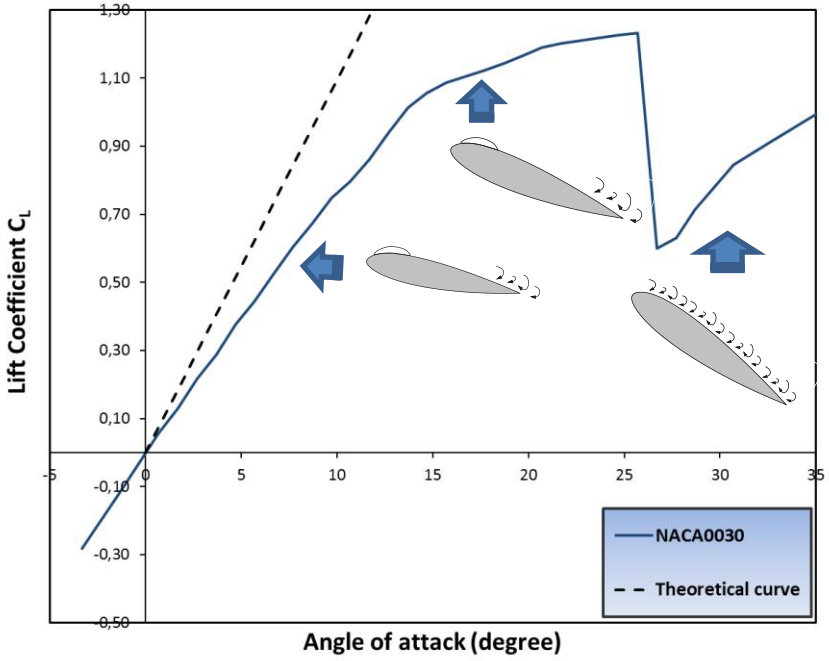

Figure 6.7: Leading edge stall characteristics for the NACA 030 airfoil with consequent lift performance (Re = 290,000).

The lift curves and flow visualizations indicate that the flow characteristics over airfoil upper surfaces are a consequence of laminar separation bubbles and trailing edge flow separation characteristics. By increasing the airfoil thickness, the leading edge radius increases becoming smoother, and leading the laminar bubble to resist to full flow separation at higher angles of attack. On other hand, an increase in airfoil thickness causes trailing edge flow separation. Thus, an increase in thickness deteriorates the pre-stall characteristics tending

to appear trailing edge flow separation, however, increases the stall angle keeping a laminar bubble at leading edge that resist attached at higher angles of attack.

The previous discussion justifies the reason why in the aircraft design literature the dependency between maximum lift coefficient and airfoil thickness presents an optimum value that reaches the highest maximum lift coefficient value. Torenbeek (1982) and Raymer (1989) show results from various airfoils at high Reynolds number ($Re = 3x10^6$) indicating that a suitable subsonic airfoil design reaches the highest C_{LMAX} keeping airfoil thickness around 13% of the chord.

This work shows, as it has been said previously, the highest maximum lift values for the thickest airfoils at flow conditions above Reynolds number 120,000. Below this flow condition, the thinner airfoils show the highest values (figure 4.58). Although aerodynamicists keep in mind around 13% of chord a good number for airfoil thickness at subsonic design, this number is related to high Reynolds number conditions ($Re > 3x10^6$). It seems that for airfoil design, at low Reynolds number (closer to UAV operational conditions), thicker airfoils are more appropriated regarding maximum lift value.

The Reynolds number effects on lift curve for airfoils NACA 0012 and NACA 0020 (figures 4.1 and 4.19) show similar behaviour. A variation in Reynolds number changes the increase on the lift curve slope caused by flow separation on the airfoil lower surface (figure 6.4). A decrease in Reynolds number increases the laminar separation bubble over the airfoil upper surface (figures 5.41 and 5.45) and the full flow separation over the lower surface at low angle of attack. As consequence, at low Reynolds number condition occurs anticipation in appearance and increases the raise in the lift curve slope (4.1 and 4.19).

Besides, a decrease in Reynolds number causes an earlier flow separation at the leading edge for both airfoils (figures 5.43 and 5.47), consequently achieving lower maximum lift coefficient values although the NACA 0020 airfoil is less sensitive. Above the Reynolds number of 100,000, the thickest NACA 0030 airfoil shows similar Reynolds number effect as thinner airfoils. In contrast, at lower Reynolds number conditions, the airfoil undergoes significant full flow separation at the leading edge even at low angle of attack, causing strong aerodynamic deterioration (figure 5.50).

6.2 Wavy airfoil pre-stall phenomenology

The understanding of pre-stall characteristics on wavy airfoils is one of the main motivations of this thesis. There is a lack of knowledge in the pre-stall regime due to fact that many researches in wavy leading edge phenomena focus on identifying potential gains in maximum lift coefficient and the understanding of the flow mechanism in the post-stall regime. This section describes the flow mechanisms found in the experimental results at pre-stall conditions as well as investigates the geometry parametric variation related to tubercles performance.

6.2.1 Secondary flow

Miklosovic et al. (2007) and Custodio (2008) said that the presence of waves on leading edges effectively create a varying leading edge sweep angle generating a spanwise flow caused by streamwise vortices. Although they attribute physically the spanwise flow to vortices created at the wavy leading edge, vortex structures are not the only flow mechanisms that cause span flow related to wavy leading edge phenomena.

Despite existing understanding in literature, the flow visualizations for a wide parameter variations (airfoil thickness, tubercle geometry, angle of attack and Reynolds number) presented in this work demonstrate distinct flow mechanisms depending on geometry and flow conditions.

Thus, since the span flow is the main characteristic of tubercle configurations, an appropriate approach in order to better understand the wavy leading edge effects are to correlate the vorticity created by tubercles with distinct phenomena.

NIEROP et al. (2008) and Rostamzadeh et al. (2014) show that the presence of wavy leading edge in airfoils generates a cyclic spanwise circulation associated with streamwise vorticity. In order to identify the flow structures that cause streamwise vorticity, the skew-induced and stress-induced mechanisms related to respectively to vorticity in the flow and anisotropy of turbulence are considered (ROSTAMZADEH et al., 2014).

The main flow mechanisms regarding wavy leading edge phenomena present skew-induced characteristics. A secondary flow introduces vorticity in the flow at the leading edge. The phenomena associated with the wavy leading edge is trigged by a spanwise flow that establishes, at the leading edge of the airfoil, a *secondary flow* as mentioned by Rostamzadeh et al. (2014) and Skillen et al. (2015) (figure 6.8) and presented in figure 6.9. This flow mechanism at leading edge leads to complex three-dimensional flow structures that affect the boundary layer development.

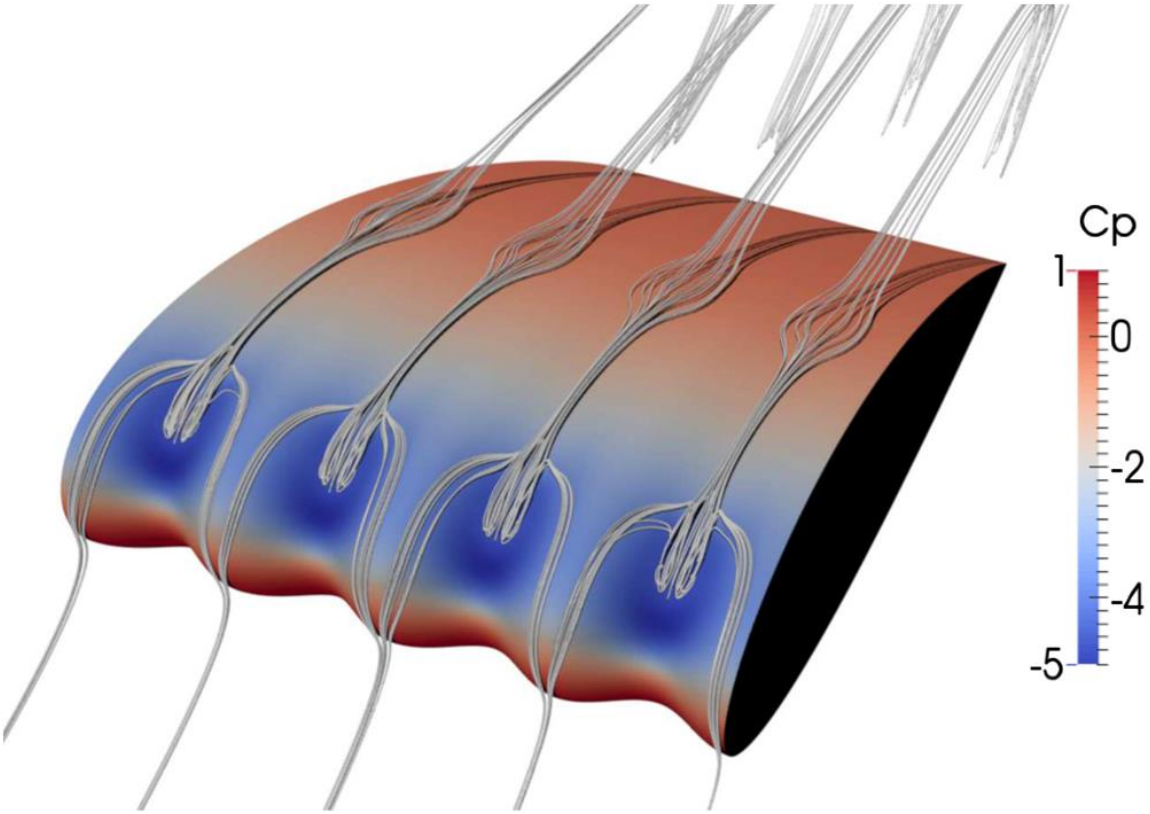

Figure 6.8: Time-averaged streamlines showing the secondary flow for NACA 0021 airfoil (α = 10° and Re=120,000). Color lines show pressure coefficient at (SKILLEN et al., 2015).

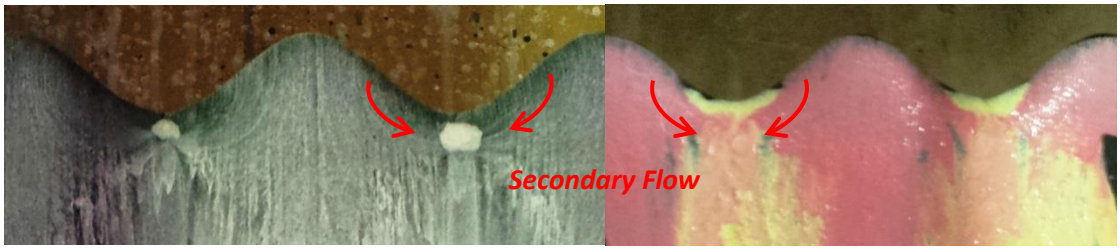

Figure 6.9: The wavy leading edge establishes a local sweep angle imposing a secondary flow represented by curved streamlines (NACA 0020; A11λ40; α = 10° and Re=290,000).

In order to understand the flow mechanisms related to wavy leading edge on airfoils in the pre-stall regime, the characteristics of the secondary flow at the leading edge are described hereafter.

The sweep angle of the wavy airfoil is the initial cause of the drastic changes on boundary layer when compared to a smooth configuration. A general explanation for the trigger of the wavy leading edge phenomena comes from the variable leading edge sweep angle that causes a spanwise secondary flow, as in a swept wing.

The *secondary flow* forms a bi-periodic flow structure over the entire airfoil leading edge span. The oil flow visualizations (figure 6.9) show streamlines curving from peak to trough caused by the pressure gradient over spanwise (figure 6.8).

The secondary flow adds velocity in chordwise direction, thus accelerating flow from peak towards trough, increasing suction pressure in this region as shown by Karthikeyan et al. (2014) and Rostamzadeh et al. (2014). Higher suction areas lead to an increase in the adverse pressure gradient at tubercle troughs whereas lower suction at peaks leads to less severe gradient (figure 6.10).

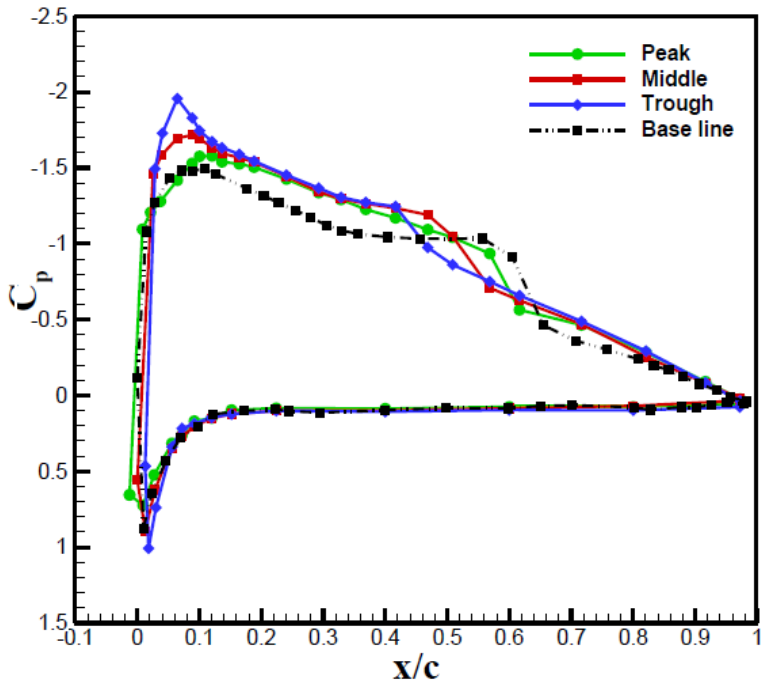

Figure 6.10: Pressure distribution (peaks, middle and trough) for NACA 4415 airfoil at angle of attack 6° and Re=120,000 (KARTHIKEYAN et al., 2014).

In the pre-stall regime, as described previously, the results show that the flow over smooth airfoils is characterized by a two-dimensional laminar separation bubble distribution. In contrast, wavy airfoils present distinct three-dimensional laminar separation bubbles at different chordwise positions downstream of the peaks and troughs (figure 6.11) as a consequence of increasing the adverse pressure gradient on troughs and decreasing it on peaks caused by the secondary flow (figure 6.11). In the present work, these characteristics are referred as *three-dimensional laminar separation bubble phenomenon.*

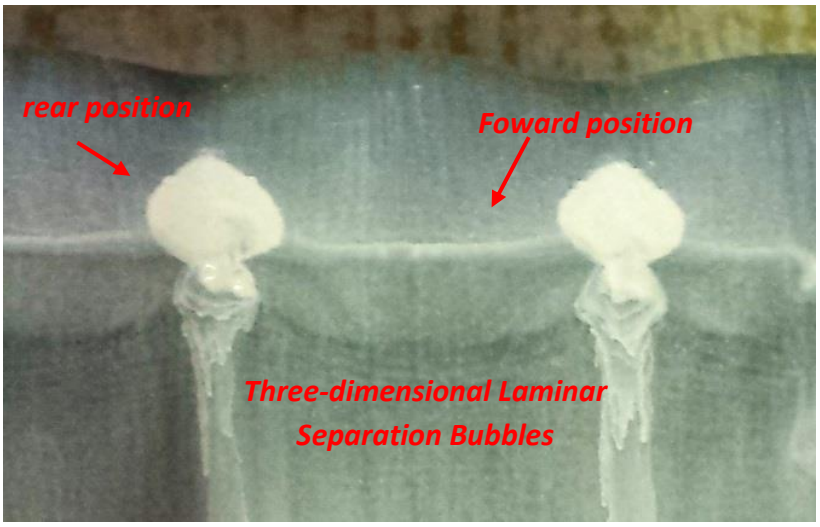

Figure 6.11: Three-dimensional laminar separation bubble structures caused by secondary flow (NACA 0030; A3λ40; α = 10º and Re=290,000).

6.2.2 Three-dimensional laminar separation bubble phenomenon

A particular case of the *three-dimensional laminar separation bubble phenomenon* was identified experimentally for the first time, at specific Reynolds number and airfoil geometry by Zverkov et al. (2008), where only laminar separation bubbles downstream of the tubercle troughs were present. However, just six years later Karthikeyan et al. (2014) confirmed for a distinct case the three-dimensional flow structures showing additional bubbles downstream of the peaks. The current work presents tests of a comprehensive parametric variation, leading to a generalization of the *three-dimensional laminar bubble structures* regarding wavy leading edge phenomena.

The oil flow visualizations show that the three-dimensional laminar separation bubble phenomenon is characterized by changes to the two-dimensional laminar bubble distribution in a smooth airfoil to a bi-periodic laminar separation bubble distribution where smaller structures appear downstream of troughs and peaks in airfoils with tubercles. In these, distinct three-dimensional laminar bubble shapes form depending on geometry (tubercle and airfoil) and flow conditions (angle of attack and Reynolds number).

In general, the three-dimensional laminar bubbles downstream of the troughs move towards the leading edge whereas the bubbles downstream of the peaks move toward the trailing edge when compared to two-dimensional bubbles at smooth airfoils.

The reason why laminar bubbles at tubercle troughs move toward leading edge is due to higher adverse gradient in this region. The effect is similar to an increase in angle of attack for a smooth airfoil: the adverse pressure gradient increases and the bubble moves toward leading edge (figure 6.2). On the other hand, at the peaks a decrease in the adverse pressure gradient shifts the laminar bubbles towards a more downstream location (figure 6.11).

The present oil visualization results are in agreement with Rostamzadeh et al. (2014) and Karthikeyanet al. (2014) that investigated the pressure distributions on wavy airfoils sections, finding laminar bubbles respectively in forward and after positions downstream of troughs and peaks (figure 6.12).

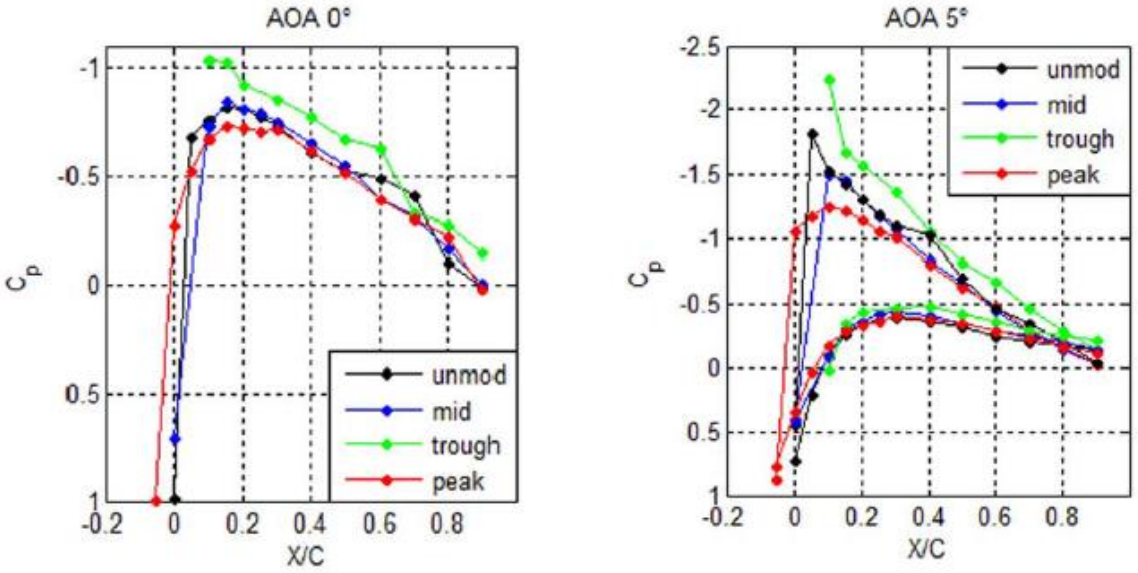

Figure 6.12: Plateau in the pressure distribution indicating laminar separation bubble (peaks, middle and trough) for NACA 0021 airfoil at Re=120,000 (ROSTAMZADEH et al., 2014).

6.2.2.1 Flow and geometry parameter effect on flow topology

The secondary flow, at each span station, determines the velocities along the chord and as a consequence also the adverse pressure gradients. Thus, the secondary flow drives distinct flow topologies as shown in figure 6.13. The next paragraphs discuss the dependency of some parameters in the formation of the secondary flow at the leading edge as result of the flow topology.

The leading edge geometry (in terms of waviness and thickness), Reynolds number and angle of attack together determine the secondary flow over the airfoil upper surface. However, considering the flow topology changes at fixed Reynolds number and airfoil thickness, the wavy geometry and angle of attack effects on flow characteristics can be observed. Figures 6.14 and 6.15 show changes in length and flow separation point of the laminar bubbles caused by a wavy leading edge for the NACA 0020 airfoil with increasing in angle of attack at Re=290,000.

The configuration A3λ40 is the only that presents laminar bubble downstream of the peaks in the entire range of angles of attack. Besides, this configuration causes minor changes in the laminar bubble position when compared to the baseline configuration. The smooth sweep angle at the leading edge adds small spanwise velocities towards the troughs and keeps the laminar separation bubbles at the locations of peaks and troughs. This characteristic also appears on the NACA 0021 airfoil for similar tubercle geometry (with longer wavelength) in a numerical simulation carried out by Rostamzadeh et al. (2014).

On the other hand, greater amplitude causes bubble reaches the local leading edge early ($\alpha = 5^{o}$), and it presents the shortest bubble length. In addition, there is an absence of bubbles downstream of the peaks as shown by Rostamzadeh et al. (2014) for similar tubercle geometry. The larger sweep angle at the leading edge of the greater amplitude adds higher spanwise velocities toward troughs and consequently forms a small bubble at the trough and attenuates the adverse pressure gradient at the peaks thus avoiding the formation of a laminar bubble.

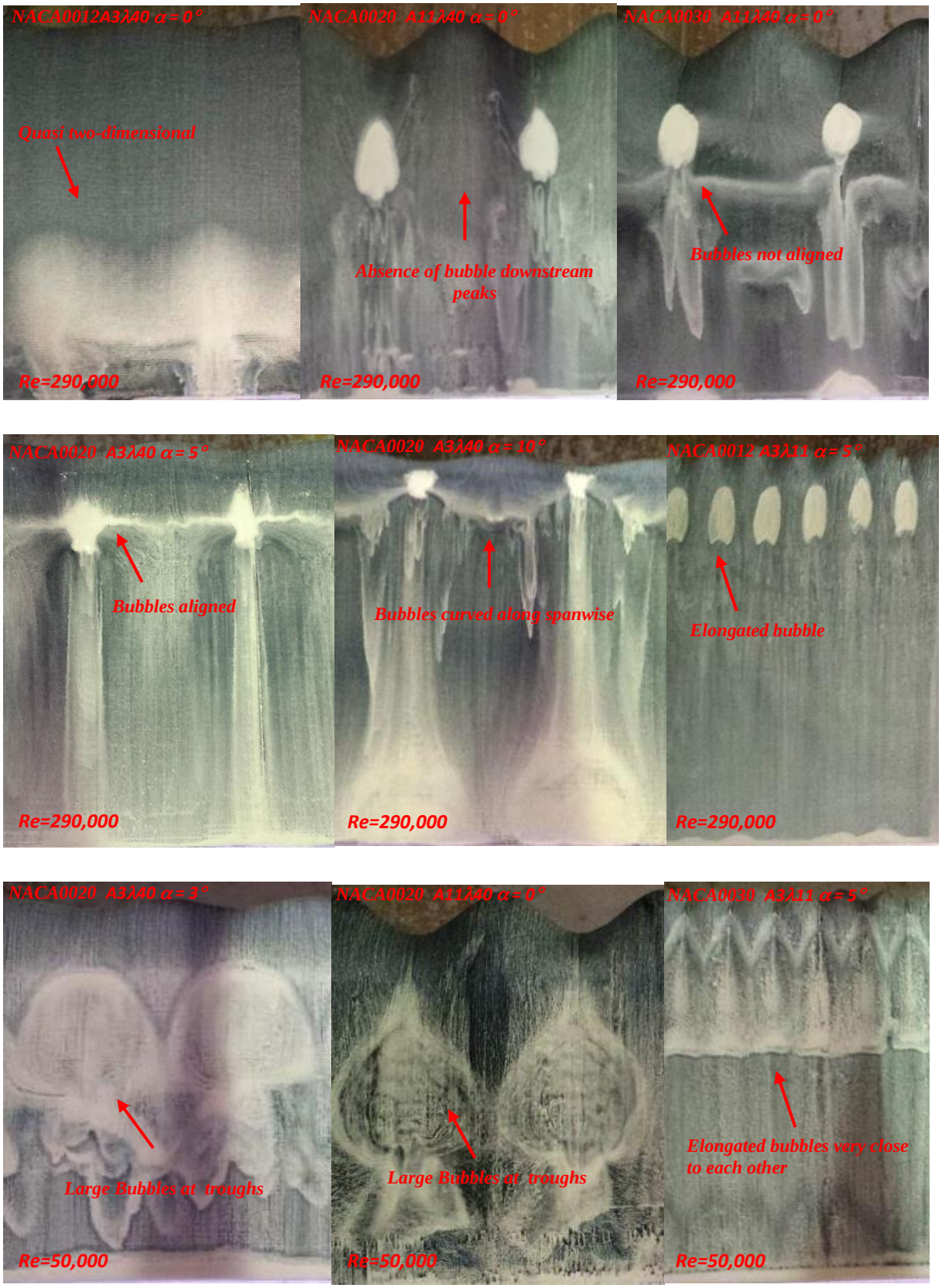

Figure 6.13: Distinct three-dimensional laminar bubble distributions caused by variation in the geometry and flow condition.

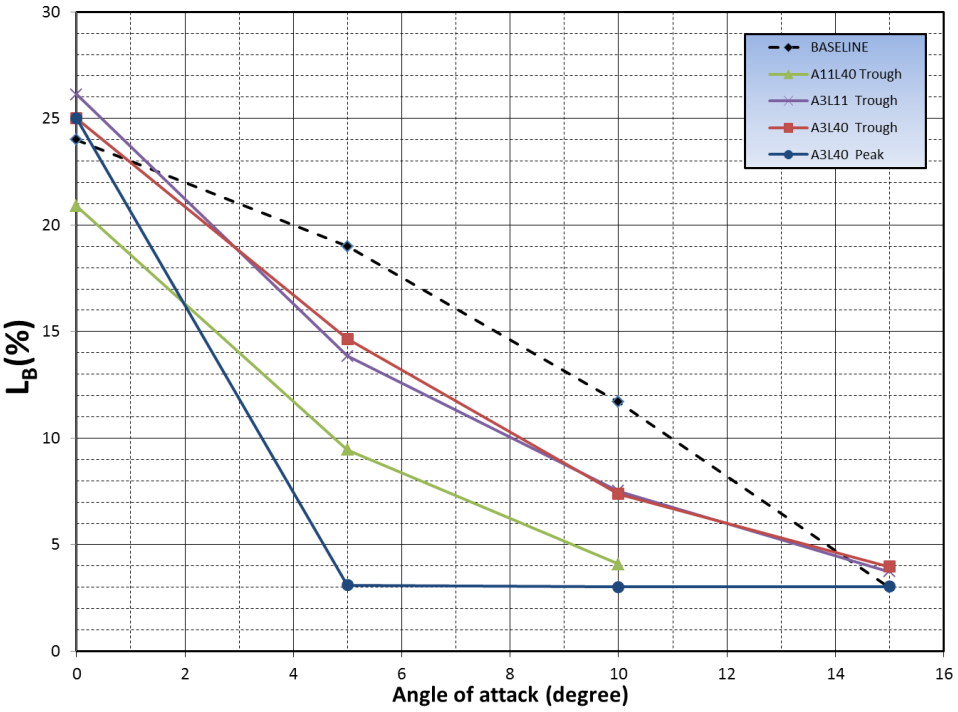

Figure 6.14: Laminar bubble separation position vs angle of attack for wavy NACA 0020 airfoil (Re=290,000).

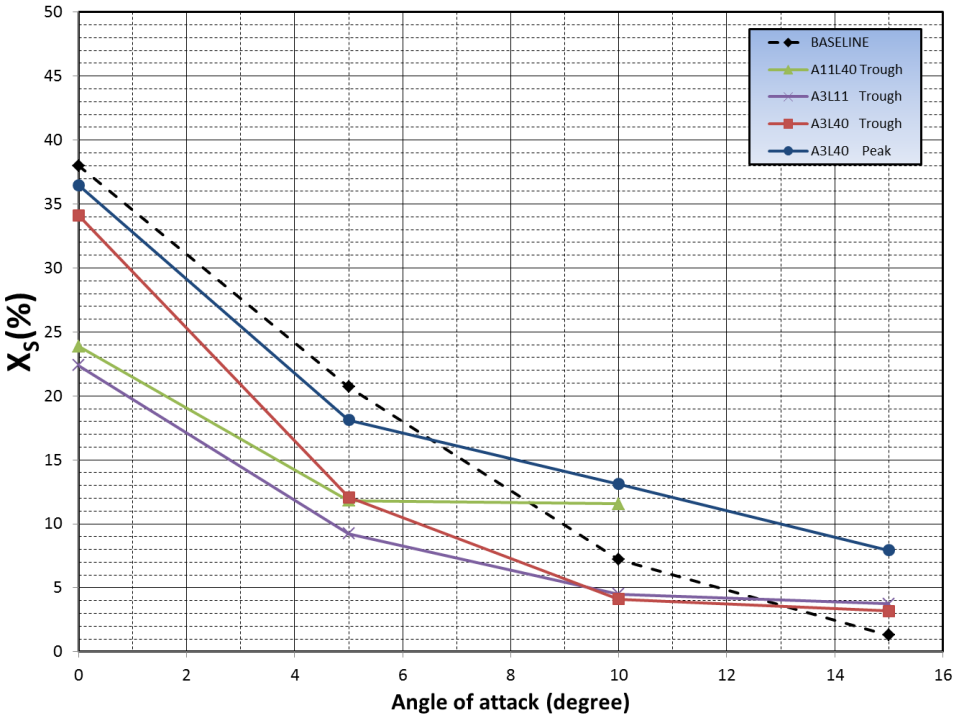

Figure 6.15: Laminar bubble length vs angle of attack for wavy NACA 0020 airfoil (Re=290,000).

Figure 6.16 shows for configuration A3λ40 in the NACA 0020 airfoil that the laminar bubbles downstream of the peaks and troughs move towards the leading edge with increasing angles of attack. In addition, the bubble decreases in length. These characteristics become similar to a smooth configuration as a consequence of increasing the adverse pressure gradient with angle of attack (figures 6.1 and 6.2).

Figure 6.16 also shows that the increase in angle of attack intensifies the streamline deflections from peak to troughs, indicating increase in spanwise flow and streamwise vorticity. As a consequence, the separation points downstream of the peaks change along the span differently from the lower angle of attack condition. Besides, the difference between flow separation points at peaks and troughs increases.

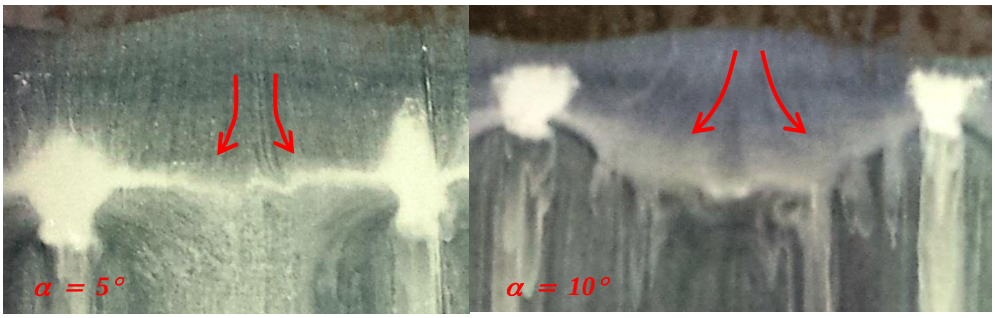

Figure 6.16: The raise in streamline deflections along span with increasing of angle of attack indicating increase in streamwise vorticity.

Although many researchers (HANSEN et al., 2009; JOHARI et al., 2007; LEVSHIN et al., 2006) studied the influence of amplitude and wavelength on wavy leading edge performance, Hansen et al. (2011) state that the amplitude-to-wavelength ratio (A/λ) is a relevant parameter in the tubercle performance. Therefore flow visualizations will be herein presented for distinct amplitude-to-wavelength ratios, since current researches did not yet evaluate the effect of this parameter on flow topology.

In fact, the parameter A/λ determines the leading edge sweep angle, and as a consequence the secondary flow. Figure 6.17 shows the sweep angle effect on flow separation point and bubble length. The configurations A11λ40 and A3λ11 have similar values of amplitude-to-wavelength ratio of 0.275 and 0.272 respectively. In both configurations, the

three-dimensional laminar bubbles reach a separation point close to the local leading edge differently as compared to configuration A3λ40 with a lower value of amplitude-to-wavelength ratio (A/λ = 0.075). Higher A/λ values cause greater flow distortion from peaks to troughs, indicating an increase in span flow and streamwise vorticity along the span, thus justifying laminar bubbles happening closer to the local leading edge in this case. In addition, a lower amplitude-to-wavelength ratio tends to generate laminar bubbles downstream from tubercle peaks. The small spanwise flow is not sufficient to decrease the adverse pressure gradient downstream of the peaks in order to prevent flow separation.

Although the parameter A/λ causes changes on flow topology increasing span flow for higher values, the bubble shape seems to not have a dependency on the amplitude-to-wavelength ratio as can be seen on figure 6.17. It is rather more appropriate to say that the amplitude-to-wavelength ratio is a measurement of vorticity for the wavy leading edge airfoils. Rostamzadeh et al. (2014) in agreement with this evidence wrote that the magnitude of peak vorticity near the leading edge is in direct proportion to the amplitude-to-wavelength ratio of the tubercle geometry.

The figure 6.17 also shows that the larger tubercle amplitude (A11λ40) presents smaller and closer bubble to leading edge as compared to smaller amplitude configuration (A3λ11) keeping similar A/λ. Thus an increase in amplitude causes a correspondent increase in the adverse pressure gradient at troughs even at same amplitude-to-wavelength ratio. This behaviour can be associated with *delta wing characteristics* where the vortex strength raises with increasing in wing root.

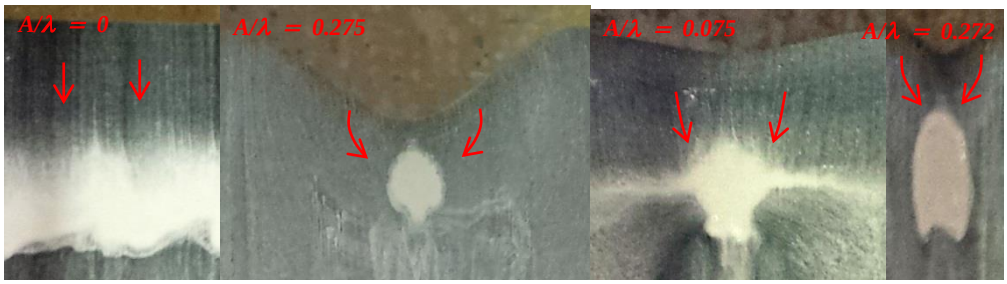

Figure 6.17: The amplitude-to-wavelength ratio effect on flow topology at leading edge (NACA 0020; α = 5° and Re = 290,000).

Previous works regarding tubercle geometry investigations considered just amplitude and wavelength as parameters of study. A measurement of leading edge radius was not yet taken into consideration as a geometric parameter.

Figure 6.18 shows the leading edge radius effect on flow topology for varying airfoil thickness. It is clear that a decrease in thickness leads to three-dimensional laminar separation bubbles, at troughs, progressively shorter and closer to the leading edge. A lower airfoil thickness implies a smaller leading edge radius, which leads to higher adverse pressure gradients which anticipate flow separation at the leading edge.

Figure 6.18: The leading edge radius effect on flow topology at A11λ40 wavy airfoil (α = 5° and Re = 290,000).

6.2.3 Flow mechanism caused by three-dimensional laminar bubbles

In the pre-stall conditions, three-dimensional laminar separation bubbles drive the flow over the entire upper surface of the wavy airfoil, influencing its performance. Although a few researchers have identified some of aspects that in combination form a complex flow mechanism (secondary flow, anisotropic turbulence and momentum exchange by vortices), there is currently a lack of understanding regarding flow topology in the pre-stall conditions. In the next subsections, the results of this work as well as previous studies will be presented in order to contribute to clear understanding of flow control mechanisms in the pre-stall conditions. In addition, some models are proposed in order to explain the flow mechanism characteristics.

Figure 6.19 shows all flow mechanisms regarding wavy leading edge in the pre-stall regime. The secondary flow, as previously mentioned, causes different boundary layer development at peak and trough along chordwise direction. At tubercle peaks, larger regions

appear to keep the laminar flow attached due to a decrease in the adverse pressure gradient. On the other hand, an increase in adverse gradient causes an earlier flow separation with turbulent reattachment at troughs. Thus, the boundary layer is re-energized throughout the span by two flow mechanisms: *a secondary flow behind peaks and a laminar separation bubble behind troughs.*

The distinct flow mechanism at tubercle peaks and troughs cause an anisotropic turbulence along the span represented by a curved line defined by a transition point far from middle peaks and the reattachment point at troughs (figure 6.19). Here, the criterion used to identify oil visualization pattern for laminar and turbulent flow is based on visualizations from Simons (2002).

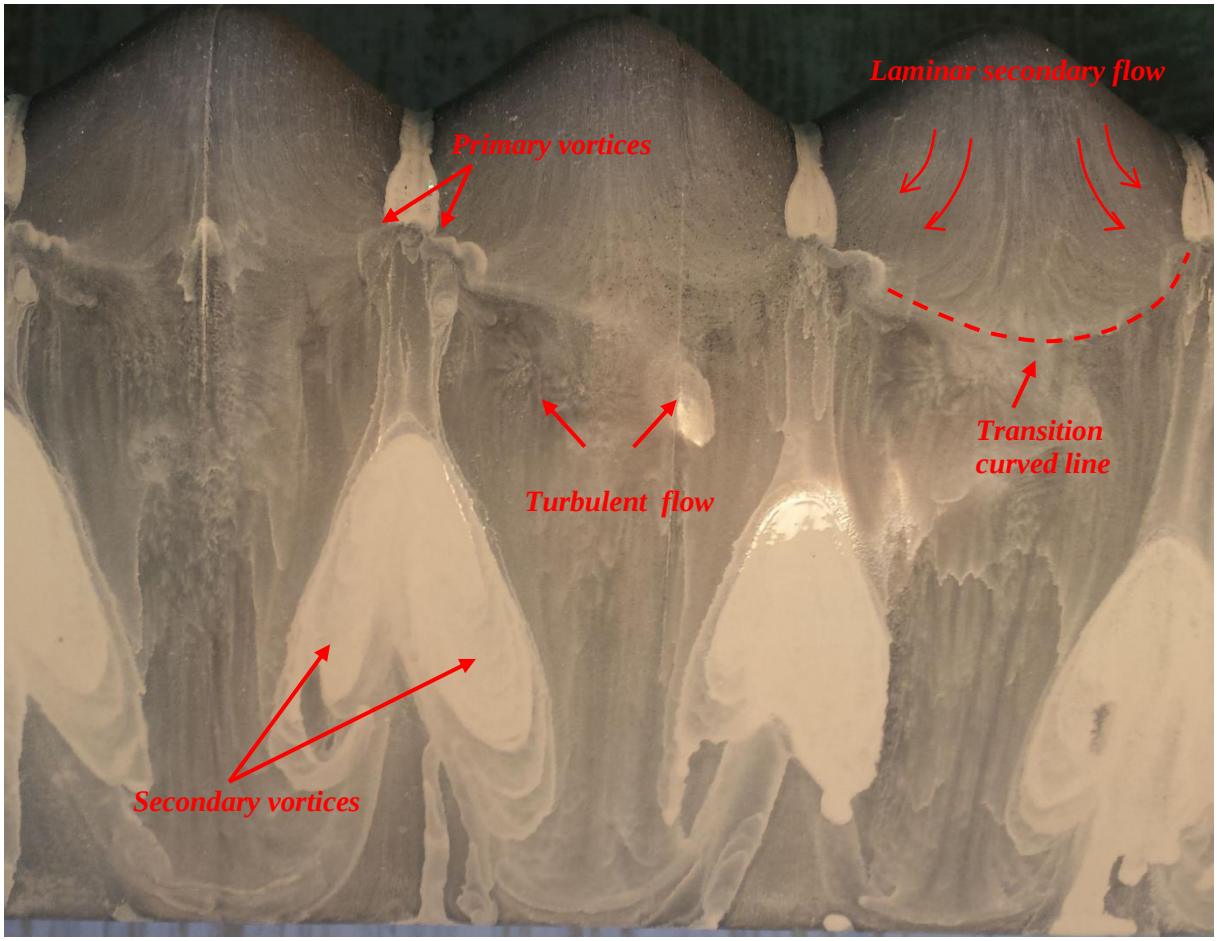

Figure 6.19: Pre-stall flow characteristics for wavy configuration A11λ40 at NACA 0030 airfoil (α =10º and Re=290,000).

Zeverkovet et al. (2008) present results in agreement with the anisotropic turbulence found in figure 6.19. They carried out RMS velocity measurements in a wavy airfoil showing that, at peaks, the boundary layer undergoes laminar-turbulent transition 30% further downstream when compared to troughs (figure 6.20). In addition, Skillen et al. (2015) present similar anisotropic turbulence results using Large Eddy Simulation in a wavy configuration (figure 2.48).

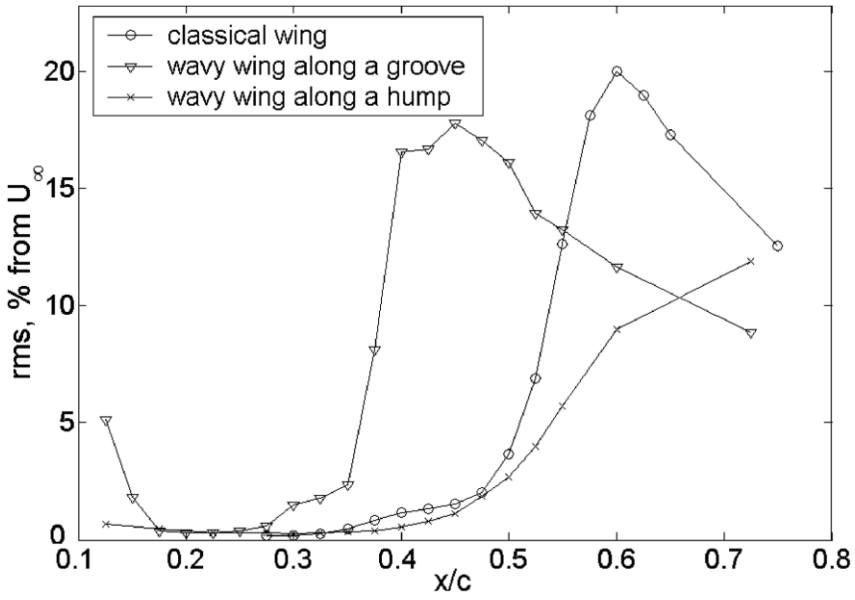

Figure 6.20: Streamwise disturbance growth presenting later laminar-turbulence transition at peak for TsAGI R-3a-12 airfoil at Re=170.000 (ZEVERKOV et al., 2008).

In addition to the secondary flow and laminar-turbulent transition downstream of the trough re-energizing the boundary layer along the span, two other skew-induced mechanisms adding streamwise vorticity were detected in oil flow visualization results and mentioned previously by Rostamzadeh et al. (2014).

The three-dimensional bubbles at troughs lead to formation of counter-rotating streamwise vortices. The observation of this structure in oil visualization results is in accordance with Rostamzadeh et al. (2014) who named the mechanism as primary vortices (figure 2.46). In addition, secondary vortices, presented by Rostamzadeh et al. (2014) as an effect of separated flow at trailing edge, are found in the results (figure 6.20).Therefore secondary flow, anisotropic turbulence, primary and secondary vortices influence the streamwise vorticity over the upper surface of wavy airfoils causing a complex three-dimensional structure (figure 6.19).

Oil flow visualization indicates the flow mechanisms aforementioned for varied flow and geometric conditions tested in this work. Although the main flow mechanisms remain valid for all test conditions, different bubble shapes caused unexpected distinct behaviour on trailing edge flow separation (secondary vortices). A pair of three-dimensional bubble patterns, hereby named *tipped-bubble* and *elongated-bubble* respectively for longer and shorter tubercle wavelength configurations, were identified. In the next subsections, the specific flow mechanisms regarding *tipped-bubbles* and *elongated-bubbles* will be discussed.

6.2.4 Tipped-bubbles

A possible vortex model presented in figure 6.21 is suggested in order to represent the flow topology for a wavy leading edge configuration of longer wavelength. A horseshoe vortex fixed at wavy leading edge (Γ_S), a horseshoe vortex fixed at the laminar bubble (Γ_B) and a pair of straight filaments (Γ_E) emerging from airfoil trailing edge are related respectively to secondary flow, primary vortices and secondary vortices.

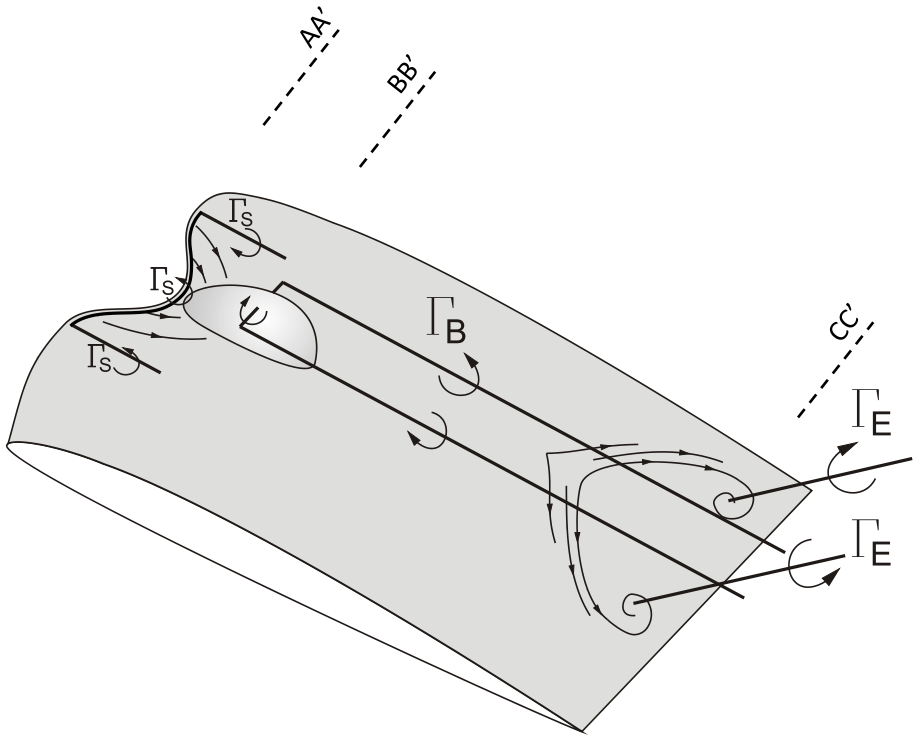

Figure 6.21:Vortex model representing the flow topology caused by tipped-bubbles.

The section AA´ represents the schemes of streamwise vorticity increase on flow over the airfoil by secondary flow (figure 6.22). The span flow establishes velocity coming from peaks to troughs. The induced velocity field can be modelled by counter-rotating vortices that induce a downwash at peaks (figure 6.19). The numerical simulations carried out by Skillen et al. (2014) present streamwise vorticity distributions caused by secondary flow similar to section AA´ modeling (figure 6.25).

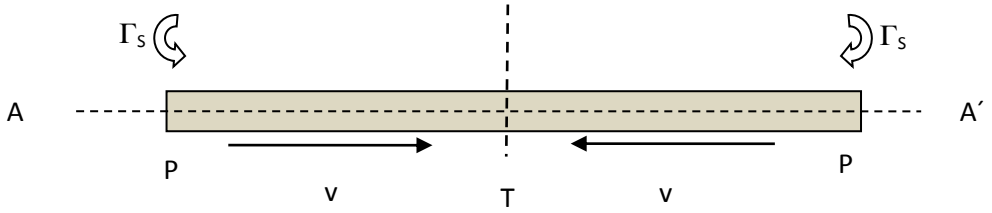

Figure 6.22: Pair of straight filaments parallel to airfoil that comes from a horseshoe vortex representing secondary flow.

The section BB´ shows the modelling of primary vortices (figure 6.23). The three-dimensional bubbles for longer wavelengths in oil flow visualizations indicate span flow from peaks to troughs, suggesting primary vortical structures based on counter-rotating vortices (CVP) inducing upwash (figure 6.24). In addition, figure 6.24 presents a wake downstream of the bubbles caused by vortex convection.

Thus, the laminar separation bubble is represented by a horseshoe vortex distribution with positive circulation in order to keep the physical condition of vortex emission downstream of the bubble. The laminar bubbles at longer wavelength are named *tipped-bubble* since their vortex distribution is similar to a wing tip.

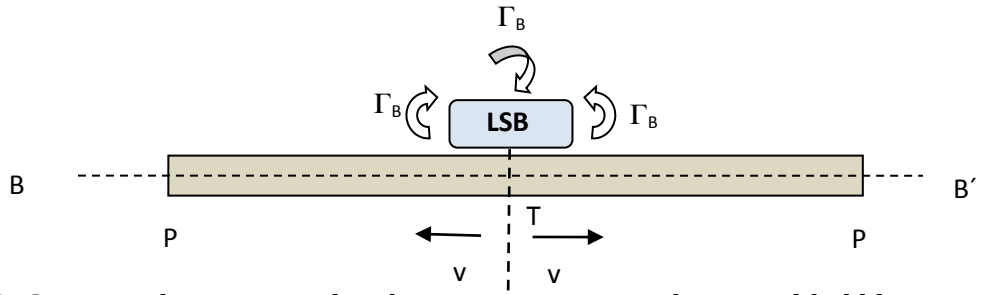

Figure 6.23: Horseshoe vortex distribution representing the tipped-bubble presenting an upwash at peaks and inducing velocities in these regions.

The figure 6.24 shows a typical *tipped-bubble* in agreement with the mathematical representation. The oil visualization indicates, near to bubble ends, fluid moving from troughs to peaks adding velocity in this region, and a dark area forming a bubble wake. These characteristics are in according with a horseshoe vortex distribution model with positive circulation.

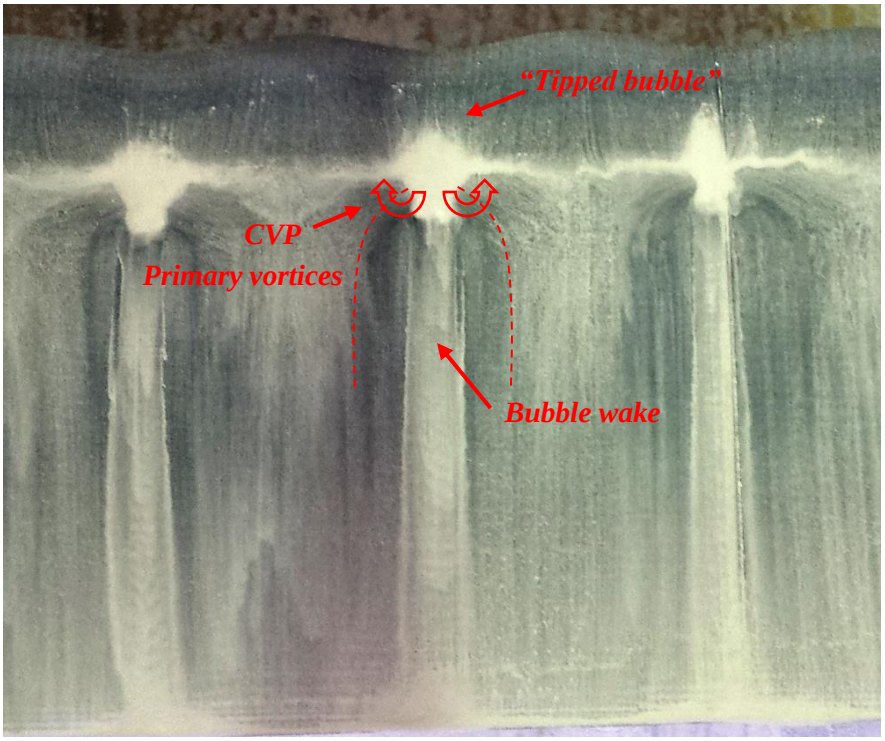

Figure 6.24: "Tipped bubble structure" for wavy configuration A3λ40 at NACA 0020 airfoil (α =5º and Re=290,000).

Skillen et al. (2014) present for a wavy airfoil in figure 6.25 streamwise vorticities downstream of the troughs that show evidence of streamwise vortices in agreement with oil flow visualization results. In addition, the flow pattern model proposed herein is in agreement with flow visualization results confirms the numerical simulation that indicates inversion of vorticity from secondary flow caused by a tipped-bubble. Although Rostamzadehet et al. (2014) identify the primary vortices in their numerical simulations, the counter-rotating vortex pair has the same vorticity signal of the secondary flow.

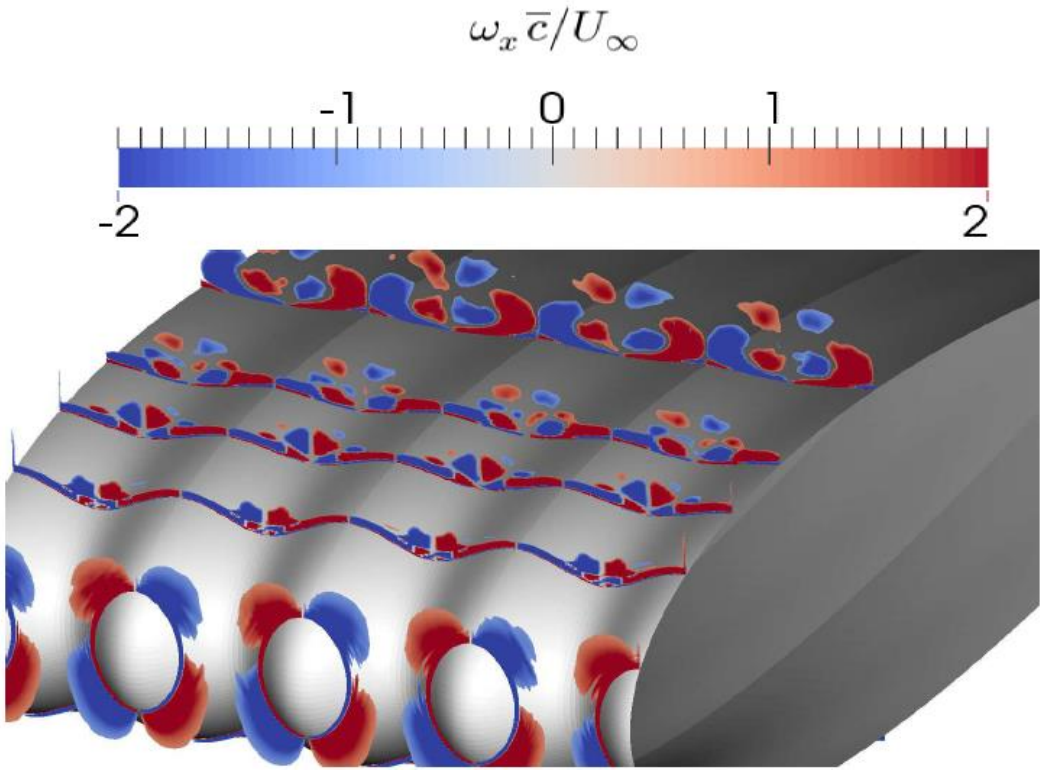

Figure 6.25: Slices colored by time-averaged streamwise vorticity (SKILLEN et al., 2014).

The source of the streamwise vortices emitted by bubbles, as suggested by Rostamzadeh et al. (2014) and Skillen et al. (2014) can be seen clearly in figure 6.26 where twin areas with absence of oil at tubercle troughs indicate the presence of a vortex pair that removes the oil in these regions.

Figure 6.26: Vortex pair removing oil from twin areas at tubercle troughs for configuration A11λ40 at NACA 0020 airfoil (α =5º and Re=290,000).

The counter-rotating vortex pair forms vortex lines convecting downstream of the bubbles, establish a region of momentum exchange along the span. Based on vortex lines obtained numerically by Rostamzadeh et al. (2014), the vortex lines at flow visualization

results can be identified (figure 6.27). In addition, the chordwise separation lines are defined by Rostamzadeh et al. (2014) as the lines of separation of the boundary layer from airfoil surface.

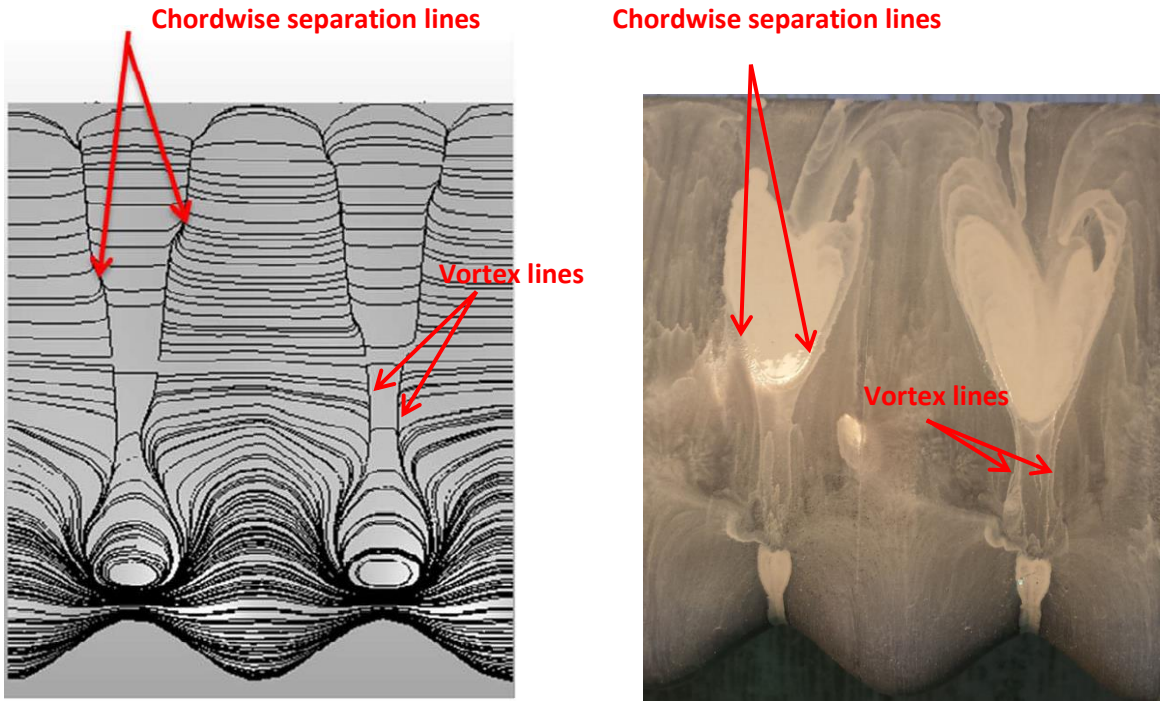

Figure 6.27: Vortex and chordwise separation lines predicted by numerical simulation (ROSTAMZADEH et al., 2014) and confirmed by flow visualization.

The trailing edge flow separation for a longer wavelength configuration presents a typical delta-shape in oil flow visualizations (figure 6.19), confirming the recent numerical results carried out by Skillen et al. (2014) and Rostamzadeh et al. (2014).Tubercle peak areas at leading edges are less susceptible to flow separation as previously discussed. In addition, the primary vortices exchange momentum, increasing velocities at this location, increasing the tendency in delaying flow separation at tubercle peaks. Thus, the distinct characteristics in resistance to flow separation at the trailing edge along the span justify a delta-shaped of the flow separation areas. Agreeing with this hypothesis, the pressure measurements for long wavelength configuration presented by Karthikeyan et al. (2014) and Rostamzadeh et al. (2014) in figures 6.10 and 6.12, respectively, confirm more favourable pressure distribution at rear chordwise position, contributing to avoid flow separation downstream from tubercle peaks.

The section CC´ (figure 6.28) represents the trailing edge flow separation in delta-shape caused by secondary vortices found at flow visualization (figure 6.19).The circulation distribution has opposite signal to the horseshoe vortex which causes a decrement in lift; the pair of vortex filament appears from the physical vortex focus. In addition, the horseshoe vortex due to bubbles continues along the trailing edge.

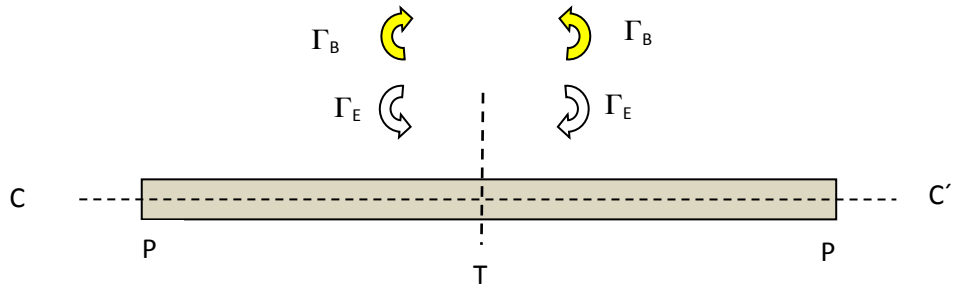

Figure 6.28: Interaction between primary and secondary vortex.

The delta-shaped trailing edge flow separation, at longer wavelength configuration, causes a significant aerodynamic deterioration at pre-stall conditions preventing the wavy configurations to reach a maximum lift coefficient value close to the smooth configuration. It is therefore important to understand the separation flow characteristics and the correlation with geometric parameters.

The oil flow visualizations for longer wavelength configurations (A3λ40 and A11λ40) on thicker airfoils NACA 0020 and NACA 0030 present earlier flow separation downstream of the tubercle troughs whereas the areas downstream of the peaks remain attached forming delta-shaped trailing edge flow separation. On the other hand, the baseline configuration keeps a two-dimensional trailing edge flow separation (figures 5.32 and 5.36).

Figure 6.29 shows clearly that the wavy leading edge configuration presents a delta-shaped flow separation area for the NACA 0030 airfoil. Besides, the tubercle configuration increases flow separation areas explaining the aerodynamic deterioration of the lift curve in the pre-stall regime for thicker airfoils, consequently decreasing the maximum lift values (figures 4.22 and 4.40).Therefore the role of tubercle on the pre-stall regime is to anticipate the trailing edge flow separation.

Increasing the angles of attack, the delta-shaped structures grow toward leading edge as a consequence of higher adverse pressure gradients remaining attached flow downstream of the peaks. In addition, the three-dimensional laminar bubble decreases in length and reaches the leading edge (figure 6.30).

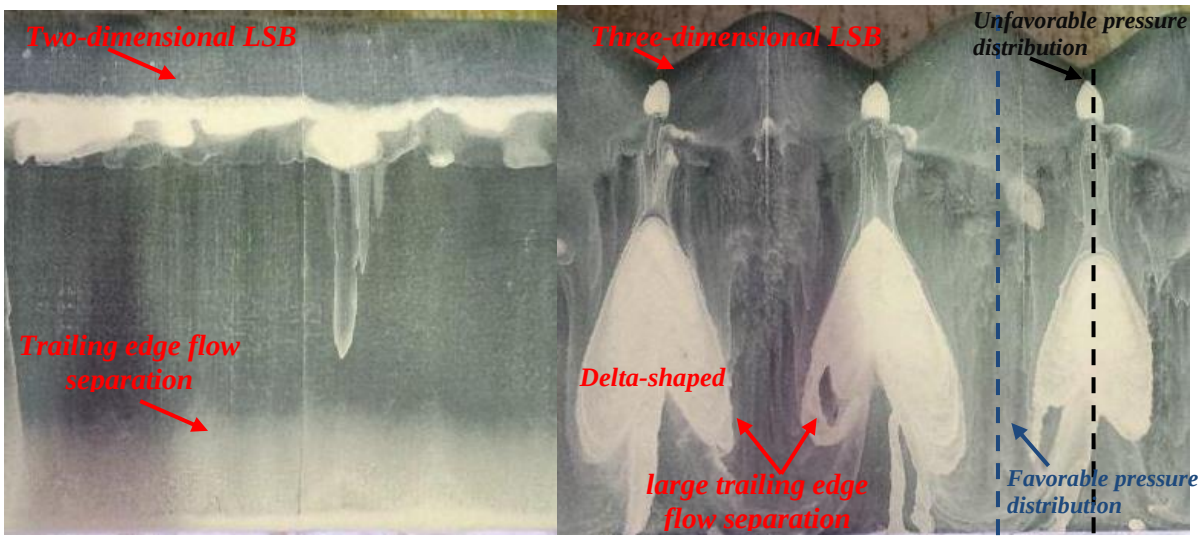

Figure 6.29: Wavy leading edge effect on pre-stall regime (NACA 0030; smooth and A11λ40; α = 10º and Re =290,000).

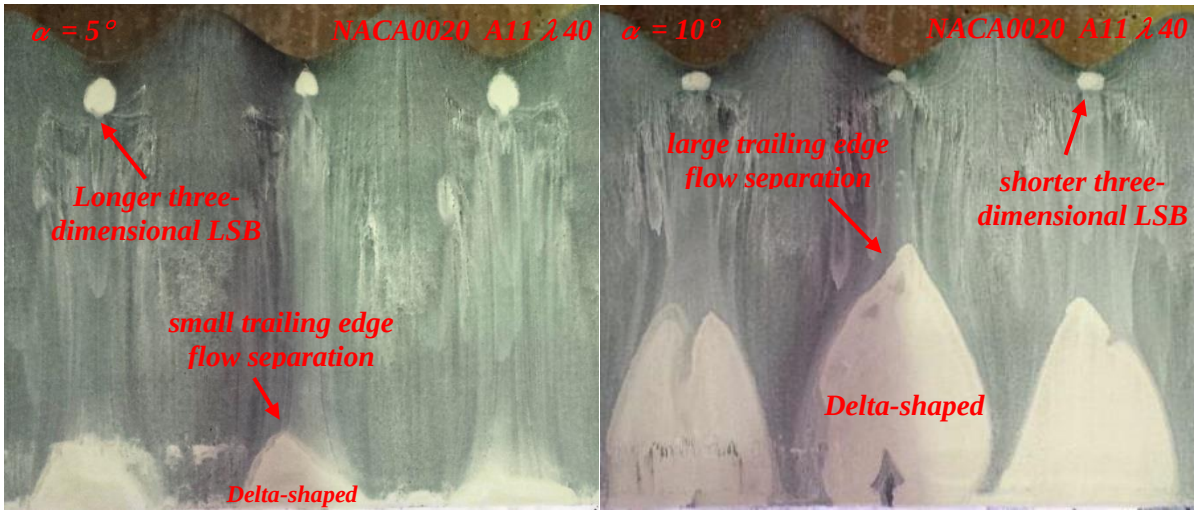

Figure 6.30: Angle of attack effect on wavy leading edge flow topology (Re =290,000).

The effect of increasing in airfoil thickness can be seen in figure 6.31. The thicker airfoil presents an earlier emergence of the delta-shaped flow separation structure at a given chordwise position compared to the thinner airfoil. Besides, as previously mentioned, a smoother leading edge radius causes a longer bubble at an after position in the thicker airfoil in comparison to the thinner airfoil.

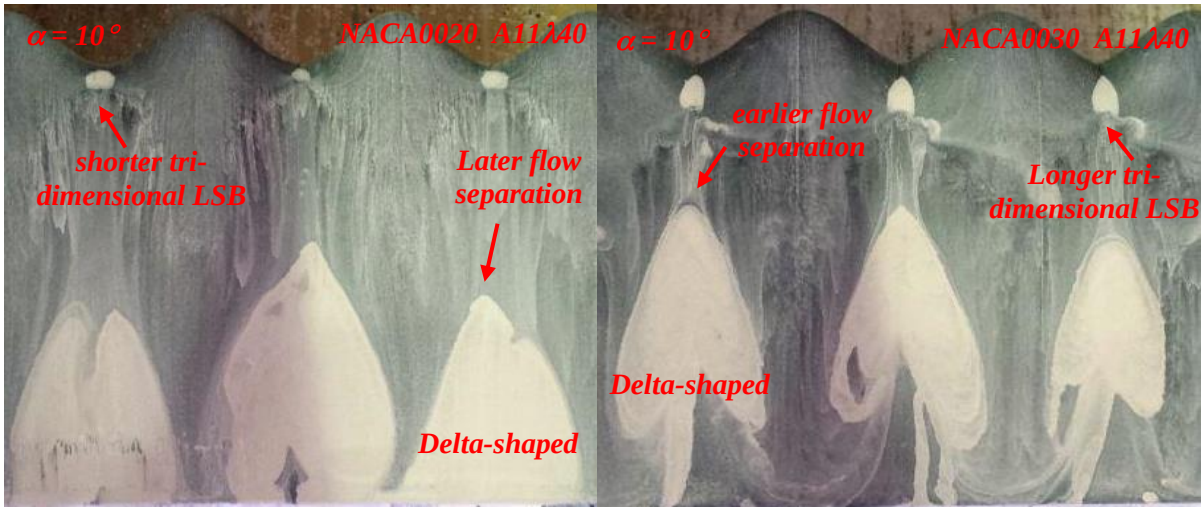

Figure 6.31: Airfoil thickness effects on wavy leading edge flow topology (Re =290,000).

As mentioned before, an increase in amplitude or amplitude-to-wavelength ratio in the tubercle causes an increase in the span flow and consequently exacerbates the adverse gradient at tubercle troughs. Figure 6.32 shows clearly the amplitude effect on trailing edge flow separation for the NACA 0020 airfoil.

Higher flow distortion can be seen on secondary flow at the leading edge for the larger amplitude (A11λ40) configuration indicating higher span flow, and consequently the higher adverse pressure gradient leads to an earlier flow separation along the chord, thus establishing stronger delta-shaped flow separation areas as compared to the smaller amplitude configuration.

This characteristic from larger tubercle amplitude dictates the worst aerodynamic performance in the pre-stall regime for all airfoil thicknesses and in the most range of Reynolds number tested in this work. Previous studies of wavy geometry effect on tubercle performance (HANSEN et al., 2009; JOHARI et al., 2007; LEVSHIN et al., 2006) indicate

lower performance for larger tubercle amplitude configurations, agreeing with the physical explanation proposed in this work.

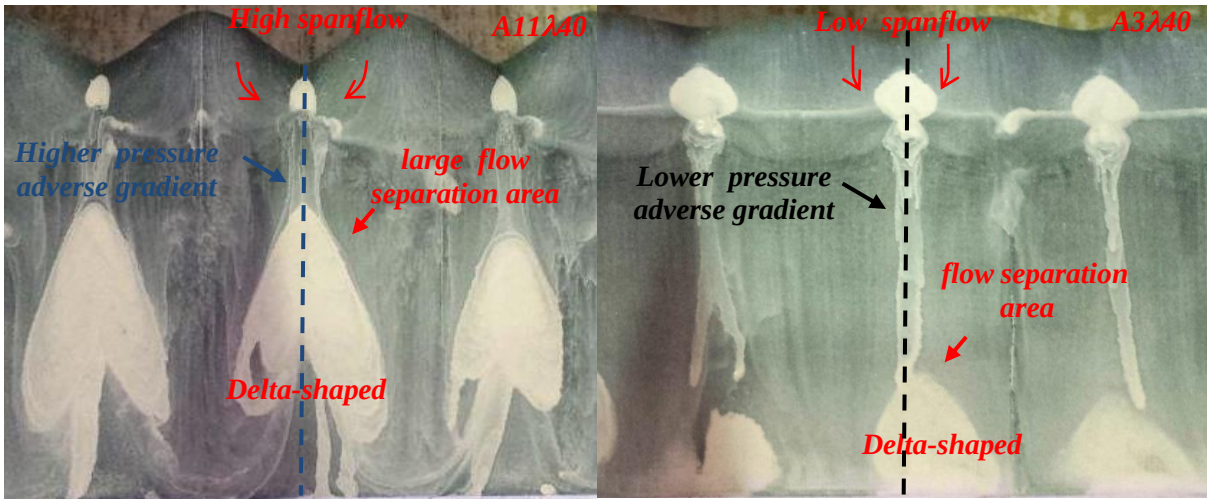

Figure 6.32: Amplitude effect on tubercle flow topology (NACA 0020 airfoil; α = 10°; Re =290).

6.2.5 Elongated-bubble

As it can be seen in figure 6.33, the flow topology for shorter tubercle wavelength configuration (A3λ11) is characterized by an elongated laminar separation bubble with distinct contour as compared to bubbles formed from longer wavelength configurations.

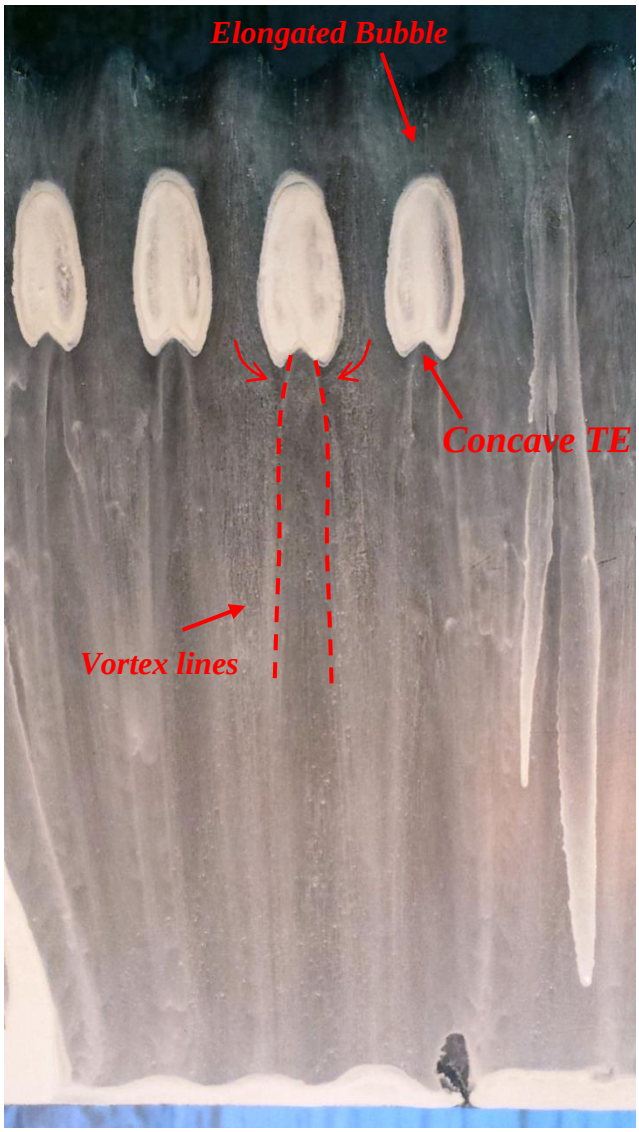

Figure 6.33: Elongated bubble topology for shorter tubercle wavelength configuration (NACA 0020; α = 5°and Re=290,000).

Since the elongated bubble presents different characteristics and cause distinct effects on trailing edge flow separations when compared to longer wavelength configuration (figure 6.39), the "bubble width-to-wavelength" ratio, named here *influence ratio* (r_i) is considered to be an important parameter for tubercle performance (figure 6.34) where a low ratio leads to

bubbles becoming very close to each other and causing important changes on the flow at tubercle peaks.

$$r_i = \frac{W_B}{\lambda}$$

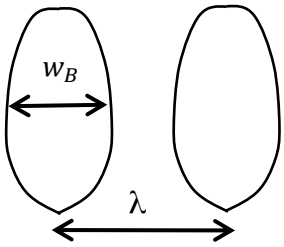

Figure 6.34: "Bubble width-to-wavelength" ratio as an important parameter causing changes on flow topology.

A narrow physical channel imposed by the distance between the elongated bubbles suggests that the flow undergoes significant acceleration in this area, and in the channel inlets the streamlines are bent outwards towards the bubbles indicating strong streamwise vorticity in this region. In addition, the oil visualization shows vortex lines downstream of the bubbles similar to the case of longer wavelength (λ40) configuration, indicating a possible counter rotating vortex pair structure (figure 6.35).

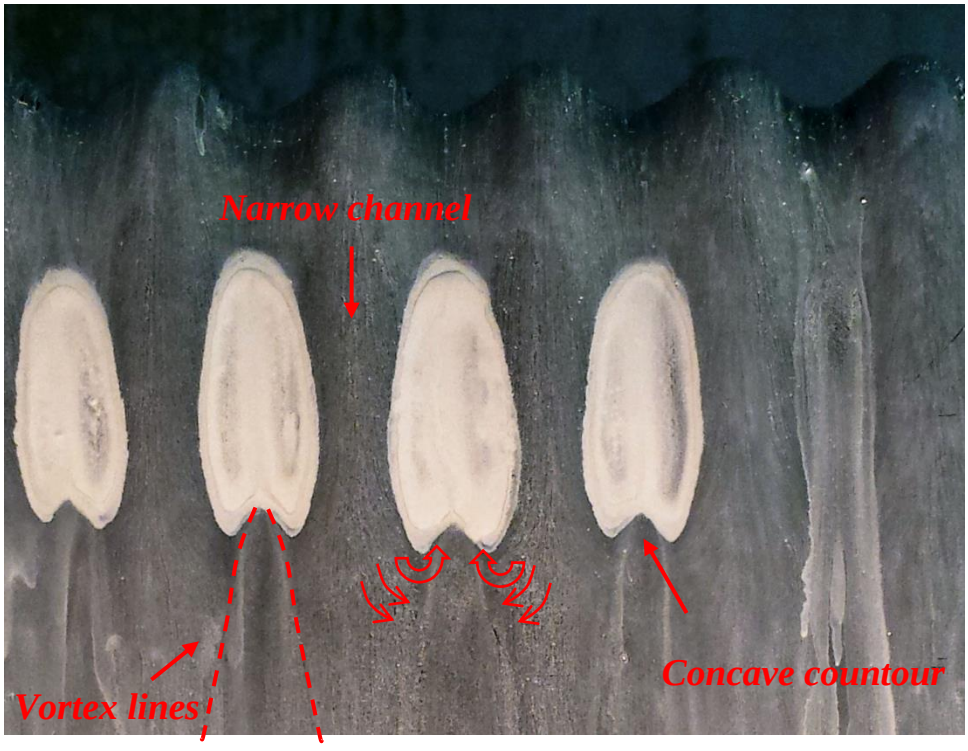

Figure 6.35: Flow mechanisms regarding the elongated bubble (NACA 0020; α = 5° and Re=290,000).

Figure 6.36 shows a possible circulation distribution model that agrees with the physical flow topology presented by elongated bubbles. A horseshoe vortex fixed at wavy leading edge (Γ_S) represents the secondary flow and a second vortex structure models the flow inside the laminar separation bubble (Γ_B). The bubble wake comes from the interaction between Γ_S and Γ_B.

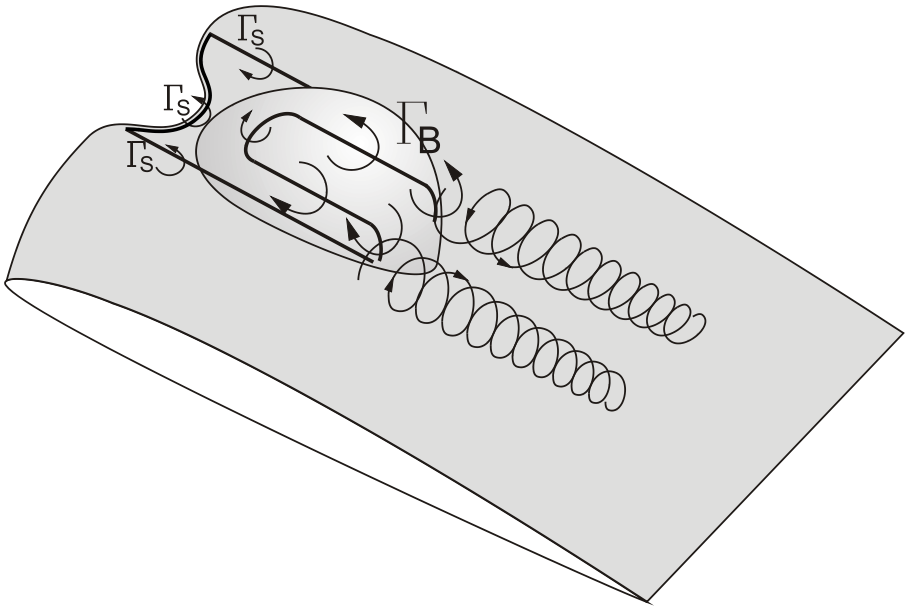

Figure 6.36: Possible circulation distribution model for elongated-bubble.

Differently from longer wavelength configurations, the configuration A3λ11 undergoes earlier trailing edge flow separation downstream of peaks attributed to elongated bubble flow mechanism (figure 5.32 and 5.36). In this direction, a possible explanation considers that the channel between bubbles carries a main role in the early flow separation at tubercle peaks for the shorter wavelength configuration.

Although the secondary flow at the leading edge causes an increase in the adverse pressure gradient at tubercle troughs suggesting areas susceptible to flow separation, the flow path at peaks undergoes additional acceleration changing the flow characteristics at the trailing edge.

After the flow decelerates at tubercle peaks due to secondary flow, it accelerates in the narrow channel between bubbles differently of the case of tipped-bubble distribution. Thus, the flow at peaks reaches higher velocities than at troughs close to trailing edge region, possibly with high adverse pressure gradients and as consequence causing an earlier flow separation at this region. Figure 6.37 shows the flow path accelerating downstream of the peaks up to reaching the trailing edge. In addition, the figure 6.38 shows a hypothetical pressure distribution along the chord at tubercle peaks, presenting more severe adverse pressure gradient at the trailing edge downstream of the tubercle peaks.

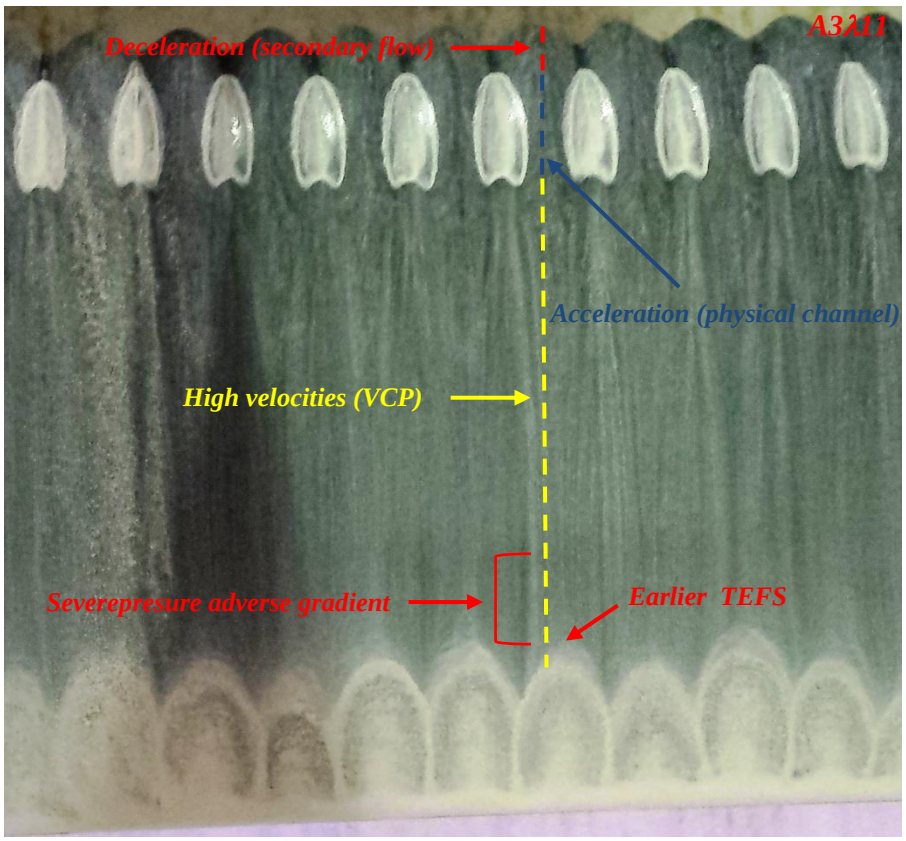

Figure 6.37: Earlier trailing edge flow separation downstream of the peaks (NACA 0030; α = 10° and Re=290,000).

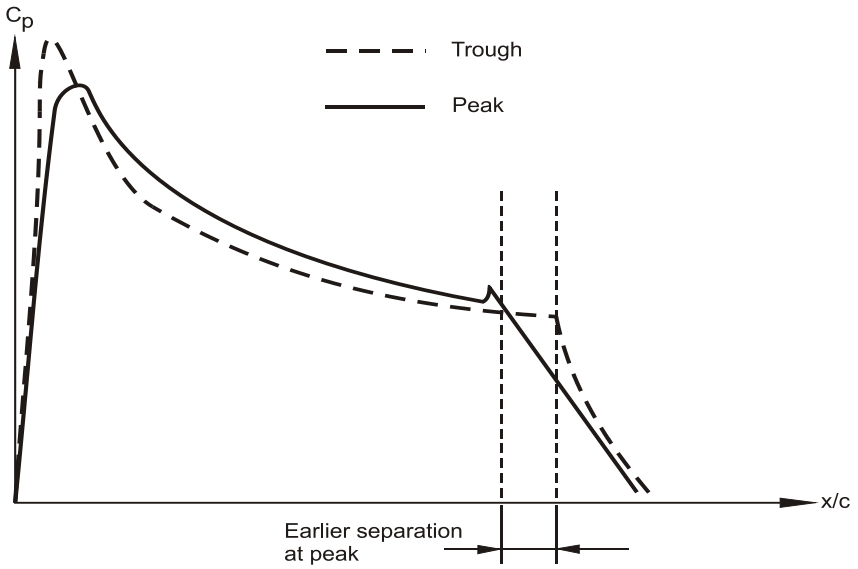

Figure 6.38: Hypothetical pressure distribution at peak and trough for shorter wavelength configuration.

The topological analysis agrees with force measurements (4.4, 4.22 and 4.40) and previous studies (LEVSHIN et al., 2006; JOHARI et al., 2007; HANSEN et al., 2009) regarding amplitude and wavelength effects on wavy leading edge pre-stall performance. The smaller amplitude and shorter wavelength appear in previous studies as optimal geometric parameters; however, the reasons were not clarified. The present topologic analysis shows that the smaller amplitude decreases the trailing edge flow separation due to lower span flow levels that cause a less severe adverse pressure gradient at troughs (figure 6.32).

On the other hand, from wavelength parameter emerges a flow mechanism that minimizes the trailing edge flow separation (figure 6.39). A possible explanation comes from flow characteristics downstream of the peaks close to the trailing edge. At tubercle peaks, the flow undergoes acceleration caused by the bubble channel so that the flow separation remains in the vicinity of the trailing edge. On the other hand, flow separation at peaks causes a span flow that tends to decrease the adverse pressure gradient at troughs and so preventing flow separation in this location. As a global effect, the shorter wavelength configuration tends to resist to the propagation of the flow separation towards the leading edge.

Thus, in general, the wavy leading edge airfoils with smaller amplitude and shorter wavelength tubercles reach better pre-stall aerodynamic characteristics and consequently higher maximum lift.

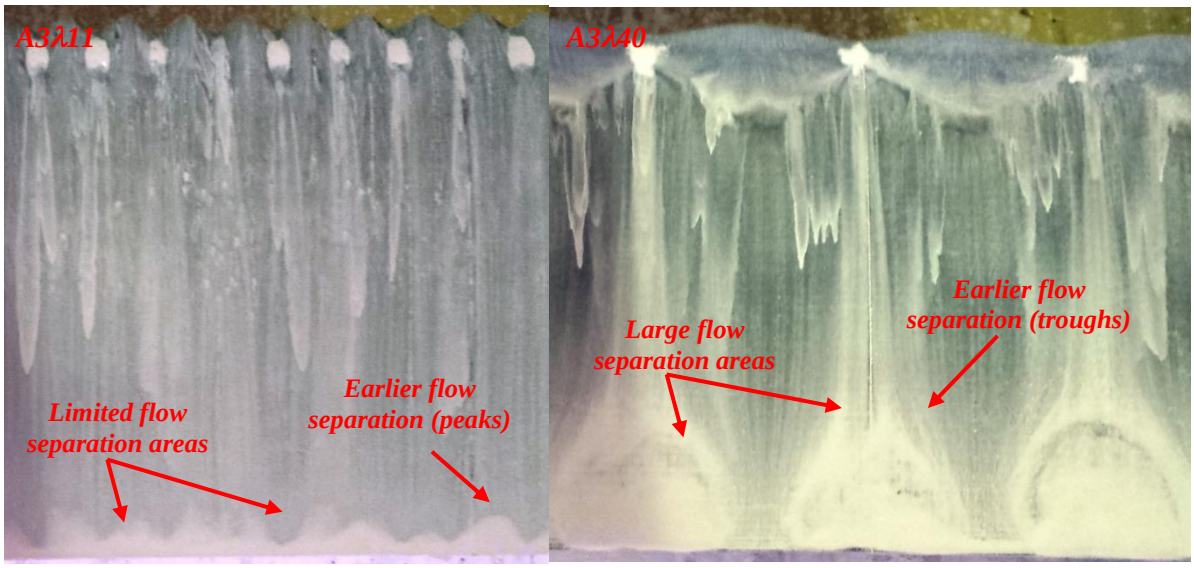

Figure 6.39: Smaller amplitude and shorter wavelength changing the flow mechanism and decreasing flow separation area (NACA 0020; $\alpha = 10°$ and Re= 290,000).

In addition, the force measurement results (4.4, 4.22 and 4.40) show that the tubercle of smaller amplitude and shorter wavelength maintains soft stall characteristics in the post-stall regime confirming previous studies (LEVSHIN et al., 2006; JOHARI et al., 2007; HANSEN et al., 2009). Thus, this configuration presents an overall optimum performance at pre-stall and post-stall regime.

6.2.6 Airfoil thickness effects

As shown in oil flow visualizations in the figure 6.29 and as mentioned before, the effect of wavy leading edge on the pre-stall regime is to anticipate the trailing edge flow separation when compared to smooth configuration, potentially causing a large aerodynamic deterioration depending on tubercle geometry. Therefore the trailing edge flow characteristics of the smooth airfoils dictate the performance of the corresponding wavy leading edge at the pre-stall regime.

In this sense, the influence of the airfoil thickness on wavy leading edge performance can be evaluated. As it was previous discussed, the thinnest NACA 0012 airfoil has *leading edge stall characteristics* where the stall propagates from the leading edge with a small trailing edge flow separation while keeping the flow fully attached through the whole of the pre-stall regime.

These characteristics lead the thin wavy airfoil to cause lower deterioration at pre-stall conditions when compared to thicker airfoils. Because the smooth configuration is resistant to trailing edge flow separation, the configurations A3λ11 and A3λ40 do not cause flow separation at the trailing edge in the pre-stall regime (figures 5.3 and 5.27); lift coefficient values remain near to the baseline airfoil up to angles of attack very close to stall angle (figure 4.4).

In contrast with the thin smooth NACA 0012 airfoil, as previously mentioned, the NACA 0020 and NACA 0030 airfoils establish a progressive trailing edge flow separation up to the leading edge where the laminar separation bubble resists up to higher angles of attack without full flow separation. This characteristic establishes worse pre-stall behaviour for thicker wavy leading edge airfoils. As the thicker baseline airfoils do not resist to trailing edge flow separation up to the stall, the wavy configurations, as noted previously, anticipate the flow separation causing aerodynamic deterioration on lift curve, starting at lower angle of attack and increasing up to the stall condition.

With increasing airfoil thickness, the flow separation tends to appear earlier at the trailing edge (figures 5.8, 5.13, 5.32 and 5.36). Thus, as the wavy configurations anticipate the trailing edge flow separation, the thickest wavy NACA 0030 airfoils develop flow separation at the leading edge earlier than NACA 0020 airfoils, thus establishing lower lift values at pre-stall regime (figures 4.22 and 4.40). Figure 6.41 shows higher trailing edge flow separation areas for the thickest wavy airfoil.

On the other hand, the thickest smooth airfoil presents higher leading edge radius in comparison to the NACA 0020 airfoil, keeping the laminar separation bubble attached at the leading edge up to higher angles of attack and increasing maximum lift coefficient values (figure 4.56). Figure 6.42 shows a longer laminar bubble further from the leading edge when compared to NACA 0020 airfoil, indicating a more resistant pattern with respect to full flow separation at the leading edge. Considering that the thickest wavy airfoil presents lower performance and its smooth counterpart reaches higher stall angle with greater lift values, it is

observed that the highest thickness configuration suffers the worst aerodynamic deterioration (figures 4.22 and 4.40).

In general, at higher Reynolds numbers, the wavy leading edge NACA 0012 airfoil, except for the larger tubercle amplitude, tends to have less aerodynamic deterioration at pre-stall conditions as compared to the thickest airfoil due to its tendency for leading edge stall, thus not showing the wavy effect in anticipating trailing edge flow separation. In addition, the greatest performance of the thickest smooth airfoils reaching the highest maximum lift add to the greatest areas of trailing edge flow separation caused by tubercles on wavy NACA 0030 leads to the worst aerodynamic deterioration on the thickest airfoil.

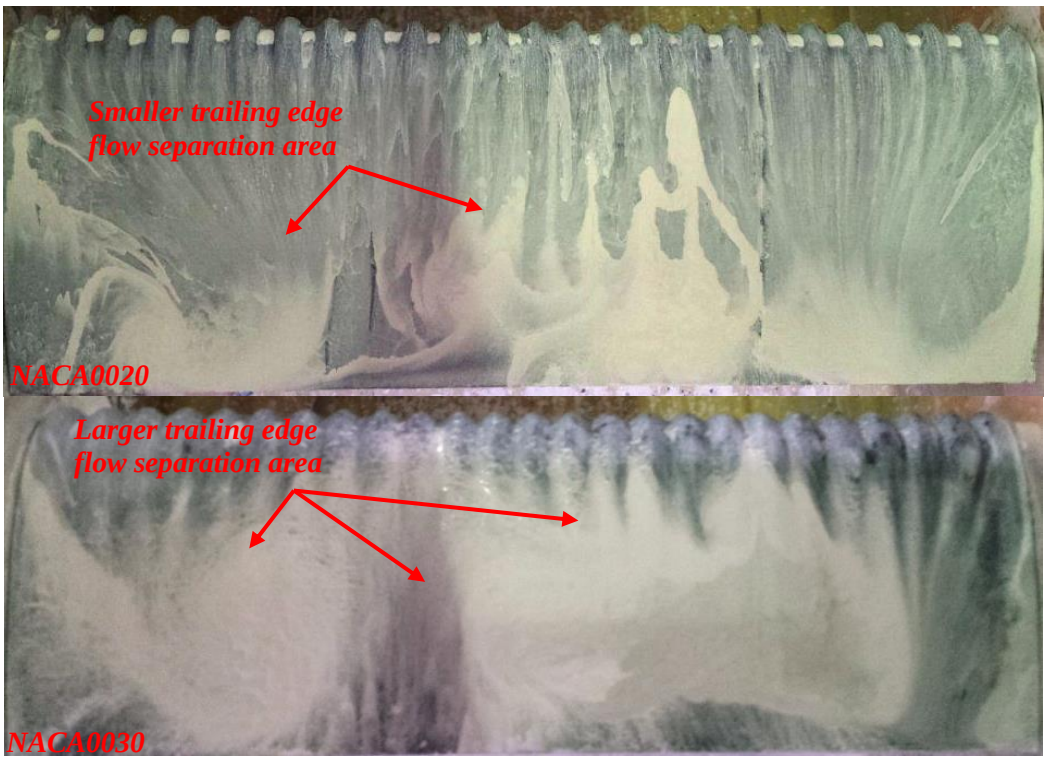

Figure 6.40: The airfoil thickness effects on flow separation at wavy airfoil (A3λ11; α =15° and Re=290,000).

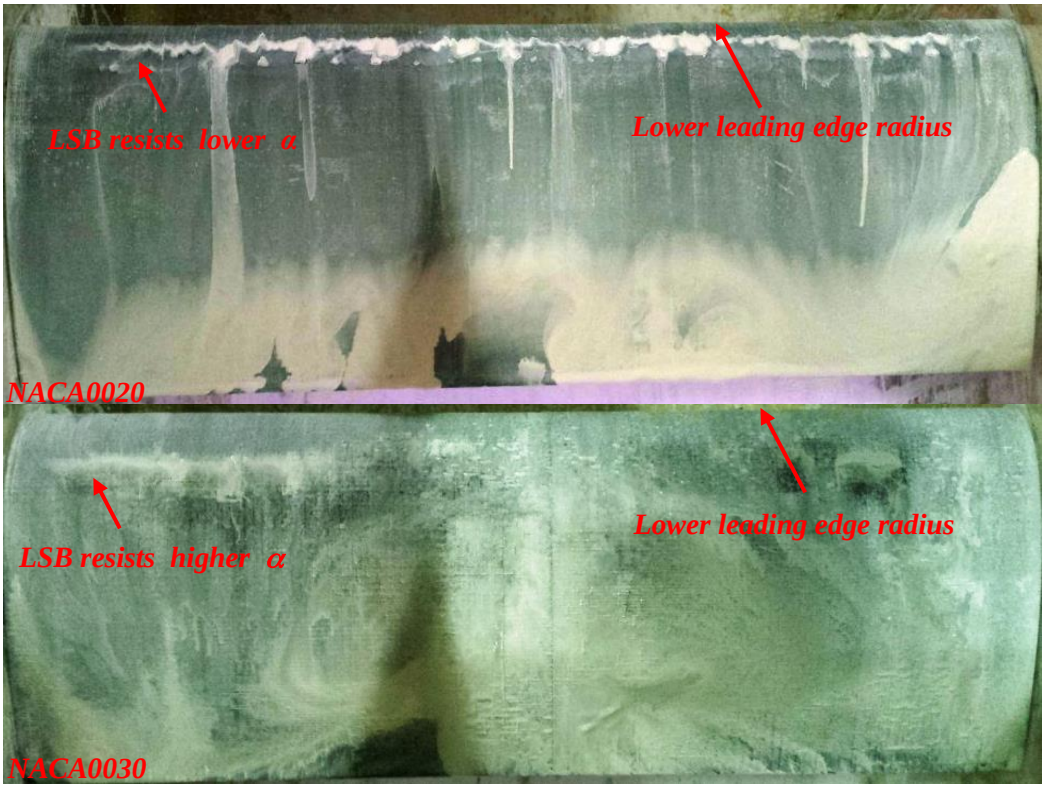

Figure 6.41: The airfoil thickness effects on flow separation at smooth airfoil (A3λ11; α =15° and Re=290,000).

6.3 Wavy airfoil post-stall phenomenology

Many researchers (CUSTODIO, 2008; FISH; BATTLE, 1995; MIKLOSOVIC et al., 2004; MIKLOSOVIC et al., 2007; PEDRO; KOBAYASHI, 2008) state that the mean flow mechanism regarding wavy leading edge phenomena is similar to vortex generators used on aircraft wings. According to these researchers, vortex structures generated by wavy leading edges are established by changing the flow topology over the airfoil in the pre-stall and post-stall regimes with varying aerodynamic efficiency. However, it was shown in the previous section that in the pre-stall regime, complex flow mechanisms occur distinct from vortical structures caused by vortex generators. Although vortical structures appear in the post-stall regime keeping high lift values for wavy leading edges confirming the hypothesis of previous researches, this section presents, in addition to the evaluation of vortical structure characteristics, an additional flow control mechanism to maintain high lift values in the post-stall regime.

The flow visualization results show that vortical structures appear on wavy airfoils in most cases in the post-stall regime. However, these flow structures also occur in the pre-stall regime for the thin NACA 0012 airfoil. The thinnest airfoil presented a flow mechanism established by a counter-rotating vortex pair (CVP) formed between peaks establishing a "tooth-shaped" (figure 6.42). In contrast, the thicker airfoils present what seems to be a unique vortical structure with a single vortex at tubercle troughs (figure 6.43).

Figure 6.42: Counter-rotating vortex pair (CVP) at wavy airfoil (NACA 0012; A11λ40; α =10° and Re=290,000).

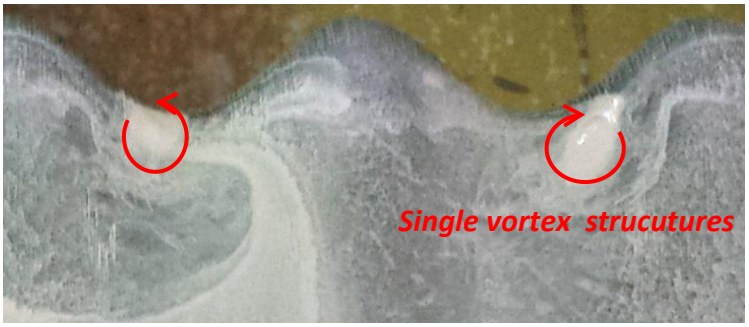

Figure 6.43: A unique vortical structure at wavy airfoil with a vortex at tubercle trough (NACA 0020; A11λ40; α =20° and Re=290,000).

Based on the observation of "tooth-shaped" structures, a possible circulation distribution model that agrees with the counter-rotating vortex pair inside flow structure is suggested (figure 6.44). The model considers a horseshoe vortex fixed at wavy leading edge representing the secondary flow (Γ_S) and a circulation distribution structure satisfying the

counter-rotating vortices and flow boundary conditions (Γ_V). Further, the interaction between Γ_S and Γ_V justify the vortex line found in flow visualizations (figure 6.45).

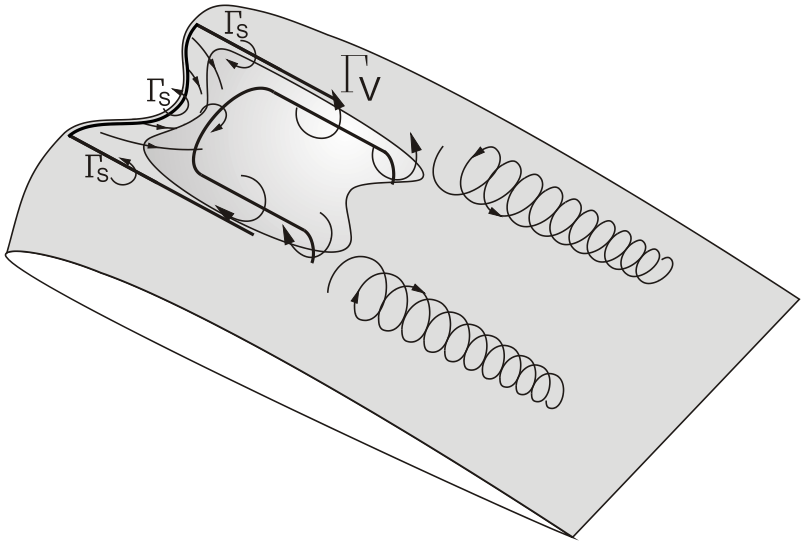

Figure 6.44: Circulation distribution model proposed for contour-rotating vortex pair (CVP).

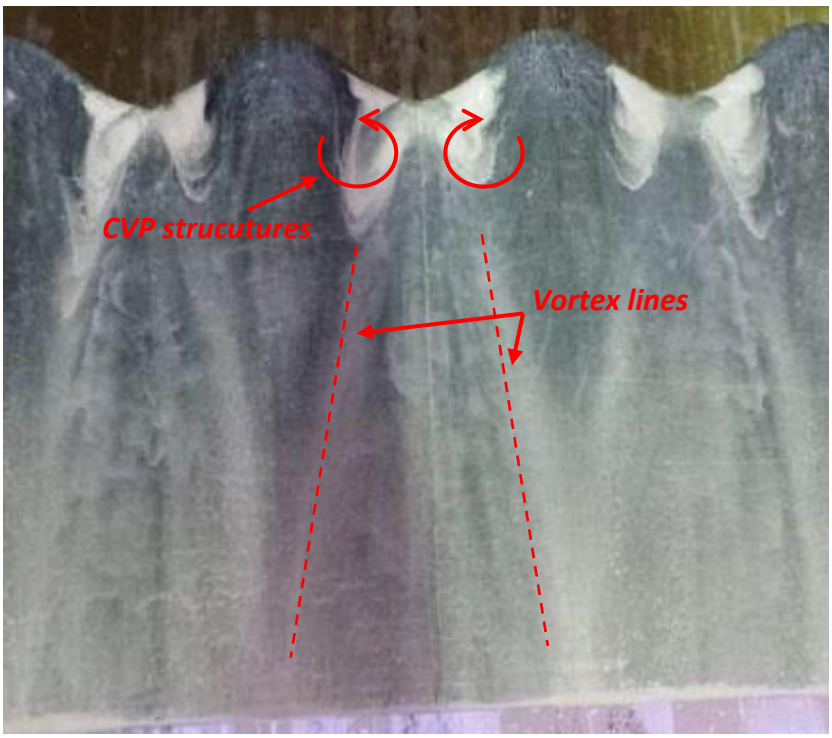

Figure 6.45: Counter-rotating vortex pair (CVP) on wavy airfoil (NACA 0012; A11λ40; α =10° and Re=290,000).

Figures 6.46-48 show the mini-tufts and oil visualizations for the airfoils NACA 0012, NACA 0020 and NACA 0030 in the post-stall regime. The mini-tufts are aligned behind peaks for all airfoil thicknesses, indicating attached flow in these regions. On the other hand, the mini-tufts present deflections at troughs characterizing flow detachment in this location.

The oil flow visualizations confirm that the flow is attached downstream of the peaks, showing an absence of oil in this region. In addition, the visualizations show the presence of vortical structures (CVP and single vortex) between tubercle peaks. These structures, generated near tubercle troughs, possibly cause momentum exchange in areas behind peaks, re-energizing the boundary layer and keeping flow attached in these locations.

As discussed by previous researchers, the vortices generated by tubercles at the leading edge seem to be similar to vortices from VG´s exchanging momentum between free flow and boundary layer downstream of the peaks. Therefore the flow control mechanism keeps the flow partially attached in areas at the airfoil leading edge, maintaining high values of the lift coefficient at greater angles of attack establishing soft stall behaviour (figures 4.4, 4.22 and 4.40)

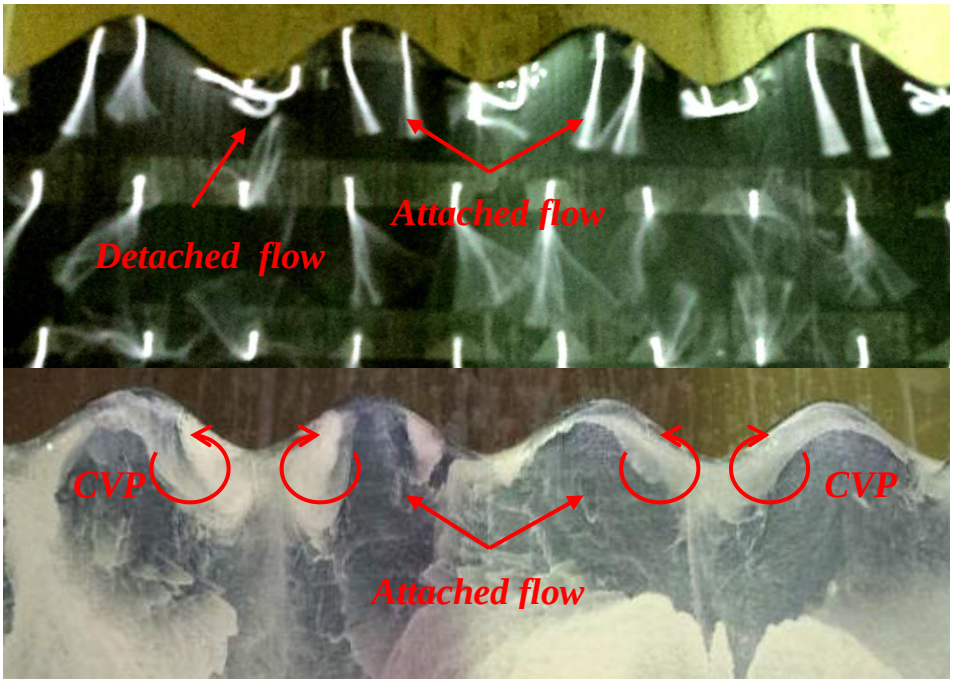

Figure 6.46: Post-stall flow characteristics for wavy configuration (NACA 0012; A11λ40; α =15° and Re=290,000).

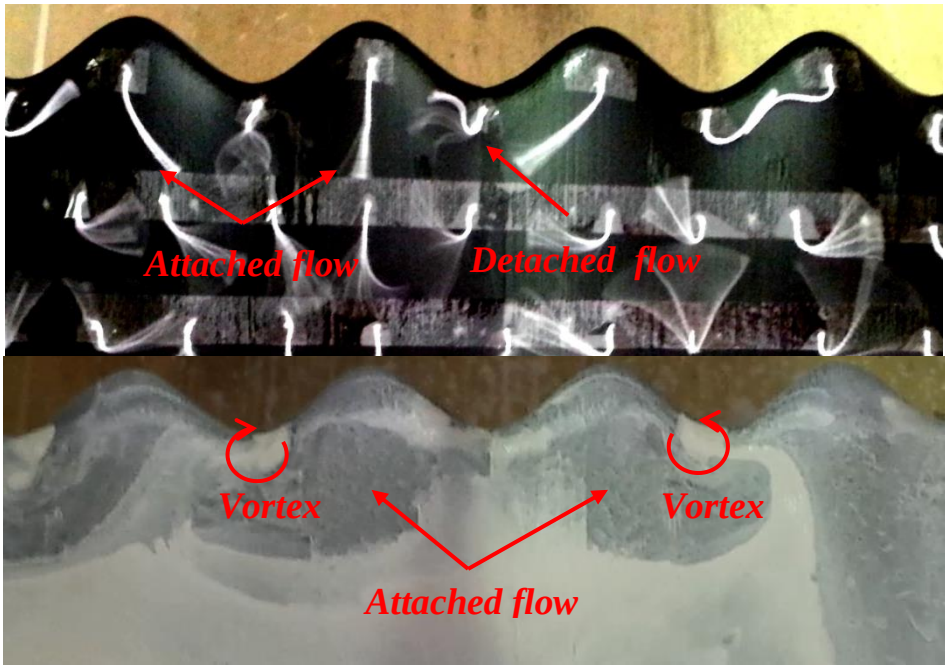

Figure 6.47: Post-stall flow characteristics for wavy configuration (NACA 0020; A11λ40; α =20° and Re=290,000).

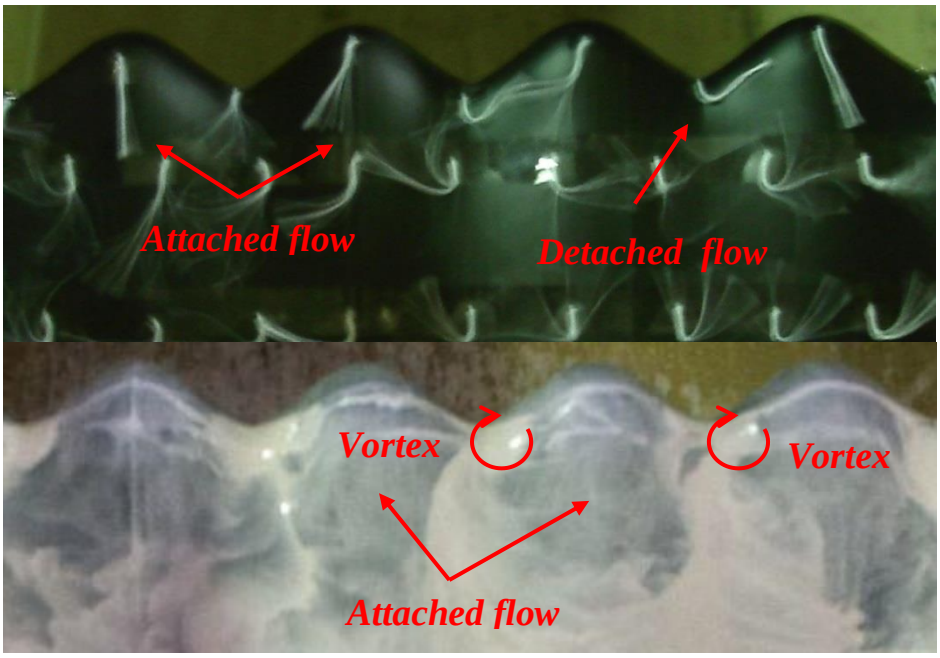

Figure 6.48: Post-stall flow characteristics for wavy configuration (NACA 0030; A11λ40; α =25° and Re=290,000).

The tubercle geometry drives the appearance of vortical structures. At greater amplitude-to-wavelength ratios (A/λ), CVP formations start at lower angles of attack. It can

be seen in figures 6.49 and 6.50 that the configurations A3λ11 and A11λ40 with similar greater amplitude-to-wavelength ratios present CVP´s structures over upper surface of the airfoils. On the other hand, figure 6.51 shows that a smaller amplitude-to-wavelength ratio (A/λ) is not able to start vortical structures between peaks, and sports a bi-periodic three-dimensional laminar bubble distribution along the span.

Configurations with higher tubercle sweep angles (A3λ11 and A11λ40) induce increment in span flow, increasing the longitudinal vorticity up to generate physical streamwise vortices. Thus, as in the pre-stall condition, the amplitude-to-wavelength ratio is indicative of vorticity strength along the leading edge. In addition, an increase in the amplitude-to-wavelength ratio intensifies the convergence of the vorticity tubes forming a unique vortex with higher vorticity strength, similarly to a finite wing.

Figure 6.49: Vortical structures at greater amplitude-to-wavelength ratio (A/λ) (NACA 0012; A11λ40; α =10° and Re=290,000).

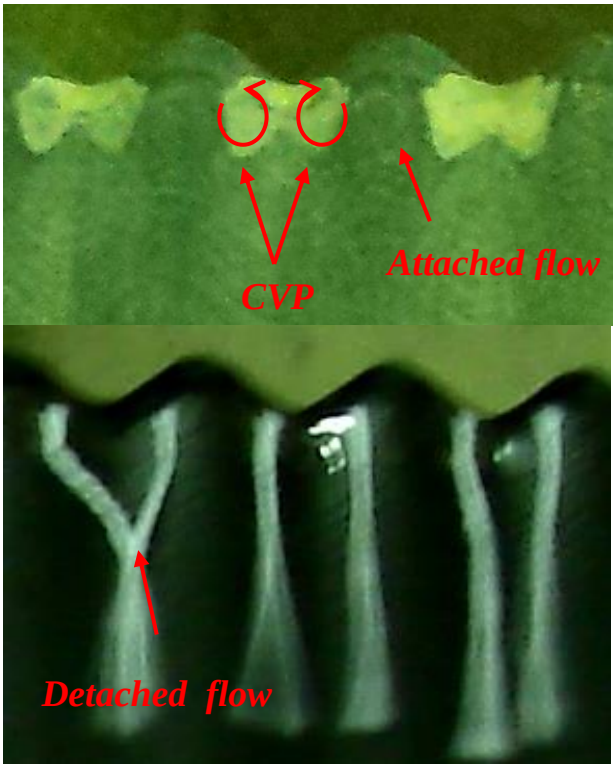

Figure 6.50: Vortical structures at greater amplitude-to-wavelength ratio (A/λ) (NACA 0012; A3λ11; α =10° and Re=290,000).

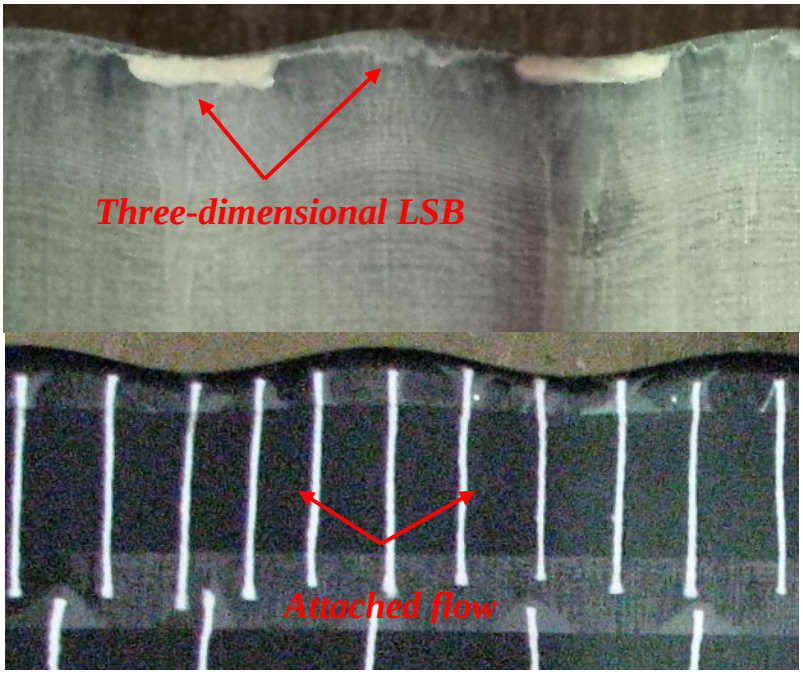

Figure 6.51: Absence of vortical structures at lower amplitude-to-wavelength ratio (A/λ) (NACA 0012; A3λ40; α =10° and Re=290,000).

Another important parameter that drives the vortical structure onset is the airfoil thickness. The thin NACA 0012 airfoil presents CVP structures at the smallest angle of attack ($\alpha = 10°$) due to, as previously discussed, the airfoil resisting to full flow separation at the leading edge up to lower stall angle (figure 6.42). In contrast, single vortices appear for NACA 0020 airfoil only at the higher angle of attack 20° (figure 6.43).

Although in most cases the three-dimensional laminar bubble distribution and vortical structures appear in the pre-stall and post-stall regimes respectively, the flow visualization results indicate that the geometric parameters at the leading edge (amplitude, wavelength and thickness) affect the flow topology so that both flow control mechanisms can occur at pre-stall and post-stall regimes. Figure 6.52 shows three-dimensional laminar bubbles even at the post-stall regime keeping flow attached at the leading edge. In this sense, this work adds a *new perspective* for flow control mechanism in the post-stall regime regarding wavy leading edge phenomena, since previous studies considered only the vortical structures as flow mechanism in order to preserve high lift values at great angles of attack.

The flow visualizations indicate that the three-dimensional laminar bubble becomes effective in keeping higher lift values at post-stall only in the case of shorter wavelength configuration at Re = 290,000 (figures 4.4, 4.22 and 4.40).

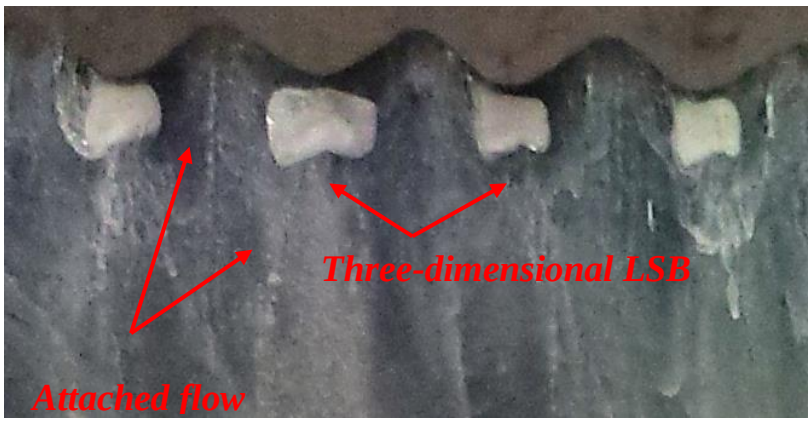

Figure 6.52: Three-dimensional laminar bubbles keeping flow attached at the leading edge in the post-stall regime (NACA 0020; A3λ11; α =20° and Re=290,000).

As discussed previously in section 6.2, the shorter wavelength configuration establishes favourable conditions caused by elongated-bubble topology that avoids flow separation, and as a consequence keeps flow attached even in areas downstream from laminar bubbles at post-stall whereas the smooth configuration presents full flow separation at the leading edge (figure 6.53).Therefore the three-dimensional bubbles, as a flow control mechanism, keep a soft stall in contrast with abrupt characteristics for the baseline airfoil (4.21).

At the lowest Reynolds number (Re=50,000), the experimental results show that the wavy leading edge configurations improve performance in the post-stall regime (figures 4.11, 4.47 and 4.29). In this case, the oil visualizations present three-dimensional laminar separation bubble distribution for all wavy configurations. This flow control mechanism is responsible for wavy airfoils to overcome the maximum lift values of the baseline configurations. These impressive results will be discussed in detail in the next section 6.4.

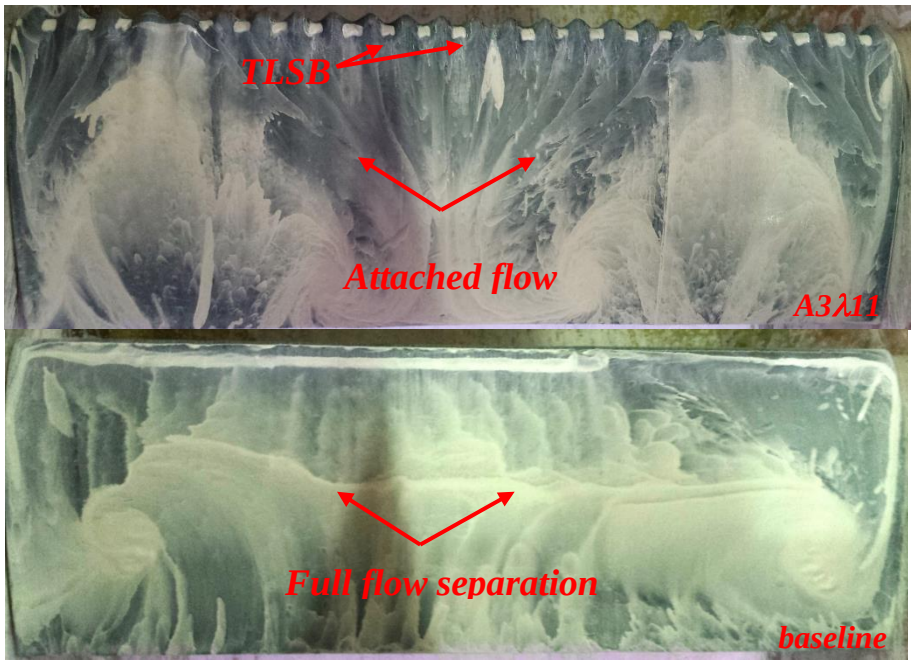

Figure 6.53: Three-dimensional laminar bubbles keeping flow attached over significant areas at post-stall regime (NACA 0020; α =20° and Re=290,000).

6.4 Reynolds number effects

The evaluation of the Reynolds number effects at distinct airfoils helped to determine an appropriate locus where the tubercle reaches optimum performance as well as to understand the locus' characteristics.

The force measurement results indicate, for all airfoil thicknesses, the best tubercle performance at the lowest Reynolds number (Re=50,000). The thinner wavy airfoils present higher maximum lift whereas the thickest wavy airfoil recovers the aerodynamic characteristics lost by the smooth configuration at this Reynolds number (figures 4.11, 4.28 and 4.47). Thus, low Reynolds number conditions are favourable as a design space for wavy leading edge airfoils.

The improvement in tubercle performance could be correlated to leading edge stall characteristics since the flow visualizations show that at the lowest Reynolds number all smooth airfoils (NACA 0012, NACA 0020 and NACA 0030) present leading edge stall characteristics diverse from those at higher Reynolds number conditions, mainly above Re=120,000, where trailing edge stall characteristics occurs.

The figures 6.54 and 6.55 show that, at the lowest Reynolds number condition (Re=50,000), the smooth NACA 0012 airfoil undergoes full flow separation at the leading edge without previous trailing edge flow separation. Moreover, the tubercles do not cause flow separation at the trailing edge near the stall condition (figure 6.54), keeping lift values close to baseline airfoil (figure 4.11).

The explanation for these characteristics comes from the discussion in section 6.2. As previously mentioned, the tubercle anticipates trailing edge flow separation. Thus, it is supposed that a wavy airfoil with characteristics of the smooth configuration, that avoid trailing flow separation in the pre-stall regime, minimizes the aerodynamic deterioration caused by tubercles.

In the post-tall regime, the wavy configuration keeps the flow attached at a large area over the airfoil upper surface in contrast with the smooth airfoil that presents full flow separation over entire airfoil surface (figure 6.55). Therefore at the lowest Reynolds number, wavy configurations cause low aerodynamic deterioration up to the stall condition and its flow control mechanism at the post-stall regime leads to wider attached flow areas as

compared to high Reynolds numbers. As a consequence, wavy configurations surpass the lift values of the baseline airfoil. The figures 5.17-24 show these characteristics for varying tubercle geometry and airfoil thickness.

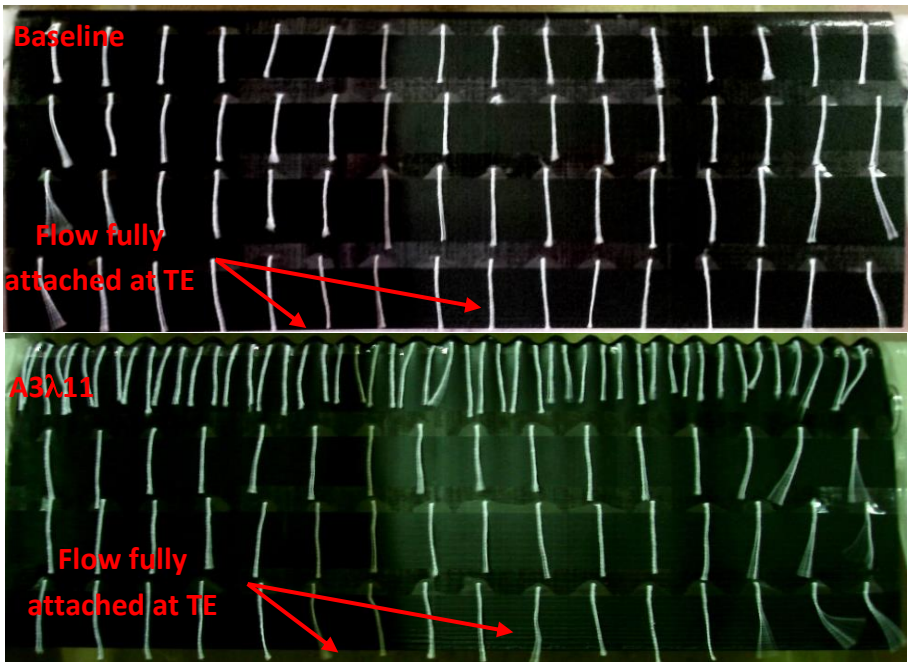

Figure 6.54: Flow fully attached over trailing edge for baseline and wavy configurations close to stall condition (NACA0012; α =9° and Re=50,000).

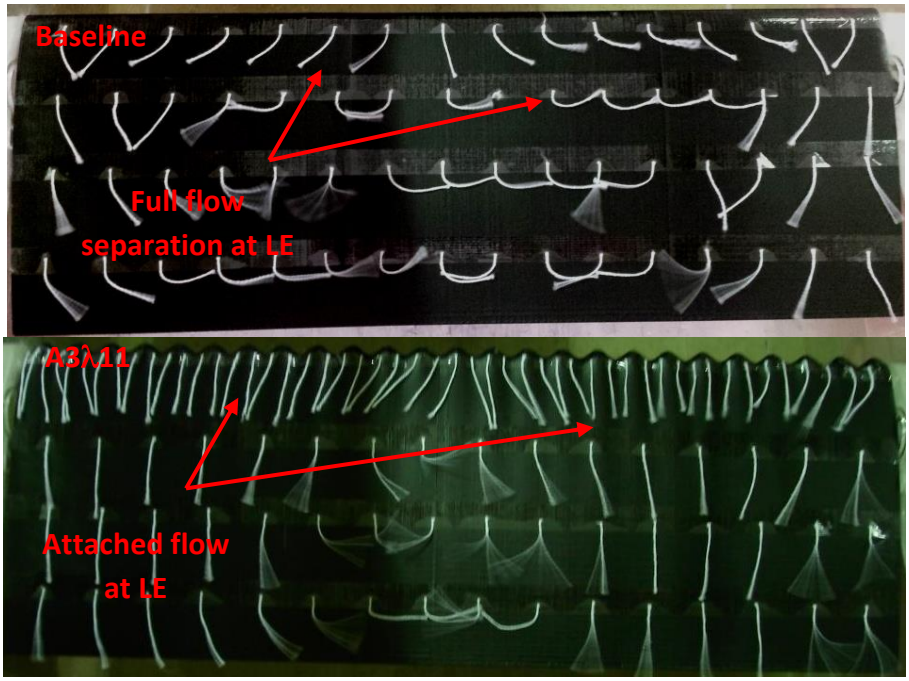

Figure 6.55: Flow topology for smooth and wavy configurations at post-stall regime (NACA 0012; α =12° and Re=50,000).

The oil flow visualizations characterize the flow control mechanism in the post-stall regime for the lowest Reynolds number condition. The results show a distinct flow control mechanism from the vortical structure cited by previous studies. All wavy leading edge configurations present three-dimensional bubble distribution at the tubercle troughs in the post-stall regime (figures 5.41-51).

As mentioned before, the three-dimensional bubble distribution as a post-stall flow control mechanism appears earlier for the shorter wavelength tubercle configuration (A3λ11) at higher Reynolds number, delaying flow separation areas downstream of the bubbles. However, although the shorter wavelength tubercle configuration at higher Reynolds number minimizes the trailing edge flow separation, caused by tubercle, at the lowest Reynolds number the leading edge flow separation condition avoids any deterioration caused by the tubercle in the pre-stall regime. Thus, this characteristic justifies an impressive performance at post-stall in terms of maximum lift values (figures 4.11, 4.29 and 4.47).

Figure 6.56 presents the three-dimensional bubbles distribution as a flow control mechanism for all wavy configurations. The smooth airfoil presents full flow separation at the leading edge whereas the wavy configuration keeps the flow attached over entire airfoil upper surface remaining higher maximum lift values compared to the baseline configuration (figure 4.28).

The wavy leading edge airfoils reach better performance at the lowest Reynolds number due to state leading edge stall characteristics favorable to tubercle effect at pre-stall and post-stall regimes.

The three-dimensional bubble flow control mechanism seems to be a way established by nature using spanwise flow or streamwise vorticity, caused by the tubercle sweep angle, to revert which would otherwise be as strong leading edge flow separation. The span flow causing decrease in pressure adverse gradient at peak and forming bubbles at trough responds as efficient flow control mechanism to keep flow attached at low Reynolds number.

The thickest wavy airfoil shows results that agree with the statement aforementioned. The NACA 0030 airfoil at Re = 290,000 and 200,000 follows the characteristics of the NACA 0020 at higher Reynolds number. However, at Reynolds 120,000, as consequence of the lower Reynolds number and due to the greater thickness, full flow separation at the leading edge occurs even at a lower angle of attack causing significant aerodynamic performance penalty

(figure 4.37). In other words, the thickest airfoil, at lower Reynolds number, does not present aerodynamic characteristics of a useful airfoil.

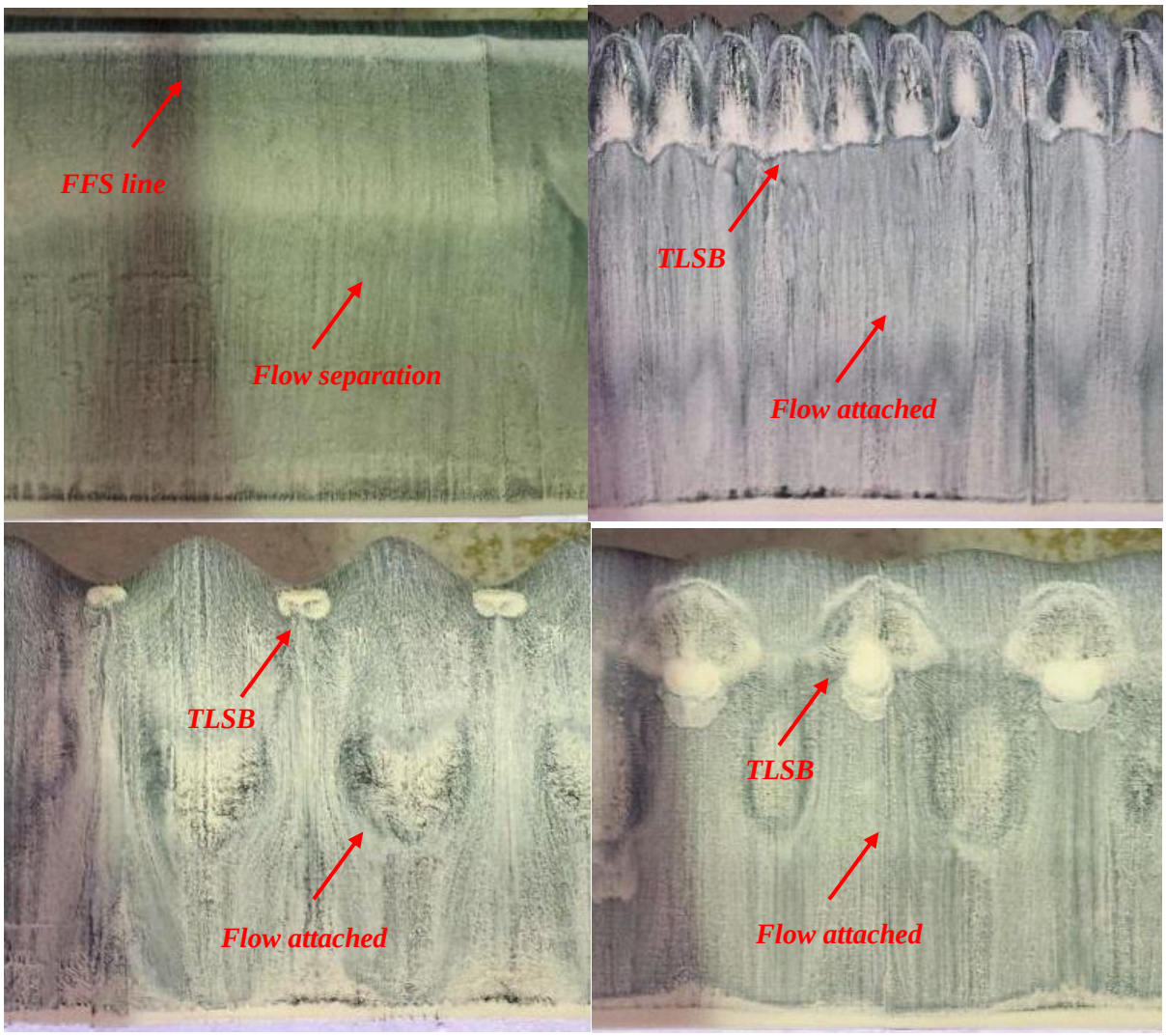

Figure 6.56: Flow topology for smooth and wavy configurations at post-stall regime (NACA 0020; α =8° and Re=50,000).

The results of this work show that at severe conditions of full leading edge separation, the wavy leading edge airfoils present great benefits in terms of aerodynamic performance (figures 4.45, 4.46 and 4.47). As previously said, at Re=120,000, the configuration A3λ11 increases the maximum lift value in 19% and the stall angle in 44%. The results present an unprecedented increase relative to literature regarding maximum lift for full-span and partial-span models.

Figure 6.57 show details of the three-dimensional bubbles that keep higher lift values for wavy configuration after premature full flow separation undergone by the smooth NACA 0030 airfoil (α=11°). The visualization confirms in the lower Reynolds number regime the three-dimensional bubble distribution working as an efficient flow control mechanism.

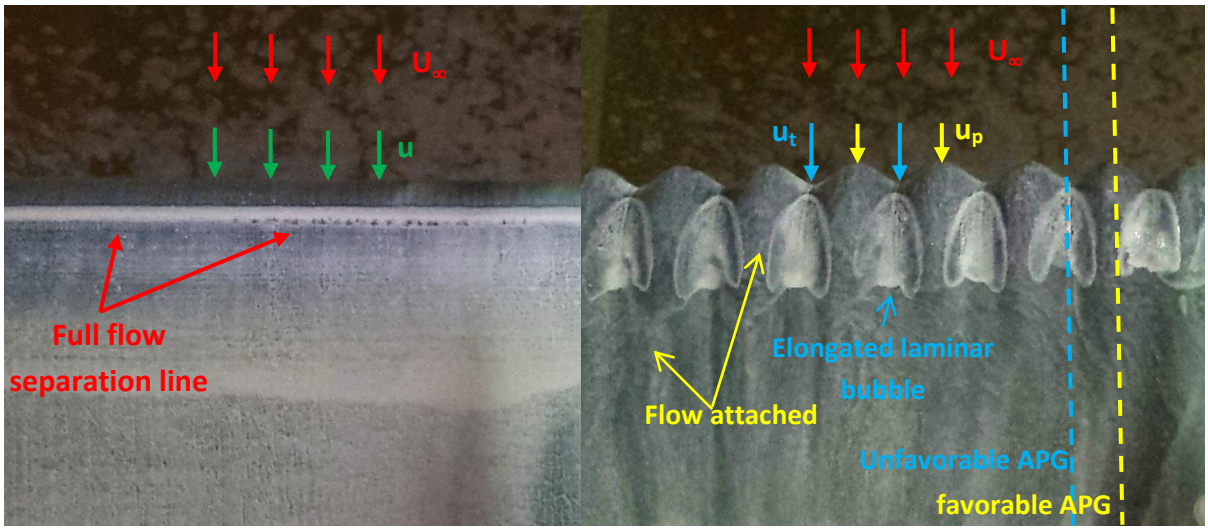

Figure 6.57: Flow control mechanics for wavy airfoil (NACA 0030; A3λ11; α =15° and Re=120,000).

In addition, decreasing the Reynolds number from 120,000 the wavy configurations recover the linearity of the lift curve since the smooth configuration presents a lift curve slope with negative values for lower angles of attack.

In agreement with desirable flow conditions for tubercle performance at lower Reynolds number, as it was discussed in the section 6.2, the wavy thin NACA 0012 airfoil reaches superior performance compared to thicker airfoils as consequence of its leading edge stall characteristics. Therefore Reynolds number conditions and airfoil thickness variation lead wavy airfoils to leading edge stall characteristics in order to reach better performance.

Figures 6.58, 6.59 and 6.60 aid a more clear understanding of the tubercle design space as well as its dependency on Reynolds number and airfoil thickness. It can be seen in figure 6.58 for the NACA 0012 an increase in performance with decreasing Reynolds number conditions. A decrease in Reynolds number anticipates the *leading edge flow separation* for smooth configuration, thus avoiding increased *trailing edge separation* at the pre-stall condition. Thus, a decrease in Reynolds number minimizes the tubercle effect in increasing

flow separation at trailing edge. At the lowest Reynolds number, as previously described, there is a benefit of increasing in maximum lift caused by the three-dimensional bubble mechanism in the post-stall regime (figures 4.11 and 5.43).

The thicker airfoils, in contrast with NACA 0012, increase aerodynamic deterioration with decreasing Reynolds number up to specific Reynolds number conditions (figures 6.59 and 6.60). This behaviour is a consequence of the *trailing edge stall characteristics* of thicker airfoils. The natural trailing edge flow separation characteristics of the thicker airfoils increase with decreasing Reynolds number. Thus, the wavy leading edge enhances its function by increasing trailing edge flow separation areas as Reynolds number decreases. This behaviour explains the increase in aerodynamic deterioration with decreasing Reynolds numbers for thicker airfoils.

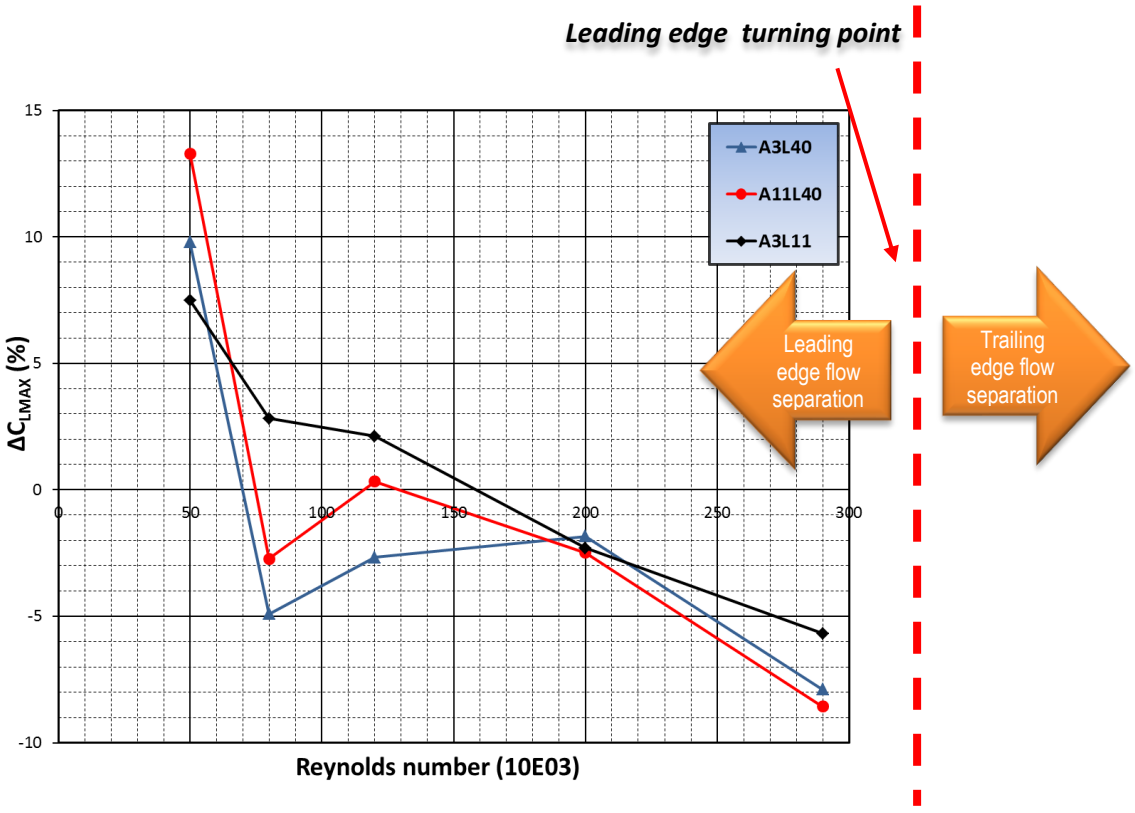

Figure 6.58: Reynolds number effect on aerodynamic deterioration in terms of maximum lift values (NACA 0012).

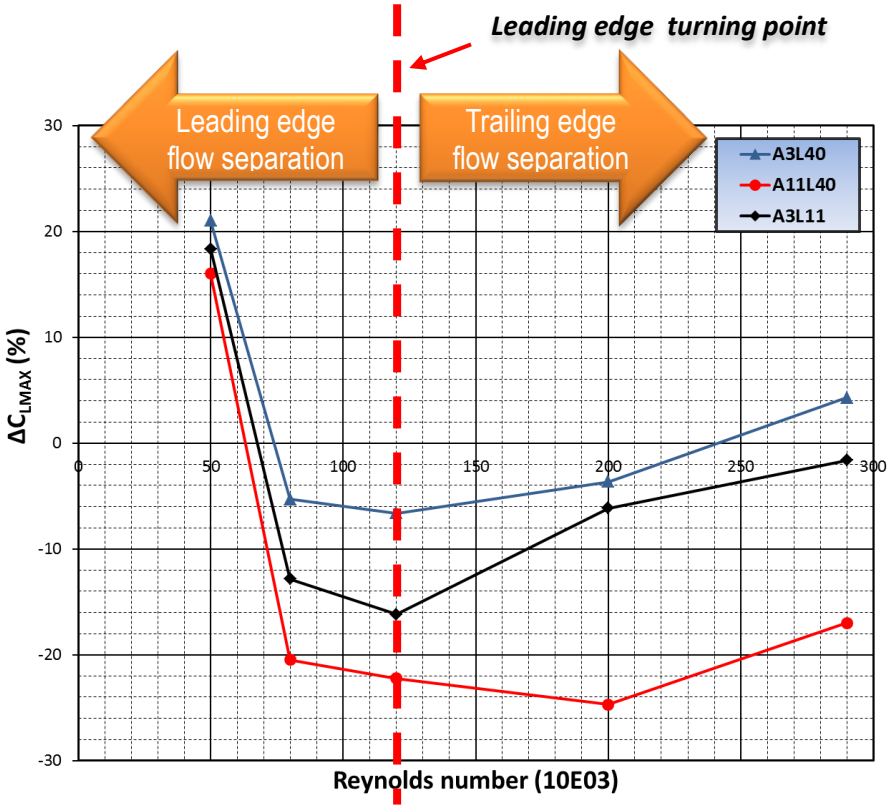

Figure 6.59: Reynolds number effect on aerodynamic deterioration in terms of maximum lift values (NACA 0020).

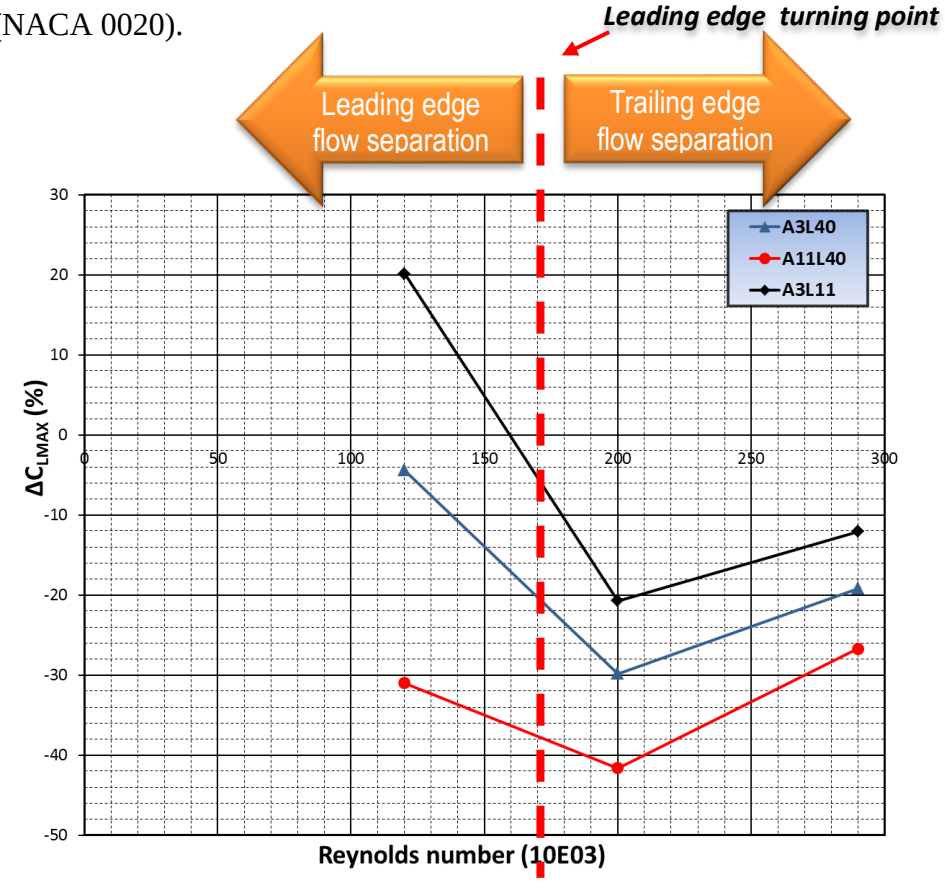

Figure 6.60: Reynolds number effect on aerodynamic deterioration in terms of maximum lift values (NACA 0030).

The wavy NACA 0020 and NACA 0030 airfoils reach the "*leading edge turning point*" at the respective Reynolds numbers of 120,000 and 200,000. At these specific Reynolds numbers, the airfoils transition from trailing edge-type to leading edge-type stall, increasing performance with decreasing Reynolds numbers (figures 6.59 and 6.60).

In contrast, the thinnest airfoil presents the leading edge turning point above Reynolds number 290,000 due to the fact that the smaller leading edge radius keeps the leading edge stall characteristic even at higher Reynolds number condition (figures 6.58). The thickest airfoil presents leading edge turning point higher than NACA 0020 airfoil due to very thick airfoils undergoing early transition for leading flow separation. Thus, the *"tubercle design space"* is defined by leading edge turning points. It can be seen in figure 6.61 a possible tubercle design space defined by leading edge turn points.

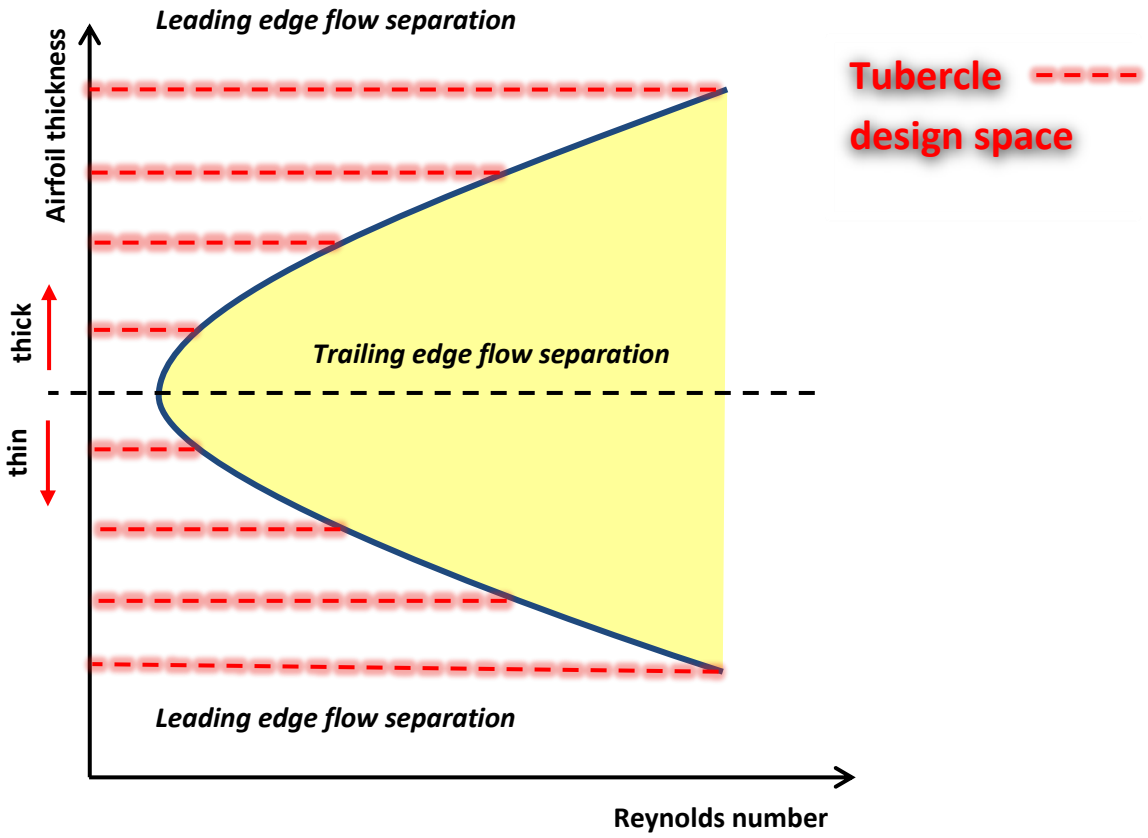

Figure 6.61: Design space for an optimum tubercle performance.

7 CONCLUSIONS

The investigations of this work starts actually with Stanway (2008) suggesting “foils operating in a short bubble stall regime will benefit more from the addition of tubercles than those operating in a trailing edge stall regime”. Stanway (2008) attributes a possible Reynolds number effect, and the consequent changes in stall characteristic, to justify lower tubercle performance on his results when compared to same partial model tested by Miklosovic et al. (2004) at higher Reynolds number conditions. He, without understanding clearly the reason for such statement, gave a remarkable insight for research in wavy leading edge phenomena.

This important statement motivated an investigation beyond humpback whale´s morphology boundaries. In this sense, as it was mentioned previously, the main aim of this thesis brought many finding due to a wide variation of conditions (Reynolds number, airfoil and wavy geometry) tested in order to evaluate the airfoil thickness effects in the low Reynolds number regime. Therefore, many aspects regarding wavy leading edge phenomena evaluate in this work need to be summarized, and they will be listed in the next paragraphs.

The airfoil thickness effects at smooth configuration, this effect presented large changes on aerodynamic characteristics of the airfoils. Low airfoil thickness leads to small values of leading edge radius establishing early full flow separation at leading edge without early flow separation at trailing edge. In contrast, a high thickness establishes a great leading edge radius delaying flow separation at leading edge for higher angles of attack. In addition, the boundary layer conditions for a higher range of angle of attack provide trailing edge flow separation up progressing toward leading edge with increasing in angles of attack. The thin airfoil characteristics result in better pre-stall performance. On the other hand, higher airfoil thicknesses present greater values of stall angle. As consequence the thickest NACA 0030 airfoil reaches the highest value of maximum lift. This suggests that an optimum airfoil thickness value in order to obtain the highest maximum lift at low Reynolds number could be distinct from the value around 13% of the chord indicated by Torenbeek (1982) and Raymer (1989) for higher Reynolds number. Thus, these results show a need of a specific airfoil for aircraft design at operational conditions of low Reynolds such as UAV and MAV operation envelope. In addition, the investigation helps to understand the thickness effects on tubercle performance in the pre-stall regime.

The role of tubercles at pre-stall regime, the force measurements and flow visualizations indicate clearly that the role of tubercles at pre-stall regime is to anticipate the trailing edge flow separation characteristics. The secondary flow caused by tubercle sweep angle causes distinct boundary layer development downstream of the troughs and peaks anticipating trailing edge flow separation at span station that presents the critical adverse pressure gradient. Thus, the tubercles drive the pre-stall condition of the airfoils and consequently the attained maximum lift values.

The airfoil thickness effects on wavy leading edge performance, the increase in airfoil thickness leads the flow separation characteristics of the smooth airfoil from leading edge stall to trailing edge stall. Therefore, the role of tubercles in the pre-stall regime determines the airfoil thickness effects on wavy leading edge performance. In other words, a thin airfoil does not present trailing edge flow separation so it is as not as sensitive to aerodynamic deterioration caused by the tubercle. As a consequence, the thinnest NACA 0012 airfoil presents small aerodynamic deterioration in the pre-stall regime when compared to thicker wavy airfoils.

Flow mechanism caused by tubercles, an important contribution of this work is related to flow mechanisms drove by the wavy leading edge airfoils. Although many previous researchers associate tubercle as vortical flow control mechanism, the results present two flow mechanisms trigger by the secondary flow: three-dimensional laminar separation bubbles or vortical structures. The flow structures can occur at any flow regime (pre-stall or post-stall conditions), however, vortical structures appears mainly at post-tall regime. Regarding three-dimensional laminar separation bubbles, this thesis confirm some few previous studies related to three-dimensional bubbles, and present for first time these structures as very efficient flow control mechanism in the post-stall regime.

Three-dimensional laminar separation bubbles in the pre-stall regime, the span flow or streamwise vorticity caused by tubercles establish higher and lower adverse pressure gradient downstream of the troughs and peaks, respectively, so forming three-dimensional bubbles. The spanwise flow depends on leading edge geometry (amplitude, wavelength and L.E radius). Therefore, distinct distributions appear by geometric effect. However, two characteristics of the laminar bubbles are identified causing different effects in performance in the pre-stall and post-tall regime. The laminar bubbles are named here as "tipped-bubbles" and "elongated-bubbles".

Tipped-bubbles, the characteristics from tipped-bubble found here for greater wavelength configurations and the consequent effect over the flow downstream them agrees with earlier trailing edge flow separation at tubercle troughs investigated by previous researchers. A numerical model (ROSTAMZADEH et al., 2014) supposing vortex emission from bubbles (primary vortices) exchange momentum along span was confirmed as well as secondary vortices caused by earlier separation at troughs forming delta-shape separation areas. The flow visualizations indicate less intense adverse pressure gradient at tubercle peaks caused by the secondary flow due to the streamwise vorticity. Additionally, primary vortices formed at bubble end to add up momentum along the span at peaks reinforcing flow condition favorable to avoid flow separation at those locations. A flow pattern model was proposed in agreement with the oil visualizations respecting spatial conservation of the vorticity strength (Helmholtz´s first vortex theorem) in order to explain the flow topology at pre-stall conditions.

Elongated-bubble, the parameter bubble width-to-wavelength ratio indicates changes on the bubble shapes as well as in the trailing edge flow characteristics of the airfoils. Thus, shorter wavelength tubercle configurations present elongated-bubbles that cause trailing edge flow separation distinct than longer wavelength configurations and in disagreement with previous studies where detached flow occurs earlier at tubercle trough. The earlier flow separation at peaks presented by the elongated-bubbles is explained here based on the acceleration caused by a narrow physical channel established due to the bubbles are very close each other. The bubble channel supposedly accelerates the flow keeping higher adverse gradient pressure near trailing edge forcing flow separation in this location. The elongated-bubble does not cause only changes on flow separation at the trailing edge along airfoil span. Moreover, the bubbles establish smaller flow separation areas along chordwise at the trailing edge when compared to tipped-bubble, so minimizing the aerodynamic deterioration caused by tubercles. The reason for elongated-bubbles minimizes the aerodynamic deteriorations caused by tubercles supposedly comes from characteristics related to higher adverse pressure gradient near trailing edge downstream of the peaks. Therefore, the flow separation remains limited near the trailing edge. Additionally, a span flow caused by flow separation at peaks decreases the pressure adverse gradient at trough minimizing the overall flow separation at trailing edge. A flow pattern model also was proposed.

The tubercle geometry effect, since first studies in wavy leading edge phenomena, researchers investigate the tubercle geometric effects on wavy leading edge performance.

Although some authors (HANSEN et al., 2009; JOHARI et al., 2007; LEVSHIN et al.; 2006) agree in establishing smaller amplitude and shorter wavelength values as optimum values to reach the best performance at pre-stall and post-stall regime, they do not carried out flow topologic analysis in order to understand these characteristics. The force measurements of this work agree with previous researchers presenting the highest maximum lift value and soft stall behaviour for configuration with smaller amplitude and shorter wavelength (A3λ11). Further, the greater amplitude and elongated-bubble characteristics bring a possible explanation for this desirable tubercle geometry. The results showed that increasing the tubercle amplitude a raise occur in the span flow causing higher adverse pressure gradient establishing earlier flow separation when compared smaller amplitude. On the other hand, a shorter wavelength configuration establishes elongated-bubbles minimizing trailing edge flow separation. Therefore, a smaller amplitude providing less span flow and a shorter wavelength establishing elongated-bubbles minimizing flow separation present the optimum tubercle geometry.

Tubercles at post-stall regime, the mini-tuft and oil visualizations confirmed vortical structures at higher angle of attack caused by tubercles working as vortex generator. The vortical structure composed by single vortices or counter-rotating vortex pair located between peaks keep flow attached downstream of the peaks justifying greater lift values at post-stall regime. However, at the highest Reynolds number (Re=290,000) the configuration (A3λ11) presents, for first time, a new flow control mechanism in the post-stall regime. A periodic elongated-bubble distribution at troughs remains significant areas of attached flow at the leading edge. It seems that the nature find a new way to deal with leading edge flow separation establishing varied areas of distinct adverse pressure gradient along span. At low Reynolds number regime this unprecedented new flow mechanism appears as the unique.

The Reynolds number effects, the results show an impressive tubercle performance at lowest Reynolds number (Re=50,000). At any tubercle geometry and airfoil thickness, the wavy leading edge airfoils present higher maximum lift values. The flow visualizations present in this Reynolds number only the three-dimensional bubbles distribution as flow control mechanism. In this flow regime, the airfoils present leading edge flow characteristics so the tubercles do not cause deterioration at pre-stall regime. Moreover, the smooth airfoil undergoes early flow separation whereas the wavy configurations present bubbles at trough and significant attached flow areas. Although at the lowest Reynolds number all wavy geometry present higher performance than smooth airfoil, the strong leading flow separation

at NACA 0030 airfoil shown the greatest increase in performance caused by tubercles reaching increase in maximum lift and stall angle values of 19.4% and 44% respectively. Therefore, this result indicates that increasing leading edge flow separation characteristics becomes more effective the tubercles as flow control mechanism.

This thesis presents higher tubercle performance for thinner airfoils and/or lower Reynolds number conditions showing clearly that these characteristics leads to tubercle operating at leading edge flow separation conditions. Thus, eight years after of Stanway (2008) speculates that leading edge stall characteristics support flow conditions to reach better tubercle performance, the results of this work establish a design space for tubercles within of the leading edge stall characteristics. In addition, the three-dimensional laminar separation bubble distribution appears as the efficient flow control mechanism that supports high tubercle performance at leading edge flow separation.

The findings of the thesis lead to questions why the humpback whale´s pectoral flipper with thick profile (NACA 63_4 21) at middle span presents high hydrodynamic performance caused by tubercles since trailing edge flow characteristics appear in similar airfoils. However, the humpback whale presents a thick airfoil at flipper tip (NACA 0020) in conditions of lower Reynolds number (small local chord). In this sense, a leading flow separation can be avoided by tubercles at tip delaying the stall progression along span as Pedro and Kobayashi (2008) show in theirs numerical simulations. Thus, this complex three-dimensional flow control at humpback whale´s pectoral flipper reinforce the desirable leading edge flow separation conditions as trigger of tubercle efficiency.

Finally, this thesis opens a new perspective to future researches in application at conditions of leading edge flow separation such as UAV and MAV.

8 FUTURE WORKS

Although important questions were answered in this work, there are others that are still open or needing further confirmation. In the sense, a great possibility for potential future works appears.

Pressure measurements were not carried out in this thesis. Future work carrying out such measurements would be able to respond many questions that the actual results are not able to. For instance, how the changes caused by tubercles affect the pressure drag. Furthermore, generally, the tubercles present a decrease in pitching moment so this effect could be investigated by evaluation of the pressure distribution changes over the airfoil upper surface. The hypothesis established that a bubble channel for shorter tubercle wavelength configuration causes severe adverse pressure gradient near trailing edge could also be confirmed.

Another important issue is turbulence investigation in new works. Although the oil visualization indicates a qualitative analysis of the anisotropy of the turbulence, accurate analysis needs to be performed measuring velocity profiles inside the boundary layer by the use of anemometry techniques. Thus, an evaluation of the changes caused by tubercles on skin friction drag could be obtained. The measurements would help to understand the anisotropy of the turbulence along the span as well. Besides, the current work shows some interesting complex flow structures (figure 5.38) where two three-dimensional laminar bubbles appears downstream from the tubercle peaks. The region between bubbles could be understood as a region of flow relaminarization. The velocity profile measurements could confirm this hypothesis. Further, velocity profile and pressure distribution measurements combined could help to evaluate the boundary layer development at peaks and troughs in detail.

As mentioned before, the wavy leading edge phenomena are caused by tubercle sweep angle that add streamwise vorticity at the boundary layer over an airfoil. Therefore, PIV measurements could give an important contribution in order to clarify the vorticity aspects along the flow at the upper surface of the airfoils. The results could add details regarding secondary flow and primary and secondary vortices by streamwise vorticity measurements.

Moreover, the streamwise vorticiy distribution could help to confirm the vorticity flow pattern models, as proposed in this thesis, or update them.

The evaluation of the airfoil thickness effects on tubercle performance indicated the thin NACA 0012 airfoil with desirable geometric characteristics to reach the leading edge flow separation (tubercle design space). However, a future work could contribute to investigate camber characteristics that lead to leading edge flow separation. Thickness and camber are the main geometric parameters that drive the aerodynamics characteristics of the airfoils. Thus, results from thickness and camber evaluation could establish guidance for design of wavy leading edge airfoils.

Based on the findings of this thesis, it supposed that, at higher Reynolds number conditions that lead to turbulent flow state, tubercles possibility do not have benefits in terms of lift performance since these condition present trailing edge flow characteristics. In this sense, there is no any study regarding wavy leading edge phenomena over flow conditions above Reynolds number 500,000. Therefore, future studies in the higher Reynolds numbers could evaluate the tubercle performance at full turbulent state and confirm the bounders of the tubercle design space established here.

Studies related to higher Reynolds number condition also could add important findings in laminar flow control investigations. Although, at turbulent flow, possibly lift deterioration occurs at higher angle of attack, in cruise conditions ($\alpha = 1.5°$) the penalty in lift tend to be minimum. On the other hand, the secondary flow establishes by tubercle sweep angle could cause large laminar areas in cruise conditions decreasing skin friction drag. Considering that this drag component could reach up to 30% of total drag at transonic and subsonic condition, studies in laminar flow control regarding tubercles appears as potential in decreasing drag.

The limitation of the force measurement system of this work led to consider in terms of drag and pitching moment values above Reynolds number 100,000. Thus, future works need to be able to measure the aerodynamics coefficients (drag and pitching moment) with accuracy at Reynolds number below 100,000 in order to investigate quantitatively the tubercles effect at this desirable design space.

The Results show that the distinct pressure distribution at peaks and troughs caused by tubercles leads to large flow differences along the airfoil span. In this sense, the proposal of

the Bolzon et al. (2015), previously discussed, regarding tubercle application in transonic and supersonic regimes, seems reasonable since large areas with pressure coefficient lower than critical pressure coefficient could concentrate the shock wave only in regions near the troughs. Thus, a potential significant decrease in wave drag needs to be investigated in future works.

REFERENCES

ABBOTT, I. H.; VON DOENHOFF, A. E.; STIVERS JR, L. S. Summary of airfoil data. NACA REPORT No. 824, 1945.

ABBOTT, I. H.; VON DOENHOFF, A. E. *Theory of wing sections*. New York: Dover Publ, 1949.

ALEXANDER, R. M. *Animal mechanics*. Oxford: Black-well Scientific Publ, 1983.

ALLEN, H. J; W. G, VINCENTI. Wall interference in a two-dimensional-flow wind tunnel with consideration of the effect of compressibility. NACA REPORT TR 782, 1944.

ALTHAUS, D.; WORTMANN, F. X. Stuttgarter profilkatalog I – Experimental results for the laminar wind tunnel of the University of Stuttgart. Friedr. Vieweg and Sohn, Braunschweig, 1972 (English version in 1981).

ANDERSON J. M.; KERREBROCK P. A. *Biomimetics in action: design and performance of an autonomous robotic fish*. In: Ayers J, Davis JL, Rudolph A, editors. Neurotechnology for biomimetic robots. Cambridge (MA): MIT Press, p. 297–308, 2002.

ANDERSON JR, J.D. *A history of aerodynamics and its impact on flying machines*, first edition, Cambridge: Cambridge University Press, 1997.

ATTINELLO, J. S. *Design and engineering features of flap blowing installations, in Boundary layer and Flow Control*. *Its Principles and Application* , ed. G.V. Lachmann, New York: Pergamon Press, v. 1, p. 463–515, 1961.

BARLOW, J. B.; RAE JR, W. H.; POPE, A. *Low-speed wind tunnel testing*, third edition, New York: John Wiley & Sons Inc., 1999.

BLAKE, R. W. *Animal mechanics*. Oxford: Black-well Scientific. Publ, 1983.

BNADYOPADHYAY, P.R. Trends in biorobotic autonomous undersea vehicles. *IEEE Journal of Oceanic Engineering*, v. 29, p. 1-32, 2004.

BOLZON, M. D.; KELSO, R. M.; ARJOMANDI, M. Tubercles and their applications. *Journal of Aerospace Engineering*, 2015.

BRENDEL, M; MUELLER, T. J. Boundary-layer measurements on an airfoil at low Reynolds numbers. *Journal of Aircraft*, v. 25, n. 7, p. 612-617, 1988.

BRENDEL, M.; MUELLER, T. J. Transition phenomena on airfoils operating at low chord Reynolds numbers in steady and unsteady flow. *Numerical and Physical Aspects of Aerodynamic Flows IV*. Berlin: Springer-Verlag, p. 333-344, 1989.

BUSHNELL D. M.; MOORE K. J. Drag reduction in nature. *Ann Rev Fluid Mech*, v. 23, p. 65-79, 1991.

CANTWELL, B. J. Organized motion in turbulent flow. *Annu. Rev. Fluid Mech*., v. 13, p. 457-515, 1981.

CARMICHAEL, B. H. Low Reynolds number airfoil survey. NASA REPORT, v. 1, 1981.

CHEN, J.H; LI, S. S.; NGUYEN, V. T. The effect of leading edge protuberances on the performance of small aspect ratio foils. *Proceedings of the 15th International Symposium on Flow Visualization*, Minsk, Belarus, 2012.

CRABTREE, L. F. The Formation of Regions of Separated Flow on Wing Surfaces. Technical Report, R and M No 3122, 1959.

CUSTODIO, D. *The effect of Humpback whale-like leading edge protuberances on hydrofoil performance*, Thesis (Master) – Worcester Polytechnic Institute, 2007.

CUSTODIO, D.; HENOCH, C.; JOHARI, H. Aerodynamic characteristics of finite-span wings with leading edge protuberances. *Proceedings of the 50th AIAA Aerospace Science Meeting*. Nashville, Tennessee: AIAA Paper 2012-0054, 2012.

DANIEL, T. L.; WEBB, P. Physics, design, and locomotor performance. In: Dejours P, Bolis L, Taylor CR, Wiebel ER, editors. Comparative physiology: life in water and on land, New York: Liviana Press, Springer, p. 343-369, 1987.

DANTEC. Probe catalog. Publication number 9607 E.

DANTEC 57H00. Traversing system. Instruction manual

DELGADO, H. E. C.; ESMAEILI, A.; SOUSA, M. M. Stereo PIV measurements of low-aspect-ratio low-Reynolds-number wings with sinusoidal leading edges for improved computational modeling. *Proceedings of the 52nd AIAA Aerospace Science Meeting.* National Harbor, Maryland: AIAA Paper 2014-1280, 2014.

DOLPHIN, W. F. Foraging dive patterns of the humpback whale, megaptera novaeangliae, in Southeast Alaska: cost-benefit analysis. *Can. J. Zool*. 66: 2432-2441, 1988.

DROPKIN, A.; CUSTODIO, D.; HENOCH, C. W.; JOHARI, H. Aerodynamic Characteristics of finite-span wings with leading edge protuberances. *AIAA Journal of aircraft*, v. 49, n. 5, 2012.

EDEL, R. K; WINN, H. E. Observations on under-water locomotion and flipper movement of the humpback whale, megaptera novaeangliae, *MAR. Biol*.48:279-287, 1978.

FISH, F. E. Transitions from drag-based to lift-based propulsion in mammalian aquatic swimming. *American Zoologist*, v. 36, p. 628-641, 1996.

FISH, F. E. Limits of nature and advances of technology in marine systems: what does biomimetics have to offer to aquatic robots ? *Applied Bionics and Biomechanics*, v. 3, p. 49-60, 2006.

F. E. Fish. Biomimetics: Determining engineering opportunities from nature. *Proceedings SPIE Conference, Biomimetics and Bioinspiration*, v. 7401, n. 740109, 2009.

Fish, F. E; Battle, J. M. Hydrodynamic design of the humpback whale flipper. *Journal of Morphology*, v. 225, p. 51-60, 1995.

FISH, F. E.; HOWLE, L. E.; MURRAY, M.M. Hydrodynamic flow control in marine mammals. *The annual meeting of the Society for integrative and comparative Biology*, v. 48, p. 788-800, 2008.

GAD-EL-HAK, M. Modern developments in flow control. *Applied Mechanics Reviews*, v. 49, p. 365–379, 1996.

GAD-EL-HAK, M. *Flow Control: Passive, Active, and Reactive Flow Management*, first edition, New York: Cambridge University Press, 2000.

GENÇ, M. S; KARASU, I; AÇIKEL, H.H. An experimental study on aerodynamics of NACA2415 aerofoil at low Re numbers. *Experimental Thermal and Fluid Science*, v. 39, p. 252-264, 2012.

GERAKOPULOS, R. J. *Investigating flow over an airfoil at low Reynolds numbers using novel time-resolved surface pressure measurements*, Thesis (Master) – University of Waterloo, 2011.

GLAUTER, H. Wind tunnel interference on wings, bodies and airscrews. ARC R&M 1566, 1933.

GODARD, G.; STANISLAS M. Control of a decelerating boundary layer. Part 1: optimization of passive vortex generators. *Aerospace Science and Technology*, v. 11, p. 181-91, 2006.

GUERREIRO, L. E. G. *Controle passivo de perda em Micro-Veículos Aéreos usando bordos de ataque sinusoidais*. Thesis (Master) – Instituto Superior Técnico, 2010.

HAIN, J. H. W; CARTER, G. R.; KRAUS, S. D.; MAYO, C. A. Feeding behaviour of the humpback whale, megaptera novaeangliae, in the western North Atlantic. *Fish. Bull* 80: 259-268, 1982.

HANSEN, L. H. *Effect of leading edge tubercles on airfoil performance*, Thesis (Doctoral) – University of Adelaide, 2012.

HANSEN K. L.; KELSO R. M.; DALLY B. B. An investigation of three-dimensional effects on the performance of tubercles at low Reynolds number. *Proceedings of the 17th Australasian Fluid Mechanics Conference*. Auckland, New Zealand, 2010.

HANSEN K. L.; KELSO R. M; DALLY B. B. Performance variations of leading-edge tubercles for distinct airfoil profiles. *AIAA Journal of Aircraft*, v. 49, n.1, p. 185-94, 2011.

HANSEN K. L.; KELSO R. M.; DALLY B. B.; BATILL, S. M. the effect of leading edge tubercle geometry on the performance of different airfoils. *Proceedings of the 7th World Conference on Experimental Heat Transfer, Fluid Mechanics and Thermodynamics*, Krakow, Poland, 2009.

HORTON, H. P. *Laminar separation bubbles in two and three dimensional incompressible flow*. Thesis (Doctoral) – Department of Aeronautical Engineering Queen Mary College, 1968.

HOWELL, A. B. *Aquatic mammals*. New York: Dover Publ, 1930.

HURT JR, H. H. Aerodynamics for naval aviators. The office of the chief of naval operations aviation. Training division. U.S Navy NACA. NAVWEPS 00-80T-80, 1965.

JACOBS, E. N.; WARD, K. E.; PINKERTON, R. M. The characteristics of 78 related sections from tests in the variable-density wind tunnel. NACA REPORT No. 460, 1935.

JACOBS, E. N.; SHERMAN, A. Airfoil section characteristics as affected by variations of the Reynolds number. NACA REPORT No. 586, 1937.

JOHARI H.; HENOCH C.; CUSTODIO D.; LEVSHIN A. Effects of leading-edge protuberances on airfoil performance. *AIAA Journal*, v. 45, n. 11, p. 2634-2642, 2007.

JONES, B. M. An experimental study of the stalling of wings, ARC R&M No. 1588, 1933.

JONES, B. M. Stalling. *Journal of Royal Aeronautical Society*, v. 38, p. 753-770, 1934.

JOSLIN R. D.; MILLER D. N. Fundamentals and applications of modern flow control. *Progress in Astronautics and Aeronautics*, v. 231, 2009.

JURAZ, C. M; JURAZ, V. P. Feeding modes of humpback whale, megaptera novaeangliae, in southeast Alaska, *Sci. Rep*. Whales Res. Inst. 31:69-83, 1979.

KARASU, I.; GENÇ, M. S.; AÇIKEL, H. H.; AKPOLAT, M. T. An experimental study on laminar separation bubble and transition over an aerofoil at low Reynolds number. *Proceedings of the 50th AIAA Applied Aerodynamic Conference.* New Orleans, Louisina: AIAA Paper 2012-3030, 2012.

KARTHIKEYAN, N.; SUDHAKAR, S.; SURIYANARAYANAN, P. Experimental studies on the effect of leading edge tubercles on laminar separation bubble. *Proceedings of the 52nd AIAA Aerospace Science Meeting*, National Harbor, Maryland: AIAA Paper 2014-1279, 2014.

KUBO, Y.; MIYAZAKI, M.; KATO, K. Effects of endplates and blockage of structural members on drag forces. *Journal of wind engineering and industrial*, v. 32, n. 3, p. 329-342, 1989.

LEATHERWOOD, S.; REEVES, R. R.; PENIN, W.; EVANS, W. E. *Whales, dolphins and porpoises of the Easter North Pacific and adjacent artic water*, New York: Dover, 1988.

LEVSHIN, A.; CUSTODIO, D. Effects of leading edge protuberances on airfoil performance. *Proceedings of the 36th AIAA Fluid Dynamics Conference and Exhibit*, San Francisco, California: AIAA Paper 2006-2868, 2006.

LIGHTHILL, J. *Introduction to the scaling of aerial locomotion*. In T.J. Pedley (ed). Scale effects in animal locomotion. London: Academic Press, p. 365-404, 1977.

LISSAMAN, P. B. S. Low-Reynolds-number airfoils. *Annual Review of Fluid Mechanics.* v. 15, p. 223-239, 1983.

LOFTIN JUNIOR, L. K. Quest for performance: the evolution of modern aircraft. NASA SP-468, 1985.

MASKEL, E. C. A theory of the blockage effects on bluff bodies and stalled wings in a closed wind tunnel. ARC R&M 3400, 1965.

MCARTHUR, J. *Aerodynamics of wings at low reynolds numbers*, Thesis (Doctoral) – University of Southern California, 2007.

McCULLOUGH, G. B; GAULT, D. E. Examples of three representative types of airfoil-section stall at low speed. NACA REPORT No. 2502, 1951.

MCFARLAND, M. W. The Papers of Wilbur and Orville Wright, Including the Chanute-Wright Papers, McGraw-Hill Companies, 2001

McMASTERS, J. H.; HENDERSON, M. L. Low-speed single-element airfoil synthesis. *Technical Soaring*, v. 4, n. 2, p. 1–21, 1979.

MIKLOSOVIC, D.S.; MURRAY, M.M.; HOWLE, L.E. Experimental evaluation of sinusoidal leading edges. *Journal of Aircraft*, v. 44, n. 4, p. 1404-1407, 2007.

MIKLOSOVIC, D.S.; MURRAY, M.M.; HOWLE, L.E.; FISH, F.E. Leading-edge tubercles delay stall on Humpback whale (Megaptera Novaeangliae) Flippers, *Physics of Fluids*, v. 16, n. 5, p. 39-42, 2004.

MUELLER, T. J.; BATILL, S. M. Experimental studies of separation on a two-dimensional airfoil at low Reynolds numbers. *AIAA Journal*, v. 20, n. 4, p. 457–463, 1982.

MUELLER, T. J.; DELAURIER J. D. Aerodynamics of small vehicles. *Ann Rev Fluid Mech*, v. 35, p. 89-111, 2003.

MURRAY, M.; GRUBER, T.; FREDRIKSSON, D. Effect of Leading Edge Tubercles on Marine Tidal Turbine Blades. *Proceedings of the 63rd Annual Meeting of the APS Division of Fluid Dynamics*. American Physical Society, 2010.

NIEROP, E.A.V., ALBEN, S., BRENNER, M.P. How Bumps on Whale Flippers Delay Stall: An Aerodynamic Model. *Physical review letters 100*, 054502, 2008.

NORBERG, U. M, *Vertebrate flight: mechanics, physiology, morphology, ecology and evolution*. Berlin: Springer-Verlag, 1990.

O´MEARA, M. M.; MUELLER, M. M. Laminar separation bubble characteristics on an airfoil at low Reynolds numbers. AIAA *Journal*, v. 25, n. 8, p. 1033-1041, 1987.

PEDRO, H.T.C; KOBAYASHI, M.H. Numerical study of stall delay on humpback whale flippers. *Proceedings of the 46th AIAA Aerospace Sciences Meeting and Exhibit*. Reno, Nevada: AIAA Paper 2008-584, 2008.

RAYMER, D. P. *Aircraft Design: a conceptual approach*. AIAA education series, 1989.

RIEGELS, F. W. *Airfoil Sections*. Butterworths, London, 1961.

ROBINSON, S. K. Coherent motions in the turbulent boundary layer, *Annu. Rev. Fluid Mech*., v. 23, p. 601-639, 1991

ROSTAMZADEH, N.; HANSEN, K. L; KELSO, R. M.; Dally, B. B. The formation mechanism and impact of streamwise vortices on NACA 0021 airfoil's performance with undulating leading edge modification. *Physics of fluids*, v. 26, n. 107101, 2014.

SCARBOROUGH, J.B. *Numerical Mathematical Analysis*, third edition, p. 429, Johns Hopkins, Baltmore, Md., 1955.

SCHLICHTING, H; GERSTEN, K. *Boundary layer theory*, 8th edition, New York: Springer-Verlag, 2000.

SCHMITZ, F.W. Aerodynamik des flugmodells. C.J.E. Volckmann Nachf. E. Wette, Berlin-Charlottenburg, 1942.

SHARMA, M. D; PODDAR, K. Experimental investigations of laminar separation bubble for a flow past an airfoil. *Proceedings of the ASME Expo 2010: Power for Land, Sea and Air Conference*. Glasgow, UK, 2010.

SIMONS, M. *Model aircraft aerodynamics*, fifth edition, Dorset: Special Interest Model Books, 2002.

Skillen, A.; Revell, A.; Pinelli, A.; Piomelli, U.; Javier, J. Flow over a wing with leading-edge undulations. *AIAA Journal*, v. 53, n. 2, p. 464-472, 2014.

STANSBY, P.K. The effect of endplates on the base pressure coefficient of a circular cylinder. *The Aeronautical Journal*, v. 78, n. 757, p. 36-37, 1977

STANWAY, M. J. *Hydrodynamic effects of leading edge tubercles on control surfaces and in flapping foil propulsion*, Thesis (Master) – Massachusetts Institute of Technology, 2008.

SWANSON, T.; ISAAC, K.M. Biologically inspired wing leading edge for enhanced wind turbine and aircraft performance. *Proceedings of the 6th AIAA Theoretical Fluid Mechanics Conference*. Honolulu, Hawaii: AIAA Paper 2011-3533, 2011.

SWATTON, P.J. *Principles of flight for pilots.* first edition, Chichester: John Wiley & Sons Ltd, 2011.

TANI, I. Low-speed flows involving bubble separations. *Progress in Aerospace Sciences*, v. 5, p. 70-103, 1964.

TAUBES G. Biologists and engineers create a new generation of robots that imitate life. *Science*, v. 288, p. 80-83, 2000.

TOMILIN A. G. Mammals of the U.R.S.S and adjacent countries, v. IX: Cetacea, 1957.

TORENBEEK, E. *Synthesis of subsonic airplane design*. Delft University Press Klumer Academic Publishers, 1982.

TORRES, G. E; MUELLER, T.J. Aerodynamic characteristics of low aspect ratio wings at low Reynolds numbers. Fixed and Flapping Wing Aerodynamics for Micro Air Vehicle Applications. *Progress in Astronautics and Aeronautics AIAA*, v. 194, p. 115-141, 2001.

TORRES, G. E; MUELLER, T.J. Low-aspect-ratio wing aerodynamic at low Reynolds numbers. *AIAA Journal*, v. 42, n. 5, p. 865-873, 2004.

TRIANTAFYLLOU G. S; TRIANTAFYLLOU M. S. An efficient swimming machine. *Scientific American*, v. 272, p. 64-70, 1995.

TRUE, F. W. *The whalebone whales of the western North Atlantic*, Washington, DC: Smithsonian Institute Press, 1983.

VOGEL, S. *Life in moving fluids.* Boston: Willard Grant Press, 1981.

VON DOENHOFF, A.E.; TETERVIN, N. Investigation of the variation of lift coefficient with Reynolds number at moderate angle of attack on a low-drag airfoil. NACA Wartime Rep. L-661, 1942.

VON MISES, R. *Theory of flight*. New York: Dover Publ, 1945.

WATTS, P.; FISH, F. E. The influence of passive, leading edge tubercles on wing performance, *Proceedings of the Twelfth International Symposium on Unmanned Untethered Submersible Technology*, Durham New, Hampshire, 2001.

WEBB, P. W. Hydrodynamics and energetics of fish propulsion. Bull. Fish. Res. Bd. Can. 199:1-159, 1975

WEBER, P.W.; HOWLE, L.E; MURRAY, M.M; MIKLOSOVIC, D. S. Computational evaluation of the performance of lifting surfaces with leading-edge protuberances. *AIAA Journal of aircraft*, v. 48, n. 2, p. 591-600, 2011.

Whitford, Ray. *Design for air combat*, first edition, London: Jane´s Publishing Company Limited, 1987.

Williams, T.M. The evolution of cost efficient swimming in marine mammals: limits to energetic optimization. *Philos Trans R Soc Lond B Biol Sci*, v. 353, p. 193-201, 1999.

WINN, H. E; REICHLEY, N. E. Humpback whale megaptera novaeangliae. *Handbook of Marine Mammal*, v. 3, p. 241-273, 1985.

WU, J. Z; VAKILI, A. D.; WU, J. M. Reviw of the physics of enhancing vortex excitation. *Prog. Aerospace Sci*, 28:73-131, 1991.

ZVERKOV, I.; ZANIN, B.; KOZLOV, V. Disturbances growth in boundary layers on classical and surface wings. *AIAA Journal*, v.46, n.12, p. 3149-3158, 2008.